REPORT DOCUMENTATION PAGE

1. Recipient's Reference	2. Originator's Reference	3. Further Reference	4. Security Classification of Document
	AGARD-LS-131	ISBN 92-835-1461-0	UNCLASSIFIED

5. Originator	Advisory Group for Aerospace Research and Development North Atlantic Treaty Organization 7 rue Ancelle, 92200 Neuilly sur Seine, France

6. Title	THE PERFORMANCE OF ANTENNAS IN THEIR OPERATIONAL ENVIRONMENT .

7. Presented at	Ankara, Turkey on 19–20 October 1983; Athens, Greece on 24–25 October 1983; and Brussels, Belgium on 27–28 October 1983.

8. Author(s)/Editor(s)	9. Date
Various	September 1983

10. Author's/Editor's Address	11. Pages
Various	250

12. Distribution Statement	This document is distributed in accordance with AGARD policies and regulations, which are outlined on the Outside Back Covers of all AGARD publications.

13. Keywords/Descriptors	
Antennas	Performance

14. Abstract

Lecture Series No.131, concerned with the performance of antennas in their operational environment, is sponsored by the Electromagnetic Wave Propagation Panel of AGARD and implemented by the Consultant and Exchange Programme.

Antennas can provide gain in any direction, and the effect of the operating environment on this parameter is fundamentally important for the performance of radio systems. Yet the effect of the environment on antennas is often overlooked. The performance of the antennas is more usually specified in terms of its operation over a perfectly conducting flat ground plane.

This Lecture Series covers: techniques for measurement/prediction (numerical and experimental modelling); performance of fixed and transportable antennas (terrain effects, masts and buildings effects, re-radiation by supporting towers); performance of mobile antennas (effects of supporting platforms such as aircraft, ships and automobiles); performance of antennas in plasmas.

AGARD-LS-131

AGARD-LS-131

AGARD

ADVISORY GROUP FOR AEROSPACE RESEARCH & DEVELOPMENT, Paris

7 RUE ANCELLE 92200 NEUILLY SUR SEINE FRANCE

AGARD LECTURE SERIES No.131

The Performance of Antennas in their Operational Environment

NORTH ATLANTIC TREATY ORGANIZATION

DISTRIBUTION AND AVAILABILITY
ON BACK COVER

NORTH ATLANTIC TREATY ORGANIZATION

ADVISORY GROUP FOR AEROSPACE RESEARCH AND DEVELOPMENT

(ORGANISATION DU TRAITE DE L'ATLANTIQUE NORD)

AGARD Lecture Series No.131

THE PERFORMANCE OF ANTENNAS

IN THEIR OPERATIONAL ENVIRONMENT

THE MISSION OF AGARD

The mission of AGARD is to bring together the leading personalities of the NATO nations in the fields of science and technology relating to aerospace for the following purposes:

— Exchanging of scientific and technical information;

— Continuously stimulating advances in the aerospace sciences relevant to strengthening the common defence posture;

— Improving the co-operation among member nations in aerospace research and development;

— Providing scientific and technical advice and assistance to the North Atlantic Military Committee in the field of aerospace research and development;

— Rendering scientific and technical assistance, as requested, to other NATO bodies and to member nations in connection with research and development problems in the aerospace field;

— Providing assistance to member nations for the purpose of increasing their scientific and technical potential;

— Recommending effective ways for the member nations to use their research and development capabilities for the common benefit of the NATO community.

The highest authority within AGARD is the National Delegates Board consisting of officially appointed senior representatives from each member nation. The mission of AGARD is carried out through the Panels which are composed of experts appointed by the National Delegates, the Consultant and Exchange Programme and the Aerospace Applications Studies Programme. The results of AGARD work are reported to the member nations and the NATO Authorities through the AGARD series of publications of which this is one.

Participation in AGARD activities is by invitation only and is normally limited to citizens of the NATO nations.

PREFACE

Lecture Series 131 on the performance of antennas in their operational environment is sponsored by the Electromagnetic Wave Propagation Panel of AGARD and implemented by the Consultant and Exchange Programme.

Antennas can provide gain in any direction, and the effect of the operational environment on this parameter is fundamentally important for the performance of radio systems. Yet the effect of the environment on antennas is often overlooked. The design of the antenna is often specified in terms of its operation over a perfectly conducting flat ground plane, which if the antenna is to be used on three-dimensional bodies or in a complex environment, has little to recommend it except cost.

The Lecture Series will cover: techniques for measurement/prediction of antenna performance (experimental modelling and in situ measurements); performance of fixed and transportable antennas (terrain effects, masts, building effects, re-radiation by supporting towers); performance of mobile antennas (effects of supporting platforms such as automobiles, ships, aircraft); non-linear scatterers; and performance of antennas in plasmas. The LS is concluded by a round table discussion at the end of the presentation on each day.

Appreciation is expressed to all who assisted in the organization of this Lecture Series as well as the compilation of this volume, to lecturers, AGARD staff and other collaborators and to those who attended the LS, since lectures must be given to an audience and it is the interested response of the audience that makes the LS successful.

JOHN S.BELROSE
Lecture Series Director
August 1983

LIST OF SPEAKERS

Lecture Series Director: Dr John S.Belrose
Communications Research Centre
P.O. Box 11490, Station "H"
Ottawa, Ontario, Canada K2H 8S2

SPEAKERS

Prof. Keith G.Balmain
Dept. of Electrical Engineering
University of Toronto
Toronto, Ontario, Canada M5S 1A4

Dr Ray J.King
Lawrence Livermore National Laboratory
P.O. Box 808
Livermore, California 94550, USA

Prof. S.J.Kubina
Concordia University
EMC Laboratory
Loyola Campus
7141 Sherbrooke St. W.
Montreal, Quebec H4B 1R6

Dr Jeremy A.Landt
Weapons Advanced Concepts
Los Alamos National Laboratory
Los Alamos, NM 87545, USA

Prof. Dr -Ing. Heinz Lindenmeier
Hochschule der Bundeswehr München
Fachereich Electrotechnik
Hochfrequenztechnische systems
Werner-Heisenberg-Weg 39
8014 Neubiberg, FRG

Dr E.K.Miller
Electronics Engineering Department
Lawrence Livermore National Laboratory
P.O. Box 808
Livermore, California 94550, USA

Dr R.H.Ott
Propagation Studies Department
COMSAT Laboratories
Clarksburg, M.D. 20871, USA

Mr M.J.Sidford
Royal Aircraft Establishment
Radio & Navigation Dept., P160 Bldg.
Farnborough, Hants, GU14 6TD, UK

CONTENTS

OVERVIEW

by

Dr. John S. Belrose
Communications Research Centre
P.O. Box 11490, Station "H"
Ottawa, Ontario, CANADA K2H 8S2

The working environment in which an antenna is installed may substantially modify such antenna parameters as radiation efficiency, impedance, pattern, etc., and while re-radiation from structures in the nearby environment can be in the near field, it is usually the performance of the antenna in the far field that is desired. An important class of antennas, e.g. the Beverage or wave antenna, however relies on the ground to enhanse the received signal. In this case the ground must be considered a significant part of the antenna system, and cannot be in the field region. While much work has neglected or ignored environmental effects this is not always the case, and for some requirements the effects of the environment are considerable and most important. The need for more accurate antenna design, taking into account such second order effects, and the availability of modern numerical modelling techniques have combined to lead antenna design from an empirical art to a mathematical science. Numerical modelling is particularly important for parametric studies, for antenna system responses to a complex electromagnetic threat environment (of particular importance for the Military), by application of computer generated waveforms, and for accounting for linear and non-linear scatterers in the nearby field of the antenna. Advances in antenna performance must be matched by improved electrical measurements, and there has been infact significant recent developments in antenna metrology. There is a continuing need for antenna modelling measurements, for measurements in situ, and for dynamic antenna measurements where the performance of antennas on a moving vehicle is desired. Antennas on large man-made satellites immersed in the earth's ionospheric and magnetospheric plasma environment lead to many unexpected and non-linear antenna environmental effects.

This Lecture Series will address this subject, provide an overview of current knowledge, and as well, each lecture will contain a reference list to key published works, so that the student engineer, designer, researcher, may delve more fully into the subject than is possible to cover in this brief Lecture Series.

SCALE MODELLING AND FULL SCALE MEASUREMENT TECHNIQUES WITH
PARTICULAR REFERENCEE TO ANTENNAS IN THEIR OPERATIONAL ENVIRONMENTS
by
John S. Belrose
Communications Research Centre
P.O. Box 11490, Station "H"
Ottawa, Ontario, K2H 8S2
Canada

ABSTRACT

Recent advances in antenna design and the need for more accurate prediction of performance of antennas in their operational environment has increased the need for improved electrical measurements, and there has been a significant accompanying development in antenna metrology. Some of these developments, those relevant to the theme of these lectures, will be reviewed here.

1. INTRODUCTION

Recent advances in numerical modelling techniques have reduced but not eliminated the need for scale modelling of antennas. Scale modelling enables second-order practical effects to be taken into account, and is particularly useful when the prediction of an antenna in its operational environment is difficult or impractical. This situation frequently exists: (1) for antennas located on large supporting structures, such as ships, land vehicles, aircraft, and large man-made satellites; and (2) antennas situated near large conducting structures such as highrise buildings, power transmission lines, other towers and antenna systems, which influence their properties. Another problem in which modelling can be employed, at least as a first step in a study, relates to moving systems, or changing environments, instability of the supporting vehicle or surrounding medium. Such studies may compel an unreasonable amount of in-situ experimental data, which require statistical treatment, and while in the end such studies may have to be carried out, model measurements provide a necessary basic understanding of the effects of the environment.

Most parameters can be modelled, without undue difficulty, excepting poor conductors like real earth, which is less easily scaled as it is necessary to increase the conductivity in proportion to the decrease in wave length and linear dimensions, while maintaining the dielectric constant unchanged. An important class of antennas, such as ground-based vertical monopoles and travelling wave "Beverage" antennas are strongly influenced by the ground, which determines their radiating properties and influences wave propagation and coupling between antennas situated on the ground. The ground itself, therefore, must be considered as a significant part of the antenna system. In these cases, measurements need to be made in full scale, in-situ.

The lecture will review modelling techniques, and methods to measure antenna patterns, impedance, currents on antennas and re-radiating structures, and antenna-to-antenna isolation. We will also review the techniques that have been developed to facilitate measurements in full scale, and techniques to recognize and allow for multipath and re-radiation problems from other structures in the antennas environment.

2. MODELLING TECHNIQUES

The theory of scale modelling has been established by Sinclair[1]. Generally the model is reduced in size from the full-scale antenna, but whether reduced or increased, the requirements are the same. Sinclair showed that, in scale modelling, wavelength, capacitances and inductances are reduced in proportion to the linear dimensions, while conductivities are increased in the same ratio. Other parameters such as gains, impedances, beam widths, sidelobe levels, current distribution on the antenna, dielectric constants, and permeabilities remain unchanged in a perfect model. If the conductivity of the full-sized antenna is good, the scaled model must have very good conductivity. While silver-plated conductors are sometimes used, since this effect often makes little practical difference, copper conductors are usually employed. Poor conductors like real earth are less easily scaled as it is necessary to increase the conductivity while maintaining the dielectric constant, and the modelled "earth" beneath the antenna must extend over a distance and to a depth that is sufficient, to distance beyond those that influence the far-field pattern of the antenna. For transmission at low elevation angles above the horizon, this distance is many wavelengths which could include the whole of the antenna pattern range.

In studies of the performance of antennas in their operational environments measurements are made in the near field of the antenna, although usually it is the effect of the local environment on the far-field pattern that is desired. Antenna measurements, including modelling techniques are well described in the literature. A most extensive and exhaustive treatment of these and other topics can be found in the IEEE Standard Test Procedures for Antennas[2], in a summarized journal paper[3], in the IEE Handbook of Antenna Design[4], and in a book on microwave antenna measurements[5].

Most of the studies have been concerned with modelling the antenna and its supporting structure (such as ships, aircraft[6], automobiles[7], and large man-made satellites), which influence the properties of antennas. However, recently modelling studies have been made on the effects of re-radiation on the performance of MF broadcast antennas[8], in which it has been necessary to model extended structures such as power transmission lines . In such circumstances it is necessary to estimate from the results of a practical model for a power line of limited length the effects of a very long line; and as well decisions have to be made on how realistic the model should be. This latter remark applies also to vehicular antennas, since construction of realistic models takes time and costs money. In many cases it is difficult to construct a simulated environment due to its complexity, and usually good judgement is required in determining how well simplified models simulate the antenna's surroundings.

It is usual to measure the performance of the antenna independent of its environment to determine if it has the same characteristics as expected for a full-sized antenna e.g., as predicted, from theoretical modelling. Often a flat ground plane is used, which is useful for monopole or ground plane antennas; however the free-space performance of antennas can also be inferrred, if the model can be cut in half along a plane of symmetry, by the method of images.

Alternatively the free-space performance of the antenna can be measured in an anechoic chamber, which is particularly useful at the higher frequencies (>500 MHz), or on outdoor elevated test ranges. In the measurement of radiation patterns the feed cable may perturb the measured quantities appreciably. In some cases the scale model can be arranged to transmit from a battery operated transmitter. However if swept frequency measurements are required to examine resonances in the supporting structures or antenna bandwidth, the scaled model may contain a receiver from which a modulated or demodulated signal must be measured. A modern approach is to use a semiconductor laser, and transmit the signal by direct modulation via an optical fibre[9]. Sometimes it is necessary to measure phase as well as amplitude. Since laser devices are available having bandwidth up to 1.25 GHz, it is technically possible nowadays to transmit the RF signal directly, without detection (Hill, private communications).

The support for the model should receive particular attention if the pattern nulls are to be accurately determined. Another complicating factor arises from the fact that most measurement instrumentation employ a coaxial input (unbalanced) whereas antennas frequently modelled have to be fed in a balanced manner. While baluns are used for such circumstances, they must be carefully constructed to achieve the required unbalanced-to-balanced transformation[10]. Coaxial baluns used at VHF and UHF are not very useful for wideband measurement, since they are narrowband devices. The primary function of a balun is to block the current path between the inside and outside surfaces of the coaxial shealth. Although many baluns employ some form of coupling transformer, an alternative is to insert an RF choke in the outer conductor of the feed line. The simplest choke is formed by coiling up a few turns of the feedline, starting where it connects to the antenna terminals. An improvement over the choke-balun is obtained by placing several ferrite beads or sleeves around the coaxial feedline. The beads introduce a high impedance in series with the braid outer surface. This configuration, which is useful at VHF, effectively isolates the external output terminal of the feedline from the input end. (See Ref. 11).

Some of the special problems mentioned above, and other details on modelling techniques are further discussed below.

3.   OUTDOOR TEST RANGES

In the literature a variety of outdoor test ranges have been described, devised for various applications. Here we consider three types: a ground level antenna pattern range, an elevated ground plane and "free space" elevated ranges.

3.1   Ground Level Ranges

The National Research Council's ground level antenna pattern range at Ottawa, sometimes called the "ship range" since it was constructed to measure the pattern of HF antennas on ships, is a good example of a ground level antenna pattern range. In this application it is a good modelling range, since an accurate ship's model can be constructed (Fig. 1), and the wire grid ground screen well simulates the excellent conductivity of the ocean. The range is on the surface of the ground. It is about 21 x 60m, with a 6m turn table, flush with the surface of the wire grid ground screen located 17m (to its centre) from one end of the range. The source antenna for measuring the azimuthal pattern on the ground plane is a corner reflector, designed to illuminate the turn table, located at the centre of the far edge of the range. A rotatable boom for elevation pattern measurement is arranged so that it can be swung in a hemispherical rotation over the turn table. To measure azimuthal pattern at fixed elevation angles the boom is fixed, and the turn table rotated. The dipole antenna mounted on the rotatable boom (Fig. 2) can be turned to measure the vertically polarized ($E\theta$) field, or the horizontally polarized ($E\phi$) field. Clearly an antenna pattern can only be measured in only one plane at a time. For ships, the vertical pattern is measured from port-to-starboard or forward to aft. For aircraft, the coordinate system adopted are the directions of the roll, pitch and yaw axis (Fig. 3), and these planes are sometimes referenced when measurements are made for other vehicles, e.g. automobiles! If the range employs digital recording techniques, computer graphic methods can be utilized to generate three dimensional pattern displays which are useful for some purposes.

The edges of the rectangular shaped ground screen are terminated in the surrounding earth, to minimize reflection.

The measurements of the vertical pattern is more subject to error than the ground level azimuthal pattern, and this difficulty is accentuated in the measurement of the pattern null. Reflections from the edges of the ground screen, from surrounding objects (fences, buildings) and from the coaxial cable running up the inside of the boom are possible sources of error. This subject is further addressed below (Section 5).

3.2   Elevated Ground Plane

While in principle it is possible to design a ground level range in such a way that measurement instrumentation (and personnnel using the range) could be beneath the ground screen, to facilitate the measurement of impedance, or to probe the currents on radiating and re-radiating structures, in practice an elevated ground screen is more practical from a mechanical design point (pumps would be required to keep water from underground structures and dug-outs, and such a range would not be useful in winter).

In Fig. 4, we show a view from the centre of a large elevated ground plane, to show the open construction so that currents on modelled structures can be probed from beneath. This facility, which is still under development at the Communications Research Centre, Ottawa, is about 30m in diameter. The ground screen is polygonal in shape (sixteen sides), and it is elevated about 2m with a measurement hut located in the centre (beneath ground screen).

The measurement of the elevation pattern (θ plane) is not so far possible on this antenna range, but is intended to construct an A-frame or gantry positioner so that this measurement can be made. A choke is usually required along the edge of the ground screen to prevent reflections from its edges, and to prevent currents from being excited on the rear side of the ground plane. A ragged edge or triangular tooth construction, should be used. Surface current absorbers can be employed for such application[12], at least for small ground planes. The absorbers operate by reducing the amplitude of the currents flowing along the ground screen before they encounter the edge discontinuity. Surface current absorbers are characterized by being in the form of a thin sheet having high magnetic permeability.

3.3. "Free Space" Elevated Ranges

Elevated ranges are used to simulate free-space, and are designed to suppress contributions from the surrounding environment (from the support towers, ground reflected signals, etc.). Such ranges over smooth terrain are not very practical except for measuring rather directive antenna systems, since rather high support structures must be employed. The design goal is that the range in front of the test antenna should not intercept any energy contained in the main lobe of the source antenna. In fact the first null in the radiation pattern of the source antenna should be directed toward the base of the test antenna tower. Otherwise, it is necessary to employ diffraction or redirection fences (Fig. 5) or by covering the Fresnel zones around the bounce point by absorber material, which is effective but an expensive method of reducing ground reflections.

In some applications, such as between adjacent mountains or hill tops the ground terrain may be irregular. For these cases, it is more difficult to locate the specular reflection points (points that reflect energy toward the test antenna). A brief account of the USAF RADC Newport Test Facility[13], 42 km east of Griffiss AFB, NY will provide some insight into the application and use of such a range. The overall test facility (shown in Fig. 6) is located on two hill tops, about 2150m apart, with a 122m deep valley in between. The steep slope of the terrain (Fig. 7) immediately in front of the test sites permits the test environment to simulate free space, which for aircraft simulates actual flight conditions. The overall facility comprise two ranges, a "pattern range" and a "section range". Each makes use of Building 1600 on Tanner Hill. Various air frames can be mounted on the heavy-duty three axis positioner on top of a 6m tower on Irish Hill; an isolation tower at another site on this hill provides a capability of supporting large antennas for ground-mounted use, or light test beds, consisting of air frame mockups or small air frames. Various air frame stores (inert weapons, wing tanks, etc.) can be mounted on the air frames in various configurations. While the terrain is favorable, for some measurements it is necessary to employ anti-reflection or RF screening fences. The requirement for fencing is dependent on frequency, depression angles in elevation of aircraft on the pedestal respective to the transmit/receive antenna, etc. Prior to the measurement, it is necessary to predict reflection points on the range considering all the above factors. A series of RF fencing is then placed on the range (Fig. 8) in these approximate locations with fine exact placements through actual field probing and measurements.

While a great deal of time, effort and money is required to construct and prove in such a free-space range, once the facility is available measurements can be taken under a very controlled measurement environment, since the dynamics of actual flying are not factors. The ranges are well defined with ambiguities such as multipath, etc. being zero or small in the final data. A complete antenna pattern, 360° in azimuth at one elevation angle can be measured in 12 minutes. This would equate to 12 hours of actual flight time to accumulate sufficient data for one antenna pattern. In the case of fighter class aircraft two flights would be necessary to obtain 12 hours of data. This causes other factors of considerable importance to be factored in, such as weather temperature inversions, equipment performance, etc. which would effect the quality of the data. There is thus a tremendous cost-saving through the use of these ranges, regarding the non-use of expensive flight time involving air crew and fuel. In addition and perhaps the most important the data are very accurate (McGregor, private communications).

3.4 Dynamic and On-Site Measurement of Antenna Patterns

The measurement of the complete three-dimensional radiation pattern of a full scale antenna on its operational site is a laborious and expensive task. It is necessary to make such measurements when the antenna radiation pattern is significantly affected by the site on which it is located, in studies of antennas which are strongly influenced by the finite conductivity of real earth[14], or as for the MF broadcast band, the measurement of proof of performance patterns as required by international treaty requirements.

Broadcast consultants have traditionally measured the azimuthal pattern of MF broadcast stations by the method of transporting field intensity measurement equipment (Fig. 9) to many locations in a 360° azimuth about the antenna, and by measuring along a number of radial paths in a few directions. This latter measurement is required to eliminate site errors on individual measurements, and to account for the influence of the conductivity of the ground on field strength measurement remote from the antenna. The measurement of the pattern of a complicated array is obtained in greater detail than can be obtained from such radial measurements from the fixed site measurements, by transmitting alternatively on a single tower (omni-directional pattern) and on the multi-tower array (directional pattern). Since the single tower is usually one of the towers in the multi-tower directional array, care must be taken that re-radiation from the unused towers does not disturb its omni-directional pattern[15].

Measurement of the azimuth and elevation pattern of HF and VHF antennas can be measured by employing equipment towed by an aircraft. The received signal strengths employing the antenna under test (AUT) are measured employing an airborne transmitter. An aircraft tows a vertically or horizontally polarized transmitting dipole (see Fig. 10) called a XELEDOP (transmitting elementary dipole of arbitrary polarization[14],[16],[17].

To develop azimuthal patterns with XELEDOP, the antenna must be towed concentrically around the AUT at various heights and distances. A cut of the vertical pattern can be obtained by flying across the AUT at a given height (typically 3 km for HF measurements) along a bore site, correcting results for spatial attenuation, and for the changing angle between the XELEDOP dipole and the AUT ray direction, which is required for vertical polarization. A detailed antenna vertical plane pattern in the main beam of the antenna can also be measured using a dipole suspended from a balloon.

It is also possible to measure the inflight pattern of antennas on aircraft, but here the flight dynamics complicate the measurement. For accurate measurement the aircraft must carry a pod mounted on it which records the roll, pitch and yaw of the aircraft as it flies. This data is merged with the ground data to permit the pattern to be related exactly to the position of the airborne platform (the aircraft).

The USAF RADC operate such a system, which they call Precision Antenna Measuring System (PAMS) which is located at Verone, N.Y.. It is a dynamic antenna measurement system, since operational aircraft have to fly against it to obtain data. A system of this type is necessary in addition to the static facilities described above for two reasons. First, not all air frames are available for mounting, and second, the time element necessary to obtain an air frame and mount it in order to meet testing time schedules. PAMs has the total capability to evaluate complete airborne systems, performing in an operational mode. It has also a limited capability to measure radar cross-sections (RCS). If interest is only the airborne antennas, other PAMs associated subsystems called the Airborne Signal Sources, which are stable CW sources can be attached to the airborne antennas in lieu of the operational system. This eliminates the inaccuracies which may occur due to fluctuations in the weapon system performances. Since at some frequencies coupled with factors not associated with static facilities such as aircraft altitude, distance from the measurement facility, etc., multipath does have to be addressed. Before using the facility a study has to be made, and a program developed which predicts the multipath expected. Once proven-in, the program can be used to factor out multipath contributions and present the true signal in the data (McGregor, private communications).

4. INDOOR TEST RANGES

4.1 Anechoic Chambers

The purpose of a radio anechoic chamber is to simulate a reflectionless indoor free-space environment in which the interaction between electromagnetic waves and many different devices, antennas, vehicles supporting antennas, radar-cross section measurements, as well as electromagnetic compatibility (EMC) studies can be carried out under controlled conditions. An early summary of the development of absorbing materials and anechoic chambers is given by Emerson[18]. A recent review of anechoic chambers, and as well of a variety of antenna measurement techniques is given in the previously referenced chapter by Appel-Hansen et al.[4]

Using todays state-of-the-art absorbers chamber designs can simulate "free-space" with regard to amplitude and phase uniformity to a very high degree. Chambers are used at frequencies as low as 30 MHz and as high as 100 GHz. The lower frequency limit requires pyramidal absorbers having thicknesses as great as 6m. Chambers range in size up to 6m x 6m in cross-section and to more than 50m in length.

The most advanced chambers utilize computers to generate and move a variety of signals and targets so as to simulate system operation in close-to-actual real world environments. In the area of interest in this lecture, measurements can be made of the radiation patterns for modelled aircraft antennas, for example in Fig. 11 we show a photograph of a 1/12 scale model of CF104 fighter aircraft, on which a crossed slot antenna is modelled. The measurement technique is to first measure the pattern of the antenna on a flat plate surface (Fig. 12), and then employing a battery operated transmitter mounted inside the model (Fig. 13), to measure the pattern for the aircraft-borne antenna (Fig. 14). The measurements are facilitated by use of a three-axis insulated support tower or positioner. In Fig. 15 we show a complete satellite-borne antenna system inside an anechoic chamber.

This particular chamber is a part of the CRC David Florida Laboratory Spacecraft Test Facilities. One wall of the test chamber is demountable behind which is an electrically-transparent window. A 40m high steel tower is located 152m from the test chamber, along a line normal to the RF window. An air conditioned hut is located at the 27m level, which contains various microwave power sources. High gain antennas at this level point to the centre of the chamber. The facility design, operated as an antenna test range, is such that antenna patterns can be measured down to 1.5° beamwidth at 14 GHz, as can be seen by application of the commonly related formula

$$R = 2 D^2/\lambda$$

where D is the aperture of the antenna required to obtain the beamwidth specified at the operating wavelength λ. R is the length of the range required to test the antenna.

4.2 Other Enclosed Field Devices

Enclosed field devices and probes for the generation and measurement of fields for radiated susceptibility testing have been recently reviewed by Alden[19]. While metallic enclosures are not useful for antenna measurements, we include reference to this class of indoor test facility since they are useful to calibrate the performance of electric and magnetic field probes. Also some of the problems

associated with measuring the signal picked up by such probes, such as ensuring that transmission line to the probe does not upset the field measurement, is common to both radiated susceptibility and antenna measurement methodology.

5. EVALUATION OF ANTENNA TEST RANGES

The most common method of evaluating an antenna test range is to measure the pattern for known antennas. For ground plane ranges convenient reference antennas are a $\lambda/4$ vertical monopole and a $\lambda/2$ horizontal dipole. Measurements should be carried out at a number of frequencies over which the range is to be used.

As mentioned earlier limitations of the antenna pattern range show up most clearly on elevation patterns. As an example we show in Fig. 16 the pattern for a quarter wave monopole at 835 and 861 MHz, measured on the NRC ground level antenna pattern range previously described. Notice that the ripple or notching on the trace for the pattern maximum (graph in relative signal strength in dB) is about $\pm 1/2$ dB, and this is typical for other ranges. The scatter signal into the null is also evident, and it is clear that this null-filling is frequency dependent.

The filling-in of a null gives a signal level equal to the strength of the scattered signal alone, while the notching arises from the interference between the scattered and the direct signal. Suppose that E_1 is the strength of the out-of-phase scattered signal. In terms of dB relative to the main lobe, the scattered signal is given by[20]

$$S = 20 \log_{10} \frac{E_1}{E_0}$$

and the notch depth is given by

$$N = 20 \log_{10} \frac{E_0 - E_1}{E_0}$$

Eliminating E_1/E_0 from the above expressions gives the following

$$10^{N/20} + 10^{S/20} = 1$$

or, in the form most frequently used

$$S = 20 \log_{10} \left(1 - 10^{N/20} \right)$$

Because of the symmetry the same formula can be used to calculate N as well as S.

For a notch depth of -0.5 dB the scattered signal S = -25 dB. It can be seen that the signal in the null is about this magnitude.

If this scattered signal adds to the main lobe, the resulting increase in total signal level (in dB normalized as before) is

$$I = 20 \log_{10} \frac{E_0 + E_1}{E_0}$$

And eliminating E_1/E_0 gives

$$10^{I/20} = 1 + 10^{S/20}$$

The above formula is not symmetric.

The usual method of calibrating an anechoic chamber antenna range is to measure the pattern of an antenna of known directivity at various points in the chamber. By displacing the antenna so as to create a difference in phase between the direct and reflected signals, the magnitude of the reflected signal may be determined from the patterns. A "quiet zone" can then be specified within the chamber where the reflected signal is X dB below the direct signal. The disavantage of this method is that the reflected signal magnitude depends on the directivity of the calibrating antenna. The user must be careful in relating the calibration data to the antenna he wishes to test, unless both have the same directivity. It is useful therefore to calibate the chamber for antennas of various directivity, low, medium and high gain antennas. An alternative method, but not so readily accomplished with simple pattern measurement equipment, is to probe the field inside the chamber for uniformity of amplitude and phase, employing a broad beamwidth antenna. The reflectivity of the walls can also be measured.

For elevated outdoor antenna ranges the magnitude of the reflected wave, relative to the direct wave can be obtained in a number of ways. If the support tower has a vertical track along which the probe antenna can be moved, the signal strength is measured at a fixed frequency as the probe antenna is moved. Again this postion change will result in a phase difference between the direct and the scattered wave. The spatial period of the signal received as the antenna is moved vertically (or horizontally) in the intended test aperature provides a measure of the reflection angle. (See Fig. 17). The magnitude of the interference pattern, as discussed above provides a measure of the scatter signal relative to the direct signal. Alternatively, employing broad-band antennas a frequency sweep will provide phase differences between direct and indirect waves. Again the calibration of this range is dependent on the directivity of the reference antenna, and so a detailed calibration procedure is required, particularly if the optimum locations of diffraction fences are to be located.

6. INSTRUMENTATION AND MEASUREMENT TECHNIQUES

A wide range of instrumentation is used for antenna measurements, extending from simple largely home constructed equipments used by radio amateur experimenters[21] to sophisticated precision instrumentation, designed specifically for antenna and antenna test range applications, that nowadays are frequently under microprocessor or computer control. The instrumentation and techniques that are refered to here are those which the author and his colleagues have used, and in particular are a part of the antenna test ranges specifically mentioned above.

6.1 Measurement of Antenna Impedance

RF impedance measurements at HF, and below have traditionally been made employing an RF bridge, but such an instrument is inconvenient for automatic measurement and for frequency sweep applications since it must be "balanced" (initial as well as final balance) each time the frequency is changed. Techniques employed at HF and above that overcome this problem are based on measurement of voltage and currents using transmission line theory in terms of forward and reflected waves. To measure impedance it is necessary to measure the phase and amplitude of these two travelling waves, and impedance is conventionally read by means of a Smith chart overlay on a polar display. The instruments for making such impedance measurements are called network or vector analyzers, and sophisticated equipments under computer or microprocessor control are available; e.g. Hewlett-Packard Model 8505A or the Rhode & Schwarz Model ZPV analysers can be used, which operate over a frequency range of about 0.5 to over 1000 MHz.

The Hewlett Packard RF impedance analyser Model 4191A is a particularly versatile instrument for impedance measurement in this frequency range, since it is a dedicated instrument designed specifically for this application. It can be used as a stand alone instrument controlled by its own microprocessor, or as a systems instrument by means of an IEEE interface, under the control of a computer, e.g. the HP Model 85 desk top computer. Two features of this instrument that are particularly useful are automatic error compensation and electrical length compensation. With the latter, it is possible, using short leads with equipment located beneath the ground plane, to effectively move the measurement port to the input terminals of the antenna. This is important for antenna modelling at VHF and UHF, since even a feed through coaxial connector becomes a measureable part of the circuit, and effects the indicated impedance. Internal software provides for optional data display of impedance: for example $|Z|-\theta$ or $R \pm jX$ ohms; or a conventional Smith Chart display for the engineer that prefers this representation.

A word of caution. This instrument employs APC-7 coaxial connectors which are high quality connectors, but they must be kept very clean, or else false measurements can be made (even the initial calibration can be in error). The curves in Fig. 18 show the impedance of a 4 dB gain collinear monopole, and the impedance seen through 4.1m of feeder coaxial cable.

6.2 Measurements of Current Distribution

The current distribution on antennas and on parasitically excited re-radiating structures can be measured by employing dimensionally small magnetic loops, of diameter $d < \lambda/50$, as current probes, connected to a phase and amplitude measurement receiver system. The Hewlett-Packard Model 8505A network analyser, mentioned above can also be employed for such measurements, since basically it is a 3-channel receiver for measuring phase and amplitude with a 100 dB dynamic range.

To make current distribution measurements on modelled antennas, one must employ an elevated ground screen, so that the instrumentation can be located beneath radiating or re-radiating structures. Even so great care must be taken to make reliable measurements. The following discussion uses an example of current measurements made on a modelled power transmission line, excited by a nearby monopole, Fig. 19,since some of the difficulties in making such measurements are revealed (Tilston [22]).

A power transmission line (see Fig. 20) behaves like a resonant structure, since a tower, the connecting skywire(s), the adjacent tower, and the image of this half-loop in the ground can be one wavelength, or multiples of one wave length long. A modelled power line (scale factor 200) was built and measurements were made of the current distribution induced on it by the monopole antenna. Initial current measurements encountered objectional power pick up on the probe shield, that was located on top of the ground screeen. A fix to the problem was obtained by minimizing the amount of cable on the ground screen, and by making secure grounds to the probe shield with the ground screen.

Several current probes were assessed (see Fig. 21). Each was dimensionally small in terms of wavelengths, being $\lambda/50$ at the second resonance of the structure (168.3 MHz). The subminax cable on the fibreglass rod did not have sufficient capture strength although its cross-polarization was 20dB. The balun type, although the signal strength was stronger than with the subminax, resulted in no stronger signal than the probe constructed of semi-rigid cable. The semi-rigid cable type was the best of the probes constructed in terms of signal strength and ease of useage. It also had the best cross-polarization ratio being of the order of 30dB.

Tests were conducted by measuring the swept frequency response employing one probe, and then placing a second probe against the measured structure and noting the difference to the first response. The semi-rigid probe had little effect, whereas the Tektronix P6022 current probe had a dramatic effect on the structure, causing magnitude changes of up to 10dB and frequency shifts in peak signal level.

The measured current distribution on the skywires for a 2-and a 3-tower power line at first resonance (87 MHz) and second resonance (168.3MHz) are shown in Figs. 22 and 23. Notice that the current at the λ resonance is a minimum at the centre of the span, whereas at the 2λ resonance the current at the centre of the span is a maximum. Notice that difficulties in measuring the currents are found at the position on the skywire near to where it joins to the cross arm at the top of the tower. Consider for example measurements for the λ resonance at the tower skywire junction as depicted in Fig. 24(a). Truly the current probe only captures 1/2 the current on the skywire, since only 1/2 of the probe is

illuminated. Thus the current magnitude measured is 6 dB less than the true value. At locations too close to tower-skywire junction (see Fig. 24(b)), the signal magnitude is not what it should be. In particular at the 10 cm location the H field from the tower interferes with the H field from the skywire. At the current probe the interference is destructive with the amount of error increasing as the tower is approached.

This difficulty is particularly marked for measurements at the 2λ resonance, since the current on the skywire at the 10 cm distance is a minimum. Since the probe gives inaccurate readings at the junction of the skywires and the tower, separate readings were taken of the base current and the current on the centre tower at the top. When these current readings at the top were corrected for the diameter, a corrected curve to the measured is obtained which is close to the cosine curve plotted on the graph (Fig. 23).

6.3 Measurement of Pattern and Antenna Gain

To measure the radiation pattern, the antenna under test (AUT) must be used as a receiving (or transmitting) antenna, and the source (or field probe) antenna, located at a distance (>2 D^2/λ) must be rotated about the AUT by an antenna positioner. A spherical coordinate system is usually used. The NRC antenna pattern range, the RADC test range and the CRC anechoic chamber (David Florida Laboratory) employ equipments manufactured by Scientific Atlanta, a company that specialized in manufacture of a variety of programmable microwave receivers, polar or X - Y chart recorders, and antenna positioners that can be operated manually or in computer controlled systems (such as the series 2020 antenna analyser). The received signal can be recorded on a linear scale (voltage or power), or on a logarithmic scale over a 60dB dynamic signal range.

The Hewlett-Packard RF Network Analyser Model 8505A, although not specifically designed for this purpose, can also be used as a signal source and receiving system (with 100 dB dynamic range), and this instrument is particularly useful for antenna pattern and gain measurements if used with the dedicated storage-normalizer (Model 8501A) module, and with a desk top controller providing computer graphics capability.

For vertical polarized antenna gain measurements a quarter wave monopole antenna (with elevated feed to provide exact 50 ohm matching) is the best reference antenna (gain is 5.161 dBi). For horizontally polarized antennas, a half wave dipole is the simplest basic reference antenna; however proper account has to be taken of the direct-and-ground-reflected-waves, when comparing the gain of an AUT with a standard gain dipole.

When the horizontal dipole antenna is $\lambda/4$ above the ground plane, overhead ($\theta = 0°$), the direct and ground reflected waves are in phase, and so the measured field is double that in free space (gain =6dBd). This reference antenna is the one commonly used by the author.

For elevated free space ranges stand gain horns, parabolic antennas, or broadband log periodic antennas specifically designed for VHF and UHF antenna test ranges are available from a number of commercial companies, e.g. Scientific Atlanta.

6.4 Measurement of Antenna-to-Antenna Isolation

A measurement that is important for certain applications is the antenna-to-antenna isolation, e.g. between antennas on aircraft and ships. Obviously this measurement can be made in a number of ways. One method employed by the author makes use of the Hewlett-Packard Model 8505A network analyser, since the measurement can be made directly (phase and amplitude (dB)). As noted above this instrument is in effect a 3-channel receiver, and the amplitude (and phase) of the signal in each channel can be measured or the ratio (in dB) between the amplitude in one channel and the amplitude in the reference channel. A directional coupler is used to sample the signal on one antenna, and the signal received on the other antenna is measured.

7. ANTENNAS IN THEIR OPERATIONAL ENVIRONMENTS:
Some Practical Examples

While this lecture is not intended to be an overview on the performance of antennas in their operational environments and on the interaction between antennas and their platforms (e.g. vehicular antennas), we conclude by some selected examples which show a strong influence of the environment on the antenna performance.

7.1 Effects of Supporting Towers on the Radiation
Patterns of Simple Wire Antennas

Wire antennas, such as a horizontal dipole are commonly used for point-to-point short to long range communications. At MF and low HF frequencies the horizontal dipole is typically supported by metal towers, having a height of about $\lambda/4$ for short to medium distance communications by way of skywave. If these towers are grounded, which is usual for lightning protection, they could affect the radiation pattern significally; yet the antenna engineer has ignored this effect. He is normally concerned with the field that is a maximum in directions broadside to the plane of the dipole, and since this field is horizontally polarized and the towers are vertical, little interaction would be expected.

A horizontal dipole however, radiates a vertically polarized field in the directions of the plane of the dipole. Since this field is vertical polarized it would be expected to couple well with the vertical towers, and the radiation pattern in this plane could be markably affected.

A half wave horizontal dipole was modelled at 200 MHz and the radiation pattern measured on the NRC ground level antenna pattern range[23],[24]. The dipole was $\lambda/4$ above the ground plane and a coaxial balun was employed. The vertical radiation patterns are shown in Fig. 25. These are tracings of the measured

patterns on a linear field strength scale. The scalloping on the curves is a range imperfection (discussed above). The solid lines are the patterns for non-conducting (wooden) towers (denoted on the diagram as insulated towers); the broken lines are for grounded $\lambda/4$ high metal conducting towers. Notice that the effect of the conducting towers is to decrease but only slightly, the horizontally polarized overhead field strength ($\theta = 90°$); and that the conducting towers result in a significant modification to the vertically polarized field pattern. With non-conducting towers there is little low angle radiation ($\theta < 10°$), whereas with conducting towers there is significant radiation at the horizon ($\theta = 0°$); of magnitude about OdBd, with a deep null in the pattern at 40°.

Similar effects were measured for other wire antennas, such as delta loops[24]. The effects shown here are a maximum, since towers were grounded, the ground plane perfectly conducting and the towers were approximately a resonant height. Since the impedance of the antenna would be affected by the conducting towers, and this was not measured or taken account of in the measured patterns, an exact agreement with numerical modelling would not be expected, but there was good agreement with theory (for the delta loop antenna which was the only configuration numerically modelled).[24]

7.2 Vehicular Antenna

Since vehicles, such as automobiles, tanks, ships, aircraft, etc., are metal structures, the electrical properties of antennas (current distribution, impedance, radiation pattern and efficiency) mounted on them would be expected to be strongly influenced by the support platform. The frame of an automobile at MF and lower HF frequencies is an inadequate ground plane, which is physically small in terms of wavelengths, and it is "insulated" from the ground beneath it by the rubber tires of the vehicle. Track vehicles are "grounded" but imperfectly so by sliding contact with the track (if it is metal). Metal ships are physically large and provide an adequate ground plane, but the super structure and hull of the ship can significantly affect the pattern of HF antennas mounted on them. Aircraft structures, particularly helicopters, markedly affects the pattern of VHF and UHF antennas mounted on them.

7.2.1 Automobiles

At HF the influence of the ground is significant, particularly since antennas employed are electrically short monopoles, and the aizmuthal pattern is affected, especially for rear bumber mounted or trunk mounted antennas[25]. The aizmuthal pattern can be as much as 5dB greater in the direction of the long axis of the automobile. Clearly the influence of the ground beneath will decrease as the vehicle becomes electrically large. Webster[26] has shown that at 30-76 MHz currents throughout the whole of the vehicle were significant. For practicle purposes the effect of the varing ground constants can be neglected above about 100 MHz[7].

A basic understanding of the influence of the ground beneath rubber tired land vehicles might be found from studies of the curent distribution on counterpoise wire systems, since currents can be measured on elevated wire systems. However, except for the study of Doty et.al.[27], who made measurements at only one frequency (1.8 MHz), no specific data have been found on current distributions on the counterpoise wire systems. These authors have shown that the currents on a 48 radial wire system (see Fig. 26) were far from equal, and they have shown that the currents on counterpoise radial are probably related to the conductivity of the ground beneath them.

Effects of VHF and UHF frequencies are largely due to the shape and lack of symmetry of the vehicle, considered as a ground plane beneath the antenna. An extreme example of pattern distortion is shown in Fig. 27, which is for a cowl mount antenna at 800 MHz[28]. The cowl mount is the worst location. Notice that the pattern null is, as might be expected, diagonally opposite the antenna location.

Vehicular communications in heavy built up areas poses problems: for out-of-sight paths the reception of a distant repeater or base station signal contains many multipath components, which can affect the "gain" of vehicular antennas;[29] for elevated base stations (on top of high rise buildings) the dominant mode may be over the roofs of buildings and diffraction into the street below, thus affecting the range of vertical angles over which the signal is received[30].

In Figs. 28 and 29 we show some results on the relation between signal fading and effective gain of a 4 dB 800 MHz collinear over a $\lambda/4$ monopole. The gain antenna was a $\lambda/2$ element over a $\lambda/4$ element with a phasing coil, in rural and urban environments. In the rural environment measurements were made in open terrain, on a road where there was a clear view of the transmitting antenna (signal was measured in a moving vehicle), and at about the same distance but behind a 1 km thick grove of evergreens. Notice that behind the wooded area the signal-fading was greater and the apparent gain (dB over a quarter-wave) was less. In the urban area (about 16 km from the transmitting antenna, which was located on the outskirts of the city), measurements were made on streets that were perpendicular and parallel to the direction of propagation. On parallel streets the fading was less than on perpendicular streets and the expected gain of the collinear was greater (infact the expected gain was measured, 4dB over a $\lambda/4$). The vertical collinear achieves gain by vertical stacking. Measurements were also also made employing twin half-delta loops[31] arranged to provide an omni-directional pattern. This antenna achieves gain by in phase horizontally spaced elements. The twin half delta loop array yielded identical gain with the collinear for the unobstructed line-of-sight path, but even less gain in the multi-path environment; suggesting that the multi-path signal came from scatters in the horizontal plane....that is the signal coherence distance was less in the horizontal than in the vertical plane. The fact that the line-of-site unobstructed path gave a gain>4dB is probably an antenna-ground-plane interaction, effecting the at-the-horizon gain of the quarter wave[32].

Finally, it should be noted that in both sets of measurements in the urban environment the transmitter was out-of-sight. The difference between the paralled and perpendicular streets therefore is a function of the difference in the multi-path. In the parallel street situation the signal is "channeled" down the street, whereas in the perpendicular street situation the signal reaches the receiver entirely by diffraction from the roofs of buildings. The fact that antenna gain is dependent on

the spatial coherence of the received signal is to be expected, but this is a subject that has not been adequately addressed. It is clearly however, an environmental situation which is important for land mobile communications.

7.2.2 Aircraft

At HF most of the published work has been concerned with resonances in the aircraft and with design of antennas, often electrically small antennas from an impedance and matching view point[33],[34]. Little has been published on patterns for the various antennas discussed. At VHF and UHF the published work is largely concerned with radiation patterns[7],[33]. A review of modelling techniques is given by Sinclair et.al[6].

While clearly the airframe has a marked effect on the radiation pattern, dependent on the type of the aircraft, the operating frequency, the type of antenna and the location of the antenna, the effects of stores (weapons, wingtanks, etc.) on the pattern is also a major concern. In Fig. 30 we show for illustration purposes, aircraft patterns measured for a F4C USAF fighter aircraft with and without stores. Clearly external stores degrade the pattern significantly, increasing multipath and decreasing the signal radiated in some directions. These measurements were made on the RADC full scale pattern range previously described. The frequency not specifically given was in the range 1300-3000 MHz.

The application of antenna range measurements for antenna design is illustrated in Fig. 31, which shows how the strategic placement of microwave absorbing material reduces a severe multipath problem on the USAF EF111A fighter aircraft. The continuous line is the pattern without absorber material for a wing glove mounted antenna (frequency in the range mentioned above). The dashed line illustrates how this pattern was improved by stratigically located microwave absorber material in wing areas. Radar absorbing material (RAM) is also used to reduce radar cross-sections, however little information on these applications has appeared in the literature in view of the significance to the military.

7.2.3 Ships

Many communications and navigation antennas used on marine vessels operate in the HF, VHF and UHF ranges. Since a ship, particularly a metal ship, is a large conducting body, the performance of the antenna (radiation pattern) will be significantly modified by the vehicle on which it is mounted. This is particularly the case for vertical antennas, since the ship superstructure, such as masts, smokestacks, etc. are vertical structures. A vertical antenna fed against an upper deck of a metal ship is in effect a grounded monopole with elevated feed, but the lower part of the monopole, the body of the ship is a physically large, in terms of wavelengths. The "ground" is the ocean on which the ship is floating, which is a good conducting medium.

Ships need omni-directional antennas in order to be able to communicate with stations on any bearing. Simple vertical antennas are commonly employed, but few communications engineers realize how much the radiation pattern can be changed from that expected. As an illustration, look at Fig. 1 which is a 1/48 scale model of a Canadian (Navy) Frigate, mounted on the NRC antenna pattern range which has been previously described. Notice the two vertical whip antennas on the upper front deck. Other antennas are also shown, but we will not consider these. The diagrams in Fig. 32 show measured patterns for a vertical whip on the NRC pattern range [Wong, private communications], measured at 2,5,8 and 14 MHz, which are the equivalent full scale frequencies labelled a,b,c and d respectively. The elevation patterns measured are for the planes forward to aft and port to starboard for vertical (E_θ) and horizontal (E_ϕ) polarization. The azmuthal pattern is for vertical polarization. Notice that -

1) The E_θ field strength does not show an overhead null, characteristic of a vertical monopole, at any frequency.

2) The azmuthal pattern for the E_θ field is certainly not omni-directional, deep nulls are found at some azimuths for some frequencies.

3) There is an appreciable E_ϕ field at all frequencies. This is certainly due to the horizontal currents flowing over the superstructure and hull of the ship.

7.3 Re-radiation from Highrise Buildings, Power Transmission Lines and Other Structures on the Pattern of MF Broadcast Antennas

Highrise buildings (30x30m x 60m. high) and HV power transmission lines are resonant in the middle of the MF broadcast band. Since such structures are conductors, if they are located near to a broadcast antenna array (say a few wavelengths away) they could be expected to significantly affect the pattern of the antenna array.

The efficiency of a highrise building as a re-radiator has been discussed. Some researchers believe that it may not be high, because it may not be well grounded. This author believes that highrise buildings are an efficient wire grid structure that is indeed well grounded. Even if the building does not have much structural steel, ground wires of the electrical system run everwhere, forming a grid, and these wires are grounded to the water system piping and to sewer piping. Power transmission lines are well grounded for lightning protection, and although the RF grounding is not well documented[35],[36],[37], there are measurements which show that re-radiation from such structures can be significant[38]. Certainly model measurements, where the ground plane is perfectly conducting and the re-radiating structures are well grounded clearly show marked effects[8],[25],[39],[40].

The effects of power transmission lines on the pattern of MF broadcast antennas have been measured on the NRC antenna pattern range, at a modelling scale factor of 600 (600 MHz corresponds to 1 MHz). The physical arrangment is illustrated in Fig. 19. A photograph of this model is shown in Fig. 33. The re-radiated field was measured in two ways: by the scalloping on the expected omni-directional pattern, and directly[39]. The scatter field can be measured directly as follows. With the monopole antenna alone on the ground plane, the signal received on the probe antenna is made to be zero, by mixing with the received signal in a power adder circuit a signal from the signal generator of the right phase and amplitude. With the power transmission line on the turntable, the signal measured by the receiver is then the scatter field only, since the direct signal has been nulled out. In Fig. 34 we show measured and calculated patterns for a 5-tower power line located near to an omni-direction radiator (the MF monopole was 448m in distant and opposite the centre tower (see Fig. 19). Patterns are for frequencies near the 1 - and 2λ loop resonant frequencies for the power line (515 and 860 kHz). Clearly in the absence of the power line the radiation pattern would have been omni-directional. In Fig. 35 we show measured (and calculated) max-to-min ratios, measured from the scalloping on the pattern for a 13 tower power line, without and with detuning stubs.

The detuning stubs on the skywires (see Fig. 20) effectively places a low impedance (to ground) at the position on the structure where the shorted end of the stub is attached; and they effecively "open" the loop (considering the towers and skywires as loops) at the open end of the stub. The stub is therefore most effective if its shorted end is positioned on the structure where the current, without the stub, is a minimum (high series impedance); since its open end will then fall at the place on the structure where the current (without the stub) is a maximum (low series impedance)[41].

We have shown in Figs. 22 and 23 that the current distribution in the skywires is such that skywire detuners should be effective, and indeed they are. In the case where there are two skywires, the skywire detuner becomes a practical proposition, since one skywire can be broken by series strain insulators to form quarter wave stubs with the parallel unbroken skywire.

The effects of re-radiation from highrise buildings and towers on the directional pattern of MF broadcast arrays have been studied by Royer[42]. Compared with the effects of power transmissions lines, the effects of isolated buildings are in principle easier to compute since they behave as thick or flat monopole re-radiators or scatters. However, buildings are often grouped into complexes, and no practical method to detune them has been found. Side mounted stubs[42], and roof-top stubs and umbrella configurations[43] have been proposed.

ACKNOWLEDGEMENT

REFERENCES

1. Sinclair, G., Theory of Models of Electromagnetic Systems, Proc. IRE, 36, 1948, p. 1364.

2. IEEE Standard Test Proceedures for Antennas, ANSI/IEEE Sdt. 149-1979, distributed by Wiley-Interscience.

3. Kummer, W.H. and E.S. Gillespie, Antenna Measurements, Proc. IEEE, 66, 1978, pp. 483-507.

4. Appel-Hansen, J., E.S. Gillespie, T.G. Hickman and J.D. Dyson, Antenna Measurements, in the Handbook of Antenna Design, Vol. 1, ed. A.W. Rudge, K. Milne, A.D. Olver and P. Knight, Peter Peregrinus Ltd., London, 1982, pp. 584-694.

5. Hollis, J.S., T.J. Lyon and L. Clayton, Microwave Antenna Measurements, Scientific-Atlanta, Inc., Atlanta Georgia, July, 1970.

6. Sinclair, G., E.C. Jordan and E.W. Vaughan, Measurement of Aircraft-Antenna Patterns using Models, Proc. IRE, 35, 1947, pp. 1451-1462.

7. Burberry, A., VHF and UHF Antenna, in the Handbook of Antenna Design, Vol. 2, Ibid, Vol. 2, 1983, pp. 725-856.

8. Belrose, J.S., W. Lavrench, J.G. Dunn, C.W. Trueman and S.J. Kubina, The effects of re-radiation from highrise buildings and transmission lines upon the radiation pattern of MF broadcasting arrays, AGARD Conf. Proc. 269, Tech. Editing and Reproduction, Ltd., London, 1979, pp. 2-1 to 2-11.

9. Ono, T. and T. Shibamata, Feederless reception antenna by the use of direct modulation of laser diode, Jpn. Appl. Phys., 22, 1983, p. 545.

10. Woodward, O., Balance measurements in balun transformers, Electronics, September, 1953, p. 188.

11. Maxwell, W., Some aspects of the balun problem, QST, March, 1983, pp. 38-40.

12. Emerson, W.H., Electromagnetic wave absorbers, useful tools for engineers, in folder Eccosorb, High-loss Dielectric Microwave Absorbers, pub. by Emerson & Cuming, Canton, Mass.

14. Belrose, J.S., J. Litva, G.E. Moss and E.E. Stevens, Beverage antennas for amateur communications, QST, January 1983, pp. 22-27.

15. Royer, M., The Field Pattern along the Group Plane for CHFA's Broadcast Array as a Function of Range Range from the Array, July, 1982 (to be published).

16. Barnes, C., XELEDOP Antenna Pattern Measuring Equipment, 2 to 50 MHz, Stanford Research Institute, Menlo Park, CA., July, 1965.

17. Petrie, L.E., Equipment: Antenna Systems, AGARD Lecture Series No. 127, Specialized Printing Services, Ltd., Loughten, Essex, May, 1983.

18. Emerson W.A., Electromagnetic wave absorbers and anechoic chambers through the years, IEEE Trans. AP-21, July, 1973, pp. 484-490.

19. Alden, A., Enclosed field devices and probes for the generation and measurement of fields for radiated suceptability testing, Dept. of Communications Contracter's Report, Harry Dulmage Assoc., Ltd., December, 1979.

20. Balman, K.G., The effect of re-radiation of AM broadcast signals, Department of Communications Contract Report, University of Toronto, March, 1978.

21. ARRL Antenna Book, Pub. by ARRL, Newington, CT, 1982.

22. Tilston W.V., R. Goetz, G. Suggitt and M.A. Tilston, Model Measurements in Simulated Power Line Sites, Department of Communications Contractor's Report by TilTek Ltd., Kempville, Ontario, March, 1983

23. Belrose, J.S., The effects of metal supporting towers on the radiation pattern of simple wire antennas, Antennas and Propagation, Pt. 1 Antennas, IEE Conf. Pub. No. 195, 1981, pp. 84-87.

24. Belrose, J.S., The effect of supporting structures in simple wire antennas, QST, Dec. 1982, pp. 32-35.

25. Belrose, J.S., VLF, LF and MF Antennas, in The Handbook of Antenna Design, Vol. 2, Ibid, pp. 553-662.

26. Webster, R.E., 20-70 MHz Monopole antennas on ground vehicles, IRE Trans., AP-5, 1957, pp. 363-368.

27. Doty, A.C., J.A. Frey and H.F. Mills, Characteristics of the counterpoise and the elevated screen, IEEE Southcan/83 Conf. Record, Session 9, January, 1983, pp. 1-14.

28. Horn, D.W., Vehicle-caused pattern distortion of 800 MHz, IEEE 33rd Vehicular Technology Conference, May, 1983, pp. 197-200.

29. Belrose, J.S., Vehicular antennas for 800 MHz mobile radio, IEEE 33rd Vehicular Technology Conference, May, 1983, pp. 191-196.

30. Davidson, A.L. and T.J. Turney, Mobile antenna gain in the multipath environment at 900 MHz, IEEE Trans. VT 26, 1977, pp. 345-348.

31. Belrose, J.S., A half twin-delta loop array, QST (correspondance), April, 1983, pp. 39-40.

32. Foster, P.R. and T. Miller, Radiation patterns of a quarter-wave monopole on a finite ground plane, Antennas and Propagation, Pt. 1: Antennas, IEE Conf. Record Pub. No. 195, 1981, pp. 451-455.

33. Bollijahn, J.T. and J.V.N. Granger, Aircraft Antennas, Antenna Engineering Handbook (ed. H. Jasik), McGraw Hill, 1961, pp. 27-1 to 27-46.

34. Radford, M.F., High Frequency Antennas, in The Handbook of Antenna Design, Vol. 2, Ibid, 1983, pp. 663-724.

35. Plumey, J.P., D.J. Roubertou, J.M. Fontaine and P. Kouteyikoff, High frequency harmonic input inpedance of an antenna embedded in a conducting half-space, EMC Zurich 1983, Paper No. 9C2.

36. Fieux, R., P. Kouteynikoff and F. Villefranque, Measurements of the impulse response of grounding to lightning currents, 15th European Conf. on Lightning Protection, Uppsala, Sweden, 1979

37. Kouteynikoff, P., Resonse impulsionnelle des prises de terre aux courants de foudre, Int. Conf. on Large High Voltage Electric Systems, Stockholm, 1981.

38. Gauthier, L., Field Intensity Measurements CBL/CJBC, Toronto (3rd set), CBC Radio Canada Report ER-216, December, 1977.

39. Belrose, J.S., C.W. Trueman, S.J. Kubina, W. Lavrench and J.G. Dunn, On minimizing the effects of re-radiation from power transmission lines on the radiation pattern of MF-AM broadcasting antenna arrays, in Antennas and Propagation, Vol. 1; Antenna, IEE Conf. Pub. No.195, 1981, pp. 33-37.

40. Trueman, C.W. and S.J. Kubina, Numerical computation of re-radiation from power transmission lines at MF frequencies, IEEE Trans. on Broadcasting, BC-27, June, 1981, pp. 39-45.

41. Trueman, C.W., S.J. Kubina and J.S. Belrose, Corrective measures for minimizing the interaction of power lines with MF broadcast antennas, IEEE Trans. on EMC, August, 1983.

42. Royer, G.M., The effects of re-radiation from highrise buildings and towers upon the antenna patterns for AM broadcast arrays, IEEE Int. Symp. on EMC, Boulder, Colo., 18-20 August, 1981.

43. Kavanagh, S.J., AM Broadcast Re-radiation from Buildings, MaSc Thesis Univ. Toronto, Canada, September, 1982.

Additonal References (not cited)

Antennas for Avionics, AGARD Conf. Proceedings No. 139, Tech. Edit. and Reproduction Ltd., London, June, 1974.

Antennas for Aircraft and Spacecraft, IEE Conf. Pub. No. 128, 3-5 June, 1975.

FitzGerrel, R.G., J.R. Juroshek and R.D. Jennings, Onsite antenna measurements, MF to x-band, Antennas and Propagation, Pt.1; Antennas, IEE Conf. Pub. No. 169, November, 1978, pp. 282-286.
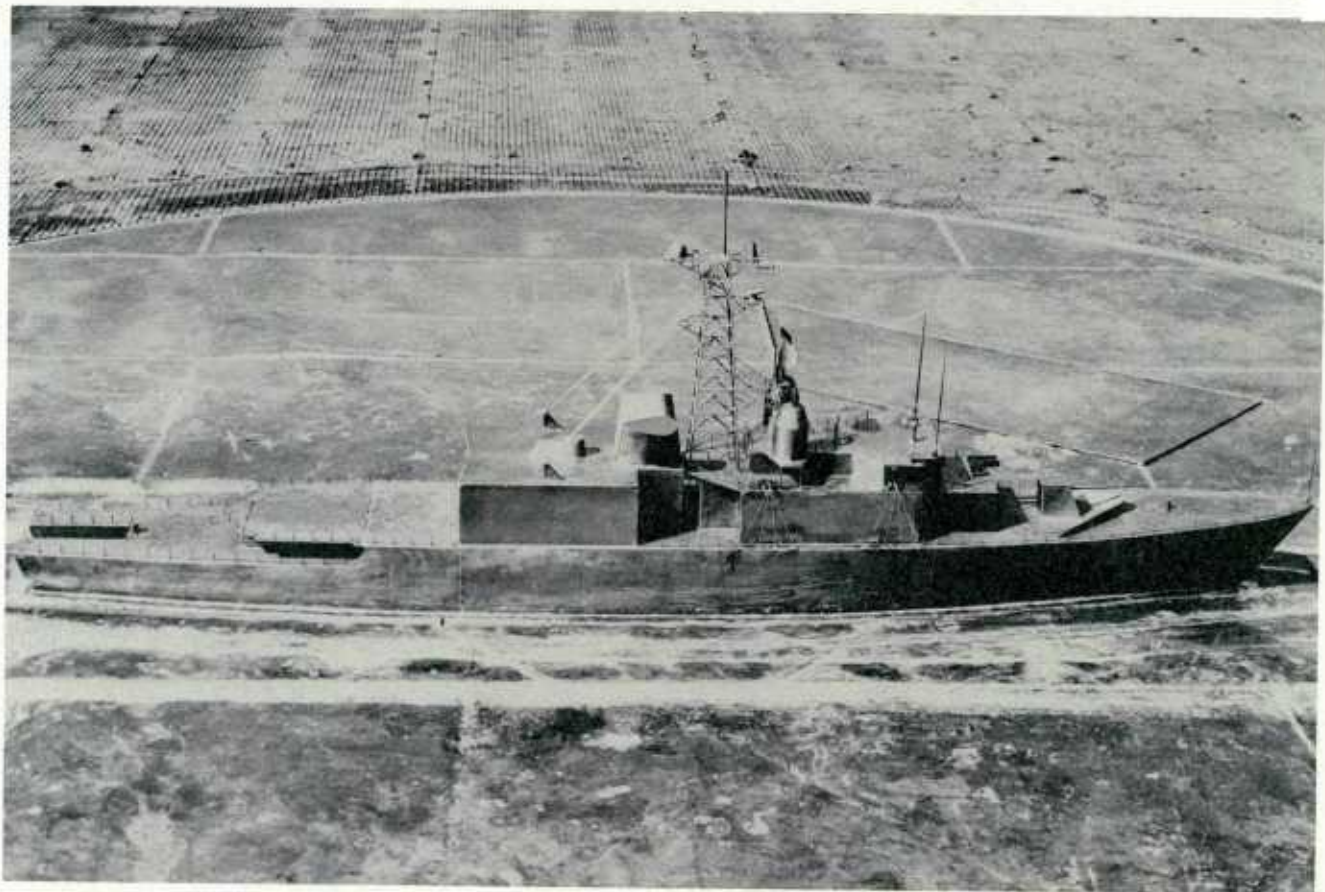
Fig. 1 A 1/48 scale model of a Canadian Frigate

Fig. 2 Photograph of the NRC ground level antenna pattern range showing the boom for measuring elevation patterns and the turntable with a 200 MHz inverted-V dipole antenna on it.

2-14
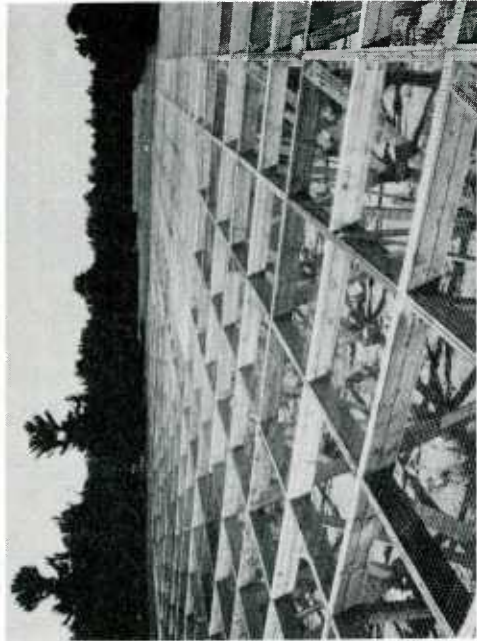
Fig. 4 Photograph taken from the centre of the CRC elevated ground plane (diameter 30m 6m above ground level)

Fig. 5 Example configuration of a 686 metre elevated range with diffraction fences (from ref. 2)
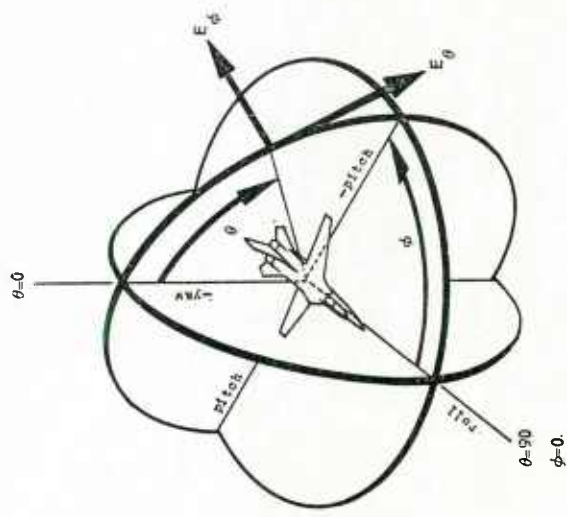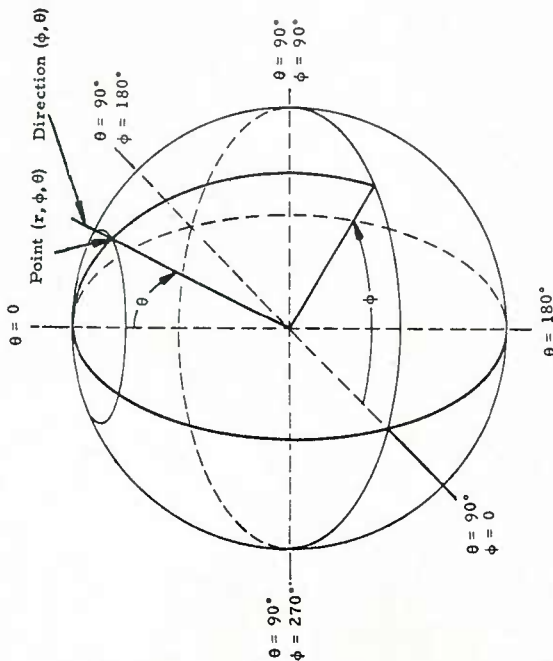
Fig. 3 Standard spherical coordinate system (upper diagram), and consolidated vehicle and antenna coordinate system (lower design)

2-15
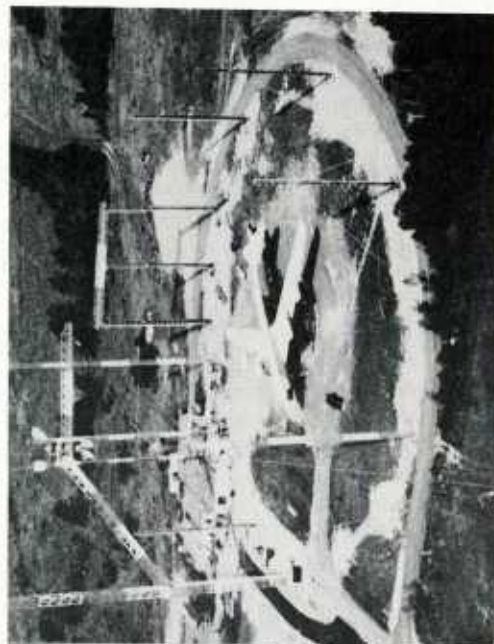
Fig. 6 Photographic view of the USAF RADC Newport antenna test facility (left) and of the Stockbridge site (above). The Stockbridge test facility not discussed in the lecture, is a single axis turntable supporting the airframe about 6m above level terrain. Patterns can be measured ±70 elevation and 0 - 360 azimuth.
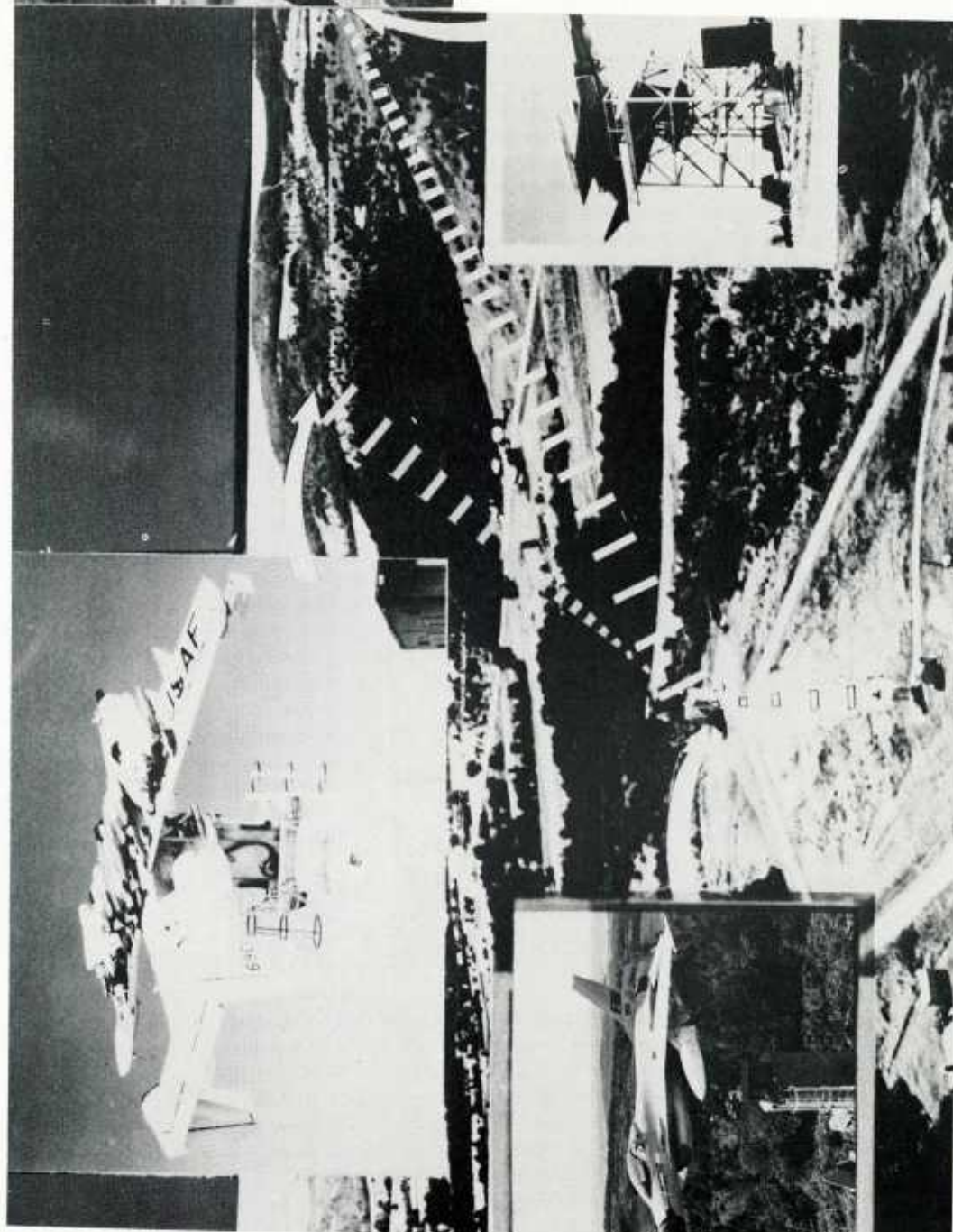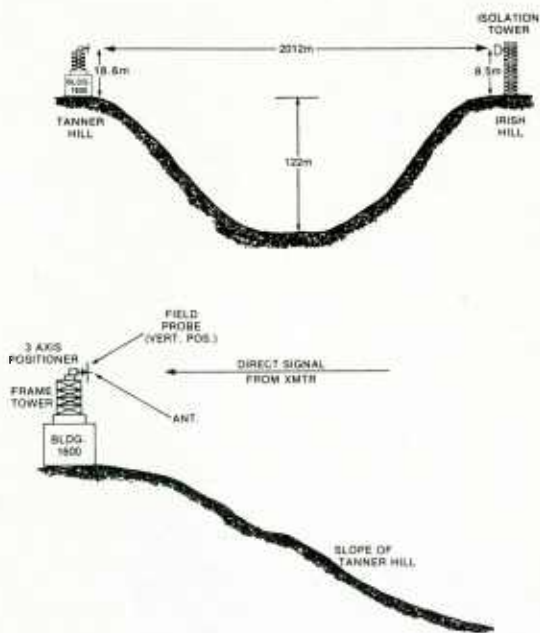
Fig. 7   Sketch showing the Newport section
range layout
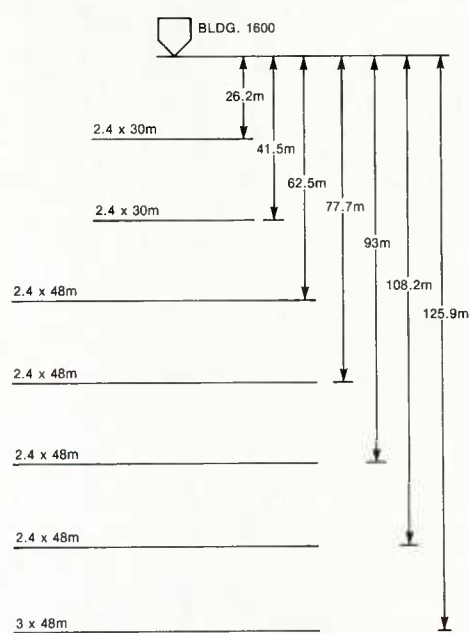
Fig. 8   Diagram illustrating the diffraction
fence configuration as employed on
the Newport section range
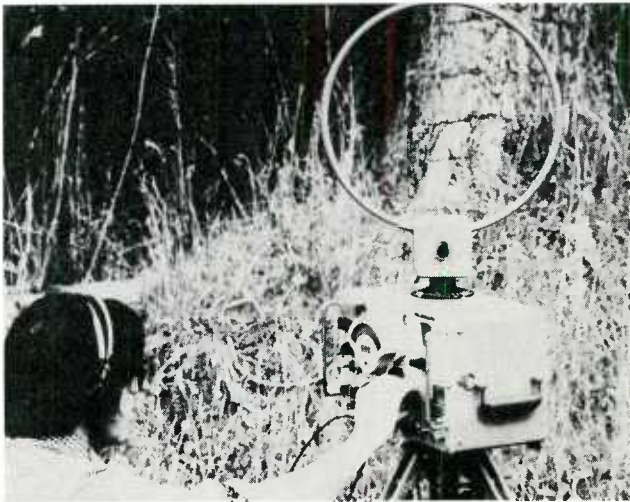
Fig. 9   Photograph of a typical MF/HF field
intensity meter with loop antenna
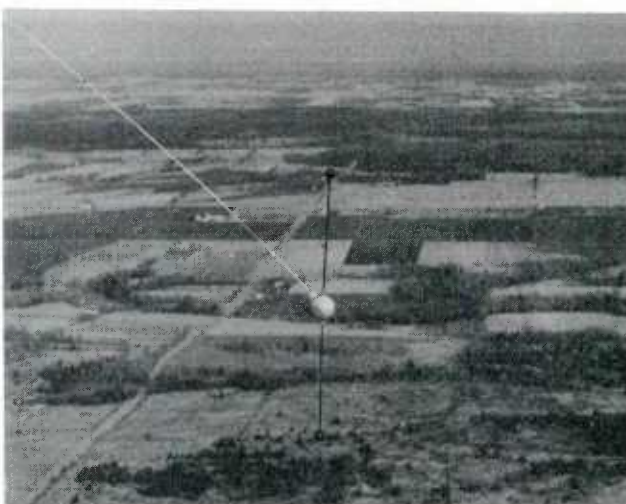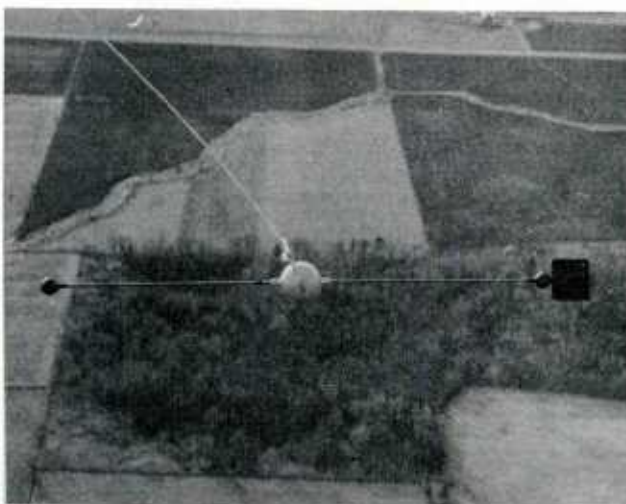
Fig. 10 Photographs illustrating a XELEDOP towed
by a small aircraft: an inflight photograph;
the horizontal dipole; and vertical dipole
configuration.

Fig. 11 A 1/12 scale model of a Canadian CF104 fighter aircraft with a crossed slot antenna on the wing.
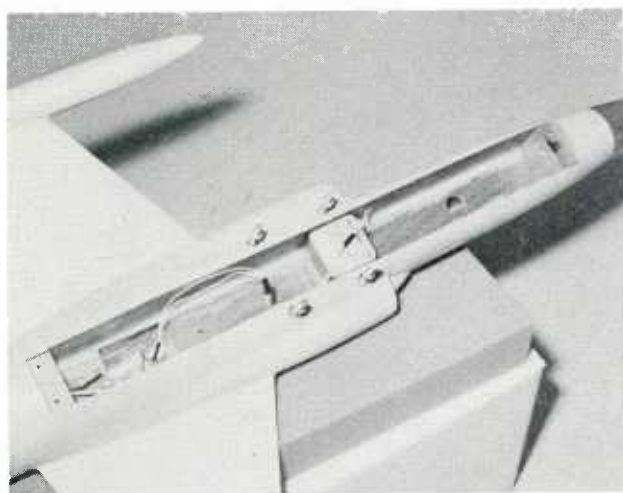
Fig. 13 Photograph illustrating the signal source/battery compartment (with batteries removed).

Fig. 12 Antenna under test on a flat plate on positioner (actually this antenna was a cavity backed spiral).
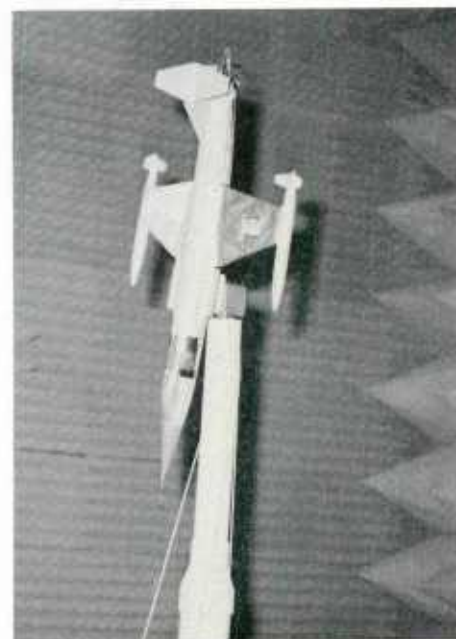
Fig. 14 Modelled aircraft on positioner
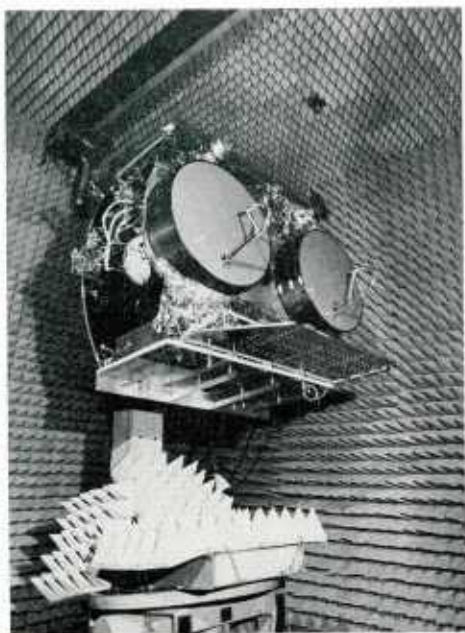
Fig. 15 CTS satellite inside an anechoic chamber, which is part of the CRC David Florida Laboratory facilities
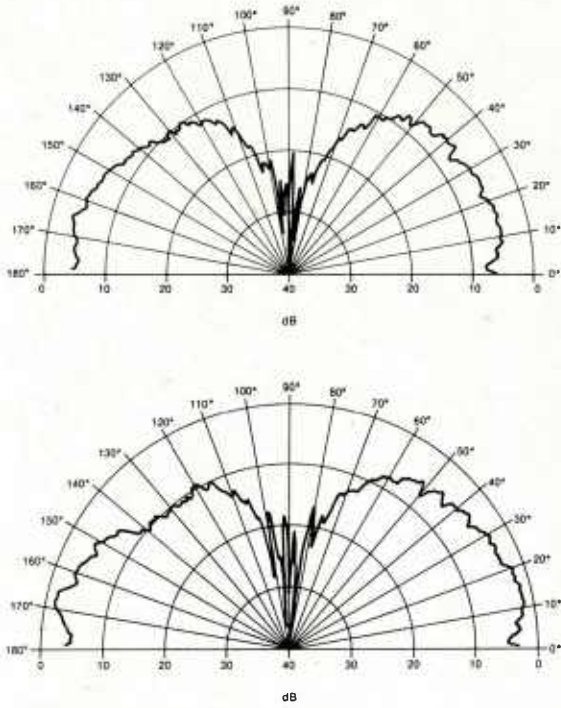
Fig. 16 Elevation pattern vertical polar-
ization for a quarter wave monopole
measured on the NRC ground level
antenna pattern range at 835MHz
(upper diagram) and 861MHz (lower
diagram)

$\alpha = \sin^{-1}\dfrac{\lambda}{\Delta h}$
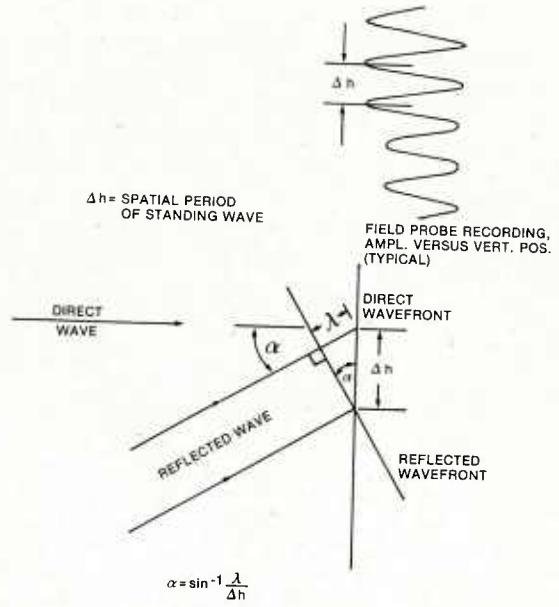
Fig. 17 Diagram illustrating the calculation
of the direction of the refected wave
from the spatial period of the standing
wave pattern measured by a vertical
moving field probe.
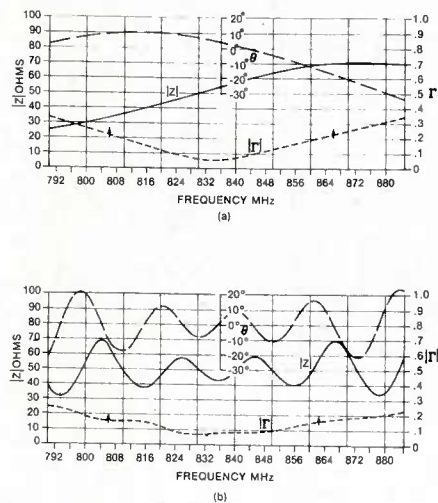
Fig. 18 Impedance $|Z|$ and θ versus frequ-
ency for an 800 MHz 4 dB gain collinear
vehicular antenna: (a) base impedance;
and (b) impedance with 4.1 metre of
feeder coax connected.
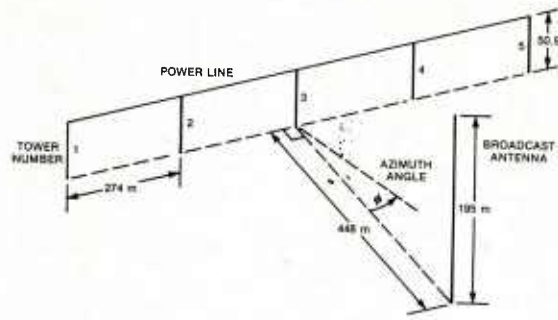
Fig. 19 Sketch illustrating a broadcast
monopole (height about $5/8\lambda$) near
to an idealized 5-tower powerline.

BENT STUB, LENGTH s = b + d
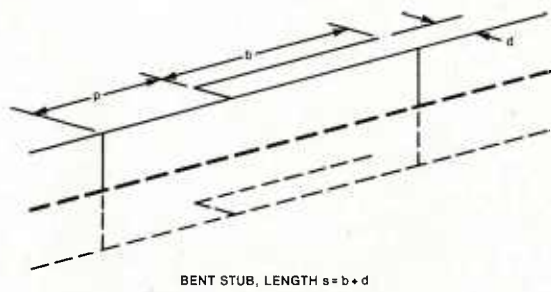
Fig. 20 Sketch illustrating a single
power line loop and its image
in the ground plane. The sketch
also illustrates a skywire
detuner (a $\lambda/4$ stub) which will
be discussed later.

3/8" SUBMINAX CABLE

1" 0.141 SEMI-RIGID CABLE

1" λ/4 @ 87 MHz BALUN TYPE

FERRITE TEKTRONIC PROBE P6022
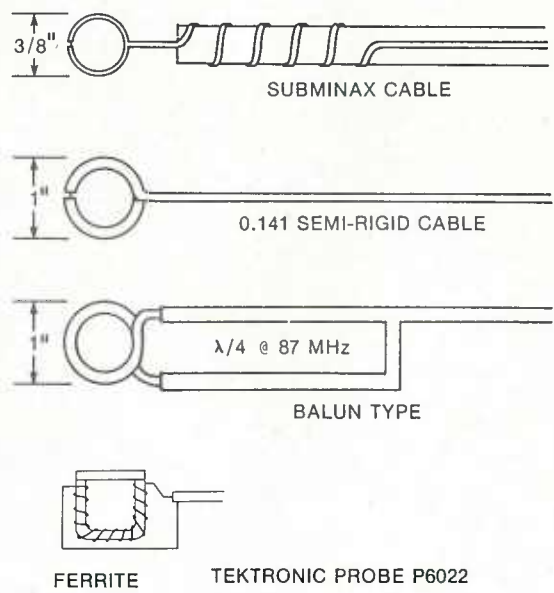
Fig. 21 Various current probes which were assessed.
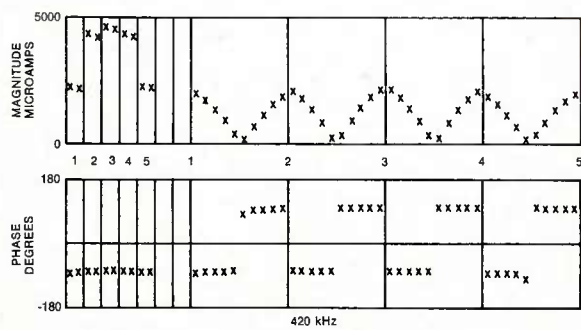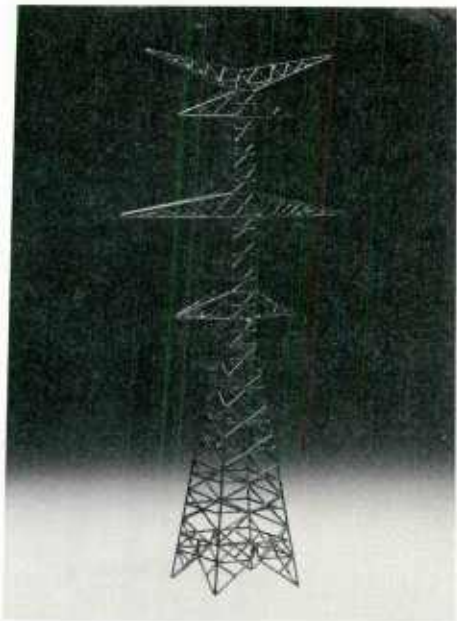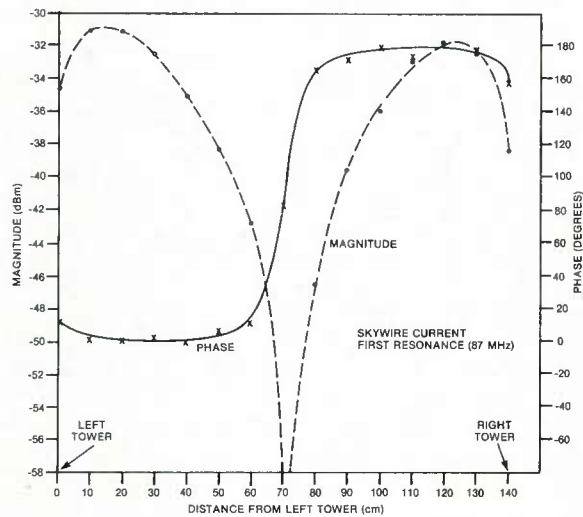
Fig. 22 Skywire current (two tower case) measured at the 1λ loop resonance frequency (87 MHz). The lower diagrams illustrate calculated currents on a 5-tower power line. The photograph shows a 1/200 scale model power transmission line tower. These towers carry two skywires on opposite ends of the upper cross-arm.
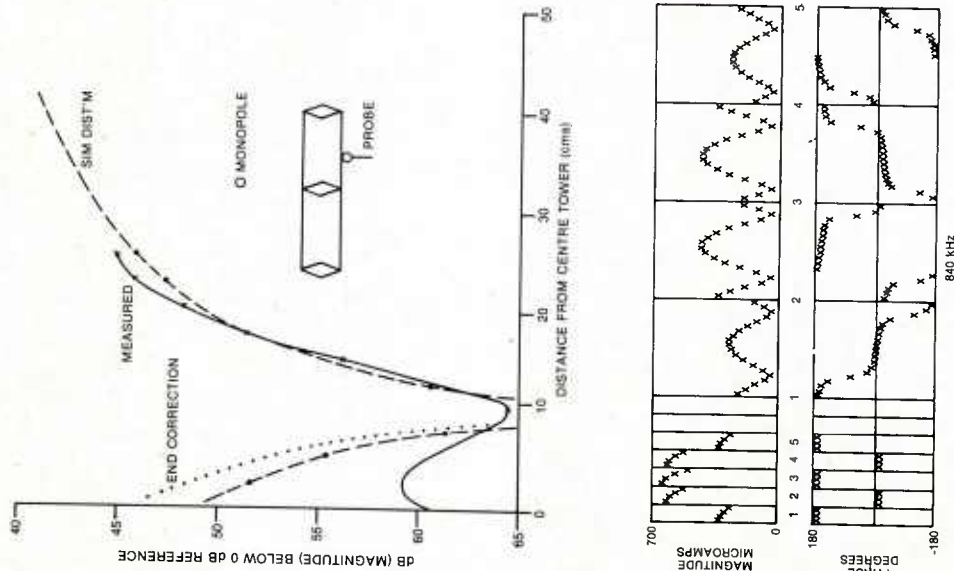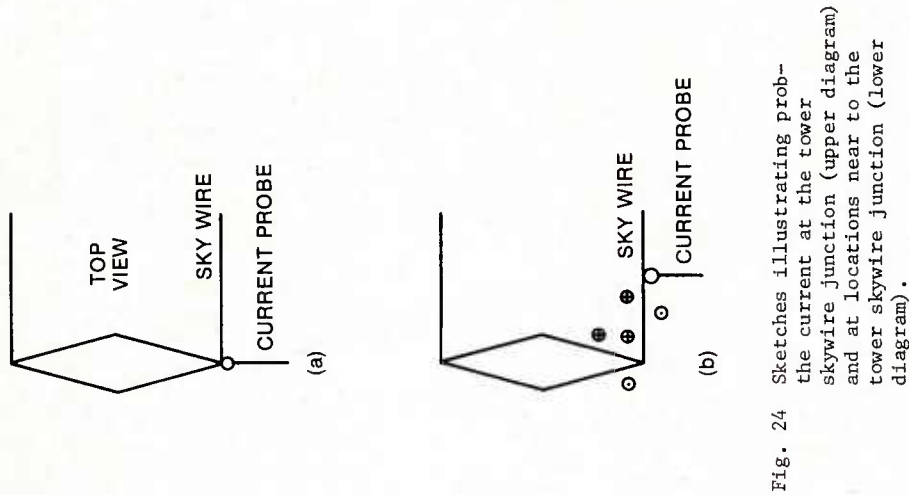
Fig. 25 Vertical patterns of a $\lambda/2$ horizontal dipole at 200MHz on the NRC ground level antenna pattern range, for conducting and non-conducting support masts. The upper diagram is horizontal polarization in the plane broadside to the dipole. The lower diagram, vertical polarization in the plane of the dipole.
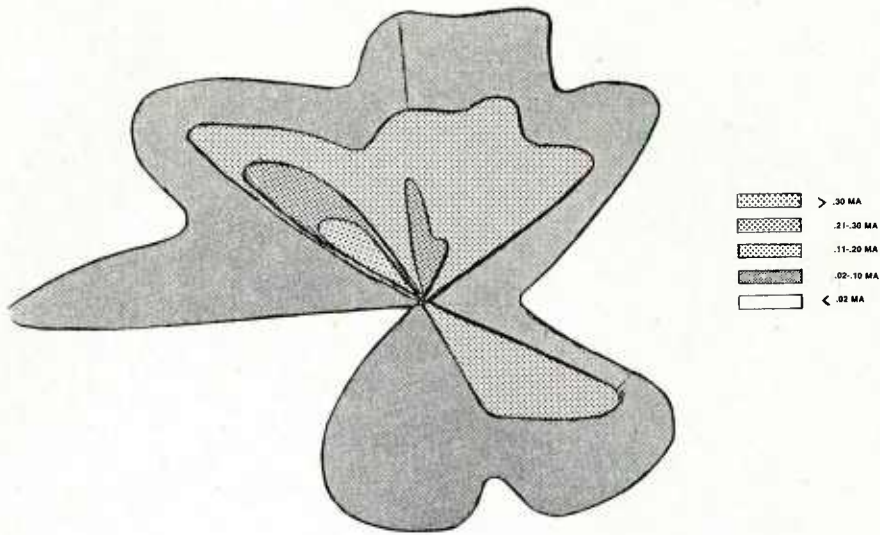

Fig. 24 Sketches illustrating problem the current at the tower skywire junction (upper diagram) and at locations near to the tower skywire junction (lower diagram).

Fig. 23 Skywire current (three tower case) measured at the 2λ loop resonance frequency (168.3 MHz). The lower diagrams illustrate calculated currents for a 5 tower powerline.

Fig. 26   Current distribution on radial wires of a 48 radial counter-poise, based on approximately 800 data points (after Doty et al[27]).
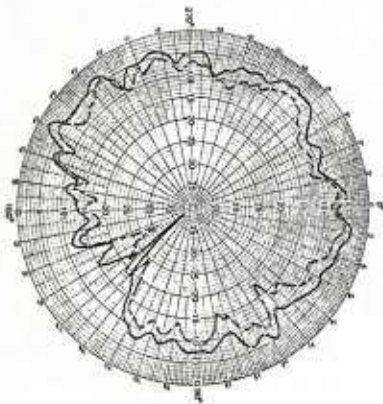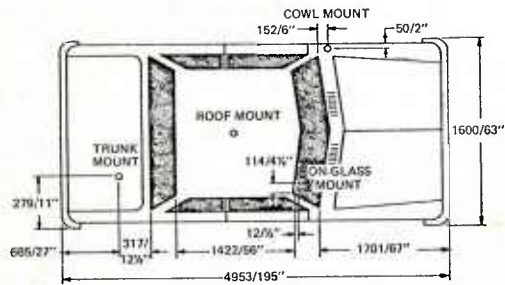

Fig. 27   Vehicle caused pattern distortion at 800 MHz for a worst case cowl mount antenna. The mounting location on the vehicle (mm/inches) is shown in the upper diagram, which is correctly oriented in relation to azimuthal pattern (lower diagram). The solid curve is a cowl mount 3 dB collinear, the dashed curve a cowl mount λ/4 monopole (after Horn[28]).
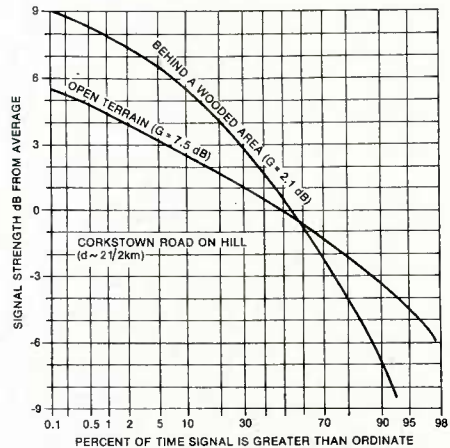

Fig. 28   Relation between signal fading and effective gain for a collinear antenna (dB over a λ/4 monopole) in a rural environment at 861MHz.

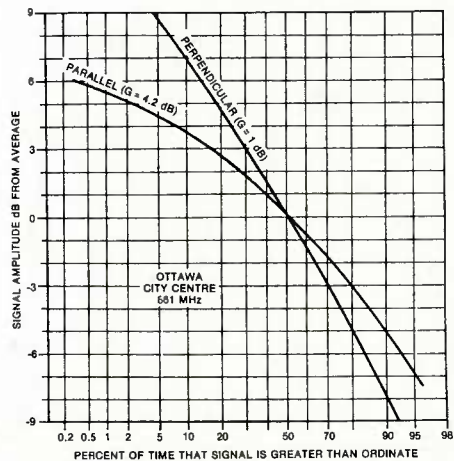

Fig. 29   Relation between signal fading and effective gain for a collinear antenna (dB over a λ/4 monopole) in an urban environment.
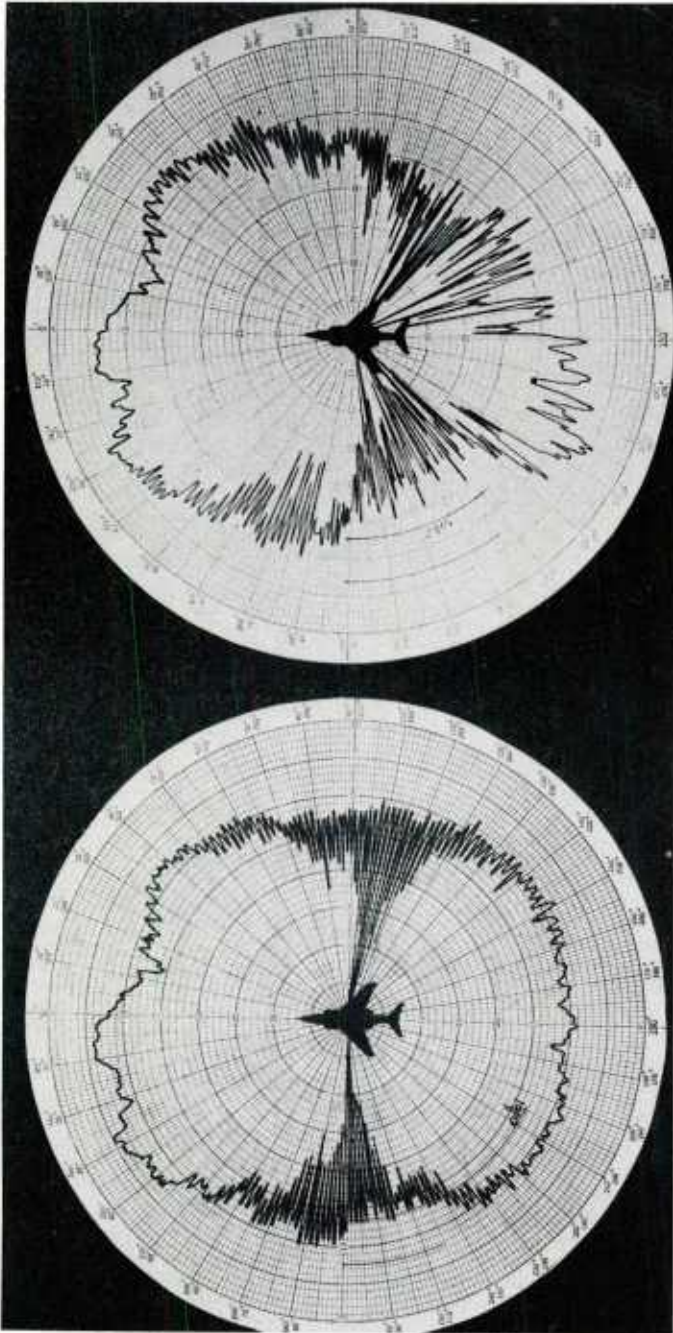
Fig. 30 Comparative antenna patterns illustrating
how the pattern has been degraded by
external stores, which is the pattern on
the right. These are measured data for
the USAF F4C airframe (after McGregor,
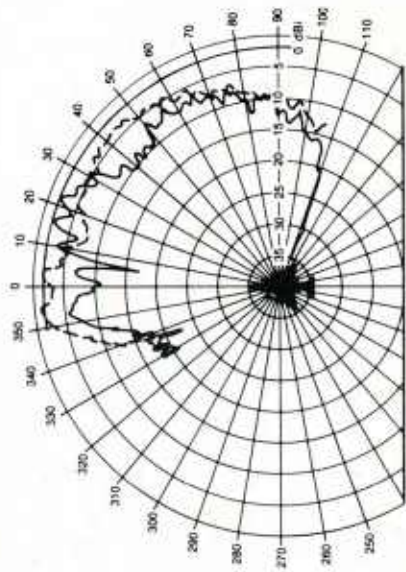private communications).

Fig. 31 Diagram showing coverage of a wing
glove mounted antenna (on a USAF
F 111A fighter aircraft), illustrating
how the pattern has been improved
(dashed line) by strategically loc-
ating microwave absorbing material in
wing areas. This is measured data
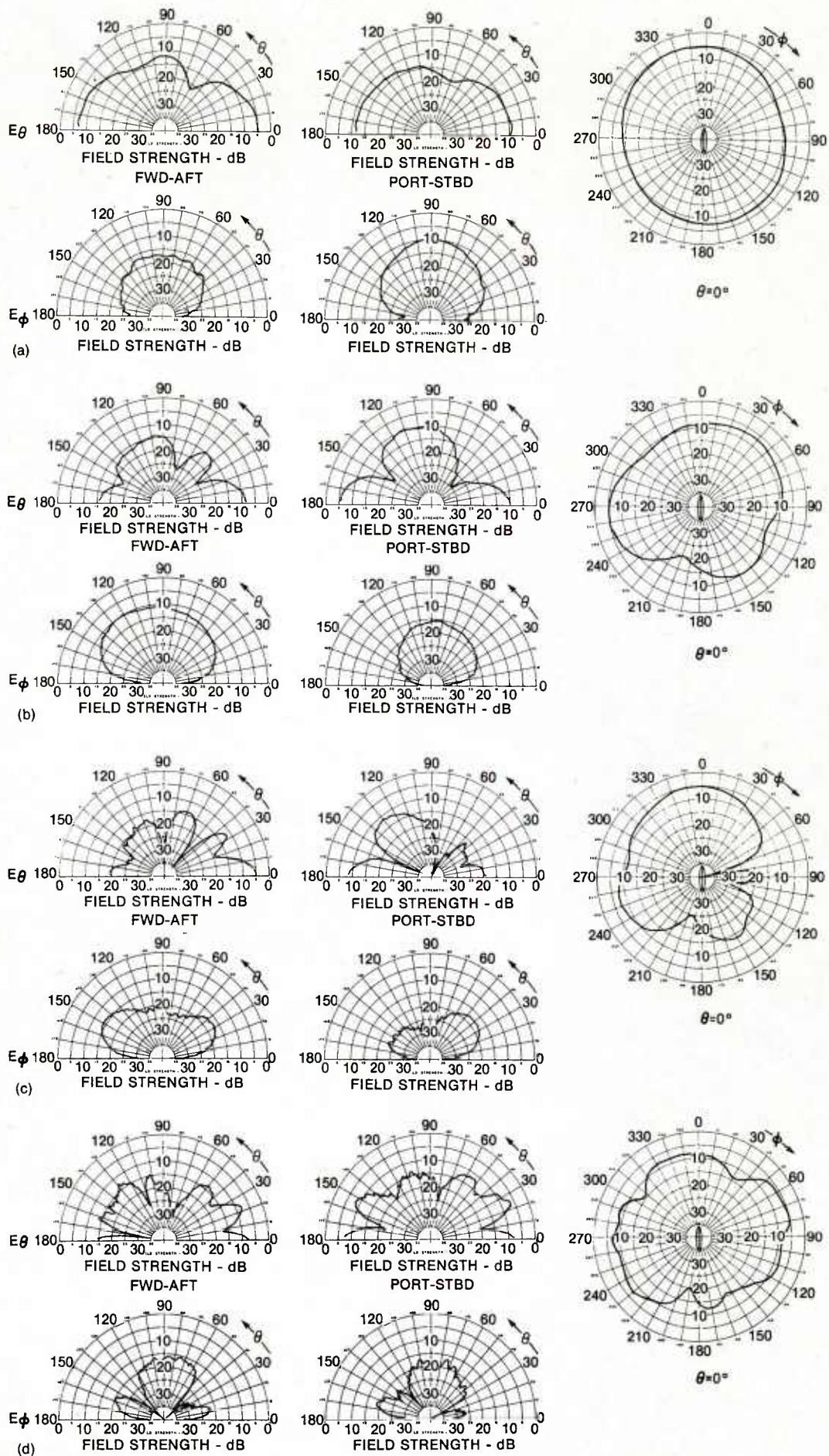(after McGregor, private communications).

Fig. 32 Antenna patterns for a standard vertical whip antenna on a Canadian frigate. These were measured for a modelled ship (see Fig. 1), on the NRC antenna pattern range. The various patterns refer to full scale frequencies: (a) 2; (b) 5; (c) 8; and (d) 14MHZ.
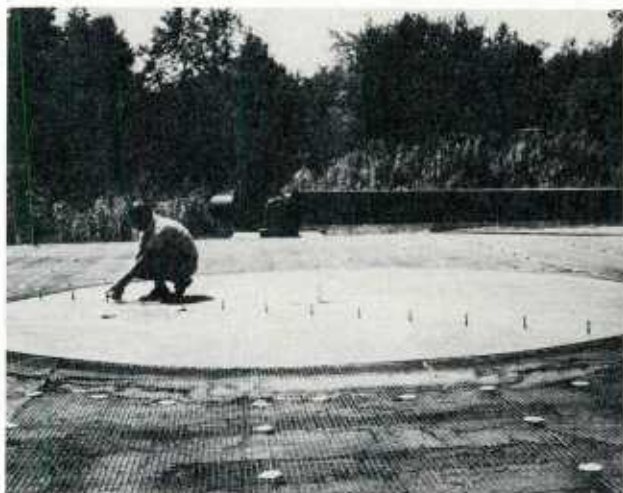
Fig. 33 Photographs of a 600/1 scale model of a power transmission line that runs nearby a MF broadcast antenna. The monopole at the centre of the turntable is surrounded by a styrofoam block to stabilize it against the wind. The upper photograph is a simplified situation; the lower photograph a more complicated model of a real situation.
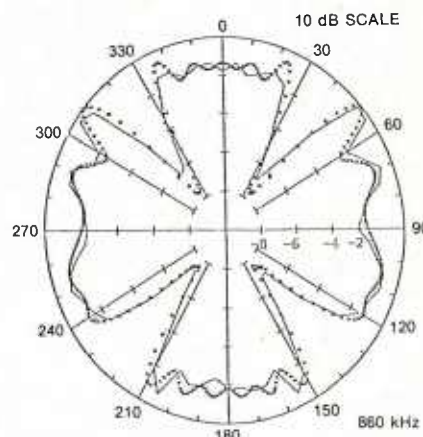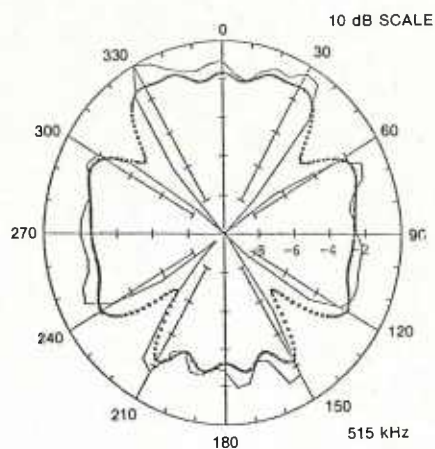

Fig. 34 Azmuthal pattern distortion for a monopole antenna caused by a 5-tower power transmission line at the 1λ (515kHz) and 2λ (860kHz) loop resonance frequencies. The solid lines were measured on the NRC ground level antenna pattern range. The crosses are the pattern predicted by a numerical method-of-moments calculation.
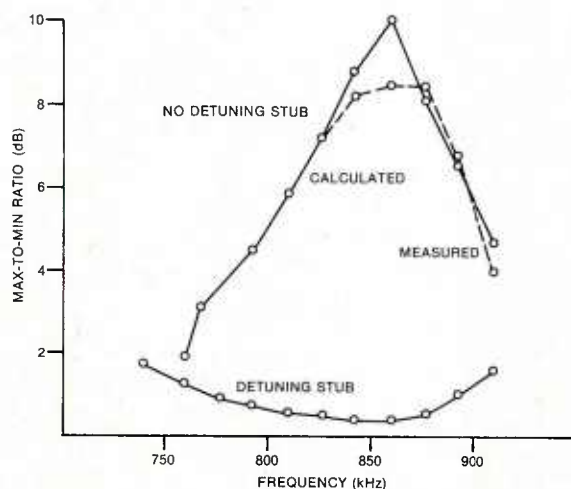

Fig. 35 Diagram illustrating how pattern distortion (max-to-min ratio measured by the scalloping of the omni-direction pattern) can be reduced by skywire detuners ($\lambda/4$ stubs). These results are for a 13-tower powerline.

CALCULATION OF GROUND WAVE ATTENUATION OVER IRREGULAR,
INHOMOGENEOUS, LAYERED MEDIA USING PROGRAM WAGNER

R. H. Ott
COMSAT Laboratories,
Clarksburg, Maryland 20871 USA

SUMMARY

A method for calculating the ground-wave field over irregular, inhomogeneous terrain has been developed, and comparisons with alternative analytical methods have been made for idealized terrain profiles such as concave parabolas, sea-land-sea paths, and single Gaussian ridges. This method employs a numerically efficient algorithm, PROGRAM WAGNER, based on an integral equation. PROGRAM WAGNER appears to be the only method general enough for calculating ground wave attenuation along detailed paths.

This paper explains the fundamentals of PROGRAM WAGNER to the user seeking to make path loss calculations. A users guide, the complete FORTRAN IV program listing, and sample input and output are included. Comparisons of computed field strengths are presented, with measured values over a path in the Netherlands at 10 frequencies from 2 to 30 MHz. Also, PROGRAM WAGNER at 5 and 30 MHz is compared with a method based on scattering from multiple knife edges. Finally, reciprocity is shown to provide necessary and useful criteria for spacing the observation points along the terrain profile.

1. INTRODUCTION

In 1952, Hufford proved that the integral equation formulation for radio wave propagation over a smoothly varying surface is reduced to the Van-der-Pol-Bremmer-Fock-Weyl-Logan-Wait residue series in the special case where the surface is spherical [1]. A numerically efficient algorithm (PROGRAM WAGNER) was developed in 1970 for an integral equation derived by using a Green's function closely related to the Sommerfeld flat earth attenuation function [2]-[5]. This integral equation has been found useful for calculating the ground wave field over irregular, inhomogeneous terrain and is the only method that appears to be general enough for detailed paths.

The following improvements have recently been made in PROGRAM WAGNER: development of linear interpolation to represent the terrain heights between the input terrain heights, versus distance, which can be obtained from existing digitized profiles; the inclusion of an effective height-gain function to account for the influence of an elevated transmitting and/or receiving antenna; and the modification of the integral equation for the case of propagation over terrain that has up to two layers in conductivity and dielectric constant, versus depth. A modification of PROGRAM WAGNER has been used to describe a theoretical method for predicting HF ground wave propagation over irregular terrain with forest, building, or snow cover [6]. This approach generalized PROGRAM WAGNER to allow for the effect of a lossy, anisotropic slab over the earth. Also, quoting Fer and Hizal, "The integral equation solution incorporated in PROGRAM WAGNER and extensively tested against measured results represents the most accurate available computer model" [7]-[12].

PROGRAM WAGNER is based on an integral equation that is a forward stepping solution in x [13]. Thus, values for the attenuation function are obtained at these values of x and are most useful for frequencies below about 30 MHz. For higher frequencies, the variability of the ground wave in time and space becomes large, and an accurate point-to-point prediction is difficult. A recent report has described an area prediction model for VHF, UHF, and SHF frequencies [14].

This paper briefly reviews the formulation of the integral equation. Results are shown for the following conditions: propagation from a forest to a clearing; two smooth paths of 60 and 80 km in the Netherlands, where comparisons with measurements are available from 2 to 30 MHz; and an irregular terrain in southern West Germany, where comparisons with multiple knife-edge diffraction are given. A users guide, program listing, and sample input and output for PROGRAM WAGNER are presented.

2. THE INTEGRAL EQUATION AND PROGRAM WAGNER

The attenuation function $f(x)$ is the ratio of the vertical electric field to twice the free-space field, E_O. The integral equation for $f(x)$ is ([9], also see Figure 1)

$$f(x) = W(x,0) - \sqrt{2\pi/ik} \int_0^x f(\xi) \ e^{-ik\phi(x,\xi)} \left\{ y'(\xi) \ W(x,\xi) \right.$$

$$\left. - \frac{y(x) - y(\xi)}{x - \xi} + [\Delta(\xi) - \Delta_a] \ W(x,\xi) \right\} \left[\frac{x}{\xi(x - \xi)} \right]^{1/2} d\xi \qquad (1)$$

where

$$\phi(x,\xi) = \frac{[y(x) - y(\xi)]^2}{2(x - \xi)} + \frac{y^2(\xi)}{2\xi} - \frac{y^2(x)}{2x}$$

$$W(x,\xi) = 1 - \sqrt{\pi p}\ w(-\sqrt{u})$$

$$p = -ik\Delta^2(\xi)\ (x - \xi)/2$$

$$u = p\left[1 - \frac{y(x) - y(\xi)}{\Delta(x - \xi)}\right]^2 \quad ;\ \xi < x$$

$$w(-\sqrt{u}) = e^{-u}\ \text{erfc}(i\sqrt{u})$$

$$= \frac{1}{i\pi} \int_{-\infty}^{\infty} \frac{e^{-t^2}\ dt}{\sqrt{u} + t} \quad ;\ \text{Im}(\sqrt{u}) > 0$$

$$\Delta(\xi) = \begin{cases} \dfrac{\sqrt{\eta - 1}}{\eta} & \text{, vertical polarization} \\ \\ \sqrt{\eta - 1} & \text{, horizontal polarization} \end{cases}$$

$$\eta(\xi) = \varepsilon_r(\xi) - \frac{i\ 18(10^3)\sigma(\xi)}{f(MHz)}$$

$$f = \text{frequency (MHz)}$$

$$\sigma(\xi) = \text{ground conductivity (MHo/m) as a function of distance}$$

$$\varepsilon_r(\xi) = \text{dielectric constant as a function of distance.}$$

In the above integral expression, $w(-\sqrt{u})$ is integrated along the path shown in Figure 2 [15].

For a flat terrain, $y(\xi) = y(x) = 0$ and $f(x)$ is

$$f(x) = 1 - i\sqrt{\pi p}\ w(-\sqrt{p}) \tag{2}$$

$$p = -ik\Delta^2 x/2$$

When $|p|$ is large

$$f(x) \sim \frac{-1}{2p} \quad ;\ -\frac{5\pi}{2} < \arg(p) < \pi/2 \tag{3}$$

Computer run time can be estimated as

$$\text{time} \propto (\text{path length})^2 \cdot (\text{frequency})^2 \tag{4}$$

A simple result for $|p|$ large and an elevated source, h_a, and an elevated receiver, h_r, is

$$f(x) \sim \frac{-1}{2p}\left(1 + ik\Delta h_a\right)\left(1 + ik\Delta h_r\right) \tag{5}$$

Appendix A contains a users guide, a program listing, and a sample input and output for PROGRAM WAGNER.

3. RECENT COMPARISONS

3.1 JUNGLE-CLEARING

Results are shown in Figure 3 for propagation from a forest or jungle to a clearing. The jungle profile versus distance, $h(x)$, together with the constitutive parameters of the jungle and ground are shown in the insert. A continuous transition from the jungle to the clearing was assumed, since this more nearly corresponds to a real situation.

In Figure 3, the magnitude of the attenuation function, $w(d)$, normalized to twice the free-space field (field over a flat perfect conductor) is plotted versus the horizontal distance, d, in meters. For comparison, the magnitude of the attenuation function, as given by the inhomogeneous term alone in the integral equation (1), is plotted versus distance, d. This would be the attenuation versus distance for no clearing. Note that two oscillations in the attenuation curve occur near the clearing. This corresponds to an interference effect as the radio wave propagates over the rounded edge of the clearing. Whether the full amount of this interference would occur in a real situation

is questionable, since, as indicated previously, some penetration of the waves at the transition region may occur. As the distance increases, the attenuation function undergoes a recovery caused by a redistribution in height of the radio energy.

3.2 SMOOTH PATHS IN THE NETHERLANDS

Measurements of field strength and bit error rate have recently been carried out on paths of 60 and 80 km in the Netherlands. Frequencies ranged from 2 to 30 MHz, and both vertical and horizontal polarization were transmitted and received. Both paths had the same transmitter, and the two paths were nearly in line. An examination of topographic maps of the area revealed that both paths were through smooth (less than a few meters in elevation change) unforested terrain with no cities. The main feature of interest was a section of low ground conductivity (dry, sandy soil) at the end of the 80-km path. The path was modeled with two smooth sections, as shown in Figure 4. No ground conductivity measurements were made, but the values $\varepsilon_g = 15$ and $\sigma_g = 10^{-2}$ S/m for the 70 km of good ground and $\varepsilon_g = 3$ and $\sigma_g = 10^{-4}$ S/m for the remaining section of poor ground were assumed [6].

In Figures 5 through 7, the magnitude of the attenuation function, f, is shown along the path for three different frequencies. As is usual, the attenuation function is defined as the ratio of the vertical electric field to the electric field over flat, perfectly conducting ground. Both the transmitting and receiving antennas are assumed to be located at the surface, and the measured data are adjusted to account for the antenna heights by assuming the height-gain function. Only the integral equation solution takes into account the poor ground section shown in Figure 4. In each case, the integral equation result shows a rapid drop in field strength beyond 70 km because of the decrease in ground constants. The measured data are consistent with this drop, but a detailed comparison is not possible because measurements are available only at 60 and 80 km. It appears that the ground conductivity and dielectric constant for the first 70 km were too high. Lower values would have provided a better fit with the measurements.

For comparison in Figures 5 through 7, the spherical earth and flat earth results are shown for a uniform path. Because the integral equation solution assumes no backscatter, it should agree with the sperical earth theory over the first 70 km. The accuracy of the integral equation solution becomes more difficult to maintain at higher frequencies and over longer paths. At 30 MHz, it was necessary to sample approximately every 40 m (or 4 wavelengths) along the path to obtain the imperfect agreement shown in Figure 7. This resulted in 2,000 sample points along the path and an execution time of approximately 15 minutes on the CYBER 750 computer.

3.3 IRREGULAR TERRAIN IN WEST GERMANY

The path considered in greatest detail was a 56.6-km path in West Germany from Inneringen to Boblingen. The terrain profile shown in Figure 8 was generated from the files of the Defense Mapping Agency. This profile agrees with the profile that was obtained by hand from 1:50,000 scale maps of the area. The ground parameters were $\varepsilon_r = 10$ and $\sigma_g = 10^{-2}$ S/m. To check PROGRAM WAGNER, the multiple knife-edge algorithm of Vogler [16] was evaluated at 11 points along the path. In Figures 9 and 10, the results of the Vogler algorithm and PROGRAM WAGNER are compared for 5 and 30 MHz. The agreement is slightly better at 30 MHz, but is satisfactory even at 5 MHz. Hill [6] used reciprocity to check PROGRAM WAGNER for this path and found that reciprocity was satisfied at 2 MHz, with some differences at 20 MHz.

4. CONCLUSIONS

Past calculations [2],[17]-[20] have shown the usefulness of PROGRAM WAGNER for predicting the performance of antennas on cliffs, near sloping beaches, near clearings, in forest-covered and vegetated media, and on a snow overburden. Future applications of PROGRAM WAGNER to cases where the topography in the vicinity of an antenna is an important factor will yield better guidelines for siting antennas. According to Hill [6], "The only method which appears to be general enough for detailed predictions over arbitrary paths is the integral equation method."

REFERENCES

[1] Hufford, G. A., "An Integral Equation Approach to the Problem of Wave Propagation Over an Irregular Surface," Q Appl Math, Vol. 9, 1952, pp. 391-404.

[2] Ott, R. H., "An Alternative Integral Equation for Propagation Over Irregular Terrain," Radio Sci, Vol. 5, No. 5, May 1970, pp. 767-771.

[3] Ott, R. H., "An Alternative Integral Equation for Propagation Over Irregular Terrain, 2," Radio Sci, Vol. 6, No. 4, 1971, pp. 429-435.

[4] Ott, R. H., "A New Method for Predicting HF Ground Wave Attenuation Over Inhomogeneous, Irregular Terrain," U.S. Department of Commerce, Research Report No. OT/TRER 7, January 1971 (NTIS Access No. AB721179).

[5] Ott, R. H., "Fock Currents for Concave Surfaces," IEEE Trans Ant Prop, Vol. AP-22, No. 2, March 1974, pp. 357-360.

[6]   Hill, D. A., "HF Ground Wave Propagation Over Forested and Built-Up Terrain," U.S. Department of Commerce, NTIA Report No. 82-114, 1982.

[7]   Fer, A. F. and A. Hizal, "Medium Wave Ground Wave Propagation Model--Numerical and Experimental Results," AGARD Conference Proc, No. 332, EPP Symposium on Propagation Aspects of Frequency Sharing, Interference, and System Diversity, Issy-les-Moulineaux, France, October 18-22, 1982, pp. 14-1 to 14-8.

[8]   Ott, R. H., "Ground Wave Propagation Over Irregular, Inhomogeneous Terrain: Comparisons of Calculations and Measurements at Frequencies From 121 kHz to 50 MHz," AGARD Conference Proc, No. 269, EPP Symposium on Terrain Profiles and Contours in Electromagnetic Wave Propagation, Edited by A. W. Biggs, Spatind, Norway, September 10-14, 1979, pp. 8-1 to 8-12.

[9]   Ott, R. H., L. E. Vogler, and G. A. Hufford, "Ground-Wave Propagation Over Irregular, Inhomogeneous Terrain: Comparisons of Calculations and Measurements," U.S. Department of Commerce, NTIA Report No. 79-20, 1979.

[10] Ott, R. H., "Theories of Ground Wave Propagation Over Mixed Paths," AGARD Conference Proc, No. 269, EPP Symposium on Terrain Profiles and Contours in Electromagnetic Wave Propagation," Edited by A. W. Biggs, Spatind, Norway, September 10-14, 1979, pp. 6-1 to 6-9.

[11] Ott, R. H., "Analysis of Ground Wave Propagation Over Irregular, Inhomogeneous Terrain," AGARD Conference Proc, No. 144, EPP Symposium on Electromagnetic Wave Propagation Involving Irregular Surfaces and Inhomogeneous Media," Edited by A. N. Ince, The Hague, Netherlands, March 25-29, 1974, pp. 25-1 to 25-6.

[12] Ott, R. H., L. E. Vogler, and G. A. Hufford, "Ground-Wave Propagation Over Irregular, Inhomogeneous Terrain: Comparisons of Calculations and Measurements," IEEE Trans Ant Prop, Vol. AP-27, No. 2, March 1979, pp. 284-286.

[13] Wagner, C., "On the Numerical Solution of Volterra Integral Equations, J Math and Physics, Vol. 32, 1953, pp. 289-401.

[14] Hufford, G. A., A. G. Longley, and W. A. Kissick, "A Guide to the Use of the ITS Irregular Terrain Model in the Area Prediction Mode," NTIA Report No. 82-100, 1982.

[15] Abramowitz, M. and I. A. Stegun, Handbook of Mathematical Functions, NBS Applied Mathematics Series 55, U.S. Government Printing Office, June 1964.

[16] Vogler, L. E., "The Attenuation of Electromagnetic Waves by Multiple Knife-Edge Diffraction," NTIA Report No. 81-86, 1981.

[17] Ott, R. H., and J. R. Wait, "Excitation Mechanisms for Transmission Through Forest-Covered and Vegetated Media," U.S. Department of Commerce, Office of Telecommunications, Boulder, Colorado, Technical Report No. ACC-ACO-8-73, (NTIS Access No. AD771915), 1973.

[18] Ott, R. H., and J. R. Wait, "A First Approach to the Propagation of Lateral Waves in an Inhomogeneous Jungle," U.S. Department of Commerce, Office of Telecommunications, Technical Memorandum No. 73-154, 1973.

[19] Ott, R. H., "Radiation Fields From HF Coastal Antennas," U.S. Department of Commerce, Office of Telecommunications, Technical Memorandum No. 74-174, June 1974.

[20] Bussey, H. E. and R. H. Ott, "A Brief Treatment of a Vertical Dipole in or on a Snow Overburden," U.S. Department of Commerce, NBS Report No. 10742, March 1972.
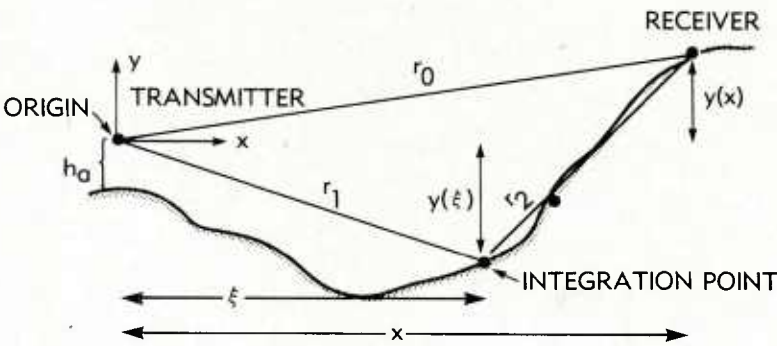
ACKNOWLEDGMENT

3-5

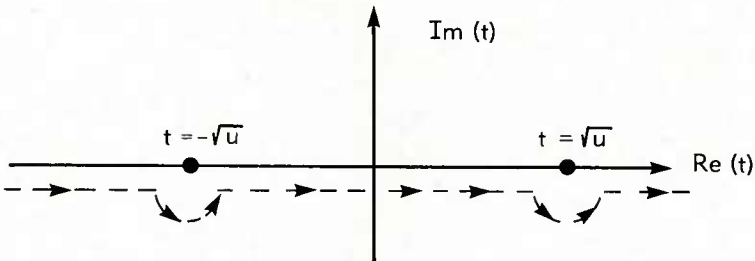Figure 1. Great Circle Path Geometry for Integral Equation

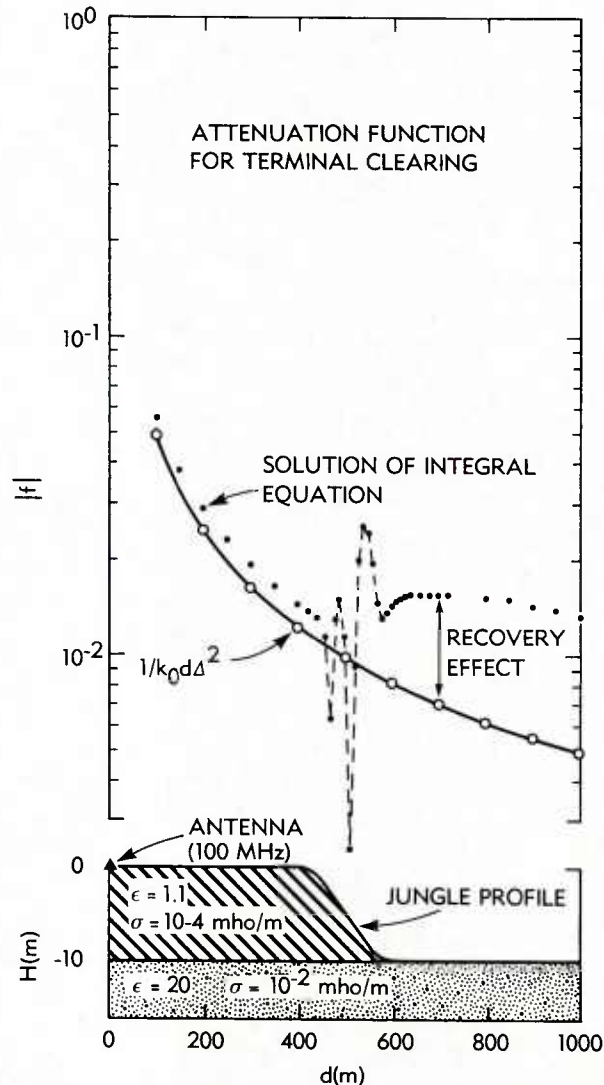Figure 2. Complex t-Plane Path for Integral Representation of $w(-\sqrt{\bar{u}})$

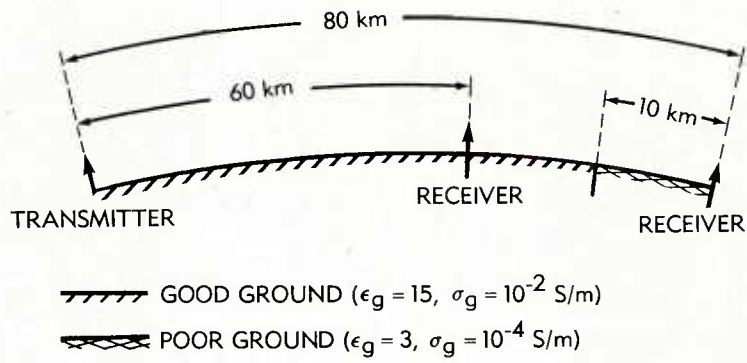Figure 3. Attenuation Function for Terminal Clearing

Figure 4. Smooth Path in the Netherlands With Receiving Sites at 60 km and 80 km
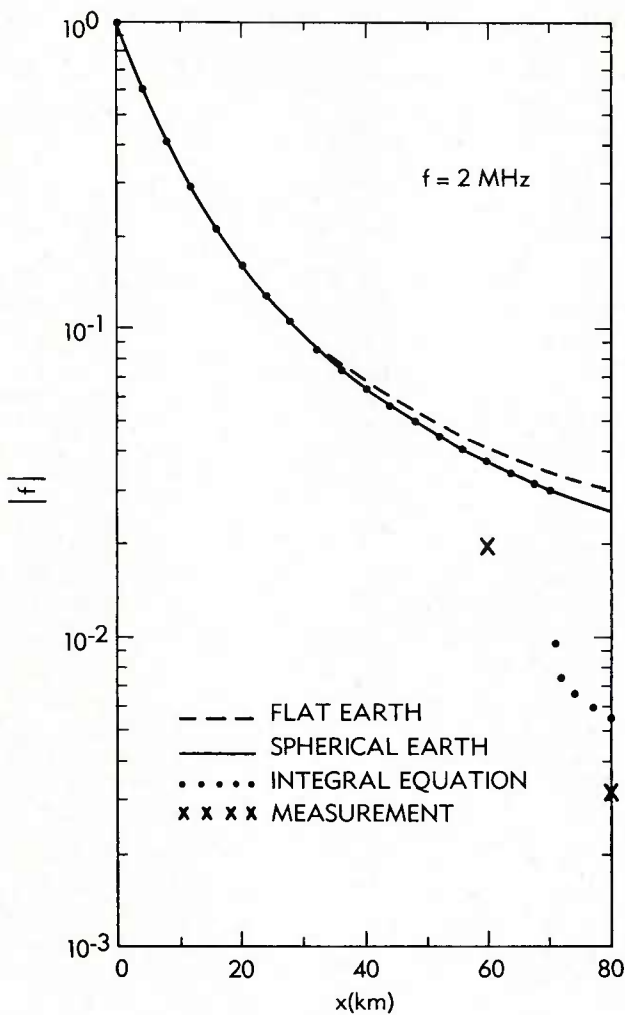

Figure 5. Comparison of Measurements With Three Theories at 2 MHz for a Smooth Path in the Netherlands
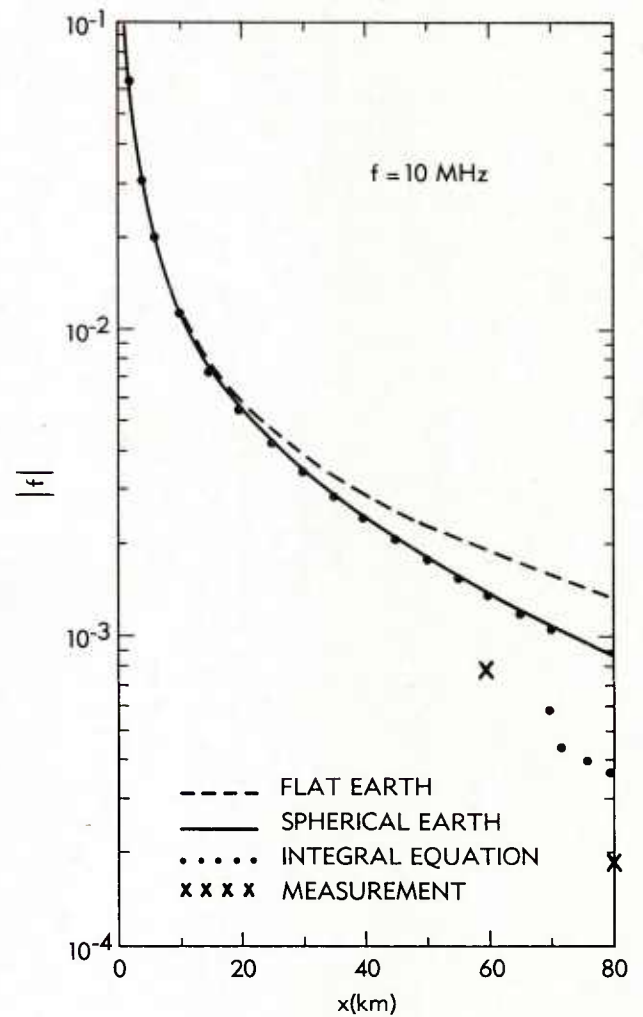
Figure 6. Comparison of Measurements With Three Theories at 10 MHz for a Smooth Path in the Netherlands
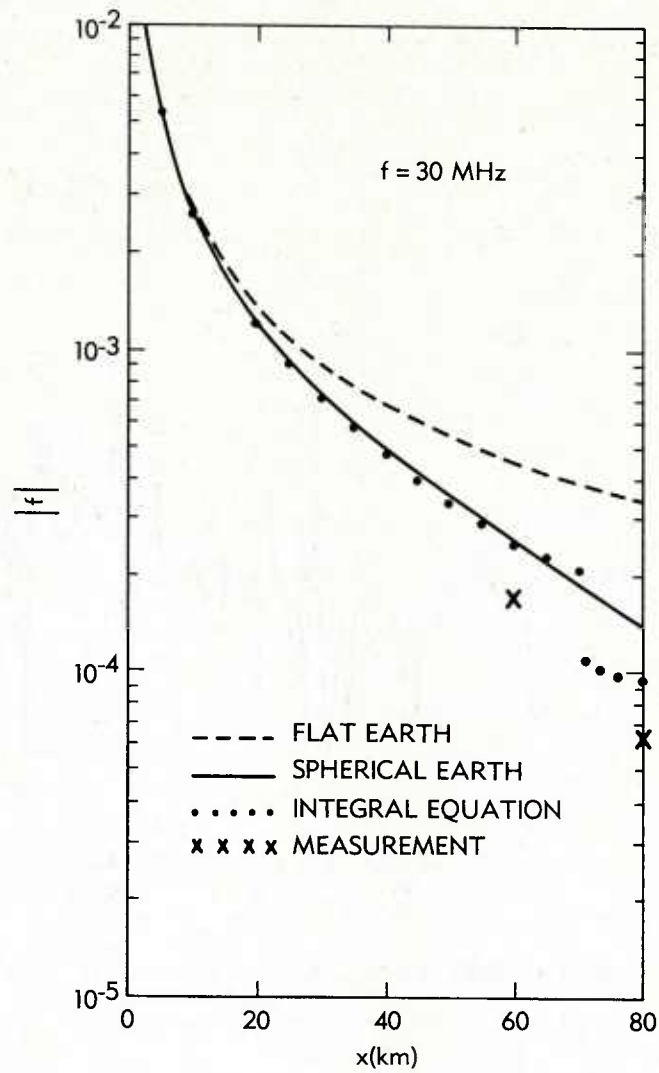
Figure 7.   Comparison of Measurements With Three Theories at 30 MHz
            for a Smooth Path in the Netherlands
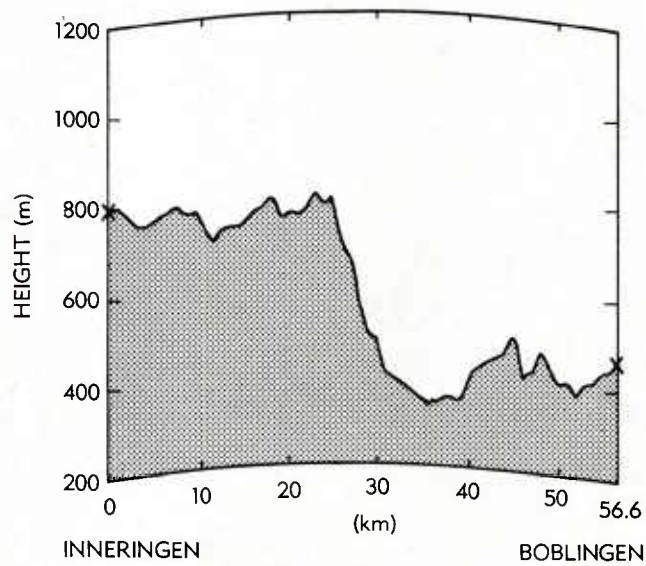

Figure 8.   Terrain Profile for the Path From Inneringen to Boblingen
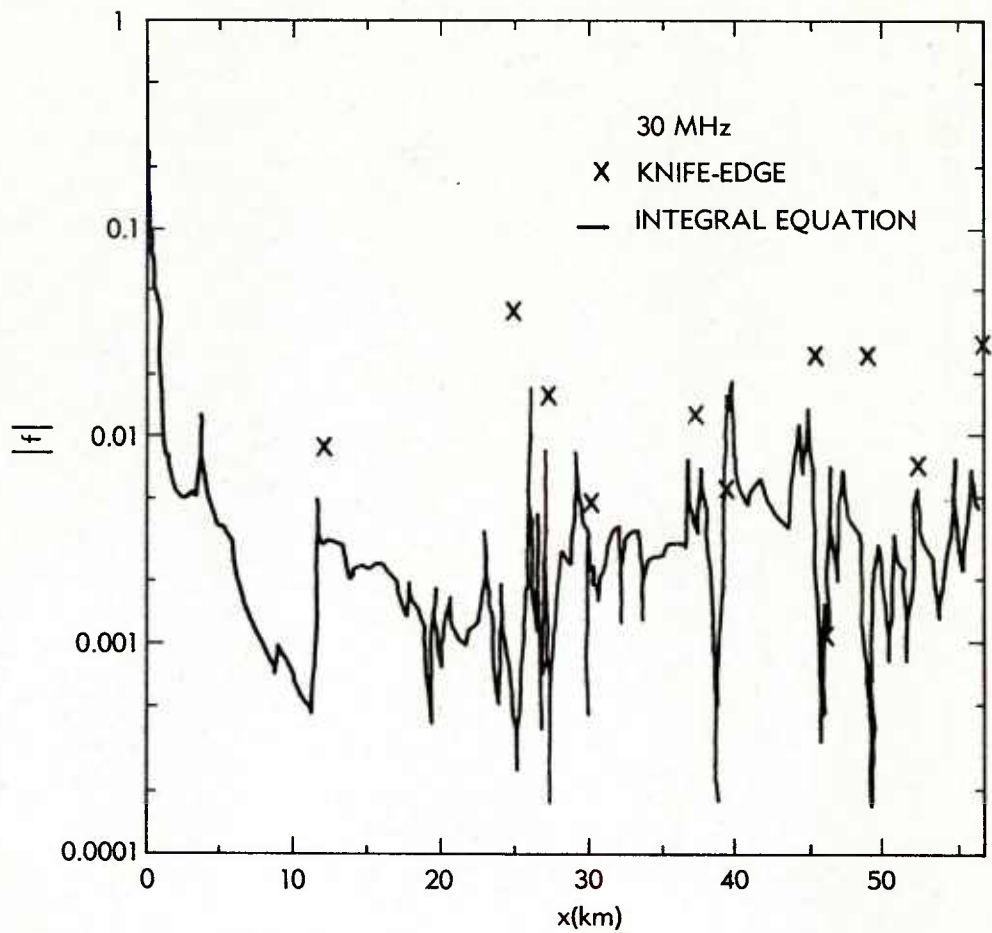
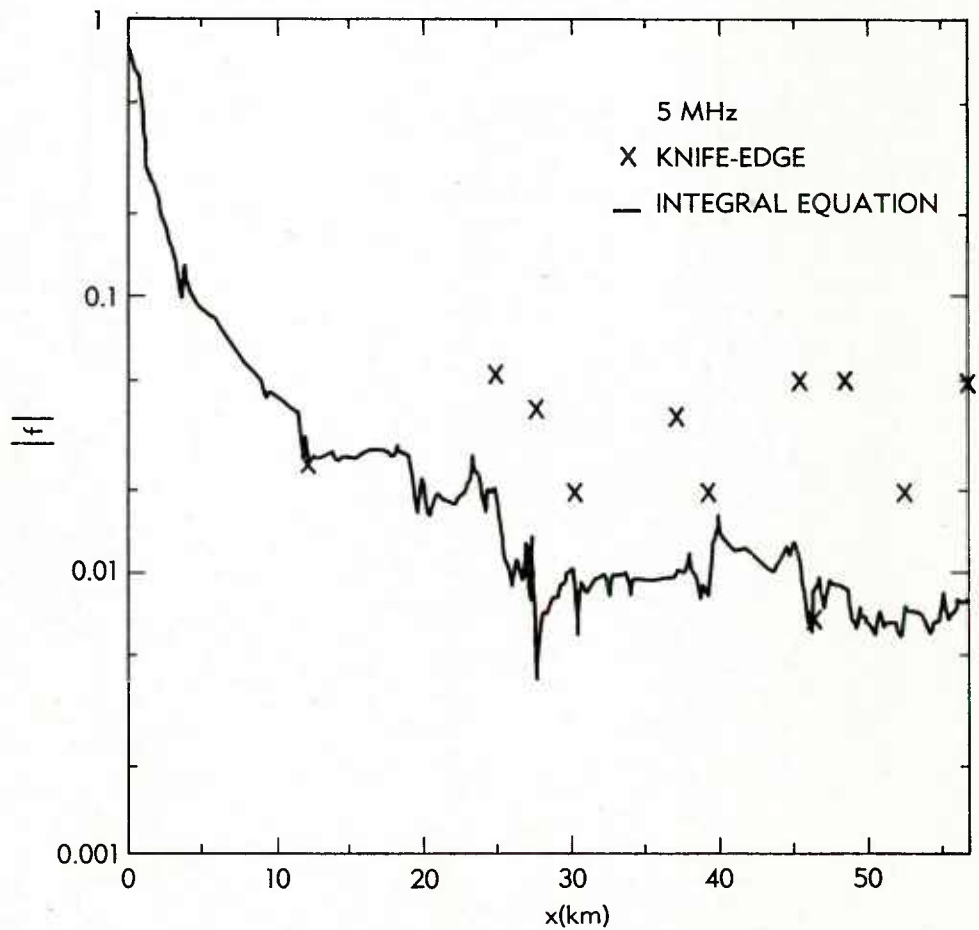Figure 9.   Inneringen to Boblingen With 40-m Spacing at 30 MHz (8/10/82)

Figure 10.   Inneringen to Boblingen With 200-m Spacing at 5 MHz (8/12/82)

APPENDIX
PROGRAM WAGNER

A.1 USERS GUIDE

This section describes the input data for PROGRAM WAGNER. Most of the quantities described are shown in Figure 1. Note that, on Card 3, the antenna heights are given in reference to the local elevation, rather than to sea level.

Card 1: KIND, TC (I10, F10.0)
    KIND = Beginning type of distance at which F(x) will be evaluated.
        1 is specified on next cards
        0 is equidistant
    TD = Total distance in kilometers

Card 2A: X(I)   (8F10.5)
    X(I) = Specific distances in kilometers at which F(x) will be evaluated.
    If KIND = 1, use these cards to begin giving specific distances until you are
        done or want to change to equidistant points.
        Terminate this set of distances with a 0.

Card 2B1: NED (I2)
    NED = Number (limited to 50) of consecutive sections with F(x) evaluated at
        equidistant points.
        (This should agree with the number of pairs of DEP and FINT.)

Card 2B2: (DEP(I), FINT(I), I = 1, NED) (8F10.0)
    DEP(I) = Distance in kilometers at which this set of equidistant points ends.
    FINT(I) = Interval of these equidistant points in kilometers.
    If KIND = 0, use these cards to begin.

(Note: A series of 2A and 2B cards may be needed to reach the total distance given on card 1).

Card 3: HA, FREQ, HAR, AKM (4F10.5)
    HA = Transmitter antenna height in kilometers = $h_a - D$
    FREQ = Frequency in megahertz
    HAR = Receiver antenna height in kilometers = $h_r - D$
    AKM = Earth radius in kilometers

Card 4: ID (8A10)
    ID = Path identification

Card 5: N, IXUNITS, IZUNITS, REFEL (3I10, F10.1)
        N = Number of points on terrain profile
    IXUNITS = 0, distance input in kilometers
         = 1, distance input in statute miles
    IZUNITS = 0, height input in meters
         = 1, height input in feet
    REFEL = Reference elevation in IZUNITS (= height at d = 0)

Card 6 to N: (X(I), I = 1, N) (4(F10.2, F10.0))
        X(I) = Terrain distances in IXUNITS
        Z(I) = Terrain heights in IZUNITS

Card M+1: NGC (I10)
    NGC = Number of sets of ground constants (limited to 50)

Card M+2 to end: (DX(I), SIGX(I), EPSX(I), I = 1, NGC)
        (4(F7.0, F7.4, F6.0))
        DX(I) = Maximum distance in kilometers for given set of ground
            constants
        SIGX(I) = Sigma of ground = σ_g
        EPSX(I) = Epsilon of ground = ε_g

A.2 PROGRAM LISTING

FILE: WAGNER   FORTRAN   A   COMSAT COMPUTER CENTER

```
      DIMENSION IPOL(2)
      DIMENSION ADAB(3),ADGH(3)
      DIMENSION F(2000),R13(2000),R14(2000),R15(2000),R16(2000),
     1R17(2000),R18(2000),R19(2000),R20(2000),R21(2000),
     1FLDS(1000),DKM(1000)
      COMMON/C1/HA,AKM
      COMMON /C2/D,H,HP
      COMMON /C3/DELTAR,WAVE
      COMMON /C4/FREQ,POL
      COMMON /C5/NG,AB(48),GH(48)
      COMMON /C6/N,X(2001),INDEX
      COMMON /INPUT/ DUMM(10320),ID(8),REFEL
```

```
      COMMON /GCX/ NGC,DX(50),ETAX(50),DELTAX(50),SIGX(50),EPSX(50)
      COMPLEX ETAX,DELTAX
      DOUBLE PRECISION DAB,DGH
      COMPLEX PEWH,P,ALAMZ,SUM,DELTAR,ETAR
      COMPLEX KERNL,P0,P1,P2,P3,P4,CTMP
      COMPLEX PP,ETA,DELTA
      DATA ADAB/.9061798459,.5384693101,0./
      DATA ADGH/.2369268851,.4786286704,.56888888888/
      CANG(Z) = ATAN2(AIMAG(Z),REAL(Z))
      NG = 5
      DATA IPOL(1)/4HVERT/
      DATA IPOL(2)/4HHORZ/
C
C
C              READ GAUSSIAN QUADRATURE ABCISSAS AND WEIGHTS
C
      NR = (NG+1)/2
      DO 1 L = 1,NR
      DAB = ADAB(L)
      DGH = ADGH(L)
      J = NG-L+1
      AB(L) = DAB
      AB(J) = -AB(L)
      GH(L) = DGH
    1 GH(J) = GH(L)
C
C         CALL SUBROUTINE TO SET UP DISTANCE ARRAY X IN METERS
C         START WITH X(2). X(1) = 0. HAS ALREADY BEEN SET.
C         THE DISTANCES DO NOT HAVE TO BE EQUALLY SPACED.
C         SUBROUTINE DISTX SHOULD MAKE SURE N LE 2000.
C
    4 X(1) = 0.
      P(1) = (1.,0.)
      CALL DISTX
C
C         MAKE SURE THERE ARE AT LEAST 4 DISTANCES
C
      IF (N.GE.4) GO TO 2
      WRITE (6,18)
      CALL EXIT
C
    2 SQRTX2 = SQRT(X(2))
      SQRTX3 = SQRT(X(3))
      SQRTX4 = SQRT(X(4))

      D1 = SQRT(X(2)*X(3)*X(4))*(X(2)*(SQRTX4-SQRTX3)+X(3)*(SQRTX2-SQ
     1RTX4)+X(4)*(SQRTX3-SQRTX2))
      R1 = X(3)*X(4)*(SQRTX4-SQRTX3)/D1
      R2 = X(2)*X(4)*(SQRTX2-SQRTX4)/D1
      R3 = X(2)*X(3)*(SQRTX3-SQRTX2)/D1
      R4 = (X(2)*(SQRTX4**3-SQRTX3**3)+X(3)*(SQRTX2**3-SQRTX4**3)+X(4)
     1*(SQRTX3**3-SQRTX2**3))/D1
      R5 = SQRT(X(3)*X(4))*(X(3)-X(4))/D1
      R6 = SQRT(X(2)*X(4))*(X(4)-X(2))/D1
      R7 = SQRT(X(2)*X(3))*(X(2)-X(3))/D1
      R8 = (SQRTX2*(SQRTX3**3-SQRTX4**3)+SQRTX3*(SQRTX4**3-SQRTX2**3)+
     1SQRTX4*(SQRTX2**3-SQRTX3**3))/D1
      R9 = SQRT(X(3)*X(4))*(SQRTX4-SQRTX3)/D1
      R10 = SQRT(X(2)*X(4))*(SQRTX2-SQRTX4)/D1
      R11 = SQRT(X(2)*X(3))*(SQRTX3-SQRTX2)/D1
      R12 = (SQRTX2*(X(4)-X(3))+SQRTX3*(X(2)-X(4))+SQRTX4*(X(3)-X(2)))
     1/D1
      DO 3 M = 5,N
      M1 = M-1
      M2 = M-2
      DELTA1 = X(M)-X(M1)
      DELTA2 = X(M)-X(M2)
      D2 = (DELTA1-DELTA2)*DELTA1*DELTA2
      R13(M) = X(M1)*X(M2)*(X(M2)-X(M1))/D2
      R14(M) = X(M)*X(M2)*(X(M)-X(M2))/D2
      R15(M) = X(M)*X(M1)*(X(M1)-X(M))/D2
      R16(M) = (X(M1)**2-X(M2)**2)/D2
      R17(M) = (X(M2)**2-X(M)**2)/D2
      R18(M) = (X(M)**2-X(M1)**2)/D2
      R19(M) = (X(M2)-X(M1))/D2
      R20(M) = (X(M)-X(M2))/D2
    3 R21(M) = (X(M1)-X(M))/D2
C
C         READ SOURCE HEIGHT, FREQUENCY, AND POLARIZATION
C    COL          DESCRIPTION
C    1-10         SOURCE HEIGHT, KM
C    11-20        FREQUENCY, MHZ
C    21-30        POLARIZATION, 1. = VERTICAL, 2. = HORIZONTAL
```

```
C       31-40      RECEIVE ANTENNA HEIGHT(M)
C       41-50      EARTH RADIUS(KM)
C
        READ (5,19) HA,FREQ,POL,HAR,AKM
        IQT = 0
        HAR = HAR*1.E+3
        HA = HA*1.E3
        KPOL = POL
        ALAM = 2.997925E2/FREQ
        WAVE = 6.283185307/ALAM
        ALAMZ = ((0.7071067812,0.7071067812)/SQRT (ALAM))
C
C            LOOP ON DISTANCE
C
        DO 14 I = 1,N
        INDEX = I
        IF (I .NE. 1) GO TO 51

        CALL TERAN2(X(I),H,HP,ETA,DELTA,ETAR,DELTAR,COND,EPS)
        WRITE (6,20)FREQ,IPOL(KPOL),AKM,HA,HAR
        GO TO 52
   51   CALL TERANE (X(I),H,HP,ETA,DELTA,ETAR,DELTAR,COND,EPS)
   52   CONTINUE
        IF (I.EQ.1) GO TO 14
        D = X(I)+(H**2)/(2.*X(I))
        F(I) = FEWH(H,X(I))
        IF (I.LE.6) GO TO 13
C
C                J = 2 THROUGH 4
C
        SUM = (0.,0.)
        DO 9 J = 2,4
        P0 = (0.,0.)
        P1 = (0.,0.)
        P2 = (0.,0.)
        P3 = (0.,0.)
        K = J-1
        XP2 = 0.5*(X(J)+X(K))
        XM2 = 0.5*(X(J)-X(K))
        DO 7 M = 1,NG
        X0 = XP2+AB(M)*XM2
        CTMP = KERNL(X0)*GH(M)
        P1 = P1+CTMP*SQRT(X0)
        P2 = P2+CTMP*X0
        P3 = P3+CTMP*SQRT(X0)**3
        IF (K.NE.1) GO TO 6
        X0 = 0.25*X(J)*(1.+AB(M))**2
        P0 = P0+SQRT(X0)*KERNL(X0)*GH(M)
        GO TO 7
   6    P0 = P0+CTMP
   7    CONTINUE
        P1 = P1*XM2
        P2 = P2*XM2
        P3 = P3*XM2
        IF (K.NE.1) GO TO 8
        P0 = P0*SQRT(X(J))
        GO TO 9
   8    P0 = P0*XM2
   9    SUM = SUM+P0+R4*P1+R8*P2+R12*P3+F(2)*(R1*P1+R5*P2+R9*P3)+F(3)*(R2*
       1P1+R6*P2+R10*P3)+F(4)*(R3*P1+R7*P2+R11*P3)
C
C                J = 5 THROUGH I-1
C
        I1 = I-1
        DO 11 J = 5,I1
        P0 = (0.,0.)
        P2 = (0.,0.)
        P4 = (0.,0.)
        XP2 = 0.5*(X(J)+X(J-1))
        XM2 = 0.5*(X(J)-X(J-1))
        DO 10 M = 1,NG
        X0 = XP2+AB(M)*XM2
        CTMP = KERNL(X0)*GH(M)
        P0 = P0+CTMP
        P2 = P2+CTMP*X0
   10   P4 = P4+CTMP*X0**2
        P0 = P0*XM2
        P2 = P2*XM2
        P4 = P4*XM2
   11   SUM = SUM+F(J-2)*(R15(J)*P0+R18(J)*P2+R21(J)*P4)+F(J-1)*(R14(J)*
       1P0+R17(J)*P2+R20(J)*P4)+F(J)*(R13(J)*P0+R16(J)*P2+R19(J)*P4)
```

```
C
C                   J = I
C
      THETA = ASIN (SQRT(X(I1)/X(I)))
      CTHETA = COS (THETA)
      P0 = (0.,0.)
      P2 = (0.,0.)
      P4 = (0.,0.)
      DO 12 M = 1,NG
      TEMP = 1.-0.25*CTHETA**2*(1.+AB(M))**2
      X0 = X(I)*TEMP
      CTMP = SQRT(X(I)  -X0)*KERNL(X0)*GH(M)
      P0 = P0+CTMP
      P2 = P2+CTMP*TEMP
   12 P4 = P4+CTMP*TEMP**2
      P0 = P0*CTHETA*SQRT(X(I))
      P2 = P2*CTHETA*SQRT(X(I))**3
      P4 = P4*CTHETA*SQRT(X(I))**5
      F(I) = (F(I) -ALAMZ*(SUM+F(I-2)*(R15(I)*P0+R18(I)*P2+R21(I)*P4)+F(I
     11)*(R14(I)*P0+R17(I)*P2+R20(I)*P4)))/(1.+ALAMZ*(R13(I)*P0+R16(I)*P
     12+R19(I)*P4))
   13 AMP = CABS(F(I))
      PHA = CANG(F(I))
      FF = (1.+(0.,1.)*DELTA*WAVE*HAR)*F(I)
      RR1 = CABS(FF)
      RR2 = 20.*ALOG10(WAVE*X(I)/RR1)
      BLT = RR2
      FLDS(I) = 139.37+20.*ALOG10(FREQ) -RR2
      DMI = X(I)*.00062137
      DKM(I) = X(I)*.001
      ZFT = (X(I)*X(I)*1.E-3/(2.*AKM)+HA+REFEL+H)*3.2808
      WRITE (6,22) X(I),H,ZFT,COND,EPS,AMP,PHA,DMI,FLDS(I),BLT
   14 CONTINUE
C
      GO TO 4
C
   18 FORMAT (' NUMBER OF DISTANCES LESS THAN 4')
   19 FORMAT (5F10.5)
   20 FORMAT ('1FREQUENCY = ',F10.2,16X,A4,'POLARIZATION',8X,'EARTH RADI
     CUS = 'F8.3,'KM'/
     C1X,'TRANSMITTER ANTENNA HEIGHT = 'F8.3,' METERS',10X,'RECEIVER ANT
     CNNA HEIGHT = 'F8.3,' METERS'//
     39X,'X',10X,'Z',9X,'HT',5X,'CONDUCTIVITY',3X,'DIELECTRIC',15X,'F(X)
     4'17X,'FIELD STRENGTH',2X,'BTL'/
     58X,'(M)',8X,'(M)',8X,'FT',8X,'(MHO/M)',6X,'CONSTANT',8X,'MAG',
     613X,'ARG',11X,'MI',3X,' (DBU)')
   22 FORMAT (F12.2,F10.1,F10.1,F14.6,F13.4,E18.8,E16.8,F7.1,
     12F8.2)
      END



      COMPLEX FUNCTION KERNL(X0)
      COMMON/C1/HA,AKM
      COMMON /C2/D,H,HP
      COMMON /C3/DELTAR,WAVE
      COMMON /C4/FREQ,POL
      COMMON /C5/NG,AB(48),GH(48)
      COMMON /C6/NX,X(2001),I
      COMPLEX FEWH,DELTA,DELTAR,ETA,ETAR
      CALL TERANE (X0,H0,HP0,ETA,DELTA,ETAR,DELTAR,COND,EPS)
      XMS = X(I) -X0
      HD = H-H0
      R1 = SQRT(X0**2+HA**2)
      RW = WAVE*(X0+((H0**2)/(2.*X0))+XMS+((HD**2)/(2.*XMS))-D)
      KERNL = CMPLX(COS (RW),-SIN (RW))*SQRT(X(I)/(R1*XMS))*((HP0+DELTA-
     1DELTAR)*FEWH(HD,XMS)-(HD/XMS))
      RETURN
      END
```

900.00	-54.5	5249.5	0.015000	15.0000	0.89832675E+00	-0.40818995E+00	0.6	112.85	29.99
1000.00	-55.2	5247.1	0.015000	15.0000	0.89445102E+00	-0.43279403E+00	0.6	111.89	30.94
1100.00	-56.0	5244.8	0.015000	15.0000	0.89020157E+00	-0.45671582E+00	0.7	111.02	31.81
1200.00	-56.7	5242.4	0.015000	15.0000	0.88591230E+00	-0.47971582E+00	0.7	110.23	32.61
1300.00	-57.4	5240.1	0.015000	15.0000	0.88161707E+00	-0.50186628E+00	0.8	109.49	33.35
1400.00	-58.2	5237.8	0.015000	15.0000	0.87738550E+00	-0.52318311E+00	0.9	108.80	34.03
1500.00	-58.9	5235.4	0.015000	15.0000	0.87319326E+00	-0.54376853E+00	0.9	108.16	34.67
1600.00	-59.6	5233.1	0.015000	15.0000	0.86905110E+00	-0.56367981E+00	1.0	107.56	35.27
1700.00	-57.6	5239.9	0.015000	15.0000	0.88034618E+00	-0.56403762E+00	1.1	107.15	35.69
1800.00	-57.6	5239.9	0.015000	15.0000	0.87420177E+00	-0.58561122E+00	1.1	106.59	36.25
1900.00	-57.6	5239.9	0.015000	15.0000	0.86969483E+00	-0.60427928E+00	1.2	106.07	36.76
2000.00	-57.6	5239.9	0.015000	15.0000	0.86568522E+00	-0.62193573E+00	1.2	105.59	37.25
2100.00	-57.5	5240.5	0.015000	15.0000	0.86560857E+00	-0.63461369E+00	1.3	105.16	37.67
2200.00	-56.7	5243.2	0.015000	15.0000	0.86545861E+00	-0.64658052E+00	1.4	104.76	38.08
2300.00	-55.9	5245.9	0.015000	15.0000	0.86372697E+00	-0.66009593E+00	1.4	104.35	38.48
2400.00	-55.1	5248.6	0.015000	15.0000	0.86144900E+00	-0.67395091E+00	1.5	103.96	38.87
2500.00	-54.3	5251.4	0.015000	15.0000	0.85885978E+00	-0.68788135E+00	1.6	103.58	39.25
2600.00	-53.5	5254.1	0.015000	15.0000	0.85610259E+00	-0.70173180E+00	1.6	103.21	39.62
2700.00	-52.7	5256.8	0.015000	15.0000	0.85320294E+00	-0.71548498E+00	1.7	102.86	39.98
2800.00	-51.9	5259.5	0.015000	15.0000	0.85020292E+00	-0.72910666E+00	1.7	102.51	40.33
2900.00	-51.1	5262.3	0.015000	15.0000	0.84713900E+00	-0.74256498E+00	1.8	102.17	40.66
3000.00	-50.3	5265.0	0.015000	15.0000	0.84403098E+00	-0.75584894E+00	1.9	101.85	40.99
3100.00	-49.5	5267.7	0.015000	15.0000	0.84086990E+00	-0.76898503E+00	1.9	101.53	41.31
3200.00	-48.7	5270.4	0.015000	15.0000	0.83769393E+00	-0.78193021E+00	2.0	101.22	41.61
3300.00	-47.9	5273.2	0.015000	15.0000	0.83447576E+00	-0.79473114E+00	2.1	100.92	41.91
3400.00	-47.1	5275.9	0.015000	15.0000	0.83126330E+00	-0.80734318E+00	2.1	100.63	42.21
3500.00	-46.3	5278.6	0.015000	15.0000	0.82803285E+00	-0.81979674E+00	2.2	100.34	42.49
3600.00	-45.5	5281.3	0.015000	15.0000	0.82479894E+00	-0.83209097E+00	2.2	100.06	42.77
3700.00	-44.7	5284.1	0.015000	15.0000	0.82155335E+00	-0.84423214E+00	2.3	99.79	43.04
3800.00	-43.9	5286.8	0.015000	15.0000	0.81830394E+00	-0.85621870E+00	2.4	99.52	43.31
3900.00	-43.2	5289.5	0.015000	15.0000	0.81507206E+00	-0.86803269E+00	2.4	99.26	43.57
4000.00	-42.4	5292.2	0.015000	15.0000	0.81184697E+00	-0.87970668E+00	2.5	99.01	43.82
4100.00	-41.6	5295.0	0.015000	15.0000	0.80860567E+00	-0.89125013E+00	2.5	98.76	44.07
4200.00	-40.8	5297.7	0.015000	15.0000	0.80539334E+00	-0.90264213E+00	2.6	98.52	44.32
4300.00	-40.0	5300.4	0.015000	15.0000	0.80216825E+00	-0.91391826E+00	2.7	98.28	44.56
4400.00	-39.3	5303.1	0.015000	15.0000	0.79897237E+00	-0.92503941E+00	2.7	98.04	44.79
4500.00	-38.5	5305.9	0.015000	15.0000	0.79577529E+00	-0.93603599E+00	2.8	97.81	45.02
4600.00	-37.7	5308.6	0.015000	15.0000	0.79258549E+00	-0.94691938E+00	2.9	97.59	45.25
4700.00	-36.9	5311.3	0.015000	15.0000	0.78942180E+00	-0.95766121E+00	2.9	97.37	45.47
4800.00	-36.1	5314.0	0.015000	15.0000	0.78625870E+00	-0.96830261E+00	3.0	97.15	45.69
4900.00	-35.4	5316.8	0.015000	15.0000	0.78310668E+00	-0.97881502E+00	3.0	96.93	45.90
5000.00	-34.6	5319.5	0.015000	15.0000	0.77996719E+00	-0.98922747E+00	3.1	96.72	46.11

KIND =   0   TOTAL DISTANCE(KM) =   0.0
NUMBER OF DISTANCES LESS THAN 4

PHYSICAL MODELING OF EM PROPAGATION OVER NONHOMOGENEOUS TERRAIN*

by
R. J. King
Lawrence Livermore National Laboratory
P. O. Box 5504, L-156
Livermore CA 94550

SUMMARY

To obtain experimental data for comparison with the theoretical results obtained from mathematical groundwave propagation models, it is often expedient to conduct experiments on laboratory models using microwaves. Besides the obvious convenience and reduced cost, practical difficulties encountered in full-scale experiments are avoided (e.g., weather and other uncontrolled parameters such as path nonhomogeneities, earth curvature, buildings, right-of-ways, etc.). There is no need to use exact similitude scaling; the media and geometries are generally chosen to test the limits of the theory's validity.

The design of several such models in the frequency range of 4-5 GHz will be discussed, and the experimental results will be compared with the corresponding theory. Specific examples are propagation over planar and curved surfaces (including stratified media, e.g., layered earth, sea ice, etc.), mixed paths (including media having abrupt discontinuities such as land-sea boundaries, gradual nonuniformities such as sloping beaches, off-path discontinuities such as islands, lakes and peninsulas), uniaxially anisotropic media, and media having an index of refraction near unity such as heavy vegetation.

When using such models, instrumentation systems and field probing techniques are key factors in their success. These will also be discussed.

1. INTRODUCTION

To supplement and verify theories of propagation in the natural environment, controlled experimental laboratory models can be a powerful and inexpensive tool. Such models are particularly useful for the evaluation of specific critical factors, e.g., the constitutive parameters of the media, obstacle shapes, frequency, polarization, etc. They also have the obvious practical convenience of avoiding unknown and uncontrolled parameters such as the weather, path nonhomogeneities, earth curvature, buildings, right-of-ways, etc. Guidance in the formulation and the verification of corresponding mathematical models are aided using geometrically scaled experimental models. Exact similitude scaling is generally unnecessary; the media and geometries are conveniently chosen to test the limits of validity in the theory.

The intent here is to review some techniques for modeling propagation problems and to show the utility of models, particularly in reference to the use of the surface impedance concept. In both experimental and mathematical models the surface impedance, Z_s, is an effective and economic means of accounting for the boundary conditions between media. This is because Z_s does not uniquely specify the underlying media or its geometry; these can be more or less arbitrarily chosen as convenient to give a prescribed Z_s. Thus, only part of the problem needs to actually be modeled. The rest of the problem is modeled via Z_s. All of the examples given here illustrate this point. However, precautions must be taken to ensure that the experimentally modeled Z_s is indeed that which is intended; this leads to a need for reliable and accurate synthesis methods, and means for experimental verification of the synthesized Z_s. This problem is also addressed.

An excellent overview of the art of modeling is given in Chapter 12 of the recent book by King and Smith [1981]. It emphasizes the art of modeling media and the characteristics of modeled media. The present paper complements King and Smith's work, particularly in reference to modeling the surface impedance. It concludes with a brief discussion of microwave instrumentation and experimental techniques which has proven valuable in carrying out laboratory measurements on models.

2. THEORY OF MODELING - A SUMMARY

There are infinitely many ways to model; size scaling is usually the paramount factor. Since VHF through microwaves is generally the range of frequencies most suitable for laboratory studies, the size of the real-world problem is scaled down at lower frequencies and scaled up at higher (e.g., millimeter and optical) frequencies. However, the frequency (ω) and size (r) need not be scaled by the same factor, in which case the permittivity (ε) and/or permeability (μ) must also be scaled. If the size is scaled, the conductivity (σ) must also be scaled. Sinclair [1948] and King and Smith [1981] give a complete analysis of simulation rules, which are briefly summarized here.

Let

$$\bar{E}_m = k_E \bar{E}_f \qquad \sigma_m = k_\sigma \sigma_f \qquad \bar{r}_m = k_\ell \bar{r}_f$$

$$\bar{H}_m = k_H \bar{H}_f \qquad \epsilon_m = k_\epsilon \epsilon_f \qquad \omega_m = k_\omega \omega_f \qquad (1)$$

$$\mu_m = k_\mu \mu_f$$

where subscripts m and f refer to the modeled and full-sized systems respectively. The dimensionless scaling constants k_E, k_H, etc., refer to the quantity being scaled. When the scaling relations in (1) are inserted into the field equations, the corresponding equations in the full-sized system are satisfied if

$$k_\sigma = \left(\frac{1}{k_\ell}\right)\left(\frac{k_H}{k_E}\right), \quad k_\epsilon = \left(\frac{1}{k_\ell k_\omega}\right)\left(\frac{k_H}{k_E}\right) \text{ and } k_\mu = \left(\frac{1}{k_\ell k_\omega}\right)\left(\frac{k_E}{k_H}\right) \qquad (2)$$

Most materials which are convenient for modeling are nonmagnetic ($\mu_m = \mu_0$), as are those for the full-sized system, so if we take $k_\mu = 1$, then $k_\epsilon = (k_H/k_E)^2$. When one of the materials is air in the full-sized system it is also generally convenient to use air in the scale model, so if we take $k_\epsilon = 1$, then $k_H/k_E = 1$. For these choices then,

$$k_\sigma = 1/k_\ell = k_\omega \qquad (3)$$

Thus, if the frequency is scaled upward by the factor k_ω, then the conductivity must also be scaled upward and the physical dimensions must be scaled downward by the same amount. Also note that at an interface between media the ratio of appropriate tangential $\bar{E}$ and $\bar{H}$ fields gives the surface impedance, and for the choice where neither ϵ or μ are scaled such that $k_\epsilon = k_\mu - k_H/k_E = 1$, the surface impedance is invariant,

$$Z_{sf} = \left.\frac{E_f}{H_f}\right|_{tang.} = \left.\frac{E_m}{H_m}\right|_{tang.} = Z_{sm} \quad . \qquad (4)$$

Thus, we can choose a one-to-one scaling of Z_s, μ and ϵ, while σ must be scaled according to (3). This also implies a one-to-one scaling of the loss tangents $\sigma/\omega\epsilon$ of all media, i.e. $\tan\delta_m = \tan\delta_f$.

When only the ratio k_H/k_E is specified, the scaling is said to be "geometric." In addition, if either k_H or k_E is specified, the scaling is "absolute." Absolute scaling is necessary only when measuring absolute field values, as in the measurement of power. For our purposes, only the relative fields are needed, so geometric scaling is sufficient.

3. PROPAGATION OVER THE EARTH

Laboratory scale models have been particularly useful for studying the propagation of LF and VLF waves over the earth. The two major reasons are cost and that it is difficult if not impossible to find full-scale situations which correspond to the analytical models to be verified. Here, some examples are cited which demonstrate the excellent results obtainable from laboratory models. Scaled frequencies in the mid-microwave range (e.g., 4 to 10 GHz) generally yield models suitable for laboratory studies, and the instrumentation is usually readily available at minimum cost.

Here, the main objectives are to verify the theory for the corresponding mathematical model, to give guidance in the formulation of the theory, or to provide approximation methods where no theory or inadequate theory exists. Accordingly, the laboratory models are generally chosen as extreme cases and do not necessarily represent any particular real-world situation.

3.1 Earth-Ionosphere Waveguide

Schwartz and Brown [1971] modeled the propagation of vertically polarized VLF waves in
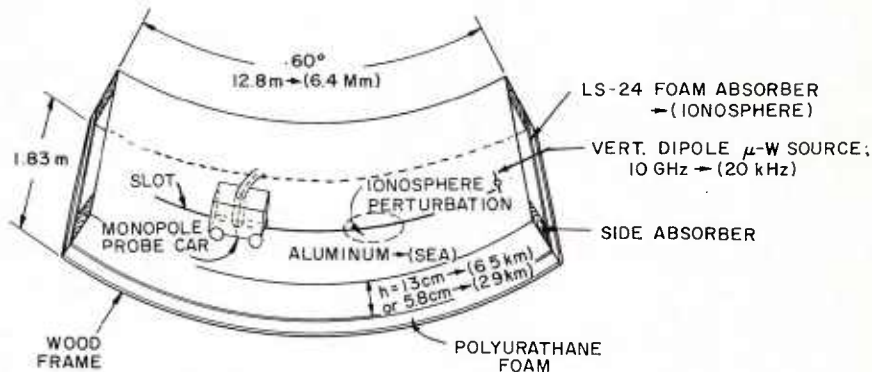

Figure 1. Cylindrical earth - ionosphere waveguide model used by Schwartz and Brown [1971]. Not drawn to scale.

the earth-ionosphere waveguide using a frequency of 10 GHz, scaled from 20 kHz ($k_\ell = k_\omega^{-1}$ = 5 x 10^{5}). The curved earth of radius 6.4 Mm was simulated using an aluminum sheet corresponding to a highly conducting sea, bent into a cylindrical shape as shown in Fig. 1. The theory suggests that propagation over the great circle of a sphere is essentially the same as propagation in the azimuth direction over a cylinder, if disturbances are not too far off the great circle path [King and Wait, 1976].

Modeling the ionosphere is no simple task, because the dielectric constant and conductivity are anisotropic and vary with height in a complicated way. However, for VLF the ionosphere behaves as a sharply bounded reflecting surface at an appropriately determined effective height. A search for modeling materials revealed that a commercially available microwave absorbing foam (Emerson and Cumming, LS-24) displays a reflection coefficient very close to that of a typical daytime ionosphere for incidence angles in the range of 70-90° from the ionosphere normal. For a reflection height of 65 km, this range corresponds to distances along the propagation path of 1200 km or more. This·is an example where the ionosphere's surface impedance was modeled over the main range of interest.

Amplitude and phase measurements of the vertical electric field vs. distance were made using a monopole antenna protruding through a slot in the aluminum, driven by a motorized car. Figure 2 shows some typical results for the amplitude using a reflection height of 65 km. Similar results were obtained for a severely depressed ionosphere height of 29 km. The agreement with the corresponding theory is excellent, thereby establishing the validity of both the theory and the experimental model. Having done this, a gradual depression centered at 1850 km and extending over a diameter of 800 km at a height of 25 to 65 km was modeled, representing a small ionospheric depression. The results are shown in Fig. 3. As no theory was available for this case, the model was truly an effective analog means for observing the effects of this complicated problem.
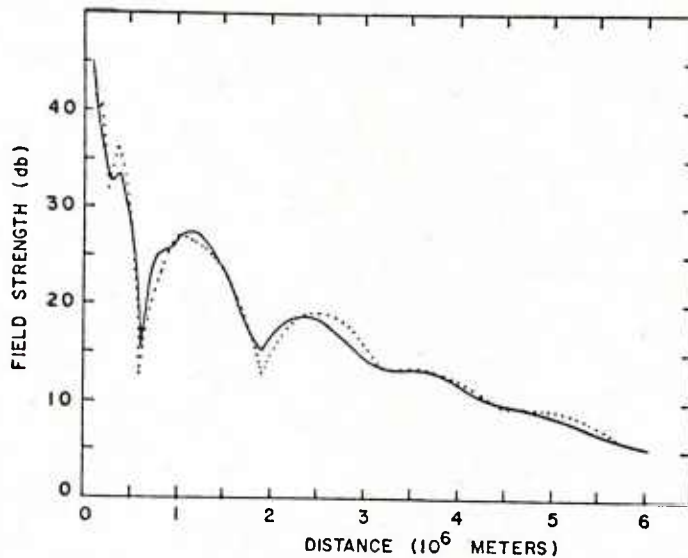
Figure 2. Amplitude vs distance for a 20 kHz signal propagating in the model shown in Fig. 1. Full-scale day-time ionosphere height is 65 km. Solid curve is theoretical calculation for an exponential ionosphere β = 0.3, a reference height of 74 km and point dipole source. Dotted curve is model experimental data for vertical transmitting and receiving dipoles 3.75 km long. °1971 American Geophysical Union.
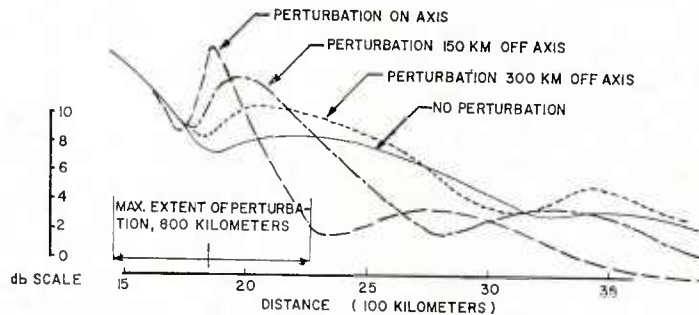

Figure 3. Amplitude vs distance for a 20 kHz signal propagating in the model shown in Fig. 1, showing the effect of an ionospheric depression. Normal ionosphere height is 65 km. Perturbation height is 25 to 65 km, cylindrically symmetric about a normal to the earth's surface. °1971 by the American Geophysical Union.

Propagation of horizontally polarized VLF (15 kHz) waves over long ice-covered paths in Antarctica was modeled at 4 GHz by Webber and Peden [1969]. As shown in Fig. 4, the nearly perfectly reflecting night-time ionosphere was modeled by a metal boundary at a height of 16 cm (81 km) above the simulated ice. The earth's curvature was not modeled and the source was a tapered horn. They chose scaling factors of $k_\mu = 1$, $k_\omega = 2.67$ x 10[5] and

$k_\ell = 1.976 \times 10^{-6}$, so $k_E/k_H = 0.528$ and $k_\epsilon = (0.528)^{-2} = 3.59$. Thus, air in the full-sized waveguide should be scaled to $(\epsilon_{air})_m = 3.59$. Fine aluminum oxide powder is a close approximation having $\epsilon = 3.6$ and a small loss tangent. The dielectric constant of antarctic ice at -25° C was taken as 3 and $\tan \delta_f = 1$. Thus, $(\epsilon_{air})_m \cong 11$ and $\tan \delta_m = 1$. Through experimentation, it was found that a 2:1 volume ratio of carbon dust and silica sand gives the desired properties. Rows of holes for inserting a monopole probe were drilled at four distances from the source and along the center axis (not shown). The experimentally measured amplitude and phase were in excellent agreement with the theory. From the measurements, they were able to determine the constant phase fronts and hence direction of the -3 dB energy flow lines as sketched in Fig. 4.
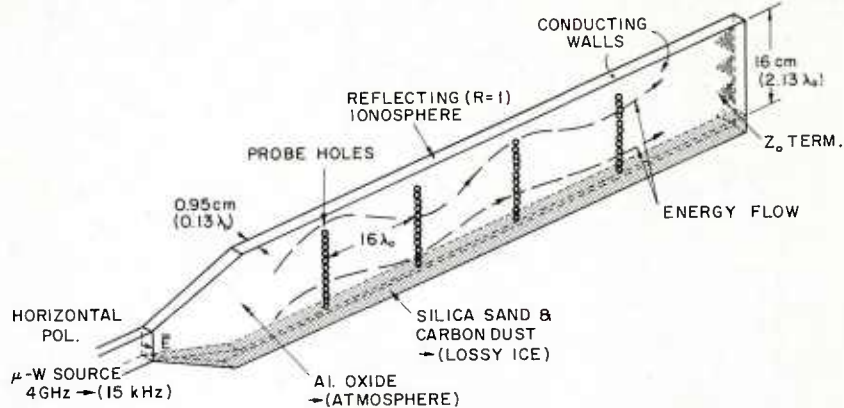
Figure 4. A 4 GHz model of the earth-ionosphere waveguide used by Webber and Peden [1969] for studying propagation of horizontally polarized waves at 15 kHz. °1969 IEEE.

Winder, et al., [1966] also used the carbon-silica sand combination to model a horizontal VLF dipole buried in the ice. The radiation pattern was measured at 3 GHz, without including the ionosphere.

Actually, Bahar [1966] was the first to build a two-dimensional model of the earth-ionosphere waveguide similar to that shown in Fig. 4. Bahar recognized that if a parallel conducting plate waveguide is symmetric about its longitudinal axis, the TE_{10}^z mode is dominant and the tangential magnetic field is zero over the symmetry plane (Fig. 5). Thus, the horizontal polarized TE_{10}^z mode in the waveguide is actually the dual of the TM_{10}^z _vertically_ polarized lowest order mode in the earth-ionsphere waveguide plus its mirror image. The center plane of symmetry represents the well conducting earth in the dual model where $E_t = 0$.
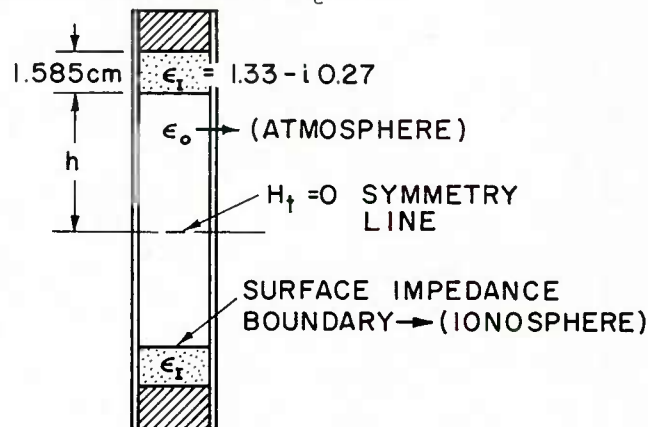
Figure 5. Cross section of Bahar's [1966] dual mode waveguide. Metal-backed lossy dielectric slabs simulate the finite impedance of the ionosphere and its image. Symmetry line simulates the earth where $E_t = 0$ in the large scale dual. Not drawn to scale.

The remaining task is to model the surface impedance of the ionosphere in the dual sense. Bahar was able to show that for the TM_{10}^z mode, the effective dielectric constant of an equivalent sharply bounded ionosphere is $\epsilon_f = 1-j$. Thus, in the dual model a permeability of $\mu_m = 1-j$ is needed. While a few ferrite material exhibit such a permeability, they all have a dielectric constant considerably greater than unity. The surface impedance of the ionosphere is related to the surface admittance in the dual model by

$$z_I^{TM_{10}} = \eta_0^2 Y_{dual}^{TE_{10}}$$

where η_0 is the intrinsic impedance of free space. Using a stratified structure made up of a dielectric absorber backed by a perfect conductor, Bahar was able to show that $z_I^{TM_{10}}$ is correctly modeled for the values of ϵ_I and thickness shown in Fig. 5. Strictly, this

modeled surface impedance is only applicable for the TM_{10}^Z mode which grazes the ionosphere. However, it is also a close approximation for the next few higher order modes for which Z_I varies with the incidence angle.

The cosine-shaped profile shown in Fig. 6 simulated a night-to-day transition for propagation from left to right using a model frequency of 9 GHz. Figure 7 shows the amplitude of the horizontal electric field as sampled through holes drilled along the axis. Agreement with the theory is excellent.
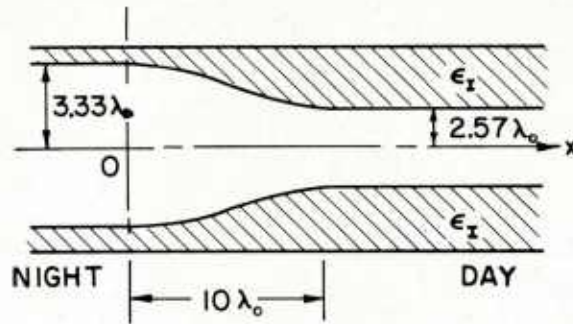

Figure 6. Profile of a night-to-day transition in Bahar's [1966] dual mode waveguide. Not drawn to scale.

3.2 Groundwave Propagation

Early ground wave model studies dealt with the field amplitude and phase vs. distance for propagation over abrupt (e.g., land-sea) boundaries on a plane earth [King and Maley, 1965, 1966; King, et al., 1965, 1966; Maley and Ottesen, 1964], including irregular shapes such as islands, peninsulas, etc. [King and Tsukamoto, 1966]. The theory for the field very close to the earth's surface is now thoroughly confirmed for these models. The modeling techniques used laid the foundations for later studies which dealt with related problems such as mixed-path height-gain effects, propagation over mixed-paths on
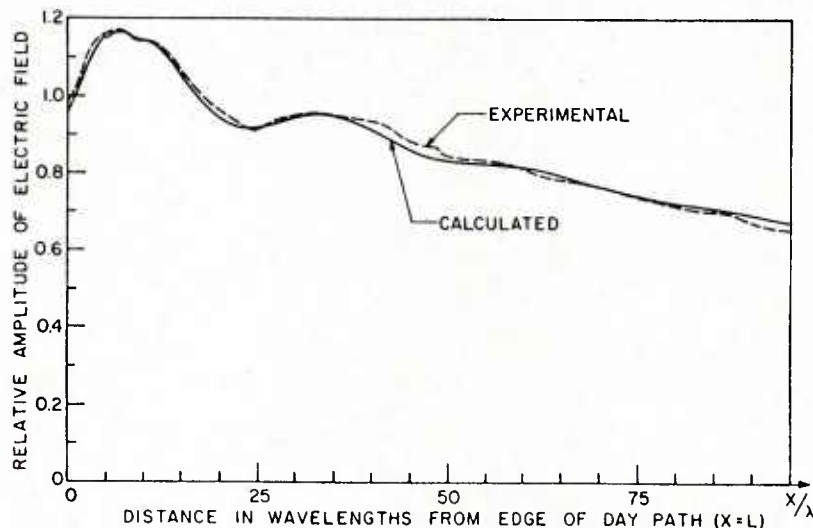
Figure 7. Amplitude variations for the night-to-day transition shown in Fig. 6. From Bahar [1966].

cylindrical surfaces, propagation over low density media and gradually changing surfaces. Since air constitutes the upper half space, it is convenient to choose $k_\epsilon = k_\mu = 1$. Then $Z_{sm} = Z_{sf}$ according to (4). The philosophy and salient features of some of these studies are briefly described next.

Figure 8 shows a typical laboratory model and monostatic instrumentation system used for surface wave and groundwave propagation studies. An electrically modulated scattering antenna (e.g., a dipole loaded by a switched PIN diode) is used as a field probe. Modulation of the junction impedance is usually in the AF range, accomplished via resistive leads oriented normal to the electric field using nylon lines. The probe can be moved or rotated to measure the desired field component, without disturbing the field. Operation of the homodyne receiver is discussed in Sec. 7.

Field vs. Distance. Prior to microwave model studies, experimental data for mixed-path groundwave propagation was meager. As noted earlier, such data is essential to evaluate the adequacy of the theory, without the unwanted effects of nonuniform terrain. The experimental models simulate, as closely as possible, the mathematical model used in formulating the theory. The frequency used was 4.2937 GHz ($\lambda \doteq 7$ cm). Tap water was used to simulate imperfect dielectric ground ($Z_S = 42 + j\, 3.45$), while aluminum plates
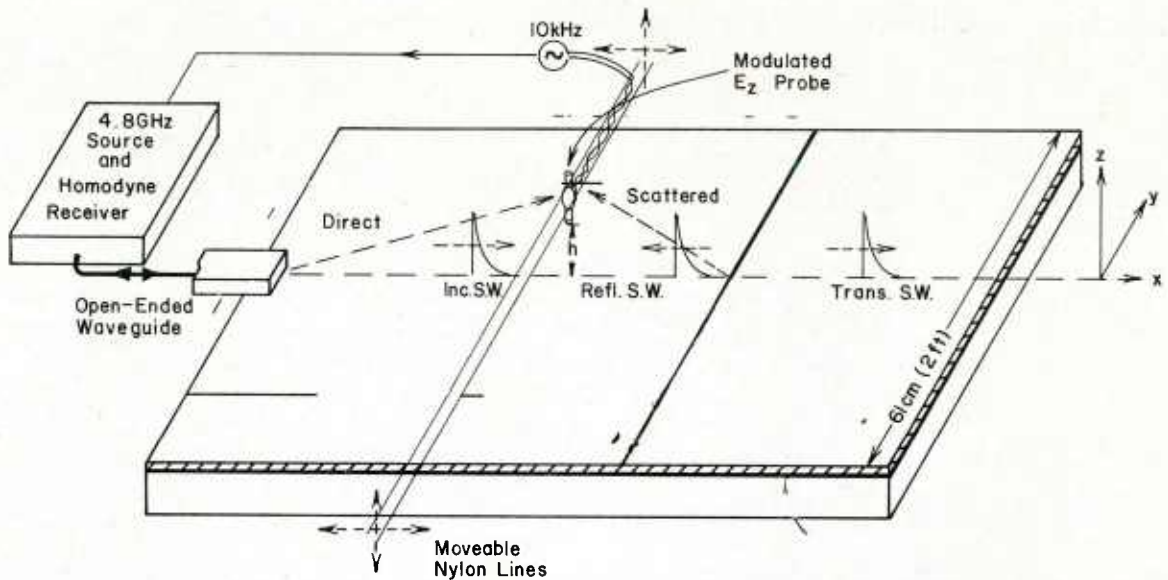
Figure 8. Typical laboratory model and instrumentation used for surface wave and groundwave propagation studies. °1982 American Geophysical Union.

simulated nearly perfectly conducting sea. In these experiments, the modulated scatterer shown in Fig. 8 was mounted on a small polystyrene foam block, and the movable nylon control line extended normal to the boundaries. The leads used to modulate the diode extended back along the nylon line in the direction of propagation. A strip of mylar film covered the path over which the foam block traversed. This provided a firm support for the light weight foam block when traversing the water portion of the path, and eliminated the water meniscus at the boundaries.

Figure 9 shows some typical results for propagation over a three-section (sea-land-sea) path at normal incidence to the abrupt boundaries [King, Maley and Wait, 1967]. A small standing wave is evident to the left of the first boundary. Otherwise, these results show that homogeneous path theory is accurate between the source and the first boundary. Between the first and second boundaries the field suffers additional attenuation due to the losses of the imperfect ground. Two-section theory accurately predicts this excess attenuation.
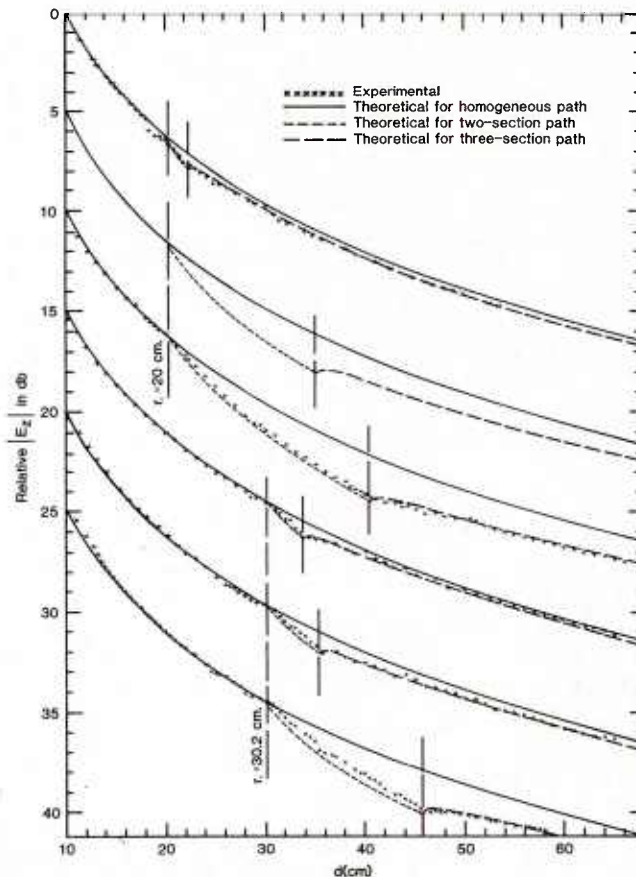
Figure 9. Relative $|E_z|$ vs distance for propagation over three-section mixed paths comprised of aluminum ($Z_s = 0$) — water ($Z_s = 42 + j\ 3.45$) — aluminum. $\lambda_o = 6.98$ cm. [King, Maley and Wait, 1966].

The experimental data is slightly higher than the two-section theory in Fig. 9. This can be attributed to the change of the self-impedance of the dipole scatterer as it moved from water to aluminum. Since the dipole is very close to the surface, there is substantial electrostatic coupling between it and the underlying medium. Consequently, as the dipole traverses over different media this coupling changes, causing the self-impedance and hence the scattering properties of the dipole to change. This effect can be minimized by raising the dipole slightly, but this causes an equally undesirable height-gain effect to occur. Later dipole scatterer designs minimized this coupling effect [King, 1978].
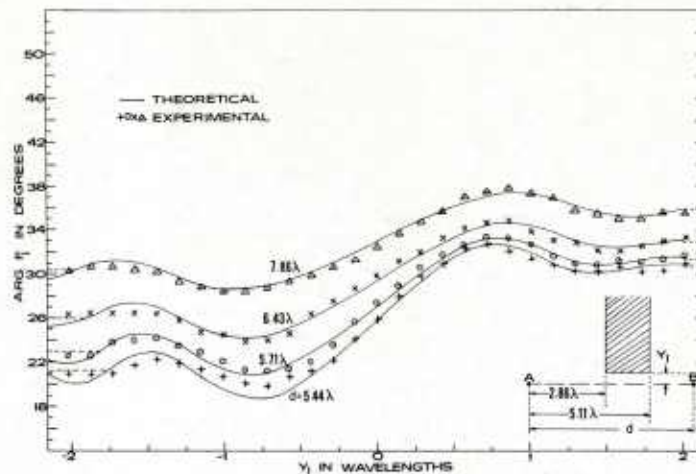
Figure 10. Relative variation of phase of attenuation function vs Y_1 for propagation near an infinite conducting strip ($Z_S = 0$) surrounded by water ($Z_S = 42 + j\ 3.45$). $\lambda_0 = 6.98$ cm. [King and Tsukamoto, 1966].

Beyond the second boundary, the field tends to recover and the experimental results compare well with the three-section path theory. Similar modeling results for oblique propagation over two-section paths are given in King and Maley [1966].

Off-path nonhomogenieties were simularly modeled by King and Tsukamoto [1966]. Some typical results for propagation near an aluminum half-strip surrounded by water are shown in Figs. 10 and 11. This configuration models propagation over lossy land ($Z_S = 42 + j\ 3.45$) near a bay of highly conducting sea water ($Z_S = 0$). In Fig. 10, the parameter is d, the separation distance between the transmitting and receiving antennas A and B and the variable is Y_1, the distance of the edge of the aluminum strip from the line connecting A and B. Variations of the phase of the overall attenuation function, F_I, are clearly evident, especially when the transmitter and receiver are close together (i.e., $\pm 7°$ for d = 5.44 λ_0). This phenomenon could have noticable effect in navigation systems which monitor the phase of the received signal, since it implies an apparent change in the direction of arrival. Asymptotic values of the phase for a strip which extends to infinity on both sides of the direct path ($Y_1 = -\infty$) are indicated on the left, while the asymptotic values for no strip ($Y_1 = \infty$) are indicated on the right.
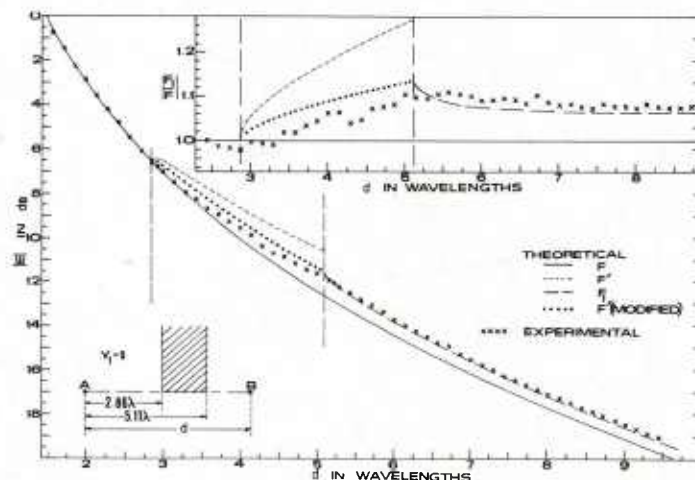

Figure 11. Relative variation of $|E_z|$ for propagation across the end of a conducting strip ($Z_S = 0$) surrounded by water ($Z_S = 42 + j\ 3.45$). $\lambda_0 = 6.98$ cm. [King and Tsukamoto, 1966].

Figure 11 shows how the amplitude of the field varies vs. d, holding the position of the half-strip fixed at $Y_1 = 0$. Also shown in the inset are the same data plotted as the ratio $|F_I/F|$. This is the overall attenuation function when the half-strip is in place, relative to the attenuation function in the absence of the strip. This clearly shows the differences between the theoretical and experimental data. When the receiver is to the

left of the strip, the attenuation function, F, for a homogeneous path compares well with the experimental data. There is no theory for a half strip, but the theory for a two-section path, F', is shown as the receiver traverses over the end of the strip. Because of symmetry, the attenuation function should be F'(modified) = F'/2. There is significant difference between F'(modified) and the experimental data, but this is again due to the change in self-impedance of the dipole scatterer as it passes in near proximity of the aluminum strip. To the right of the strip, the experimental data compares quite well with the theory using F_I. Actually, the theory for F_I is not expected to be valid within about $\lambda_0/2$ of the rear boundary, but the comparison of experimental and theoretical data are still quite good in this case.

Height Gain. Well-known theory for groundwave propagation over a uniform plane earth is usually divided into three parts: the direct wave, the specular wave reflected at angle ψ_r from the horizon, and a non-geometrical-optics term which is generally referred to as the Norton Surface Wave. Beyond the induction region of the source, the first two terms are exact, so any approximations or restrictions imposed are relegated to the Norton wave term. Full-scale as well as model experiments have shown that the theory accurately predicts the behavior of the field amplitude vs. distance, d, as close as $d = \lambda$ from the source. However, little experimental data existed confirming its ability to predict the amplitude of the field with height above the earth's surface. Accordingly, a 4.76 GHz model was designed to test these aspects of the theory [King, et al., 1973, Part 1]. From the theory, it is anticipated that the greatest error will occur for surfaces which are "highly inductive," i.e., $\pi/4 < \arg Z_s < \pi/2$. Rarely does arg (Z_s) exceed 50-60° in the real world; such a highly inductive impedance is usually associated with a low-loss medium overlying a more conductive layer, e.g., ice over the sea. The model chosen was a plane surface of 7/64 inch (2.8 mm) Plexiglas lying on tap water. As shown at the top of Fig. 13, the water was contained in a sealed 1 x 1.33 x .04 m Plexiglas tank covered with the Plexiglas sheet ($\epsilon_r = 2.6$) representing the low-loss medium. The 4 cm thick layer of water beneath represented the underlying reflective medium of essentially infinite depth. The resulting normalized surface impedance for grazing incidence, as calculated using parallel stratified media theory, is

$$\Delta_0 = (Z_s/\eta_0)\Big|_{\psi_r = 0} = 0.213 \exp(j\,53.4°)\quad.$$

To simulate a vertical electric dipole source, an open-ended waveguide was laid flat on one end of the tank. The variation of the vertical electric field vs. receiver height, h_2, above the surface was measured using a vertical modulated scattering dipole and homodyne detection (Fig. 8).

Figure 12 compares some typical height-gain experimental results with (a) the total theory comprised of the sum of the direct and reflected waves and the Norton surface wave, (b) the approximate height gain factor $G(h_2) = 1 + jk\Delta_0 h_2$ as obtained using the first two
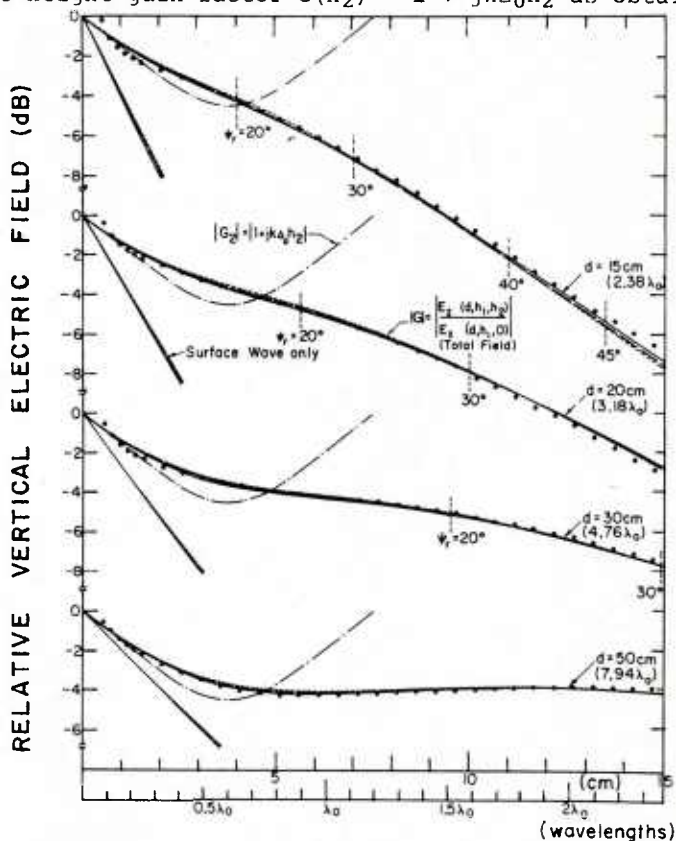
RECEIVING ANTENNA HEIGHT, h_2

Figure 12. Relative $|E_z|$ vs height h_2 for TM propagation over a moderately inductive surface at close to moderate ranges. $\Delta_0 = 0.213 \exp(j\,53.4°)$. [King, et al., 1973; King and Wait, 1976]; •1973 American Geophysical Union.

terms of a Maclaurin series expansion for the total field, and (c) the variation of the Norton wave only, neglecting the direct and reflected waves. The agreement between the experimental data and the total theory is remarkable. For heights less than 1 cm, the scattering properties of the modulated dipole are altered by its proximity with the surface. For $\Psi_r > 30°$, the free space radiation pattern of the open-ended waveguide source begins to deviate from that of a dipole assumed in the theory. At these angles, the Norton wave is insignificant compared to the direct and reflected fields. Thus, the small deviations at larger values of Ψ_r can be attributed to the difference in source radiation patterns. It is also seen that G is valid only if $|k\Delta_0 h_2| \ll 1$, and that the height variation of the surface wave term only is a very poor approximation until large ranges ($d > 10\lambda$) are reached.

Using this same model, height-gain measurements were also made for propagation over abrupt mixed-paths [King, et al., 1973; Part 2]. By simply sticking adhesive-backed aluminum foil on part of the Plexiglas top, a conducting sea was simulated over that region. Mixed-path groundwave theory is applicable only at points on the surface; height effects are not included. However, in the homogeneous path studies it was shown that $G(h_2)$ accurately predicts the height-gain for $|k\Delta_0 h_2| \ll 1$, e.g., see Fig. 12. This suggests that the height-gain for mixed-paths can be approximated using G, and this hypothesis was tested using the mixed-path model. Some typical field vs. distance results are shown in Fig. 13 for various receiver heights, h_2. Since $\Delta_0 = 0$ and $G = 1$ over the first part of the path, the theory for the field on the second part of the path is adjusted downward by an amount given by $|G|$ using the local impedance of the second part. In the case where $h_2 = 0.5$ cm it was necessary to correct the experimental data by the proximity effect noted earlier. This data shows that near the surface where $|k\Delta_0 h_2| \ll 1$, G accurately predicts the local height-gain for distances greater than about one wavelength from the boundary. From Fig. 12, note that G ceases to accurately predict the height-gain for $h_2 \geq 2$ cm. Thus, for $h_2 = 2$ cm in Fig. 13, the use of G gives some error. Also shown is the case of propagation from metal to water. Since Arg Δ_0 for water is quite
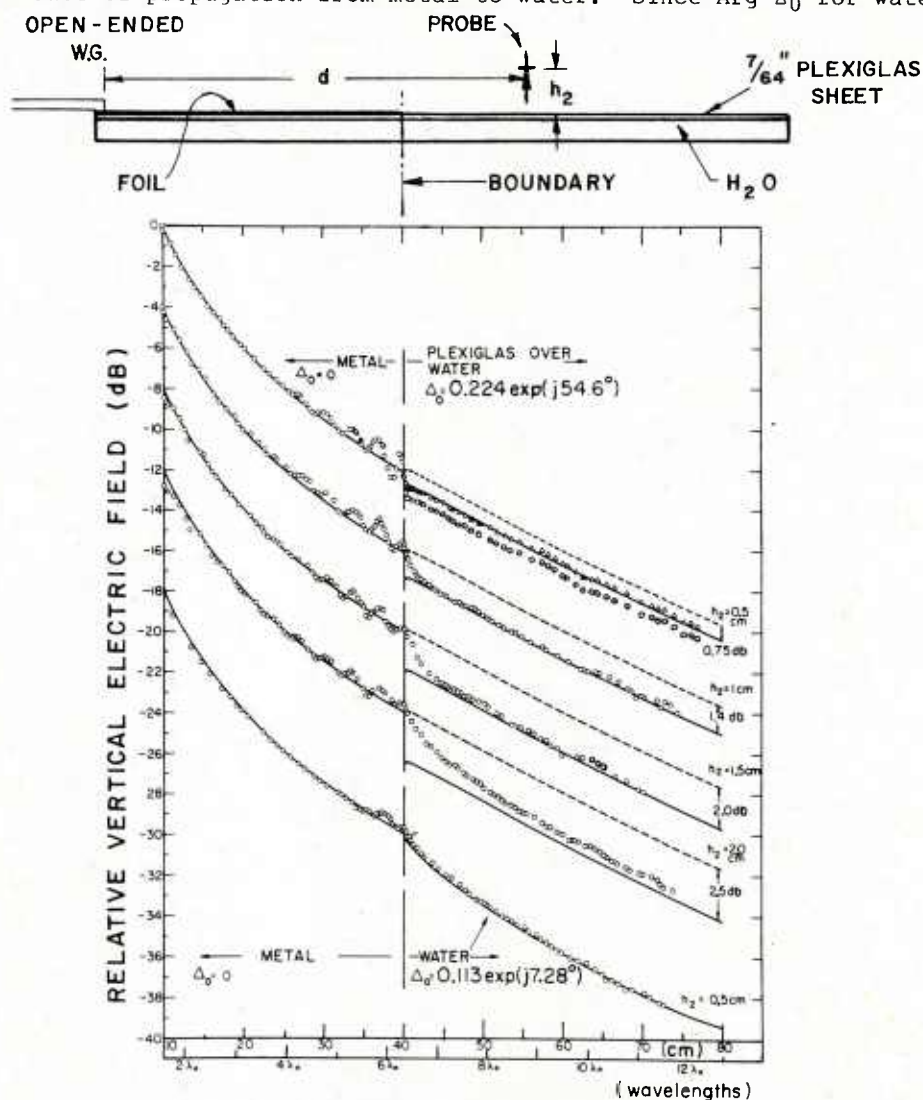

DISTANCE FROM TRANSMITTING ANTENNA, d

Figure 13. Relative $|E_z|$ along mixed paths for various receiving antenna heights, h_2. Legend: ooo Raw experiment; ΔΔΔ experiment adjusted by probe proximity effect; --- theory on the surface; ___ theory adjusted by local height-gain factor $|G|$ [King, et al., 1973]; ©1973 American Geophysical Union.

small, the G factor is approximately unity for $h_2 = 0.5$ cm. It also happens that the proximity factors were identical for metal and water at $h_2 = 0.5$ cm. Therefore, no corrections were necessary.

Similar model experiments were carried out on a cylindrical water tank having a radius of 20 λ (Fig. 14), corresponding to 1 kHz in the full-scale real earth situation [King, et al., 1974]. Thus, if the theory proves accurate for this model, it will be even more accurate for VLF and LF propagation. Figure 15 shows some experimental height-gain data for propagation over cylindrical homogeneous paths comprised of either metal (aluminum foil) or Plexiglas-over-water. The residue series theory for a spherical earth agrees well with the experiments in the shadow and penumbra regions, but agreement becomes poorer as
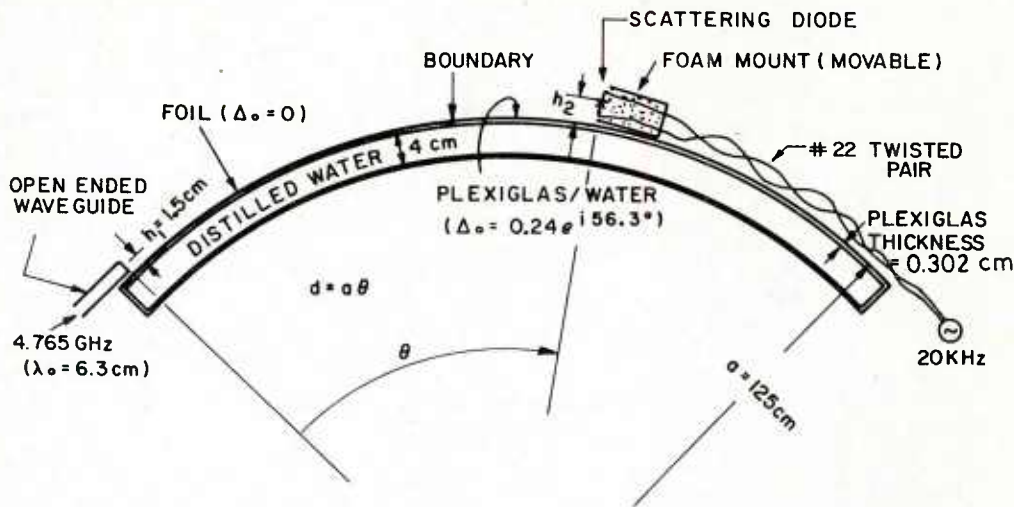
Figure 14. Cross-section of a cylindrical Plexiglas water tank model. An open-ended waveguide simulated a radial dipole source and a modulated scattering dipole was used to probe the radial electric field [King et al., 1974]; °1974 IEEE.
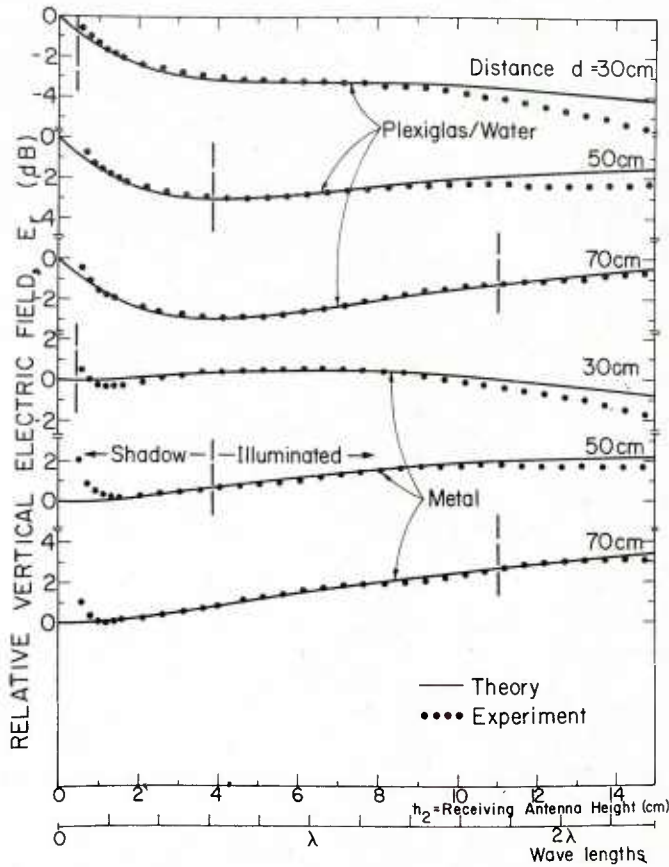
Figure 15. Relative radial electric field E_r for propagation over cylindrical (experimental) and spherical (theory) homogeneous paths comprised of either metal or plexiglas over water [King et al., 1974]; °1974 IEEE.

the observation point moves into the illuminated region where an excessive number of residue terms is needed. Other experiments were conducted to confirm that the residue series is able to predict the field amplitude vs. distance for both homogeneous and mixed paths, and the height-gain for mixed paths. The results were reassuring.

Low-Density Media. Propagation over low-density media has relevance to HF propagation over heavy vegetation. The material chosen was a 2.5 cm thick sheet of commercially available microwave graded foam absorber (Emerson and Cumming AN-75) approximately 1 m^2 in area. Again, an open-ended waveguide (4.765 GHz) placed on one edge served as an equivalent vertical electric dipole source.

It has been shown [King and Wait, 1976, pp. 133-161] that a low-density medium having an index of refraction near unity can support a groundwave of precisely the same form as when the refractive index is large, e.g., the earth. As the refractive index of the foam absorber used was unspecified by the manufacturer, wave tilt measurements were first conducted. For homogeneous surfaces on which no reflected waves exist, the complex wave tilt W ($\equiv E_x/E_z$) of a TM wave propagating at grazing incidence is equal to the normalized surface impedance. The measurements determined this impedance as

$$\Delta_0 = \frac{1}{n^2} [n^2-1]^{1/2} = 0.625 \exp(j0°)$$

from which the effective refractive index can be computed as $n^2 = \varepsilon_r = 1.60 \exp(-j\ 36.9°)$. Measured height-gain data is compared with ground-wave theory in Fig. 16 using the previously determined value of Δ_0. The case for $\Delta_0 = 0$ is also shown for comparison. Below $h_2 = 1.5$ cm the scattering probe's proximity to the surface causes some measurement error.
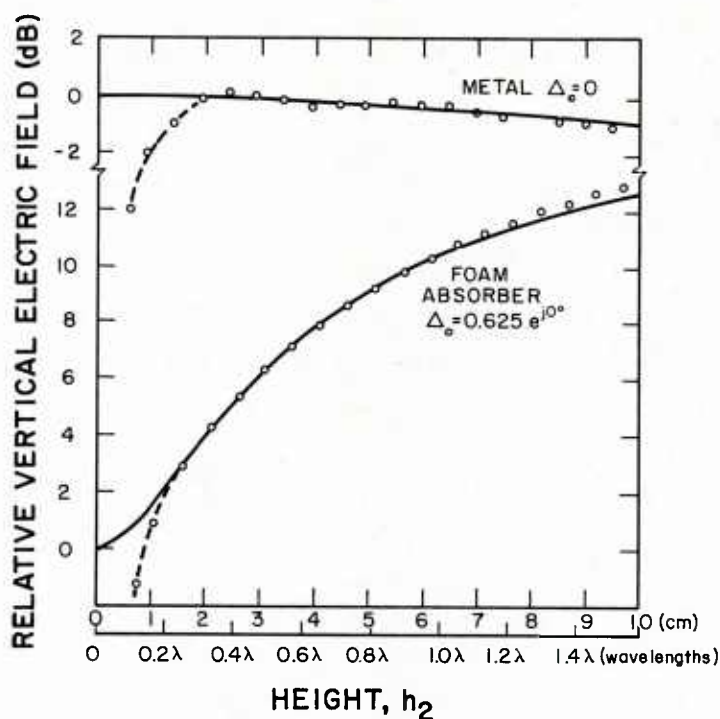
Figure 16. Height-gain data for a TM wave propagating over a flat uniform sheet of microwave absorbing foam and a perfect conductor. Distance = d = 42.7cm (6.8λ), and $h_1 = 1.5$cm (0.237λ) [King and Wait 1976]; ●1976 Academic Press.

To further test the hypothesis that a Norton surface wave can propagate over a low density medium, a 4 m long flat polystrene path was constructed in a radio anechoic chamber at the Technical University of Denmark. Details of the experimental setup are given in Krogager et al. [1980]. Figure 17 shows some results for a frequency of 3 GHz. The free space or direct field varies as d^{-1} as shown, while the sum of the direct and specularly reflected field decreases at a much greater rate. When the Norton wave is added, the experimental and theoretical data agree well using a dielectric constant of $\varepsilon_r = 1.015$ for the foam. This data should be regarded as preliminary; other experiments are in progress.

Figure 18 shows some cylindrical surface mixed-path data, where the metal part of the path is adhesive-backed aluminum foil laid on the foam absorber. The theory used is the residue series for propagation over mixed paths on a spherical earth. Because of the different proximity effect factors for metal and foam, it was necessary to correct the experimental data empirically. Although these corrections are crude, the comparison between experiment and theory is satisfactory except possibly at large ranges when the second part was metal. In this case, the field is entirely radiated and so unattenuated reflections from the end of the model were observed.
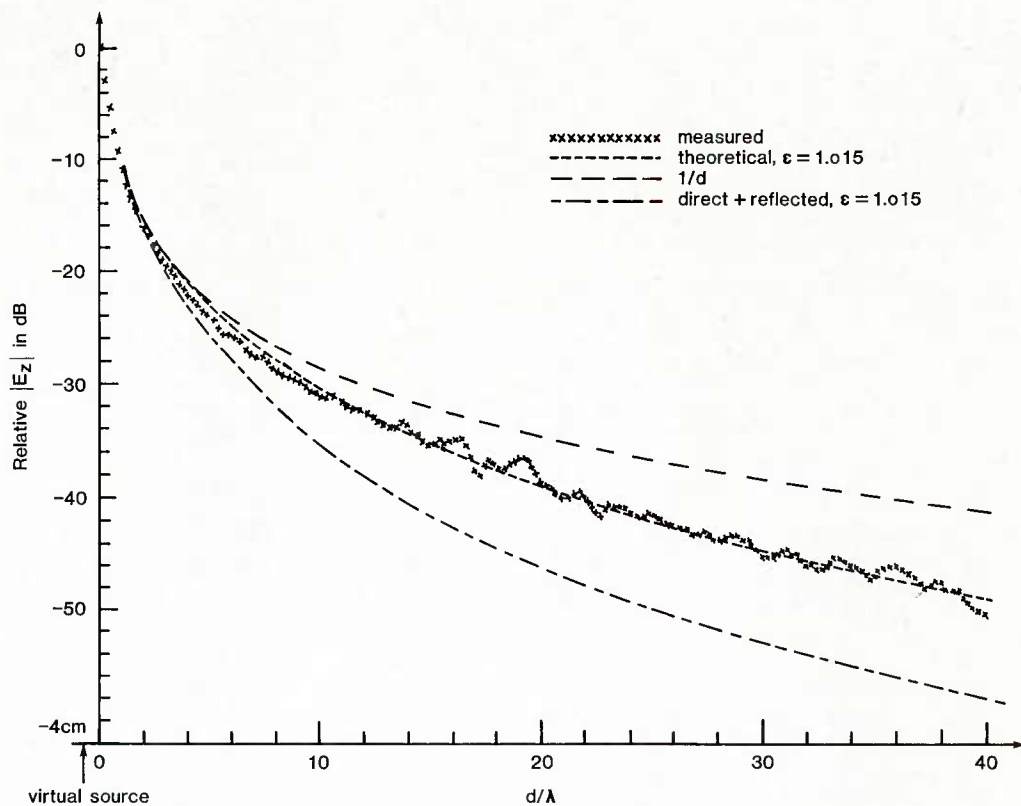
Figure 17. Vertical electric field vs distance of propagation over a low-loss foam path. The open-ended waveguide represents a virtual dipole source at d = -4 cm.

4. PROPAGATION OVER GRADUALLY VARYING SURFACES

Besides groundwave propagation over abrupt boundaries, a more general problem is the effect of nonuniform surfaces in which the material characteristics or geometry change gradually. Equivalently, this means that the surface impedance is variable. Typical examples of nonuniform surfaces are a land-sea beach where the water depth is varying, radial-wire ground systems beneath radiating antennas, and terminations and transitions on guided wave structures such as surface and leaky wave antennas.

4.1 Dielectric Wedge

When an antenna is situated near a coastline, the varying depth of water at the beach may have some effect on the radiation pattern as well as the groundwave field. We seek an economical and efficient way to describe the varying surface impedance of the beach. Taking a worst case again, a model consisting of a dielectric wedge above a perfect conductor was chosen. The objective of the experiment was to see if the surface impedance could be accurately predicted using parallel-stratified media theory in which the local thickness h(x) (= x tan δ) of the dielectric is used, where δ (= 1°) is the acute wedge angle. The inset in Fig. 19 shows the geometry. The dielectric was Plexiglas (ϵ_r = 2.6, loss tangent = 5.4 x 10^{-3}). The final wedge was 32 cm wide and 80 cm long. The end was terminated in microwave absorber to minimize reflections. Full details of the design and experiment are given in King and Hustig [1971].

Again using a homodyne detection system (4.75 GHz) in conjunction with a modulated scattering dipole probe and an open-ended waveguide source, the wave tilt was measured over the wedge region. The scattering dipole was 0.19 λ long, centered 0.25 λ above the surface to avoid proximity effects. It was suspended between two nylon lines (Fig. 8) which were oriented parallel to the wedge apex. The lines could be rotated about their axis so that the dipole rotated in the plane of incidence. By measuring the tilt angle and the ratio of the major to minor axes of the polarization ellipse, the wave tilt was found. Since there are no reflections to the right of the apex, and the increasing wedge depth tends to trap the diffracted field, the wave tilt is expected to be very close to the normalized surface impedance for small impedances.

The amplitude results are shown in Fig. 19 for propagation in the direction of increasing wedge depth. The theory for the plane wave solution is that obtained using parallel stratified media theory [King and Hustig, 1971; Thiel, 1982]. It is assumed that the wave tilt W(x) is equal to the normalized surface impedance Δ(x) for grazing incidence, given by
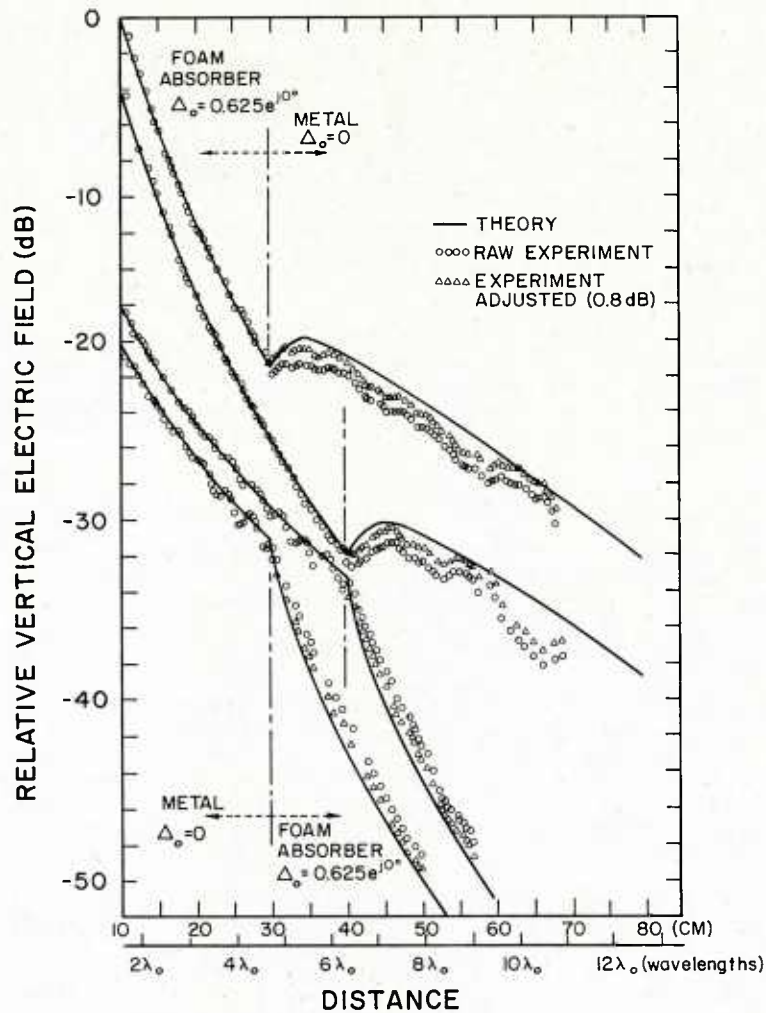
$$\Delta(x) = \Delta_1 \tanh[u_1 h(x)] \tag{5}$$

Figure 18. Radial electric field E_r vs great circle distance for a TM wave propagating over cylindrical mixed-paths composed of foam absorber and metal. Curvature radius = 123.4 cm; source height h_1 = 1.5 cm.; receiving antenna height h_2 = 0.9 cm. ⊕1982 American Geophysical Union.
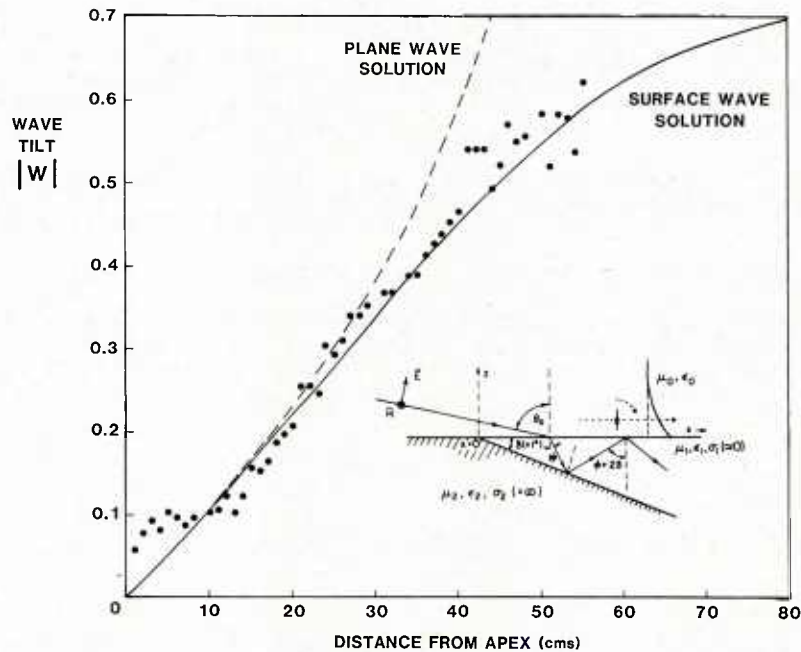

Figure 19. Electric field wave tilt for grazing incidence (θ_0 = 90°) of a 4.75 GHz wave on a grounded dielectric wedge. Propagation is in the direction of increasing wedge depth. Experimental and plane wave data is from King and Hustig [1971]. The surface wave theory is from Thiel [1982].

where

$$\Delta_1 = \frac{\gamma_0}{\gamma_1} \left[1 - \left(\frac{\gamma_0}{\gamma_1} \right)^2 \right]^{1/2} \tag{6}$$

is the normalized impedance of the upper medium when it is infinitely thick. The propagation constants of air and the slab are γ_0 and γ_1, respectively. The $\tanh[u_1 h(x)]$ factor accounts for the finite local thickness $h(x)$ of the slab over the conductor, and $u_1 [= (\gamma_1^2 - \gamma_0^2)^{1/2}]$ is the vertical propagation constant in the slab. The experimental data generally agrees well with the plane wave solution for $|W(x)| < 0.35$, beyond which a more accurate theory is needed.

Although not shown in Fig. 19, the measured Arg $W(x)$ was between 80-90°, so the field has a strongly excited trapped surface wave component which decreases rapidly with height. Near the apex, the field is loosely bound, becoming more tightly bound with increasing x. It is logical then to approach the problem using trapped surface wave theory [Thiel, 1982]. In this theory, (5) and (6) still apply, but now the vertical propagation constant in the slab is

$$u_1(x) = \left\{ \gamma_1^2 - \gamma_0^2 [1 + x^2(x)] \right\}^{1/2} \tag{7}$$

where $X = -j\Delta$, is the normalized surface reactance. For $X > 0.3$, this is significantly different than that for the plane wave analysis. Obviously, the solution of (5) and (7) is transcendental. Finally, it is not difficult to show that for a surface wave.

$$W_{(x)} = \frac{\Delta(x)}{[1 - \Delta^2(x)]^{1/2}} \tag{8}$$

Numerical computations for $|W(x)|$ as computed by [Thiel, 1982] are also shown in Fig. 19. The improved fit with the experimental data for larger dielectric thicknesses indicates that a very significant trapped surface wave is present. The wedge apex apparently acts as a magnetic line source which launches this wave. The deviation of the experimental data from the theory near the apex is the result of scattering from the apex. This radiation tends to inflate $|W|$ close to the boundary, a phenomenon observed again recently [Thiel et al., 1982].

When propagating in the direction of decreasing wedge depth (not shown), the two theorys fail completely because they make no distinction in the propagation direction. In this case, a geometrical optics solution works best, although it does not predict Arg $Z_s(x)$ well [King and Hustig, 1971]. The experiments give -110° < Arg W < -100°, indicating a highly capacitive surface with a negative real part. This is attributed to severe scattering (e.g., leakage) from the wedge which was not present for the opposite direction of propagation.

In the natural world, the experimental model shown in Fig. 19 represents a sloping wedge of ice on sea water. However, since parallel stratified media theory seems to work well for propagation in the direction of increasing wedge depth for this extreme case, when $|\Delta| < 0.35$, it should also be quite adequate when applied to propagation from land to a sloping beach because; (a) the refractive index of the water is large, which causes the refracted field to propagate essentially vertically in the wedge, (b) water, especially sea water, has a considerably greater loss tangent which diminishes the amplitude of reflections from the bottom, (c) the reflection coefficient at the bottom between the water and sand is less than in the dielectric wedge-metal model and (d) the angle is generally greater than 1° which means there will be fewer internally scattered modes.

These experiments also point out another important feature -- the impedance of nonuniform surfaces is dependent on the direction of propagation. The implications of this, in relation to reciprocity, are considered in King and Hustig [1971].

5. WAVE TILT MEASUREMENTS IN THE PRESENCE OF REFLECTIONS AND SCATTERING

The measurement of the wave tilt, W, of EM waves is one of the first methods to be used for remotely sensing the substructure of the earth near its surface. This is because of its one-to-one relationship to the normalized surface impedance for a horizontally uniform earth. For a TM^x wave propagating in the x-direction,

$$W \equiv \frac{E_x}{E_z} \quad \text{and} \quad \Delta \equiv \frac{-1}{\eta_0} \frac{E_x}{H_y} \tag{9}$$

where the z-axis is normal to the surface. Thus, if $E_z = -\eta_0 H_y$, as is the case for uniform surfaces at grazing incidence, then $W = \Delta$, and if we take

$$\Delta = \frac{1}{n^2} [n^2 - 1]^{1/2}$$

corresponding to a grazing plane wave, as seen from (6), this provides a means of calculating the effective refractive index of the earth, n^2.

However, when the surface is not uniform, scattering and reflections can occur which can alter the wave tilt at points far removed from the scatterer and/or reflector. If one continues to regard it as equal to the normalized surface impedance, misinterpretations of the earth's local substructure can result [Thiel, et al., 1982]. To show this, wave tilt

measurements were made on a worst case model on which the local surface impedance is known and constant. The model was constructed using grounded artificial dielectric slabs. These slabs were constructed like a pin (fakir's) bed consisting of thousands of headless pins which were inserted into a polyform support covered with adhesive-backed aluminum foil to form the ground plane. By choosing the proper density and height of the pins, a wide range
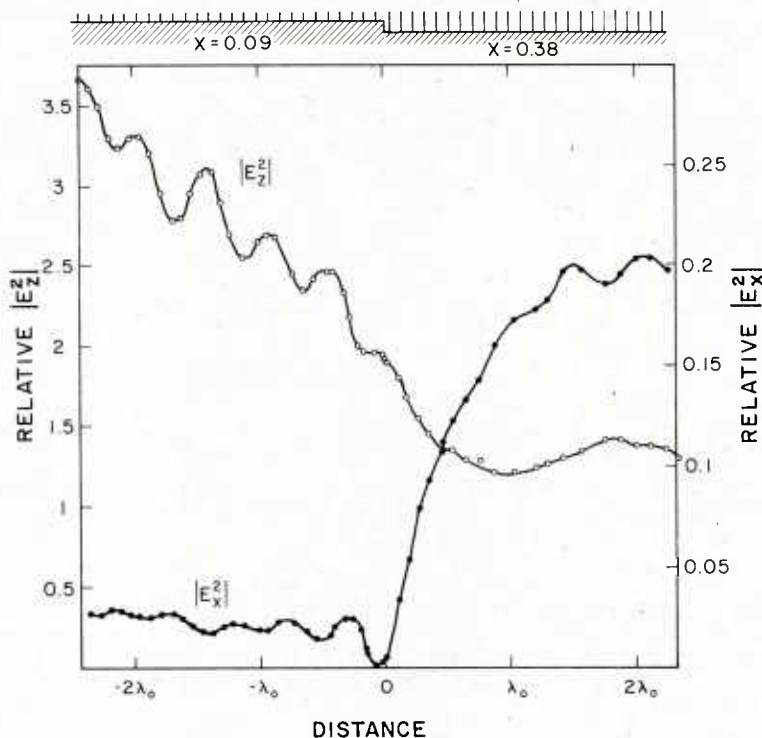

Figure 20. Measured horizontal $|E_x^2|$ and vertical $|E_z^2|$ electric fields for a TM^x surface wave propagating over the two-section pin bed reactance structure shown at the top. The constant values of normalized reactance are X = 0.09 for X < 0 and X = 0.38 for x > 0. Frequency = 4.8 GHz. •1982 American Geophysical Union.

of local surface reactances can be synthesized. Details of the synthesis procedure and confirming experiments are given in King and Park [1981] and King et al. [1983]. Here, it is sufficient to remark that the diameter and spacing of the pins is such that propagation is below cutoff in the lateral (x and y) directions within the slab. Vertical propagation, however, is permitted and yields a reactive surface impedance $Z_s = j\eta_0 X$, the magnitude of X being chiefly determined by the local pin height.

The profile of the two-section structure tested is shown at the top of Fig. 20. The length of the scattering dipole was 0.2λ, centered at a height of 0.26λ which was sufficient to avoid proximity errors. Since the homodyne system measures the square of the field component along the dipole, the square of these components was plotted directly in Fig. 20. Two features are noteworthy. First, there is a strong standing wave of $|E_z^2|$ to the left of the boundary. Second, $|E_x^2|$ vanishes very near the boundary and then gradually recovers and oscillates to the right of the boundary.
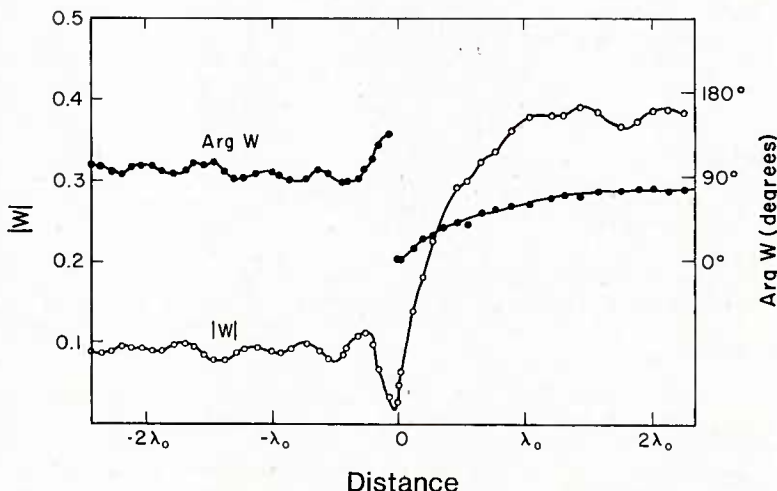
Figure 21. Measured wave tilt for the surface reactance structure shown in Fig. 20. •1982 American Geophysical Union.

From the measured amplitude and phase of E_x and E_z, the wavetilt was calculated according to (9) and the results are plotted in Fig. 21. Again, notable features are the undulations of both the amplitude and argument of W to the left of the boundary, the apparent 180° flip of the phase of W at the boundary, and then the magnitude and argument of W gradually approaches steady state values to the right of the boundary.

To understand the undulations in W to the left of the boundary, consider the total TM^x magnetic field of a one-dimensional source,

$$\bar{H}^t = \bar{a}_y H_y (e^{-vz-j\beta x} + Re^{-vz+j\beta x}) \tag{10}$$

where $v = k_0 X$ and $\beta = k_0(1+X^2)^{1/2}$. The first term is the incident surface wave propagating toward the right, the second term is a reflected surface wave propagating toward the left, and R is the reflection coefficient. Using the Maxwell-Ampere law,

$$E_x^t = -j\eta_0 X\, H_y (e^{-vz-j\beta x} + Re^{-vz+j\beta x}) \tag{11}$$

and

$$E_z^t = -\eta_0 (1 + x^2)^{1/2} H_y (e^{-vz-j\beta x} - Re^{-vz+j\beta x}) \tag{12}$$

The wave tilt is therefore

$$W^t = \frac{jX}{(1 + X^2)^{1/2}} \left[\frac{1 + Re^{j2\beta x}}{1 - Re^{j2\beta x}} \right] \tag{13}$$

where $jX/(1+X^2)^{1/2} = W$, is the wave tilt for a uniform surface [see Eq. (8)]. Thus, the variation in the observed tilt is due to reflections. Additional experimental data are given in Thiel, et al., [1982] and Park [1982].

A similar conclusion is reached for W in the near vicinity and to the right of the boundary. Here significant radiation and scattering occurs from the boundary. Thus, $|W|$ is still varying at 2λ to the right of the boundary and Arg W has not yet settled to 90°. Of course, this is partly due to the fact that the dipole is elevated 0.26λ above the surface. Finally, the apparent 180° flip in Arg W occurs where $|E_x|$ vanishes. Thus, track of the phase is lost.

Of course, propagation over the earth is somewhat more complicated, since the amplitude and phase variation of the incident, reflected and scattered fields are different. Also, for a uniform earth, $W = \Delta_0$ and $|\Delta_0^2| \ll 1$ is required. But this surface wave model serves to make the point that observed variations in the wave tilt, which might be interpreted as due to local variations in the subsurface structure of the ground, can actually be due to reflections and/or scattering from a nonhomogeniety at some distance away.

6. SYNTHESIS OF SURFACE IMPEDANCES

The preceding section particularly points out the utility and need for simple and accurate methods for synthesizing surface impedances. This amounts to precribing desired boundary conditions, and implies control over the guiding, radiating and scattering properties of the surface. Field distributions on the surface can then be prescribed, as can radiation patterns.

Ideally, synthesized impedances at an interface should be a local function of position, and independent of the angle of incidence and the shape of the body. The grounded anisotropic artificial dielectric (pin bed) largely fulfills these requirements [King, et al. (1983)]. In addition, by filling the space between the pins with lossy dielectrics, any impedance in the right half plane should be synthesizable.

Synthesized surface impedances would obviously be of great value when designing laboratory models such as those described in the previous section. But besides this, they would also be useful in other applications, such as the design of the main body, and reflectionless tapers and terminations on guided wave structures (e.g., surface and leaky wave antennas), and the design of absorbers and reflectors.

7. HOMODYNE INSTRUMENTATION

Probing field distributions without disturbing the field itself is a difficult task. The use of a small electrically modulated scattering antenna in conjunction with a coherent system for detecting the backscattered signal is a simple, flexible and practical means of making such measurements. The probe can be either an electric dipole or a loop for measuring $\bar{E}$ or $\bar{H}$ fields respectively. It is easily moved and/or oriented to measure any desired component of the field without the disturbing effects of supports, cables, receivers, mixers, etc.
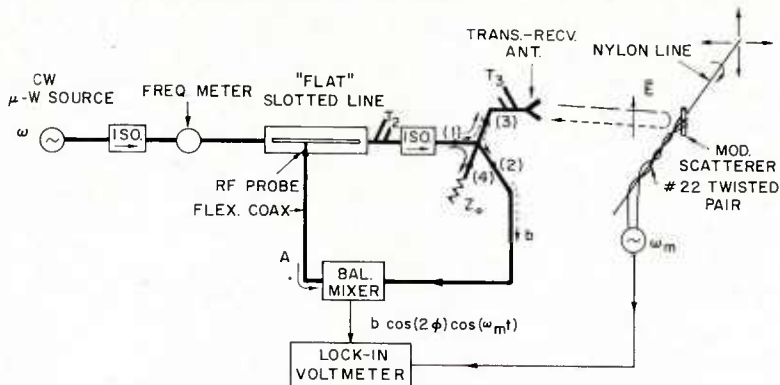
The terminals of the scattering antenna are usually loaded by a PIN diode. Amplitude modulation is accomplished by switching the junction impedance of the diode at an AF rate via resistive leads which are oriented perpendicular to the electric field. A detailed discussion on the design and use of modulated scatterers is given in [King, 1978].

The microwave homodyne instrumentation shown in Fig. 22 has proven to be a simple, accurate and sensitive means for measuring the relative amplitude and phase of the field

scattered from the probe. The CW microwave source output of about one watt is split by the magic tee, and radiated by the transmit-receive antenna. A minute amount of the amplitude modulated signal, b, which is scattered by the probe finds its way back into the transmit-receive antenna. There it is split by the magic tee and half passes to the balanced mixer where it is mixed with a portion of the original CW signal, A, routed via the RF probe in the slotted line and a flexible coaxial cable. Acting as a phase sensitive (homodyne) detector, the output of the mixer is of the form [King, 1978].

$$b \cos(2\phi) \cos(\omega_m t) \hspace{4cm} (14)$$

where b is proportional to the squared amplitude of the field component scattered by the probe, e.g., $b \propto |\overline{E} \cdot \overline{\ell}|^2$ when using an electric dipole, and $\overline{\ell}$ is a unit vector in the direction of the dipole axis. The angle 2ϕ is the round-trip phase difference between the reference A and the backscattered wave at the location of the mixer. This phase is easily varied by moving the RF probe along with "flat" slotted line which serves as a simple but accurate combined phase shifter and power divider.

Figure 22. Simple double-channel homodyne instrumentation system for measuring amplitude and phase of electric field distributions. •1982 American Geophysical Union.

To make amplitude measurements, 2ϕ is adjusted to make $\cos(2\phi)$ in (14) equal to unity and this maximum is tracked as the position of the scattering probe is varied. Similarly, to track the phase, 2ϕ is continuously adjusted via the slotted line probe to make $\cos(2\phi = 0)$. The corresponding change in 2ϕ is then read from a position indicator on the slotted line.

Tuning of the system is straightforward. By turning the modulator off and temporarily connecting a power meter to port 2 of the magic tee, tuner T_3 is adjusted to minimize the power at port 2. Tuner T_2 is adjusted to obtain a SWR of unity on the slotted line, as sensed by temporarily connecting a power meter to the RF probe. Penetration of the RF probe should be set such that the reference signal, A, is slightly below the point where the output noise of balanced mixer begins to increase noticeably. Typically, A ranges from 7 to 12 dBm. These adjustments insure the greatest sensitivity and dynamic range, and minimum system error.

The mixer output (14) can be monitored with a high-gain narrow-band voltmeter centered at ω_m. A lock-in voltmeter is quite effective since it is a phase sensitive detector in which the bandwidth can be very narrow, typically 10 Hz. Thus, the overall system is doubly coherent and the stability of the microwave and modulating sources is relatively unimportant. For a 10 Hz bandwidth, the overall system sensitivity is of the order of -140 dBm. The modulation frequency is chosen well above the noise corner of the mixer diodes, e.g., 10 kHz for Schottky diodes.

The microwave source power can be reduced and/or the dynamic range can be increased by 6 dB by using a circulator instead of a magic tee. The system shown in Fig. 22 has been found to function quite well when making manual measurements. By using two balanced mixers fed in quadrature phase, the phase sensitive homodyne system shown in Fig. 22 can be made phase insensitive [King, 1978; Park, 1982]. This permits rapid mapping of field amplitude and phase distributions without the inconvenience of manual adjustment of the slotted line probe to track the maxima or the nulls respectively. With proper trim adjustments of the amplitude and phase of the two balanced mixers, the measurement system can be made error-free [King, 1982b]. For automated measurements where the amplitude, phase and polarization are measured simultaneously and independently in real-time, see King and Yen [1981].

REFERENCES

1. Appel-Hansen, J. and R. J. King, "Experimental Study of Surface Wave Propagation on a Low-Permittivity Medium," Electronics Letters, 15(4), [1979], pp. 101-102. Also, Proceedings of the AGARD Symposium on "Terrain Profiles and Contours in EM Wave Propagation," Spatind, Norway, Sept. 10-14, AGARD-CP-269, pp. 9-1 - 9-4.

2. Bahar, E., "Progagation of VLF radio waves in a model earth-ionosphere waveguide of arbitrary height and finite surface impedance boundary: Theory and experiment," Radio Science 1(8), [1966], 925-938.

3. King, R. J., "Physical Modeling of Propagation Over the Earth," Radio Science, 17(5), (Special issue on Mathematical Models of Radio Propagation), [1982a], 1103-1116.

4. King, R. J., "Error Analysis of Phase-Insensitive Coherent (Homodyne) Detectors," IEEE Trans. on Instrumentation and Measurement, IM-31(3), [1982b], 212-214.

5. King, R. J., Microwave Homodyne Systems, Peregrinus Press, Southgate House, Stevegage, Herts., England, [1978].

6. King, R. J., "Wave-tilt measurements," IEEE Transactions on Antennas and Propagation, AP-24(1), [1976], 115-119.

7. King, R. J., D. V. Thiel and K. S. Park, "The Synthesis of Surface Reactance Using an Artificial Dielectric," IEEE Trans. on Antennas and Propagation, AP-31(3), [1983] 471-476.

8. King, R. W. P. and G. S. Smith, Antennas in Matter, 727-765, MIT Press, Cambridge, MA, [1981].

9. King, R. J. and Y. H. Yen, "Probing amplitude, phase and polarization of field distributions in real time," IEEE Transactions on Microwave Theory and Techniques, MTT-29(11), [1981], 1225-1231.

10. King, R. J. and K. S. Park, "Synthesis of surface reactances using a grounded pin bed structure," Electronics Letters, 17(1), [1981], 52-53.

11. King, R. J. and J. R. Wait, "Electromagnetic groundwave propagation; theory and experiment," Symposia Mathematics XVIII, Academic Press, N.Y., [1976], 184-193.

12. King, R. J., S. H. Cho, D. L. Jaggard, G. E. Bruckner and C. H. Hustig, "Experimental data for groundwave propagation over cylindrical surfaces," IEEE Trans. on Antennas and Propagation, AP-22(4), [1974], 551-556.

13. King, R. J., S. H. Cho and D. L. Jaggard, "Height-gain experimental data for groundwave propagation: 1, Homogeneous paths," Radio Science, 8(1), 7-15; "2, Heterogeneous paths," [1973], 17-22.

14. King, R. J. and C. H. Hustig, "Microwave surface impedance measurementsof a dielectric wedge on a perfect conductor," Canadian Journal of Physics, 49(7), [1971], 820-830.

15. King, R. J., S. W. Maley and J. R. Wait, "Experimental and theoretical studies of propagation of groundwaves across mixed paths," in Electromagnetic Wave Theory, J. Brown, Ed., Pergamon Press, New York, [1967], 217-224.

16. King, R. J. and S. W. Maley, "Model experiments on propagation of groundwaves across an abrupt boundary at oblique incidence," Radio Science 1(1), [1966], 111-115.

17. King, R. J. and W. I. Tsukamoto, "Groundwave propagation across semi-infinite strips and islands on a flat earth," Radio Science 1(7), [1966], 775-778.

18. King, R. J., S. W. Maley and J. R. Wait, "Groundwave propagation along three-section mixed paths," Proc. IEEE, 113(5), [1966], 747-751.

19. King, R. J. and S. W. Maley, "Model experiments on propagation of groundwaves across an abrupt boundary at perpendicular incidence," Radio Science J. Res. NBS 69D(10), [1965], 1375-1381.

20. Krogager, E., J. Appel-Hansen and R. J. King, "Precision Measurement of Surface and Lateral Waves," Conf. Proc. on Precision Electromagnetic Measurements, Braunschweig FRG, [1980], 23-27.

21. Maley, S. W. and H. Ottesen, "An experimental study of mixed-path groundwave propagation," Radio Science J. Res. NBS, 68D(8), [1964], 915-918.

22. Park, W. S., Instrumentation of Phase-Insensitive Homodyne Detection for Measuring Microwave Electric Fields, M. S. Thesis, Dept. of Electrical and Computer Engineering, University of Wisconsin, Madison, [1982].

23. Schwartz, K. and G. L. Brown, "A laboratory model for VLF propagation experiments," Radio Science, 6(7), [1971], 709-716.

24. Sinclair, G., "Theory of models of electromagnetic systems," Proc. IRE 36(11), [1948], 1364-1370.

25. Thiel, D. V., "Surface Impedance and Wave Tilt Interpretation over Horizontally Stratified Media", J. of Electrical and Electronics Engineering, Australia, IE Aust. and IREE Aust., 2(4), [1982], 240-244.

26. Thiel, D. V., K. S. Park and R. J. King, "Wave-tilt fluctuations near a vertical discontinuity in a flat ground plane," IEEE Transactions on Geoscience Electronics GE-20(1), [1982], 131-134.

27. Webber, G. E. amd I. C. Peden, "VLF mode analysis using a ceramic dielectric model of the earth-ionosphere waveguide," <u>IEEE Trans. on Antennas and Propagation</u>, AP-17(5), [1969], 613-620.

28. Winder, D. E., I. C. Peden and H. M. Swarm, "A 3 GHz scale model of submerged VLF antenna using lossy ceramic powder," <u>IEEE Trans. on Antennas and Propagation</u>, AP-14(4), [1966], 507-509.

ACKNOWLEDGEMENTS

INTERACTION OF ANTENNAS WITH MASTS UNDER SPECIAL CONSIDERATION OF THE SENSITIVITY AND NONLINEAR EFFECTS IN SHIP BORNE RECEIVING SYSTEMS

by
H.K.Lindenmeier
University of the Bundeswehr Munich
8014 Neubiberg,Germany FRG

SUMMARY

The minimum required height of active and passive rod antennas is presented as a function of the environmental noise. A high linearity of the system is necessary to suppress intermodulation and crossmodulation effects being generated by high level signals radiated from the transmitters on the ship. In many cases this problem can only be solved by selective means at the front end of a receiving system. An appropriate solution is found in a "fast tunable active receiving antenna." The effective height, the antenna impedance and the vertical pattern of an antenna mounted on top of a mast are influenced in an undesired way. The available dynamic range of the receiving system is reduced considerably by the interaction of the mast and the antenna. Due to the resonant effects of the mast-antenna-structure this reduction factor is frequency dependent and increases with increasing height of the mast. In addition there is a severe disturbing influence of the mast on the vertical diagram of the rod antenna on this mast. Passive broadband rod antennas should not be mounted on a mast at all. With an active antenna however the effect of the mast on the antenna properties can be reduced. In contrary to rod antennas loop antennas can be advantageously decoupled from the mast by symmetrical mounting on top of a rotationally symmetrical mast.

1. SENSITIVITY AND MINIMUM REQUIRED ANTENNA HEIGHT.

The determining parameter for the efficiency of a communication channel is the channel capacity C_c which is a function of P_d/P_u with P_d representing the desired signal power and P_u representing the total undesired power of distortions in this channel at the output of the receiving system. With every receiving system as displayed in Fig. 1 additional distortions occur which indeed are not of the character of white noise, however, reduce the capacity of the communication channel in a similar way. In Fig. 1 the distortions to be considered are listed. Beside the received external noise power P_A and beside the electronic noise P_a of the active antenna and the receiver noise P_r as well distortions P_i and P_{ir} which are caused by nonlinear effects in the active antenna and in the receiver respectively are also included. In /9,11/ all distortions have been summarized and the signal-to distortion ratio reads

$$\frac{E_d^2}{\overline{e_u^2}} = \frac{E_d^2/\overline{e_A^2}}{1 + \dfrac{\overline{e_a^2}}{\overline{e_A^2}} \cdot (1+ \dfrac{\overline{e_r^2}}{\overline{e_a^2}} + \dfrac{E_i^2}{\overline{e_a^2}} + \dfrac{E_{ir}^2}{\overline{e_a^2}})} \qquad (1)$$

In Equ. (1) the desired signal is expressed by the signal fieldstrength E_d and all distortions are expressed by fictitious equivalent distortion fieldstrengths of a respective fictitious plane wave at the receiving location incident from the direction of maximum reception. Distortions of random character are described by median square fieldstrength values while an intermodulation distortion has the character of an undesired rf carrier and therefore is expressed by an effective fieldstrength value being produced by undesired signal carriers E_u as an effect of nonlinearity /9/ . From Equ.(1) design considerations for the antenna can be derived for optimization of the channel capacity.

1.1 Minimum required height of resonant antennas

In practice the required snr-bandwidth, the realizable Q-factor, and the antenna temperature T_A at the location of reception are known. From this the minimum required radiator bandwidth can be computed. For a rod radiator the minimum required height h_{min} has been evaluated in /12/ for different situations of external noise. The curve in Fig. 2 shows that the required height of a receiving antenna at no frequency exceeds 80 cm for average values of T_A and at lower frequencies is much less than the required height of a transmitting antenna. If a capacity C is effective in parallel to the terminals of a capacitive radiator with capacity C_A this capacity C may be regarded a part of the radiator the effective bandwidth of which is reduced by this to

$$b_{ro}' = b_{ro}/(1+C/C_A) \qquad (2)$$

This effect reduces both the efficiency and the available snr-bandwidth as well. From this point of view inductive tuning of a capacitive radiator is preferable to capacitive tuning. The same is true with the capacitive tuning of a magnetic dipole. A similar bandlimiting effect occurs if the radiator is loaded by a transmission line as in Fig. 4. The influence of the line increases with increasing ℓ/h. In order to compensate for this effect the increase of antenna height indicated at the scale at the right hand side of Fig. 4 would be necessary. Therefore minimum antenna height is only obtained if the line at the base of the radiator is avoided.

1.2 Extremely broadband active receiving antennas /7,9,10,11/

In a certain frequency range, the impedance of the passive antenna part is located within the boundary circle for noise matching represented by $snr/(snr)_{max} = 1/2$ at the operational frequency regarded. The fact that very large boundary circles exist at lower frequencies gives rise to the idea that the active element could be directly connected to the radiator and the impedance of the radiator is not transformed by means of a more complicated antenna structure or any excitation network. In the case of the capacitive radiator in Fig. 6 the optimum snr is obtained by choice of an appropriate active element and its bias in such a way that the noise characteristics satisfy the impedance condition with a radiator of minimum size.

Fig. 6 shows the equivalent circuit of a short active rod antenna with rod capacitance C_A with directly connected FET-emplifier. C_a represents the inevitable input capacitance of the amplifier which should be as small as possible, since the required length of the rod is proportional to the factor $(1 + C_a/C_A)$. With this principle broadband antennas have been designed covering the frequency range from 10 kHz to 100 MHz. The equivalent noise fieldstrength due to the amplifier noise voltage v_a is obtained from

$$\sqrt{\overline{e_\alpha^2}} = \sqrt{\overline{v_\alpha^2}} \cdot (1+C_a/C_A)/h_{eff}$$

where h_{eff} = effective height of the passive antenna part.

1.3 Minimum required height

If $\overline{v_\alpha^2}$ is expressed by an equivalent noise resistance R_e, h_{min} of an active rod antenna of height h reads /19/

$$\frac{h_{min}}{\lambda_o} \approx \frac{h_i}{\lambda_o} \cdot \left[1 + \frac{1}{2} \cdot \left(\sqrt{1 + \frac{4C_a}{c \cdot h_i}} - 1 \right) \right] \quad , \tag{3}$$

with $c = C_A/h$ representing the antenna capacitance and h_i representing the ideal height for $C_a = 0$

$$\frac{h_i}{\lambda_o} = \sqrt{\frac{T_o}{T_A}} \cdot \sqrt{\frac{R_e}{Z_o}} \cdot \sqrt{\frac{3}{\pi}} \qquad Z_o = 120 \ \pi\Omega. \tag{4}$$

In contrary to that the minimum required height of a short passive rod antenna, being directly connected at its base to the inner conductor of a coaxial line and feeding a receiver with noise figure F_r, varies with $\sqrt[4]{T_o/T_A}$ /19/ :

$$\frac{h_{min}}{\lambda_o} \approx 0.43 \cdot \sqrt[4]{\frac{T_o}{T_A} \cdot \frac{(F_r - 1)}{(Z_L/50\Omega) \cdot (c/10pF/m)^2}} \tag{5}$$

Z_L: characteristic impedance of line and receiver

A comparison of the uninterrupted curves in Fig. 3 shows that the minimum required height of the active antenna is much lower than that of the passive antenna. Even though the active antenna operates broadband the required height does not differ very much from the curve in Fig. 2, which is valid for narrow band receiving antennas being tuned to the actual frequency.

1.4 Optimum location of antenna amplifier /7,11,19/

It is well known that with a rod monopole of given total height h_t maximum h_{eff} is not found if the feeding gap is located at the base of the rod. At this location, however, maximum antenna capacitance C_A is measured. Considering the emf in combination with the voltage dividing effect between the passive antenna part and the amplifier input in Fig. 6 it is obvious that there is a location at height h_{Mopt} for optimum snr at the active antenna output. h_{Mopt} reads roughly

$$\frac{h_{Mopt}}{h_t} \approx (1 + \frac{C_a}{c \cdot h_t}) - \sqrt{(1 + \frac{C_a}{c \cdot h_t})^2 - 1} \tag{6}$$

and is displayed in Fig.5

1.5 Nonlinear effects in active antenna and receiver elements /9,10,11,13/

Nonlinear effects can be avoided either by selective means or by means of a high reverse feedback, which has to be designed in a way that the sensitivity of the active antenna is not diminished. In the very vicinity of a transmitting station an undesired fieldstrength of up to 100 V/m may occur. In these cases for an undisturbed operation the active antenna must be tuned. In /21/ design considerations of a highly selective active antenna are presented and it is shown that nonlinear effects in the ferrite tuning elements become a severe problem. In general, however, the active antenna should operate broadband. In this case a broadband reverse feedbacked antenna amplifier is necessary.

With the circuit in Fig. 6 the reverse feedback resistance $R_a^* + Z_L$ contributes to the noise of transistor T_1', the forward transconductance of which is g_m. The equivalent noise fieldstrength e_α of the active antenna reads

$$\sqrt{\frac{e_a^2}{B}} \approx \frac{1}{h_{eff}} \cdot (1 + C_a/C_A) \cdot \sqrt{4\,k\,T_o/g_m} \cdot$$
$$\cdot \sqrt{1 + \frac{G_r}{\beta_2 \cdot \beta_{34}}} \; , \tag{7}$$

where the last factor describes the influence of the reverse feedback on the noise. With increasing negative reverse feedback factor $G_r = V_{11}/V_{12}$ the ratio of the voltage V_{11} between the terminals 2 and 2' and the steering voltage V_{12} at transistor T_1' increases. The influence of V_{11}/V_{12}, however, is reduced by the influence of $\beta_2 \cdot \beta_{34}$, where β_2 and β_{34} represent the current amplification factor of transistor T_2' and T_3', T_4' respectively.

In the following the "small signal linearity characteristics" of the active antenna are estimated in form of the suppression of intermodulation products $a_{2,3}$ in dB with respect to 2nd order and 3rd order effects respectively caused by two undesired fieldstrenths $E_u = E_{f1} = E_{f2}$ in Fig. 7. There is no theoretical limitation of the obtainable G_r and the achievable $a_{2,3}$ which depend completely on the circuit design and the semiconductors available. A further very important characteristic of an active antenna is its dynamic range which characterizes the difference between the noise level at the one end and the maximum tolerable undesired signal at the other end. The maximum tolerable undesired signal is that value $E_{ut2} = \sqrt{E_{f1} \cdot E_{f2}}$ the second order intermodulation product of which equals the noise level $\sqrt{e_a^2}$ of the active antenna. A similar value with respect to a third order intermodulation product at the frequencies $2f_1 \pm f_2$ and $f_1 + 2f_2$ respectively reads

$$E_{ut3} = \sqrt{E_{f1}^2 \cdot E_{f2}} \text{ and } E_{ut3} = \sqrt{E_{f1} \cdot E_{f2}^2}$$

respectively. Consequently the dynamic of nth order is defined to be

$$d_n = 20 \cdot \log \frac{E_{utn}}{\sqrt{e_a^2}} \; , \tag{8}$$

which is illustrated in Fig. 7.

With many cases in practice the receiving system is more endangered by "large signal nonlinear effects", such as broadband crossmodulation from a nearby located transmitting antenna. In this case the tolerable rms-value E_{uc} of an undesired amplitude modulated signal is regarded causing a 20 dB suppressed undesired modulation factor on the desired signal carrier.

1.6 Optimum antenna height of broadband antenna

For a given antenna amplifier the minimum required height h_{min} also represents the optimum antenna height h_{opt} if nonlinear effects are taken into account. This can be shown by means of Fig. 8 , where the power contributions P_d , P_A and P_a for a given fieldstrength situation are plotted versus the height h of an active rod antenna in a logarithmic display. In addition the intermodulation distortions P_{i1} , P_{i2} and P_{i3} for different values of interfering signals $E_{u1} > E_{u2} > E_{u3}$ are displayed. The dash-dotted curves describe the sum of distortions, and the distance from the desired power level P_d represents the actual signal-to-distortion ratio obtained with the respective value of E_u . This signal-to-distortion ratio is displayed by the curves in the lower part of the schematic. h_{min} describes the point where $P_a = P_A$. Increasing the antenna height above h_{min} P_d/P_u may be diminished severely by nonlinear effects but can never be increased to an extent of practical interest. h_{min} represents that height where maximum available P_d/P_u can be obtained and the tolerable interfering fields of amplitude E_u are maximum which means $h_{min} = h_{opt}$.

If the antenna is mounted upon a slim mast as displayed in Fig. 9 all characteristic fieldstrength values such as the equivalent noise fieldstrength and the maximum tolerable fieldstrength, are reduced by the factor "b" in dB due to the height effect of the mast.

This means that the sensitivity of the receiving system is increased by this factor, whereas, the linearity of the antenna is reduced by the same factor, and according to equ. (8), the dynamic of the antenna remains unaltered by this effect. Obviously the above considerations about the optimum antenna height should take the height of the mast into account. In the frequency range where h_M is short compared to the wavelength the factor b is independent from the frequency, and the antenna rod can be shortened to compensate for the effect of the mast. Because of the comparatively narrow band resonances a too high and very slim mast should be avoided in practice /7/ . This will be shown in the following chapter.

2. ROD ANTENNAS ON MASTS /22/

2.1 Summary of undesired effects

If a rod antenna is mounted on a mast the effective height, the antenna impedance and the vertical pattern are influenced in an undesired way. In the following this influence will be shown for a variety of conical masts which are frequently found on board of a ship and will be displayed in form of a catalogue.

By means of Fig.8 it was shown that there is an optimum antenna height for every receiving system. If the antenna height is greater than this value the receiving system is endangered by intermodulation effects, and if the antenna height is less the sensitivity of the receiving system is not satisfactory. The great advantage of small active antennas is the frequency independent effective antenna height and the frequency independent vertical pattern which are due to the shortness of the antenna in comparison with the wavelength. As a result of this it is possible to adapt the passive antenna part by appropriate choice of the antenna height to the active antenna part broadband. This provides the optimum dynamic for the receiving system which can be obtained with a given antenna amplifier in a wide frequency range. With passive antennas, which, according to Fig.3, must be chosen much higher, neither the effective height nor the vertical pattern are constant within the required frequency range. Therefore with a given receiver of a certain dynamic the dynamic of the receiving system cannot be designed optimum in a wide frequency range.

If an antenna is mounted on a mast the mast is integrated into the antenna structure and has to be considered a part of the antenna. Therefore with passive and active antennas as well the available dynamic range of the receiving system is reduced considerably by the interaction of the mast and the antenna. Due to the resonant effects of the mast-antenna-structure this reduction factor is frequency dependent and increases with increasing height of the mast. In addition there is a severe disturbing influence of the mast on the vertical diagram of the rod antenna on this mast. The catalogue to be presented will also show the beam splitting effect of the mast on the vertical diagram. This results very often in an undesired suppression of ground wave reception and a strong undesired main beam at higher elevation angles. At higher frequencies even a series of undesired lobes have to be considered.

2.2 Effective height of rod antenna on a mast

As already explained in Ch. 1.6 and in Fig. 9 the linearity of the receiving system is reduced if the effective height of the passive antenna part mounted on a mast is greater than the effective height of the same antenna mounted on a conducting area. Therefore the frequency dependance of the effective height of a short rod antenna mounted on a mast is studied in Figs.12 -15. Most informative is Fig. 12 where the effective heights of a slim 1m rod mounted on a slim 15 m high mast and the same rod mounted on a conical mast of same height are compared. The effective height of the rod on the mast is defined as the ratio of the emf measured at the base of the rod antenna over the electric fieldstrength of the incident wave at the elevation angle zero. Fig. 12 shows the effective height versus the frequency. At the frequency where the mast is of a quarter wavelength there is a resonance, which in the case of the slim mast of .8 cm diameter is much greater than with a conical mast of 67.5 cm diameter at the base and 15 cm diameter at the upper end. At the frequency where the masts are of half a wavelength a deep minimum of the effective height is obtained. At three quarter of a wavelength again there is a maximum and the figure shows that the effective height oscillates within quarter wavelength steps with a descending tendency towards higher frequencies. The slim mast of .8 cm diameter which in practice might be realized by means of a non conductive mast with a cable of .8 cm diameter the resonances are much more pronounced than with the thicker conical mast. Therefore the more frequently used conducted conical mast is preferable to the nonconductive mast with antenna cable. A comparison of Figs. 13, 14 and 15 shows that the influence of the mast is increased with increasing physical height. At low frequencies the height factor is obtained from Equ. (6). The curves in Figs. 12 - 15 are true with a 1 m rod which is frequently applied to active receiving antennas. The basic effects however are also true for higher rods which are used as passive antennas. The resonances of the effective heights can be physically explained by an electric line which is short circuited at its end. The short circuit is represented by the conductive connection of the conductive mast with a conductive ground plane which for example may be the body of a ship. At the upper end the mast is unloaded. A short circuited line into which rf energy is coupled produces a resonant voltage at the unloaded end.

Therefore at a quarter wavelength the resonant mast in the field of the incident wave produces a high voltage at its upper end going along with a high secondary fieldstrength exciting the rod antenna at this end. The bandwidth of this resonance depends on the slenderness of the mast. Therefore the bandwidth of the resonance of the effective height is determined by the bandwidth of the resonance of the mast.

2.3 Current distribution

The current distribution along the mast and the short rod are displayed in Fig. 16 -20 in phase φ and absolute value I. Fig. 16 and 17 show the current distributions in the receiving case for the slim and the conical mast at very low frequencies. Fig. 18 presents the current distribution at a quarter wavelength resonance and Fig. 19 and Fig. 20 at a half wavelength resonance and three quarter resonance respectively.

2.4 Vertical pattern and antenna impedance

The curves for the effective heights give only an information about a horizontal incident wave. In order to learn the emf of the antenna for waves with arbitrary elevation angles the vertical diagram has to be studied. For a mast of 15 m height these diagrams are displayed in Fig. 21 - 26. At low frequencies up to 4.5 MHz the vertical diagram resembles that of a Hertzian monopole. With increasing frequency the vertical diagram is splitted into several undesired sidelobes. Therefore at several frequencies the good reception of incident waves of low elevation angles can not be guaranteed. This effect is very disturbing since a broadband design of the transmission channel under these circumstances is impossible. There are also resonant effects of the antenna impedance which for a mast of 10 m height is plotted in Fig. 27.
There are also resonant effects of the antenna impedance which for a mast of 10 m height is plotted in Fig. 27. In Figs. 28 - 31 the vertical pattern of an antenna on a 10 m high mast are displayed. Again it can be seen that the desired vertical pattern is only available at frequencies below 10 MHz. In a similar way Fig. 32 - 34 and 35 - 36 show the impedance diagram and the vertical patterns for 7 m and 4 m high masts respectively.

In many cases it is possible to avoid a mast of great height and the antenna can be mounted on a short cylindrical mast of only less than 2 m height. Fig. 37 describes the effective height and the measured antenna capacity if the total height of mast and antenna is 3 m and the location of the antenna terminals is chosen at a special height h_M. In Fig. 38 and Fig. 39 the effective heights of a 1 m rod on a 2 m high and a 1 m high mast respectively are plotted. It can be seen that the structure displayed in Fig. 39 is satisfactorily frequency independent. A mast of this height can be considered tolerable for a receiving system.
With active antennas it is possible to suppress the influence of a higher mast by means of a brodband decoupling circuit. In this case an additional ground plane being realized by means of horizontal radials are necessary.
If for any reasons the installation of the antenna on a higher mast can not be avoided the dynamic range of the active antenna or the receiver respectively has to be increased. This requires the application of a selective active antenna.

3. DESIGN CONSIDERATIONS ON SELECTIVE ACTIVE RECEIVING ANTENNAS /23/

3.1 Fieldstrength sensitivity

By means of the equivalent circuit (Fig.40) of the selective active antenna the fieldstrength sensitivity can be obtained. The short rod antenna is described by its effective height h_{eff}, which is half of the geometrical height h and by R_A and C_A, the equivalent elements for the impedance of the antenna. The resonant circuit is formed by the inductance L and C_A, C_p and C_a/t^2. C_a represents the input capacitance of the amplifier which is transformed by the (ideal) transformer t:1. This transformer makes various ways of coupling between the amplifier and the resonant circuit possible. Among others the winding capacity of L is part of C_p. V_{na} is the equivalent noise source of the amplifier, the losses of the inductance L are described by R_L and its noise source V_{mL}, the equivalent temperature of which is the ambient temperature T_o.

At the resonant frequency $f_r = \omega/2\pi$, which is identical with the receiving frequency, the noise contribution of the inductance of quality factor Q can be expressed by an equivalent noise fieldstrength $\overline{e_Q^2}$ with a channel bandwidth B

$$\overline{e_Q^2} = \left(\frac{2}{h}\right)^2 \cdot \frac{4kT_oB}{\omega_r C_A Q} \cdot \left(1 + \frac{C_P}{C_A} + \frac{C_a}{t^2 C_A}\right) \tag{8}$$

and the appertaining equivalent noise fieldstrength due to the noise contribution of the amplifiers $\overline{e_T^2}$ reads as:

$$\overline{e_T^2} = \overline{e_Q^2} \cdot \frac{R_{na}\omega_r C_A t^2}{Q} \cdot \left(1 + \frac{C_P}{C_A} + \frac{C_a}{t^2 C_A}\right) \tag{9}$$

Herein $R_{na} = \overline{V_{na}^2} / (4kT_o B)$ according to Nyquist's formula represents the equivalent noise resistance of the transistor. As a consequence the equivalent noise fieldstrength of the selective active antenna is

$$\overline{e_a^2} = \overline{e_Q^2} + \overline{e_T^2}. \tag{10}$$

From equs. (8) and (9) the deteriorating effect of C_p and C_a can be seen. Sensitivity as well as the later on evaluated dynamic range seriously depend on the transformer ratio t. In Fig. 41 curves of $\overline{e_Q^2}$ (dotted), $\overline{e_T^2}$ (dashed) and $\overline{e_a^2}$ (uninterrupted) are plotted dynamic d. The typical curvature obtained for the total noise can be subdivided into three regions. Best sensitivity for given height of the antenna, or minimum antenna height for requested sensitivity respectively, will be obtained in region II of $\overline{e_a^2}$. In this region of values of t the effects of the amplifier capacity and the amplifier noise as well are negligible. However, as will be shown below, it is not advantageous, to chose t of this region, since the dynamic range of the system is not as good as possible.

The optimum dynamic will be reached if t is chosen of region III in fig.41 where the noise source of the amplifier is dominating the fieldstrength sensitivity. In order to compensate the reduced sensitivity, the antenna can be made a bit higher. A t of region I is of no practical interest, since a worse sensitivity is combined with a reduced dynamic, additionally.

In general it is avoided by frequency planning to operate with neighboured receiving and transmitting stations, the frequencies of which are very close together. Thus, undesired signals about 10% and 20% apart from the receiving frequency can be considered as worst case for third order intermodulation, and signals at 0.9 f_r and 1.9 f_r as worst case for second order intermodulation, respectively.
Considering an amplifier from an active broadband antenna with the above mentioned dynamic characteristics and a selective circuit of Q = 100 for example the tolerable fieldstrength of the undesired signals can be 14 V/m for third order and 3 V/m for second order intermodulation distortion, repectively. With the active broadband antenna the appertaining values of only 0.55 V/m and 0.055 V/m are obtained.

With greater frequency deviation of the undesired signals from the receiving frequency the dynamic increases considerably with selective active antennas.
The obtainable improvement of dynamic is displayed in Fig.42.

3.2 Minimum required height for optimum sensitivity

In /19/ fieldstrength sensitivity and minimum required antenna height taking the external noise into account have been derived for active broadband antennas. With some changes in nomenclature the sensitivity can be expressed by:

$$\overline{e_{ab}^2} = \left(\frac{2}{h_b}\right)^2 \cdot \left(1 + \frac{C_{Pb}}{C_{Ab}}\right)^2 \cdot 4kT_o BR_n \tag{11}$$

$$\text{with } h_b \approx h_i \cdot \left[1 + \frac{1}{2}\left(\sqrt{1 + \frac{4C_{Pb}}{c \cdot h_i}} - 1\right)\right] \tag{12}$$

$$\text{and } h_i = \lambda_o \cdot \sqrt{\frac{T_o}{T_A} \cdot \frac{R_n}{Z_o} \cdot \frac{3}{\pi}} \tag{13}$$

T_A is the external noise temperature, Z_o represents the wave impedance ($Z_o = 120\pi\,\Omega$) and $c = C_A/h = C_{Ab}/h_b$ the capacitance of the rod per antenna height h or h_b respectively.

$\overline{e_{ab}^2}$, h_b, C_{Ab} and C_{pb} are the corresponding values of the broadband antenna as $\overline{e_a^2}$, h, C_A and C_p are of the selective antenna. R_n represents the equivalent noise resistance of the noise source of the amplifier.
In chapter 3.1 it has been shown, that minimum antenna height of the selective active antenna will be obtained in region II of Fig. 41. In this region $\overline{e_a^2}$ reads as

$$\overline{e_a^2} = \left(\frac{2}{h}\right)^2 \cdot \frac{4kT_o B}{\omega_r C_A Q} \cdot \left(1 + \frac{C_P}{C_A}\right) \tag{14}$$

Considering best sensitivity possible in both cases, which will be obtained with negligible values of C_ρ and $C_{\rho b}$, equivalent fieldstrength sensitivity will be reached, if the height of the selective active antenna (h_{min}) is chosen with respect to Equ. (14).

$$h_{min}/m = \sqrt[3]{(h_i/m)^2 \cdot \frac{1}{\omega_r \cdot 10 \text{ pF} \cdot \frac{C}{10 pF/m} \cdot Q \cdot R_n}}$$ (15)

The minimum required height of selective active antennas (Q = 50 and Q = 100) is plotted versus frequency in the frequency range from 100 kHz up to 100 MHz in Fig. 43 (dashed curves). Compared to the height of the active broadband antenna (h_i, dotted curve, R_m = 100 Ω), it can be seen, that only beyond 10 MHz the selectivity leads to smaller antennas, whereas below 1 MHz, due to the losses of the inductance the selective antenna has to be considerably longer. h_ρ in Fig. 43 represents the required height of a passive antenna system according to /19/.

4. LOOP ANTENNAS /23/

In contrary to rod antennas loop antennas can be advantageously decoupled from the mast by symmetrical mounting on top of a rotationally symmetrical mast as to be seen in Fig. 44. In order to provide an omnidirectional horizontal diagram a pair of crossed loop antennas have to be applied. With passive loop antennas the required diameter is unsuitable large for application in a mobile receiving system as on board of a ship. For this reason an active loop antenna of only 0.8 m in diameter has been developed which covers the frequency band from 1 MHz to 30 MHz broadband. A special coupling between the loop and the amplifier provides maximum signal-to-noise ratio. By means of a highly linear antenna amplifier a wide dynamic range can be realized which is not reduced if the antenna is mounted on a mast.

4.1 Fieldstrength-sensitivity

Fig. 45 shows the basic circuit diagram of a broadband active loop antenna. The FET in grounded-gate circuit symbolizes an electronic circuit with low input impedance. Its noise contribution can be described by an equivalent noise voltage source in series. At the output of this amplifier stage a highly linear low noise transistor amplifier is cascaded. An appropriate transformer coupling between the amplifier and the loop in combination with a smallest possible load capacitance C are the determining factors for broadband sensitivity optimization. The analysis of the noise concentrates on the noise contribution of the conductance G, which is described by Nyquist's formula $\overline{i_{rG}^2} = 4kT_o BG$. The shot noise of the FET, described by an equivalent noise source in series to the input, reads as $\overline{u_{re}^2} = 4kT_o BR_e$, with R_e representing the equivalent noise resistance in this circuit. R_e is approximated by $R_e \approx (1 + g_m/R_c)/g_m$. Herein g_m = forward transconductance, and R_c = channel resistance. Under the assumption of a negligibly small noise contribution of the gate leakage current the equivalent noise-fieldstrength of the active loop antenna reads as:

$$\frac{E_a}{\sqrt{B}} \approx \frac{1}{h_{eff1}} \cdot \sqrt{4kT_o} \cdot \sqrt{R_e \cdot \frac{[1-(\frac{\omega}{\omega_o})^2]^2}{t^2} + \frac{1}{Q^2 \cdot t^2 \cdot G} \cdot (\frac{\omega}{\omega_o})^2}$$ (16)

with h_{eff} = $2\pi A/\lambda$ representing the effective height of the passive loop with area A. As a result of the inevitable capacitor C and the transformed loop inductance an undesired resonance is formed at frequency ω_o with a quality factor Q = $\omega_o C/G$. Curves of the equivalent noise fieldstrength of the active loop antenna for a channel bandwith of B = 1 Hz are plotted versus frequency in Fig 46. Optimum sensitivity is obtained with a transformation ratio of 1:12 assuming a minimum possible capacitance of 2 pF, which is only realistic if a gallium-arsenide FET is applied to the circuit. The external noise fieldstrength has been found to be -42 dBμV/m by CCIR and is represented by the dash-dotted line in Fig 46.

4.2. Effective height of the active loop antenna

After the analogy of passive receiving antennas the electromotoric force at the output (2 and 2' in Fig. 45) in relation to the electric fieldstrength E can be defined as the effective height of the active loop antenna $h_{eff a}$. With the impedances as defined in Fig. 45 $h_{eff a}$ reads as: $h_{eff a}$ = $V_{22'}(Z_L + Z_A)/(Z_L \cdot E)$. With active antennas the impedance ratio $(Z_L + Z_A)/Z_A$ can be realized to be frequency independent without any problems. This reduces the problem of a broadband frequency independent output voltage $V_{22'}/E$ in the circuit in Fig. 45 to the problem of a frequency independent transistor current I/E. Under the assumption of a $G \ll g_m$, which in practice is always true, this current can be described as follows:

$$I \approx E \cdot A \cdot \frac{1}{L_i \cdot t \cdot C_o} \cdot \frac{1}{\sqrt{1 + [Q \cdot \frac{G}{g_m}(\frac{\omega}{\omega_o} - \frac{\omega_o}{\omega})]^2}} \qquad (17)$$

L_i: inductance of the loop. c_o: light velocity

If $Q' = Q \cdot G/g_m$ is regarded the effective quality factor of the circuit it can be realized that in contrary to the sensitivity performance the resonant character is of only negligible influence on the signal behaviour of the active loop antenna. With the optimum dimensioned antenna in Fig 46 (t=12,C=2 pF) the variation of h_{eff_a} is far less than 1 dB in the regarded frequency range. Hence the circuit in Fig.45 satisfies the required sensitivity and the required flatness of the amplitude response versus frequency as well.

4.3. Linearity and preferential application of active loop antennas.

Fig.47 presents the basic circuit of a realized antenna amplifier. A highly linear symmetrical amplifier with high impedance input is applied as a second amplifier stage. Due to the limited linearity characteristics of this amplifier the total second order dynamic has been found to be 100 dB.

The ratio of the electric fieldstrength of a nearby located vertically polarized transmitting antenna, and the equivalent noise fieldstrength of the receiving system can be regarded as a related distortion level. With this definition the obtainable gain in dynamic range, which is available if a receiving loop antenna is applied instead of a receiving rod antenna, can be found by the negative difference of these related distortion levels. This difference is plotted in Fig. 48 versus the distance from a 7 m high transmitting rod antenna.

REFERENCES

/1/ H. Meinke, To the definition of an active antenna, Nachrichtentechn. Z. 29 (1976),S.55.

/2/ J. R. Copeland, W. J. Robertson, R. G. Vertraete, Antennafier arrays, IEEE Trans. Antennas and Propagation AP-12 (1964), S.227-233.

/3/ H. Meinke, Noise in nonreciprocal, amplifying receiving antennas, Nachrichtentechn. Z. 21 (1968), S.322-329.

/4/ H. Lindenmeier, Some examples of low noise, transistorized receiving antennas, Nachrichtentechn. Z. 22 (1969), S.381-387.

/5/ G. Flachenecker, A lightning protected transistorized receiving antenna, Nachrichtentechn. Z. 22 (1969), S.557-564.

/6/ F. Landstorfer, Short transistorized receiving antennas in the frequency range from 30-200 MHz, Nachrichtentechn. Z. 23 (1969), S.694-700.

/7/ H. Lindenmeier, The transistorized receiving antenna with a capacitive high impedance amplifier an optimum solution for receiving at low frequencies, Nachrichtentechn. Z. 27 (1974), S.411-418.

/8/ H. Lindenmeier, Optimum Bandwidth of Signal-to-noise ratio of receiving systems with small antennas, AEÜ 30 (1976), S.358-367.

/9/ H. Lindenmeier, Small signal properties and sensitivity of an active broadband receiving antenna with a wide range of linearity. Nachrichtentechn. Z. 30 (1977), H. 1, S.95-99.

/10/ H. Lindenmeier, Characteristic quantities for valuation of the linearity properties of active broadband antennas with a wide range of linearity, Nachrichtentechn. Z. 30 (1977), H. 2, S.169-173.

/11/ H. Lindenmeier, Design of electrically small broadband receiving antennas under consideration of nonlinear distortions in amplifier elements, Ant.a.Prop.Soc.Int.Symp. at Amherst 1976, pp. 242-245.

/12/ H. Lindenmeier, Relation between minimum antenna height and bandwidth of the signal-to-noise ratio in a receiving system. Ant.a.Prop.Soc.Symp. at Amherst, pp. 246-249.

/13/ H. Lindenmeier, New methods to solve the nonlinearity problem in active receiving antennas, Summaries of Papers 1978, Int.Symp.on Ant.a.Prop,Sendai,Japan. I.E.C.E. of Japan, pp. 525-529.

/14/ F. Landstorfer, H. Lindenmeier and H. Meinke, Transistorized antennas at mocrowave frequencies, Nachrichtentechn. Z. 24 (1971), S.5-9.

/15/ H. Lindenmeier, Principle and properties of modern car antennas, Nachrichtentechn. Z. 27 (1974) H. 1, S.17-23.

/16/ H. Lindenmeier and H. Meinke, Electronic car antennas of today, Funkschau 48 (1976), S.578-580.

/17/ H. Lindenmeier, Small active car antennas for electronically tunable receivers and for standard receivers, IERE Conf. Proc. No. 40, pp. 37-45, (1977).

/18/ G. Bodemann, H. Lindenmeier, Adcocksystem with active antennas for mobile applications, AEG Scientific Report, AEG-Telefunken 50 (1977) 4/5, pp. 158-165.

/19/ H. Lindenmeier, The short active receiving antenna an appropriate element for application in antenna arrays. IEE Conference Publication Number 169, pp. 91-95 (1978).

/20/ M.M. Dawond et al, Realization of superdirectivity from active and passive array antennas, IEE Conference Publication Number 169, pp. 25-29 (1978).

/21/ J. Hopf, H. Lindenmeier, Fast tunable active receiving antenna, URSI-Symposium on Electromagnetic Waves 1980, Munich.
/22/ K. Woweries, Evaluation of short rod antennas on conical masts. Diploma-thesis 1973, Technical University of Munich.

/23/ J. Hopf, H.K. Lindenmeier, Active loop antennas. IEEE Conf. on. antennas a. Propagation, May 1982, Albuquerque New Mexico. pp.560 - 563.
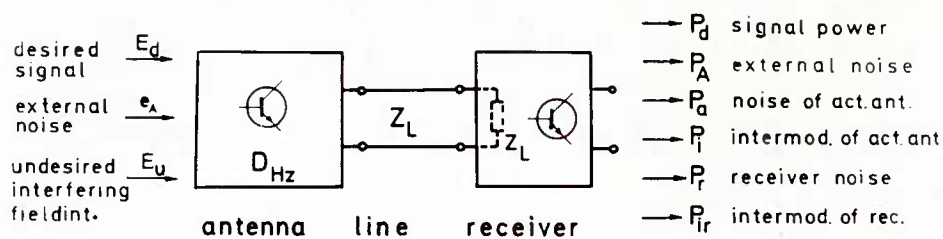
Fig. 1
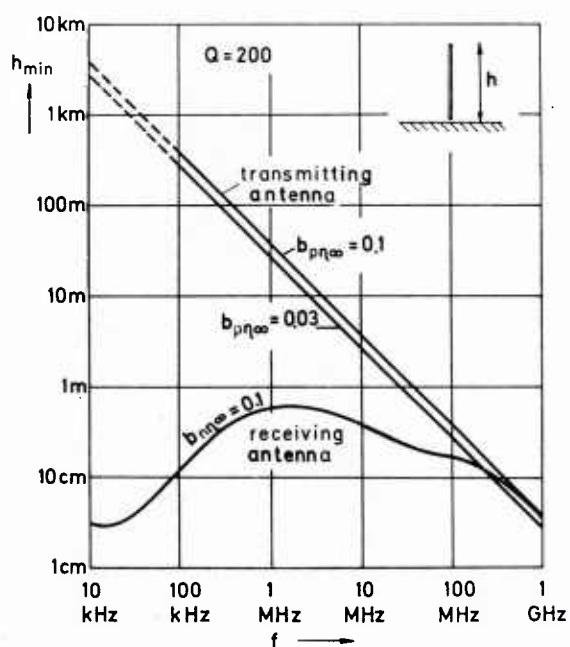
Fig. 2
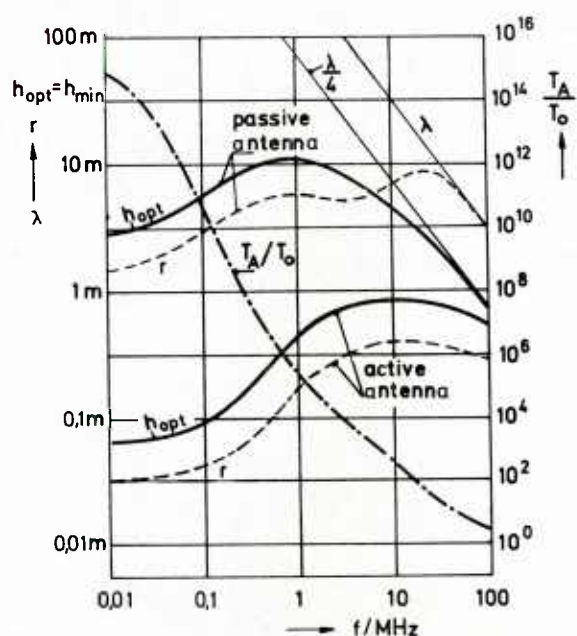
Fig. 3
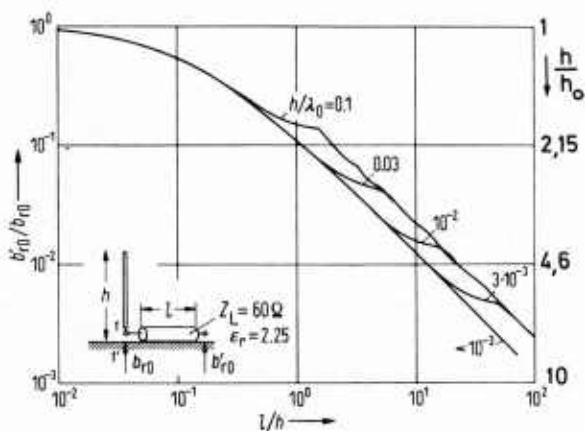
Fig. 4
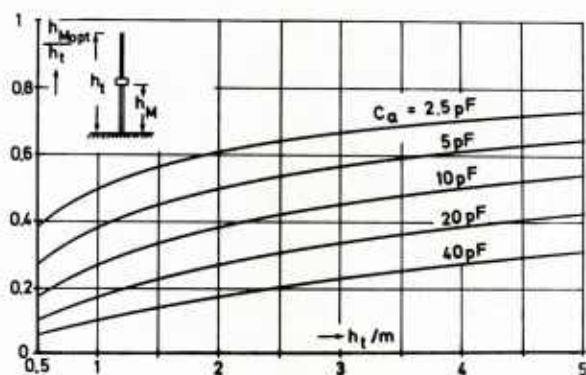
Fig. 5
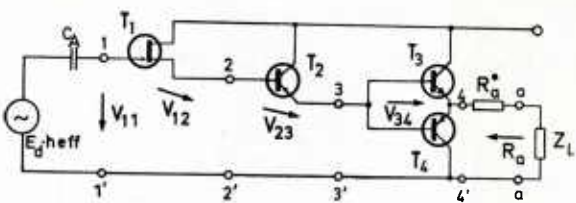
Fig. 6
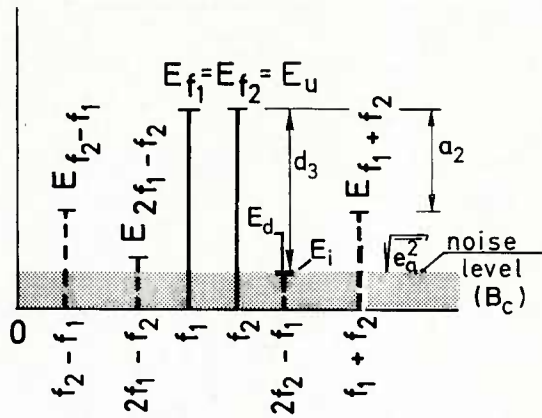
Fig. 7
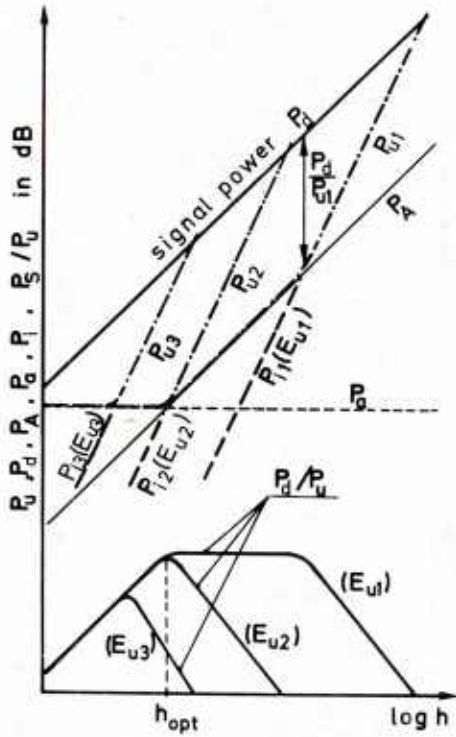
Fig. 8
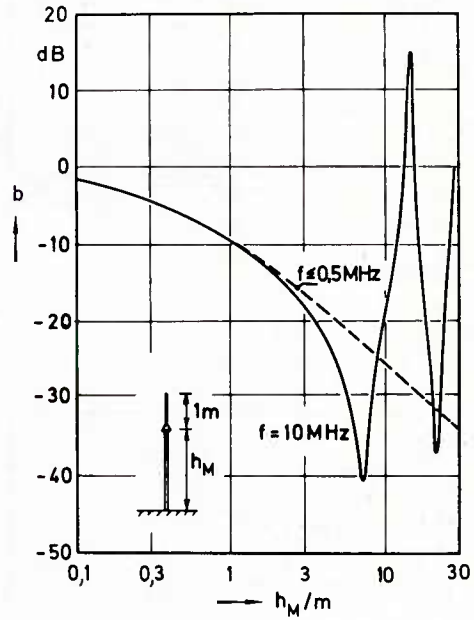
Fig. 9
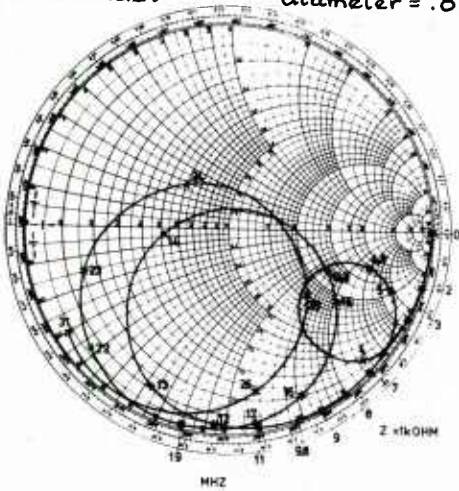
Fig. 10
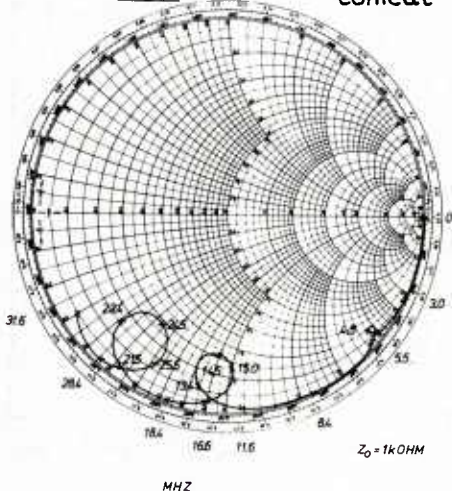
Fig. 11
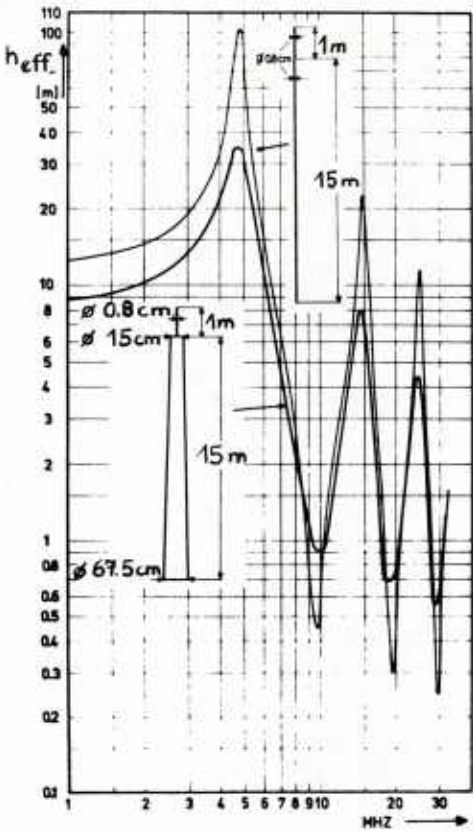
Fig. 12
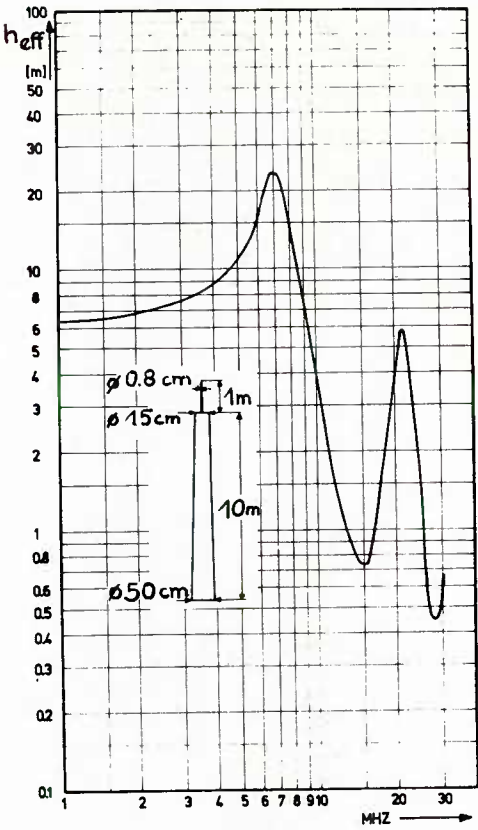
Fig. 13
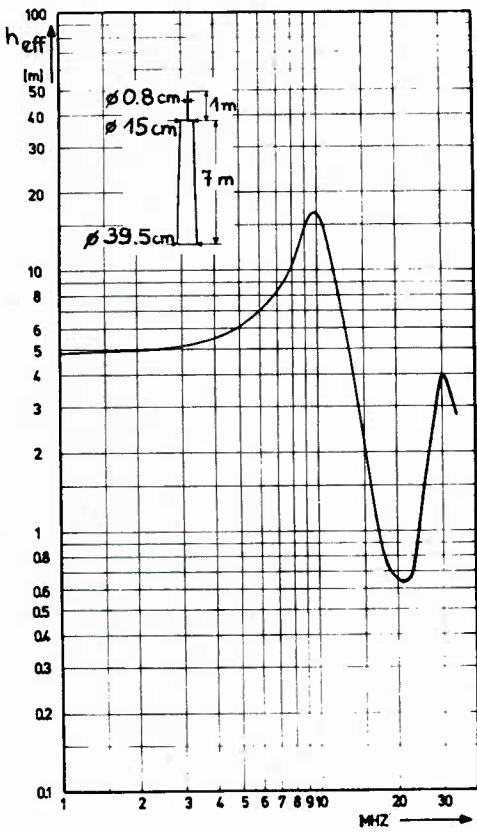
Fig. 14
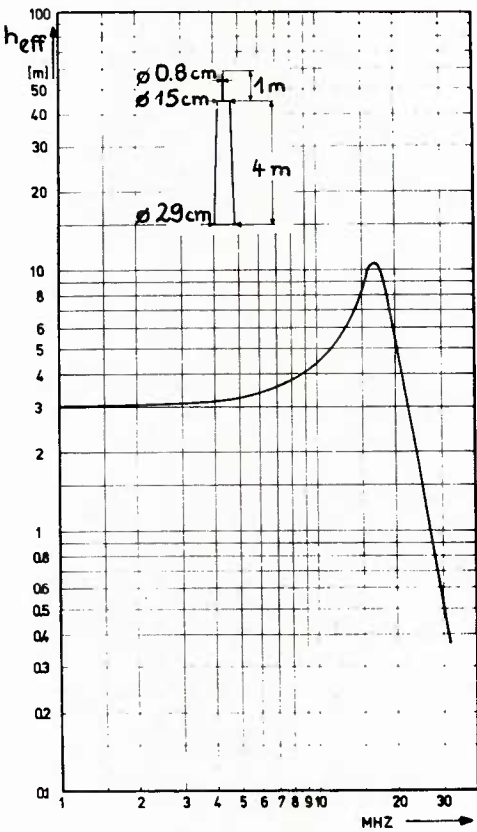
Fig. 15
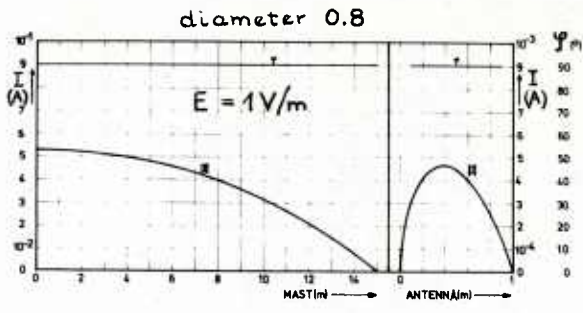
Fig. 16
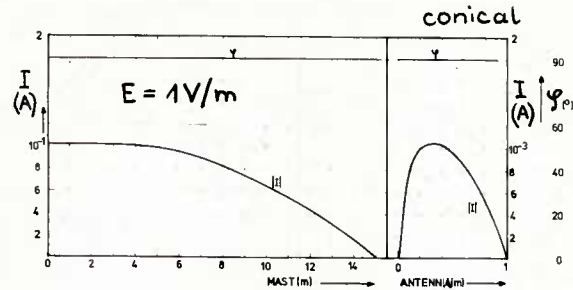
Fig. 17
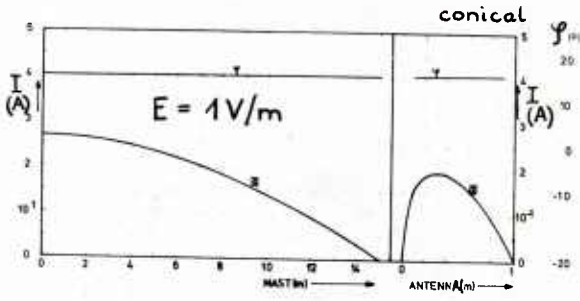
Fig. 18
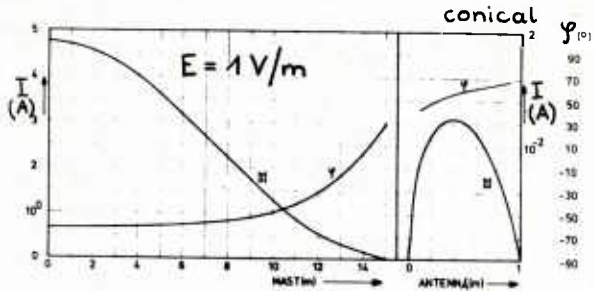
Fig. 19

Fig. 20

Fig. 21

Fig. 22

Fig. 23

☐ 24,0 MHz

15 METER

Fig. 24

☐ 26,6 MHz

15 METER

Fig. 25

☐ 30,0 MHz

15 METER

Fig. 26

10 METER

$Z_0 = 1 kOHM$

MHZ

Fig. 27

☐ 0,1 MHz
+ 3,0 MHz
X 4,5 MHz
Y 7,5 MHz

10 METER

Fig. 28

☐ 7,5 MHz
+ 9,9 MHz
X 12,6 MHz
Y 15,0 MHz
• 17,4 MHz

10 METER
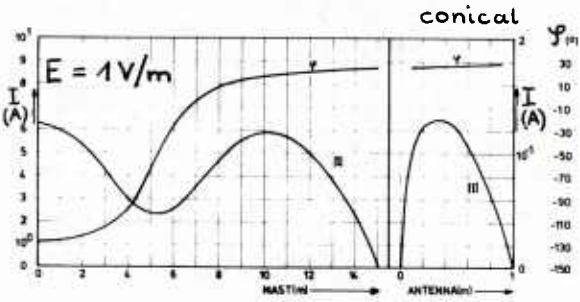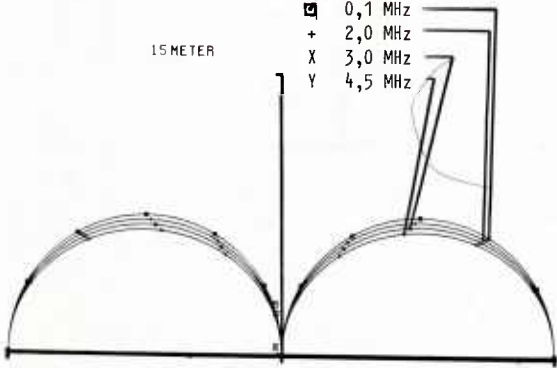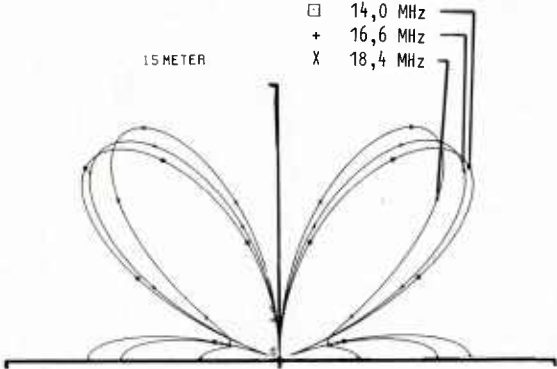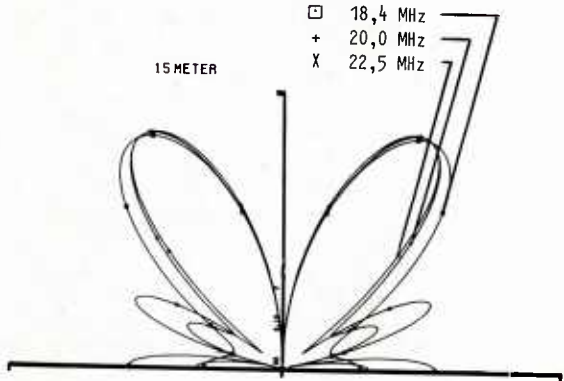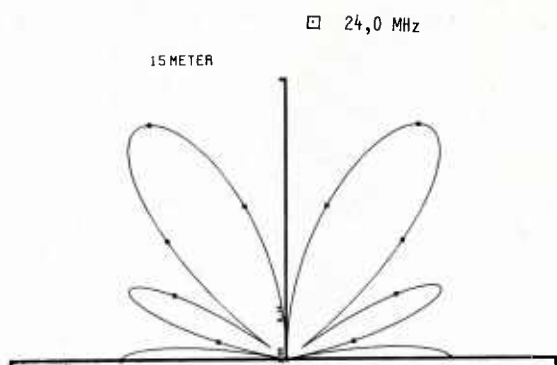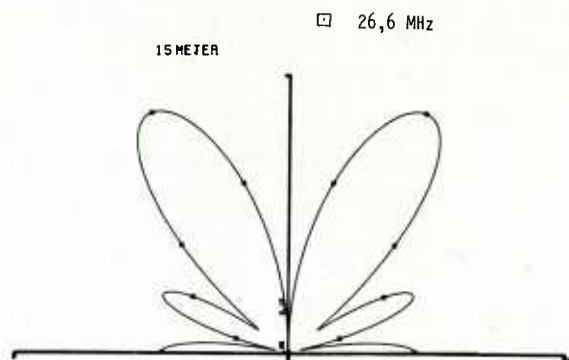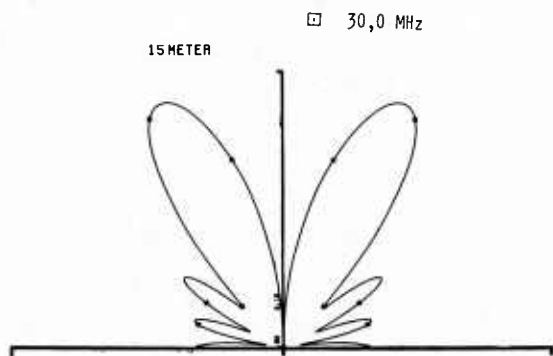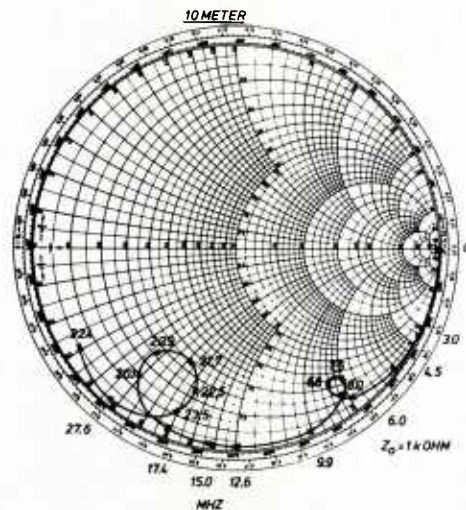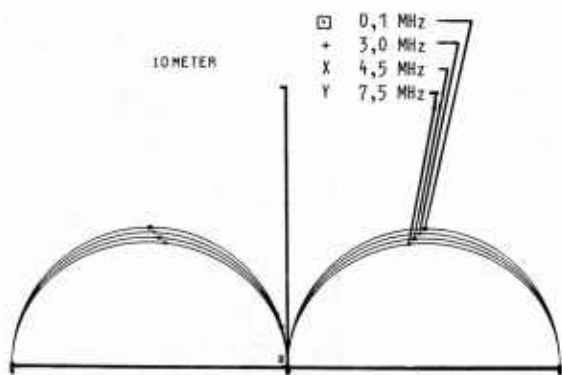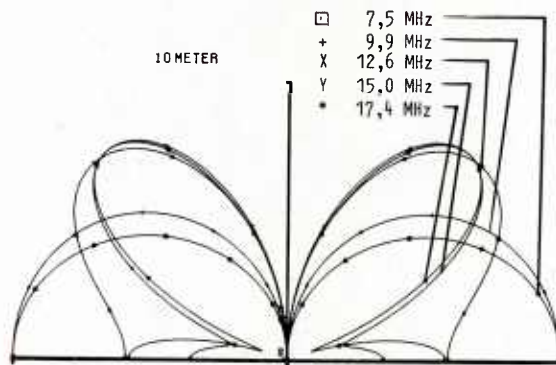
Fig. 29
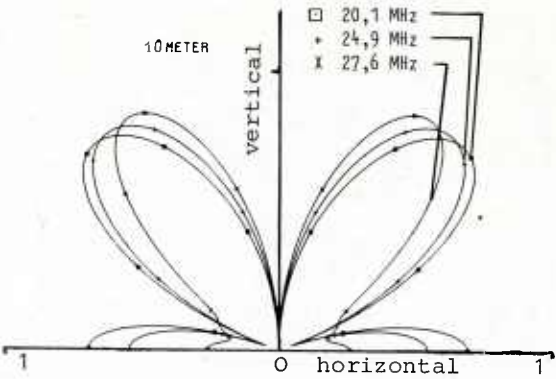
Fig. 30
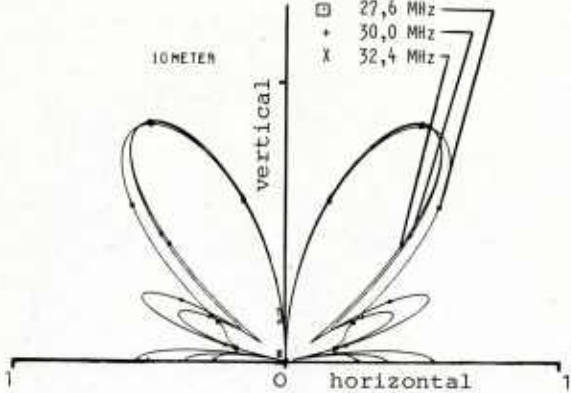
Fig. 31
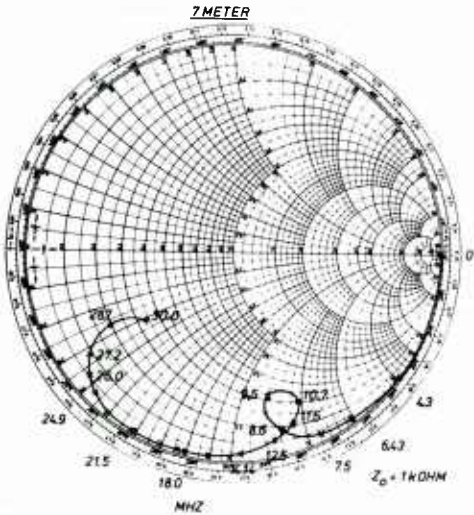
Fig. 32
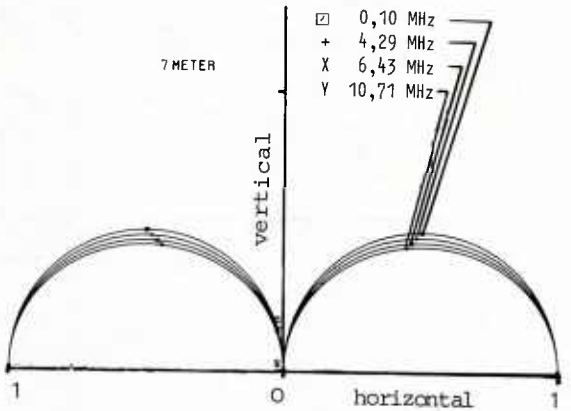
Fig. 33
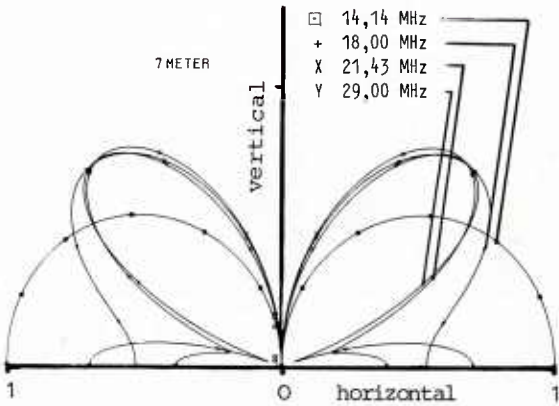
Fig. 34
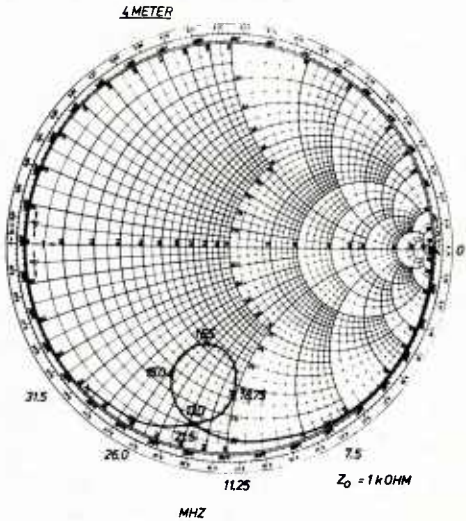
Fig. 35
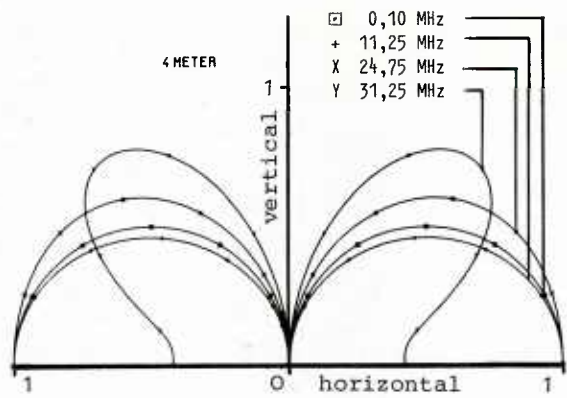
Fig. 36
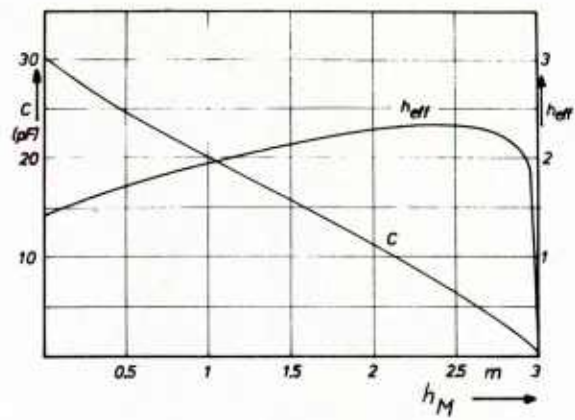
Fig. 37
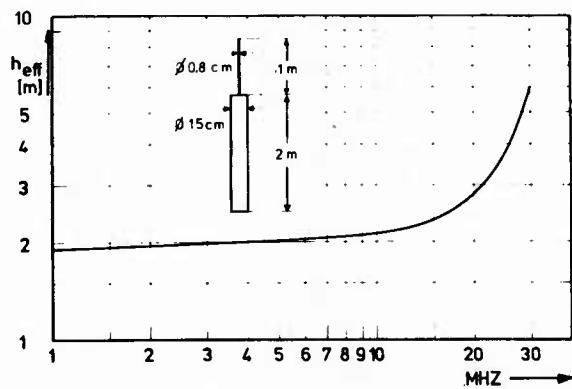
Fig. 38
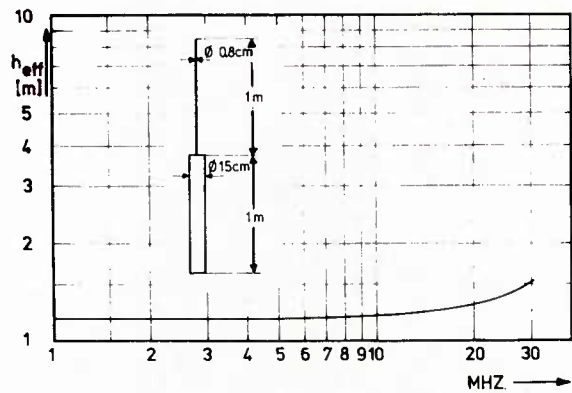
Fig. 39
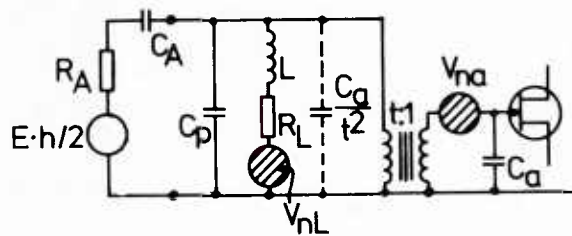
Fig. 40
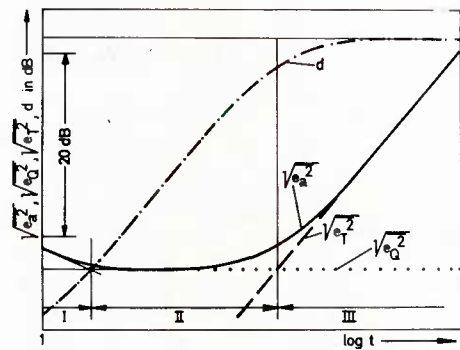
Fig. 41
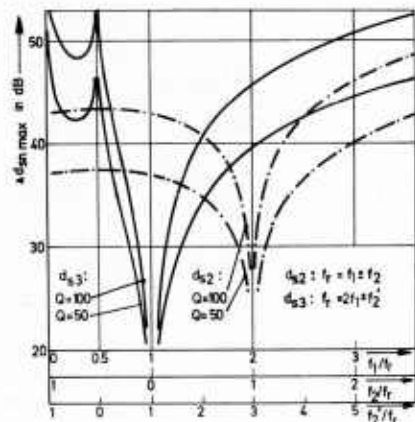
Fig. 42
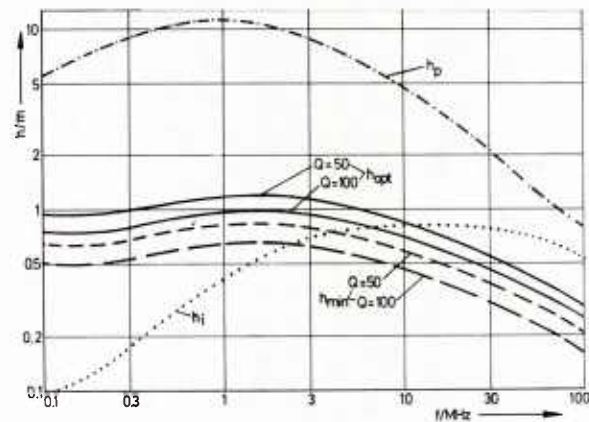
Fig. 43

Fig. 44
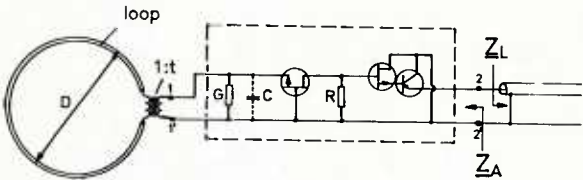
broadband active loop antenna

Fig. 45
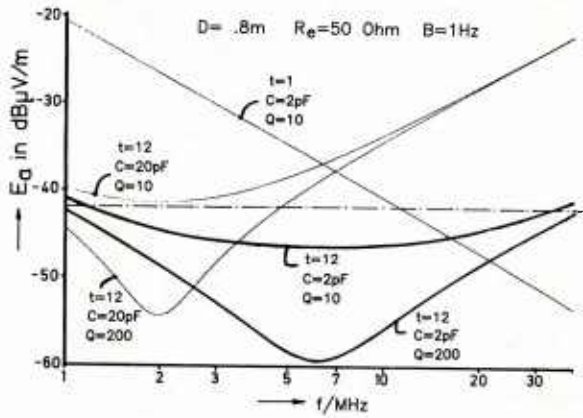
fieldstrength sensitivity
of broadband active loop antennnas

Fig. 46
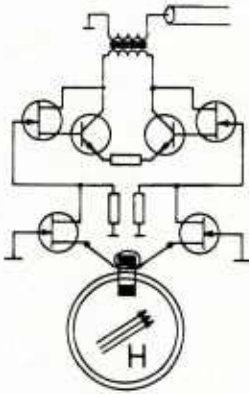
realized antenna

Fig. 47
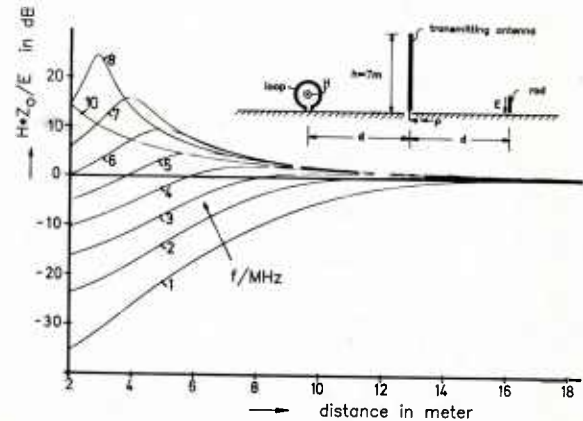
related interfering field intensity

Fig. 48

INFLUENCES OF THE AIRFRAME ON THE PERFORMANCE OF ANTENNAS FOR AVIONICS

by

M. J. Sidford
Radio and Navigation Department
Royal Aircraft Establishment
Farnborough
Hants, GU14 6TD
UK

SUMMARY

The performance of antennas mounted on airframes is an important factor in the design of airborne radio systems, and should be considered at an early stage in the study and definition of the system requirements for any particular aircraft and associated operational scenario. This is becoming critical as the number of systems and their complexity increases, and as the number of associated antennas required is further multiplied in the application of such techniques as adaptive array signal processing.

This paper highlights the influences of the airframe environment on antenna properties such as radiation pattern, gain, impedance, polarisation and coupling, and means of quantifying such influences are discussed. Related electromagnetic structure-dependent effects due to non-linear junctions, and the use of carbon fibre composite materials are also considered.

The limitations of system performance resulting from airframe-antenna interaction are difficult to quantify, since detailed knowledge of particular system parameters, associated hardware, and operational scenarios is required. Although this is beyond the scope of this paper, sufficient indications are given to alert those concerned with selection, design and installation of aircraft radio systems to some of the potential problem areas.

1 INTRODUCTION

Aircraft antennas serve avionics systems operating at frequencies from about 10 KHz to 18 GHz and above. Table 1 indicates the range of systems, many of which are required in the radio fit of a modern military aircraft. Recent helicopter studies have, for example, indicated the need for more than 35 antennas to meet a variety of operational requirements. Knowledge of the influence of the airframe on the performance parameters of these antennas is therefore sought by system designers in the definition of such projects, and by aircraft manufacturers in balancing the structural and aerodynamic aspects of siting and installation against the achievement of satisfactory electromagnetic performances. Such knowledge is obtained through the use of a necessarily wide range of techniques, since the airframe represents only a fraction of a wavelength at, say, 2 MHz, where the airframe itself is an integral part of the radiating structure, to over a thousand wavelengths at microwave frequencies, where for a radar antenna for example, interaction with the airframe may be limited to local radome effects. The intention here is to deal mainly with the quasi omnidirectional systems in the communications, navigation and identification system bands below 1.6 GHz, where airframe interaction is at a high level.

The following sections deal in turn with the influences of the airframe in relation to parameters normally used in the characterisation of antenna performance.

2 ANTENNA RADIATION PATTERNS

An antenna such as a dipole has a known radiation pattern in free space, and a first estimate of a system power budget may be based on such simplified models. The presence of the airframe adds a scattered component to the direct signal, which imposes positive and negative modulations on the radiation pattern as a function of frequency and direction. The performance of a system must then be judged on a statistical basis, making use of measured or computed radiation pattern data.

2.1 Radiation pattern determination

2.1.1 Scale modelling

This is a well established technique in which an aircraft and antenna are scaled down and the measurement frequency scaled up to maintain the size:wavelength ratio constant. Radiation patterns are then measured on an antenna range. It is rarely possible to model fine detail of the aircraft structure (rivetted panels, moving surfaces, details of cockpit, radomes, etc) and the conductivity can not usually be scaled by the same factor. Lack of fine detail is not significant where such detail has dimensions which are much shorter than a wavelength, or where it is remote from the vicinity of the antenna. However, care must be taken in cases where near-resonant structures (slots between movable control surfaces and mainframe, removable panels, other antennas, protrusions, etc) are within a few wavelengths of the antenna under test. On the question of conductivity, smooth copper surfaces exhibit sufficiently high reflectivity to represent metallic aircraft for all practical purposes.

Scaling factors between 1/5 and 1/30 are commonly employed. Difficulties arise if the antenna itself is difficult to model - for example a 1/10 scale version of a 1.5GHz circularly polarised shallow profile antenna for satellite reception may be difficult to construct. In such cases, physically more bulky antennas of approximately equivalent radiation pattern (eg open ended waveguide) may be employed, the restrictions of cutting large recesses in models not being as critical as in operational aircraft. For complex antennas, arrays, or when the antenna operating frequency scales to more than 30 GHz, sectional mock-ups or even complete representations of, say, the underside of a fighter may be needed.

Indeed in some US ranges, full size aircraft may be mounted on azimuth turntables. A turntable accepting helicopters and fighter aircraft has been constructed at RAE.

Antenna ranges today vary in complexity and cost from ad-hoc open air types, to those which employ automated high precision positioning and spherical near field scan processing software. Information on such ranges is widely reported, and is not reviewed here. One question often raised, however, concerns the minimum length suitable for aircraft antenna model ranges. Radiation pattern measurements of a monopole on a model fighter aircraft were made at an RAE range at distances ranging from $1.2d^2/\lambda$ to $0.1d^2/\lambda$, d being taken as the maximum dimension of the model. Fig 1 illustrates two of the patterns obtained. Similar results were obtained theoretically in a British Aerospace study in which GTD was employed to compute true far field patterns and those observed down to $0.1d^2/\lambda$. Both theory and practice indicate that measurements may be made to the accuracy required for the majority of communications systems down to ranges of $0.1d^2/\lambda$. Care has to be taken, however, if precise angles and depths of nulls in the radiation pattern are critical to a particular system performance.

Model scaling factors are preferably chosen to bring the measurement frequency into a region where either the range is anechoic (eg in a chamber with absorbent lining), or where directional antennas may be used to avoid ground reflections. This is not always possible, particularly in modelling HF antennas where even 1/50 scale models result in measurement frequencies as low as 100 MHz. To give an example, RAE required to measure the levels of vertically polarised HF radiation from a helicopter in the presence of a much stronger horizontally polarised component using a 1/30 scale model. On the outdoor horizontal range, normally used, the strong ground reflection at the 60 MHz measurement frequency was heavily dependent on polarisation and was variable depending on ground conditions. This, coupled with the cross polar reponse of the measurement antenna and its mounting structure made the measurement of relative horizontal and vertical polarisations inaccurate. A 5 metre vertical range was therefore constructed in which the model was supported and rotated vertically above a carefully balanced horizontal dipole which was mounted above a flat horizontal ground plane at ground level. This arrangement gave far greater symmetry to the propagation of the orthogonal polarisations. The only asymmetry due to the wooden supporting structure introduced acceptably low errors, a dipole-to-dipole to check indicating cross-polar levels of the order of -40 dB irrespective of orientation[1].

2.1.2 Sectional full-scale models

When antennas themselves are difficult to scale down or when the scale frequency becomes too high for the range instrumentation, full-scale models of parts of the airframe may be employed. As an example, an antenna intended for a microwave system requiring forward sector cover only was measured at RAE on the nose section of a fighter aircraft. Comparison of the azimuthal radiation patterns with and without a metal pitot tube protruding from the nose clearly demonstrates the perturbing effect of the tube in the forward direction (Fig 2).

2.1.3 Mathematical modelling

Other lectures in this series review this subject, and the comments below are restricted mainly to modelling programs at RAE.

A wire grid computer program was developed in 1974 by D. Forgan[2]. The method used allows the airframe to be modelled as a grid of up to 340 segments each of maximum length 0.1λ. Various criteria together with empirically derived 'rules of thumb' concerning grid layout and wire radius, have allowed after a long period of iteration between model measurement and computer program adjustment a fair degree of confidence to be obtained in this program for the prediction of HF radiation patterns of loops, notches and wires on metal aircraft and helicopters. It is debatable whether wire grid/surface patch programs can yet be applied completely automatically to new problems with high confidence factors - particularly for impedance calculation. It is a matter of taking a particular program getting to know its strength and weaknesses, and developing a feel for its accuracy for particular types of problem over a period of time.

The wire grid and other numerical integral equation techniques are limited by computer resources to frequencies where the aircraft length is of the order of a wavelength. Where aircraft dimensions are large compared with a wavelength, corresponding to antennas of 1 GHz and above on an airframe, geometric theory of diffraction techniques may be used (eg Ref 3). Good agreement has been obtained in many instances with scale model measurements, but a degree of program 'adjustment' is still required - every aircraft, antenna and site is to some extent a 'special case'. Nevertheless, at a system design stage in a new project, such programs are proving useful as indicators of possible antenna siting problems. For example, calculations of relative strengths of contributions to airframe multipath, as a function of source direction, resulting from wings, tailplane etc, have been useful recently in estimating dispersive effects in adaptive nulling antenna systems.

Between frequencies at which the assumptions of wire grid and GTD methods apply (typically in the 30 MHz to 300 MHz range), there is currently no satisfactory modelling technique - particularly in regions close to airframe resonances. In an attempt to tackle problems of VHF homing antennas on helicopters, some studies in Industry have recently been undertaken to investigate finite element integral equation methods[4]. In these methods, a finite element boundary integral equation is formulated, based on the electric field integral equation. Variational principles are invoked to ensure a stationary minimum energy solution, giving, it is claimed, improved modelling of a physical surface, more accurate current density modelling, better numerical stability and greater algorithmic simplicity than moment methods. Analysis has been restricted so far to scattering from simple two- and three-dimensional shapes with dimensions of the order of a wavelength.

2.1.4 Airborne trials

It is sometimes necessary to measure installed performance of antennas on military aircraft by means of transmissions from their normal communications equipments. Although this can be useful in

determining general characteristics of radiation patterns, serious gaps in coverage etc, results are seldom sufficiently comprehensive and accurate to provide good data for detailed corre lation with scale measurement, and mathematical modelling techniques.

The problem is concerned with the number of variables:

(a)   aircraft range, bearing and elevation from ground station;

(b)   aircraft attitude in yaw, pitch and roll planes;

(c)   propagation factors associated with ground multipath from objects and other antennas in the vicinity of the ground antenna, ground conductivity, and at some frequencies, atmospheric ducting;

(d)   amplitude and frequency stability of transmission;

(e)   measurement receiver stability, linearity, calibration accuracy and data recording techniques;

(f)   interferences from other transmissions - authorised or otherwise.

In principle (a) can be overcome by precision radar tracking (or even laser tracking) from the ground station, appropriate corrections being applied for the separation of the tracker and the measurement antennas; (b) can be accounted for by continuous recording of outputs against time from an inertial platform in the aircraft; (c) could be reduced to low levels if it were possible to select a flat, open geographical environment for a ground installation containing the isolated measurement antenna only, and for HF, incorporating large surface mesh ground planes to prevent variability of vertical radiation pattern with ground wetness conditions; (d) and (e) can be overcome by use of specialised calibrated measurement receivers, and stable transmitting sources whose output power is continuously monitored; (f) necessitates the parallel recording of spectral level data in a frequency band centred around the wanted measurement frequency. All the information required to determine angle, range and field strength needs to be time synchronised in a recording system for subsequent computer analysis. This means that either the aircraft and ground sensor outputs are recorded separately against accurate clock information, or the aircraft transmits its sensor data to the ground station via a separate communication link.

Needless to say, provision of such facilities is expensive, and it is usually not possible to fit the necessary additional equipment, or to interface with the necessary sensors in service aircraft. Furthermore, continuous transmission is often not permissible on the grounds of interference with existing operational systems; for example, continuous transmissions in the IFF or TACAN bands could interfere with civil SSR and DME systems. Problems are also encountered due to air space limitations which often make the execution of complex flight envelopes impracticable.

Radiation pattern measurements are made in RAE aircraft equipped for experimental flying, by receiving a monitored ground transmission and recording the received signal strength in the air together with aircraft heading and bank angles; time marked track plots using the normal aircraft navigation system record the aircraft position relative to the transmitter. Diffraction fences designed to provide a sharp lower cut off in the elevation plane pattern of the ground transmitting antenna have sometimes been employed. These reduce ground illumination and consequently provide a uniform field in a region sufficiently large to accommodate orbital flight patterns. For HF measurements, a field calibration method has been devised in which airspace is first calibrated using vertical dipoles or horizontal loops with built-in stable oscillators suspended below a helicopter; transmissions from aircraft in that airspace can then be compared in strength with these references at a ground receiving antenna site, range and bearing data being supplied by a tracking radar.

The azimuthal plane radiation pattern is frequently the most useful in an airborne communication system; it is usually recorded either at discrete points (typically every 10°) by flying a 'daisy' pattern where the aircraft is straight and level on a number of headings at the centre of the pattern, or in continuous orbit centred at many orbit diameters from the ground measurement site. In the former case, much can be missed in terms of pattern nulls and fine detail by coarse sampling, and in the orbiting case, the aircraft is banked in the turn, and the pattern plane is inclined to the horizontal by the aircraft bank angles. To avoid random variations due to bank changes associated with maintaining a circular track relative to ground, constant bank turns are preferable, appropriate corrections being made for downwind drift in post-flight analysis of the aircraft track.

2.2   Impact of radiation pattern on system performance

Any aircraft radio link power budget should include a margin for aircraft antenna pattern variation. However in air-to-air, and air-to-ground transmissions, to allow for intended maximum range to be upheld continuously in all possible manoeuvres usually results in a requirement for undesirably high transmitter power, with all its attendant problems (EMC, drain on aircraft prime power, heat dissipation, unit size, etc). It is first necessary, therefore, to consider the operational scenario, and determine if there are likely to be preferred directions in which the communication link will be particularly vital (eg in flying toward an enemy and communicating back to ground stations or surveillance aircraft in the tailward sector). Antenna siting and transmitter powers should certainly be made appropriate for such cases. Away from these cases, there will usually be a general need for communication capability for a high percentage of the time during various types of operational sortie. To estimate the statistical effect of antenna radiation pattern on performance under such circumstances, the spherical radiation pattern must be analysed to give percentage of the angular coverage above specified gain levels; this information suitably weighted to account for assumed scenarios (for example an aircraft will usually spend more time near level flight than banked at 60°, and there may be one spread of ranges more important than others) must then be built up into an estimate of the probability of successful communication as a function of transmitter power and antenna site.

Unfortunately, such detailed analysis has not usually been undertaken in many existing systems. Only in recent years have the necessary automatic spherical pattern recording and computer analysis been developed, and these are being applied to new systems.

Radiation pattern shaping imposed by the aircraft environment affects homing and direction finding systems more critically than most other radio systems. Let us consider two cases – UHF helicopter homing, and VHF direction finding by interferometry.

A helicopter is not usually a symmetrical structure either as a whole, or in detail around the preferred site for a UHF homing antenna pair. One major disturbance of the symmetry may well be the presence of other antennas. Fig 3 shows the effect of a nearby antenna on the performance of a UHF homing system, indicating the disturbance and consequent slewing of the forward crossover point of two patterns obtained by a quadrature feed arrangement. Since the aircraft is flown in a direction to mini- mise the difference in the signal levels received via the two patterns, an error in flight direction results.

Direction finding by interferometry involves measurement of relative phase between signals arriving at a number of antenna pairs. Having decided on the accuracy with which it is required to measure the source direction – say ±0.5° – it is then necessary to ensure that the relative phase error introduced by airframe multipath is less than the change in relative phase as the source swings from (θ – 0.5°) to (θ + 0.5°) for an element pair in a free space environment. Relative phase measurements of element pairs mounted under the fuselage of a scale model large aircraft produced the results that a separation of 11λ is required to achieve an azimuth plane accuracy of 0.5° rms in the presence of the airframe. This corresponds to airframe multipath levels up to –15 dB on the direct signal. Such large spacings of course generate multiple ambiguities which have to be resolved by antennas with intermediate spacings, and if angular accuracy is to be maintained over 360°, a planar rather than linear array aperture is required. The perturbing effect due to scattering from interferometer array antennas not in use at any instant may be minimised by arranging an effective open circuit at their bases.

3   ANTENNA GAIN AND EFFICIENCY

If an antenna structure is lossless, and perfectly matched to the transmitter/receiver, its gain can, of course, be determined from the radiation pattern. The spherical pattern is integrated to obtain a level corresponding to the same power radiated from an isotropic source (the isotropic level), the directive gain in any particular direction then being determined from the radiation pattern power level in that direction relative to the isotrope. As stated earlier, most airborne communication, navigation and identification systems depend on low gain antennas, since their response needs to be quasi 'omni-directional'. For cases where an aircraft is not expected to manoeuvre rapidly in its operational role (for example in the case of early warning radar surveillance aircraft), elevation plane beam narrowing may sometimes be employed to improve azimuthal plane gain. There will usually be sufficient 'splash-over' of power into directions above and below the aircraft to allow for communication at the short ranges normally associated with such directions.

Of more concern in this section is gain reduction associated with ohmic losses in the antenna, its associated structure, its tuning, matching and feed networks. The efficiency of the antenna in this con- text is defined as the ratio of the total radiated power to the forward power delivered by the trans- mitter. It is the factor by which the directive gain obtained by radiation pattern integration is reduced by resistive losses. Achievement of high efficiency is particularly difficult in HF transmission. A fighter aircraft or helicopter is typically less than 0.2λ long at the lower end of the HF band. Currents may be coupled to the airframe using wires, probes, loops, slots and notches. At the low end of the band, wires and probes are electrically short and have large capacitive reactance which has to be tuned out with series inductance; loops, slots and notches are inductive and are tuned with parallel capacitance. In practice, to cover the multioctave HF band, both capacitance and inductance is usually required in tuning and matching unit networks. The series ohmic loss introduced in the tuner may typically be of the order of an ohm, whereas the radiation resistance of, say, a notch on a fighter aircraft is typically in the order of 10^{-3} ohms in the low part of the HF band. Fig 4 gives some example radiation resistances. The efficiency of the antenna at 2 MHz may therefore be less than 0.1% as a result of tuning unit losses alone. Additional losses occur in the antenna structure itself, particu- larly at joints situated near high current regions – for example at the feed point of a notch antenna. Problems have occurred in the past due to corrosion at such joints in notch antenna feeds resulting in cleaning procedures being included in appropriate service maintenance schedules.

3.1   Measurement of blade antenna efficiency

Blade antennas such as may be used for applications from 100 MHz to 1.2 GHz are normally of rela- tively high efficiency, although absolute gain is rarely specified by manufacturers. In fact, the accurate measurement of efficiency is not a simple matter; direct measurement of radiated power by far field pattern integration over the sphere is inaccurate in most instances due to reflections from the range and mounting arrangement. A method commonly adopted is comparison against a standard – such as a $\lambda/4$ stub monopole on the same ground plane – usually in the azimuth plane only. With care such methods can be accurate provided the antenna under test has a closely similar radiation pattern to the stub. However, this may not be the case with, say, a notch fed plate, or a sleeve fed monopole where the maxi- mum current region is raised above the ground plane thus affecting the latter's edge contribution to the radiation pattern.

A method proposed by Wheeler[5] involves placing a conducting hemispherical shell over the antenna on its ground plane, thus short circuiting the radiation. The antenna efficiency is derived by measure- ment of the reflected power at the antenna's termination with and without the short circuit. The method assumes the short circuiting cover does not alter the current distribution and hence the loss in the antenna, and that there are no losses in the conducting shell or the joints between it and the antenna ground plane. The latter may not be true, particularly at frequencies associated with high Q resonances.

Although the method can be useful for quick, approximate measurements, it is not regarded as reliable for accurate efficiency measurement.

The above measurement techniques have been studied in Industry for RAE. .The use of spherical near field scanning, radar cross section, time domain (pulse excitation) and calorimetric methods were also considered. A general conclusion reached was that the most accurate (and least disputable) method involves the use of spherical near field scanning to measure the total radiated power[6]. However such a facility may be too expensive for an aircraft antenna manufacturer to provide, and in this case comparison with a standard calibrated at a central near field scan facility was recommended.

3.2 Effects of efficiency on system performance

The above considerations apply to efficiency measurement of aircraft blade antennas to accuracies better than 1 dB from VHF up to 1.2 GHz. However, the expense of providing a facility with such precision is rarely justified in the light of performance degradations which occur in installed environments. Losses in joints between the antenna base and the aircraft skin, in connectors, and in cables can swamp antenna inefficiency in many cases, and of course scattering from the airframe can produce many decibels of deviation from the free space radiation patterns. Fig 5 indicates the percentage of azimuthal coverage as a function of relative gain for a blade antenna on a small aircraft. If a system antenna gain requirement of say 0 dB is specified, it can be seen that each decibel lost due to antenna inefficiency, cable losses, etc reduces the azimuthal cover by about 20%. These gain losses have a less dramatic effect in the statistical performance of the overall system, however, since the system antenna gain requirement is specified to achieve the desired maximum range, and for a large percentage of the time, ranges less than this maximum will occur in operational use. Furthermore, the system may not degrade catastrophically at signal levels a little below their nominal threshold. Nevertheless, the importance can be seen of good antenna design and carefully specified codes of practice for installation of the antenna on an aircraft to reduce gain loss to a minimum.

A quite separate requirement for high efficiency occurs in high power transmitting systems. Here the antenna must not overheat, resulting in either 'burn out' or mechanical fatigue failure over many transmission cycles. This can be a problematical requirement in some electrically small antennas employing inductive tuning elements. Again referring to HF, achievement of high efficiency to avoid heating problems and the need for excessive transmitter powers is more important than achievement of high efficiency for reception. In the latter case, efficiency has to be high enough to allow the limiting noise in the system to be external noise – usually a less stringent requirement than for transmission.

4 ANTENNA IMPEDANCE

In general, except in cases where transmitting or receiving electronics is closely integrated with the antenna structure, the requirement is to match the antenna impedance to 50 ohm transmission line. An antenna manufacturer may specify the matching of his antenna to such a line in terms of the VSWR in the line, with the antenna mounted on some specified ground plane. Two questions arise here; firstly, how critical is the dimension and shape of the ground plane in determining the match, and secondly, how closely does the match so specified relate to the installed performance of the antenna? A study undertaken for RAE determined the variation of impedance of monopole antennas due to the scattering from edges and corners of arbitrarily shaped flat ground planes[7]. In the theoretical analysis, a hybrid technique combining moment method and near field geometrical theory of diffraction was used. In particular it was found that for a monopole on a ground plane one wavelength square at the lowest frequency (f_{min}) in the band to be measured, an optimum region around 0.32λ from one edge and 0.44λ from the orthogonal edge could be found where the amplitude of the impedance perturbation due to the edges and corners was less than 2 ohms from f_{min} upwards (Fig 6). Such a technique could be stated in specifications, allowing realistic comparison between different manufacturers' antennas. However, we have not obtained a general theoretical treatment of impedance perturbations on aircraft structures, since in most cases for fuselage mounted blade antennas the perturbation has not been found in practice to be a limitation to antenna performance. A case where some variation might be expected, is that of a blade antenna mounted on top of a tail fin[8]. In such cases, manufacturers should provide impedance information for antennas mounted on mock-up sections.

4.1 Effects of impedance mismatch on system performance

For reception purposes, VSWRs of up to 3:1 will still allow 75% of the power available from a perfectly matched antenna to be delivered to the receiver. More stringent VSWR requirements usually apply to transmission, since a high standing wave ratio can lead to excessively high voltages on transmitter output stages with possible resultant damage. The VSWR of a transmitting antenna is therefore usually governed by the transmitter specification, and values in the range 1.5:1 to 2.0:1 are typical.

5 POLARISATION

Vertical polarisation is chosen for most line-of-sight communication links, since omni-azimuthal radiation patterns are most conveniently formed with vertical monopole and dipole types of antenna element and low angle coverage of ground antennas may be optimised. Where predominantly downward coverage is required, horizontal polarisation may be employed (eg in 75 MHz marker beacon reception used in runway approach aids, where the ground transmitter is overflown). In HF communication via Skywave, it is usually more important to design for as high an efficiency as possible, rather than for any specific polarisation. In applications where HF ground wave propagation is exploited (eg in short range low altitude helicopter-to-ship links) generation of vertical polarisation in the low HF band is required, usually presenting considerable design and siting problems.

Satellite communication links with aircraft employ circular polarisation to avoid fading due to the Faraday Rotation effect in the ionosphere. Although circular polarisation is only necessary at one end of the link in this respect, power is wasted due to polarisation mismatch if circularly polarised

antennas are not employed at both ends. The power lost due to polarisation mismatch amounts to a maximum of only 0.5 dB for up to 3 dB axial ratio of the polarisation ellipses of the transmitting and receiving antennas. Although these low mismatch losses are achievable with mechanically steered reflector aircraft antennas, greater losses result when conformal phased arrays are employed.

Satellite communications for aircraft is not widely used to date, both for reasons of cost and potential vulnerability to jamming in the military environment. In the latter case, systems are being considered for the future which employ SHF or EHF bands where wide bandwidths, narrow beamwidths and null steering could be exploited to provide jamming protection. The cost of the associated aircraft antennas and the feasibility of achieving the stringent performance requirements in the airborne environment is a major research topic in its own right. In the US, technical feasibility has been demonstrated in experimental installations employing mechanically steerable antennas mounted under large radomes.

At frequencies around 300 MHz, UHF satellite communications is possible using simple blade antennas, or shallow profile crossed-slot cavity-backed structures. At around 1.5 GHz, reception of signals from Navstar Global Positioning System satellites is also possible using quasi hemispherical coverage low gain antennas. A problem encountered in such systems is concerned with loss of gain due to polarisation mismatch at low elevation angles. If a single top-of-fuselage antenna site is assumed, the horizontally polarised component of polarisation of a flush mounted or shallow profile antenna is heavily attenuated in directions parallel to the aircraft skin. Even if the $E\theta$ field pattern is perfectly semi-circular for all ϕ planes, this results in a 6 dB reduction of gain at the horizon for circularly polarised incident signals. An alternative employed by RAE for L-band Aerosat experiments in 1975 and more recently for Navstar reception is to have a dual antenna installation - each antenna being a slot dipole[9] mounted at 45° around the fuselage from the zenith. This avoids the excessive polarisation mismatch loss of gain except for narrow azimuthal sectors in nose and tail directions, maintaining gain above isotropic levels for the majority of the hemisphere. Of course, the complication of selection of the appropriate antenna depending on aircaft-satellite geometry is added.

6   ANTENNA TO ANTENNA COUPLING

Modern military aircraft employ a multiplicity of radio systems and the operation of a number of these systems without mutual interference requires knowledge of the coupling between each transmitter and each receiver likely to be in simultaneous use. This coupling may be considered by two mechanisms. In the first, linear coupling, it is assumed that the transmitter produces an output in its operating band only (ie with no significant harmonics or noise outside that band) and that there is no generation of harmonics or intermodulation products by non-linearities in cables, connectors, antennas and aircraft structure. Hence coupling is determined by signal power level arriving at the terminals of various receivers due to specified source frequencies and powers at the transmitter terminals. In this case coupling may take place by imperfect screening of the 'black boxes' themselves, via power supplies, through inadequate screening of cables and connectors, and finally between the antenna structures themselves. It is this last coupling which concerns us here, and on which some work was carried out for RAE - both in measurement of its magnitude and in the development of empirical formulae for its calculation. This is briefly described in the next section, but a fuller consideration of the general topic is given in Dr Kubina's lecture.

The second coupling mechanism includes the same coupling paths as those mentioned above, but occurs at frequencies other than those nominally specified at the transmitters. Hence transmitters at frequencies f_{T_1}, f_{T_2}, f_{T_3}, etc may induce power in receivers at the different frequencies f_{R_1}, f_{R_2}, f_{R_3}, etc to which the receivers are tuned. Such coupling is due to out-of-band spurious outputs from the transmitters and/or generation of intermodulation products and harmonics through non-linearities in cables, connectors, antennas and their associated structures. In this category, I can also report some general conclusions based on work carried out for RAE[10,11].

6.1   Linear coupling

The coupling between antennas in this case is governed by the geometry of their siting on the airframe and the impedances of the antennas (both in the design band and, where appropriate, out of that band). Such coupling was measured using low power signal generators, 10 dB 50ohm pads at the antenna terminations and wideband measurement receivers for a variety of VHF, UHF and TACAN band antennas on five types of aircraft. In-service broad band nominally omni-azimuthal communications and navigation antennas were used. These measurements provided a data bank from which estimates could be made for other sitings on other aircraft. To assist in this process, an empirical formula was developed which gave values of isolation within, +9 to -20 dB on the measured values for about 70% of the antenna pair/ frequency combinations measured. A sample measurement is shown in Fig 7 of the coupling of a UHF antenna under the fuselage of a Wessex helicopter with a V/UHF antenna on top of the tail. It is to be noted that the measured out-of-band coupling is also represented reasonably by the empirical formula due to a factor based on a treatment by Siarkiewicz and Adams[12] of coupling between arbitrary length monopole-type antennas.

A coupling problem of particular interest in the UK concerns co-located HF transceivers. The whole airframe plays such an integral part in the radiation mechanism that poor isolation would be expected between systems. To quantify the problem, the coupling between five HF antennas fitted to the RAE Comet aircraft was measured. The antennas were as shown in Fig 8 - a wing root notch, a tail fin notch and three wires. In the case of the notch antennas transmission was made at selected frequencies across the band via a tuning unit into one notch, the received power into a 50 ohm system via a tuning unit from the other notch being measured as the latter's tuned frequency was swept through the band (Fig 9). Due in part to the different modes excited by the two notches (one notch in the horizontal plane, the other vertical) in-band isolation of about 20 dB is achieved. This is not so for the almost parallel wire antennas (Fig 10) where coupling was measured with the transmitting antenna tuned and matched, whilst, as in practical usage, the receive antenna tuning unit was by-passed to achieve broader reception bandwidths. This illustrates the need for transceiver systems with very high specification tunable RF filters if

simultaneous transmission and reception - albeit at different frequencies in the band - is required from such highly coupled wire antennas.

6.2   Non-linear coupling

For nearly all measurements referred to above, where power oscillators and transmitters were used as sources, the harmonic content of the sources swamped any harmonic generation attributable to non-linearities in cables, connectors, antennas and airframe. It was concluded that there was room for improvement in spectral purity of transmitters, employing filters if necessary. An important point emerges here. Harmonic levels generated by a transmitter are usually specified into a 50 ohm measurement system, whereas an antenna impedance may be a widely different value (usually not specified) outside its nominal operating band. Design of filters needs care for the same reason - ie that the termination impedance may be variable with frequency and from one installation to another. Absorbtive types of filter where out-of-band power is diverted into matched loads are preferable to constant K designs. There may sometimes be unfortunate combinations of circumstances where high coupling detrimental to system performance can occur; for example a UHF transmitter with high third harmonic level driving an antenna unfortuitously matched to the source impedance at the harmonic frequency could desensitise an IFF receiver. Such problems can usually be rectified by appropriate filtering.

It may become important to quantify the level of harmonic generation other than within the transmitter, particularly in aircraft where the complexity and number of transmitting systems (including frequency hopping and spread spectrum systems) is likely to be high. To date, however, this non-linear coupling mechanism does not appear to have presented any serious problems in UK aircraft communication systems, probably due to a degree of awareness coupled with appropriate codes of practice in system installation.

7   ELECTROMAGNETIC IMPLICATIONS OF THE USE OF COMPOSITE MATERIALS IN AIRCRAFT STRUCTURES

The use of composite materials in airframe construction is receiving serious consideration in the aircraft industry for the purposes of weight and cost reduction. A variety of materials are being considered from insulating plastics to carbon fibre reinforced composites which are moderately conducting.

An aircraft skin performs both a screening function and is an integral part of the radiating structure of most broad beamwidth antennas. Use of insulating materials will expose internal metallic structure, such as earthing frames for power supply returns, which may have RF resonances disturbing antenna performance. Lack of adequate ground plane may necessitate the use of dipole rather than monopole antennas. Lack of airframe screening may result in the need for improved screening of other aircraft electrical and electronic systems, and associated cables, both to protect them from fields radiated by the antennas, and to avoid internally generated RF interference entering radio receivers via the antenna.

Carbon fibre composites (CFC) have high strength-to-weight ratio, and are receiving particular attention as a material for use in aircraft construction. There is a range of materials and corresponding electrical properties, but as a general guide, planar conductivities of lamina composites are lower than those normally recognised as good conductors by around three orders of magnitude. Although individual laminae are anisotropic (the fibres being laid undirectionally) a multi-ply laminate will exhibit bulk electrical properties which can for practical purposes be regarded as isotropic and homogeneous in the plane of the sheet. Typically, dc resistivity of such samples is of the order 10^{-5} ohm metres in the plane of the sheet. Perpendicular to the plane of the sheet (ie across the fibres) the resistivity is higher by three orders of magnitude or more depending on the material.

From the antenna radiation viewpoint, experiments at RAE have indicated that at 100 MHz and above, performance of the commonly employed broadband blade antennas is for practical purposes equivalent to their performance on metal aircraft. For electrically small antennas with high circulating currents, however (eg HF notches at 2 MHz) significant loss of efficiency may result unless good electrical bonding (CFC to CFC, and CFC to metal) and local metallisation is employed (see section 7.1).

From the linearity viewpoint, tests undertaken for RAE have shown that single sheets of CFC laminate when irradiated with high power at UHF produce no measureable re-radiation at second and third harmonic frequencies, even when mechanically stressed, whereas levels 20 dB to 40 dB above the measurement system noise level are observed for jointed aluminium structures. Observable harmonic levels were only obtained with a cracked sheet, and with two sheets lightly touching at their edges. It appears, therefore, that if this linearity advantage of CFC is realised, a significant reduction in intermittent EMC problems arising from IMP effects should be attainable in CFC aircraft.

7.1   Efficiency of HF notch antennas in CFC tail fin

Two 2-metre triangular tail fin mock-ups were constructed, one in CFC material and the other in aluminium. A tuning unit was bolted within the notch on each fin in turn, the fin being mounted near the end of a 14 metre length of Comet fuselage mounted on a turntable. By measurement of the radiated field strength in the azimuth plane and comparison with a standard calibrated loop radiator at the same height and range, absolute levels were assigned to radiated power. Hence, with knowledge of the input power, the overall efficiency of antenna plus tuning unit was obtained at a number of frequencies. Fig 11 shows results obtained. The lowest curve relates to the original tail fin in which all CFC joints were glued, the next curve to the same fin in which glued joints around the notch were bolted through using countersunk bolts, thereby reducing joint resistance. The third curve relates to the CFC structure, but with an aluminium lining around the notch inner surface. The top curve is for the all aluminium structure. It can be seen that the glue bonded CFC structure was about 10 dB less efficient at 3 MHz than the all-aluminium structure, but that this difference was reduced to about 2 dB with an aluminium lining[13]. Above 16 MHz, no significant difference in efficiency existed between the various structures. A frequency dependent loading of the elements in the wire grid mathematical model of the tail fin which

gave calculated efficiencies for the notch structure similar to those measured was derived (Fig 12) although it should be emphasised that this loading will not necessarily be applicable in other cases.

8   AIRFRAME MULTIPATH AND ADAPTIVE ANTENNAS

As technology advances, the incorporation of sophisticated antenna array signal processing into airborne radio systems is becoming increasingly feasible. Such techniques are generally motivated by a requirement to improve ECM resistance of systems by spatial nulling of jamming transmissions. Whereas there is a wealth of literature relating to signal processing algorithms in which a free space array is assumed, the impact of airframe multipath and dynamics is less well defined.

8.1   Aircraft dynamics

The speed at which the processing electronics must adjust the phase and amplitude weights in each antenna array element channel prior to summation of the element signals in order to maintain a null pointed toward a jammer is readily calculable for a free space array as a function of array aperture in wavelengths and angular rate of change of jammer direction. The latter is generally dominated by aircraft attitude variation rate – the most rapid being the roll rate. The effect of airframe multipath is to increase the effective aperture of the array, to dimensions approaching those of the airframe. The angular rate of change of number, amplitude, phase and time delay of significant contributions to indirect signals is a complex theoretical problem, to which one approach is the use of GTD modelling. As a rough guide, response times in the range 1 ms to 100 ms are typically estimated to be necessary at UHF to maintain narrow bandwidth nulling at a 30 dB level during moderate manoeuvres.

8.2   Airframe multipath

Fig 13 shows two possible responses from an adaptive array in cancelling a direct jamming signal of bandwidth B Hz and a single multipath reflection with time delay   seconds. In the first, B is small, such that the direct signal and its reflection are highly correlated. In this case, nulls are not formed in the direction of the direct and multipath arrivals, but rather the array processor will arrange a vector balance between the two, cancelling one against the other. The radiation pattern will have a null between the two signals, for which only a single degree of freedom is required in the beamformer.

In the second, B is large, such that the direct signal and its reflection are uncorrelated. The first null in the autocorrelation response of band limited noise occurs for B = 1. Hence a jamming signal with 10 metre (33 ns) delay time from, say, a tail fin scattered signal received at an array on the forward fuselage in a system where the adaptive processor is attempting to null a bandwidth of 30 MHz will be uncorrelated with the direct arrival, and will appear as a separate jamming source. Two nulls will be formed by the processor, necessitating two degrees of freedom. Hence, for several multiple returns there is a reduction in the number of jammers which can be completely cancelled from a specific array and weighting network, or alternatively an increase in the residual power in the null. Fortunately, most systems can be treated as having a sufficiently narrow instantaneous bandwidth to keep the multipath correlated. Furthermore, an approximate analysis of radiation patterns for an array on the top fuselage of a small aircraft has shown that there is on average a reduction of amplitude of multipath return with increasing time delay. This effect tends to compensate for the increase in the uncorrelated component in the determination of the residual null power which would be obtained with an adaptive array.

Another effect which multipath may have is in the generation of cross polarisation components in the composite antenna/structure radiation patterns. These components may introduce effectively different path delays into the element channels relative to the direct signal, and similar effects on finite bandwidth signals mentioned above would be observed.

An appreciation of phase and amplitude perturbations which occur due to the airframe may be obtained by examination of scale model measurements of a two element array of monopoles mounted on the fuselage of a small aircraft . Fig 14 shows the distribution of the difference between measured results on the aircraft and calculated free space array values, compounded from measurements at 15 frequencies, four antenna pair spacings and three directions.

CONCLUDING REMARKS

This lecture has briefly reviewed some of the factors influencing antenna performance in the airborne environment. The electromagnetic problems are however only one aspect of the subject. Far greater problems often occur in siting and installing the antenna, since this may involve costly structural modifications (particularly in retrofit situations) careful calculation of aerodynamic effects, provision for cables, etc. It is desirable that an antenna fit is designed as an integral part of the airframe, and attempts have been made at this in new airframes. Unfortunately, it is often found that replacing a protruding blade antenna with a flush mounted structure, for example, has severe penalties in terms of weight, serviceability, and often electromagnetic performance. Similarly, the concept of serving the majority of radio systems from a single broad band antenna does not appear attractive, since a single site might not provide the optimum coverage for the various radio functions, and additional filters required for system isolation add complexity and weight. Nevertheless, good cases for flush mounted and broad band multifunction antennas well integrated with the airframe do occasionally exist, and it is to be hoped that full consideration is given to this concept in future integrated avionics systems.

REFERENCES

1   D.E.T. Nichols and M.S. Smith: Design and performance of a vertical range for radiation pattern measurement using aircraft scale models, RAE Technical Report 77052, April 1977.

2   D. Forgan: Computation of the performance of HF aerials mounted on aircraft. Unpublished MOD(PE) Report, August 1974.

3   W.D. Burnside, N. Wang and E.L. Pelton: Near field pattern analysis of airborne antennas, IEEE Trans on Antennas and Propagation, Vol AP28, No.3, May 1980.

4   G.Y. Philippou, R. Bustamente and R. Chignell: Recent developments in high frequency electro-magnetic field analysis by finite element methods, IEE Digest 1983/48, May 1983.

5   H.A. Wheeler: The radiansphere around a small antenna, Proc IRE, pp 1325-1331, August 1959.

6   R. Chignell, G.Y. Philippou, R. Bustamente: A novel precise method of measuring the efficiency of arbitrary low gain antennas, Proc IEE International Conference on Antennas and Propagation, York, April 1981.

7   R. Chignell and G.Y. Philippou: The characterisation of corner diffraction coefficients by the measurement of antenna impedance, Proc IEE, International Conference on Antennas and Propagation, November 1978.

8   G. Maile and R. Chignell: The impedance properties of fin-cap antennas, Proc IEEE APS Conference, Quebec, June 1980.

9   M.J. Sidford: A radiating element giving circularly polarised radiation over a large solid angle, IEE Conference Publication No.95, March 1973.

10   D.W. Smithers and D.A. Bull: Antenna to antenna coupling in aircraft radio systems, IEE International Symposium on EMC, pp 274-281, 1979.

11   D.W. Smithers and D.A. Bull: Aerial isolation – a study of the interaction between co-sited aerials, Radio and Electronic Engineer, Vol 49, No.6, pp 289-296, June 1979.

12   K.R. Siarkiewicz and A.T. Adams: Analysis and prediction of coupling between co-located antennas, IEEE Fourteenth EMC Symposium Record, pp 315-320, 1972.

13   J.I.R. Owen: Efficiency measurements of a HF notch aerial in a carbon fibre composite tail fin, IEE International Conference on Antennas and Propagation, pp 93-96, April 1983.

14   M.J. Sidford: Airframe multipath effects in airborne adaptive antenna arrays, IEE International Conference on Antennas and Propagation, pp 149-152, April 1981.

Table 1
SOME AIRBORNE RADIO SYSTEMS AND THEIR NOMINAL FREQUENCY BANDS

Communications		Navigation	
System	Frequency band	System	Frequency band
HF comms	2–30 MHz	Omega nav	10–14 kHz
VHF (FM) tactical comms and homing	30–76 MHz	Approach and landing aids	75 MHz 108–118 MHz 328–336 MHz
VHF comms	118–136 MHz		≈5 GHz
Sonobuoy data link and homing	136–174 MHz	TACAN/DME	960–1215 MHz
		Navstar GPS	1227–1575 MHz
UHF comms and homing	225–400 MHz	Radar altimeter	≈4 GHz
JTIDS – secure data comms	960–1215 MHz	Doppler nav	≈13 GHz
Identification			
IFF	1030–1090 MHz		
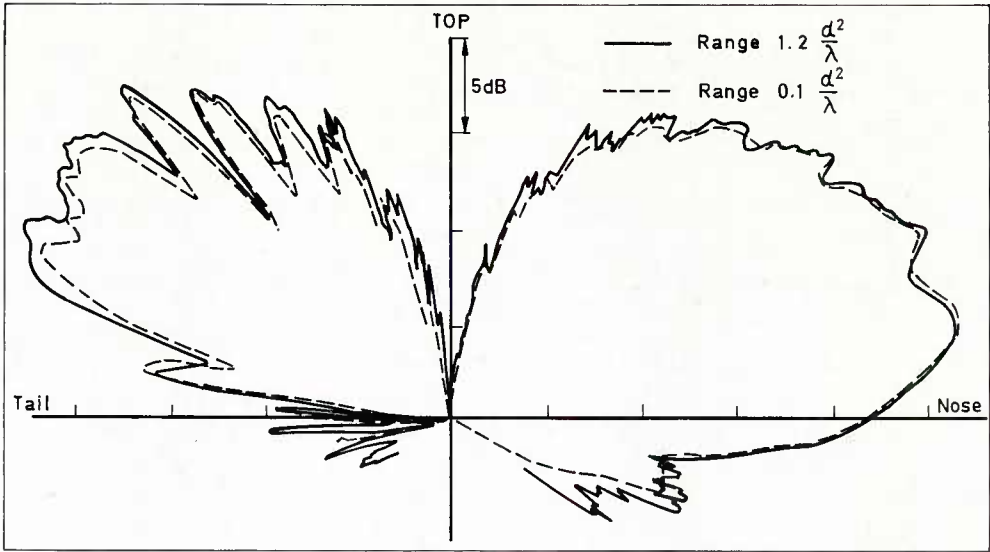
Fig 1   Pitch plane patterns of a monopole antenna on the top fuselage of a fighter of length d.
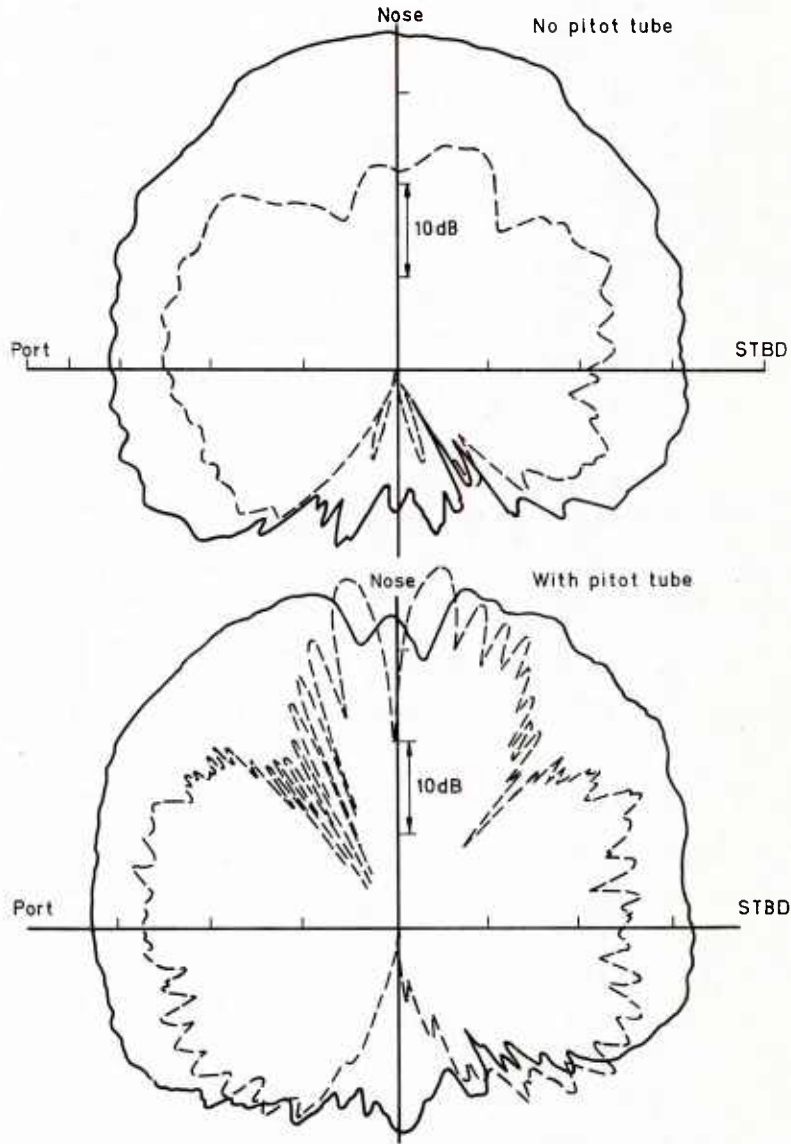
Fig 2   Radiation patterns of microwave antenna on nose of fighter aircraft.
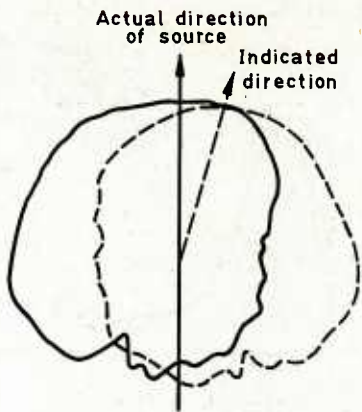
Fig 3   UHF Homing error due to nearby asymmetrically sited antenna.
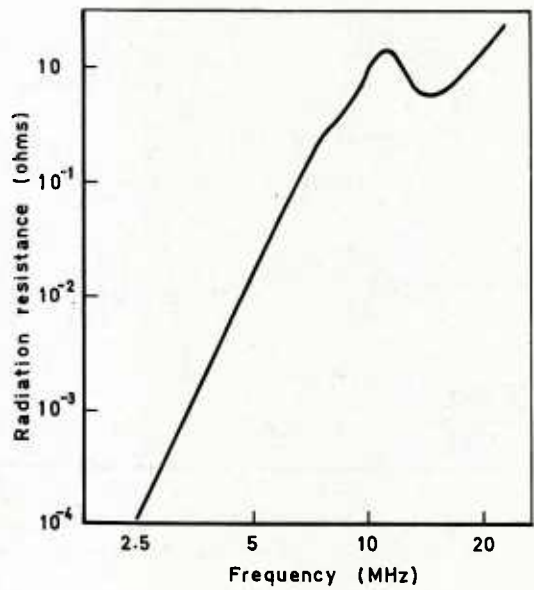
Fig 4   Typical radiation resistance of a HF notch antenna
on a small fighter aircraft.
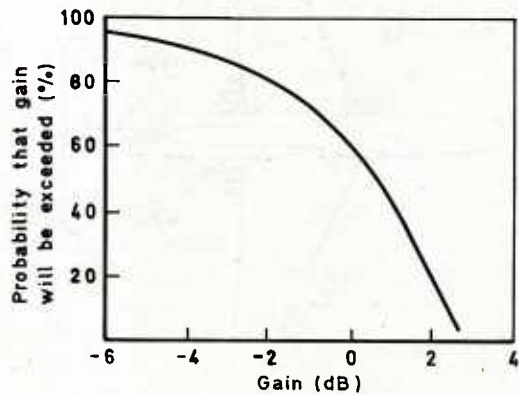
Fig 5   Gain probability distribution in azimuth plane
for blade antenna on small aircraft (1 GHz).
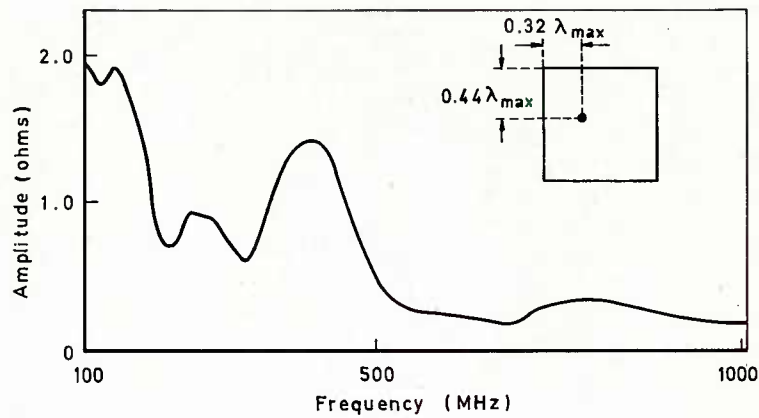
Fig 6   Impedance perturbation amplitude for a monopole placed in 'optimum' position on
a 3 metre square ground plane.
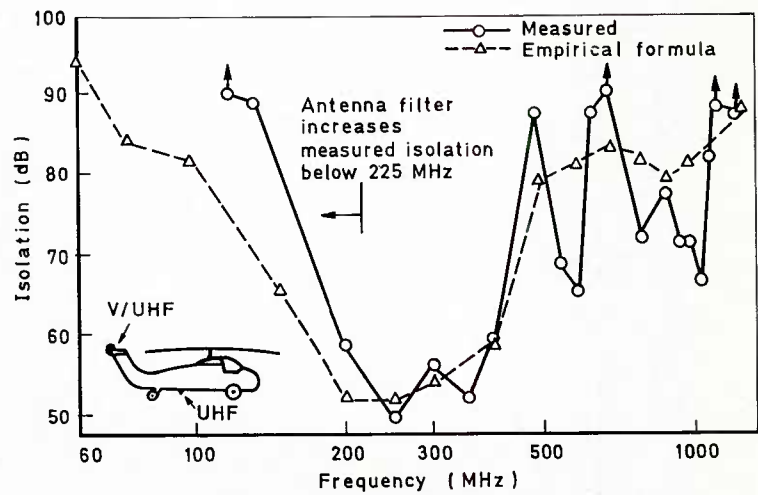
Fig 7   Lower UHF to tail V/UHF antenna isolation – Wessex helicopter.
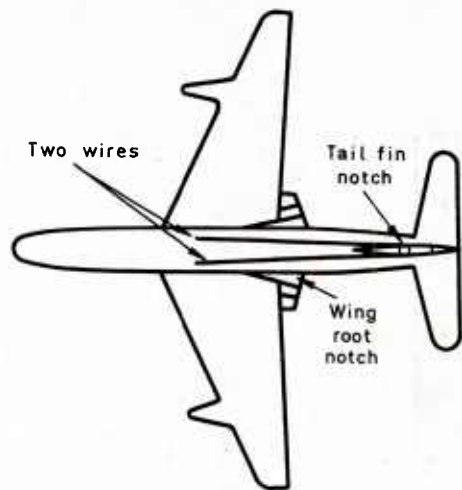
Fig 8   HF antennas on RAE Comet aircraft.
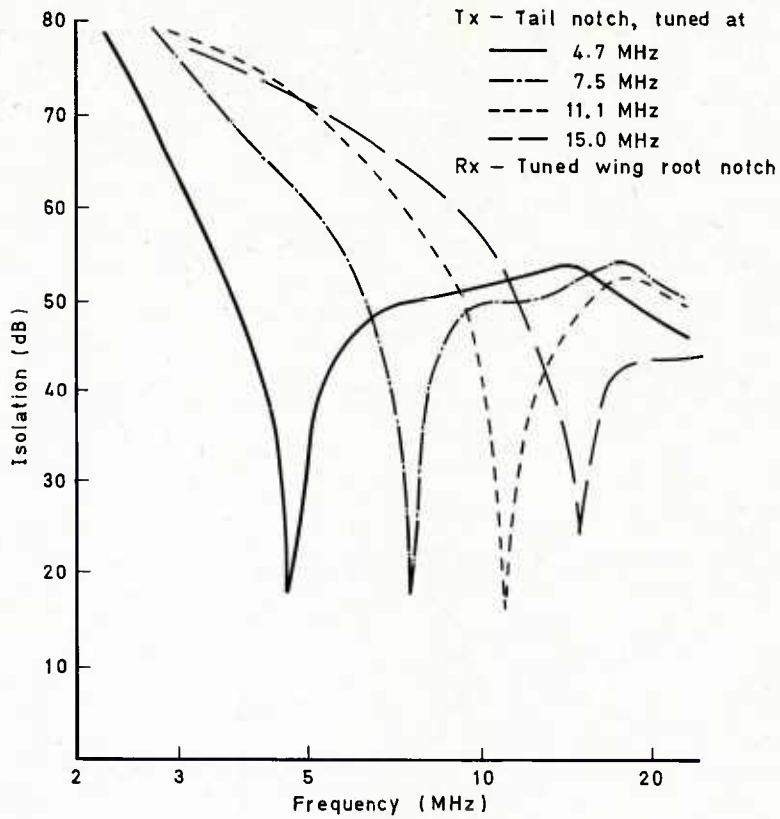
Fig 9 HF antenna isolation, Comet aircraft, in-flight measurements.
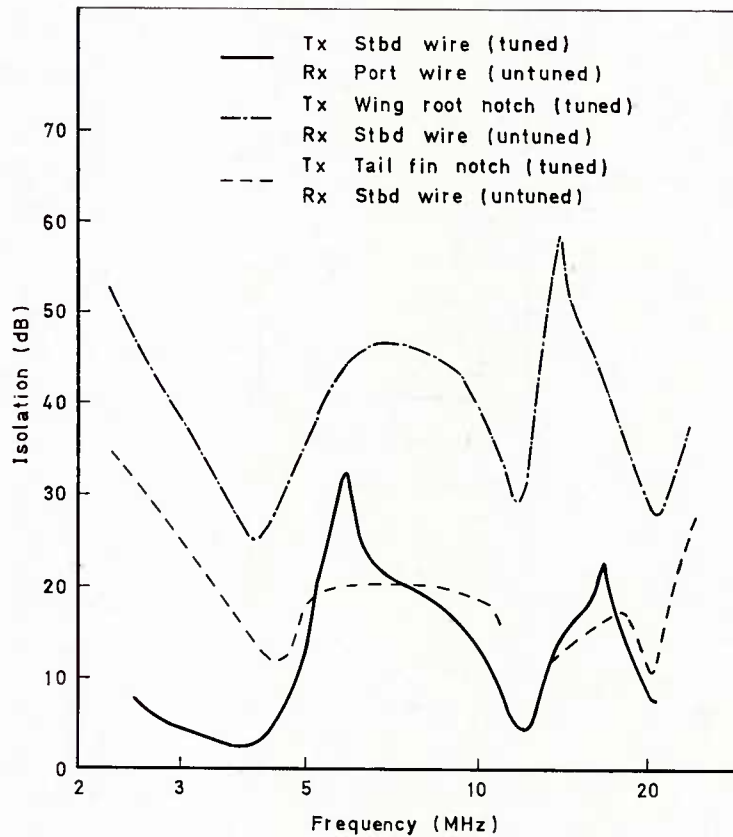
Fig 10 HF antenna isolation, Comet aircraft, in-flight measurements.
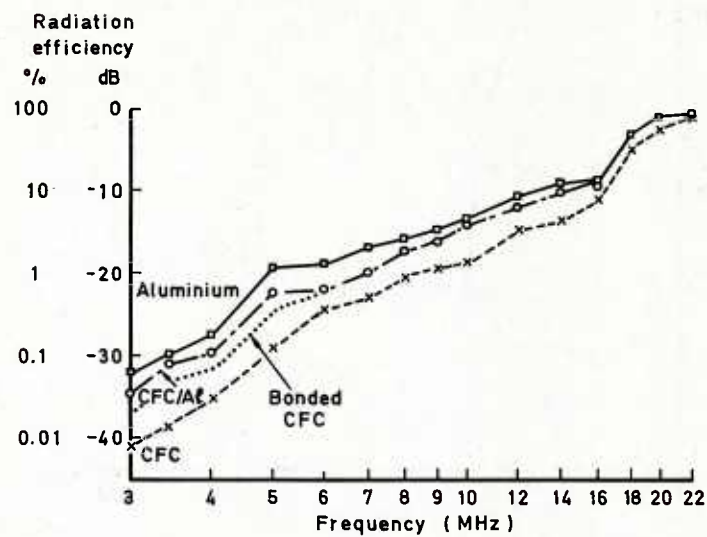
Fig 11 Radiation efficiencies of notch antennas in carbon fibre composite and aluminium structures.
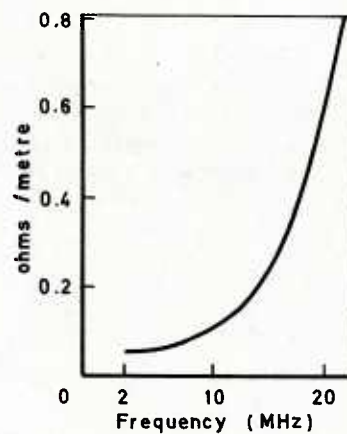
Fig 12 Wire grid loading for carbon fibre composite material.
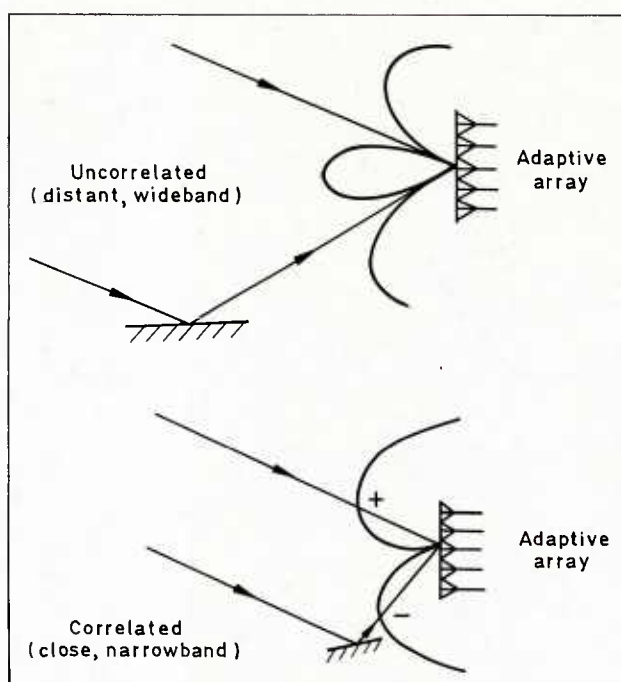
Fig 13   Airframe multipath effects on an adaptive array.
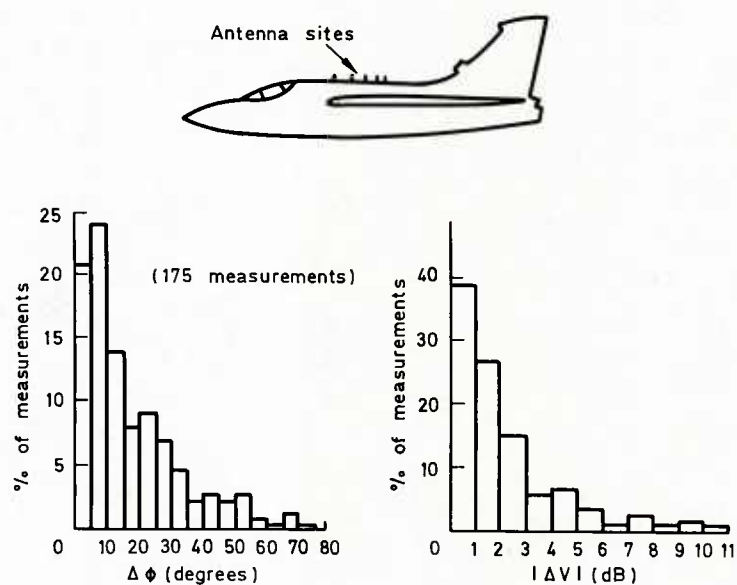
Fig 14   Deviation of relative phase and amplitude at array elements from free space values
due to airframe multipath (model measurements).

Numerical Modeling Techniques for Antennas*

E. K. Miller
Electronics Engineering Department
Lawrence Livermore National Laboratory
University of California
Livermore, California   94550

ABSTRACT.   An overview of wire-antenna computer modeling
is given for infinite media and half-space type problems.
The formulation and numerical solution methods are
summarized, and applications are demonstrated with
numerous examples.

1.   INTRODUCTION

Numerical methods based on integral-equation formulations are receiving increasing
acceptance for application to real-life electromagnetic radiation and scattering
problems.   Computer codes have been developed and validated for both surface and wire
geometries in both the frequency and time domains for modeling infinite, homogeneous
medium problems.   Some of these basic procedures have also been extended to the
analysis of structures located near a planar interface.   In this presentation we will
discuss the general topic of computer models from a frequency-domain viewpoint for wire
antennas in free space and located near the ground-air interface.   Some preliminary
considerations are discussed in Section 2, followed by a brief summary of a specific
formulation and numerical treatment in Section 3, with sample numerical results given
in Section 4.

2.   PRELIMINARY CONSIDERATIONS

The derivation of an integral equation for a wire structure can be accomplished in
many ways.   What is basically involved is the writing of Maxwell's equations in
integral form so that the scattered or secondary fields are given in terms of integrals
over induced source distributions.   By expressing the secondary field over loci of
points where the behavior of the total field (incident or primary plus secondary) is
known via boundary or continuity conditions, an integral equation for the induced
source is obtained in terms of the primary field.   Two broad general classes of
integral equations are obtained, depending upon whether the forcing function (primary
field) is electric or magnetic.   An electric forcing function gives rise to a Fredholm
integral equation of the first kind, in which the unknown appears only under the
integral.   A magnetic forcing field gives rise to a Fredholm integral equation of the
second kind, in which the unknown also appears outside the integral.   While derivatives
of the unknown may occur as well, these equations are commonly called integral
equations, rather than integro-differential equations as would be strictly correct.

Generally speaking, it has been found that the magnetic field type of integral
equation is better suited for smooth, closed surfaces than it is for thin-plate or
shell geometries and wires [1].   The converse is generally true of the electric-field
type of integral equation.   It is the latter then that is more commonly employed for
treating wire structures.   Also involved in developing wire integral equations are the
approximations that (1) the circumferential current is negligible; (2) the circum-
ferential variation of the longitudinal current can be ignored; and (3) the thin-wire
or reduced kernel can be used in place of the actual surface integration.

Many analytically equivalent integral equations for wires based upon the electric
field can be derived.   Three of the most commonly employed are the Hallen or vector
potential type [2], the mixed potential version [3], and the Pocklington integral
equation [4].   All are solved within the framework of the moment (or matrix) method but
each exhibits distinctive characteristics which must be taken into account in its
numerical treatment.   The Hallen equation, for example, can produce results using a
pulse current basis of accuracy comparable to those obtained from the Pocklington
equation solved with a three-term (constant, sine, and cosine) basis for simple
structures [5].   The Hallen equation is not, however, readily extendable to the complex
geometries that the Pocklington equation can handle [6].

Although pulse-current [4] and linear-current [7] bases have been quite widely
used, and can under suitable circumstances be essentially equivalent, they are not as
efficient for modeling traveling wave structures, regardless of the integral equation
employed, as are sinusoidal bases which possess nonconstant derivatives and which can
closely resemble the actual current solution.   Sinusoidal bases have appeared in
subsectional or subdomain form in both the three-term expansion mentioned above and in
the piecewise sinusoidal [8,9] or two-term form.   Fourier series have also been studied

as complete-domain sinusoidal bases, but have not been widely adopted because they require more integration effort than subsectional bases and can lead to ill-conditioned matrices [4].

The weight or test functions most often used have been delta functions, although Galerkin's method with both linear [7] (two-term) and sinusoidal [8] (two-term) functions has also been quite widely applied. The term "point matching" refers to the use of delta-function weights. A comparison of numerical convergence rates for several common methods applied to a straight-wire scatterer is shown in Fig. 1 [10].

In addition to the problem of choosing basis and weight functions, there are other special aspects of the numerical development which must be considered when selecting a code for computer modeling. Three of these aspects are discussed below.

2.1 JUNCTION TREATMENT

Any subsectional approach which employs finite-difference operators in the integral equation or other than a pulse current basis necessitates special consideration of both simple (two wires) and multiple (three or more wires) junctions. What is essentially required is a way to relate in some physically and mathematically reasonable way the current basis of each subsection (segment) to those of its neighbors. When pulse bases are used in the mixed-potential integral equation, the finite-difference operator spans two segments and thus leads to a charge which involves the two corresponding pulse-current samples [3]. For two- or three-term bases, the condition of current amplitude and slope continuity at each simple junction leads to equations which permit all the constants in the current expansion to be given in terms of current samples at the segment junctions or centers, respectively [5]. A slightly different handling of the three-term basis was developed by Yeh and Mei [11], in which the current is extrapolated from a given segment to the adjacent segment centers, but which is otherwise basically the same.

When a multiple junction is concerned, the treatment can get considerably more involved. The pulse-basis approach mentioned can be extended to the multiple junction by dividing the total junction charge between the junction segments according to the ratio of the logarithm of their individual areas to the sum of the logarithms of their areas [12]. The two-term expansions have been applied to multiple junctions by overlapping M - 1 of the bases a pair at a time at an M-segment junction [7]. Application of the three-term expansion to the multiple junction was originally accomplished using the Yeh and Mei simple-junction procedure by incorporating a composite segment having the averaged length and total current of the M - 1 connected segments [13]. More recently, the logarithmic-area-ratio approach was adapted to the three-term expansion for multiple junctions, while a spline treatment is used to handle simple junctions [14].

2.2 SOURCE MODELS

Determination of quantities such as absolute gain, efficiency, radiated power, input power, etc. requires not only the antenna current distribution but also the input characteristics, particularly the feedpoint impedance (or admittance). The feedpoint admittance can be found in various ways, but when using the integral-equation approach it is usually defined in terms of source-region current per unit of terminal voltage. In order to calculate this quantity, a realistic source model is needed that not only provides an appropriate means for numerically exciting the antenna but also permits ready evaluation or specification of the effective terminal voltage. Thus if, as in a point-matching procedure, the excitation arises as a tangential field on the source segment of length Δ, the driving voltage might be assumed to be $-E^I\Delta$ if E^I is constant on the source segment and zero elsewhere. This assumption may not always be valid, however, with the result that the actual voltage can only be obtained by integrating the tangential field in the vicinity of the source segment [5]. Somewhat less ambiguity should arise from Galerkin-type approaches where the boundary conditions are integrated, so that the classical delta function source might be numerically approximated. An alternate source model for point matching is provided as a current slope discontinuity, which also approximates a delta-function source field [15]. The current bases, junction treatment, and weight functions can all influence the usefulness of these alternate source models. In case of uncertainty, once the current distribution has been found, the impedance might be computed from the classical EMF method, although at the expense of the additional integration which this entails.

Two other source models are worth mentioning. Upon noting that a source renders the linear system of equations inhomogeneous so that it has a nontrivial solution, one obvious choice is a specified current at some point on the structure [16]. Another is to drive the antenna with an explicit transmission line. In the latter case the exciting field is removed from the antenna structure, but a source is still needed to excite the transmission line itself.

2.3 INTEGRATION

Integration is understandably an essential part of the moment method, being involved in applying the integral operator to the current bases, and in a Galerkin

method in evaluating the inner product of this result with the weight functions. For most wire programs, these operations, which lead to the generalized impedance matrix, dominate the total solution time for numbers of unknowns less than ~200. It is thus important that the integration time be minimized consistent with the overall accuracy requirements.

One way to approach this goal is to choose appropriate bases and weight functions. The two-term sinusoidal current basis, for example, requires no numerical integration when the Pocklington integral equation is used together with point marching. This particular combination is not very accurate, however [17]. By adding the constant term, much better results are obtained, with the slight additional expense of the numerical integration required to find the longitudinal field of this current term; the radial component can be analytically expressed. Alternatively, use of a sinusoidal weight function [8] also gives much improved results and requires numerical integration at most, of sine and cosine integrals. The piecewise linear basis used with the mixed-potential equation cannot be analytically integrated, but good results are obtained with four-point rectangular integration of both the operator and inner-product integrals [7]. In addition, instead of applying a numerical integration to the self-term, a series expansion which gives a closed-form expression can be used [3]. When numerical integration is resorted to, various adaptive routines and special techniques are available to improve efficiency [18].

3. WIRE ANTENNA ANALYSIS

3.1 INFINITE, HOMOGENEOUS, ISOTROPIC MEDIA

It can be appreciated that there are many options available to the analyst concerning the integral equation to be selected and its numerical treatment in developing a computer model for application to wire antennas. In order to limit this discussion to a reasonable length, our attention will be primarily directed to an approach based on the Pocklington integral equation solved using a three-term subsectional basis (constant, sine, and cosine) and point matching.

A brief overview of the relevant equations and numerical treatment used for free space and various interface theories and some special topics is given in this section. Numerical results follow in Section 4.

The Pocklington-type integral equation for a wire structure of contour $C(\bar{r})$ can be expressed in the form

$$\hat{s} \cdot \bar{E}^I(s) = \frac{i\omega\mu}{4\pi} \int_{C(\bar{r})} I(s')G_0(s,s')ds'; \quad s\epsilon C(\bar{r}) + a(\bar{r}) \tag{3.1}$$

where

$$G_0(s,s') = [\hat{s} \cdot \hat{s}' + \frac{1}{k^2}(\hat{s} \cdot \nabla)(\hat{s}' \cdot \nabla)]g_0(\bar{r},\bar{r}') ,$$

$$g_0(r,r') = \frac{e^{-ikR}}{R} ,$$

$$R = |\bar{r} - \bar{r}'| \geq a(\bar{r}) ,$$

$$\hat{s} = \frac{\nabla C(\bar{r})}{|\nabla C(\bar{r})|} ,$$

and

$$\hat{s}' = \frac{\nabla C(r')}{|\nabla C(r')|} ,$$

where as usual k is the infinite-medium wave member, the permeability and permittivity are denoted by μ and ϵ, $a(\bar{r})$ is the wire radius at $\bar{r}$, and $\bar{E}^I$ is the incident electric field.

Reduction of this equation to matrix form involves these steps:

(1) Approximating $C(\bar{r})$ as a piecewise linear sequence of N segments of length Δ_i, i = 1, ... , N, so that

$$C(\bar{r}) \simeq \sum_{i=1}^{N} \Delta_i \hat{s}_i ,$$

with $\hat{s}_i$ the unit tangent vector to $C(\bar{r})$ at $\bar{r} = \bar{r}_i$ (use of straight segments is not mandatory, but it is very convenient in simplifying the current integration);

(2)   Introducing the subsectional bases

$$I_i(s') = A_i + B_i \sin [k(s' - s_i)] + C_i \cos [k(s' - s_i)]$$

to represent the unknown current (the final unknowns will be the N-sampled current values $I_i = A_i + C_i$, $i = 1, \ldots , N$, (or their equivalents) at the center of each of the N segments);

(3)   A current interpolation procedure whereby the individual A_i, B_i, and C_i constants are expressed in terms of the sampled current values;

(4)   Use of the N delta-function weights $\delta(s - s_j)$, $j = 1, \ldots , N$, to obtain an Nth-order impedance matrix of N independent field equations (note that the weight functions sample the field at the segment centers, and are thus "collocated" with the current sample locations);

(5)   Specification of the N incident or primary field vector components $E = \bar{E}^I(s_j)$ $\cdot \hat{s}_j$, $j = 1, \ldots , N$, which are the tangential fields at the N segment centers;

(6)   Matrix manipulation to obtain an admittance equivalent of the impedance matrix; and

(7)   Computation of the current distribution and whatever field components are desired.

The total computer solution time is well approximated by $AN^2 + BN^3$, where the "A" term corresponds to step (4) and the "B" term to step (6). For the code under the consideration here and for a CDC-7600 computer, $A \approx 4 \times 10^{-4}$ sec and $B \approx 2 \times 10^{-6}$ sec. It is useful to observe that this segmentation of the structure into N segments yields the equivalent of an N-port network for describing its electromagnetic properties, from which valuable insight can be obtained.

3.2   PERFECTLY CONDUCTING HALF-SPACE

Equation (3.1) as written applies to wire structures excited as antennas or scatterers and located in infinite, isotropic, homogeneous media of arbitrary (possibly lossy) permittivity and permeability. It can easily be extended to permit the modeling of magnetic or electric image planes. For example, the perfectly conducting ground analog of Eq. (3.1) is, for an antenna elevated above a ground plane at $z = 0$,

$$s \cdot \bar{E}^I(s) = \frac{i\omega\mu}{4\pi} \int_{C(\bar{r})} I(s') [G_0(s,s') + G_I(s,s'*)] ds', \qquad (3.2)$$

where

$$g_I = \frac{e^{-ikR*}}{R*} ,$$

$$R* = |\bar{r} - \bar{r}'*| ,$$

$$\bar{r}'*(x,y,z) = \bar{r}'(x,y,-z) ,$$

$$s'* = \frac{\nabla C(\bar{r}'*)}{|\nabla C(\bar{r}'*)|} .$$

Similar forms can be written for a magnetic interface and for an interior right-angle corner. If the corner angle is otherwise arbitrary but related to π as an integer multiple, a discrete spectrum of angular images is obtained, but the essence of the integral equation form is preserved [19]. Precisely the same line of approach can also be used for interior problems where the wire structure is located between two parallel magnetic or electric planes [20].

3.3   IMPERFECTLY CONDUCTING HALF-SPACE

A problem which is not so computationally simple to handle, but which is of perhaps greater practical interest, is that of an antenna located (buried or elevated) near the ground-air interface. This is a topic of considerable longevity in electro-

magnetics; a formal solution was worked out for this problem in 1909 by Sommerfeld [21]. The numerical complexity of evaluating the Sommerfeld integrals (which appear in the integral-equation kernel) for arbitrary source and observation-point locations and ground parameters, however, has prevented the Sommerfeld theory from being routinely used for such problems. Consequently, while some progress has been made in applying the Sommerfeld theory, alternate approches to the antenna-ground problem have also been pursued. Some of these various methods are briefly discussed below.

3.3.1 The Sommerfeld Theory

Details of the steps in deriving the Sommerfeld integrals may be found elsewhere [22]. Here we will simply write one version of Eq. (3.1) which accounts for the interface reflected field via the Sommerfeld theory; alternate forms are also available, differing essentially in how the perfect-ground image terms are handled. It is

$$\hat{s} \cdot \overline{E}^I(s) = \frac{i\omega\mu}{4\pi} \int_{C(\overline{r})} I(s')ds' \left\{ G_0(s,s') + G_I(s,s'*) \right.$$

$$+ \left(\cos \beta + \frac{1}{k^2} \frac{\partial^2}{\partial s \partial z} \right) \sin \beta' \ g_{Hz} - \cos \beta' \ g_{Vz}$$

$$\left. + \sin \beta' \left[\sin \beta \cos (\alpha - \alpha') + \frac{1}{k^2} \frac{\partial^2}{\partial s \partial t'} \right] g_{Ht} \right\} , \tag{3.3a}$$

with

$$g_{Ht} = 2 \int_0^\infty \frac{\lambda}{\gamma + \gamma_E} J_0(\lambda\rho) \ e^{-\gamma(z+z')} d\lambda, \tag{3.3b}$$

$$g_{Hz} = \frac{-\cos(\phi-\alpha')}{k^2} \int_0^\infty \frac{\gamma - \gamma_E}{\varepsilon_E\gamma + \gamma_E} J_1(\lambda\rho) \ e^{-\gamma(z+z')}\lambda^2 d\lambda ,$$

$$\tag{3.3c}$$

$$g_{Vz} = 2 \int_0^\infty \frac{\gamma_E}{\varepsilon_E\gamma + \gamma_E} J_0(\lambda\rho) \ e^{-\gamma(z+z')} \frac{\lambda}{\gamma} d\lambda ,$$

$$\rho = \sqrt{(x - x')^2 + (y - y')^2 + a^2} ,$$

$$\phi = \tan^{-1} [(y-y')/(x-x')] ,$$

$$\gamma = \sqrt{\lambda^2 - k^2} ,$$

$$\gamma_E = \sqrt{\lambda^2 - \varepsilon_E k^2} ,$$

where $\alpha = \alpha(\overline{r})$ and $\beta = \beta(\overline{r})$ are the direction angles of the wire at $\overline{r}$, $\hat{t}'$ is the horizontal projection of $\hat{s}'$, J_n is the Bessel function of order n, and with the permittivity of the lower half space relative to the upper free-space medium denoted by ε_E. The permeabilities of the two half spaces are assumed to be equal.

The presence of the double integral in Eq. (3.3), particularly the Sommerfeld portion, makes it quite time-consuming and sensitive to evaluate. In spite of that, the basic moment method can be used to solve it, but in addition to the usual constraints imposed on current sampling, it is necessary to take into account the source distance from the interface, as this parameter can influence both the Sommerfeld-integral evaluation and the model segmentation. The more general problem of an antenna which penetrates the interface or where objects lie in both half spaces requires obtaining both the field reflected from it and transmitted across it. Treatment of this problem is similar to that just described, and so it is not discussed here.

3.3.2 Sommerfeld Interpolation

Much effort has been devoted to reducing the computational expense of evaluating the Sommerfeld integrals which appear in Eq. (3.3). For the most part, this has involved analytical manipulation of the integrals and is intended to obtain forms more suitable for computation or approximation. Such approaches usually have had limited success because the constraints employed in deriving them restrict their scope of applicability.

A quite different approach which exploits the inherent smoothness of the Sommerfeld-integral contributions to the field, however, has demonstrated that efficiency, accuracy and flexibility are not mutually incompatible [23]. This approach is based on interpolation in the two-dimensional space (ρ, z + z') of the Sommerfeld field values which, as shown in Eqs. (3.3b - 3.3d), are dependent spatially only on ρ and z + z'. By computing and prestoring Sommerfeld field values on a grid of points which contains the antenna of interest, it is possible to perform the integration of Eq. (3.3a) without further resort to the Sommerfeld integrals themselves.

Although initial tests of the interpolation procedure employed a rectangular grid, additional study has shown a polar grid to work even better [24], an example of which is given in Fig. 2. And, the computer times involved are indeed remarkable, considering that results obtained using this approach are essentially rigorous insofar as the Sommerfeld field contributions are concerned. For example, suppose the computer time needed to model a given antenna in free space is T, then the time needed to model the same antenna over ground, using this approach is $\sim(2-4)$T, once the interpolation grid has been computed, which itself uses a time $\sim$T. Furthermore, the grid can be stored for subsequent re-use for other heights or orientations of the same antenna, or for modeling other antennas, and the interpolation procedure works well for wires within a thousandth of a wavelength or less of the ground plane [24]. Finally, it can be extended to the cross-interface problem where an antenna penetrates the interface or two objects lie on either side of it. In this case, the transmitted fields are functions of the three variables ρ, z and z'. Treatment of the latter problem is similar to the approach just described so it is not discussed here.

3.3.3 Modified Image Theory

In many cases, although they may not be always easy to identify a priori, the rigor represented by Eq. (3.3) is unnecessary; various approximations will be found adequate. The accuracy actually required of the computer model may be debatable, but it is probably reasonable to seek something on the order of experimental error. One approach which has been found to agree within 10-15% of the Sommerfeld results for input impedance of simple antennas, and so which appears useful in view of the above observation, is the reflection coefficient approximation [25,26]. It involves representing the interface-reflected fields in terms of their perfect-ground images multiplied by the Fresnel plane-wave reflection coefficients for the TE and TM field components evaluated at the specular reflection point. This approximation leads to the integral equation given below:

$$\hat{s} \cdot \overline{E}^I (s) = \frac{i\omega\mu}{4\pi} \int_{C(\overline{r})} I(s') \, [G_0(s,s') + R_M G_I(s,s'^*) + (R_E - R_M) \sin \beta \sin \beta'$$

$$\times \sin (\phi - \alpha) \sin (\phi - \alpha') \, g_I(\overline{r},\overline{r}'^*)] \, ds' \quad , \qquad (3.4)$$

where R_E and R_M are the TE and TM reflection coefficients given by

$$R_E = \frac{\sqrt{\varepsilon_E - \sin^2 \theta} - \cos \theta}{\sqrt{\varepsilon_E - \sin^2 \theta} + \cos \theta} \quad ,$$

$$R_M = \frac{\varepsilon_E \cos \theta - \sqrt{\varepsilon_E - \sin^2 \theta}}{\varepsilon_E \cos \theta + \sqrt{\varepsilon_E - \sin^2 \theta}}$$

with θ the angle of incidence with respect to vertical. (Although Eqs. (3.3) and (3.4) are written expressly for the reflected field, similar expressions can be developed for the field transmitted across the interface, but their accuracy may not be acceptable).

Since the reflection-coefficient integral Eq. (3.4) differs only trivially from that for the perfect-ground case given by (2), it may be appreciated that its numerical solution is obtained with almost equal efficiency, in marked contrast to the situation which holds for the Sommerfeld theory in its usual form. The reflection coefficient approximation is, in addition, applicable to a laterally inhomogeneous ground with little further complication. Layered grounds can also be handled using this approach.

3.3.4 Interface Source Distribution

The Sommerfeld theory is not the only rigorous formulation which can be derived for the antenna-ground problem. Some variations of that approach, which still involve integral-type elementary source solutions, are summarized by Banos [27]. A completely different method of treatment which results in integration in real space (the interface) rather than wave-space integration (the Sommerfeld or λ integral) can be postulated. One way is to treat the interface tangential fields as unknown in addition to the antenna current distribution itself. One can then solve for these surface sources together with the antenna current by applying the moment method to the coupled integral equations which result. An obvious disadvantage of this approach is that many more unknowns require consideration, an infinite number in principle, but finite in practice since only the region near the antenna needs be modeled. Advantages are that the computer-time penalty imposed by the interface-related calculation is relatively independent of antenna size, and the Sommerfeld integrals are entirely circumvented, with no nested numerical integrals being encountered.

One form of the integral equation which results from this treatment is

$$\hat{s} \cdot \overline{E}^I(s) = \frac{i\omega\mu}{4\pi} \int_{C(\overline{r})} I(s')G_0(s,s')ds' - \frac{\hat{s}}{4\pi} \cdot \int_A \{i\omega\mu[\hat{z} \times \overline{H}(\overline{r}')]g_0(\overline{r},\overline{r}')$$

$$- [\hat{z} \times \overline{E}(\overline{r}')] \times \nabla' g_0(\overline{r},\overline{r}') - [\hat{z} \cdot \overline{E}(\overline{r}')]\nabla'g_0(\overline{r},\overline{r}') \, da'\}; \quad s \in C(\overline{r}) + a(\overline{r}) \qquad (3.5a)$$

$$\hat{z} \times \frac{i\omega\mu}{4\pi} \int_{C(\overline{r})} I(s')\overline{G}_0(\overline{r},s')ds' = \frac{1}{2\pi} \hat{z} \times \int_A \{i\omega\mu[\hat{z} \times \overline{H}(\overline{r}')] \, g_1(\overline{r},\overline{r}')$$

$$- [\hat{z} \times \overline{E}(\overline{r}')] \times \nabla'g_1(\overline{r},\overline{r}') - [\hat{z} \cdot \overline{E}(\overline{r}')]\nabla'\tilde{g}_2(\overline{r},\overline{r}')I \, da'\}; \quad r \in A \qquad (3.5b)$$

$$- \hat{z} \times \nabla \times \frac{1}{4\pi} \int_{C(\overline{r})} I(s')\overline{G}_0(\overline{r},s')ds' = \frac{1}{2\pi} \hat{z} \times \int_A \{i\omega\epsilon[\hat{z} \times \overline{E}(\overline{r}')] \, g_2(\overline{r},\overline{r}')$$

$$+ [\hat{z} \times \overline{H}(\overline{r}')] \times \nabla'g_1(\overline{r},\overline{r}') + [\hat{z} \cdot \overline{H}(\overline{r}')]\nabla'g_1(\overline{r},\overline{r}')\} \, ds'; \quad \overline{r} \in A$$

where

$$g_1 = g_0 + g_E \, , \qquad g_2 = g_0 + \epsilon_E g_E \, , \qquad \tilde{g}_2 = g_0 + g_E/\epsilon_E$$

$$g_E = \exp[-ik\sqrt{\epsilon_E}R]/R$$

Also A is an area on the $z = 0$ ground plane under the antenna, $\overline{E}(\overline{r}')$ and $\overline{H}(\overline{r}')$ are the ground-plane source distributions, and

$$\overline{G}_0(\overline{r},s') = [\hat{s}' + \frac{1}{k^2} \nabla(\hat{s}' \cdot \nabla)]g_0(\overline{r},\overline{r}') \, .$$

Note that the surface integrals in the latter two of the above equations must be evaluated in a principal-value sense.

3.3.5 Surface Source Approximations

In the same way that the reflection-coefficient approximation follows in a straight-forward way from the rigorous Sommerfeld theory, approximations to the interface source distribution analysis discussed above naturally suggest themselves. Two we consider here are the surface-impedance and physical-optics approximations.

3.3.6 Surface-Impedance Approximation

Under the condition that the surface impedance concept is valid $[(\sin^2\theta)/\epsilon_E \ll 1]$ [28], the tangential components of the electric and magnetic fields at the surface are to a good approximation related as

$$E_{tan} = -H_{tan}Z_{surf},$$

where

$$Z_{surf} = \eta/\sqrt{\epsilon_E} \quad ,$$

with η the upper medium wave impedance.

Upon employing this relationship in (3.5) the surface integral equations decouple and the number of surface unknowns is decreased by half. A corresponding reduction in the order of the overall linear system is thus achieved, with a potential significant saving in both the computer storage and solution time. Either of the two surface equations can be retained for use together with the structure-related integral equation. For convenience we might select the electric-field equation since then all required interaction coefficients involve the electric field only.

3.3.7 Physical-optics Approximation

Even further simplification of (3.5) can be achieved by invoking a physical-optics type of approximation for the surface fields. But in contrast to the usual physical-optics magnetic field, which is given by $H_{tan} = 2H_{tan}^{inc}$, we instead use

$$H_{tan} = (1 + R)H_{tan}^{inc} \quad ,$$

with R the reflection coefficient together with the surface impedance approximation for E_{tan} to allow for a finite ground conductivity. This permits the total-surface field distribution to be expressed in terms of the currents on the wire structure and leads to the same number of unknowns as for the Sommerfeld theory, but with the advantage of a much simpler integral-equation kernel. A perfect-ground type of integral equation could be derived by decomposing the surface source contribution to the fields on the structure into a part due to the perfect ground (due to $2H_{tan}^{inc}$), which can be analytically integrated to give the usual perfect ground image, and a perturbation term $(R - 1)H_{tan}^{inc}$, which will require numerical integration. While in general we might use a Fresnel reflection coefficient for each incremental source and surface path, it would be simpler, and not inconsistent with approximations already employed, to everywhere approximate R by its normal incidence form. Note that by appropriate pairing of source and observation points on the wire structure and use of a single reflection coefficient evaluated at their specular point, we would obtain the reflection coefficient approximation already discussed.

3.3.8 The Compensation Theorem

Application of the compensation theorem to ground-plane problems has received considerable attention [29-31]. It has been used to determine the input impedance of vertical monopoles located over various ground configurations, including determining the effect of ground-screen size. However, more general antenna problems have evidently not been attempted with this theory. The reason for this lies, apparently, not in limitations inherent in the theory itself, but in its numerical implementation. A ground plane integral is involved, which, for all but the simplest situations, requires numerical evaluation.

The compensation theorem "is essentially an exact perturbation technique in which the fields in the unperturbed state are known" [31]. If the unperturbed state is the case of a perfectly conducting ground plane and the perturbed state is the actual ground problem of interest, then we obtain for the antenna input impedance

$$Z' = Z + \frac{1}{I^2} \int_A \overline{H} \cdot \hat{z} \times \overline{E}' \, da \quad ,$$

where the primes denote perturbed quantities and I is the feedpoint current. Since the perfect-ground magnetic-field distribution can be accurately solved for, evaluation of Z' hinges on finding $\overline{E}'$. This is usually accomplished by using the surface impedance approximation, i.e., $E'_{tan} = -H'_{tan} \times Z_{surf}$, and then assuming $H'_{tan} \simeq H_{tan}$. These steps facilitate the calculation and permit use of the perfect-ground result as a sort of canonical solution to find the antenna impedance for the finitely conducting ground.

3.4 SPECIAL TOPICS

In addition to the above topics, there are other problem areas concerning wire-antenna computer modeling that deserve attention. Some of them are summarized here.

3.4.1 Wire Grids

Hardly had the initial wire integral-equation models been developed, than were they used for modeling wire-grid objects [4,32]. Two types of wire-grid applications naturally occur. One is where the object is actually a wire grid, as in a wire-grid reflector for an antenna, for example. The other, and the one more frequently employed, is where a solid conducting body or shell, for modeling purposes, is represented by a wire grid. This latter application involves two approximations, the physical one of replacing a continuous surface with a grid, and the numerical one involved in a computational solution. Of the two approximations, the physical one is probably the more limiting, although the errors of both can be reduced as the grid size is reduced or the number of unknowns is increased [1].

One uncertainty of modeling continuous surfaces with wire grids is that of choosing the most appropriate wire size to use. The surface impedance of a wire grid is a function of both the wire radius and grid opening. Thus, changing either of these parameters can affect the electromagnetic behavior of the surface [1]. One guideline for the most appropriate ratio of segment length to wire radius is 2π, for which value the surface areas of the grid and the surface being modeled are equal. The ratio that works best seems to depend upon both the analytical formulation and numerical treatment employed [33].

3.4.2 Ground Screens

The compensation theorem has been employed in various ways to analyze ground-screen effects as mentioned above. Ground screens can also be analyzed rigorously by including the wires of which they are comprised as part of the antenna model, for which some sample results are presented in Section 4. However, it may not be practicable to use this approach for ground screens containing many wires. As an alternative, the reflection-coefficient approximation might be more appropriate. It offers an easily implemented procedure for analyzing a broad class of ground-screen configurations with greater efficiency than available in general from the compensation theorem.

What is essentially required in order to include the ground-screen influence in the reflection-coefficient calculation is a modified reflection coefficient which takes into account the reflecting properties of the screen-ground combination. This is possible if the surface impedance of the combination is known. For ground screens whose wires are in good electrical contact with the soil, the effective surface impedance Z'_{surf} may be taken to be [34]

$$Z'_{surf} \approx \frac{Z_{surf} \, Z_{screen}}{Z_{surf} + Z_{screen}} \quad ,$$

where Z_{screen} is the screen impedance. For a radial screen having N wires of radius a, the screen impedance at distance ρ from the center is given by [34]

$$Z_{screen} \approx \frac{i\mu\omega\rho}{N} \ln (\rho/Na) \quad .$$

A corresponding formula for a parallel grid of wires, whose center spacing is d, is

$$Z_{screen} \approx \frac{i\mu\omega d}{2\pi} \ln (d/2\pi a) \quad .$$

Meshes consisting of locally orthogonal wires having different spacings might be treated as anisotropically conducting planes whose principal-direction impedances are obtained from the parallel-wire formula using their corresponding spacings. From Z'_{surf} we infer an effective ground permittivity for use in computing the Fresnel reflection coefficients, and are thus able to include the screen in the integral-equation calculation. The anisotropic case requires decomposition of the TE and TM fields into components along the orthogonal screen wires [35]. Note that this method fails for vertical antennas located at the center of a radial screen.

An alternative possibility is offered by the work of Astrakhan [36] who derived reflection coefficients for infinite-plane wire grids. His results, given in terms of TE-TE, TM-TM, TE-TM, and TM-TE reflection coefficients can be modified to include the effect of the ground itself and used in the reflection-coefficient approximation. Other useful results are given by Wait [37] who studied the properties of a wire grid located near ground.

3.4.3 The Layered Ground

Reflection coefficients are of course available for a layered ground. For the special case of only two layers, and where the surface impedance approximation holds, the effective surface impedance is given by [38]

$$z'_{surf} \approx z_{surf} \frac{\sqrt{\varepsilon_1} + i\sqrt{\varepsilon_2} \tan kh \sqrt{\varepsilon_1}}{\sqrt{\varepsilon_2} + i\sqrt{\varepsilon_1} \tan kh \sqrt{\varepsilon_1}} ,$$

with ε_1 and ε_2 the relative permittivities of the two layers and h the

thickness of layer 1.

3.4.4 Geometrical Theory of Diffraction

The geometrical theory of diffraction (GTD) does not have obvious application to antenna-ground problems. There are however, two areas where GTD may be beneficial: (1) ground-screen edge effects (diffraction) on input impedance and low-angle radiation; and (2) effects of large scale terrain variations, e.g., diffraction at a cliff. Application of GTD to both areas has been studied by Thiele [39]. His approach was to combine GTD with the moment method to find the effect of the edge-diffracted field on the current distribution of a monopole antenna located on a wedge. This leads to an integral equation modified from that for free space by inclusion of the diffracted fields, given in terms of the antenna current, in the total tangential electric field on the antenna. Thus, no additional unknowns are involved. The far field is treated in a similar manner. Results obtained to date are encouraging, although use of the technique to analyze a real ground screen awaits derivation of diffraction coefficients for a perfectly conducting half-plane lying on a lossy interface. Some progress has been made for the case of a half-plane lying on a lossless slab [40].

3.4.5 Backscreen Evaluation

It is fairly common practice to employ backscreens to improve HF antenna performance. Backscreens are typically constructed of arrays of parallel, vertical wires whose spacing and diameter are selected to maximize the antenna's front-to-back ratio or some other measure of its performance. The backscreen parameters so chosen have necessarily been based on design criteria derived from experimental measurement and some simplified analysis for a limited number of cases [41], and are thus unlikely to truly optimize the resulting antenna characteristics. Computer modeling offers some possibilities for improving this aspect of antenna design.

One approach that might be considered would be that of including the backscreen wires in the computer model. This could provide a very realistic representation of the overall antenna-backscreen system, but at a considerable increase in computer time, especially if extensive parametric studies were to be performed.

As an alternative, the parametric evaluation could be instead based on a two-dimensional integral equation, using infinite wires or strips for the backscreen and antenna members. The effects of spacing and size of the backscreen elements, backscreen width, antenna position, frequency, etc. could be much more efficiently studied, while many physical features important in the actual three-dimensional configuration could be retained. After identifying parameter values of greatest apparent interest, it might be then useful to perform limited calculations for the three-dimensional geometry to ensure the essential validity of the two-dimensional results. Another possible alternative which is worth mentioning is the application of image theory to the backscreen as well as to the interface. This is basically equivalent to a two-dimensional screen model, while it retains the three-dimensional aspects of the actual antenna.

3.4.6 Impedance Loading

In many cases of interest, the antenna may be connected to impedance loads of various kinds, or may even itself be lossy enough so that it cannot be accurately modeled as being perfectly conducting. These situations can be accommodated in the computer model by subtracting an appropriate voltage drop $z_{ij}^{(L)} I_j$ from the source term E_i, where $z_{ij}^{(L)}$ is the load impedance. When there are no mutual impedance effects, such as those due to transformer or transmission line interconnection, then $z_{ij}^{(L)} = \delta_{ij} z_{ij}^{(L)}$, i.e., the $\bar{\bar{z}}^{(L)}$ matrix becomes diagonal. Lumped loads are simply specified in terms of their resistive and reactive components. Their treatment is similar to that accorded sources, since the two can be viewed as mathematically equivalent. Distributed loads which might be used to model wire losses can be derived from the wire properties [42].

3.4.7 Sheathed Wires

Another problem of relevance, especially for antennas located in lossy media such as ground or sea water, is that of a wire coated by a dielectric layer. One possible approach might be to model the sheath in the same way as a lossy wire, by a suitably derived impedance load [42]. An alternative, more rigorous approach has been taken by

Richmond [43], who models the sheath with a radially directed polarization current, reasoning that the tangential field, being much smaller, is by comparison of negligible import. Since the radial sheath fields which determine this current are known in terms of the charge density on the wire, no additional unknowns are introduced. One simply obtains a modified integral equation which can be solved in the usual way.

3.4.8 Time Domain Analysis

Previous discussion has dealt exclusively with frequency-domain formulations. It is worthwhile to point out that many of these problems can also be attacked from a time-dependent or time-domain viewpoint [44-47]. As one outcome of such an effort, there can be derived time-dependent integral equations which correspond closely to their frequency-domain counterparts. The solution procedure, while also developed from the moment method, is significantly different in that a solution is obtained as an initial-value problem via time stepping. This leads to results which are valid for only a single incident field or source configuration but over a band of frequencies, in contrast with the more familiar frequency-domain approach of which the converse is true. Solutions may consequently be obtained more efficiently in the time domain than in the frequency domain for certain types of problems, especially for wire structures analyzed as antennas. The modeling of nonlinear loads is also well suited to a time-domain approach [48,49].

4. NUMERICAL RESULTS

In the context of practical applications, judgment on the relative merits of a particular computer model must ultimately depend upon the comparison of calculated results with independent data, preferably experimental, although other analytically or computationally derived results may suffice. Unfortunately, reliable experimental data is not always available so that in many instances we may have to resort to various "computer experiments" and physical intuition when attempting to validate a numerical procedure. In the discussion which follows, we present numerical results for a variety of problems, accompanied where possible by measured data, to demonstrate the general applicability of the computer modeling approach for wire antennas. The order of presentation will follow that of Section 3 above. Original sources for the results included are cited wherever possible. Any results for which citations are not given are unpublished works of the author and his colleagues.

4.1 INFINITE, HOMOGENEOUS, ISOTROPIC MEDIA

Problems which involve isolated antennas in infinite, homogeneous media are not frequently encountered, since, more often than not, environmental influences due to ground planes or the installation are important. Nevertheless, this kind of problem does provide a good, controlled check on the accuracy of computer calculations.

Various infinite-medium applications of wire integral-equation models are presented in Figs. 3-12. Two examples which incorporate transmission lines, one to compare with analytic results and the other to exhibit source-model differences for a dipole, are given in Figs. 3 and 4. Results for the resonance frequency of a zig-zag dipole are presented in Fig. 5, while a comparison of the input impedance of a Vee-loaded dipole as obtained from several independent computer models is included in Fig. 6. A test application of using a wire model for a lossy medium is demonstrated in Fig. 7, where a plasma-immersed dipole is modeled and compared with an analytic result. Two examples of modeling a circular loop antenna are included in Figs. 8 and 9, where the effects of capacitive loading and a near-field computation are demonstrated respectively. A more complicated curved-antenna structure is treated in Fig. 10, which depicts the current distribution on a conical spiral. The section concludes with two examples of modeling log-periodic (LP) antennas, that in Fig. 11 dealing with inductive loading to achieve reduced element size, while in Fig. 12 is presented a comparison of two models for the transmission line which connects the LP elements.

4.2 PERFECTLY CONDUCTING IMAGE PLANES

Applications involving image planes of various kinds are illustrated by Figs. 13-19. Two examples for LORAN antenna modeling are presented in Figs. 13 and 14. Various applications involving antennas used on U.S. Navy ships are demonstrated in Figs. 15-17. A different kind of use for modeling a perfect ground plane is shown in Fig. 18, where there are plotted the currents induced by a four element Yagi mounted on a ground plane. An application involving a dipole antenna located between two parallel infinite planes as presented in Fig. 19, concludes this section.

4.3 HALF-SPACE PROBLEMS

This section deals with several kinds of wire-antenna problems which involve lossy half-spaces, as presented in Figs. 20-30. In Fig. 20 is shown the impedance of vertical and horizontal dipoles as a function of height over a ground-air interface, as obtained using Sommerfeld theory, the reflection-coefficient approximation, and (in Fig. 20a),

the compensation theorem. The upper half-space gain of a horizontal dipole as it is moved to within 10^{-7} wavelengths of grounds of various conductivities is presented in Fig. 21. Results for the impedance of horizontal dipoles as a function of distance from either side of a free space and a dielectric half-space are given in Fig. 22. In Figs. 23 and 24 are shown results for a sectionalized LORAN transmitting antenna and a fan doublet, respectively. Other ground applications are illustrated in Figs. 25-27, for Beverage, vertical half Rhombic and sloping-vee antennas. A problem involving interaction across the air-ground interface is demonstrated for a ground-stake application in Fig. 28. Concluding examples of simple ground-screen models are presented in Figs. 29 and 30.

4.4 SPECIAL TOPICS

Examples of wire-grid applications are demonstrated in Figs. 31-33, for a simple cage dipole, a moderately complex wire-grid helicopter, and an elaborate wire-grid ship, respectively. In Figs. 34 and 35 are illustrated applications involving fairly dense ground screens modeled using the refection-coefecient and surface-impedance approximations. An example of a hybrid GTD-MOM application is illustrated in Fig. 36, while a backscreen computation performed to establish wire-grid modeling guidelines is given in Fig. 37. A computation for a sheathed dipole is presented in Fig. 38. Several time-domain applications are illustrated in Figs. 39-42, the first two dealing with a conical spiral antenna and wire-grid truck, and the latter two treating nonlinear loading of dipoles.

REFERENCES

1. A. J. Poggio and E. K. Miller, "Integral Equation Solutions of Three-Dimensional Scattering Problems," in Computer Techniques for Electromagnetics, R. Mittra, Ed., Pergamon Press, New York, 1973.
2. K. K. Mei, "On the Integral Equation of Thin Wire Antennas," IEEE Trans. Antennas Propagat., AP-13, 1965, p. 374.
3. R. F. Harrington, Field Computation by Moment Methods, MacMillan, New York, 1968.
4. J. H. Richmond, "Digital Computer Solutions of the Rigorous Equations for Scattering Problems," Proc. IEEE 53, 1965, p. 796.
5. E. K. Miller and F. J. Deadrick, "Some Computational Aspects of Thin-Wire Modeling," Chapter 4 in Numerical and Asymptotic Techniques in Electromagnetics. R. Mittra, Ed., Springer-Verlag, New York, 1975.
6. C. M. Butler, "Currents Induced on a Pair of Skewed Crossed Wires," IEEE Trans. Antennas Propagat., AP-20, 1972, p. 731.
7. H. H. Chao and B. J. Strait, "Radiation and Scattering by Configurations of Bent Wires with Junctions," IEEE Trans. Antennas Propagat., AP-19, No. 5, 1971, pp. 701-702.
8. J. H. Richmond, Computer Analysis of Three-Dimensional Wire Antennas, Ohio State U., Electroscience Lab, Tech. Rept. 2708-4, 1969.
9. J. H. Richmond, "A Wire-Grid Model for Scattering by Conducting Bodies," IEEE Trans. Antennas Propagat., AP-14, 1966, p. 782.
10. A. J. Poggio, R. M. Bevensee and E. K. Miller, "Evaluation of Some Thin-Wire Computer Programs," IEEE/AP-S Symposium, Atlantic, GA, Symposium Digest, 1974, pp. 181-184.
11. Y. S. Yeh and K. K. Mei, "Theory of Conical Equiangular Spiral Antennas: Part I--Numerical Techniques," IEEE Trans. Antennas Propagat., AP-15, 1967, p. 634.
12. T. T. Wu and R. W. P. King, "The Tapered Antenna and Its Application to the Junction Problem for Thin Wires," IEEE Trans. Antennas Propagat., AP-24, 1976, p. 47.
13. S. Gee, E. K. Miller, A. J. Poggio, E. S. Selden, and G. J. Burke, "Computer Techniques for Electromagnetic Scattering and Radiation Analyses," invited paper presented at The Electromagnetic Compatibility Meeting, Philadelphia, PA, 1971.
14. G. J. Burke, NEC - Numerical Electromagnetics Code for Frequency Domain Analysis, Tech. Report UCRL-80942, Lawrence Livermore Laboratory, 1978. See also G. J. Burke, A. J. Poggio, J. C. Logan, and J. W. Rockway, "NEC - Numerical Electromagnetic Code for Antennas and Scattering," IEEE APS Symposium Digest, 1974, pp. 147-150.
15. A. J. Poggio, R. W. Adams, and E. K. Miller, A Study of Antenna Source Models, Tech. Report UCRL-51693, Lawrence Livermore Laboratory, 1974.
16. G. A. Thiele, "Wire Antennas," in Computer Techniques for Electromagnetics, R. Mittra, Ed., Pergamon Press, New York, 1973.
17. R. Mittra and C. A. Klein, "Stability and Convergence of Moment Method Solutions," Chapter 5 in Numerical and Asymptotic Techniques in Electromagnetics, R. Mittra, Ed., Springer-Verlag, New York, 1975.
18. E. K. Miller and G. J. Burke, "Numerical Integration Methods," IEEE Trans. Antennas Propagat., AP-17, 1969, p. 669.
19. K. K. Chan, L. B. Felsen, S. T. Ping, and J. Schmoys, "Diffraction of the Pulsed Field from an Arbitrarily Oriented Electric or Magnetic Dipole by a Wedge," AFWL Sensor and Simulation Note 202, 1973.
20. C. D. Taylor, "Thin Wire Receiving Antenna in a Parallel Plate Waveguide," IEEE Trans. Antennas Propagat., AP-15, 1967, p. 572.
21. A. Sommerfeld, "Uber der Ausbreitung der Willen in der Drahtlosen Telegraphic," Ann. Physik 28, 1909, p. 663.

22. A. Sommerfeld, Partial Differential Equations in Physics, Academic Press, New York, 1964.

23. J. N. Brittingham, E. K. Miller, and J. T. Okada, "A Bivariate Interpolation Approach for Efficiently and Accurately Modeling Antennas Near a Halfspace," Electron. Lett. 13, 1977, pp. 690-691.

24. G. J. Burke, E. K. Miller, J. N. Brittingham, D. L. Lager, R. J. Lytle, and J. T. Okada, "Computer Modeling of Antennas Near the Ground," Electromagnetics 1, 1981, pp. 29-49.

25. E. K. Miller, A. J. Poggio, G. J. Burke, and E. S. Selden, "Analysis of Wire Antennas in the Presence of a Conducting Half Space: Part I. The Vertical Antenna in Free Space," Can. J. Phys. 50, 1972, p. 879.

26. E. K. Miller, A. J. Poggio, G. J. Burke, and E. S. Selden, "Analysis of Wire Antennas in the Presence of a Conducting Half Space: Part II. The Horizontal Antenna in Free Space," Can. J. Phys. 50, 1972, p. 2614.

27. A. Baños, Dipole Radiation in the Presence of a Conducting Half-Space, Pergamon Press, New York, 1966.

28. R. J. King, "Electromagnetic Wave Propagation over a Constant Impedance Plane," Radio Sci. 4, 1969, p. 225.

29. G. D. Monteath, "Application of the Compensation Theorem to Certain Radiation and Propagation Problems," Proc. IEE 98 Part IV, 1951, p. 23.

30. R. Mittra, Vector Form of Compensation Theorem and Its Application to Boundary Value Problems, Department of Electronics Engineering, University of Colorado, Boulder, Scientific Rept. 2, AFCRL 575, 1961.

31. R. J. King, "On the Surface Impedance Concept," Proc. Conf. Environmental Effects on Antenna Performance, Boulder, Colorado, J. R. Wait, Ed., 1969.

32. R. L. Tanner and M. G. Andreasen, "Numerical Solution of Electromagnetic Problems," IEEE Spectrum 4, No. 9, 1967, p. 53.

33. K. S. H. Lee, L. Marin, and J. P. Castillo, "Limitations of Wire-Grid Modeling of a Closed Surface," IEEE Trans. On EMC, EMC-18, 3, 1976, p.123.

34. J. R. Wait, "Characteristics of Antennas over Lossy Earth," in Antenna Theory, R. E. Collin and F. J. Zucker, Eds., McGraw-Hill, New York, 1969, pp. 386-437.

35. E. K. Miller and F. J. Deadrick, Computer Evaluation of LORAN-C Antennas, Lawrence Livermore Laboratory, Rept. UCRL-51464, 1973.

36. M. I. Astrakhan, "Reflecting and Screening Properties of Plane Wire Grids," Radio Engineering 23 (1), (translated from the Russian), 1968, p. 76.

37. J. R. Wait, "Theories of Scattering from Wire Grid and Mesh Structures," Electromagnetic Scattering, Academic Press, New York, 1978, p. 253.

38. J. R. Wait, Electromagnetic Waves in Stratified Media, Pergamon Press, MacMillan Co., New York, 1962.

39. G. A. Thiele and T. H. Newhouse, "A Hybrid Technique for Combining Moment Methods with the Geometrical Theory of Diffraction," IEEE Trans. Antennas Propagat., AP-23, 1975, pp. 62-69.

40. R. D. Coblin and L. W. Pearson, "Diffraction by a Perfectly Conducting Half-Plane Residing on a Dielectric Slab," USNC/URSI National Radio Science Meeting Digest, 1983, p. 51.

41. E. B. Moullin, Radio Aerials, Oxford University Press, New York, Ch. 5 and 11, 1949.

42. E. S. Cassidy and J. Fainberg, "Backscattering Cross Sections of Cylindrical Wires of Finite Conductivity," IRE Trans. Antennas Propagat. AP-8, 1960, p. 1.

43. J. H. Richmond, Radiation and Scattering by Thin-Wire Structures in the Complex Frequency Domain, Ohio State University, Department of Electronics Engineering, Electro Science Laboratory, Rept. 2902-10, 1973.

44. C. L. Bennett and W. L. Weeks, "Transient Scattering from Conducting Cylinders," IEEE Trans. Antennas Propagat., AP-18, No. 5, 1970, pp. 627-633.

45. E. P. Sayre and R. F. Harrington, "Time-Domain Radiation and Scattering by Thin Wires," Appl. Sci. Res. 26 (6), 1972, pp. 413-444.

46. E. K. Miller, A. J. Poggio, and G. J. Burke, "An Integro-Differential Equation Technique for the Time Domain Analysis of Thin Wire Structures, Part I. The Numerical Method," J. Computational Phys. 12, 1973, p. 24.

47. A. J. Poggio, E. K. Miller, and G. J. Burke, "An Integro-Differential Equation Technique for the Time-Domain Analysis of Thin Wire Structures. II: Numerical Results," J. Computational Phys. 12, 1973, p. 210.

48. J. A. Landt, E. K. Miller and F. J. Deadrick, "Time-Domain Modeling of Non-Linear Loads," IEEE Trans. Antennas Propagat., AP-31, 1983, pp. 121-126.

49. E. K. Miller and J. A. Landt, "Direct Time-Domain Techniques for Transient Radiation and Scattering from Wires," Proc. IEEE 68, No. 11, 1981, pp. 1396-1423.

50. E. K. Miller, G. M. Pjerrou, and E. S. Selden, "On the Versatility of Thin-Wire Electric Field Integral Equation Techniques," IEEE/G-AP Symposium, Austin, Texas, Symposium Digest, 1969, pp. 17-24.

51. S. Gee, E. K. Miller, and E. S. Selden, Computer Analysis of Loaded Loop and Conical Spiral Antennas, MBAssociates, San Ramon, California, Tech. Rept. MB-R-70/38, 1970.

52. R. L. Fante, J. J. Otazo, and J. T. Mayhan, "The Near Field of the Loop Antenna," Radio Sci. 4, 1969, p. 697.

53. E. K. Miller, R. M. Bevensee, A. J. Poggio, R. Adams, F. J. Deadrick, and J. A. Landt, An Evaluation of Computer Programs Using Integral Equations for the Electromagnetic Analysis of Thin Wire Structures, Lawrence Livermore Laboratory, Rept. UCRL-75566, 1974. See also Air Force Weapons Lab Interaction Note 177.

54. K. G. Balmain, "Dipole Admittance for Magnetoplasma Diagnostics," IEEE Trans. Ant. Prop. AP-17, 1969, pp. 389-392.

55. G. J. Burke and A. J. Poggio, <u>Computer Analysis of the Twin-Whip Antenna</u>, Lawrence Livermore Laboratory, Rept. UCRL-52080, 1976.
56. G. J. Burke and A. J. Poggio, <u>Computer Analysis of the Bottom-Fed Fan Antenna</u>, Lawrence Livermore Laboratory, Rept. UCRL-52109, 1976.
57. F. J. Deadrick, G. J. Burke, and A. J. Poggio, <u>Computer Analysis of the Trussed-Whip and Discone-Cage Antennas</u>, Lawrence Livermore Laboratory, Rept. UCRL-52201, 1977.
58. J. L. Willows and R. J. Lytle, <u>Design of Yagi Antennas for a Doppler Radar System that Measures Ocean System Currents</u>, Lawrence Livermore Laboratory, Rept. UCID-17024, 1976.
59. F. M. Tesche, <u>On the Behavior of Thin-Wire Scatterers and Antennas Arbitrarily Located Within a Parallel Plate Region. I. The Formulation</u>, EMP Sensor and Simulation Notes, Note 135, AFWL, Kirtland AFB, N.M., 1971.
60. G. J. Burke, W. A. Johnson, and E. K. Miller, "Modeling of Simple Antennas Near to and Penetrating an Interface," <u>Proc. IEEE 71</u>, 1983, pp. 174-175.
61. J. A. Landt, F. J. Deadrick, E. K. Miller, and R. Kirchofer, <u>Computer Analysis of the Fan Doublet Antenna</u>, Lawrence Livermore Laboratory, Rept. UCRL-74846 Preprint, 1973.
62. E. K. Miller, F. J. Deadrick, and W. O. Henry, "Computer Evaluation of Large, Low-Frequency Antennas," <u>IEEE Trans. Antennas Propagat.</u>, <u>AP-21</u>, 1973 , p. 386.
63. J. N. Brittingham, E. K. Miller, and J. T. Okada, <u>SOMINT: An Improved Model for Studying Conducting Objects Near Lossy Half-Spaces</u>, Lawrence Livermore Laboratory, Rept. UCRL-52423, 1978.
64. E. K. Miller, J. N. Brittingham, and J. T. Okada, "Explicit Modelling of Antennas with Sparse-Ground Screens," <u>Electron. Lett.</u> <u>14</u>, 1978, pp. 627-629.
65. E. S. Selden and G. J. Burke, <u>DLGN-38 Final Report</u>, MBAssociates, San Ramon, California, Tech. Rept. MB-R-75/16, 1975.
66. R. M. Bevensee, <u>Design Considerations for Parasitic Screen Antennas</u>, Lawrence Livermore Laboratory, Rept. UCID-16657, 1975.
67. J. A. Landt and E. K. Miller, <u>Transient Characteristics of the Conical Spiral</u>, Lawrence Livermore Laboratory, Rept. UCID-16461, 1974.

ACKNOWLEDGMENTS

Fig. 2. Three-dimensional aspect plot of a modified Sommerfeld-integral (I_P^H as defined in Ref. [24]). The real part of the electric field is shown on the vertical axis as a function of distance (R_1) and angle (θ) for (a) $\varepsilon_1/\varepsilon_0 = 4$ and $\sigma_1 = 0.001$ S/m and (b) $\varepsilon_1/\varepsilon_0 = 16$ and $\sigma_1 = 0$.

Fig. 1. Convergence rate for several numerical methods [10]. Quantity on the ordinate in (a) is the normalized RMS current and in (b) the RMS error in current for the number of unknowns on the abscissa, relative to a reference RMS current obtained for $N = N_R \geq 250$. Results are for a straight wire of length $L \simeq 12 \lambda$ long illuminated from broadside by a planewave. Numerical models employed are as described in the references listed.

Fig. 3. Comparison of a wire integral-equation solution for the current on a two-wire transmission line with the analytic result [50]. The line impedance is 600 ohms and the terminations are short and open circuits and matched loads. Comparable results are obtained with other load impedances. These results provide one of the few analytic checks on the thin-wire model.
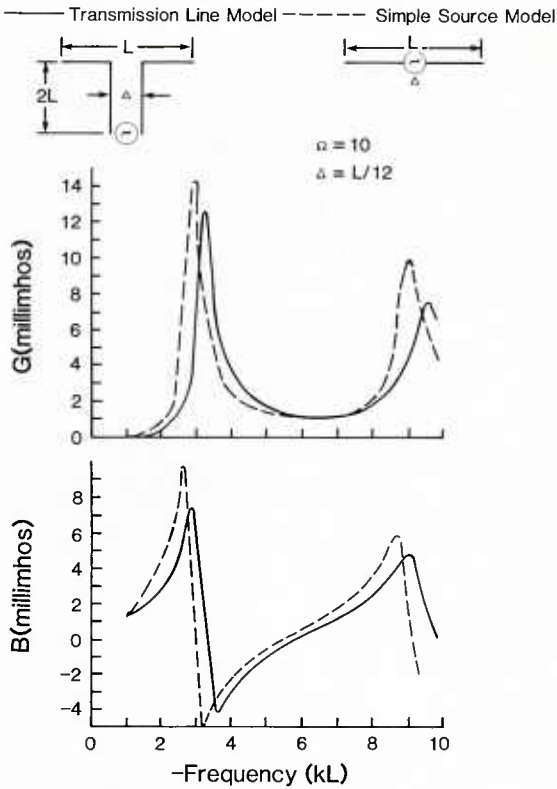
Fig. 4. Comparison of the input impedance for a dipole antenna obtained using a tangential electric-field source with that which results from connecting the antenna to a two-wire transmission line. The downward frequency shift exhibited by the transmission line results is evidently due to the capacitive loading effect of the antenna-transmission line junction.
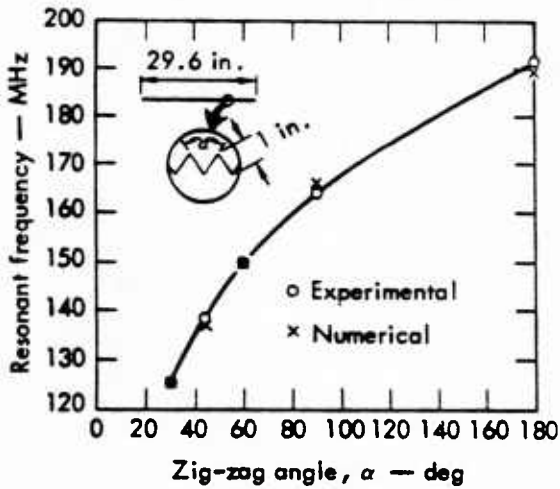
Fig. 5. Resonance frequency of a zig-zag dipole [51]. This application tests the capability of the model to accurately handle a slow-wave structure which achieves the effect of loading through structure shaping.
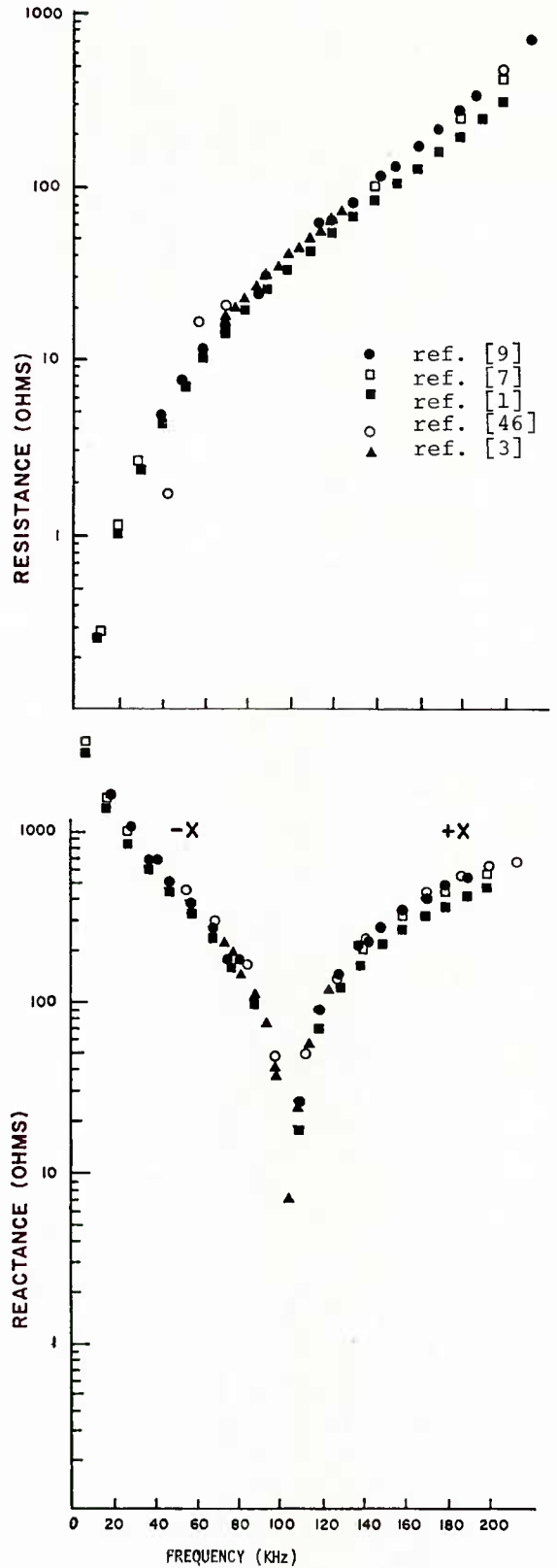
Fig. 6. Comparison of input-impedance results for a center-fed dipole having vee-shaped ends as obtained from several different computer codes, all of which employed uniformly segmented models [53]. These results demonstrate that when appropriate models are used, various treatments can produce comparable results. Some approaches can be more sensitive to model details than others, for example in requiring equal segment lengths at junctions and sources.
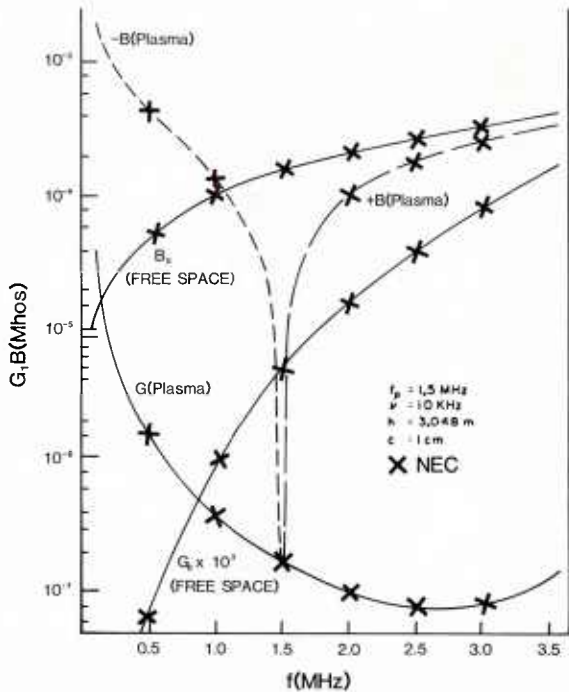
Fig. 7. Input impedance of a dipole antenna in a lossy infinite plasma. Results from the integral-equation model are in good agreement with analytical values [54], validating the numerical model's applicability to lossy media. This capability is needed for the general interface problem where part or all of an antenna may be buried in a lossy ground.
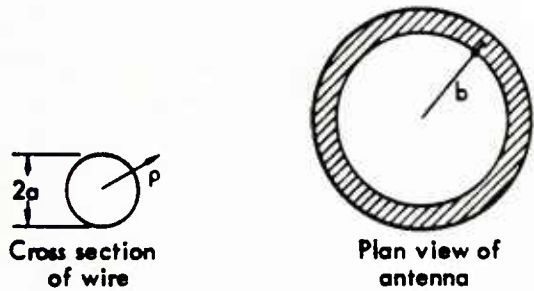
$$a/b = 3.5 \times 10^{-2}$$
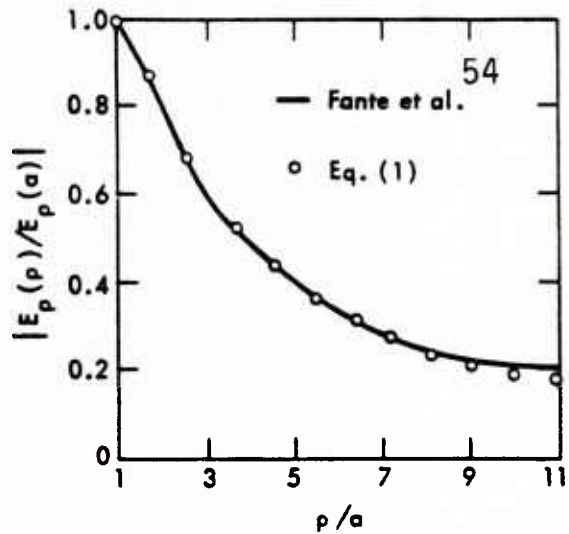
Fig. 9. The near field of a circular loop antenna [51]. Results obtained from the integral-equation model are found to agree with analytically obtained values [52].
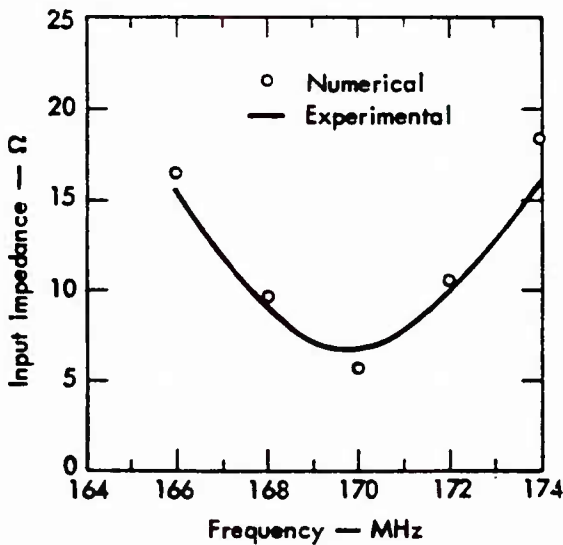
Fig. 8. Input impedance of a capacitively loaded circular loop antenna [51]. The loop is modeled as a 16-sided polygon with each segment loaded with a capacitor. This result demonstrates the capability of the numerical model to treat a distributed reactive load.
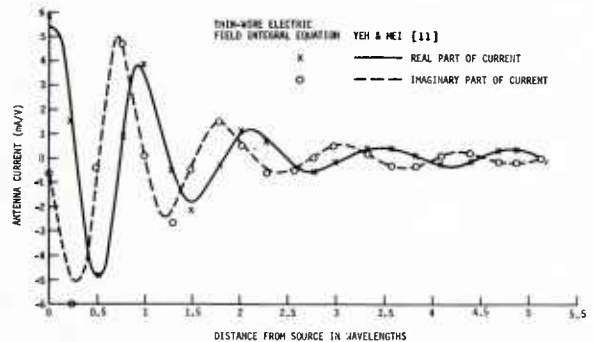
Fig. 10. Comparison of the current distribution on a conical spiral antenna as obtained using an electric-field and Hallen-type integral equations [50]. Even though the two results are in excellent agreement, the analytical difficulty of generalizing the Hallen approach for arbitrary wire geometries has restricted its application.
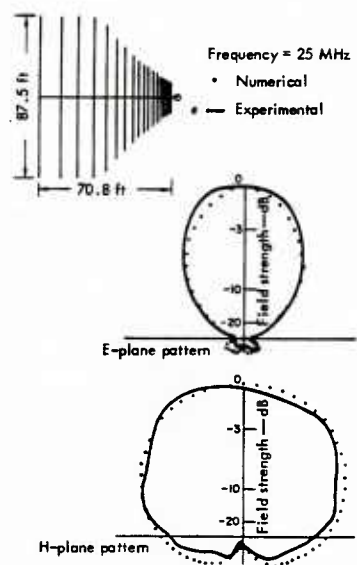
Fig. 11. Radiation pattern of a fore-shortened 19-element log-periodic antenna. The antenna size is decreased by inserting inductive loads on each of the four longest elements to reduce their resonance frequencies to those that would occur if the unloaded elements were used.
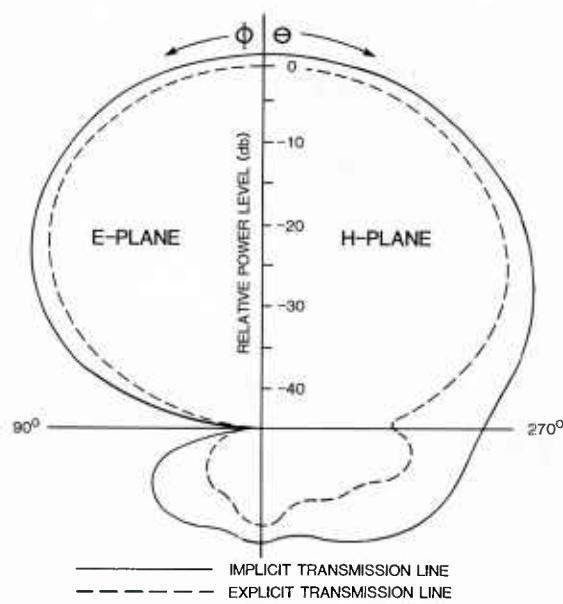
Fig. 12. Radiation patterns for 13-element LP antenna when modeled using implicit and explicit transmission-line connection of the antenna elements. In the implicit model, the transmission line is represented using the analytic equations for a two-wire line, appropriately related to the antenna feedpoint currents and driving voltages. The explicit model on the other hand, includes the actual transmission-line wires in the computation. The patterns shown are for unit-voltage excitation and the differences exhibited are due to different input impedances and radiation from the transmission-line wires. Input admittances are for (a) 7.9 - i1.7 mmhos, and (b) 7.0 - i0.9 mmhos, respectively.
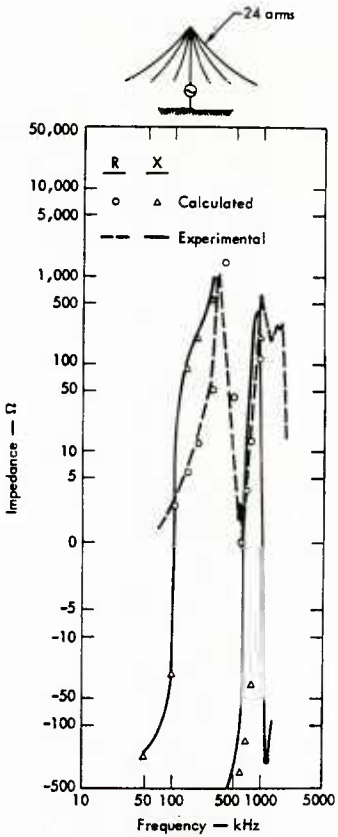
Fig. 13. Input impedance of a top-loaded monopole antenna [35]. The measurements are for an actual LORAN antenna located over real ground with a 120-wire radial ground screen, and the computations are for a perfect ground. The good agreement which is exhibited indicates that the ground screen is conductive enough to well approximate a perfect ground.
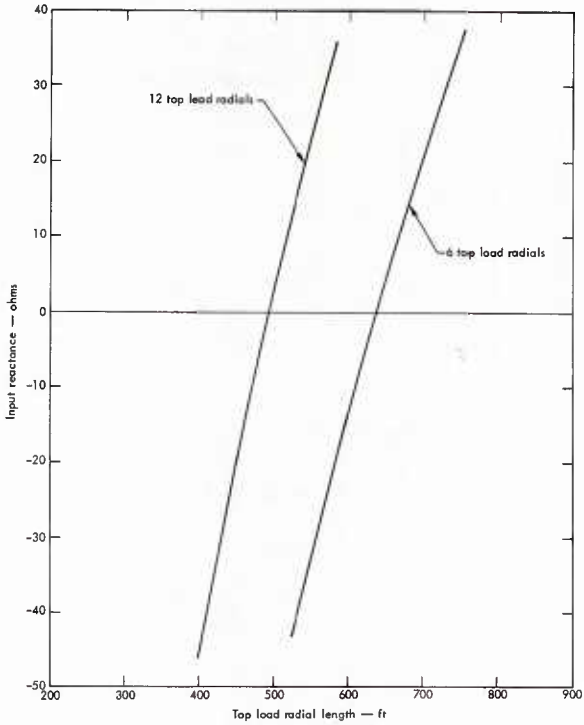
Fig. 14. Application of computer modeling to obtain a specified performance for a top-loaded monopole [62]. It was desired to find the top-load lengths using either 6 or 12 evenly spaced top-load wires that would give a -20 ohm reactance at 100 KHz.
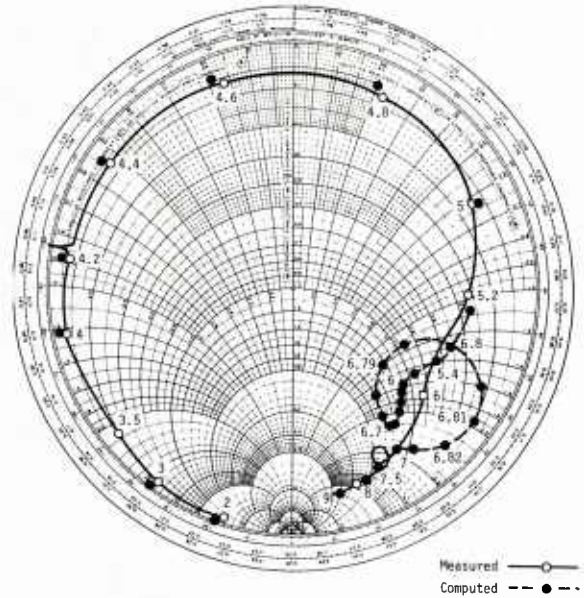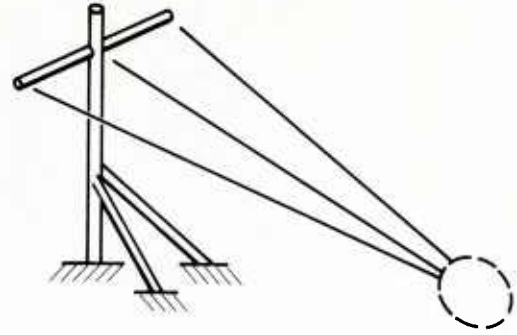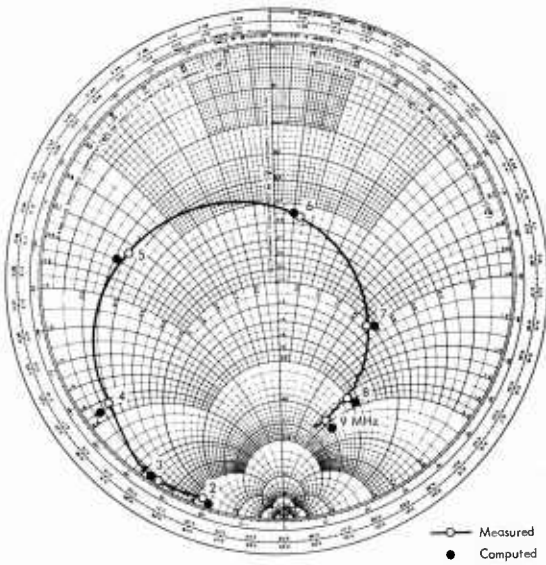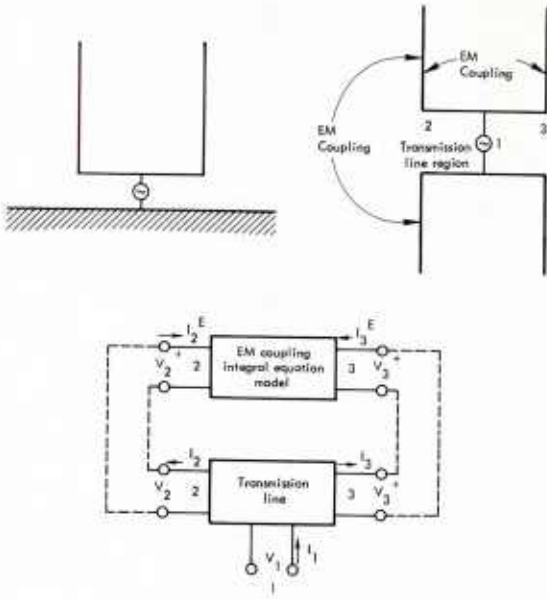
Fig. 16.   Input impedance of a bottom-fed fan antenna [56].

Fig. 15.   Input impedance of a twin-whip antenna [55] as measured and computed.   Each of the computer models used for these calculations (and for Figs. 16 and 17) was based on comparisons of the results it produced with measured data.   It is important to note that experimental results may be needed in order to select the most appropriate numerical model.
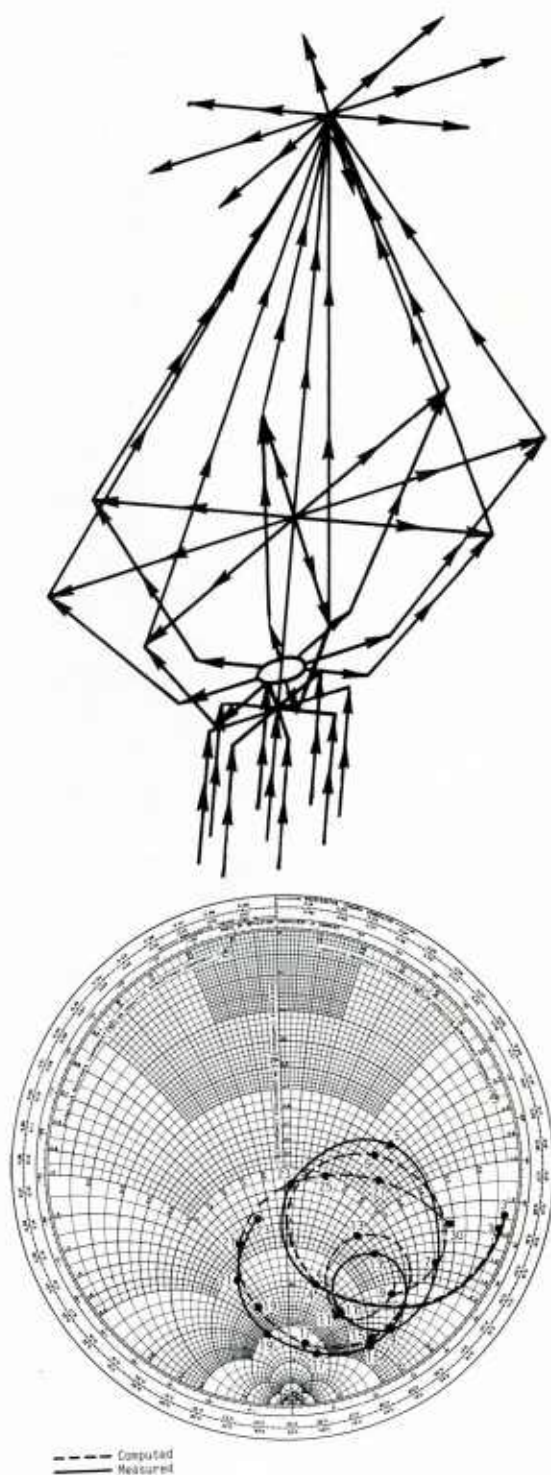
Fig. 17. Input impedance of a discone-cage antenna [57].
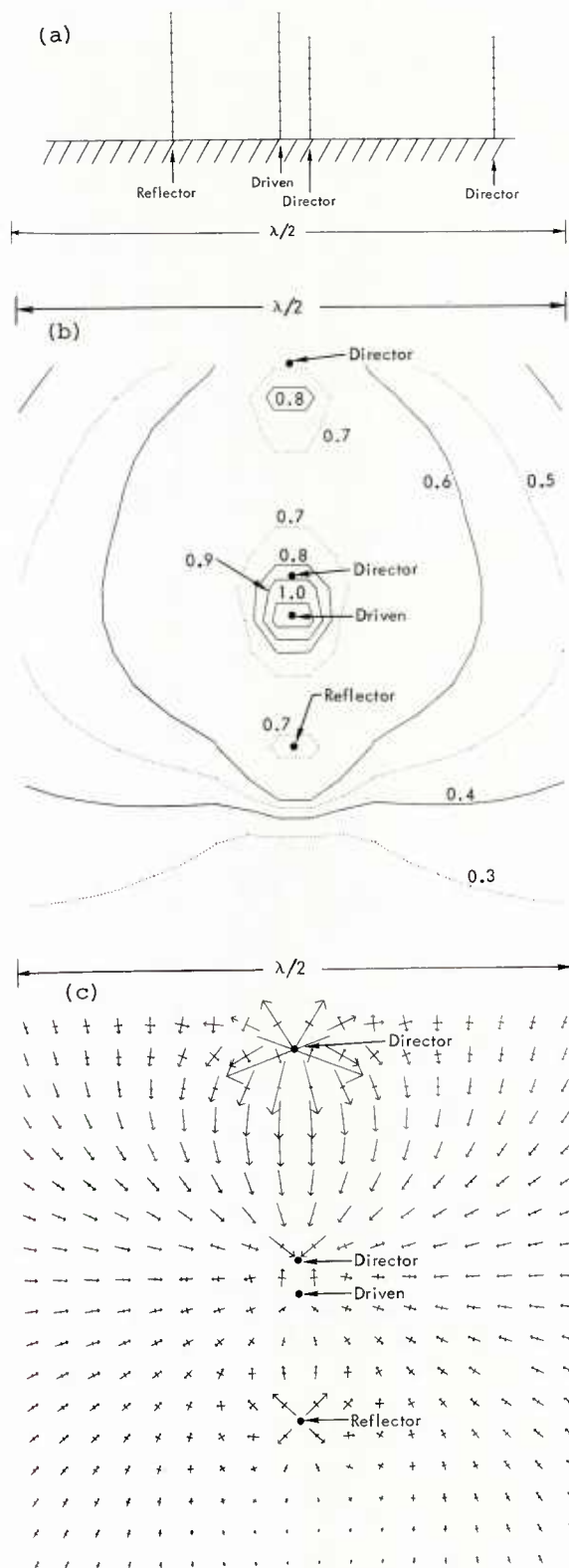
Fig. 18. Perfect ground-plane currents of Yagi antenna in (a) as a contour plot (b) and vector plot (c) [58]. The semi-major and semi-minor axes of the current vector are shown in (c), multiplied by distance from the driven element to reduce the effect of geometric attenuation. Plots like these can be useful in evaluating antenna near fields and assessing ground-screen requirements.
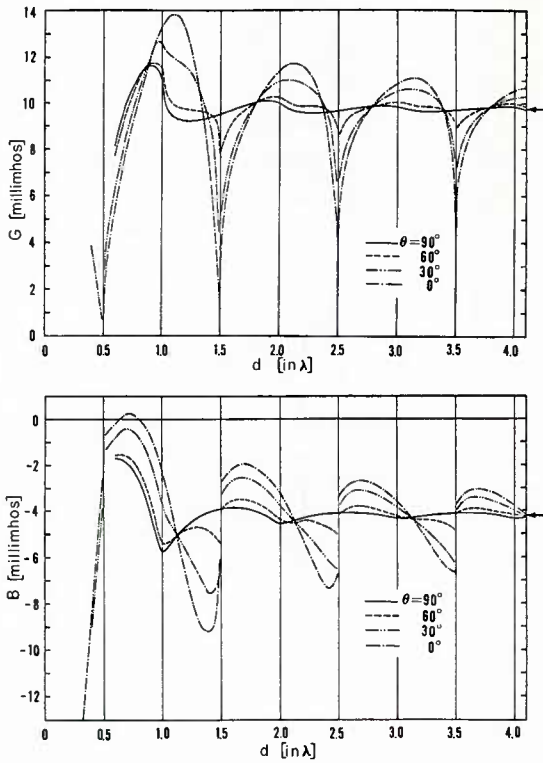
Fig. 19. Input impedance of a half-wave dipole located midway between two infinite conducting planes a distance d apart [59]. The arrows denote free-space values. This calculation involves use of a series Green's function to account for the periodic sequence of images caused by the reflecting planes.
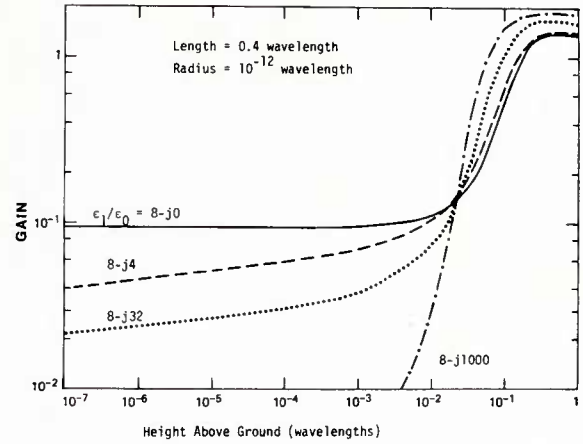
Fig. 21. Average gain (2x power radiated in upper half-space/input power) of 0.4 wavelength (5-segment) horizontal dipole as it is lowered to within 10^{-7} wavelengths of the interface for various ground parameters [60]. The gain is almost 2 for the most conductive ground, but in all cases falls off below a height of about 0.1 wavelengths due to the near-field interaction.
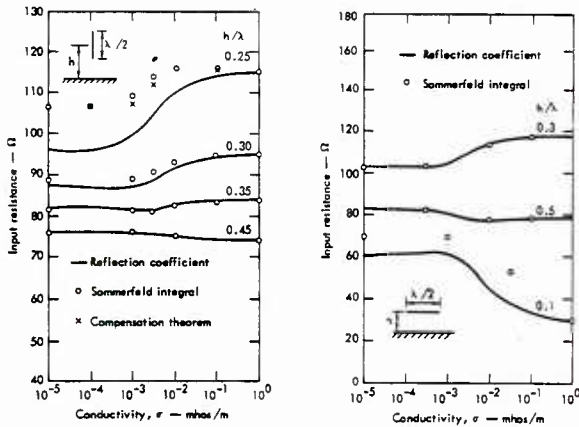
Fig. 20. Results for the input resistance of a center-fed half wave dipole over a lossy ground. Part (a) [25] is for the vertical orientation and part (b) [26] the horizontal, with f = 3.0 MHz, ε_r = 10 and a/λ = 5 x 10^{-4}. Reflection-coefficient (or modified image theory) and Sommerfeld-integral results are shown for both cases, with compensation-theorem results also included for the vertical case.
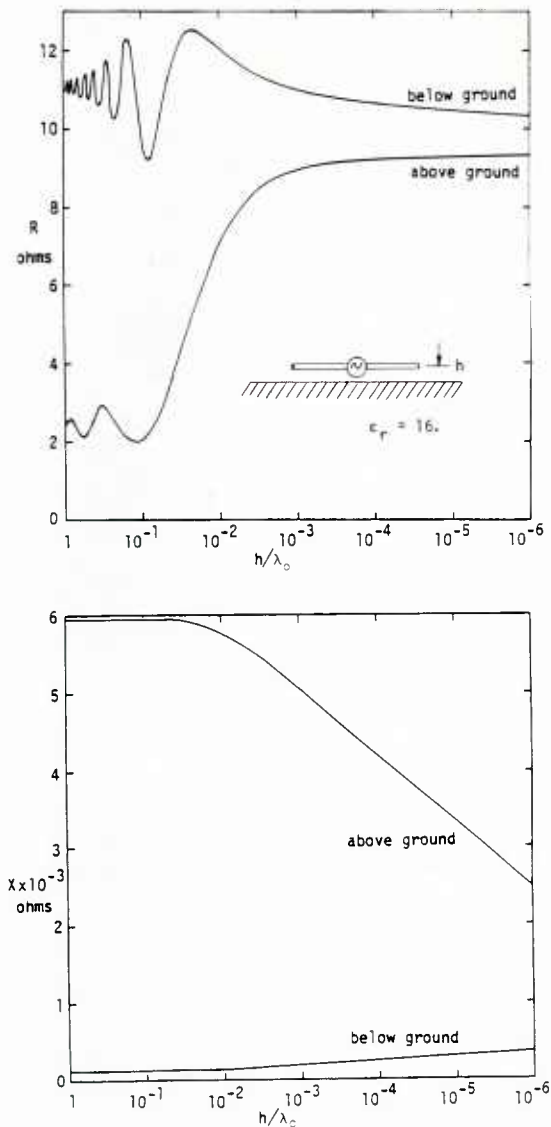
Fig. 22. Input impedance of a horizontal wire near the interface between free space and a dielectric half-space with $\varepsilon_r = 16$ [24]. Wire length is $0.1 \lambda_o$ (modeled using 5 segments), radius $10^{-8} \lambda_o$ and h is distance above or below the interface. If extrapolated, the reactance curves meet where h is approximately the wire radius. A smooth transition between resistance above and below the interface apparently depends on effects over a distance of the wire radius and cannot be modeled with the thin-wire approximation.
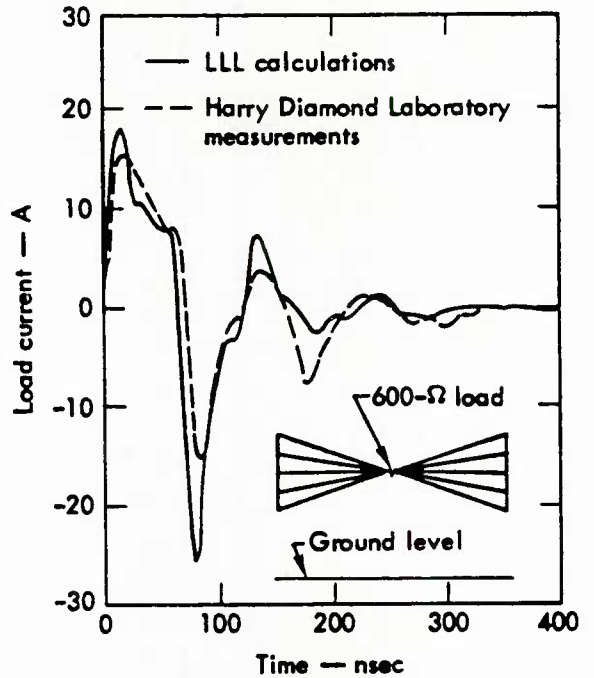
Fig. 23. EMP simulated response of the fan doublet antenna [61]. The calculation is based on a frequency-domain model for the antenna in free space, with the ground effect included only through the exciting field used in the model. The exciting field was measured at ground level in the time domain and image theory was used to estimate the actual field incident on the antenna.

(a)

690 ft

1420 ft   1420 ft

Transmitter house

(b)

Fig. 25. Current distribution on a
Beverage antenna at 0.54 and 1.6 MHz
(a) and elevation-plane radiation
pattern for f = 0.54 MHz (b) [24]. As
expected, the higher frequency increases
the current attenuation. The current
behavior at the connection points of
the antenna to the ground is approxi-
mated by setting its derivative to zero.

(c)

Fig. 24. (a) Sectionalized LORAN
Transmitter antenna geometry. (b)
Computer model. (c) Experimental and
numerical comparison of SLT antenna
impedance [62]. These computed results
use the reflection-coefficient approxi-
mation together with a surface-impedance
approximation for the ground screen,
the validity of which is indicated by
the good agreement they exhibit with
the experimental data. The frequency
shift seen in the reactance is probably
due to the source model.

Fig. 26. Vertical half-rhombic antenna (a) exhibits current distributions (b) and elevation patterns in antenna plane (c) with midpoint height (H_V) a parameter [63]. The effect of a ground stake was approximated by setting the current slope equal to zero at the ground-connection point. Increased interaction between the antenna and ground is exhibited by greater attenuation of the current.
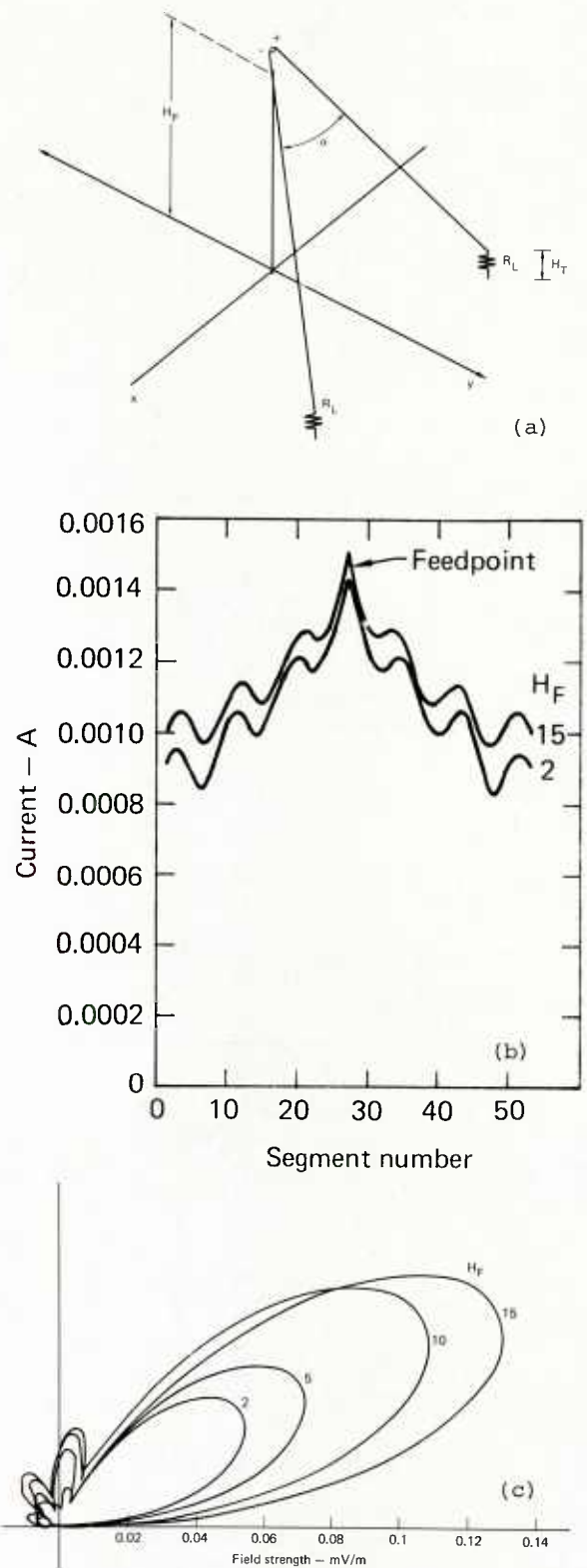
Fig. 27. Sloping-vee antenna (a) has current distribution (b) and elevation patterns in bisecting plane (c) with center height (H_F) a parameter [63]. Ground stake treatment is same as for Fig. 26. Current attenuation increases as the antenna is lowered in a fashion similar to the behavior of the vertical half-rhombic.
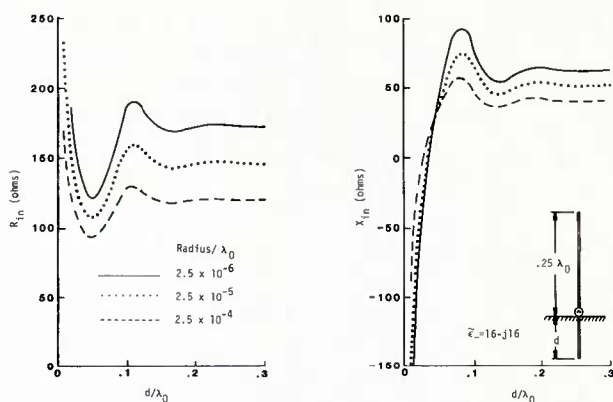
Fig. 28. Variation of the input impedance of a wire monopole as a function of ground-stake length [60]. This computation requires both the fields reflected from and transmitted through the air-ground interface.
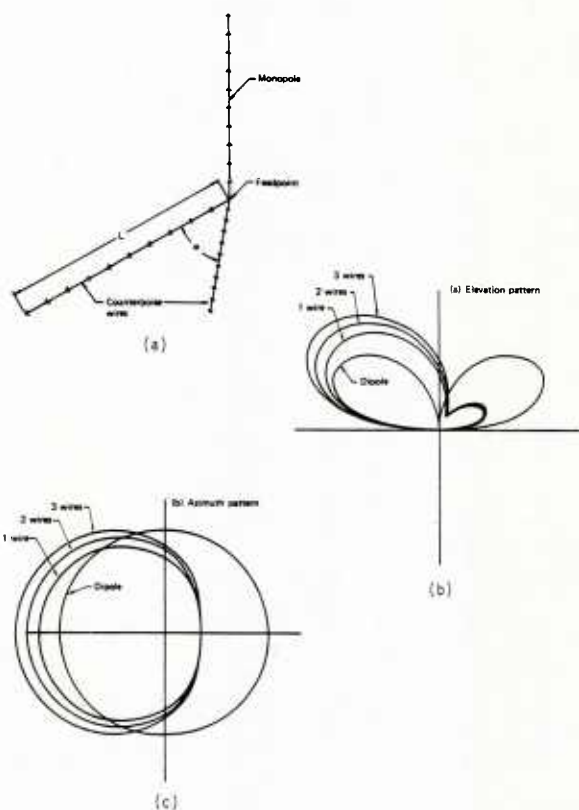
Fig. 29. (a) A computer plot of a representative monopole-screen geometry. (b) Elevation (θ) and (c) azimuth (∅ with θ = 45°) plane patterns for 1-3 screen wires with a dipole included for comparison [64]. The total included angle of the screen wires is 30°, their length is 3.0 m as is the monopole height and height above ground is 0.3 m. Results shown are for constant input power.
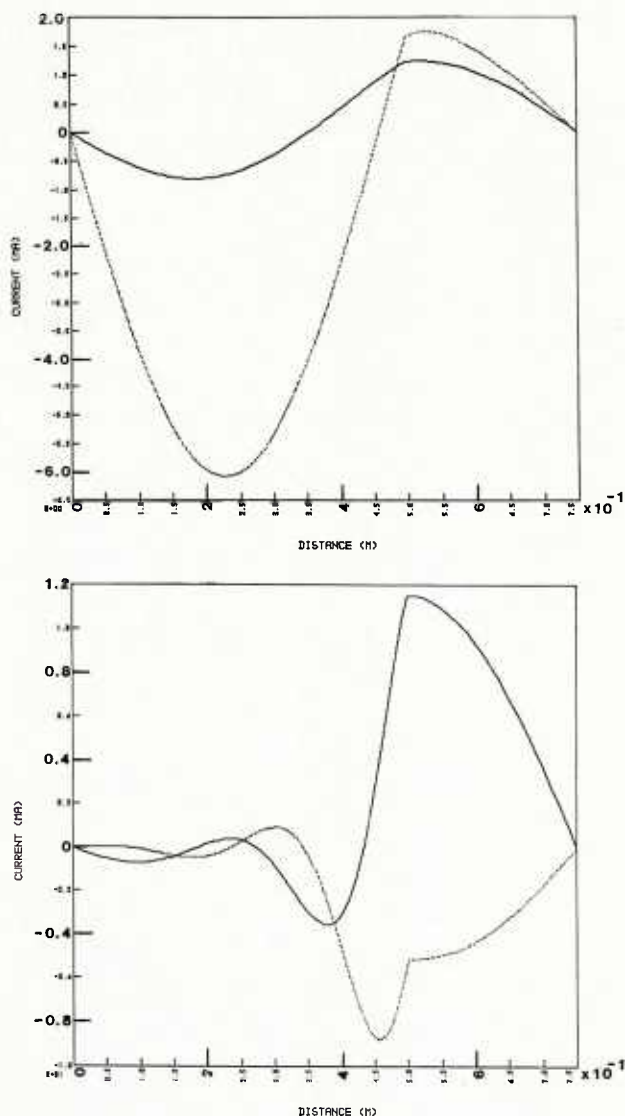
Fig. 30. Current distribution on a quarter-wave monopole driven against a ground screen consisting of six evenly spaced half-wave wires when (a) 10^{-6} λ_0 above ground, and (b) 10^{-6} λ_0 below ground [24]. A significant decrease in the wavelength of the screen-wire current can be observed for the buried case, compared with the above-ground result. There is also an accompanying increase in the radiation efficiency, changing from ∿11% to ∿18% as the screen is moved from 10^{-3} λ_0 above to 10^{-3} λ_0 beneath the interface.
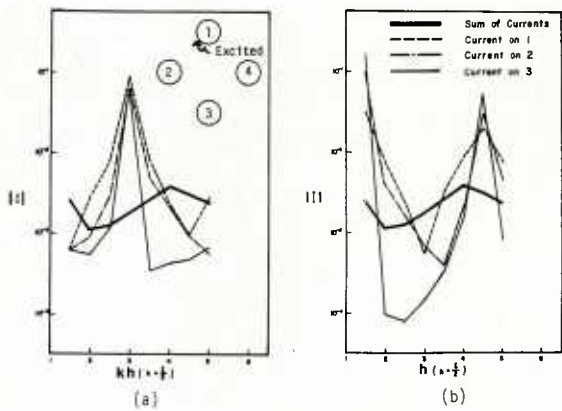
Fig. 31. Current on 4-wire dipole used to model a single thick wire for fatness parameter $\Omega = 6$: (a) wire connected at ends, (b) wires open at ends. These results highlight the possibility for transmission-line mode currents to be produced on grid-like objects, especially when the excitation is asymmetric.

Fig. 33a. A calculational model of a large vessel consisting of 829 wire segments that approximate the electrical current paths on the ship [65].
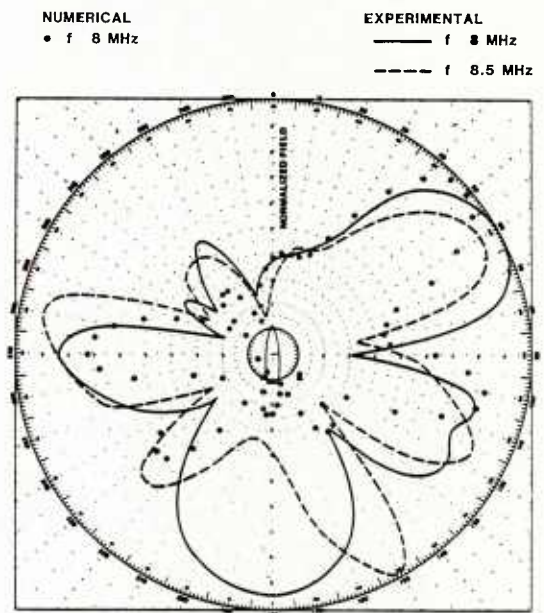
Fig. 33b. Azimuthal pattern for the twin-whip antenna on the 829 segment grid model of Fig. 33a at 8 MHz compared with experiment. The sensitivity of the measured results to varying the frequency emphasizes the need to avoid comparisons at a single value of a parameter such as frequency, angle or position.

Fig. 32 Wire-grid helicopter model computations [1]. Model depicted in (a) yields patterns compared with measured data in (b). These results are reasonably good, but can deteriorate with increasing frequency as the grid openings become larger in wavelengths.
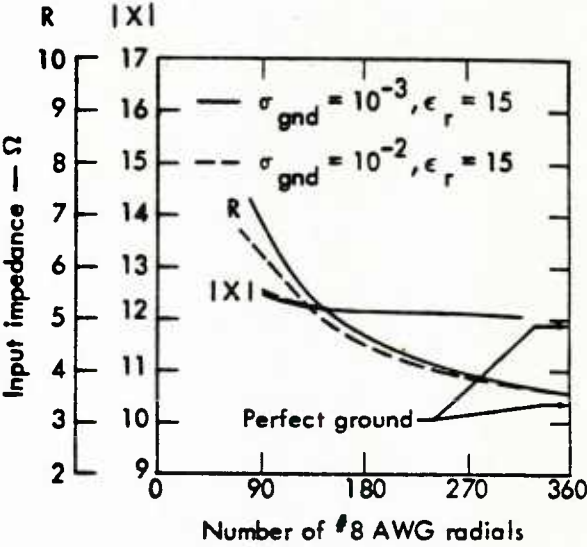
Fig. 34. Influence of the ground screen on the sectionalized LORAN transmitting antenna [35]. Results are based on the combined reflection-coefficient and surface-impedance approximations for the ground and ground screen, respectively. Computations like these can indicate how many wires are needed in a ground screen.
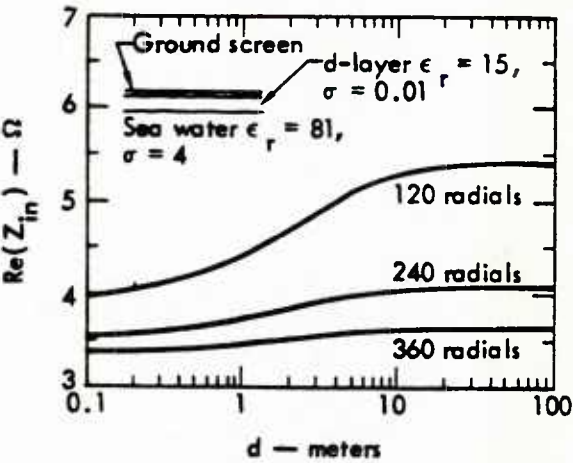
Fig. 35. Effect of subsurface sea water on the sectionalized LORAN trans-mitting antenna [35]. These results are in qualitative agreement with mea-sured values. The model can be used to establish ground-screen requirements to stabilize antenna resistance within specified limits.
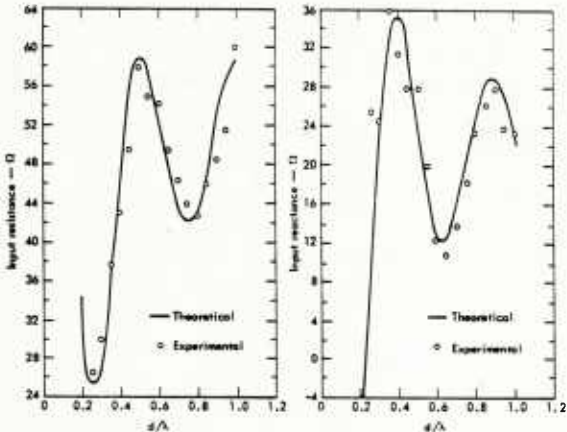
Fig. 36. Application of the combined moment-method and GTD technique [39]. These results are for an octagonal plate (of radius d) with a monopole at the center (fixed physical radius). h = 0.25 λ; a = 0.1524 cm.
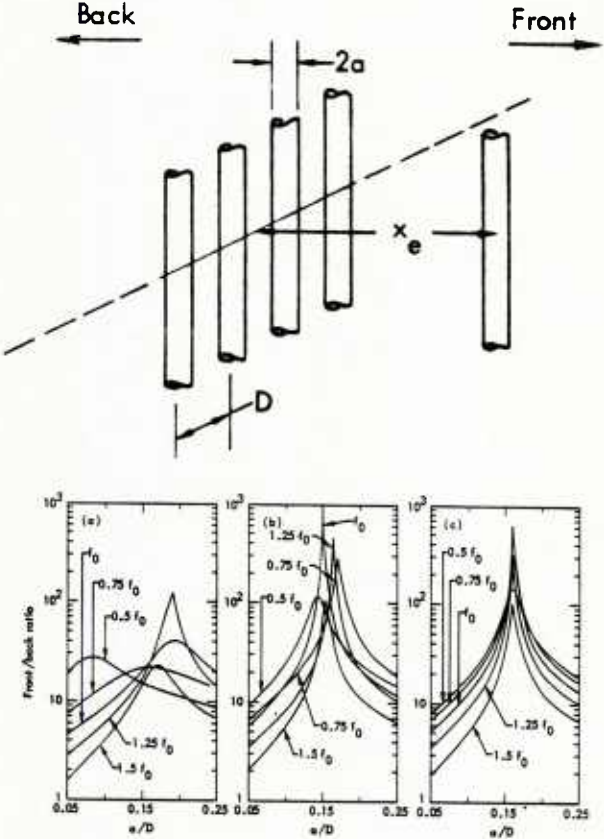
Fig. 37. Some results from a back-screen optimization study [66] for front/back ratio of screen antenna vs a/D, at various frequencies about f_0. (a) Definition of screen-antenna parameters plotted in (b), (c) and (d). At f_0, $D/\lambda_0 = 0.16$, $x_e/\lambda_0 = 0.25$. (b) 10 wires in screen. (c) 30 wires in screen. (d) 50 wires in screen. Note the front-to-back ratio peaks at a/D ~ 1/2 π, where the screen wires have a surface area approximately equal to the frontal area of the screen.
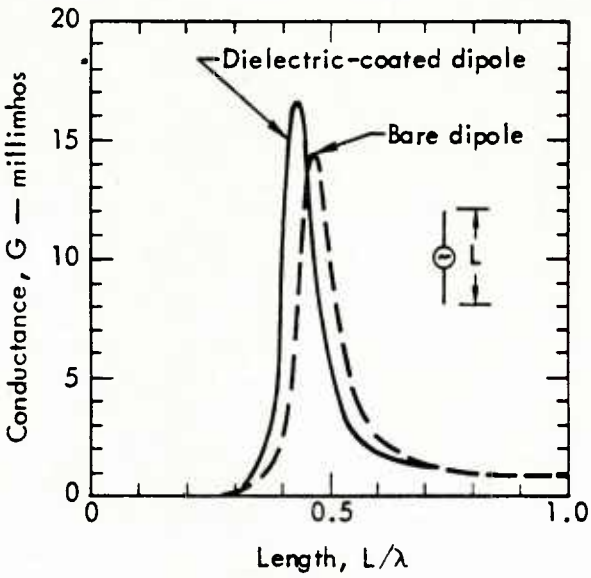
Fig. 38. Input resistance of bare and sheathed wire as a function of fre-quency [43]. As expected the loading effect of the sheath decreases the resonance frequency. Wire diameter d = L/100; outer diameter of dielectric sheath D = 2d; permittivity of shell $\epsilon = 4\epsilon_0$.
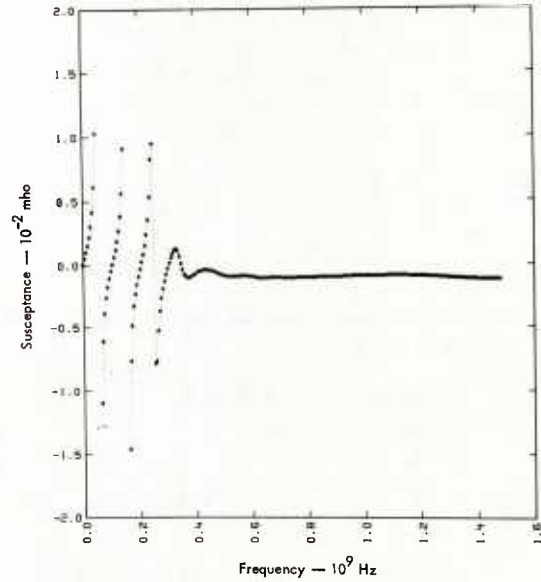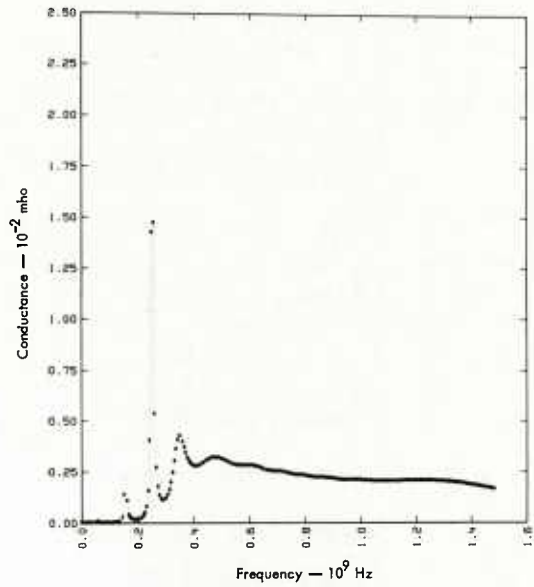
Fig. 39. Time-domain computer results for a conical spiral [67]: (a) Transient feedpoint current excited by a Gaussian pulse from a 350-Ω gene-rator. (b) Far-field radiation in bore-site direction. (c) Conductance. (d) Susceptance. (c) and (d) are obtained from a Fourier transform of (a) with the generator impedance removed.
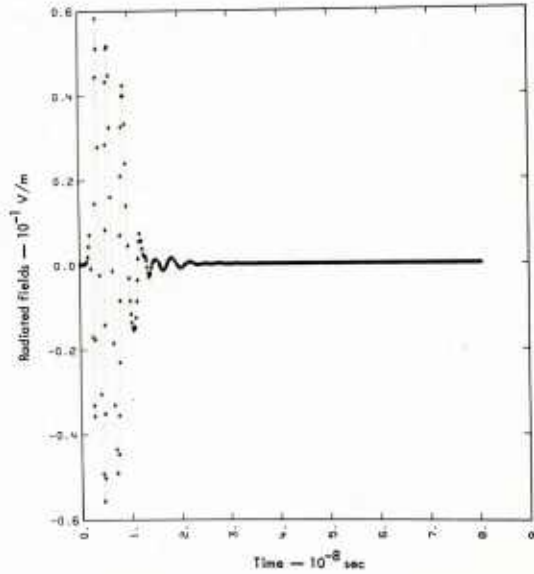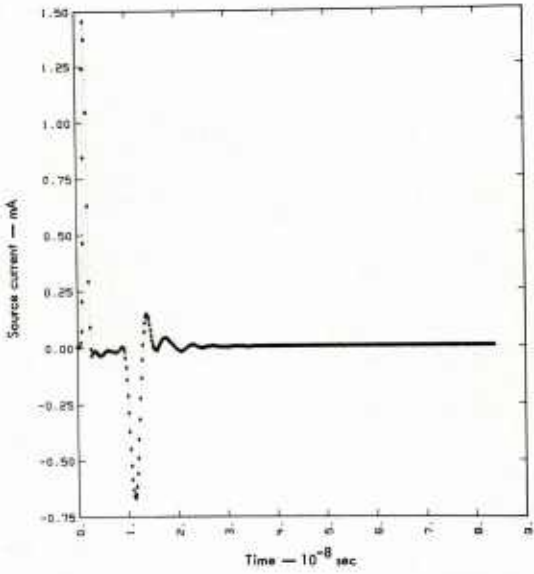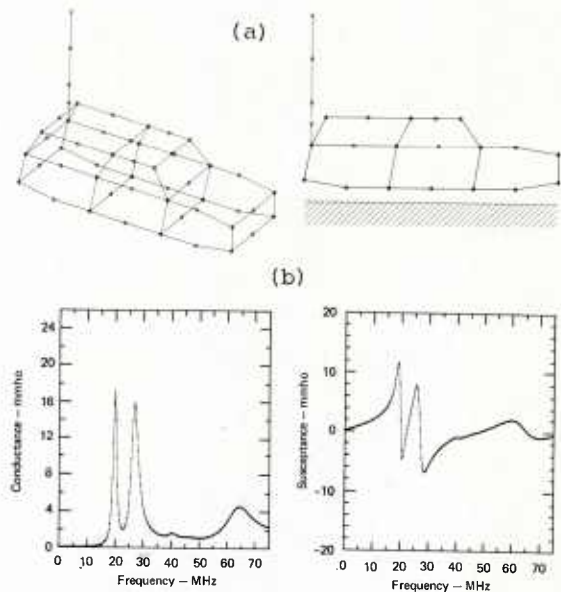
Fig. 40. Wire-grid truck model over perfect ground (a) yields input admittance (b) from time-domain calculation [49]. Results approximate the behavior of a CB antenna connected to rear bumper of light utility vehicle.
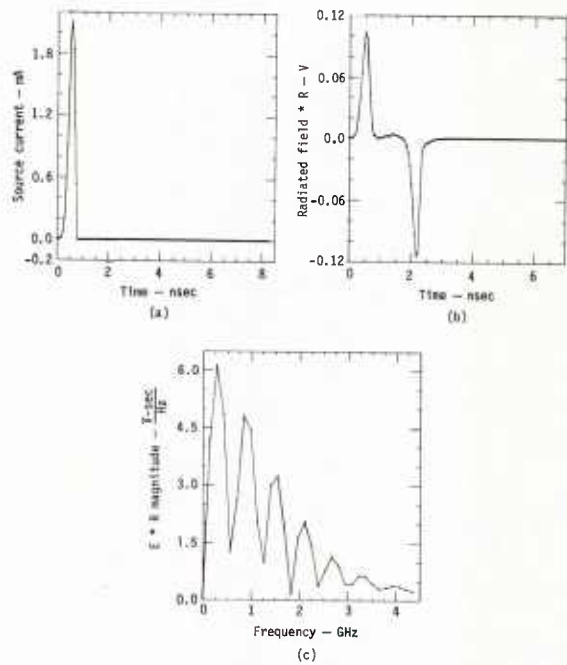
Fig. 41. Demonstration of nonlinear time-domain model of dipole (1 m long) which conducts current in only one direction. The model incorporates 60 ideal diodes and exhibits possibility of pulse shaping using such loads. Feedpoint current (a) produces initial radiated pulse (b) due to Gaussian exciting voltage at center while second pulse is caused by stopping of the charge as it reaches dipole ends, resulting in a notched spectrum (c).
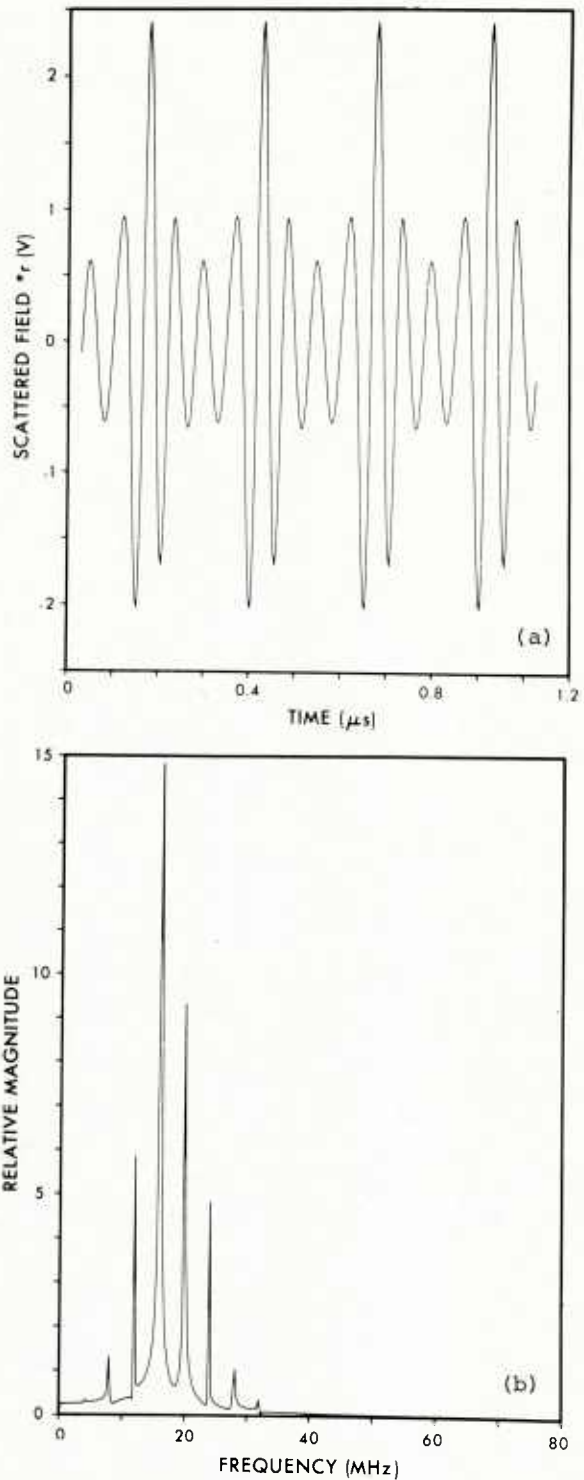
Fig. 42. Time waveform (a) and frequency spectrum (b) of broadside field (f = 16 MHz) scattered from dipole center-loaded by a sinusoidally time-varying (f_{mod} = 4 MHz) resistance [48]. Modulation effect of the load produces sidebands at intervals of the difference frequency between the incident-wave frequency and the modulation frequency. There is the possibility of transferring all the scattered power to frequencies different from that of the incident wave.

NUMERICAL MODELING TECHNIQUES FOR HALF-SPACE (GROUND) PROBLEMS*

E. K. Miller,** G. J. Burke,** R. J. King** and N. C. Mathur†

**Lawrence Livermore National Laboratory
P. O. Box 5504, L-153, Livermore, CA 94550

†Communications Laboratory, Dept. of Electrical Engineering and Computer Science
University of Illinois at Chicago, Chicago, IL 60680

SUMMARY

In the frequency range below a few hundred MHz, the earth-air interface can significantly affect the EM characteristics of a nearby object. The characteristics most likely to be affected are: 1) the object's current distribution and input impedance (if an antenna); and 2) the near and far fields that it produces. The problem of modeling both the object-ground near-field interaction and the ground screens used to reduce or control this interaction is discussed here.

The basic model (Part I) employed for the object-ground interaction uses a thin wire approximation to the electric-field integral equation in which the kernel includes the interface effect via the usual Sommerfeld integrals. Both the reflected and transmitted fields are accounted for so that objects on both sides of the interface, or even penetrating the interface, can be modeled.

Another approach (Part II) to modeling a ground system uses the surface impedance Z_s to represent the boundary conditions at the interface. To permit applications to a generic set of problems, $Z_s(\rho)$ is permitted to vary arbitrarily in the radial direction. A one-dimensional integral equation is first used to solve for the tangential magnetic field on the interface. This field is then used in a two-dimensional integral to find the radiation patterns for arrays of vertical dipoles over ground screens.

The analytical development and numerical treatment of each approach are summarized, and numerous examples are given to illustrate the results that can be obtained.

PART I

1. INTRODUCTION

The capability of modeling antennas near to and penetrating a plane boundary such as the earth-air interface has long been needed. While the analytical solution of this problem is well established, its rigorous computational treatment is only now becoming practicable. In this presentation, we outline the basic problem, describe a numerical approach to modeling it, and present some representative results. For simplicity, our discussion is addressed to wire objects only, although the method used to include the interface is more general, being applicable to conducting surfaces and penetrable bodies as well. The computer model described below is incorporated in NEC (Numerical Electromagnetic Code), a widely used modeling code.

2. ANALYTICAL DEVELOPMENT

It is convenient to develop the treatment for a wire object penetrating an interface as a sequence of extensions to that of the same object located in free space. The discussion here (and in Section 3 on the numerical procedure) therefore considers a wire: 1) in free space; 2) in a lossy infinite medium; 3) near an interface; and 4) penetrating an interface.

2.1 Free Space

Our approach is to employ an integral equation to obtain the current distribution induced on an object by a monochromatic ($e^{j\omega t}$ time variation) source. For wires whose radius (a) is small with respect to the wavelength (λ), the Pocklington form of the electric field integral equation has been found to work well [1]. It can be written for free space in the form

$$\hat{s} \cdot \vec{E}_\infty^I(\vec{r}) = - \hat{s} \cdot \vec{E}_\infty^D(\vec{r}); \quad \vec{r} \varepsilon C(\vec{r}) \tag{1a}$$

where

$$\vec{E}_\infty^D(\vec{r}) = \int_{C(\vec{r})} I(s')\hat{s}' \cdot \overline{\overline{G}}_\infty^D(\vec{r},\vec{r}')ds' \tag{1b}$$

In addition

$$\overline{\overline{G}}_\infty^D(\vec{r},\vec{r}') = C_1(\nabla\nabla/k_0^2 + \overline{\overline{I}})g_\infty \tag{2}$$

$$g_\infty = \exp(-jk_0 R)/R$$

$$\bar{\bar{I}} = \hat{x}\hat{x} + \hat{y}\hat{y} + \hat{z}\hat{z} \quad ,$$

$$R = \left| \vec{r} - \vec{r}' \right| \quad ,$$

$$k_0^2 = \omega^2 \mu_0 \epsilon_0 \quad ,$$

and

$$C_1 = -j\omega\mu_0/4\pi \quad ,$$

where the subscript ∞ denotes an infinite medium quantity.

Also, I is the induced current, $\vec{E}_\infty^I$ is the exciting field, $\hat{s}$ and $\hat{s}'$ are unit vectors tangent to the wire at s and s', and $\vec{r}$ and $\vec{r}'$ are vectors to the points s and s' on the wire contour $\vec{C}$. $\bar{\bar{G}}_\infty^D$ is the dyadic Green's function for the electric field at $\vec{r}$ due to a current element at $\vec{r}'$.

The thin-wire approximation has been employed in reducing the original two-dimensional surface integration to the one-dimensional line integration shown in Eq. (1). This approximation involves the assumptions that: 1) the longitudinal current has negligible circumferential variation; 2) the circumferential current is negligible; 3) the tube of current flowing on the wire can be replaced by a filament flowing on the wire axis, while the boundary condition is matched on the wire surface, so that $R \geq a$.

2.2 Wire in Lossy, Infinite Medium

Typical grounds are lossy, so that our model of the general interface problem requires that it allow for the complex wave number

$$k = k_0 \sqrt{\tilde{\epsilon}_\infty}, \text{ where } \tilde{\epsilon}_\infty = \epsilon_r - j\frac{\sigma}{\omega\epsilon_0} \quad .$$

Because the interface model includes the infinite-medium fields of an object as part of the total field, it therefore follows that capability to model a lossy, infinite medium is needed to handle objects buried in a lossy half space. The analytical capability for doing this is already encompassed by Eq. (1), if the free space wave number k_0 is replaced by the medium wave number k above. The numerical impact of this change is non-trivial, but straightforward, as is discussed in Section 3.2 below.

2.3 Wire Near an Interface

The free space (or infinite medium) integral equation (1) can be extended to handle a wire located near the boundary between two half spaces by modifying the kernel to include the fields scattered from the interface. Various image approximations have been used for this purpose (e.g., see [2], [3]), but their limitations are so restrictive that the rigorous Sommerfeld integrals are required in general. Thus, we use in place of Eq. (1), when $z \cdot z' \geq 0$, for source and observation points above ground (+) or below ground (-),

$$\hat{s} \cdot \vec{E}_\pm^I(\vec{r}) = -\hat{s} \cdot \vec{E}_\pm^D(\vec{r}) - \hat{s} \cdot \vec{E}_\pm^R(\vec{r}); \quad \vec{r}\epsilon C_\pm(\vec{r}) \quad , \tag{3a}$$

where the direct field $\vec{E}_\pm^D$ is given by Eq. (1b) with $k_0 \rightarrow k_\pm = k_0\sqrt{\tilde{\epsilon}_\pm}$ and $\tilde{\epsilon}_\pm = \epsilon_\pm - j\frac{\sigma_\pm}{\omega\epsilon_0}$. The field component due to the interface is

$$\vec{E}_\pm^R(\vec{r}) = \int_{C_\pm(\vec{r})} I_\pm(s')\hat{s}' \cdot \bar{\bar{G}}_\pm^R(\vec{r},\vec{r}')ds' \quad , \tag{3b}$$

with

$$\bar{\bar{G}}_\pm^R(\vec{r},\vec{r}') = \frac{k_\mp^2 \, k_\pm^2}{k_+^2 + k_-^2} \bar{\bar{G}}_\pm^I(\vec{r},\vec{r}') + \bar{\bar{R}}_\pm(\vec{r},\vec{r}') \quad , \tag{4a}$$

$$\bar{\bar{G}}_\pm^I(\vec{r},\vec{r}') = -\bar{\bar{I}}_R \cdot \bar{\bar{G}}_\pm^D(\vec{r},\bar{\bar{I}}_R \cdot \vec{r}') \quad , \tag{4b}$$

$$\bar{\bar{I}}_R = \hat{x}\hat{x} + \hat{y}\hat{y} - \hat{z}\hat{z} \quad .$$

$\bar{\bar{R}}_\pm$ involves the Sommerfeld integrals and is constructed from the following vector components for horizontally and vertically oriented dipoles

$$R_{\pm\rho}^V = \frac{C_1}{k_\pm^2}\frac{\partial^2}{\partial\rho\partial z} k_+^2 V_\pm^R \quad , \tag{5a}$$

$$R^V_{\pm z} = \frac{C_1}{k^2_\pm} \left(\frac{\partial^2}{\partial z^2} + k^2_\pm\right) k^2_\mp V^R_\pm \qquad , \tag{5b}$$

$$R^H_{\pm \rho} = \frac{C_1}{k^2_\pm} \cos \phi \left(\frac{\partial^2}{\partial \rho^2} k^2_\pm V^R_\pm + k^2_\pm U^R_\pm\right) \qquad , \tag{5c}$$

$$R^H_{\pm \phi} = \frac{-C_1}{k^2_\pm} \sin \phi \left(\frac{1}{\rho} \frac{\partial}{\partial \rho} k^2_\pm V^R_\pm + k^2_\pm U^R_\pm\right) \qquad , \tag{5d}$$

$$R^H_{\pm z} = - \cos \phi \ R^V_{\pm \rho} \qquad , $$

where the source is at $\vec{r}' = z'$, $\hat{z}$ and the field is evaluated at $\vec{r} = \rho(\cos \phi \ \hat{x} + \sin \phi \ \hat{y}) + z\hat{z}$. The superscript on R indicates a vertical (V) or horizontal (H) current element and the subscript indicates the cylindrical component of the field vector. The horizontal current element is along the x axis.

The Sommerfeld integral terms are

$$U^R_\pm = \int_0^\infty D_1 (\lambda) \exp[-\gamma_\pm|z + z'|]J_0 (\lambda\rho)\lambda d\lambda \qquad , \tag{5e}$$

$$V^R_\pm = \int_0^\infty D_2 (\lambda) \exp[-\gamma_\pm|z + z'|]J_0 (\lambda\rho)\lambda d\lambda \qquad , \tag{5f}$$

with

$$D_1(\lambda) = \frac{2}{\gamma_+ + \gamma_-} - \frac{2k^2_\pm}{\gamma_\pm(k^2_+ + k^2_-)} \qquad , $$

$$D_2(\lambda) = \frac{2}{k^2_- \gamma_+ + k^2_+ \gamma_-} - \frac{2}{\gamma_\pm(k^2_+ + k^2_-)} \qquad , $$

and

$$\gamma_\pm = (\lambda^2 - k^2_\pm)^{1/2} \qquad . $$

The terms $U^R_\pm$ and $V^R_\pm$ differ from those commonly used [4] by having static terms subtracted. The term subtracted from $V^R_\pm$ lets that integral converge as ρ and $z + z'$ approach zero with only an R^{-1} singularity in the second derivatives of $V^R_\pm$. The term subtracted from $U^R_\pm$ does not alter the singularity but completes the $\overline{\overline{G}}_I$ term in Eq. (4).

2.4 Wire Penetrating an Interface

Besides reflecting from it, fields are transmitted through the interface. As long as the object is located wholly in one half space, the transmitted fields need not be considered in the solution for current. But when the object penetrates the interface, or there are two (or more) objects located on opposite sides of the interface, the transmitted fields must then be included. Upon adding the transmitted fields, the integral equation (3a) becomes:

$$\hat{s} \cdot \vec{E}^I_\pm(\vec{r}) = -\hat{s} \cdot \vec{E}^D_\pm(\vec{r}) - \hat{s} \cdot \vec{E}^R_\pm(\vec{r}) - \hat{s} \cdot \vec{E}^T_\pm(\vec{r}); \quad \vec{r}\epsilon C_\pm(\vec{r}) \tag{6a}$$

where

$$\vec{E}^T_\pm(\vec{r}) = \int_{C_\mp(\vec{r})} I_\mp(\vec{s}')\hat{s}' \cdot \overline{\overline{T}}_\pm(\vec{r},\vec{r}')ds' \tag{6b}$$

and $\overline{\overline{T}}_\pm(\vec{r},\vec{r}')$ accounts for the Sommerfeld integral contributions to the transmitted field with sign subscript chosen for the observation medium (with the source in the other as indicated by the $\mp$ sign on I and C). It is constructed from the following expressions:

$$T^V_{\pm \rho} = C_1 \frac{\partial^2}{\partial\rho\partial z} V^T_\pm \qquad , \tag{7a}$$

$$T^V_{\pm z} = C_1 \left(\frac{\partial^2}{\partial z^2} + k^2_\pm\right) V^T_\pm \qquad , \tag{7b}$$

$$T^H_{\pm \rho} = C_1 \cos \phi \left(\frac{\partial^2}{\partial \rho^2} V^T_\pm + U^T_\pm\right) \qquad , \tag{7c}$$

$$T^H_{\pm \phi} = -C_1 \sin \phi \left(\frac{1}{\rho} \frac{\partial}{\partial \rho} V^T_\pm + U^T_\pm\right) \qquad , \tag{7d}$$

$$T^H_{\pm z} = -C_1 \cos \phi \frac{\partial^2}{\partial \rho \partial z'} V^T_\pm \quad , \tag{7e}$$

where

$$V^T_\pm = 2 \int_o^\infty \frac{e^{-\gamma_- |z'| - \gamma_\pm |z|}}{k^2_- \gamma_+ + k^2_+ \gamma_-} J_0(\lambda \rho) \lambda d\lambda \tag{7f}$$

$$U^T_\pm = 2 \int_o^\infty \frac{e^{-\gamma_- |z'| - \gamma_\pm |z|}}{\gamma_- + \gamma_+} J_0(\lambda \rho) \lambda d\lambda \tag{7g}$$

3. NUMERICAL TREATMENT AND VALIDATION

The numerical solution of integral equations of the kind presented above is now fairly standard in electromagnetic computer modeling. Only a brief summary is included here with detailed discussion limited, for the most part, to those aspects of the solution procedure that are new. Validation results similarly are given only where the computational procedure is significantly different from the basic case of the free space medium or where they round out the discussion.

3.1 Wire in Free Space

The Method of Moments [5] provides a way to reduce an integral equation to a linear system whose solution can be obtained using standard matrix techniques. As applied here, it involves these steps:

1. Representation of the wire contour C as a piecewise linear sequence of N segments of lengths Δ_j, $j = 1, \ldots, N$.

2. Approximation of the unknown current using a basis function expansion given by

$$I(s') = \sum_{j=1}^N P_j I_j(s')$$

with

$$P_j = \begin{cases} 1 & \text{if } |s' - s_j| < \Delta_j/2 \\ 0 & \text{otherwise} \end{cases} \quad ,$$

and

$$I_j(s') = A_j + B_j \sin[k_0(s' - s_j)] + C_j \cos[k_0(s' - s_j)]$$

The constants A_j, B_j, and C_j are so chosen, using a spline approach, that current and charge continuity is enforced along wires and the appropriate conditions are applied at junctions. Conditions on current and charge crossing an interface are discussed in Section 3.4.

3. Use of delta-function weights $\delta(s - s_i)$, $i = 1, \ldots, N$ to point match the integral equation to obtain the linear system

$$\sum_{j=1}^N Z_{ij} P_j = E^I_i \tag{8a}$$

where

$$Z_{ij} = \int_C I_j(s')\hat{s}' \cdot \overline{\overline{G}}^D_\infty(\vec{r}_i,\vec{r}') \cdot \hat{s}_i ds' \quad , \tag{8b}$$

and

$$\vec{E}^I_i = -\hat{s}_i \cdot \vec{E}^I_\infty(\vec{r}_i); \tag{8c}$$

with

$$i,j = 1, \ldots, N \quad \cdot$$

In the solution procedure, the matrix elements Z_{ij} are computed and the matrix is factored into upper and lower triangular factors. E^I is then specified, either as an incident wave or a localized field representing a voltage source. The coefficients P_j are then computed by solution of the matrix equation and the current is obtained by summing the basis functions. The correctness of this procedure has been widely demonstrated for the free space environment (e.g., see [6]) so no specific validation results are given here.

3.2 Wire in a Lossy, Infinite Medium

When the medium is lossy, the numerical treatment follows the steps outlined above,

with k_0 replaced by k. Introduction of a complex wave number results in a minimal increase in computation time since the field quantities were already complex.

In Fig. 1 a comparison is shown of the results obtained from the numerical treatment discussed here with those from an analytic closed-form solution due to Balmain [7]. The admittance of a short dipole is plotted as a function of frequency for both free space and a lossy plasma. Excellent agreement is exhibited between the two sets of results, validating the numerical model for at least this specific case.

Another kind of check on the numerical model for complex wave number is to obtain the resonance frequencies of a straight wire in the complex-frequency (s = jω - σ) plane. Resonance frequencies from an independent computation [8] are found to agree closely with those obtained here, providing further validation of the extension to a lossy medium. The resonance frequencies in both cases were obtained from a search of the complex frequency plane.

3.3 Wire Near an Interface

Addition of the Sommerfeld integrals to account for the fields reflected from the interface has a substantial impact on the numerical treatment. Straightforward numerical evaluation of the Sommerfeld contributions can be time consuming, increasing the overall computer time by a factor of 100 or more relative to the same computation performed for an infinite medium [2,3].

An alternate approach, obtaining the Sommerfeld integral values by interpolation in a two-dimensional (ρ, z + z') grid of pre-stored values, has been shown to be as accurate and much more efficient [9]. Accurate interpolation for the Sommerfeld integral terms ($\bar{\bar{R}}_\pm$) in Eq. (4a) is aided by the grouping of the more singular terms with the image field $\bar{\bar{G}}_\pm^I$. This form also aids in the evaluation of the integral in Eq. (3b) since the image field can be integrated in closed form for the sinusoidal terms of the current expansion. With this method, the computer time for evaluating matrix elements is about four times that required for the same object in free space. Time to solve the matrix equation is of course unchanged. For comparison, modeling the same object located near a perfectly conducting ground plane requires about twice the computation time to evaluate matrix elements as for free space since both the direct and image fields must be computed. Details of the interpolation procedure and the Sommerfeld integral computation used to fill the interpolation grid are given elsewhere [9] and so are not included here, but an example of an interpolation grid is presented in Fig. 2 to illustrate the procedure.

Limited validation of the Sommerfeld analysis for the interface model has been given elsewhere [2,3], as it also has for the interpolation treatment [9]. While experimental data is one of the more convincing checks to use for validation purposes, it is not widely available.

One alternative to experimental validation is provided by the internal consistency check of integrating the far-field power

$$P_F = \frac{1}{2} r^2 Re \underset{Lim \ r \to \infty}{\int} \vec{E}(\bar{r}) \times \vec{H}(\bar{r})^* \cdot \hat{r} \ d\Omega \qquad (9a)$$

for comparison with the input power

$$P_I = \frac{1}{2} Re(V_I I_I^*) \qquad (9b)$$

obtained from the antenna-source model. For lossless media, any difference between these two results can be interpreted as a measure of relative solution accuracy. However, this is a necessary, but not sufficient, requirement of a valid solution.

Application of this check typically yields agreement between P_F and P_I within one percent or so, giving confidence that for lossless half spaces at least, the overall model is quite accurate. An example of its application is illustrated by the results given in Fig. 3.

3.4 Wire Penetrating An Interface

Extension of the model to a wire penetrating the interface requires evaluation of the transmitted field $E_\pm^T$ in Eq. (6a). A similar approach was taken as for the reflected field, although the implementation is more involved. Also, the basis functions in the current expansion must be modified for the condition on current and charge at the point where a wire passes through the interface as described in Section 3.4.2.

3.4.1 Transmitted Field Evaluation

In contrast to the two-dimensional dependence of the reflected fields as can be seen in Eq. (5), the transmitted fields depend on three coordinates: ρ, z, and z'. This is because the source and observation distances from the interface are multiplied by different z-dependent wave numbers in the Sommerfeld integrals (see Eq. 7). Consequently, the number of values in the interpolation table is on the order of the 3/2 power of that for the reflected field. Interpolation still results in a large reduction in computation time since, in the method of moments solution, values over a limited range of coordinates tend to be

used repeatedly.

With this dependence on three parameters, it is particularly important to use a numerical treatment that yields accurate field values with a minimum number of evaluations of the Sommerfeld integrals. Using interpolation, this is accomplished by removing the singularity and dividing out the dominant phase factor as was done for the reflected field above ground. The transmitted field, however, can in some cases have a complex phase behavior described asymptotically by one ray traveling principally in the upper medium, above the straight line from source to observer, and another ray on or below the straight-line path. Since this phase dependence cannot be removed by division, an approach of least-squares approximation was developed which can be viewed as parameter estimation with a model chosen from the known behavior of the field.

At sufficiently large distances from the source, the field can be obtained directly from asymptotic approximations. Such approximations were used to permit truncating the interpolation and least squares approximation tables. These three methods, interpolation, least squares approximation and asymptotic approximation are combined in the present code to cover the range of source and observation point coordinates for the transmitted field. The technique, described briefly below, represents a trade-off between accuracy, complexity and computation time, and could probably continue to be refined with as much additional work as one cared to spend.

In the following, as is done in the code, we will consider only the case of a buried source and elevated observer, since the fields for elevated source and buried observer can be obtained from the former case through reciprocity.

Three-Dimensional Interpolation. The transmitted field components in Eqs. (7a) through (7e) are dominated at small distances in $R_T = [\rho^2 + (z - z')^2]^{1/2}$ by the derivatives of $V_\pm^T$ which have R_T^{-3} singularities. Hence, to smooth the interpolated functions and ease the requirement for interpolation accuracy, an analytically integrable term is subtracted from the integrand of $V_\pm^T$. The resulting integral is nonsingular as R_T goes to zero and the second derivatives of $V_\pm^T$ are singular as R_T^{-1}. The modified version of $V_\pm^T (\tilde{V}_+^T)$ is

$$\tilde{V}_+^T = 2 \int_0^\infty \left[\frac{e^{-\gamma_+|z| - \gamma_-|z'|}}{k_+^2 \gamma_- + k_-^2 \gamma_+} - \frac{e^{-\gamma_+|z-z'|}}{\gamma_+ (k_+^2 + k_-^2)} \right] J_0 (\lambda\rho) \lambda d\lambda$$

$$= V_+^T - \frac{2}{k_+^2 + k_-^2} \frac{e^{-jk_+R_T}}{R_T} \tag{10}$$

Substitution of $\tilde{V}_+^T$ for V_+^T in Eqs. (7a) through (7e) and multiplication by R_T to suppress the singularity results in the following functions of ρ, z and z' to which interpolation is applied:

$$I_\rho^V = C_1 R_T \frac{\partial^2}{\partial\rho\partial z} \tilde{V}_+^T \tag{11a}$$

$$I_z^V = C_1 R_T \left(\frac{\partial^2}{\partial z^2} + k_+^2\right) \tilde{V}_+^T \tag{11b}$$

$$I_\rho^H = C_1 R_T \left(\frac{\partial^2}{\partial\rho^2} \tilde{V}_+^T + U_+^T\right) \tag{11c}$$

$$I_\phi^H = -C_1 R_T \left(\frac{1}{\rho} \frac{\partial}{\partial\rho} \tilde{V}_+^T + U_+^T\right) \tag{11d}$$

$$I_z^H = -C_1 R_T \frac{\partial^2}{\partial\rho\partial z'} \tilde{V}_+^T \tag{11e}$$

As R_T approaches zero, these quantities remain finite and their limits are

$$I_\rho^V = C_1 \left(C_3 \frac{1-\sin\theta}{\cos\theta} - C_2 S \cos\theta\right) \tag{12a}$$

$$I_z^V = C_1 \left(C_3 - C_2 S \sin\theta\right) \tag{12b}$$

$$I_\rho^H = C_1 \left(C_3 \frac{\sin^2\theta - \sin\theta}{\cos^2\theta} + C_2 S \frac{\sin\theta (1+\cos^2\theta)-1}{\cos^2\theta} +1\right) \tag{12c}$$

$$I_\phi^H = -C_1 \left[(C_2 S - C_3) \frac{1 - \sin\theta}{\cos^2\theta} + 1\right] \tag{12d}$$

$$I_z^H = -C_1 \left(k_-^2 C_3 \frac{1-\sin\theta}{\cos\theta} + k_+^2 C_2 S \cos\theta\right) \tag{12e}$$

where $\theta = \tan^{-1} \dfrac{|z - z'|}{\rho}$,

$\qquad S = z'/R_T$,

$\qquad C_2 = \dfrac{k_-^2 - k_+^2}{k_+^2 + k_-^2}$,

and

$\qquad C_3 = k_+^2 C_2 / (k_+^2 + k_-^2)$

When, for $|k_- R_T|$ less than about 3, values for the quantities in Eqs. (11a) through (11e) are obtained by interpolation and subsequently divided by R_T and combined with the subtracted terms, the resulting errors in the field are considerably smaller than when the total field is obtained by interpolation.

For larger values of R_T, however, the subtracted term can dominate, since it is not attenuated by loss in the medium, and the interpolation error can be magnified. Thus, for larger values of R_T the field components of Eqs. (7a) through (7e) are obtained directly by interpolation.

Two different interpolation-point grids have been used. In an early version of the code, which produced some of the results presented here, the interpolation was performed in a set of coordinates derived from ρ, z, and z' such that approximately equal distances are covered in the upper and lower media as measured in the respective medium wavelengths and the quantities can be defined when R_T is zero. These coordinates are

$\qquad R' = [\rho^2 + (z - |k_-/k_+| z')^2]^{1/2}$

$\qquad \theta' = \tan^{-1} [(z - |k_-/k_+| z')/\rho]$

$\qquad x' = z/(z - |k_-/k_+| z')$

For R' from 0 to 0.2 λ_o the quantities in Eqs. (11a) through (11e) are obtained by interpolation with increments of 0.02 λ_o in R'. From 0.2 λ_o to 1.0 λ_o quantities from Eqs. 7a through 7e are obtained with increments of 0.1 λ in R'. In either case, increments in θ' are 10 degrees from 0 to 90 degrees, and increments in x' are 0.1 from 0 to 1.0.

In the present code, it was found more convenient to use coordinates ρ, z and z' to join the interpolation region with the least squares and asymptotic approximation regions. The values for $R_T = 0$ in Eqs. (12a) through (12e) are subtracted from Eqs. (11a) through (11e) so that the point $\rho = 0$, $z = 0$, $z' = 0$ in the interpolation grid has the value zero. Interpolation is used for the region

$\qquad 0 \le \rho \le 2\pi/|k_-|$

$\qquad 0 \le z \le 2\pi/|k_-|$

$\qquad 0 \le |z'| \le 2\pi/k_+$

with three sub-regions:

1. $0 \le |z'| \le .4(2\pi)/|k_-|$; interpolation for the difference between Eqs. (11) and (12)

2. $.4(2\pi)/|k_-| < |z'| \le 2\pi/|k_-|$; interpolation for the quantities in Eqs. (7) divided by $\exp(-jk_-|z'|)/R_T^2$

3. $2\pi/|k_-| < |z'| \le 2\pi/k_+$; interpolation for the quantities in Eqs. (7) divided by $\exp[-jk_-(\rho^2 + z'^2)^{1/2}]/R_T^2$

Three-dimensional linear interpolation is used on these grids. Outside of this interpolation region, the field is evaluated by least squares or asymptotic approximation.

<u>Asymptotic Approximation</u>. Asymptotic approximations for Sommerfeld integrals have been used by many investigators in forms ranging from simple first order approximations, known as reflection coefficient and transmission coefficient approximations [4] to higher order uniform interface asymptotic approximations. The forms used here were chosen to be valid on the interface and to cover transmitted field paths without limit on the maximum depth in the ground.

For asymptotic approximation, the integral for $V_\pm^T$ in Eq. (7f) (and similarly $U_\pm^T$) can be written in the form

$$V_\pm^T = \int_{-\infty}^{\infty} G(\lambda) e^{-F(\lambda)} d\lambda \qquad\qquad\qquad (13a)$$

where

$$G(\lambda) = \frac{\lambda H_o^{(2)}(\lambda\rho) \exp(j\lambda\rho)}{k_-^2\gamma_+ + k_+^2\gamma_-} \tag{13b}$$

and

$$F(\lambda) = \gamma_{\mp}|z'| + \gamma_{\pm}|z| + j\lambda\rho \tag{13c}$$

When ρ is sufficiently large, $G(\lambda)$ can be considered slowly varying relative to the exponential in Eq. (13a) and an approximation for the integral can be derived by the method of steepest descent. The integral is thus approximated in terms of contributions from the neighborhood of saddle points which are solutions of the equation

$$F'(\lambda) = 0 \tag{14}$$

The procedure is complicated by the existance of two branch points, $\lambda = k_+$ and $\lambda = k_-$, and a pole at the zero of the denominator of G. In general two saddle points must be considered. The first, λ_1, represents a ray that travels at a steep angle up to the interface and then at a shallower angle in the upper medium. The second, λ_2, represents a ray that travels at a shallow angle in the lower medium and then upward to the observer. The λ_2 ray attenuates exponentially above the interface (since $Re(\lambda_2) > k_+$) and is strongly attenuated in a lossy medium. In a lossy medium both rays are complex.

Rather than develop the complete asymptotic approximation for an integral of this form, an approximation was derived considering the λ_1 saddle point together with the pole but isolated from the λ_2 saddle point. Higher order terms were included in the contribution of the λ_1 saddle point. This part of the approximation thus includes the usually dominant ray and the surface wave. A first order approximation was then added for the λ_2 saddle point which can be important when z is small relative to ρ and z'. When ρ is small relative to z the first order approximation for the λ_1 saddle point is used with higher order terms obtained by interpolating between the higher terms for a larger value of ρ and higher order terms from an approximation for $\rho = 0$. When ρ and z are small relative to z', only the first order approximation for λ_1 is used since a more involved analysis would be required for higher order terms.

These asymptotic approximations yield errors less than a few percent for ρ greater than about 0.5λ to $1\lambda_o$ or for z greater than about $1\lambda_o$ to $2\lambda_o$. For small ρ and z, errors are less than 10 to 20 percent for $|z'|$ greater than about $1\lambda_o$ to $2\lambda_o$.

Least Squares Approximation (Parameter Estimation). For efficient interpolation the interpolated functions were made as smooth as possible, by suppressing the singularity and phase factor, to better match the linear or higher order interpolation functions. As an alternative, we might consider a model-based procedure. The basic difference is to employ interpolation functions chosen on physical or mathematical grounds to be close to the expected field behavior. The function amplitudes are obtained by enforcing a match to Sommerfeld integral values. If suitable model-based interpolation functions can be found, the possibility exists that the number of stored data values can be greatly reduced.

A form for such functions is suggested by the asymptotic approximations. The rays corresponding to the saddle points λ_1 and λ_2 have phase factors of the form

$$P_1(\rho,z,z') = e^{-F(\lambda_1)} \quad ,$$

$$P_2(\rho,z,z') = e^{-F(\lambda_2)} \quad ,$$

where λ_1 and λ_2 are solutions to Eq. (14) for the particular ρ, z, and z'. In addition, the field will involve spreading factors, such as R_1^{-n} for P_1 and R_2^{-n} for P_2 with n = 1, 2, 3, where

$$R_1 = [\rho^2 + (z - |k_+/k_-|z')^2]^{1/2} \quad ,$$

$$R_2 = [\rho^2 + z'^2]^{1/2} \quad ,$$

and angle factors such as 1., z/R_T, z^2/R_T, z'/R_T, ρ/R_T, etc. The field may then be approximated by a sum of functions

$$\tilde{E}(\rho,z,z') = \sum_n A_n f_n(\rho,z,z')$$

where each f_n is a product of a phase factor, a spreading factor, and an angle factor. The coefficients A_n are determined to provide a least squares fit of $\tilde{E}$ to field values computed by evaluating Sommerfeld integrals. $\tilde{E}$ can then be used to interpolate or extrapolate from the computed points that were fit. If the f_n are good approximations to the field behavior, then considerably fewer computed points should be needed for a given accuracy than with polynomial interpolation.

This method is effective for extrapolation as well as interpolation, as illustrated in Fig. 4. Both low frequency (P_1) and high frequency (P_2) components are present and are matched by the approximation.

In the present code, this least squares approximation is used from the outer boundary

of the interpolation region out to $3\lambda_0$ in ρ, $2\lambda_0$ in z and to a depth of about $2\pi/|k_-|$ in z'. The method is applied in three subregions. Two, with a boarder on the interface, involve a least squares fit of 32 terms while the third, for small ρ and z greater than $2\pi/|k_-|$ involves 28 terms with no P_2 factors. The Sommerfeld integrals are fit at a total of 196 points which is far fewer than would be needed for simple inter- polation over the region.

3.4.2 Current and Charge Conditions at the Interface

To model a wire penetrating the interface the basis functions of the current expansion, described in Section 3.1, must be modified to conform to the appropriate conditions on current and charge at the point of penetration. These conditions can be derived from the continuity required of the tangential electric and magnetic fields at the interface.

The condition on curent is determined by considering the azimuthal magnetic field of the current which, for a vertical wire, is tangent to the interface. Continuity of the magnetic field across the interface requires continuity of current (assuming $\mu_+ = \mu_- = \mu_0$), or

$$I_+ = I_- \tag{15}$$

where

$$I_+ = I(z_\pm \rightarrow 0)$$

Similarly, a radial electric field is produced by the charge on the wire and is tangent to the interface when the wire is vertical. Continuity of the radial electric field across the interface requires that

$$\frac{q_+}{q_-} = \frac{\varepsilon_+}{\varepsilon_-}$$

where q_+ and q_- are linear charge densities on the wire and ε_+ and ε_- are the real dielectric constants of the media. The continuity relation on the wire, taking account of the conduction current into the medium, is

$$I'_\pm = -j\omega q_\pm \, \tilde{\varepsilon}_\pm/\varepsilon_\pm$$

where

$$\tilde{\varepsilon}_\pm = (\varepsilon_\pm - j\frac{\sigma_\pm}{\omega\varepsilon_0}) \quad .$$

Hence, the condition on the derivative of current, which is needed to define the basis function, is

$$\frac{I'_+}{I'_-} = \frac{\tilde{\varepsilon}_+}{\tilde{\varepsilon}_-} \quad . \tag{16}$$

These conditions are strictly valid only for the vertical wire. They have been used for oblique penetration, however, and appear to be the most reasonable conditions compatible with the thin wire approximation.

Two kinds of checks were made to assess the validity of the treatment of the penetrating conductor. One involved an independent formulation for a vertical circular cylinder penetrating the interface [10]. The cylinder was modeled with the electric field integral equation as a surface, without invoking the thin wire approximation. A Galerkin's technique was employed to solve for the current using piecewise linear basis and weight functions. This solution ensured continuity of current but placed no constraint on the derivative of current. Interface effects were included via the Sommerfeld integrals but these were evaluated independently of the routines used in NEC.

The solution for current obtained from this model revealed a variation in accord with Eq. (16). The overall current distribution was in close agreement with that obtained from NEC when the cylinder radius was small enough to satisfy the thin-wire approximation. It was found, however, that considerably more samples were needed in the vicinity of the interface to obtain convergence in the solution with the cylinder code than with NEC where the condition of Eq. (16) is built in. An example of results obtained using the Galerkin technique [10] as compared with the thin-wire treatment is presented in Fig. 5.

The other check was to evaluate the electric field both radial and tangential to the wire due to the computed current. This was done for normal and oblique angles of penetration. The results, some of which are presented in Fig. 6, show no significant anomaly in the field until the penetration angle exceeds about 60° from normal. Even then, the perturbation in the field is small in an integral sense relative to the source field. Any perturbation in the condition of Eq. (16) produced a noticable increase in the field tangential to the wire at the interface.

4. REPRESENTATIVE APPLICATIONS

There are many practical problems to which a model of the kind discussed above can be productively applied. Some representative results for antenna, geophysical and EMP simulation applications are given here.

4.1 Antenna Applications

4.1.1 The Monopole on a Ground Stake

One of the motivations for developing a capability for modeling a wire penetrating an interface was to model ground stakes, typically metal rods driven into the ground, that are used with many HF and VHF antennas. Before this capability was developed such antennas were often modeled by omitting the ground stake and setting I_+ to zero where the wire ended on the upper side of the interface. This condition is compatible with Eq. (16) in the limit $\sigma_- \to \infty$ and usually leads to a reasonable solution for the current distribution if $\sigma_-/\omega\epsilon_0$ is large. Hence it is useful for obtaining the radiation pattern, although radiation from the ground stake is neglected. Setting I_+ equal to zero, however, does not lead to an accurate calculation of input impedance, which typically depends on segment length and which exhibits no definite convergence as N increases. While the more accurate ground-stake model developed here is itself not completely general, including the thin-wire approximation as it does, it is consistent with other aspects of the overall numerical treatment and leads to a converged and apparently accurate solution.

Some results to illustrate these points, as well as to demonstrate the importance of being able to model a ground stake, are included in Fig. 7. There the current distribution is shown on a vertical quarter-wave monopole driven against a ground stake of varying lengths. The input impedance results corresponding to these cases are given in Fig. 8.

The effect of a variable ground stake length is displayed in more detail in Figs. 9-11. Input impedances are presented in Fig. 9 and the radiation resistance R_R and ground-loss resistance R_G are given as Fig. 10 where

$$R_R = \frac{r^2}{|I_I|^2} \underset{r\to\infty}{\text{Lim}} \int \text{Re}[\overline{E}(\overline{r}) \times \overline{H}^*(\overline{r})] \cdot \hat{r}\, d\Omega \qquad, z > 0$$

for source current I_I and $R_G = R_I - R_R$. It is also useful to derive the radiation efficiency η_R, defined by

$$\eta_R \equiv \frac{R_R}{R_I}$$

which is plotted in Fig. 11. Note that the efficiency exhibits an increasing sensitivity to the wire radius as the ground conductivity increases.

4.1.2 The Antenna on a Ground Screen

Ground screens are used to stabilize antenna impedance, improve radiation efficiency, and control the radiation, besides providing a point against which to drive the antenna. Their effects are presently analyzed using various approximations such as the screen equivalent surface impedance and the compensation theorem. This situation is not surprising, since it has been difficult to treat a single wire near an interface, let alone the large collection of wires which may comprise a typical ground screen. Approximate analyses have, in the past, provided much useful date for dense ground screens [11]. The more vigorous analysis described here can provide a check on these approximations. If full advantage is taken of the symmetry of a monopole on a radial screen, then screens with over 100 radials could be modeled in very reasonable computation time. Since only partial use is made of symmetry in the present code a maximum of 16 radials are considered in the results presented here. Some preliminary results were previously presented for a space ground screen consisting of just a few ($\leq$ 4) wires with the antenna and screen above the interface [12]. Here, we study a more general situation including the case of an elevated antenna driven against a buried ground, as illustrated in Figs. 12-13.

For low ground conductivity, the effect of the ground screen is seen to be strongly dependent on the electrical lengths of the radial wires. Furthermore, the transition from a k_+ wave number for current to a k_- wave number occurs over a very small change in vertical position of the radials with respect to the interface.

4.2 Geophysical Applications

An area in which there is a continuing need for the capability to predict the response of objects buried in the ground due to various kinds of incident fields is that of geophysical exploration. Electric, magnetic and electromagnetic fields, due both to the natural earth's background and man-made causes, have been used to probe into the ground. Two kinds of approaches are discussed below, field measurements and impedance probing.

4.2.1 Field Measurements

One approach to subsurface probing is to measure the electric and/or magnetic field near the interface, as the probe is moved over it in a raster-like fashion. The detection of a buried object then depends on the perturbation it may produce in the total field.

Computations were performed for three different underground objects, or targets, a vertical pipe, a horizontal pipe, and horizontal crossed pipes. The effects of varying the frequency, burial depth, pipe length, and conductivity were examined. Three probing fields were considered, one due to a vertical antenna 10 km from the target, another a horizontal

antenna 100 m away, and a plane wave incident at an angle of 45°. Various field components were examined, both above and beneath the interface. Some representative results of these computations are presented in Figs. 14-16.

In Fig. 14 is shown a typical result for the vertical pipe. Corresponding results are shown in Figs. 15 and 16 for the horizontal pipe and the crossed pipes, respectively. Clear evidence is seen in each of the presence of the buried target. The level of the field perturbation (relative to the source field) is only a few percent, however, so that measurement noise could substantially reduce target detectability.

4.2.2 Impedance Measurements

Another kind of approach to geophysical probing is to measure the input impedance of a sensing antenna. In this case, the probing field is produced by the antenna itself, with its impedance changes providing the detection mechanism. Some results to illustrate this approach are shown in Fig. 17.

Again, the changes being measured are generally only a few percent of the background or nominal value, indicating the need to assess the effects of measurement noise. It would be useful to conduct a systems assessment to determine the sensitivity of overall system's performance on the various factors involved.

4.2.3 EMP Simulator Modeling

A wide variety of simulators have been used for testing the effects of Electromagnetic Pulse on various systems. One specific example is SIEGE, which was intended for application to buried objects such as missile silos. It consists basically of vertical wires buried in the ground and excited from a horizontal wire to which they are connected.

Some simplified versions of this simulator were modeled, for which representative results are given in Fig. 18. There is demonstrated the effect of completely burying the simulator relative to locating the horizontal portion above ground. Computer models of this kind can be helpful in evaluating design tradeoffs.

5. CONCLUDING REMARKS

The development and application of a computer model for testing objects located near, or penetrating, the earth-air interface has been described in this paper. An integral equation provides the basis for the computer model, and its solution is obtained using the moment method.

The effect of the ground is included using the Sommerfeld integrals, which appear as part of the integral equation kernel. An innovative procedure is used to provide an accurate and efficient computation of these fields. It is based on a combination of intepolation, model-based parameter estimation and an asymptotic expansion. A charge discontinuity condition is employed to ensure continuity of the tangential electric field at the interface due to the wire current. The result is a computer model which can provide accurate results for problems involving penetrating conductors at a computer cost of only ~4-8 times that required for the same object in free space.

REFERENCES

1. E. K. Miller and F. J. Deadrick, "Some Computational Aspects of Thin-Wire Modeling," Chapter 4 in Numerical and Asymptotic Techniques in Electromagnetics, edited by R. Mittra, Springer-Verlag, New York (1975).
2. E. K. Miller, A. J. Poggio, G. J. Burke and E. S. Selden, "Analysis of Wire Antennas in the Presence of a Conducting Half Space: Part I. The Vertical Antenna in Free Space," Canadian Journal of Physics, 50, pp. 879-888 (1972).
3. E. K. Miller, A. J. Poggio, G. J. Burke and E. S. Selden, "Analysis of Wire Antennas in the Presence of a Conducting Half Space: Part II. The Horizontal Antenna in Free Space," Canadian Journal of Physics, 50, pp. 2614-2627 (1972).
4. A. Banos, Dipole Radiation in the Presence of a Conducting Half-Space, Pergamon Press, New York (1966).
5. R. F. Harrington, "Field Computations by Moment Methods," MacMillan, New York (1968).
6. A. J. Poggio and E. K. Miller, "Integral Equation Solutions of Three-Dimensional Scattering Problems," in Computer Techniques for Electromagnetics, edited by R. Mittra (Pergamon Press, New York), Chapter IV (1973).
7. K. G. Balmain, "Dipole Admittance for Magneto Plasma Diagnostics," IEEE Trans Ant. Prop., AP-17, pp. 389-392 (1969).
8. F. M. Tesche, "On the Analysis of Scattering and Antenna Problems Using the Singularity Expansion Technique," IEEE Ap-s Trans., Ap-21, pp. 53-62, (1973).
9. G. J. Burke, E. K. Miller, J. N. Brittingham, D. L. Lager and R. J. Lytle, "Computer Modeling of Antennas Near the Ground," Electromagnetics, 1, pp. 29-49 (1981).
10. W. A. Johnson, "Analysis of a Vertical, Tubular Cylinder Which Penetrates an Air-Dielectric Interface and Which Is Excited by an Azimuthally Symmetric Source," to be published in Radio Science.
11. J. R. Wait and W. A. Pope, "The Characteristics of a Vertical Antenna with a Radial Conductor Ground System", Appl. Sci. Res., Section B, Vol. 4, (1954).
12. E. K. Miller, J. N. Brittingham, and J. T. Okada, "Explicit Modeling of Antennas with Sparse Ground Screens," Elect. Lett. Vol. 14, pp. 627-629.
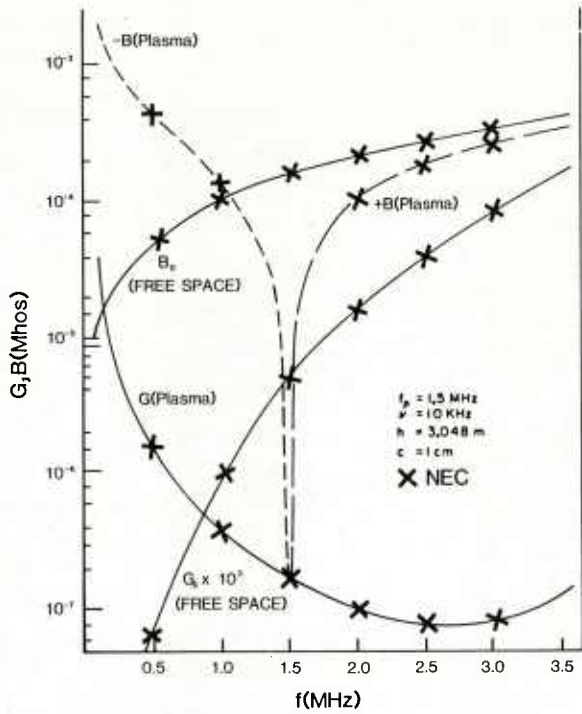
Figure 1. Comparison of results from present treatment and analytic solution [7] for linear dipole antenna in lossy plasma and free space. Antenna half length is 3.048 m, radius is 1 cm, plasma frequency is 1.5 MHz and electron collision rate is 10^4/sec.
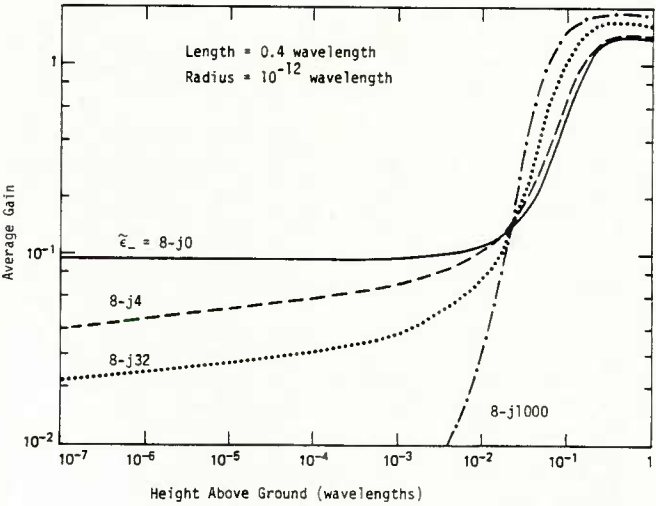
Figure 3. Upper half-space gain (defined as $2P_F$ in the upper medium divided by P_I) of a horizontal dipole as a function of distance from the interface. Radiated power, obtained by integrating over upper and lower half-spaces, is within one percent of the input power P_I for the lossless case. The average gain is seen to exhibit great sensitivity to distance from the interface, especially for larger ground conductivity. As ground conductivity is further increased the height of the dipole at which the gain drops will decrease.
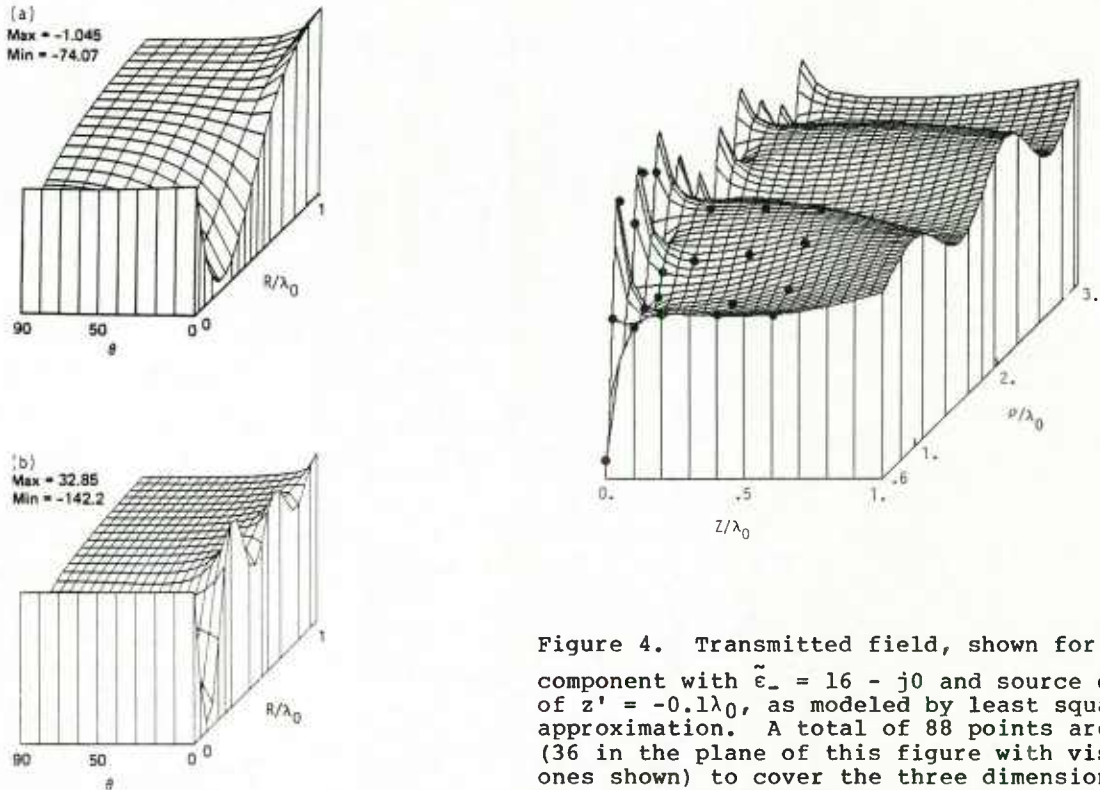
Figure 2. Real part of I_ρ^H for frequency = 10 MHz and (a) $\varepsilon_- = 4$ and $\sigma_- = .001$ S/m and (b) $\varepsilon_- = 16$ and $\sigma_- = 0$.

Figure 4. Transmitted field, shown for T_ρ^V component with $\tilde{\varepsilon}_- = 16 - j0$ and source depth of $z' = -0.1\lambda_0$, as modeled by least squares approximation. A total of 88 points are fit (36 in the plane of this figure with visible ones shown) to cover the three dimensional region $0.6 \leq \rho/\lambda_0 \leq 3.0$, $0 \leq z/\lambda_0 \leq 2.0$, and $0 \leq |z'|/\lambda_0 \leq 0.25$ with less than 4 percent error.

a)

b)
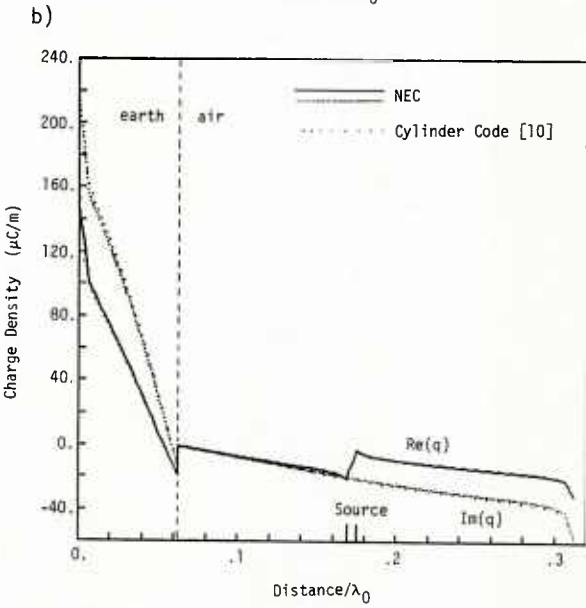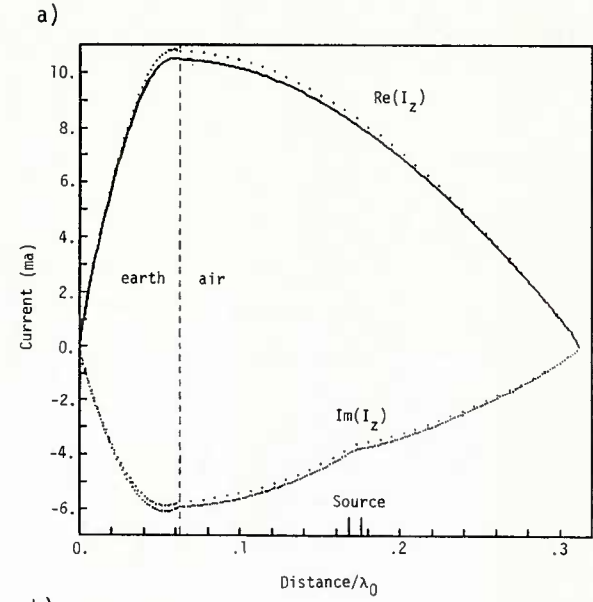
Figure 5. Comparison of current and charge
distribution from two different computations
for a vertical wire penetrating a horizontal
ground. The present treatment imposes an
implicit charge condition at the interface
[Eq. (16)], whereas only current continuity
was imposed in the other approach [10].
Validity of both treatments and the charge
condition is implied by these results.
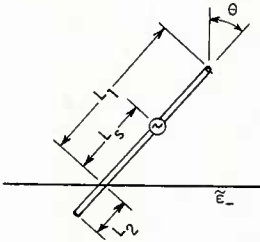
$\tilde{\varepsilon}_- = 16-j0.$

wire radius = $.00025\lambda_0$

$L_1 = .25\lambda_0$

$L_2 = .0625\lambda_0$

$L_s = .1187\lambda_0$
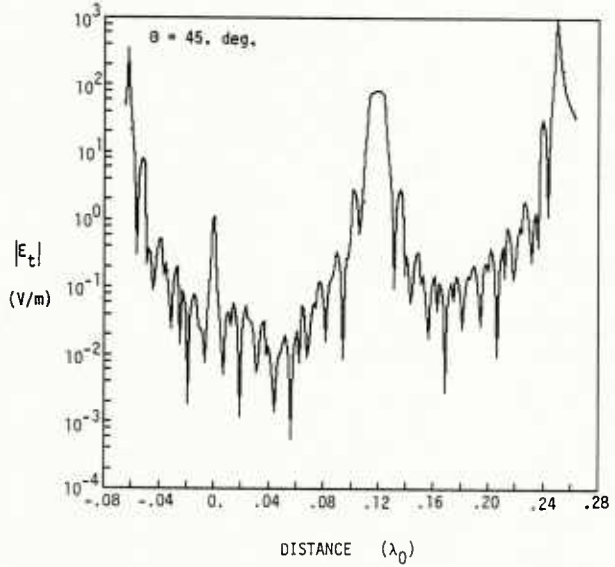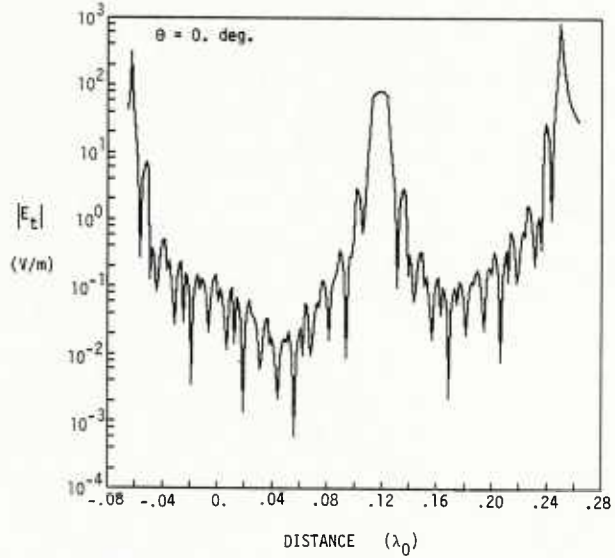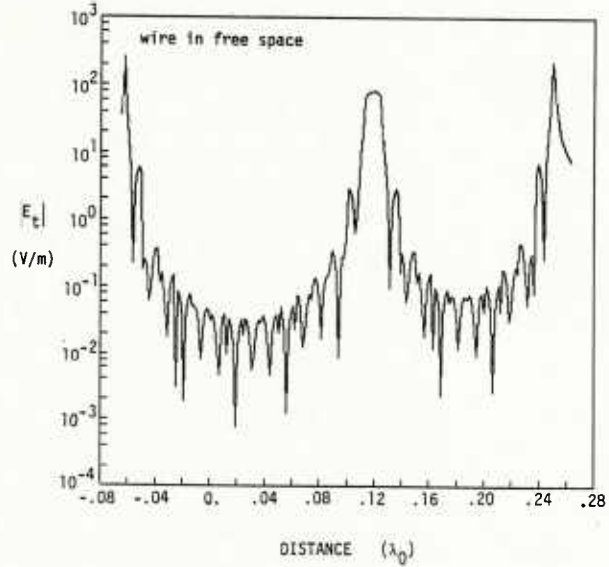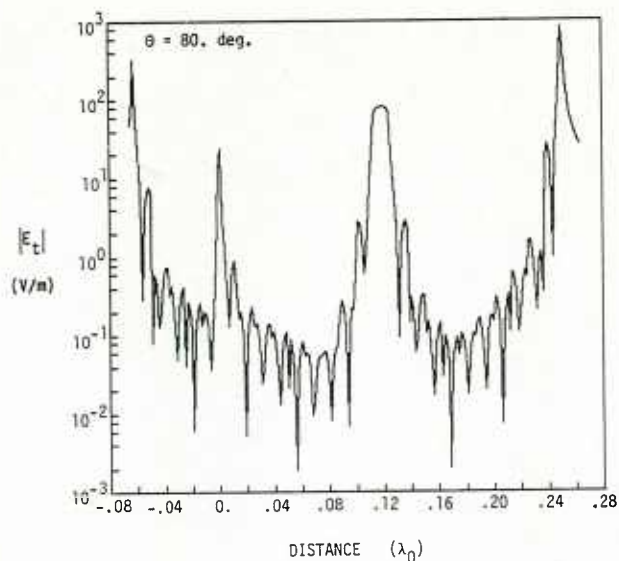
Figure 6. Tangential electric field along surface of thin wire penetrating a ground at various angles, θ, with respect to vertical, with free space shown for comparison. This error field, which should be zero outside the source region, oscillates due to the numerical treatment. A useful measure of boundary condition mismatch is to measure the error field relative to the source field, for which these results exhibit reasonable accuracy.
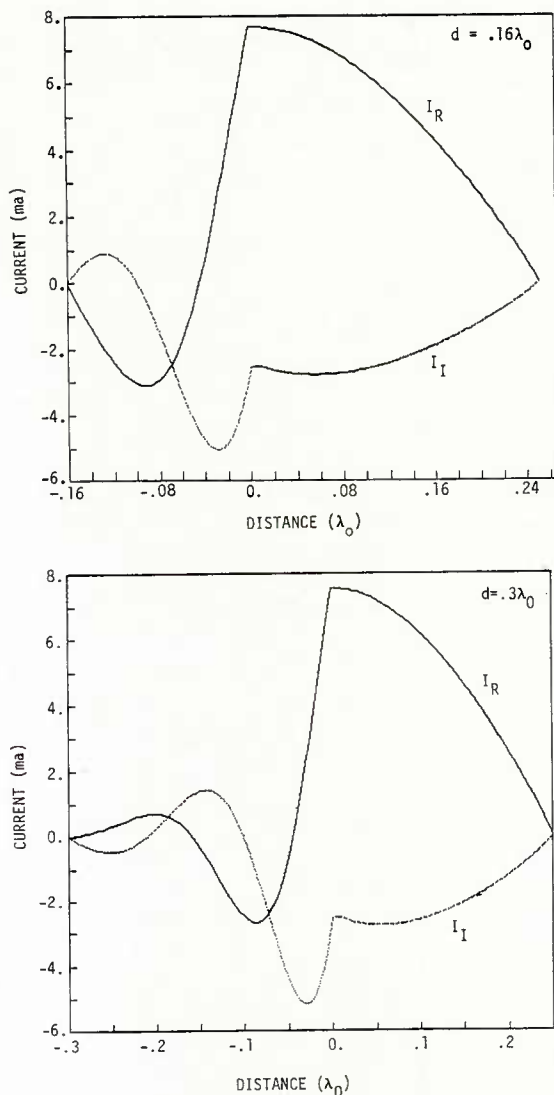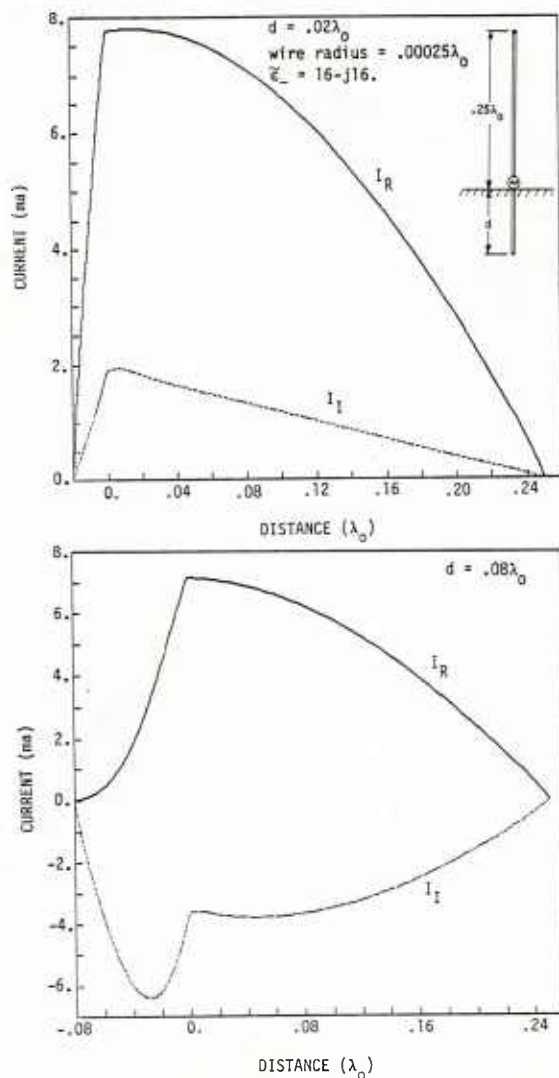
Figure 7. Current distributions on vertical quarter wave monopole for various lengths of ground stake. The present treatment produces results which are as well converged as a free space model, whereas using no ground stake and $I_+ = 0$ yields solutions very sensitive to segmentation.
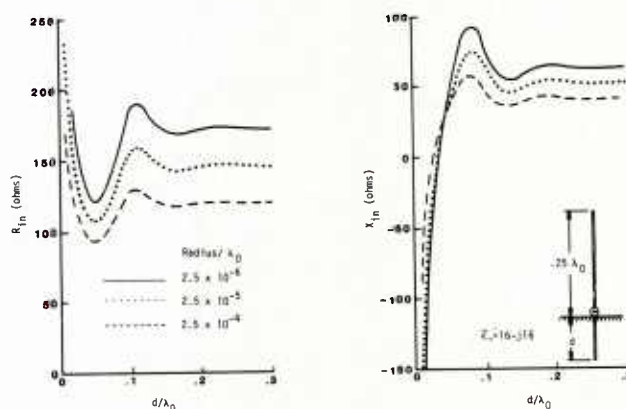
Figure 8. Input impedance of the quarter wave monopole as a function of ground stake length with wire radius a parameter. For this particular ground, a length of ~0.15% the free space wavelength or more yields an impedance essentially independent of stake length.

Figure 10. Radiation (from upper half-space power) and ground loss resistances corresponding to the cases of Fig. 9. Note the possibility of "tuning" the ground stake length to maximize the power radiated into the upper half space.

Figure 9. Input impedance of the quarter wave monopole as a function of ground-stake length with $\tilde{\epsilon}_-$ a parameter. As expected, the length of ground stake needed to stabilize the impedance decreases with increasing conductivity.
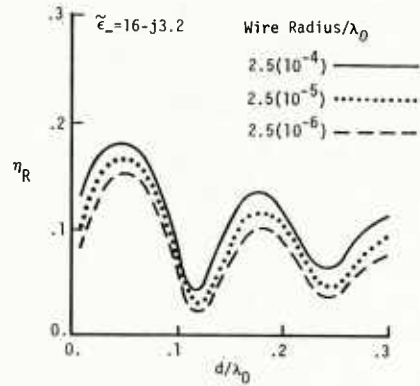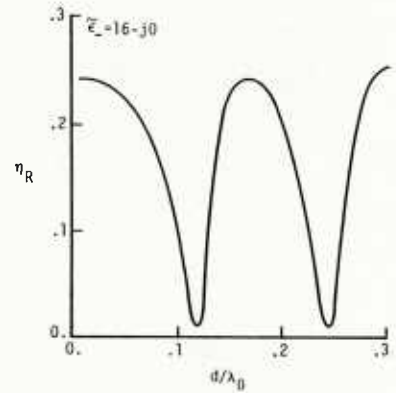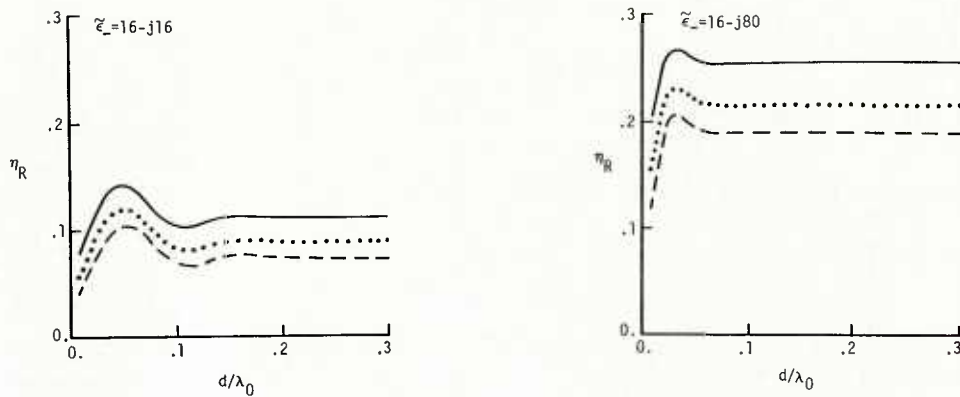
Figure 11. Radiation efficiency for the upper half space corresponding to the cases of Fig. 9. The sensitivity of the efficiency to wire radius increases with ground conductivity over the range considered here.
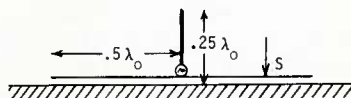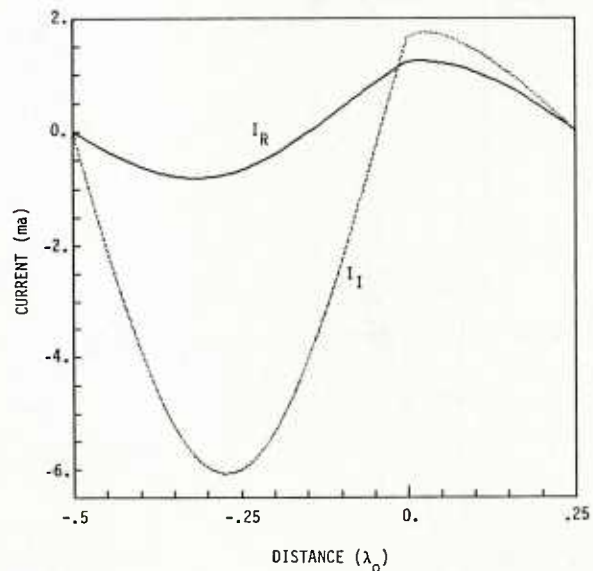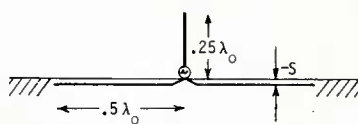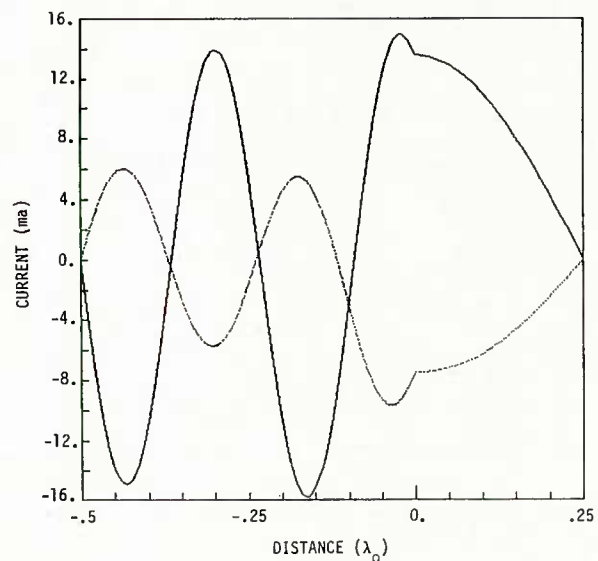
Figure 12. Current distribution on a quarter wave monopole driven against a ground screen consisting of 6 evenly spaced radial wires parallel to the ground, for (a) a screen $10^{-3}\lambda_0$ above the interface, and (b) $10^{-3}\lambda_0$ beneath it, for $\epsilon_- = 16 - j0$. The sum of the radial currents is plotted to obtain a continuous current at the monopole screen junction. It can be seen that transition from the upper to lower medium wavelength occurs within a vertical distance of $2(10^{-3})\lambda_0$.

a)

b)

$\tilde{\epsilon}_-$

16-j0 ——

16-j3.2 ••••••••••

16-j16 – – –

c)

d)
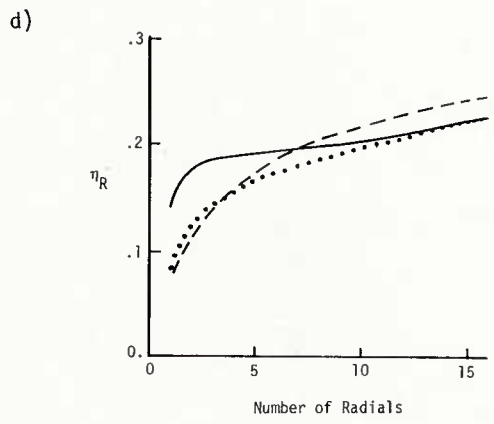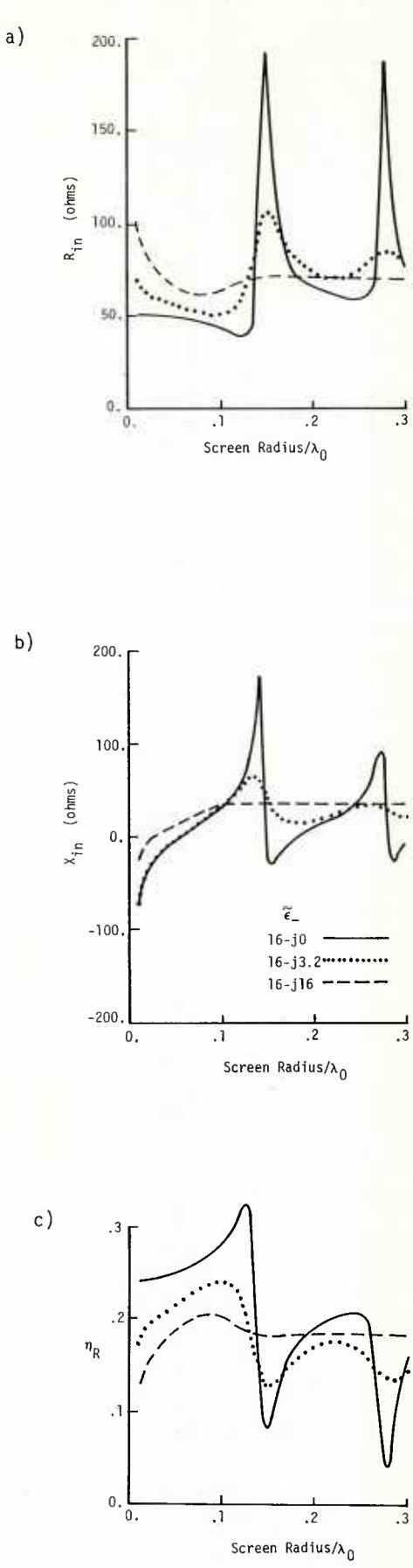
Figure 13. Input impedance and radiation efficiency of monopole on a radial wire ground screen $10^{-3}\lambda_0$ below the interface. In (a) through (c) the screen radius is varied for 6 radials having a wire radius of $10^{-7}\lambda_0$, with $\tilde{\epsilon}_-$ a parameter. Strong resonance effects are seen for low ground conductivity. In (d) the number of radials is varied for a fixed screen radius of $0.2\lambda_0$. Increasing the number of radials beyond 6 or 8 for this set of parameters yields diminishing benefit.
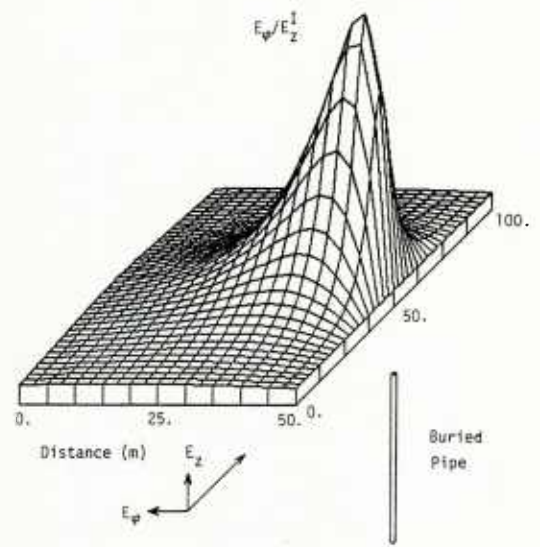
Figure 14. Typical signature (defined by the magnitude of E_ϕ relative to E_z) of buried vertical pipe (length L = 45 m, diameter d = .2 m) with upper end 5. m below the interface for $\epsilon_- = 16 - j80$ and f = 200 kHz. The magnitude of the ϕ-directed electric field normalized by the z component of incident electric field is plotted, for a vertical electric source 10 km distant. The peak perturbation, E_ϕ, relative to the incident field is 0.0012. Only the left half of the field, which is left right symmetric is plotted.
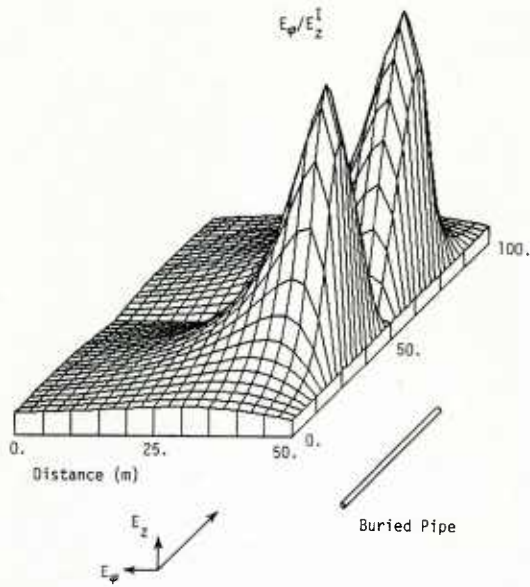
Figure 15. Signature of a horizontal pipe of L = 50 m, d = .2 m, and buried 5 m below the interface with $\tilde{\epsilon}_- = 16 - j80$ and f = 200 kHz, plotted as in Fig. 15. The two peaks in the field are associated with the ends of the pipe. The peak value of E_ϕ relative to the incident field is .039.
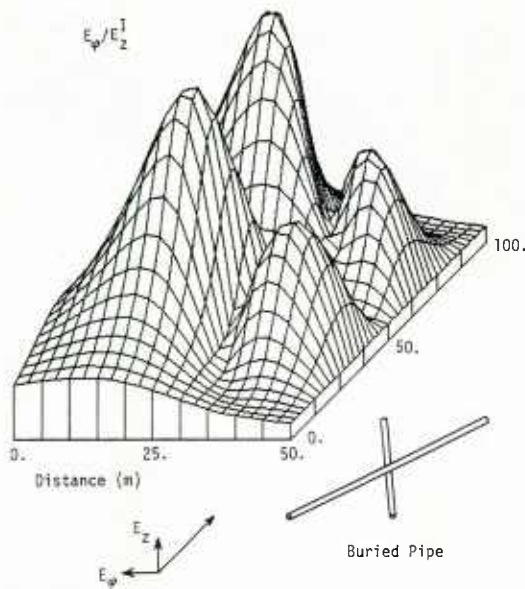
Figure 16. Signature of crossed horizontal pipes of L = 71 m and d = .2 m buried 10 m below the interface with $\epsilon_- = 16 - j80$ and f = 200 kHz, plotted as in Fig. 15. The center of the cross is at coordinates (50, 50), and the maximum of E_ϕ relative to the incident field is .014.
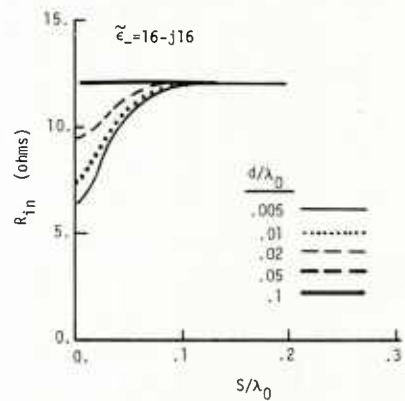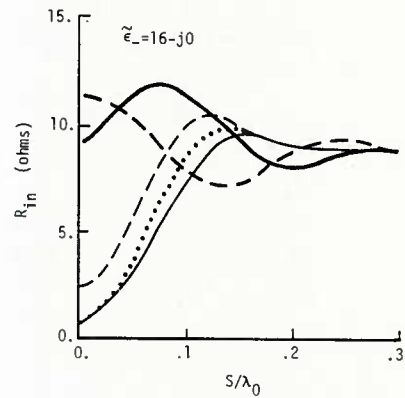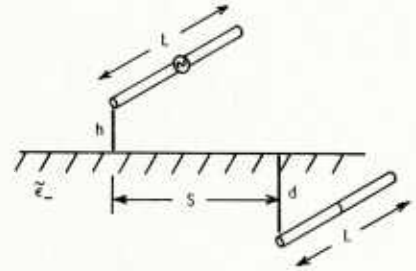
Figure 17. Resistance of an elevated dipole due to a buried wire with burial depth a parameter. The wires are parallel to each other and the interface with their centers in a common vertical plane. Wire lengths are $L = 0.125\lambda_0$, diameter $.0002\lambda_0$, with the elevated dipole $0.02\lambda_0$ above the interface.

a)

d)

b)
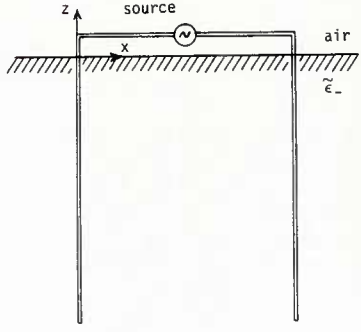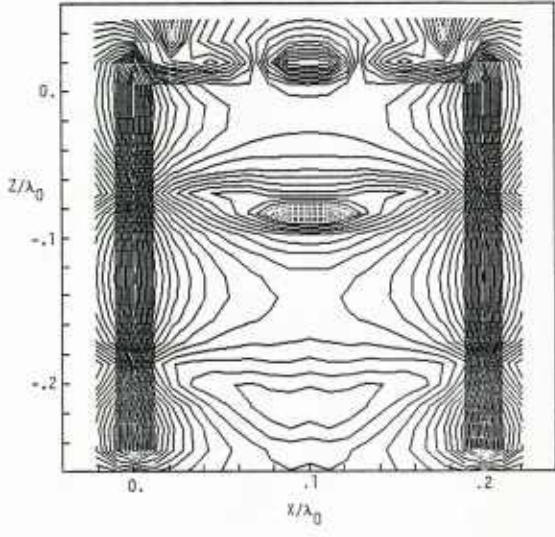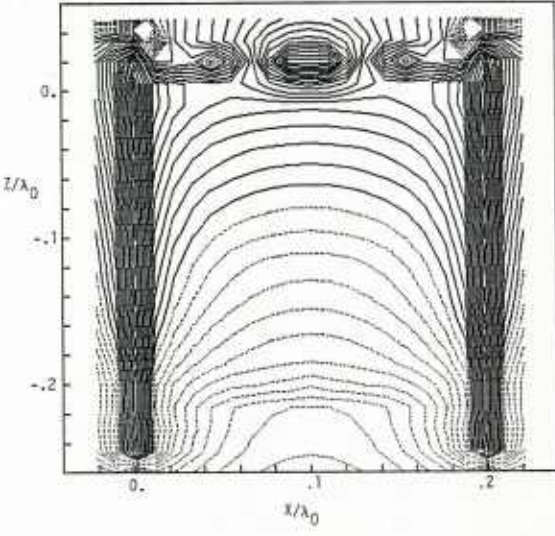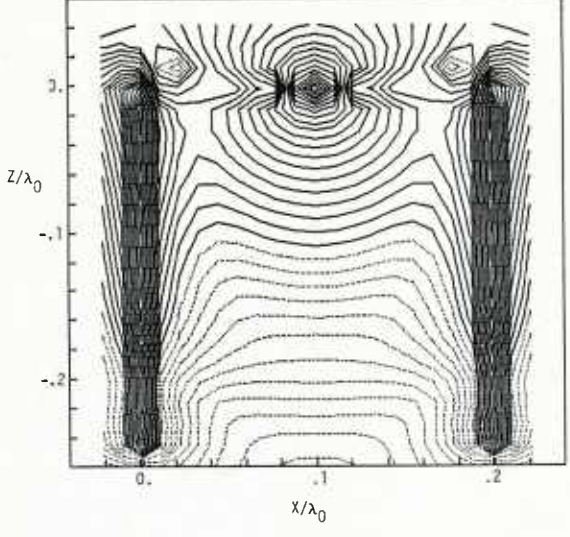
Figure 18. Contours of the magnitude of the horizontal component of electric field produced by a single-wire model of a Seige EMP Simulator. In (b) and (c) the source is $0.02\lambda_0$ above the interface and $\tilde{\epsilon}_-$ is $16 - j0$ in (b) and $16 - j16$ in (c). A standing wave is apparent for zero loss. In (d) the source is $10^{-3}\lambda_0$ below the interface and $\tilde{\epsilon}_-$ is $16 - j16$. The contour interval is 2dB in each case and the change from solid to dotted contours indicates the same field strength in each figure for a fixed voltage source.

c)

PART II
PERFORMANCE OF AN ARRAY OF VERTICAL DIPOLES
OVER A RADIAL WIRE GROUND SYSTEM*

1. INTRODUCTION

As noted in section 4.1.2 (Part I), the effects of ground screens have been extensively modeled using an effective surface impedance. This is an economical and convenient means of accounting for the combination of earth and wire radials, but is limited to situations where the grids are closely spaced (compared to the wavelength in the ground), i.e., dense grids. Thus, this technique compliments that described in Part I which considers sparce ground screens. As the more rigorous analysis of Part I becomes able to accommodate 100 radials or more, the surface impedance approach will provide a valuable check.

The specific problem studied here is the performance of an array of vertical dipoles (VEDs) over a radial wire ground system [1]. References to prior work using the surface impedance to represent the earth-radial wire combination are given in [2].

The behavior of a vertical array of antennas located over a ground system of arbitrary electrical characteristics has considerable practical significance. In HF communication and radar work, narrow beams are frequently produced by arrays. Narrow steerable beams are particularly important in HF over-the-horizon radar. The design of such arrays located over inhomogeneous ground systems is difficult and the literature on this subject is scant. It is complicated by the fact that the radiation field of a dipole located over such a ground is complex, difficult to evaluate, and also height-dependent. Thus, in effect, the problem is one of understanding the performance of an array of antennas of dissimilar radiation patterns. Here the performance of a vertical array of vertical electric dipoles (VEDs) over an inhomogeneous ground is considered. The ground properties are considered to be azimuthally symmetric but radially varying in an arbitrary manner. Recently, Teng and King [2] gave an integral formulation of the problem using the electromagnetic compensation theorem. This formulation is used here to numerically evaluate the radiation pattern of a VED located at an arbitrary height above the ground. The radiation pattern of a vertical array of 21 VEDs spaced 0.1 λ apart is studied using three different types of array excitation functions. One is the conventional equal-amplitude linear-phase excitation function suitable for arrays of identical radiators in free space or over a perfect ground. The second uses an excitation function which is the complex conjugate of the radiation field of each dipole in the direction of desired beam steering [3]. The third uses a sinusoidal amplitude excitation function with constant phase which is a special case of the complex conjugate excitation as will be shown later. The performance of the array for each type of excitation under different ground conditions is studied and observations are made on some general features of performance such as steering angle, beam size and shape, and sidelobe structure.

Use of the surface impedance and general techniques described here have also been applied to studying the radiation patterns of an HF vertical dipole near a sloping beach [4].

2. FORMULATION

In the past a number of approaches have been used to find the radiation field of a VED over an inhomogeneous ground [5-9]. The formulation used here is due to Teng and King [2] which is based on the electromagnetic compensation theorem. Details of the formulation are given in the reference cited above. However, for the sake of completeness, the basic steps are briefly summarized below.

2.1 THE INTEGRAL EQUATION

Figure 1 shows the geometry of the VED above the inhomogeneous ground which has a radially varying surface impedance in the region $0 < \rho < b$. An elemental VED with current moment $I_1 \ell_1$ is located at $\rho = 0$ and $z = h_1$. To find the magnetic field at P_2, a horizontal magnetic dipole (HMD) of moment $K_2 \ell_2$ located at ρ and $z = h_2$ is used as a test source. The $z = 0$ plane is the surface S and $z > 0$ is free space. The media for $z \leq 0$ determines the surface impedance profile,

$$Z_s'(\rho) = \eta_0 \Delta'(\rho), \tag{1}$$

where $\eta_0 = 120 \pi$, and the normalized surface impedance $\Delta'(\rho)$ varies radially in magnitude and/or argument, with no dependence on the azimuthal coordinate ϕ.

Let $\bar{E}_1$, $\bar{H}_1$, $\bar{E}_2$ and $\bar{H}_2$ be the electric and magnetic fields for the VED (source 1) and the HMD (source 2) when the medium for $z < 0$ is homogeneous with constant surface impedance $Z_s = \eta_0\Delta_1$. Also, let $\bar{E}_1'$ and $\bar{H}_1'$ be the unknown fields of the VED when the surface impedance is changed to $Z_s'(\rho)$. As the problem is TM to ρ and z, i.e., $\bar{H}_1' = \bar{a}_\phi H_{1\phi}'$, a ϕ-directed HMD test source is chosen to find $H_{1\phi}'$.

The electromagnetic compensation theorem first given by Monteath [10] and later generalized by Mittra [11] can be stated as

$$\int_S (\bar{E}_1' \times \bar{H}_2 - \bar{E}_2 \times \bar{H}_1') \cdot \hat{n}dS = \int_{R_2} [\bar{J}_2 \cdot (\bar{E}_1' - \bar{E}_1) - \bar{M}_2 \cdot (\bar{H}_1' - \bar{H}_1)]dV \qquad (2)$$

where the volume R_2 includes only source 2 and $\hat{n}$ is a unit vector normal to S. We invoke the surface impedance boundary conditions,

$$\hat{n} \times \bar{E}_1 = -\eta_0\Delta_1 H_{1\phi}\hat{a}_{1\phi} \quad \text{and} \quad \hat{n} \times \bar{E}_1' = -\eta_0\Delta'(\rho)H_{1\phi}'\hat{a}_{1\phi} \qquad (3)$$

in the unperturbed and perturbed cases respectively. In the present problem, $\bar{M}_2 = K_2\ell_2\delta(P-P_2)\hat{a}_{1\phi}$ and $\bar{J}_2 = 0$. Then, substituting (3) into (2) gives the basic working equation

$$H_{1\phi}'(\rho,h_1,h_2,\Delta') = H_{1\phi}(\rho,h_1,h_2,\Delta_1) +$$

$$+ \frac{\eta_0}{K_2\ell_2} \int_S (\Delta'(\rho_1)-\Delta_1)H_{1\phi}'(\rho_1,h_1,0,\Delta')[\hat{a}_{1\phi}\cdot\bar{H}_2]dS \quad . \qquad (4)$$

The general procedure for finding the radiation pattern using (4) is to first find the unknown field $H_{1\phi}'(\rho,h_1,0,\Delta')$ on S. This is accomplished by setting P_2 on S, and performing a stationary phase integration to reduce the resulting integral equation to one dimension. This yields a Volterra integral equation of the second kind which is solved for $H_{1\phi}'(\rho,h_1,0,\Delta')$. This result is then inserted back into (4) which is numerically integrated in two dimensions to find the radiation field $H_{1\phi}'(\rho,h_1,h_2,\Delta')$ far from the VED. The details of this procedure are summarized in the following.

The unknown field $H_{1\phi}'$ is cast into the form

$$H_{1\phi}'(\rho,h_1,h_2,\Delta') = H_{1\phi}(\rho,h_1,h_2,\Delta_1)F'(\rho,h_1,h_2,\Delta') \qquad (5)$$

where F' is an attenuation function in excess of that for propagation over Δ_1. Substituting (5) into (4) and using only the radiation terms for the fields $H_{1\phi}$ and $\bar{H}_2$ (e.g., see [12]) yields

$$F'(\rho,h_1,h_2,\Delta') = 1 + [\frac{jk}{2\pi H_{1\phi}(\rho,h_1,h_2,\Delta_1)}] \int_S (\Delta'(\rho_1)-\Delta_1) \frac{e^{-jkr_2}}{r_2} \cdot$$

$$[\frac{\sin(\phi_2)\cos(\alpha)}{\sin(\psi)+\Delta_1}] [\sin(\psi_2) + \Delta_1 F(\rho_2,h_2,0,\Delta_1)]H_{1\phi}(\rho_1,h_1,0,\Delta_1)F'(\rho_1,h_1,0,\Delta')dS,$$

where $\qquad (6)$

$$r_2 = (\rho_2^2+h_2^2)^{1/2}, \quad \rho_2 = [\rho^2+\rho_1^2 - 2\rho\rho_1 \cos(\phi_1)]^{1/2}, \quad \cos(\alpha) = (\rho_1^2+\rho_2^2-\rho^2)/(2\rho_1\rho_2),$$

$\sin(\psi_2) = h_2/r_2$, $\sin(\phi_2) = [\rho-\rho_1 \cos(\phi_1)]/\rho_2$ and the suppressed time factor is $e^{j\omega t}$. F is the Sommerfeld attenuation function and ϕ_1 is the angle between the x-axis and $\overline{OQ}$ $(= \rho_1)$, where Q is the integration point located on S. To solve (6), first put the HMD on the perturbed surface S by setting $h_2 = 0$. Then, (6) becomes a two-dimensional Fredholm integral equation of the second kind where the integration extends over the perturbed portion of S, i.e., where Δ' differs significantly from Δ_1. A stationary-

phase integration of the two-dimensional surface integration for $F'(\rho,h_1,0,\Delta')$ can be reduced to a one-dimensional Volterra integral equation of the second kind [2],

$$F'(\rho,h_1,0,\Delta') = 1 - \int_0^\rho F'(t,h_1,0,\Delta')g(\rho,t)\phi(\rho,t)dt \qquad (7)$$

where $\phi(\rho,t) = [t(\rho-t)]^{1/2}$ and

$$g(\rho,t) = (\frac{jk}{\pi})^{1/2} \frac{R^2}{\rho^{3/2}} \frac{(\Delta'(t)-\Delta_1)t^{5/2}}{(h_1^2+t^2)[t+(h_1^2+t^2)^{1/2}]^{1/2}} F(\rho-t,0,0,\Delta_1).$$

$$\frac{h_1+(h_1^2+t^2)^{1/2}\Delta_1 F(t,h_1,0,\Delta_1)}{h_1+R\Delta_1 F(\rho,h_1,0,\Delta_1)} \cdot \frac{h_1+R\Delta_1}{h_1+(h_1^2+t^2)^{1/2}\Delta_1} e^{jk[R-\rho+t-(h_1^2+t^2)^{1/2}]} \qquad (8)$$

Here, $R = (\rho^2+h_1^2)^{1/2}$ and $F(0,0,0,\Delta_1) = F(\rho,0,0,0) = F(t,0,0,0) =$

$F(\rho-t,0,0,0) \equiv 1$.

To obtain an approximate numerical solution of (7), the technique of product integration is used, e.g., the generalized trapezoidal rule [13]. Standard methods are not applicable due to the weak singularities $t^{-1/2}$ and $(\rho-t)^{-1/2}$ contained in $\phi(\rho,t)$.

Finally, the solution for $F'(\rho,h_1,0,\Delta')$ is inserted back into (6) to give $F'(\rho,h_1,h_2,\Delta')$ from which the radiation pattern can be found using (5) in (4). Note that the two-dimensional integration for $F'(\rho,h_1,h_2,\Delta')$ in (6) cannot be simplified with the stationary phase method unless $(h_1+h_2) << \rho$. Therefore, Pierce's [14] method over a planar annulus is used to perform a two-dimensional numerical integration of (6) over a perturbed circular region. Details of the numerical integration procedures using the product method and Pierce's method can be found in Teng [15] and Teng and King [2].

2.2 THE SURFACE IMPEDANCE

This formulation requires a knowledge of the normalized surface impedance of the ground. In addition to a uniform earth, the performance of arrays over a radial wire ground system is considered. The surface impedance of such a ground system is found by considering an elemental area to be locally equivalent to a parallel wire grid of spacing $d = 2\pi\rho/N$, where N is the number of radial wires and ρ is the distance from the center of the ground system. The method developed by Wait [16] for finding the surface impedance of a parallel wire grid over a homogeneous ground has been used. The details are given in Teng [15]. The combined effective surface impedance $Z'(\rho)$ is the parallel combination of Z_{grid}, the surface impedance of the parallel wire grid and Z_{ground}, the surface impedance of the homogeneous ground on which the grid is placed. Thus

$$Z'(\rho) = (Z_{grid} \cdot Z_{ground})/(Z_{grid} + Z_{ground}) \qquad (9)$$

where $Z_{ground} = \eta_0 \frac{k}{k'} C'$ \qquad (10)

and $Z_{grid} = j \frac{2\pi\rho}{N} \{\frac{\eta_0}{\lambda} [f_0 \ell n (\frac{\rho}{Nr_a}) + \Delta f] - jZ_i\}$ \qquad (11)

The various symbols are defined as follows:

$$f_0 = \frac{2C^2(C')^2}{C^2 + (C')^2 - (\frac{S}{k'})^2 \frac{[(k'C')^2 - (kC)^2]^2}{(k'C')^2 + (kC)^2}}$$

$$\Delta f = \sum_{m=1}^\infty (g_m - \frac{f_0}{m})$$

$$g_m = \frac{2C^2(C')^2}{[(C')^2 N_m + C^2 N'_m] - m^2 (\frac{S}{k'})^2 \frac{[(k'C')^2 - (kC)^2]^2}{[N_m(k'C')^2 - N'_m(kC)^2]}}$$

$S = \sin\Theta, \quad C = \cos\Theta$

$k = \omega(\mu_0 \epsilon_o)^{1/2}, \quad k' = \omega [\mu_0(\epsilon' - j\frac{\sigma'}{\omega})]^{1/2}$

$k'S' = kS, \quad C' = [1 - (S')^2]^{1/2}$

$N_m = [m^2 - (kC\frac{\rho}{N})^2]^{1/2}$

$N'_m = [m^2 - (k'C'\frac{\rho}{N})^2]^{1/2}$

$\eta_1 = [j\omega\mu_1/(\sigma_1 + j\omega\epsilon_1)]^{1/2}, \quad \gamma = [j\omega\mu_1(\sigma_1 + j\omega\epsilon_1)]^{1/2}$

$$z_i = \frac{\eta_1}{2\pi r_a} \frac{I_0(\gamma r_a)}{I_1(\gamma r_a)} = \text{Internal impedance of the wires} \tag{12}$$

I_0 and I_1 are the modified Bessel functions of the first kind and of order zero and one, respectively. The first 30 terms are adequate for the summation in Δf. The radius of each wire is r_a and Θ is the angle of incidence. The earth has electrical parameters μ_0, ϵ', and σ' and the wire has parameters μ_1, ϵ_1 and σ_1. For sufficiently high frequency such that $|\gamma r_a| \gg 1$, we can approximate z_i as

$$z_i \simeq (\frac{\omega\mu_1}{2\sigma_1})^{1/2} (\frac{1+j}{2\pi r_a}) \tag{13}$$

It is assumed that $r_a \ll d$, $|kcd| < 1$ and $|k'c'd| < 1$. The amplitude and phase of Δ' change with the angle of incidence Θ but the variation is small. With the help of these formulas the variation of $|\Delta'|$ with ρ under two different ground conditions is shown in Fig. 2. The radial wire ground system chosen throughout this paper has $N = 120$ wires of length $b = 2\lambda$ using AWG #6 copper wires ($r_a = 0.081$ in., $\sigma = 5.8 \times 10^{-7}$ S/m). An operating frequency of $f = 10$ MHz is assumed.

3. DIPOLE RADIATION PATTERNS

The influence of height on the radiation pattern of the VED is studied using the above formulation. Due to the finite conductivity of the ground, the radiated field $H'_{1\phi}$ is complex and both the amplitude and phase change with the height of the VED. This behavior is shown in Figs. 3 and 4. Five different ground situations are considered, namely, (a) a radial wire ground system on a well-conducting earth ($\epsilon_r = 15$, $\sigma = 10^{-2}$ S/m), (b) a similar ground system on a poorly-conducting earth ($\epsilon_r = 5$, $\sigma = 10^{-4}$ S/m), (c) a perfectly-conducting disc of radius 2λ over poorly-conducting ground as in (b) above, (d) a homogeneous poorly-conducting ground as in (b) with no ground system, and, (e) a perfectly conducting plane.

In general, raising the height of the dipole results in the appearance of an increased number of sidelobes while at the same time the main beam becomes narrower and gets closer to the ground. The phase increases continuously with elevation angle for dipole heights greater than 0.5λ. As the dipole height is increased, the phase change with elevation angle becomes larger until at a height of $h_1 = 2\lambda$ the phase changes through almost two complete cycles. This continuous change of phase is a direct consequence of the finite conductivity of the ground system. Radiation fields

of dipoles in free space or over perfectly conducting ground do not show a continuous phase change with elevation angle. The phase is either 0° or 180°. The phase behavior over dissipative ground is the principal difficulty in the choice of an appropriate excitation function for an array of dipoles over such a ground. A study of Fig. 4 shows that no unique phasing function for all types of grounds can be chosen for an array of dipoles which will guarantee beam steering in a particular direction.

4. ARRAY RADIATION PATTERNS

We now study the behavior of a vertical array of VEDs over a dissipative inhomogeneous ground. For this study we have considered an array of 21 dipoles uniformly spaced 0.1 λ apart with a total array height of 2 λ. The problem of choosing an appropriate excitation function for beam steering for such an array has not received much attention in the literature. FitzGerell et al. [17] have considered a vertical array of horizontally polarized antennas and have demonstrated the usefulness of a sinusoidal excitation function to achieve low-angle steering. The complex conjugate excitation function excites each element with a current which is the complex conjugate of the field produced by that element in the desired beam direction. In the case of a perfectly conducting ground, this field varies sinusoidally with the height of the dipole, so the sinusoidal illumination function is a special case of the complex conjugate excitation function.

In general, let $H_n(\theta)$ be the radiation field of the nth dipole located at height h_n. Here θ is the elevation angle. With an excitation function $W_n(\theta_0)$ suitable for producing the main beam in the direction θ_0, the array radiation pattern becomes

$$H(\theta) = \sum_{n=0}^{N-1} W_n(\theta_0) H_n(\theta) \tag{14}$$

Note that $H_n(\theta)$ is complex, and implicitly contains the phase due to the height h_n of the dipole above the ground. The conventional linear phase excitation function for a phased array is

$$W_n(\theta_0) = \exp(-j\beta h_n \sin\theta_0) \tag{15}$$

which is appropriate for an array of identical radiators in free space. If the dipoles are located over a perfectly conducting ground so that true images are formed, then [3]

$$W_n(\theta_0) = \cos(\beta h_n \sin\theta_0) \tag{16}$$

which is the sinusoidal excitation function. The complex conjugate excitation function is the choice

$$W_n(\theta_0) = H_n^*(\theta_0) \tag{17}$$

4.1 EFFECTS OF EXCITATION FUNCTION

The array radiation pattern has been studied using these three types of excitation functions and the five different ground conditions mentioned in section 3. The results are shown in Figs. 5 (low-angle steering) and 6 (high-angle steering). For low-angle steering it is seen that the complex conjugate excitation function generally produces a narrower beam as well as smaller sidelobes than the conventional excitation. Also, the actual direction of the main beam maximum agrees best with the design steering angle for the conjugate excitation (also see Table 1). Sinusoidal excitation produces distorted beam shapes as well as high sidelobes.

For high-angle steering (Fig. 6), we see that the agreement between main beam direction and steering angle is best for conjugate and sinusoidal than for the conventional excitations. For all ground systems considered, this conclusion holds. Also, the beam shapes are better and the beamwidth is narrower for the conjugate and sinusoidal excitations. Sinusoidal excitation provides the lowest sidelobe levels for high-angle steering.

It is not possible to effectively steer the beam to elevation angles higher than about 75° without creating major undesired sidelobes, or lower than about 9°, irrespective of the type of excitation function used. Finally, conjugate and sinusoidal excitations provide a larger beam steering range than does conventional excitation.

4.2 EFFECT OF GROUND SYSTEM

The type of ground system used has an influence on the width, shape, and pointing angle of the main beam at both low and high steering angles. Figure 7 illustrates this effect for the case when the complex conjugate excitation function set for steering angles of 10° and 70° is used. Similar figures drawn for other steering angles show that for low-angle steering, lower conductivity earth with or without a ground system produces a narrower beam than higher conductivity earth. Table 1 compares the pointing angles and beamwidths for various ground systems for two types of excitation. The lower limit for beam steering is about 9° for all the ground systems considered. The presence of a radial wire ground system does not improve the low-angle performance of the array. However, when the array is excited to steer the beam to high elevation angles, the presence of the radial wire ground system markedly reduces the beamwidth. Also, it brings the actual main beam closer to the steering angle chosen for the excitation function. A ground system consisting of a large number of radial wires (approaching the perfectly conducting disc ground system) gives the best beam performance at high elevation angles. These effects are functions of the radius of ground systems used [15]. Again, the beam cannot be effectively steered beyond 75° elevation without creating objectionable sidelobes, irrespective of the excitation function or the type of ground system used.

5. DISCUSSION

A study of the radiation pattern of a VED over an inhomogeneous ground system reveals that it is a function of both the height of the VED above the ground and the properties of the ground. The radiated field is in general complex and both the magnitude and phase change with height and ground properties. Thus, the design of a vertical array of VEDs over an inhomogeneous ground system is analogous to the design of an array of dissimilar antennas. Classical excitation to achieve a desired steering angle is not applicable. We have studied the behavior of the array pattern using complex conjugate and sinusoidal excitation functions and have compared the results with those for the conventional phased array excitation. For a variety of ground systems considered, both the complex conjugate and the sinusoidal excitations produce better results at high-steering angles than does conventional excitation. The performance improvement is with respect to the beam shape, beamwidth, sidelobe level, and agreement between desired and actual directions of the main beam.

It is found that over ground conditions usually encountered in practice, it is impossible to steer the beam to very low or very high elevation angles. For a 21 element array of height 2 λ, the steering limits are roughly 9° and 75°. For such an array it is found that for low elevation angles the type of ground system used has very little influence on the main beam. However, the performance is better over dry, poorly-conducting earth ($\epsilon_r = 5$, $\sigma = 10^{-4}$ S/m) than a moist, well-conducting earth ($\epsilon_r = 15$, $\sigma = 10^{-2}$ S/m). For high elevation angles a good ground system with a large number of radial wires improves the performance considerably.

The basic constituent of this preliminary study is the availability of a formulation to evaluate the fields of a VED above an azimuthally symmetric inhomogeneous ground. The complex conjugate excitation function is derived from this formulation. If ground conditions are such that the actual radiation pattern of a VED for various heights cannot be evaluated, the complex conjugate excitation function cannot be determined. In such a case, a sinusoidal excitation function appears to be a better choice than the conventional excitation.

The problem of designing an excitation function to synthesize a given beam pattern is, in general, very difficult. However, it is possible to synthesize a beam with specified nulls and/or specified (complex) radiation fields at various elevation angles. The excitation function for achieving such a beam is obtained by solving a set of equations generated from (14), viz.,

$$H(\theta_i) = \sum_{n=0}^{N-1} W_n H_n(\theta_i), \qquad i = 1,2,\ldots,m \tag{18}$$

where the array pattern $H(\theta_i)$ is specified for m elevation angles. Since H, W_n and H_n are complex, one needs 2N constraints on $H(\theta)$ (i.e., m = 2N) to determine the excitation function uniquely. However, for a given set of constraints, one can determine an excitation function W_n which will (a) satisfy the constraints if m < 2N, and (b) produce a best fit to the specifications if m > 2N. But in terms of the general problem of an antenna array design, the specifications are usually in terms of beamwidth, pointing angle, beam shape, sidelobe level, sidelobe locations, and null locations. Most of these parameters are explicit and, hence, not easily usable in solving for the excitation function W_n from (18). Thus, the design of antenna arrays over inhomogeneous ground systems needs further detailed investigation.

REFERENCES

1. R. J. King and N. C. Mathur, "Performance of an array of vertical dipoles over an inhomogeneous ground system," _Electromagnetics_, 1983 (in press).

2. Teng, C. J. and R. J. King, "Surface fields and radiation patterns of a vertical electric dipole over a radial-wire ground system," _Electromagnetics_ $\underline{1}$(1), 1981, pp. 101-116.

3. Waldman, A., "Elevation steering of the pattern of a vertical array of vertically polarized elements over a ground screen," _IEEE Trans. on Antennas and Propagation_ AP-18(1), 1970, pp. 105-107.

4. K. S. Park and R. J. King, "Radiation Patterns of an HF Vertical Dipole Near a Sloping Beach," _Electromagnetics_ $\underline{2}$, 1982, pp. 129-145.

5. Hufford, G. A., "An integral equation approach to the problem of wave propagation over an irregular terrain," _Quart. J. Appl. Math_ $\underline{9}$(4), 1952, pp. 391-404.

6. Wait, J. R. and K. Spies, "On the radiation from a vertical dipole with an inductive wire-grid ground system," _IEEE Trans. on Antennas and Propagation_, AP-18(4), 1970, pp. 558-560.

7. de Jong, G., "Electromagnetic wave propagation over an inhomogeneous flat earth (two-dimensional integral equation formulation)," _Radio Sci._ $\underline{10}$(12), 1975, pp. 925-933.

8. Rafuse, R. P. and J. Ruze, "Low-angle radiation from vertically polarized antennas over radially heterogeneous flat ground," _Radio Sci._ $\underline{10}$(12), 1975, pp. 1011-1018.

9. Balanis, C. A. and D. DeCarlo, "Monopole antenna patterns on finite size composite ground planes," _IEEE Trans. on Antennas and Propagation_ AP-30(4), 1982, pp. 764-768.

10. Monteath, G. D., "Application of compensation theorem to certain radiation and propagation problems," _Proc. Inst. Elec. Eng._ $\underline{98}$, Pt IV, 1951, pp. 23-31.

11. Mittra, R., "A vector form of compensation theorem and its application to boundary value problems," AFCRL 75, University of Colorado, Boulder, 1961.

12. King, R. J., "Electromagnetic wave propagation over a constant impedance plane," _Radio Sci._ $\underline{4}$(3), 1969, pp. 356-374.

13. Linz, P., "Numerical method for Volterra integral equation with singular kernels," _SIAM J. Numerical Analysis_ $\underline{6}$(3), 1969, pp. 356-374.

14. Pierce, W. H., "Numerical integration over the planar annulus," _J. Soc. Indus. Appl. Math._ $\underline{5}$(2), 1957, pp. 66-73.

15. Teng, C., _Ground Wave Propagation and Radiation Patterns of a Vertical Electric Dipole over a Radially Varying Surface Impedance Plane_, Ph.D. Thesis, University of Wisconsin-Madison, Madison, WI, 1978.

16. Wait, J. R., _Electromagnetic Waves in Stratified Media_, Pergamon Press, NY, 1962.

17. FitzGerrel, R. G., A. C. Wilson, L. L. Proctor, and H. V. Cottony, "An HF array antenna electronically scanned in elevation," _IEEE Trans. on Antennas and Propagation_ AP-15(6), 1967, pp. 758-766.

Table 1

Effect of Ground System and Excitation Function on Low-angle Steering

Actual Main Beam Pointing Angle (Deg)

Design Steering Angle (Deg)	1 a	1 b	2 a	2 b	3 a	3 b	4 a	4 b	5 a	5 b
0	8	9	9	8	9	8	9	8	0	0
2	8	9	9	8	9	8	9	8	0	0
4	8	9	9	8	9	8	9	8	0	0
6	9	10	9	9	10	9	9	8	0	0
8	10	11	10	9	10	9	10	9	0	0
10	11	12	10	9	10	9	10	9	0	9
12	12	14	10	10	11	10	10	9	0	14
14	14	15	11	11	12	11	11	10	0	16
16	15	16	13	13	15	14	13	12	17	17
18	16	17	17	18	18	18	18	17	17	17
20	17	19	19	20	20	20	20	20	17	18

Half-Power Beamwidth (Deg)

Design Steering Angle (Deg)	1 a	1 b	2 a	2 b	3 a	3 b	4 a	4 b	5 a	5 b
0	11.2	16.0	10.5	10.5	10.8	10.8	10.9	10.5	--	--
2	12.6	16.0	10.9	10.7	11.2	10.8	11.1	10.5	--	--
4	14.0	16.2	11.5	10.8	12.0	11.0	11.8	10.7	--	--
6	15.0	17.0	12.0	11.2	12.9	11.2	12.6	11.0	--	--
8	16.5	17.5	13.0	11.2	14.0	11.8	13.8	11.4	--	--
10	17.5	17.5	14.2	12.0	15.8	12.7	14.5	12.0	--	--
12	18.3	18.4	16.4	14.0	17.5	14.7	17.9	13.8	--	18.6
14	18.9	18.1	18.5	16.8	19.5	17.0	20.2	16.8	--	12.2
16	19.3	18.7	21.0	19.8	21.2	19.2	22.8	21.0	--	12.0
18	20.2	19.0	22.5	21.0	22.0	19.8	24.0	23.2	16.4	12.1
20	21.5	19.5	23.0	20.5	22.0	18.5	25.0	24.7	16.0	12.9

Ground Systems: (1) $\epsilon_r = 15$, $\sigma = 10^{-2}$ with radial wires, (2) $\epsilon_r = 5$, $\sigma = 10^{-4}$ with radial wires

(3) $\epsilon_r = 5$, $\sigma = 10^{-4}$ with disc, (4) $\epsilon_r = 5$, $\sigma = 10^{-4}$ homogeneous ground,

(5) perfectly conducting homogeneous ground.

Excitations: (a) Conventional, (b) Complex Conjugate
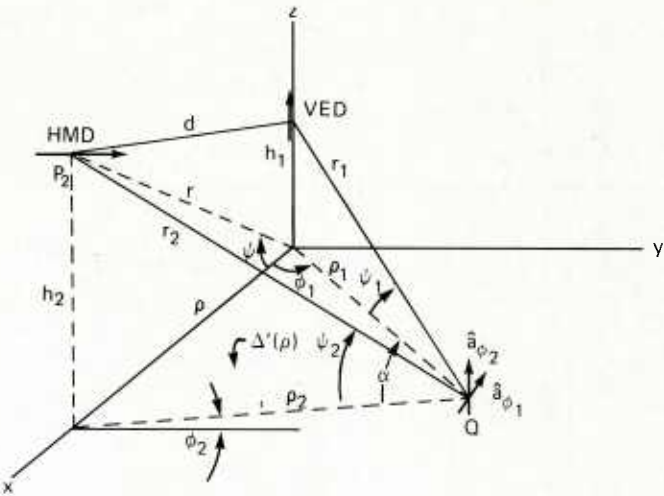
Fig. 1. Geometry of a VED over an azimuth-
ally symmetric ground having surface imped-
ance $Z_s'(\rho) = \eta_o \Delta'(\rho)$. The HMD is a test
source for measuring $H_{1\phi}'$.
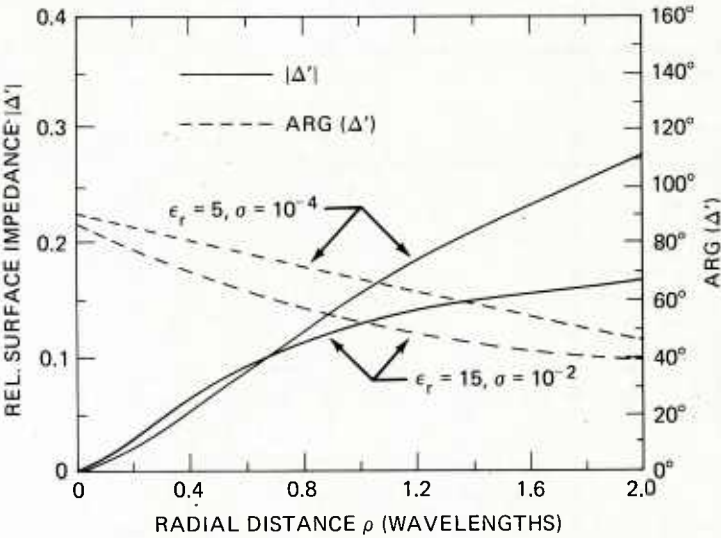
Fig. 2. Magnitude and Phase of $\Delta'(\rho)$ for a
radial wire ground system (N = 120) on well-
and poorly-conducting earth. f = 10 MHz.
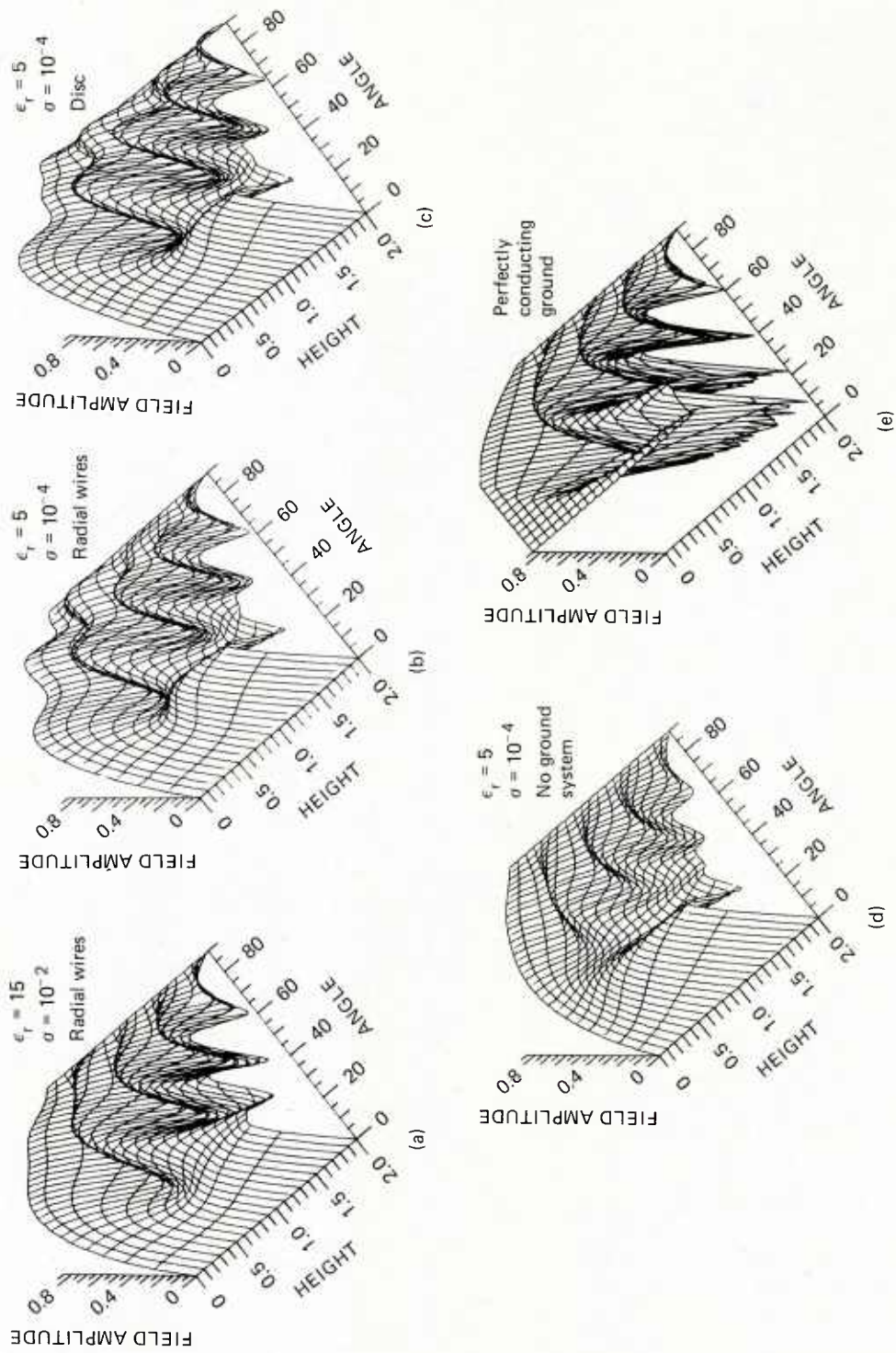
Fig. 3. Radiation pattern amplitude of a VED over various ground systems as a function of height, h_1. $f = 10$ MHz.
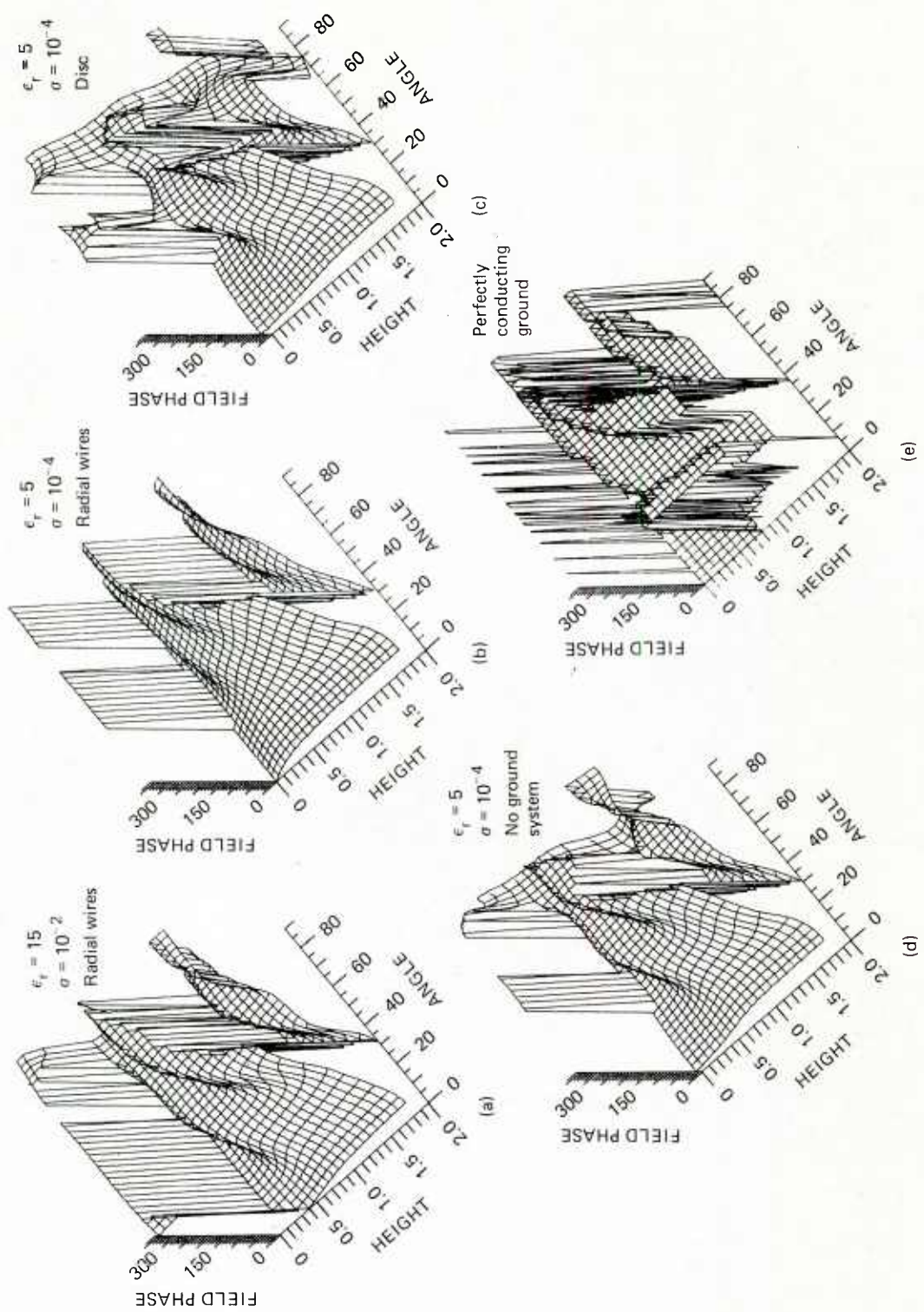
Fig. 4. Radiation pattern phase of a VED over various ground systems as a function of height, h_1. $f = 10$ MHz.
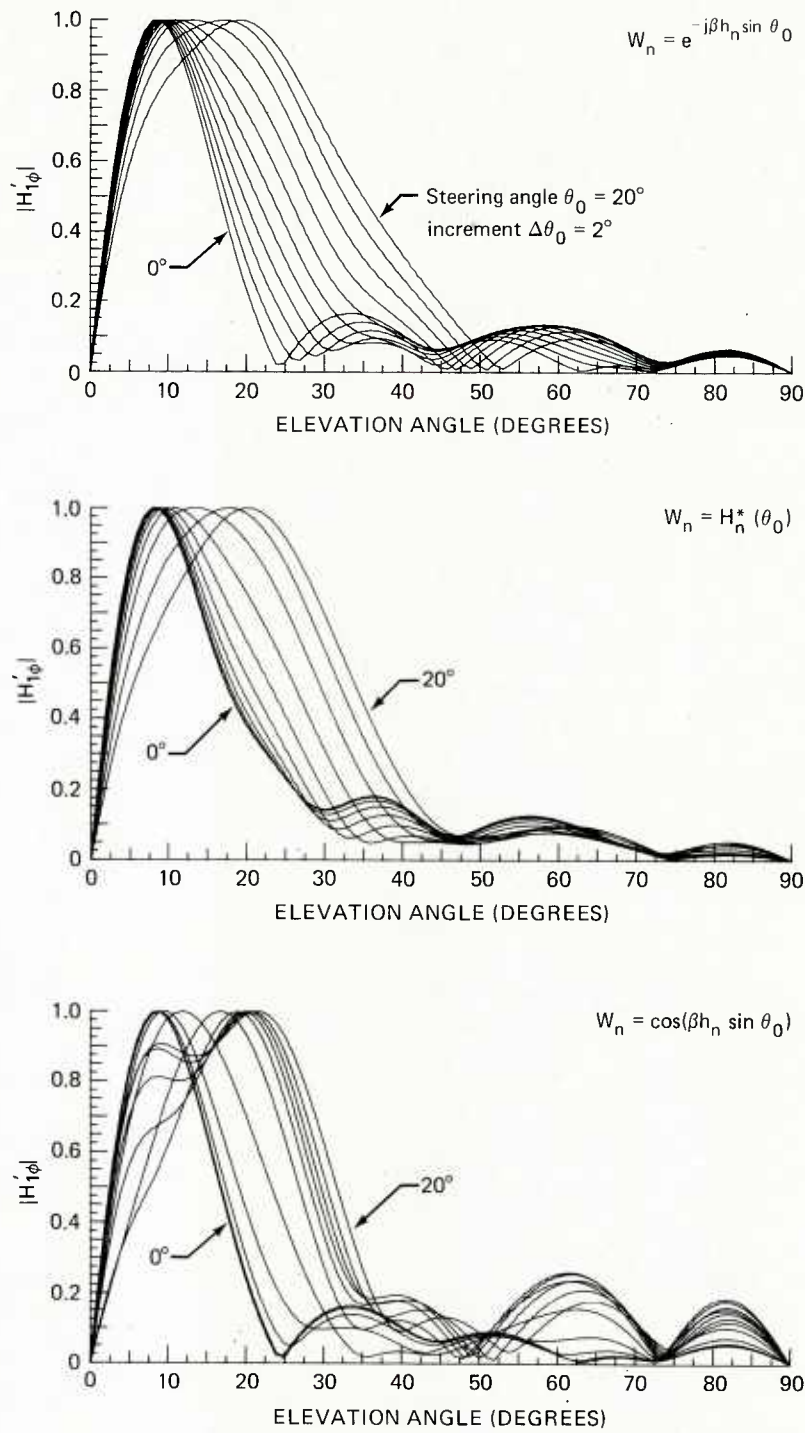
Fig. 5. Low-angle steered radiation patterns for a stacked array of VEDs centered on a radial wire ground system (N = 120, b = 2 λ) lying on poor, earth (ε_r = 5, σ = 10^{-4} S/m). f = 10 MHz.

Excitations: (a) conventional
(b) complex conjugate
(c) sinusoidal

Fig. 6. Steered radiation patterns for a stacked array of VEDs centered on a radial wire ground system ($N = 120$, $b = 2\lambda$) lying on poor earth ($\varepsilon_r = 5$, $\sigma = 10^{-4}$ S/m). $f = 10$ MHz.

Excitations: (a) conventional
(b) complex conjugate
(c) sinusoidal
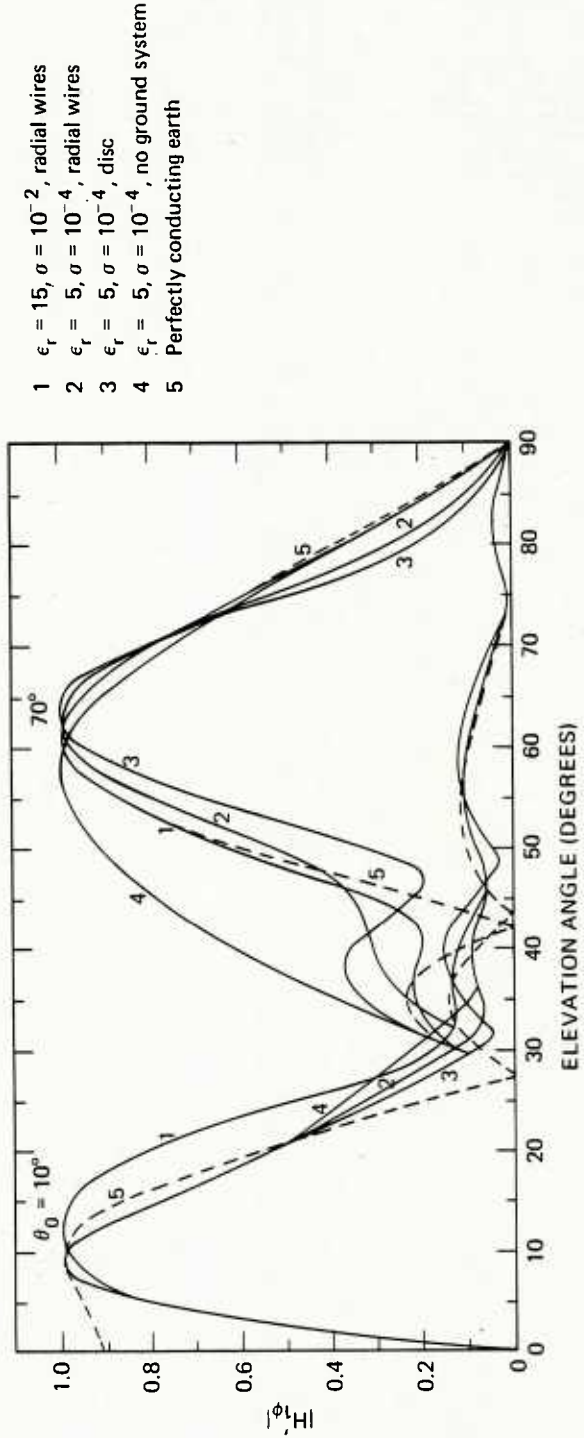
Figure 7. Low-angle (10°) and high-angle (70°) steered radiation patterns for a stacked array of VEDs on different grounds, using a conjugate excitation function. f = 10 MHz.

NUMERICAL MODELLING METHODS FOR PREDICTING ANTENNA PERFORMANCE ON AIRCRAFT

by

Stanley J. Kubina

Department of Electrical Engineering
Concordia University/Loyola Campus
7141 Sherbrooke St. W.,
Montreal, Quebec, Canada
H4B 1R6

Summary

This paper examines typical case studies that involve the application of Moment Methods to the prediction of the radiation characteristics of antennas in the HF frequency band. The examples consist of the analysis of a shorted transmission line HF antenna on a CHSS-2/Sea King helicopter, wire antennas on the CP-140/Aurora patrol aircraft and a long dipole antenna on the Space Shuttle Orbiter spacecraft. In each of these cases the guide-lines for antenna modelling by the use of the program called the Numerical Electromagnetic Code are progressively applied and results are compared to measurements made by the use of scale-model techniques. In complex examples of this type it is shown that comparisons based on individual radiation patterns are insufficient for the validation of computer models. A volumetric method of radiation pattern comparison is used that is based on criteria that result from pattern integration and that are related to communication system performance. This is supplemented by hidden-surface displays of an entire set of conical radiation patterns resulting from measurements and computations. Antenna coupling considerations are discussed for the case of the dual HF installation on the CP-140/Aurora aircraft.

The methodology of Electromagnetic Compatibility (EMC) analysis of aircraft antenna systems is summarized. An example of these high frequency GTD techniques is given with special emphasis on a computer program called Aircraft-inter-Antenna Propagation with Graphics (AAPG) that uses interactive computer graphics techniques to simplify this complex analytical task.

Preface

The powerful computer techniques that are described by Dr. Miller [1] are attractive to aerospace antenna engineers and system analysts because they offer the possibility of obtaining radiation characteristics of antennas quickly for arbitrary locations in the complex geometrical environments of helicopter, aircraft and spacecraft structures. He has realistically addressed the problem of validation of computer codes and presented the guidelines for their application in the derivation of wire-grid and surface patch models. This paper presents a user's viewpoint on the application of the low-frequency Moment Method [2] for the prediction of radiation patterns of high frequency (HF) antennas operating in the 2-30MHz range and on the application of the Geometric Theory of Diffraction (GTD) techniques for the prediction of antenna-to-antenna coupling that are used in aircraft intrasystem analysis.

Three case studies are presented that deal with the application of the computer program called the Numerical Electromagnetic Code (NEC) [3] to the modelling of an HF loop antenna on a large Sikorsky CHSS-2/Sea King helicopter, HF wire antennas on a Lockheed P-3C airframe and of a dipole on the Space Shuttle orbiter spacecraft. In the first two cases, both simple and complex wire grid models are used. Simple models have been used sometime ago [4] and examples of more complex models have been summarized by Miller and Deadrick [5]. However, in the examples presented in this paper, the results of wire-grid modelling are compared more exhaustively with the results of measurements to the degree that would be necessary for avionic system performance analysis. Both vertical and horizontal polarization field components are compared with each of these normalized to a common isotropic reference level in the computed as well as the measured results. Liberal use of illustrations is intended to emphasize the problem of bandwidth or frequency range of validity of models for systems that span several octaves. With the consequent accumulation of a massive amount of data, the user's dilemma in judging a model's adequacy is highlighted. Judicious use of system performance criteria, that use volumetric pattern integration, is offered as a practical solution that helps the discrimination process in model development, while providing simultaneously, an indication of system performance. This approach is similar to some of the self-validation techniques suggested by Dr. Miller [1] for the validation of the computer codes themselves.

The computer-generated illustrations are also intended to suggest that such use of computer graphics is invaluable for the development of the user's insight into the computer modelling process itself. In particular, the plots of computed current distributions on a dual antenna installation provide the basis for the analysis of the coupling between these systems.

The prediction of the interaction of systems on modern aircraft with many systems and often with one hundred antennas or more is a complex task for which a specialized computer-based Electromagnetic Compatibility (EMC) methodology has been developed. This field has been the subject of a separate AGARD lecture series [6]. One of the available codes, the

Intrasystem Electromagnetic Compatibility Analysis Program (IEMCAP) uses detailed modelling of system elements including antennas and cables, as well as the various mechanisms of electromagnetic transfer between them. Antenna-to-antenna coupling analysis can be carried out expeditiously by a more recent computer code called Aircraft-inter-Antenna Propagation with Graphics (AAPG) that has been specifically designed for interactive use on a mini-computer (or micro) with a graphics terminal. More extensive descriptions of this code and its use are presented elsewhere [7,8]. A summary and a typical example of coupling path analysis and its use for antenna relocation studies are given as a conclusion to this paper.

Theoretical Summary

The illustrations that follow show that the complex bodies being modelled are replaced by an equivalent grid of wires for which the NEC program computes the currents that result from the applied source excitation. The distribution of RF current must satisfy the boundary condition that the axial component of the electric field must be zero everywhere along each wire. In receiving and scattering problems, the source field is an incoming plane wave and the value of the source field is non-zero at every point on each one of the wires. In the transmit mode, the user specifies a voltage excitation at the feed point of the antenna, which is translated to a non-zero source field over a short segment of wire across the feed point, and a zero excitation elsewhere on the antenna. Dr. Miller discusses [1] the additional excitations that are available.

In the wire-grid models used with NEC, the user can either describe the model as consisting of segments of appropriate length ($\sim.1$ wavelength) or he can specify the model in terms of individual wires that must be further subdivided into segments of the required length. This latter approach produces a shorter input data set. Thus as the user specifies, the NEC program subdivides wire #k into N_k segments of equal length and assumes that the current on each segment has the functional form,

$$I_k(s') = A_{kj} + B_{kj} \sin\beta (s'-s_j) + C_{kj} \cos\beta (s'-s_j) \qquad ...(1)$$

where,

s' is the distance along the wire segment,
s_j is the center of segment #j,
β is the wave number,
A_{kj} B_{kj} C_{kj} are the set of $3N_k$ unknown complex current coefficients for wire #k.

If there are N_w wires making up the model, then the total number of unknown coefficients is:

$$3N_T = \sum_{k=1}^{N_w} 3N_k \qquad \qquad ......(2)$$

or three times the total number of segments

The secondary field from wire #k can be expressed as the Pocklington form of the integral of the (unknown) induced current on wire #k. The total secondary field is the sum of integrals for all the wires. At any point on any of the wires, the axial component of this secondary field plus the axial component of the excitation field must equal to zero. Thus,

$$\sum_{\substack{k=1 \\ \text{all} \\ \text{wires}}}^{N_w} \frac{-j\eta}{4\pi\beta} \int_{\substack{\text{wire} \\ \#k}} I_k(s')(\beta^2 \hat{s}.\hat{s}' - \frac{\partial^2}{\partial s \partial s'}) G(\bar{r},\bar{r}') ds' = -\hat{s}.\bar{E}^I(\bar{r}) \qquad ...(3)$$

where,

$\hat{s}'$ is the axial unit vector for wire #k,

$\bar{r}'$ is the position vector of point s' on wire #k,

$\bar{r}$ is the position vector of the observation point on one of the wires,

$\hat{s}$ is the axial unit vector for the wire of the observation point,
s is a 'distance along the wire' variable for that wire,

$G(\bar{r},\bar{r}')$ is the appropriate kernel function,

E^I is the source field

η is the characteristic impedance

and other terms are as defined in equation (1).

This integral must be solved for the values of the unknown current coefficients in the current function $I_k(s')$.

The values of these coefficients are found by enforcing junction constraints at the

boundary between each segment and the adjacent segments on the same wire, between segments on different wires that are adjacent to wire junctions and by the boundary conditions expressed in equation (3).

The current and charge density constraints at junctions are as follows. Within wire #k, the coefficients A_{kj}, B_{kj}, C_{kj} and $A_{k, j+1}$ and $B_{k, j+1}$ and $C_{k, j+1}$ are constrained such that moving across the segment boundary from segment #j to segment #j+1, the current is continuous and also the charge density (which is proportional to the derivative of the current) is continuous. This generates two equations for each segment boundary, or $2(N_k-1)$ equations for the wire. At a junction of "n" wires, relationships are enforced among the coefficients on the segments making up the junction such that Kirchoff's Current Law holds. In addition, in the NEC program, the King-Wu charge density constraint [9] is imposed. This relates the charge density on any wire to the charge density on any wire at the junction point, and has the form,

$$\psi_1 \rho_1 = \psi_2 \rho_2 = \psi_3 \rho_3 = \ldots = \psi_n \rho_n \qquad \ldots\ldots(4)$$

where,

ρ_1, ρ_2, ρ_3, ... are charge densities on the various wires at the junction, evaluated at the junction point, and

ψ is a radius dependent weighting factor

given by:

$$\psi = 2 \left[\ln\left(\frac{2}{\beta a}\right) - \gamma\right] \qquad \ldots\ldots(5)$$

where,

γ is Euler's constant and has the value 0.5772 and 'a' is the wire radius.

One KCL equation plus (n-1) charge density equations give total of "n" equations for a junction of "n" wires. At a free end, the current and charge densities are related, giving one equation for each free wire in the computer model. The set of segment boundary equations plus junction equations plus free end equations is a set of exactly $2N_T$ linear equations. A further set of N_T linear equations are needed to solve for the values of the $3N_T$ unknown coefficients.

These additional linear equations are found by the "Moment Method" by enforcing Pocklington's Equation at a set of N_T distinct points on the wires. Thus, equation (3) is "point matched" at the center of each segment. The complete set of $3N_T$ equations never has to be explicitly assembled or stored in computer memory, because the junction relationships are implicitly imposed in the course of constructing the point matching equations. The result is a set of only N_T linear equations which can be solved for N_T of the coefficients by the Gauss-Doolittle method. The remainder of the coefficients are explicitly found by substitution into the junction relationships.

Once the current coefficients are known, the current is tabulated at the center of each segment on each of the wires of the model. This tabulation can be used to plot the current on each wire of the model, and as noted above, such plots lend insight into the radiation behaviour of the model. The radiation patterns of the antenna are obtained by numerical integration of the RF current distribution on the model, and are presented in tabular form in the output of the NEC code. In the illustrations that follow, computer graphics is used to automatically plot the patterns directly from NEC output files and from files of digitized measurement data.

Miller [1], Miller and Deadrick [5] and the NEC manual [3] have summarized the guidelines for wire grid model development. In practice shorter segments than the usual one-tenth of the wavelength, are necessary near the source for an accurate model of the feed region. The restriction on the relative length of segments that form a junction, requires that these lengths be comparable within a factor of say five. Usually some wires in the model must be very short, and this calls for short segments on any wire that makes a junction with the short wire. Limits on wire radius are dictated by the validity of the integration techniques used in conjunction with Pocklington's Equation. At the high end when large radii are desirable for purposes of 'electromagnetic equivalence', the wire radius should not exceed the requirements of the "thin wire kernel" which is based on a uniformly distributed, axially directed current density around the periphery of the wire. This permissible diameter is of the order of one-fifteenth of a wavelength. Thus the ratio of segment length to its diameter must be maintained at ten or greater for the "thin wire" assumption to hold. NEC also has an "extended kernel" (or EK) option which calls for additional integration around the periphery of the wire. In this case this ratio can be as small as two, with some increase in execution time. The examples in this paper, for purposes of pattern computation alone, sometimes encroach on these limits with consequent noticeable degradation in modelling accuracy.

System Performance Criteria

In the early era of development of HF antennas for aircraft, Granger [10] proposed an antenna radiation pattern parameter called radiation pattern efficiency, η_p. This parameter had been obtained by analyzing the energy distribution requirements of HF antennas for long distance communication on transport aircraft. It is defined as the ratio of power radiated in both E_θ and E_ϕ in the solid angle between $\theta=60°$ and $\theta=120°$ to the total power radiated by the antenna. The standard coordinate reference system is shown in Fig.1 Thus,

$$\eta_p = \frac{\int_0^{2\pi} \int_{60}^{120} (|E_\theta|^2 + |E_\phi|^2)\, \sin\theta\, d\theta\, d\phi}{\int_0^{2\pi} \int_0^{\pi} (|E_\theta|^2 + |E_\phi|^2\, \sin\theta\, d\theta\, d\phi} \qquad \ldots\ldots (6)$$

For purposes of the ground-wave mode of propagation, it is desirable to maximize the radiated power in the vertical component E_θ. Thus an additional assessment parameter can be defined [11] that involves the ratio of the power radiated in the vertical component E_θ to the total power radiated by the antenna. It is usually denoted as "percent E-theta", $\%E_\theta$. Thus,

$$\%E_\theta = \frac{\int_0^{2\pi} \int_0^{\pi} |E_\theta|^2\, \sin\theta\, d\theta\, d\phi}{\int_0^{2\pi} \int_0^{\pi} (|E_\theta|^2 + |E_\phi|^2)\, \sin\theta\, d\theta\, d\phi} \qquad \ldots\ldots (7)$$

More directly related to the ground wave communications mode on an operational basis [12], allowing for say helicopter manoeuvring limits, is a modification of the '$\%E_\theta$' parameter, denoted as "useful percent E_θ" or $\%E_\theta^*$. This is the ratio of the power contained in E_θ between $\theta=60°$ and $\theta=120°$ to the total power radiated by the antenna, or

$$\%E_\theta^* = \frac{\int_0^{2\pi} \int_{60}^{120} |E_\theta|^2\, \sin\theta\, d\phi\, d\theta}{\int_0^{2\pi} \int_0^{\pi} (|E_\theta|^2 + |E_\phi|^2)\, \sin\theta\, d\theta\, d\phi} \qquad \ldots\ldots (8)$$

It is difficult to judge the superiority of one model over another based on individual, say azimuth plane radiation patterns at a single frequency. When examined over a considerable frequency range, the individual variations make the assessment confusing indeed. Fortuitously, the computation of the performance parameters provides single number values, that when plotted versus frequency simplify the comparison while providing meaningful numbers in the system sense. Philosophically this approach has its parallel in the power integration methods mentioned by Dr. Miller [1] for computer code validation purposes. At the EMC Laboratory of Concordia, an auxiliary computer program (ISOLEV) has been used to compute these parameters for both computed and measured patterns and it is used routinely in the "post-processing" of NEC output files in order to have these parameters available for comparison purposes. As will be seen from the illustrations, plots of these parameters are also supplemented by hidden surface plots of the entire set of radiation pattern conical cuts at the θ values that have been standardized [11] for purposes of calculating η_p.

Case Study No. 1: HF Loop Antenna on the CHSS-2/Sea King Helicopter

Introduction

Larger long-range helicopters operating at low altitudes like the CHSS-2/Sea King have a requirement for HF communications. Due to the limited length of the airframe and its irregular geometry compared to a fixed-wing aircraft, wire antennas do not offer an elegant installation design. Recently, shorted transmission line or "loop" antennas have been evaluated. Due to the nature of their impedance at low frequencies (inductive), they can be tuned with higher efficiency than open-circuited fixed wire antennas by commercial couplers designed for shunt-fed or "notch" antennas. The installation shown in Fig. 2 was tested on an operational helicopter by the Canadian Defences Forces some time ago, and formed a relevant example for numerical modelling. The particular location on the aircraft is a convenient rather than an optimized one because it coincides with the location of the feedpoint for an existing wire antenna. The installation of the tuning unit inside the aircraft involves a minimum relocation of existing equipment.

The theoretical evaluation of the radiation patterns of this type of antenna formed the master's thesis of Mr. Youssef Bahsoun [13]. It consisted of both experimental measurements and computer modelling. The experimental measurements were conducted using a 1/24-scale model with a self-contained tunable battery-powered miniature oscillator. The measurements were carried out [14] on the radiation pattern range of the National Research Council of Canada (NRCC) in Ottawa. One very useful feature of this program was the automatic generation of patterns in digital form while the conventional analog polar plots were being made. The computer modelling portion of the work examined approaches to wire-grid model topology by identifying ways to optimize and authenticate each topology variant.

This paper describes the results of simple model optimization studies and of a specific example of a more authentic complex model. This latter model was designed at RAE Farnborough [15]. The sharing by RAE of the associated description data set led to an interesting comparison of computations at different laboratories by different computer programs. The results presented here emphasize the importance of the resonance region of the model in defining model characteristics. With both models it was clear that their optimization could not be based on separate radiation patterns alone but rather performance criteria more completely related to three-dimensional (volumetric) pattern coverage.

Optimization of a Simple Model

Fig. 3a) shows the simple or 'stick' model of the Sea King helicopter. The fuselage is modelled by a single wire at its center line. The drive shaft of the main rotor blades, the sponsons, and the loop antenna located on the port side, are connected to the main fuselage wire. This makes the drive shaft wire segment 1.8m in length. The rotor blades are shown in the forward position (i.e., rotor aligned with forward part of fuselage). The tail rotor blades have been omitted for simplicity. The total number of segments making up this stick model is 78. The model is excited by a voltage source applied to wire 23 as shown in the figure. This model was first tested with a uniform radius of 0.1m at frequencies between 2.6 and 14MHz. This gave a minimum ratio of segment length to radius of 8 which dictated the use of the extended kernel in NEC. This option was in fact used throughout for the results presented herein.

The computed radiation patterns of the simple model with uniform radius showed some agreement with measured patterns at 2.6 and 4.1MHz, very good agreement at 6.0MHz and relatively poor agreement at 8.1MHz and higher. The difficulty in judging agreement of single patterns led to the examination of the computed and measured curves of $\%E_\theta$ vs. frequency as shown in Fig. 4. A parametric study of $\%E_\theta$ vs. fuselage radius at 2.6MHz established 0.3m as the desirable fuselage radius. However, with this radius the outer portion of the loop is too close to the fuselage. This manifested itself in a distortion of the E_ϕ polarization of the port side. By varying the spacing of the outer loop wire segment while noting the ratio of measured and computed E_ϕ values on the port side, an optimum wire spacing (1.2m) was established. The radius of the antenna itself was also reduced to 0.01m to coincide with its actual physical size. The model geometry is shown in Fig. 3b) where the actual radii are evident.

The results of the optimization at 2.6MHz generally apply at other frequencies. Note the close agreement of $\%E_\theta$ values shown in Fig. 5. The details of typically good results are shown in Fig. 6a) where both shape and relative magnitudes are reproduced. Fig. 6b) shows the azimuth plane results at 8.1MHz. Here although the lobe structure is similar, the locations of the nulls and maxima leave something to be desired. This particular frequency corresponds to half-wave resonance of a path from the tip of the rotor blade, along the fuselage and terminating at the rear tip of the helicopter. Better agreement would result if the path length of the computer model agreed with the actual physical path length. Such agreement in fact was corroborated in experiments with the complex model.

'Tuning' of the Complex Model

The complex model, shown in Fig. 7 was carefully derived at the Royal Aircraft Establishment (RAE), Farnborough for the study of HF wire and loop antennas. The fuselage is modelled by ten interconnected and equally spaced vertical hexagonal or octagonal sections, depending on their position along the fuselage. The nose of the helicopter is formed by joining the vertices of the front hexagon to the forward point of the model. The sponsons are modelled by a number of wires, reasonably approximating the sponsons of the actual helicopter. The tail of the helicopter is made up of two parallel wires. The tail and main rotor blades are represented by single wires. The drive shaft is a single wire joined to the corresponding section of the fuselage. The model is excited by a voltage source applied to wire No.1 as shown in the figure. The total number of segments is 335. All lengths are less than one tenth of a wavelength at 20MHz. A uniform radius of 0.1m is used for all wires except that the antenna wire radius is 0.01m.

This model was also analyzed at frequencies between 2.6 and 14MHz inclusive. The results for $\%E_\theta$ vs. frequency are shown in Fig. 8. Fig. 9 shows the azimuth patterns at 2.6, 4.1, 6.0 and 8.1MHz compared with measured results. Again the shapes as well as the relative magnitudes of E_θ and E_ϕ are produced except that there is a pronounced shift of the four-lobed E_ϕ pattern at 8.1MHz.

Two distinct investigations were carried out in order to better understand the discrepancy at 8.1MHz. In order to make sure that the solution was not contaminated by currents associated with internal resonance modes [16], the extended boundary condition was applied — six diagonal elements were inserted between diametrically opposite fuselage nodes to assure a zero field internally. No significant change in the solution values was obtained. Subsequently when the pattern was computed at nearby frequencies, it was found that best agreement was obtained at 7.8MHz, indicating a longer resonant path on the computer model than on the measurement model.

A corresponding adjustment in resonant path length was most readily carried out by shortening the rotor blades by 0.4m to achieve resonance at 8.1MHz. This resonance was verified by examining the current distribution along the blades and fuselage. Fig. 10 shows the azimuth pattern at 8.1MHz for the adjusted geometry. Note now the agreement in pattern levels and orientation. The computed %E_θ also rose to 53%, i.e., within 7% of the measured %E_θ. This agreement is also noted for example, in the total set of E_ϕ conical patterns that are shown in Fig. 11 as hidden surface plots of the measured and computed patterns.

Summary Comments

The application of available guidelines, coupled with parametric studies based on performance parameters (%E_θ) and select pattern characteristics can lead to simple models which are good indicators of antenna performance.

The detailed pattern agreement with more complex models is superior to that obtained with simple models, but at frequencies of airframe path length resource, frequency perturbation studies are necessary to identifiy and adjust resonant path lengths in the model topology. The extent of agreement thus obtained with 'tuned' models is then sufficient for the use of these models in antenna location and rotor modulation studies.

Case Study No. 2: HF Antennas on the CP-140/Aurora Patrol Aircraft

Preamble

The CP-140/Aurora,Canada's modern long range patrol aircraft is used for ASW, coastal and arctic patrol. Its counterpart in use by the U.S. Navy and other nations is called the P-3C Orion. This specific airframe dates back to the days of the Lockheed 'Electra', but the complement of avionic equipment has been up-dated many times as has the antenna installation. Figure 12 illustrates the many antennas that are on such an aircraft. The dual HF installation provides an important long-range communication capability. The antennas for this purpose remain the classic wire antennas that were introduced on earlier versions of this airframe. The requirement for simultaneous HF service (SIMOP) and the use of 1 KW transmitters require that the mutual coupling characteristics of the antennas be well known. The radiation patterns of similar antennas had been measured by Lockheed on scale-models some time ago [17] and no new measurements were undertaken as part of the development of the Canadian configuration. It was seen in Case Study No.1 that a complete radiation pattern set of principal plane and conical cuts is desirable. Such a complete data set was not available, but a partial conical set was available for an older HF antenna geometry [17] and a less complete set on the exact CP-140 configuration of Figure 12. Whereas in the helicopter shorted transmission line antenna case, the patterns were available in digitized form, the patterns for the CP-140 were in the classic analog polar plot form. This required their manual digitization (via digitizing tablet) in order to generate the useful digital data base that is used to create the illustrations that follow.

The computer modelling of this HF installation is of interest in itself and for the further development and testing of the modelling methodology because a useful measurement data set exists for validation purposes. It also has practical importance because validated computer models can be used to fill gaps in the measured pattern and coupling data. In addition results can be used for the computation of near fields that are useful for the assessment of hazards to personnel and for the assessment of the total electromagnetic environment.

It is not 'a priori' evident whether there is a single best model topology that could produce acceptable results over the total HF frequency band, 2-30 MHz. Although the use of simple models has been reported some time ago [4], the degree of agreement and the bandwidth of this agreement with measurement results is somewhat limited. Models of simple topology are attractive because they are easy to generate and inexpensive in terms of CPU time. This paper describes the results obtained by using a simple 'stick' model (74 segments) as well as a more complex model (327 segments) of the CP-140 aircraft. It will be seen that except for some anomalies, the main pattern characteristics are reproduced by the simple model over an extensive frequency range (2-20MHz). The complex model, however, produces the degree of agreement that is required for system range analysis.

Simple 'Stick' Models

Chronologically, in the work at Concordia, experimentation with simple 'stick' models was directed to the modelling of the older P-3C configuration [17] consisting of very similar port and starboard antennas. Each had a feed-point at STA 452 and approximately 23 inches off the centerline. Both antennas are about 67 ft. The port antenna terminates on the vertical stabilizer at VSS 191 and the starboard antenna terminates on the vertical stabilizer at VSS 129. The CP-140 configuration has antennas of more dissimilar lengths. The port antenna (HF1) has a feed point at STA 411., BL 28L, and is attached to an insulator at VSS 191. It is approximately 64 ft. long. The starboard antenna (HF2) originates at STA 715, BL 57 R, and terminates in an insulator near the same vertical stabilizer station (Fig. 12). It is 48 ft. long. The open ends of the antennas are separated by virtue of the V-connection of insulators at the stabilizer attachment point. It is commonly assumed that patterns of wire antennas will have similar pattern characteristics. It is always of interest however to identify the degree of similarity and to note the differences.

Experimenters who use data sets generated elsewhere and long ago often are led to question the details of the measurement. In the case of the P-3C installation [17], it was not known whether the antennas were measured singly or with the passive antenna installed and shorted or installed and terminated in 50 ohms. It is logical to assume of course that the second antenna was installed. Nevertheless, without the possibility of corroboration, all possibilities must be considered. When numerical modelling results disagree, it is difficult to identify the reasons for the disagreement.

Fig. 13 shows the stick model that was used for the P-3C installation. It has single wires for the fuselage, wings, horizontal and vertical stabilizers. In this model these wires are located along the center line of these surfaces. The model consists of 74 segments. Initially the radius of each segment was selected to be 0.1m. This is called the 'thin' simple model. It satisfies the criteria with regard to segment length to radius, ratio over the entire frequency range 2-30MHz. The segment lengths at 2MHz range from $.01\lambda$ to $.013\lambda$. The shortest segment is the feed element $(.002\lambda)$.

Fig. 14 shows representative results with this model at 2,4 and 6MHz for the port antenna. The principal plane patterns at 4 and 6 MHz agree in their main features but the relative E_θ and E_ϕ levels differ from the experimental results. At 2MHz there is a serious difference in the pattern tilt angle (E_θ) for the $\phi = 0°$ pattern. Differences of this type lead to an examination of possible parameters or topology that should be varied. It is rather surprising how many variations of these one can identify for such a simple topology.

In earlier work, the isoperimetric inequalities [18, 19] were found to be a useful guide in the choice of wire radii. Thus, the 'fat' simple model was tried. Here the radius was selected so that the model would have the same surface area. The graphics of Fig. 15 illustrates the result. It is obvious that the segment/radius criterion must be kept in mind. The lowest value is 1 and strains the limits of the 'EK' option of NEC that was used. Fig. 16 shows the principal plane patterns at 2,4 and 6MHz. The agreement is superior to that obtained with the 'thin' model. In particular, the tilt angle, of E_θ for $\phi=0°$ agrees much better with the measured value. These models were executed at 2MHz intervals to 12MHz, but at these other frequencies, the principal plane patterns on the average, had similar degrees of agreement. In Case No.1 above, the performance parameters such as $\%E_\theta$ were found to be better overall indicators of agreement. Experimental values of $\%E_\theta$ were available. Fig. 17 shows $\%E_\theta$ vs. frequency for the 'thin' (Model 2G) and 'fat' (Model 2H) models. It shows that the results of the 'fat' model track the experimental values better.

At this stage of the work, more experimental results for the CP-140 became available and it was decided to concentrate on this configuration rather than on one that is primarily of historical interest.

CP-140/Aurora Configuration - Simple Model

The Aurora model geometry is shown in Fig. 18. Because of the results noted above only a 'fat' model has been used. This model was executed at generally 2MHz increments through 30MHz. Fig. 19 shows the principal plane patterns at 2 and 6 MHz. Measured data were not available at 4MHz. The agreement is similar to that discussed above except for the port antenna at 2MHz. Note the tilt angle discrepancy. The more complete comparison of pattern shape is in the hidden surface display of Fig. 20. Note the location of maxima and minima. It can be seen once more that the comparison of individual patterns is difficult and often confusing.

Curiously enough, this simple model maintained fair agreement through the higher frequency range. An example of this can be seen in Fig. 21 at 24MHz. It was observed however that the computed results at 22MHz, shown in Fig. 22 agreed better with the measured results at 24MHz. This suggests a lengths difference in some fundamental current modes between the simple model and the aircraft. Using the complex model as a reference, the comparison of Table 2-1 shows indeed that this is so. It is seen that paths 1,2,3 and 5 are longer on the simple model. For optimization of simple models, the topology could be adjusted to bring about closer agreement. It will be considered at a later stage in the

present modelling program. It should be noted that the calcuation of impedance involves
additional guidelines [3]. In work reported elsewhere [20], the application of these
guidelines, as, to radius jumps at junctions and finer segmentation near the feed point were
indeed found necessary. In the calculations with these simple models it was found that
the computed impedance was negative for the starboard antenna at 2MHz. Reducing the radius
difference at the antenna junction produced positive values of impedance and generally
improved the agreement of the pattern results. An example of this is shown in the principal
plane results of Fig. 33. These are for the case of the radius of the fuselage reduced
by 50% from the previous 'fat' model. The improvement of the agreement is also evident
in the hidden surface plots of Fig. 24. This is for the starboard antenna. No such
positive improvement is obtained for the port antenna. Other parametric studies are now
being done in parallel with the development of a more complex model. When anomalies of
the type described occur with simple models, there is a tendency to progressively increase
the complexity of the model by inserting elements that would support other current modes.
In the case of the investigation of the CP-140 it was decided to develop a model that would
implement the guidelines more completely as well as having more representative path lengths.

Complex Model - CP-140/Aurora Configuration

Fig. 25 shows a 3-dimensional view of a 327 segment model. The main portion of the
fuselage has an octogonal section, (i.e. 8 longitudinal wires) with two upper longitudinal
wires arranged to coincide with the lateral location of the feedpoints of the two antennas.
The wing and stabilizer segmentation is such that wire lengths are .2λ in both directions
at 30MHz. The M.A.D. boom on the tail remains a single wire. Radii have been selected
to produce the equivalent surface area in the computer model. Thus radii are tapered on
the wing and stabilizer surfaces as well as the non-uniform portion of the fuselage.
Noting Dr. Miller's evaluation of computational effort [1], it takes more than 100 times
the processing time of the simple model to execute the complex model (in fact the ratio
is 750 secs to 60 secs → CYBER 174). Thus experimentation with complex models is generally
expensive in computer installations where computing time must be paid for in real currency.
Complex models also require a great deal of care in their development to forestall simple
but subtle errors in dimensions, wire overlap etc. This particular model was generated
from two-dimensional drawings via a digitizing tablet by a computer-aided design system
called DIDEC: Digitize, Display, Edit and Convert. A set of vertices and wires is
generated, simultaneously displayed, edited as necessary and finally converted to the in-
put data format of the NEC code. Reflection of surfaces and attachment of one section
to another are some of the features allowed in this CORE [21] graphics-based software.
Colour displays allow for colour coding of wires as to length or diameter in order to keep
the user aware of the guidelines and equivalences as he develops the model. By the time
a complex model is ready for execution the anticipation of the results is keen, especially
in cases such as these where anomalies are noted with the simple models. Another program
called CHECK verifies the extent to which the model conforms to the guidelines on segment
length, radius and interconnection. A typical output is shown in Table 2-2. It can be
seen that some parts of the model violate some criteria at 30MHz. How much better do we
expect the results to be? Over what frequency range?

The radiation patterns at 2 and 6MHz are shown in Fig 26. The agreement is exceptionaly
good for both HF1 and HF2. Note this is a linear scale. Patterns agree in shape, relative
values of E_θ vs. E_ϕ and with relation to the isotropic level. The anomaly in pattern tilt
at 2MHz does not appear! Fig. 27 shows similar results for 10, 15 and 20MHz and Fig. 28
shows the principal plane patterns for 24 and 30MHz. The entire set of radiation patterns
is displayed at 2 and 20MHz in the hidden surface plots of Fig. 29. The graph %E_θ vs.
frequency in Fig. 30 also shows that these values track the experimental ones fairly well.
No special attempt has yet been made to optimize this model for impedance calculation
purposes. The plot of impedance vs. frequency shown in Fig. 31 shows that some optimization
would be necessary when it is important to have reliable impedance values. This will be
one of the next steps in this model development.

Coupling Considerations

The process of trying to establish whether old measurements were done with one or
two antennas in place provides one example of coupling interactions. What is the effect
on the pattern of one antenna of the adjacent parasitic one? Calculations using NEC with
one and two antennas in place readily provide the answer. In addition, the examination
of the current distributions obtained as a solution in the two cases produces a good
appreciation of inter-antenna coupling.

Fig. 32 shows the principal plane patterns for the port antenna alone at 2MHz. Com-
parison with the patterns of Fig. 14 shows substantial pattern differences. An appre-
ciation of the reason for such differences can be obtained from an examination of the
current distributions of Fig. 33. Here we see that the addition of the second antenna
brings about an increase in the current on the driven antenna itself as well as a sub-
stantial current on the passive antenna. Thus the installation of the second antenna is
expected to produce an impedance change in the driven antenna at some frequencies in
addition to the pattern change. The induced current at the terminals of the passive
antenna will produce a terminal voltage that might be high enough to produce interference
(even with the passive antenna tuned to a different frequency) or damage the input stage
of the receiver. Input stage protection is necessary on the CP-140. Evaluation of
these effects is important to successful SIMOP operation and they are usually measured

in the development of a new installation. Fig. 34 shows a typical isolation curve from a set that had been generated for an installation similar to the CP-140. Although theoretically, it is possible to generate equivalent data with NEC, insufficient experience is available at present to judge its cost-effectiveness. Of course NEC computations can be done at any point of a development program whereas measurements of this type must be done on large scale models or the actual aircraft.

NEC can also produce explicit coupling computations [3]. The maximum coupling between any two segments (terminals) of a model can be computed. The simple model was used to compute a limited frequency sweep of coupling for the CP-140 configuration. This is an indication of "worst-case coupling" between the two antennas. The results are plotted on the measured isolation curve of Figure 34. A broader approach to EMC considerations for antennas is presented in the concluding portion of this paper. The coupling calculation can and was done simultaneously with pattern calculations.

Case Study No. 3: WISP/HF Antenna on the Space Shuttle

An Experimental Dilemma

Introduction

The Waves in Space or WISP project is a Canadian scientific mission for upper ionosphere exploration by means of an instrumented package operating from one of the cargo pallets on the orbiter spacecraft. The mission and configuration are more completely described in Dr. Balmain's paper [22]. The WISP antenna aboard the space shuttle orbiter consists of a dipole (intended to be of variable length) oriented on a port-to-starboard axis and it is fed from its pallet by a two wire transmission line. The frequency of operation can range from low kHz to 30MHz. The radiation patterns of the antenna must be known at all frequencies of the experiment and for all dipole lengths so that the scientists can fully understand the meaning of the data that will be gathered. To this end a combined experimental and numerical modelling program was organized that would supply the antenna characteristics. Scale-model (1/72) pattern measurements are being carried out on the pattern range of the National Research Council of Canada (NRCC) while concurrently computer modelling is underway at the EMC Laboratory of Concordia University. This example reports the results that are now available at 10MHz. These results illustrate progressively how the pattern of the dipole is altered by its feedline, its support pallet and finally by the entire orbiter structure. Although this in itself is instructive, in this program the experimenters at NRCC encountered a problem with balanced output from the miniaturized source used within the scale model. This brought about an interesting interplay of experimental and computer modelling in order to establish the approximate degree of unbalance. Correlation between measurement and computation brought about a special appreciation of this unusual problem and its consequences. The work to be described was carried out primarily by Dr. C.W. Trueman of Concordia University and his research assistants [23].

Antenna and Orbiter Model Development

Fig. 35a) shows the full scale dimensions of the dipole that is used at 10MHz. Fig. 35b) shows the reference co-ordinate system. At this frequency the dipole is about 0.2λ in length. For computation, nine segments are used on each arm. The radius of the wires is 0.0571 meters, full scale. Fig. 36 shows the principal plane radiation patterns for this 5.36m dipole alone at 10MHz. The patterns are shown normalized to the 0dB isotropic reference level. The patterns are oriented to coincide with the dipole's intended location on the shuttle craft and thus represent the reference pattern that the scientists would normally expect. Note the polarization purity and the sharpness of nulls.

The feedline shown in Fig. 35 carries balanced currents on the two wires. The electric field radiated by each wire of the feedline exactly cancels that of the other wire in the pitch plane ($\phi=0$). In the other planes, the 0.46 meter separation of the two wires introduces a phase shift in the field radiated by each wire that manifests itself in a non-zero far field for the feedline. Thus the feedline radiates an E_θ-component in both the roll ($\phi=90°$) and yaw ($\theta=90°$) planes. The feedline was modelled using 8 segments on each wire as shown in Fig. 37. This figure also shows the principal plane patterns of the dipole and feedline combination at 10MHz. Note the presence of the cross-polarized component in the yaw-plane pattern and the filling-in of the nulls of the dipole's pattern in the roll-plane pattern.

The cargo-bay pallet surface was modelled by several topologies, some including radial wires at the junction of the transmission line. However, the simple grid shown in Fig. 38 was found to give the same results as the others. This procedure is a self-consistency approach alluded to by Dr. Miller. The radii of the wires are such that the total surface area of the wires roughly equals the area of the pallet surface. This condition resulted in a radius of 0.14m. Note that this is approximately twice the radius of the feedline wires. Fig. 38 also shows the resulting principal plane patterns at 10MHz. The currents induced on the pallet surface fill in the nulls in the yaw-plane E_θ polarization. The level

of the cross-polarized component is raised by about 2dB. There is no change in the pitch-plane pattern because of the symmetry of current flow about the $\phi=0$ plane. In the roll-plane pattern, the pallet adds a cross-polarized component, about 25dB down from the main polarization and the nulls in the E_θ pattern are filled in by additional 2dB.

The derivation of the data set describing the physical dimensions of the orbiter was not easy. It finally resulted from the combination of data from another investigator (Ron Jenetzke, University of Chicago) and from dimensions and details on commercially

available 1/72 scale plastic models. An initial model of considerable complexity was systematically thinned approximately 40% to produce the model of 675 segments shown in Fig. 39. This "electrically equivalent" model represents the wings and stabilizer surface by a single plane of wires along the center line of these surfaces. The cargo bay doors are represented by a simple V-mesh. The engines are represented by single wires. The cargo bay floor and sides are rectangular meshes. The radii were chosen so that for one-sided surfaces, the surface area of the wires equals the surface area of the surface being represented for each of two perpendicular directions of current flow. This produced a radius of 0.28m for the wires of the fuselage. For two-sided surfaces (wings, stabilizer), the surface area was equated to the total area of both surfaces for each perpendicular direction of current flow. This resulted in a radius of 0.58m for the wires of the wing and 0.40m for those of the vertical stabilizer.

The 675 segment model required 6,276 seconds of CPU time on the Concordia CYBER 174. The resultant radiation patterns are shown in Fig. 40. In the yaw-plane pattern, a strong cross-polarized component is added, the nulls are filled-in and the principal polarization radiates less energy aft of the orbiter. This distribution is confirmed by the pitch-plane pattern which shows reduced fields both below and aft of the orbiter as a shading effect of the wings and tail surfaces. No cross-polarized component is introduced in the $\phi=0°$ pattern. The roll-plane pattern shows a strong cross-polarized component and the nulls in the principal polarization are shifted upward. Thus the main change consists of an increase in cross-polarized components and the shadowing aft and below, by the shuttle craft structure.

This series represents a classic example of pattern changes brought about by the component parts of the antenna's installation environment. Are these patterns validated by comparison with experimental measurements? Such a direct comparison was thwarted by the unusual problem of source balance that in turn produced a new use of computer modelling to corroborate the degree of this experimental problem.

Comparison and Matching of NRCC Measured Patterns

The NRCC measurements were carried out using a 1/72 scale factor model sprayed with conductive paint. A miniature, battery-operated and tunable oscillator was mounted within the model and carefully tuned to the scale frequency of 720MHz. Because commercial baluns were too large to fit within the orbiter body, an improvised coil coupling arrangement was tried to produce a balanced output from the unbalanced source. An unknown amount of unbalance was suspected. Fig. 41 shows the measured principal plane patterns corresponding to the full-scale frequency of 10MHz. The comparison with Fig. 40 shows that the measured patterns show a strong cross-polarized component in the pitch-plane and the cross-polarized components in the roll and yaw-planes do not resemble the "figure eight" patterns of the computation set. No immediate possibility existed for any serious improvement in the experimental arrangement and the results by implication, cast some doubt about the computer model.

Experimenting with unbalanced excitation of the computer model corroborated the increase of cross-polarized components and an appreciation of the resulting current flow asymmetry. A 20% imbalance (i.e., driving the feedline with 0.4 volt and 0.5 volt generators) produced the patterns of Fig. 42. Note the agreement now with the main pattern features. The cross-polarized components are comparable as is the filling-in of the nulls. The degree of similarity in these results is in fact surprising, considering that the unbalance in the feeding of the measurement model could include a phase as well as an amplitude difference, whereas the 20% unbalance in the computer model is an amplitude difference only.

This modelling investigation is now continuing with image plane techniques being used for the experimental work. The computations and measurements are being done at the high end (30MHz) of the expected experimental frequency range and nearby pallet configurations are being included for an assessment of their possible perturbing effect.

EMC Analysis: Antenna-to-Antenna Coupling

Methodology of Intrasystem EMC Analysis

Intrasystem compatibility involves the satisfactory functioning of different avionic subsystems or equipments within a major system of describable geometry such as a single aircraft, spacecraft or ground station. Undesired intrasystem coupling mechanisms arise from antenna-to-antenna, wire-to-wire, case-to-case, electromagnetic field to wire or case and common mode coupling. The ensemble can be considered to be a collection of emitters and receptors of electromagnetic energy, joined by the intentional and unintentional coupling paths. As outlined by Spina [24], the total set of interactions can be visualized as forming an Interference Interaction Sample Space as shown in Fig. 43. In this matrix of interactions between emittors and receptors, each entry T_{ij} represents the level present

at the ith receptor due to the jth emitter. The objective of EMC analysis is to identify those elements of the matrix which can result in an incompatibility, rank them as to severity in preparation for the consideration of corrective measures. Under the Intrasystem Analysis Program, the U.S. Airforce at the Rome Air Development Center has been sponsoring the development of computer techniques that are designed to make the analysis of the multitude of interactions an organized process. In particular, the Intrasystem Electromagnetic Compatibility Analysis Program (IEMCAP)[25] is designed to provide the

prediction of the T_{ij} entries by means of a frequency domain analysis that includes most of the possible coupling modes. The details of modelling emitter/receptor and filter spectra plus the coupling models are discussed by Capraro [25]. However, this comprehensive program is designed for operation in a "batch" computer mode and the user must be prepared to spend considerable time in the preparation and validation of input data and the examination of its most extensive printed output.

For the examination of antenna-to-antenna coupling alone, the Aircraft inter Antenna Propagation with Graphics (AAPG) program that has recently become available, provides a more responsive instrument for the analysis of this particular coupling mode. In the modelling of antenna characteristics, the aircraft structure and the coupling path, AAPG uses formulations similar to IEMCAP but the path computation algorithms are entirely different. Among its main advantages are its interactive mode and the ready availability of integrated displays of input and output data.

Antenna System Analysis with AAPG

By the nature of the models that are used, EMC analysis has less accuracy than the computer modelling techniques that have been discussed previously. The results are nonetheless important because of the need to identify potential incompatibilities as early as possible in an aircraft system development program and because of serious operational implications, the predictions should be conservative or fail-safe.

The transfer function T_{ij} that is computed by AAPG is called the narrowband EMI margin. It is computed as:

$$EM = P_j + TFS + SF - CL_j - CL_i - SR_i$$

where,

EM	=	EMI margin at receptor "i" due to emittor "j", dB
P_j	=	Emittor power level, dBm
TFS	=	Free space propagation factor (loss-Friis) for the emitter/receptor antenna pair being analyzed, dB
SF	=	Shading factor (loss) due to edge diffraction or creeping wave geodesic path loss over the fuselage for the emitter/receptor antenna pair, dB
CL_j, CL_i	=	Emittor and receptor cable for filter losses, dB
SR_i	=	Receptor sensitivity threshold power level, dB_m

The terms TFS, SF and CL_j and CL_i comprise the total coupling path loss $\overline{t_{ij}}$ (f) that is considered in AAPG. The aircraft model that is used has a cylinder/cone combination for the fuselage and thin planes for the wing and stabilizer surfaces as shown in the illustrations that follow. The coupling path used in these calculations can be a composite one of straight line segments, cylindrical and conical spirals, and edge diffracted rays [26]. The edge diffraction loss is based on the scalar Keller diffraction coefficient [26] and the creeping wave loss is based on an approximation derived by Hasserjian and Ishimaru [26,27]. The path computation algorithms select the path with the minimum transfer loss.

·The narrowband EMI margin applies only where there is frequency coincidence between emittors and receptors. For purposes of this computation, emittors are modelled as having a specified power level over the operating frequency band, specified fall-off beyond this at out-of-band 'skirting' frequencies and specified or default values of harmonic power levels. Emittors are modelled as having a specified power threshold level in the operating frequency band and specified fall-off in sensitivity at skirt frequencies. It is intended that spurious response be modelled by defining additional receivers (receptors) with appropriate response characteristics.

Antennas are described by a simple two-level model having a fixed main beam gain over a specified angular region in space and a fixed side lobe level over the remaining angles. This is illustrated below.

The user prepares a data set (card or disk file) that specifies the aircraft model, the antenna types, location and characteristics, and the associated emitter and receptor characteristics plus the associated cable or filter losses in a format required by AAPG. He specifies this as a file name for AAPG execution. The AAPG code was designed specifically for operation on a PDP-11 minicomputer with an RT-11 operating system and PLOT10 software driving a Tektronix 4014 display. The code requires 22k works of memory. It consists of two major software blocks: an Electromagnetic Compatibility Computation System (EMCCS) and a Graphical Data Management System (GDMS). The EMCCS computes the values of the EMI margin for all the frequency coincident combinations that are possible with the input data set and stores the associated information as disk files. These files are accessed by the GDMS for the specific displays requested by the user. A thirty system data set with an average of two antennas per emitter and receptor, takes about 20 min. to execute on a PDP-11/20.

The GDMS is a menu-driven system of four software modules: Frequency Coincidence, Antenna Location, EMI Margin and Antenna Position Input, each of which has its menu of features and displays that are called up by simple mnemonic commands [7]. The starting display results from typing S <CR>. This produces a numbered tabulation of the receivers in turn vs. the offending transmitters that have frequency coincidence with each receiver. The limits of this coincidence can be tabulated. This then bounds the T_{ij} values in frequency. Subsequent displays use the receiver/emittor numerical coding of this summary. Displays of coincidence of individual receptor/emittor pairs produce a graphical overlay of the modelled emittor and receptor characteristics. This immediately allows the verification of this input data by the user and quantifies the power level differences in the corresponding T_{ij} entry.

The antenna location display is intended for verification of the aircraft model, antenna location and antenna characteristics and as a documentation aid [7].

The EMI Margin module offers three distinct but associated templated displays. Calling up an EMI display of a specific antenna pair for a specific emittor/receptor combination produces the display shown in Fig. 44. This has appropriate and complete identification labelling of this display, a tabulation of all terms that make up the EMI margin value plus an oriented display of the aircraft, the antenna locations, plus the actual coupling path that is used in the computations. A separate block labels the associated antennas and indicates whether coupling is via main or side lobe. A close-up of the aircraft display is available for a user-specified orientation, as shown in Fig. 45. This has been selected to show another type of path. The antenna patterns can be displayed, if necessary, for purposes of their authentication and also for an appreciation of the degree of approximation used in the simple model compared with actual antenna patterns, as shown in Fig. 46. The ready display of the aircraft geometry as well as the coupling path itself, together with the tabulated values of path loss results in a heretofore unavailable ability to associate the two and results in better insight into the physical relationship in the model and its relationship to the 'real-world' of the aircraft installation [8]. The user can examine specific antenna pairs at will or cycle through the entire data set by using available and convenient 'AGAIN' and "NEXT' commands.

Antenna re-location is often considered for radiation pattern or EMC reasons, especially with the retrofit installation of new systems. The Antenna Position Input module makes re-location studies convenient for purposes of EMC analysis or design. Calling up a specific antenna in this software module, produces the display shown in Fig. 47. The current antenna position is shown in two templated views of the aircraft and its aircraft coordinates are shown tabulated. After this, the user is reminded of the antenna characteristics that are in the input file, and he can elect to confirm or change them line by line. After confirmation the session can be terminated in a 'RECOMPUTE' mode which re-cycles all the EMCCS calculations with the new antenna location as part of the data set. The user can then examine the changes in EMI margin values and obtain an appreciation of the sensitivity of location with regard to inter-antenna coupling.

Status and Future Development

Potential users should examine the displays in other papers [7,8] for a fuller appreciation of details of presentation and operation. For example the inclusion of the path length in wavelengths [8] beside the margin values, alerts the user to the degree of approximation implied by the calculations. The code is now under joint development by the Canadian Department of National Defence and the U.S.A.F., Rome Air Development Center. One of the major items for its improvement involves the incorporation of modern diffraction coefficients for the edge diffraction portion of the path loss computation. A systematic validation process has also been undertaken comparing prediction with full-scale aircraft measurements. For the code that is in present use, the data supplied by Hodes and Widmer [8] apply.

References

[1]   E.K. Miller, "Numerical Modeling Techniques for Free Space", Paper No. 7., Proceedings of AGARD Lecture Series No. 131 on 'The Performance of Antennas in their Operating Environment', October 1983.

[2]   R.F. Harrington, "Field Computation by Moment Methods", The MacMillan Co., New York 1968.

[3]   G.J. Burke and A.J. Poggio, "Numerical Electromagnetic Code (NEC)- Methods of Moments", Technical Document NOSC 116, Naval Electronic Systems Command (ELEX 3041), Naval Ocean Systems Center, San Diego, California 92152.

[4]   Yan T. Lin and Jack H. Richmond, "EM Modeling of Aircraft at Low Frequencies", IEEE Transactions on Antennas and Propagation, Vol. AP-23, No.1, January 1975.

[5]   E.K. Miller and F.J. Deadrick, "Some Computational Aspects of Thin-Wire Modeling", in 'Numerical and Asymptotic Techniques in Electromagnetics', R. Mittra (ed.), Springer-Verlag 1975.

[6]   "Electromagnetic Compatibility", AGARD Lecture Series No. 116, John F. Spina, Director, August 1981, ISBN92-835-1396-7.

[7]   Kubina, S.J. and Bhartia, P., "Computer Graphics Techniques for Aircraft EMC Analysis and Design", AGARD Conference Proceedings No. 343, 'Advanced Concepts for Avionics/ Weapon System Design, Development and Integration', Avionics Panel 45th Symposium, Ottawa, Canada, April 1983.

[8]   Hodes, Harry, and Widmer, Hans Peter, "The Solution of 'Real-World' Aircraft EMC Problems Using the AAPG Computer Code", Proceedings of NAECON 82 Conference, Dayton, Ohio, May 1982.

[9]   Wu, T.T. and King, R.W.P., "The Tapered Antenna and its Application to the Junction Problem for Thin Wires", IEEE Trans. on Antennas and Propagation, Vol. AP-24, pp. 42-45, January 1976.

[10]   Granger, J.V. "System Considerations in Aircraft Antenna Design", I.R.E. Transactions on Airborne Electronics, Vol. AE-1, pp. 1-2, December 1951.

[11]   MIL-A-9080 (U.S.A.F.), Military Specification for Antenna Liaison Communications Equipment, Feb. 1954.

[12]   Kubina, S.J. and Pavlasek, T.J.F., "Evaluation of HF Antennas for Helicopters and Small Aircraft," Proceedings of the International Conference on Antennas for Aircraft and Spacecraft, London, June 1975, IEE Conference Publication Number 128.

[13]   Bahsoun, Youssef, "Evaluation of an HF Helicopter Antenna - Measurements and Numerical Techniques", M. Eng. thesis, Faculty of Engineering, Concordia University, Montreal, Quebec, Canada, March 1982.

[14]   Bahsoun, Y. and Hazell, J., "Radiation Pattern Measurements of a Tranline Antenna on a Scale Model of the CHSS-2/Sea King Helicopter" ERB-929, NRCC No. 18883, National Research Council of Canada, Ottawa, December 1980.

[15]   Owen, J.I.R., "Wire Grid Analysis of HF Aerial for the Toronado and the Sea-King", Royal Aircraft Establishment Technical Report TR77154, Farnborough, England, October 1977 (Restricted).

[16]   Bolomey, J.C. and Tabbara, W.," Numerical Aspects of Coupling between Complementary Boundary-Value Problems," IEEE Transactions on Antennas and Propagation, Vol. AP-21, pp. 356-363, May 1973.

[17]   Carlson, R.E., "Evaluation of the Antenna System Installed on the P3V-1 Aircraft", Vol. III, Lockheed Report LR13565-(III), 22 February 1961, Lockheed California Co., Burbank, Ca., U.S.A.

[18]   Trueman, C.W. and Kubina, S.J., "AM Re-Radiation Project - Final Report", Technical Note No. TN-EMC-80-03, EMC Laboratory, Concordia University, Montreal, Canada, March 1980.

[19]   Jaggard, K.L., "An Application of Isoperimetric Inequalities to the Calculation of Equivalent Radii", Proceedings of the National Radio Science Meeting, Boulder, Colorado, November 1979.

[20]   Trueman, C.W. and Kubina S.J., "AM Re-Radiation Project - Final Report 1982-3", Technical Note EMC-83-04, EMC Laboratory, Concordia University, Montreal, Canada, August 1983.

[21]   Warren, James R., "Principles of Device - Independent Computer Graphics Software", I.E.E.E. Computer Graphics and Applications, Vol. 1, No. 4, October 1981.

[22]   Balmain, K.G., "Performance of Antenna in Plasmas", Paper No. 12, Proceedings of AGARD Lecture Series No. 131 on 'The Performance of Antennas in Their Operating Environment', October 1983.

[23]   Trueman, C.W. and Kubina, S.J., "Computation of the Radiation Patterns of the WISP/HF Dipole on the Space Orbiter - Final Report 81/82", Technical Note TN-EMC-82-03, EMC Laboratory Concorida University, Montreal, Canada, July 1982.

[24]   Spina, John F., "The EMC Concept for Weapon Systems", AGARD Lecture Series Publication AGARD-LS-116 on Electromagnetic Compatibility, September 1981.

[25]   Capraro, Gerard T., "An Intrasystem EMC Analysis Program", AGARD Lecture Series Publication AGARD-LS-116 on Electromagnetic Compatibility, September 1981.

[26]   Bogdanor, J., Siegel, M., and Weinstock G., "Intra-Vehicular Electromagnetic Compat-ibility Analysis", AFAL-TR-71-155, McDonnell Aircraft Co., St-Louis, MO, July 1971

[27]   Hasserjian, G., and Ishimaru, A.," Excitation of a Conducting Cylindrical Surface of Large Radius of Curvature", Transactions of the IRE, Vol. AP-10, No. 3, May 1962 pp. 264-273.

Acknowledgements

Fig. 2   Tranline Antenna Configuration on the CHSS-2/Sea King Helicopter

Fig. 1   Reference Spherical Coordinate System

(a)   (b)
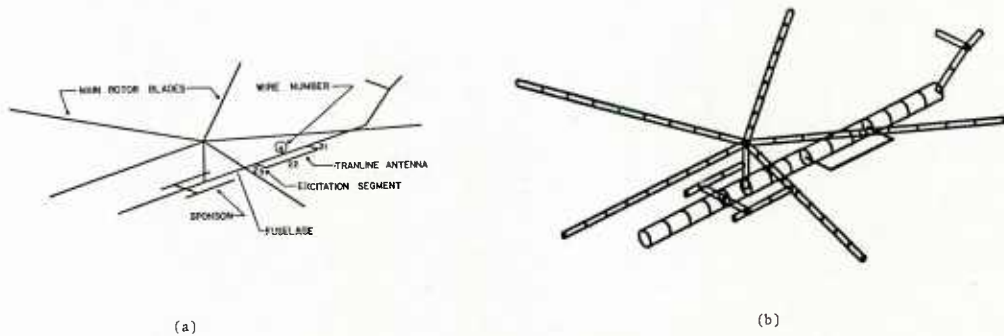
Fig. 3   Simple Model of CHSS-2/Sea King Helicopter
(a) Wire Model
(b) Radius Display
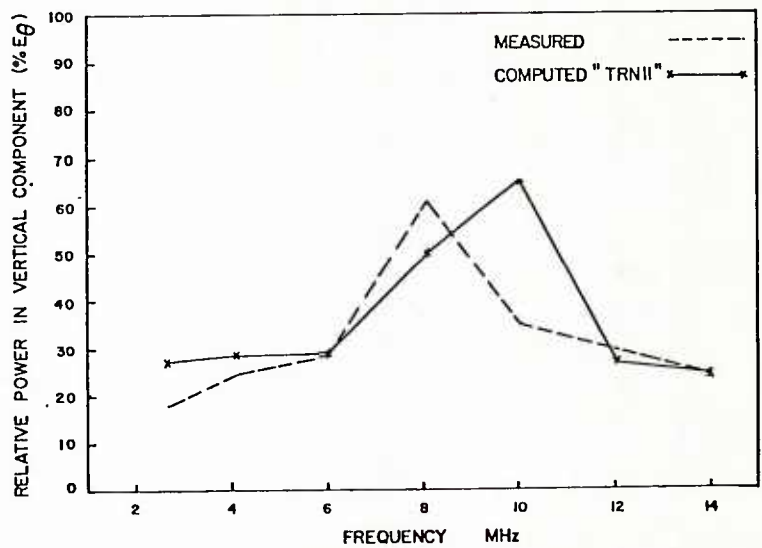
Fig. 4   % E_θ vs Frequency - Simple Model,
Uniform Radius (0.1 m)
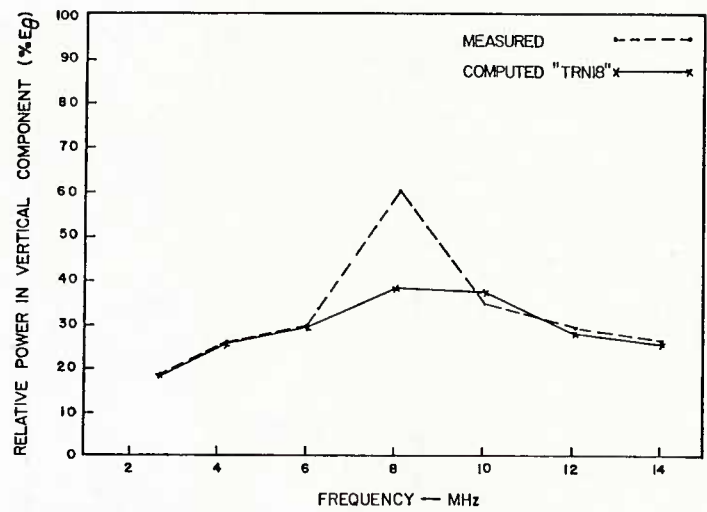
Fig. 5   % E_θ vs Frequency - Simple Model,
          Optimized Radius
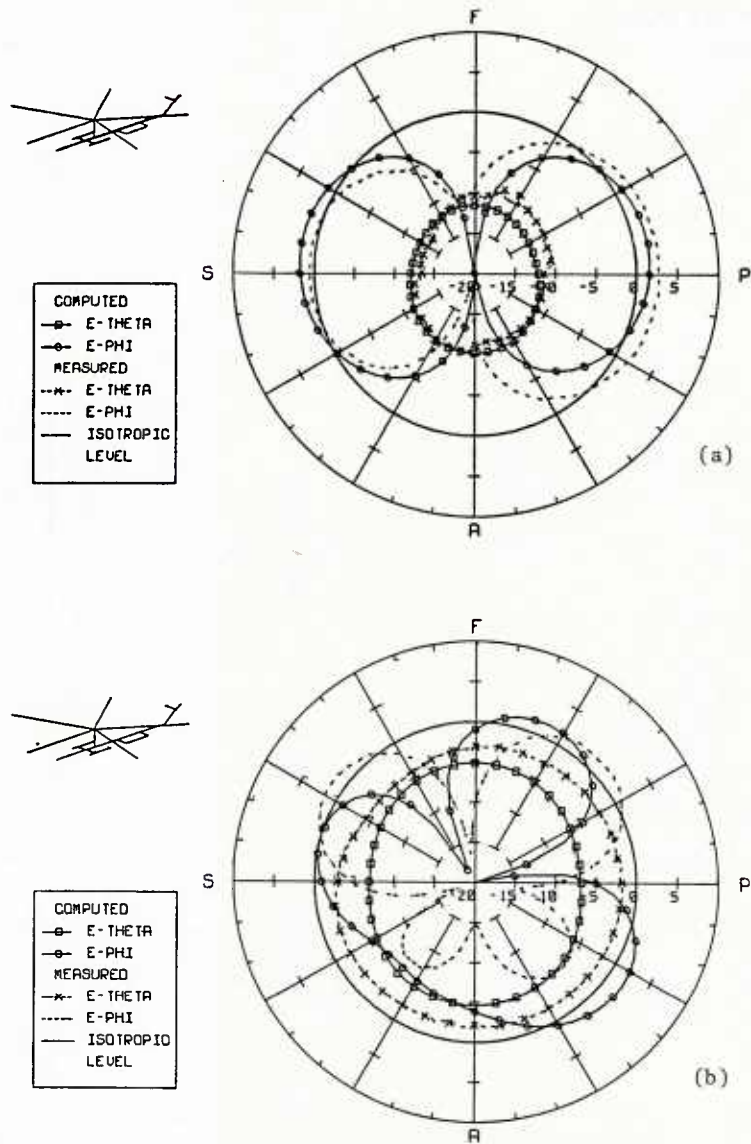
Fig. 6   Azimuth Pattern, Simple Model, Optimized Radius
          (a)   6 MHz, dB Scale
          (b)   8.1 MHz, dB Scale

(a)

(b)

Fig. 7   Complex Model of the CHSS-2/Sea King Helicopter
         (a)   Wire Representation
         (b)   Radius Representation
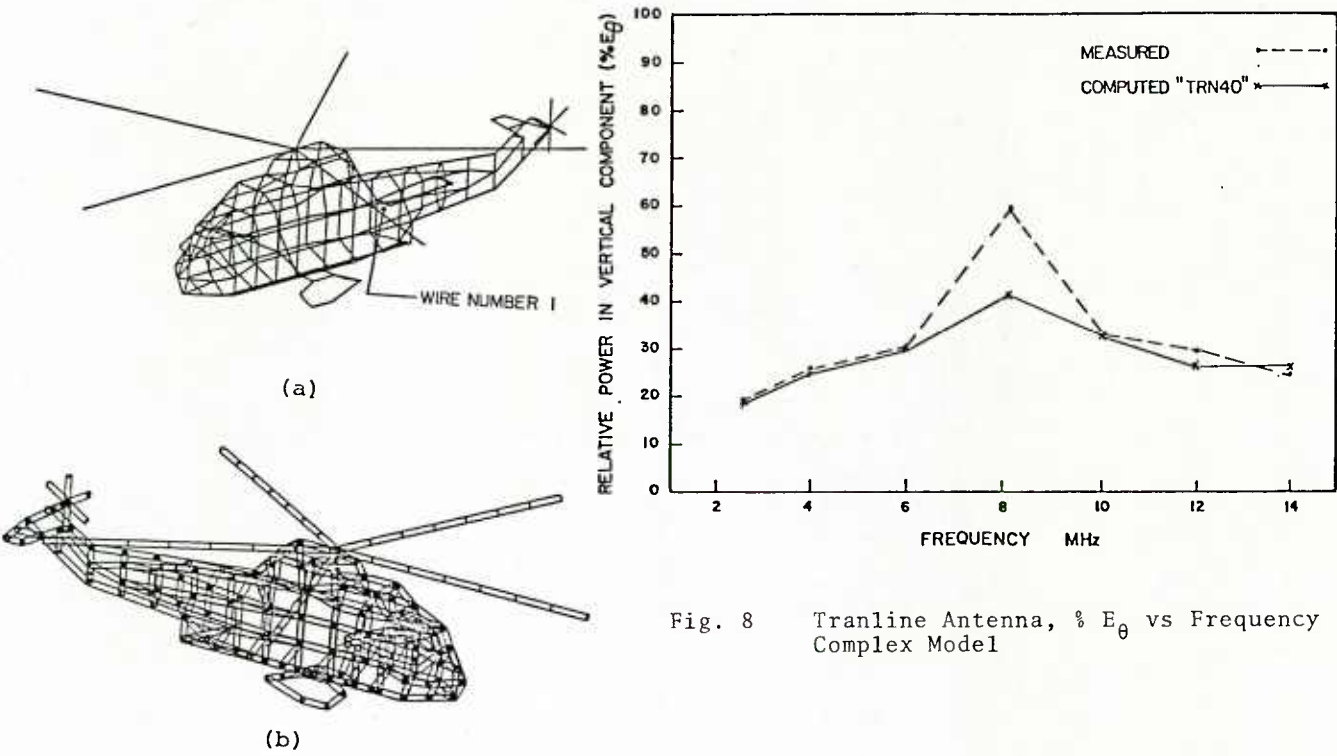
Fig. 8   Tranline Antenna, % E_θ vs Frequency
          Complex Model
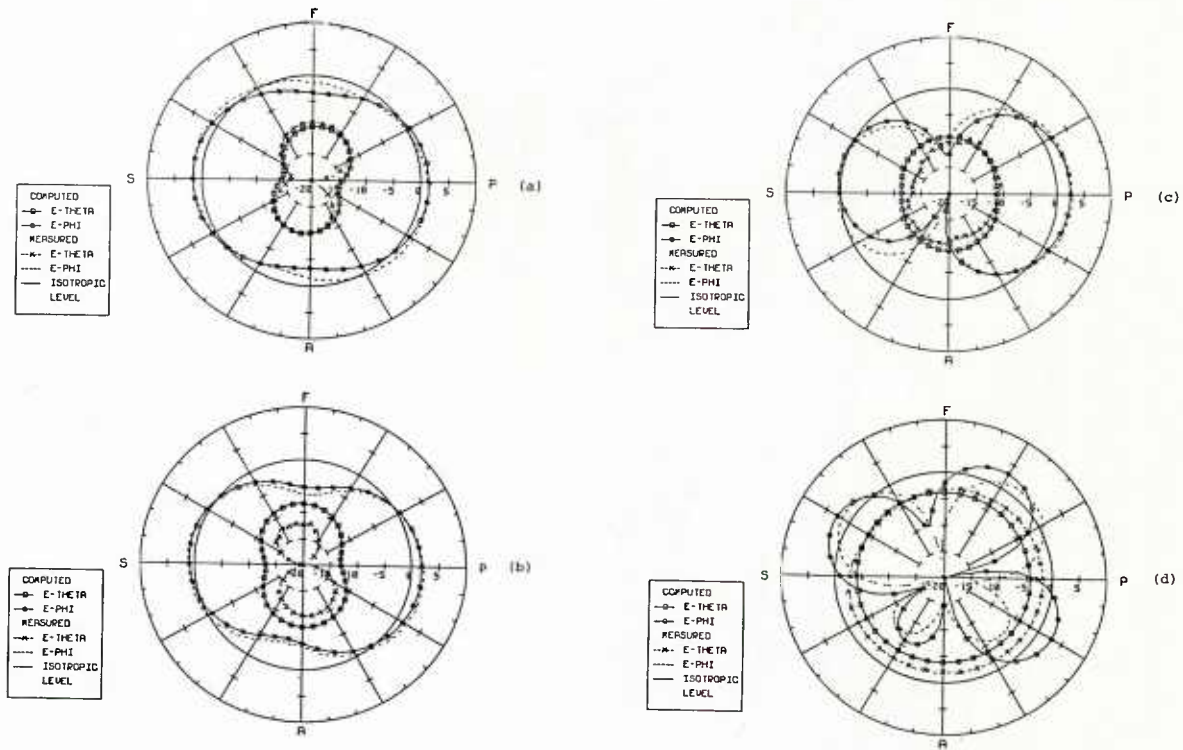
Fig. 9   Azimuth Patterns, Complex Model
          (a)   2.6 MHz, (b)   4.1 MHz, (c)   6.0 MHz,
          (d)   8.1 MHz, dB Scale
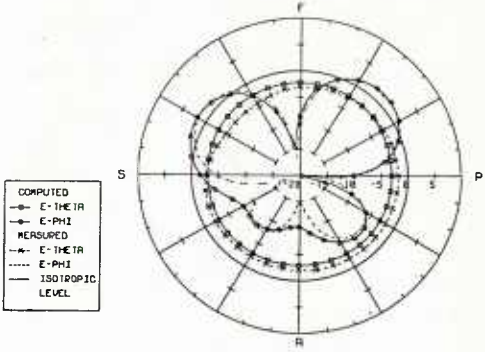
Fig. 10   Azimuth Pattern, "Tuned" Complex Model,
           8.1 MHz, dB Scale
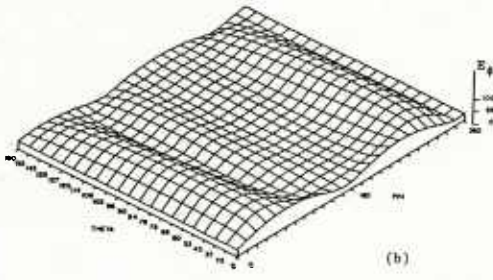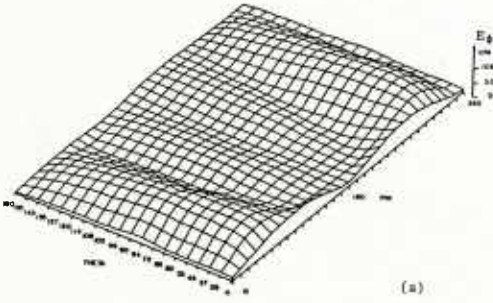
Fig. 11   Hidden Surface Plots, E_ϕ Conical Patterns
           (a) Measured,   (b) Computed
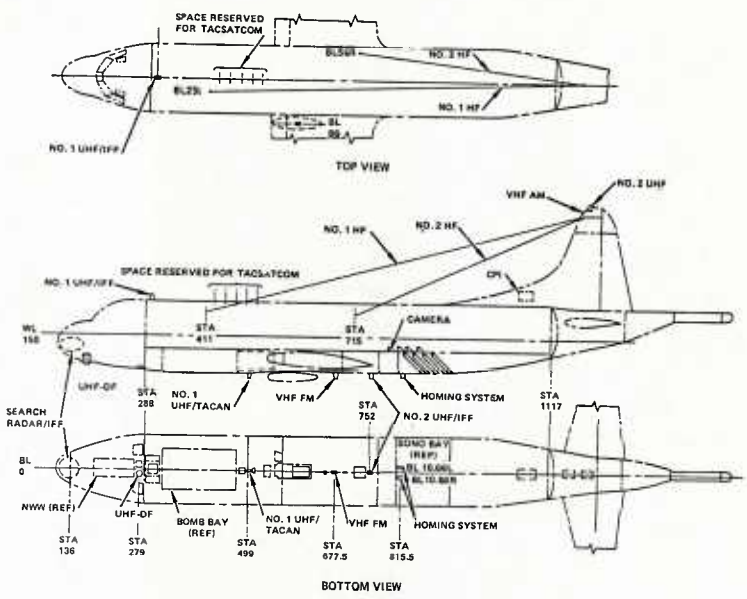
Fig. 12   P-3 Antenna Arrangement
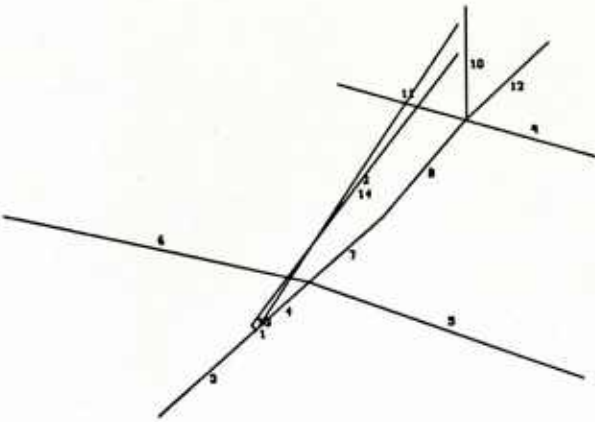
Fig. 13

Simple Stick Model - Old P-3C
Configuration

Fig. 14(a)

Principal Plane Patterns,
P-3C Thin Stick Model,
Port Antenna, 2 MHz
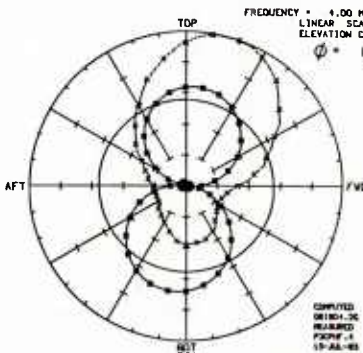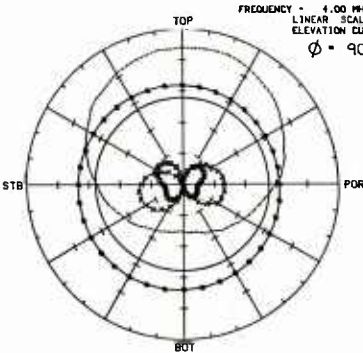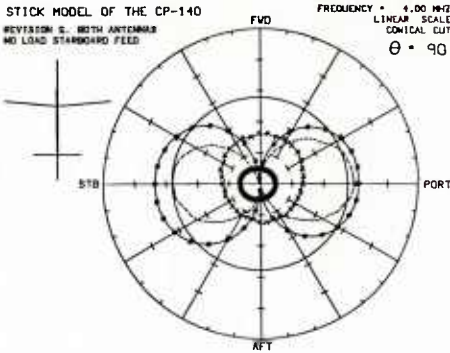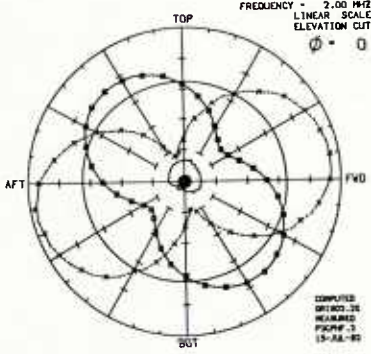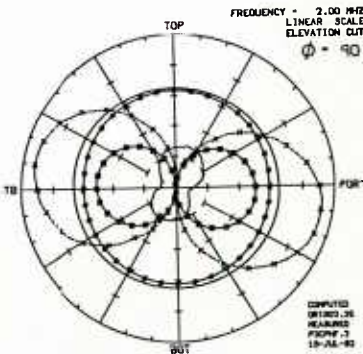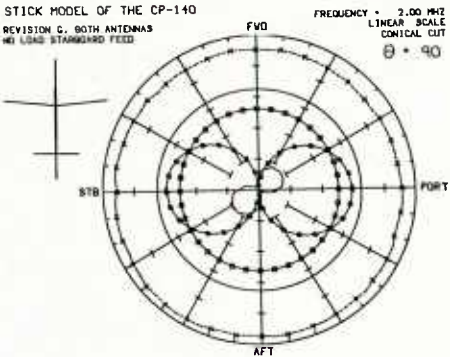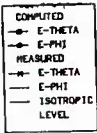
Fig. 14(b)

Principal Plane Patterns,
P-3C Thin Stick Model,
Port Antenna, 4 MHz

Fig. 14(c)

Principal Plane Patterns,
P-3C Thin Stick Model,
Port Antenna, 6 MHz
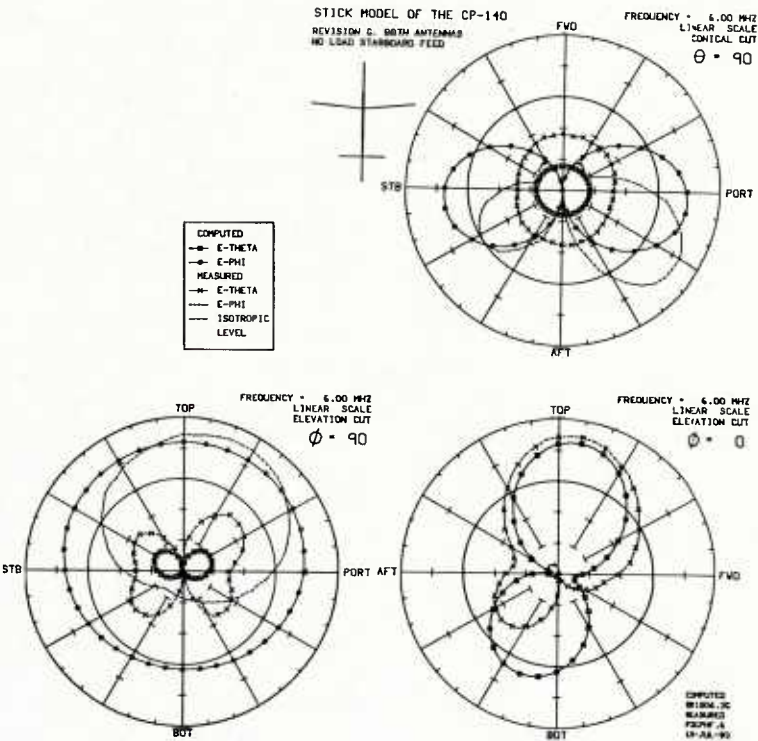
Fig. 15

"Fat" Simple Model, P-3C Configuration
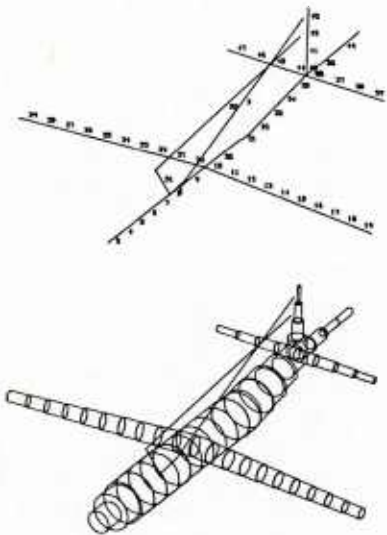
Fig. 16(a)

Principal Plane Patterns,
P-3C Fat Simple Model, Port Antenna,
2 MHz
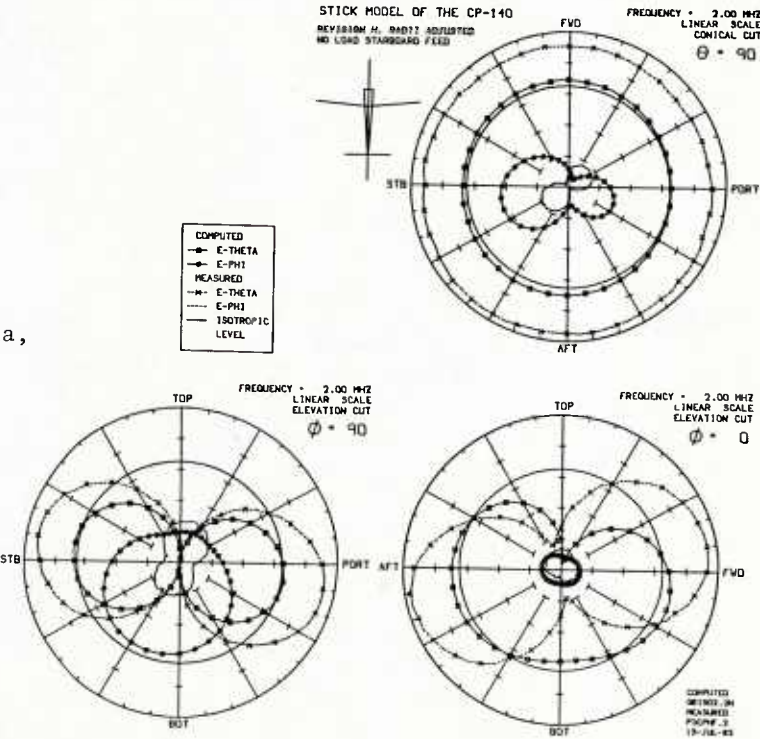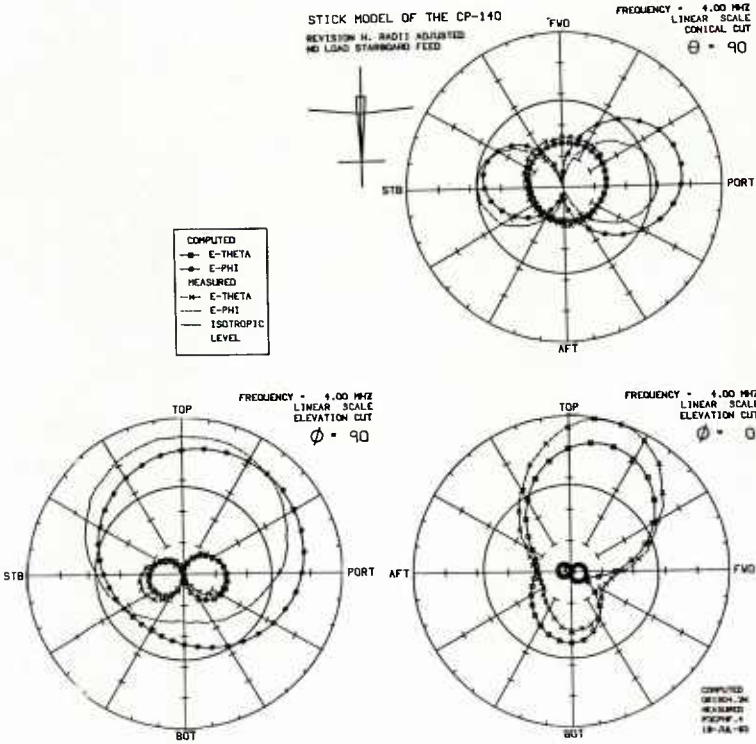
Fig. 16(b)
Principal Plane Patterns,
P-3C Fat Simple Model,
Port Antenna, 4 MHz

Fig. 16(c)
Principal Plane Patterns,
P-3C Fat Simple Model,
Port Antenna, 6 MHz
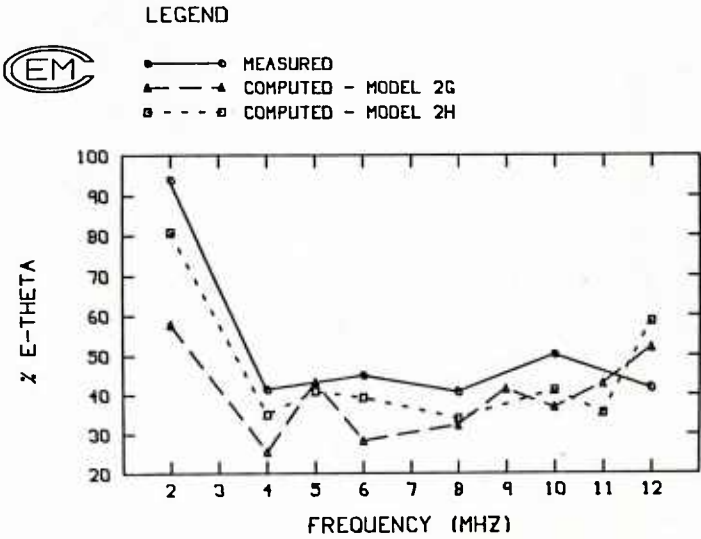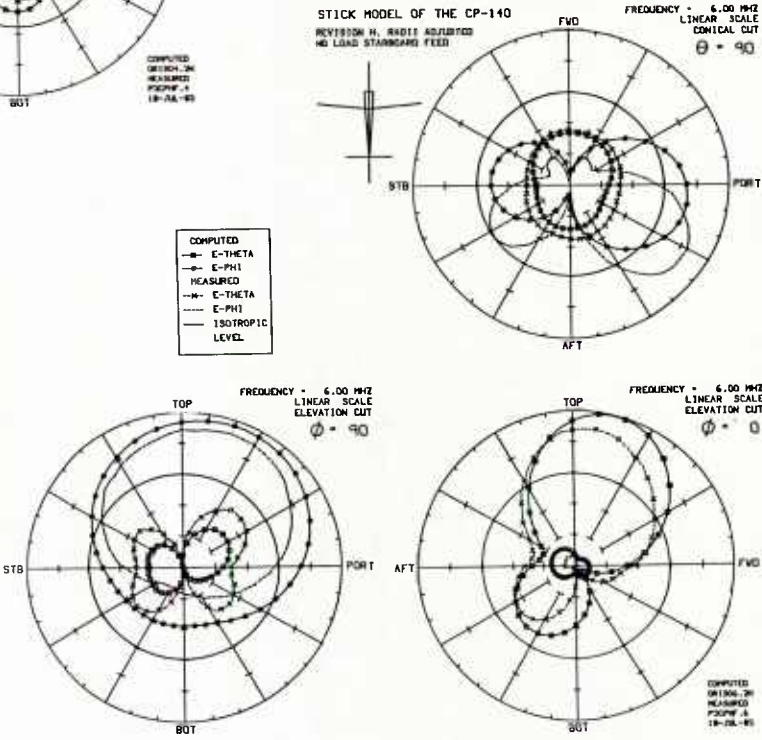
Fig. 17
% E_θ vs Frequency,
Thin (2G) and Fat (2H)
Simple Models
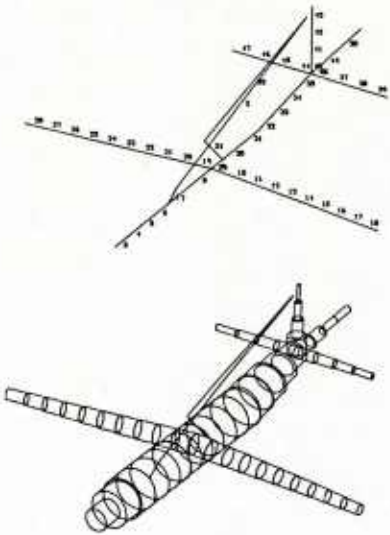
Fig. 18
CP-140/Aurora
Simple Model Geometry
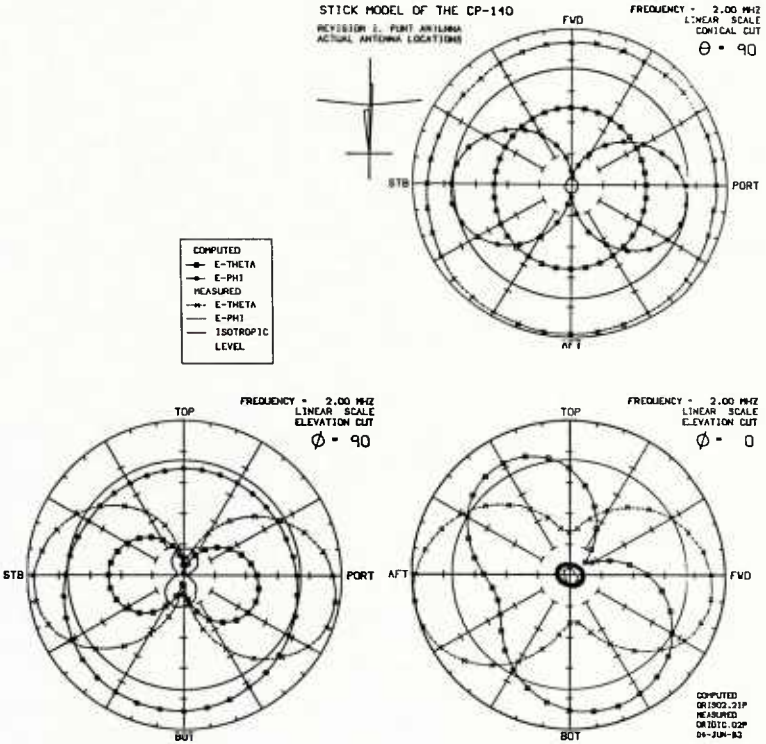
Fig. 19(a)   Principal Plane Patterns, CP-140
Simple Model, 2 MHz, Port Antenna

Fig. 19(b)

Principal Plane Patterns, CP-140
Simple Model, 6 MHz, Port Antenna
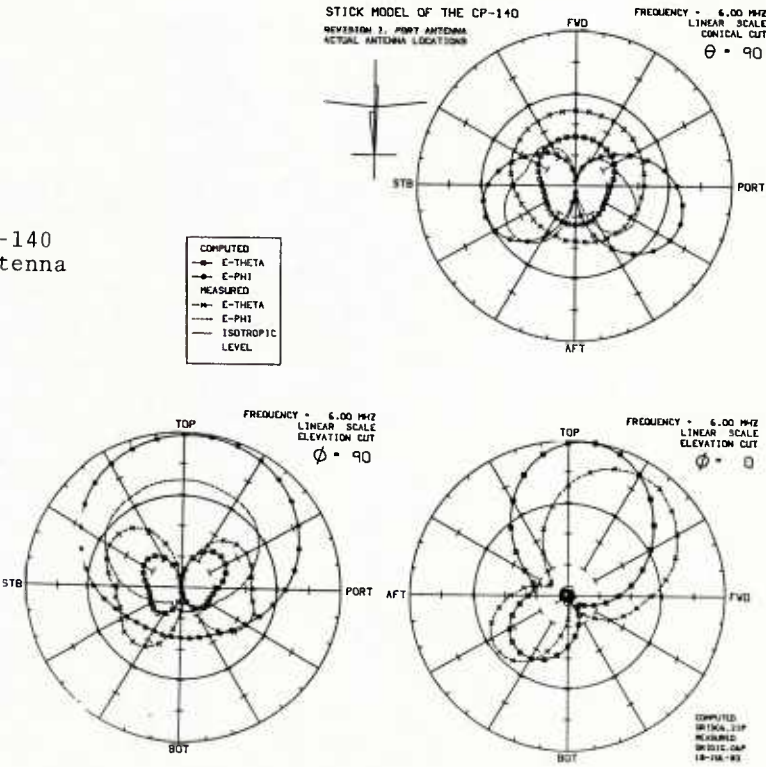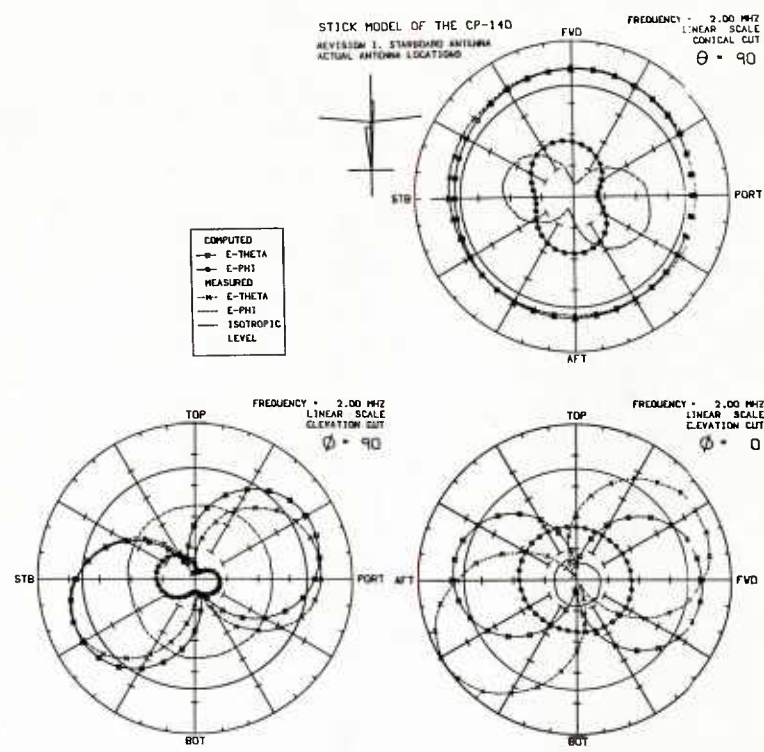
Fig. 19(c)   Principal Plane Patterns, CP-140 Simple Model,
2 MHz, STBD Antenna
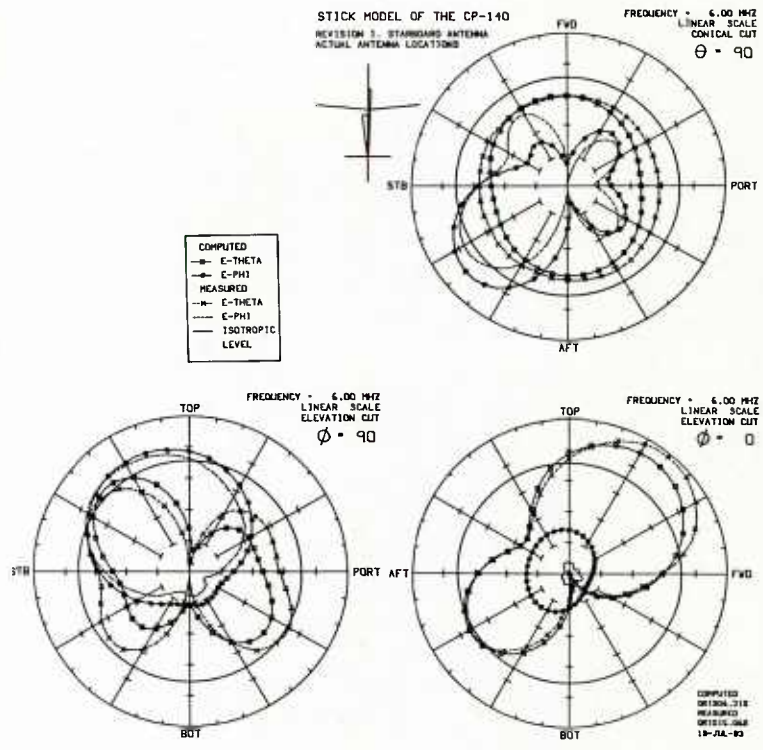
Fig. 19(d)   Principal Plane Patterns, CP-140 Simple Model,
6 MHz, STBD Antenna

Fig. 20

Hidden-Surface Display,
Conical Pattern Set -
CP-140 Simple Model,
STBD Antenna, 6 MHz
(a) Measured Patterns
(b) Computed Patterns
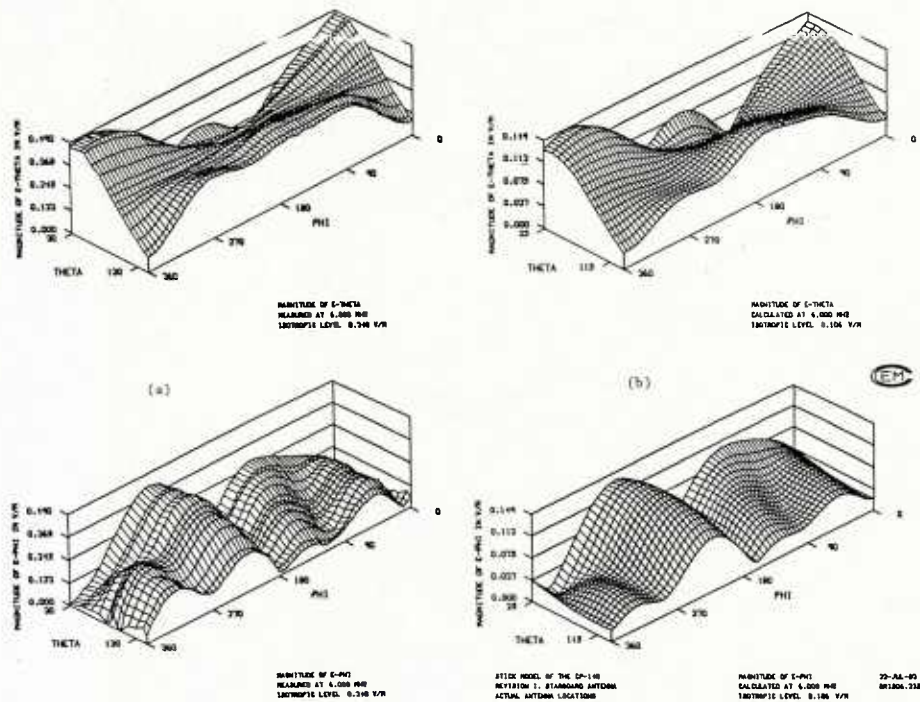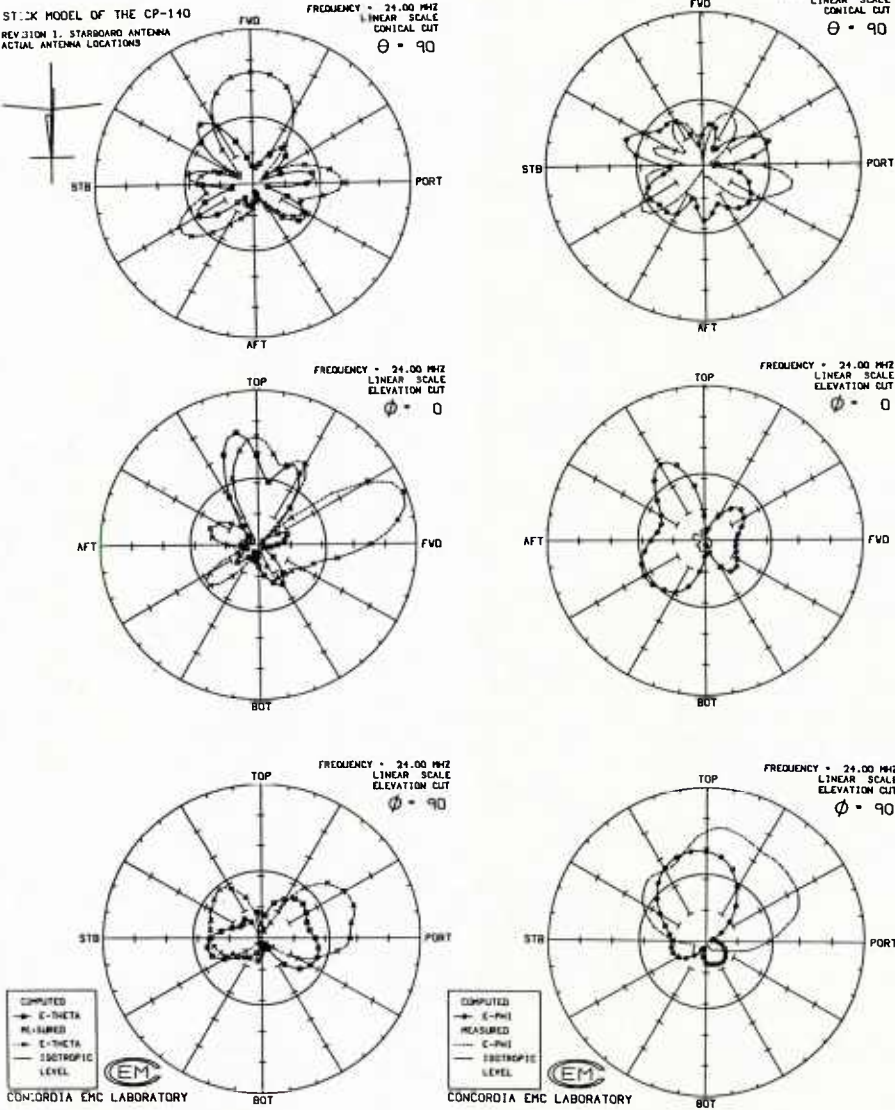
Fig. 21

Principal Plane
Patterns, CP-140
STBD Antenna,
Simple Model
24 MHz
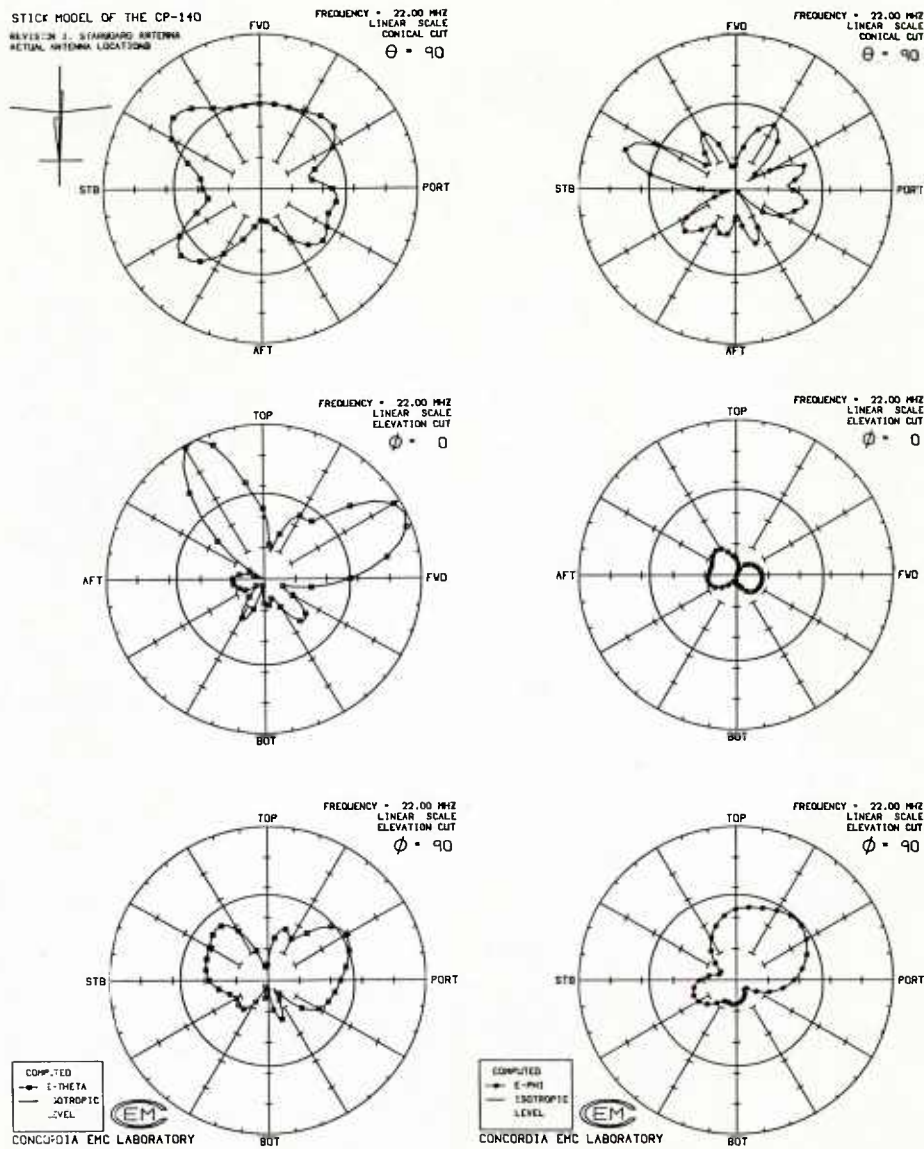
Fig. 22

Computed Principal
Plane Patterns,
CP-140 STBD HF
Antenna, Simple
Model, 22 MHz

Fig. 23

Principal Plane Patterns,
CP-140 STBD HF Antenna,
Simple Model, Reduced 50%,
2 MHz
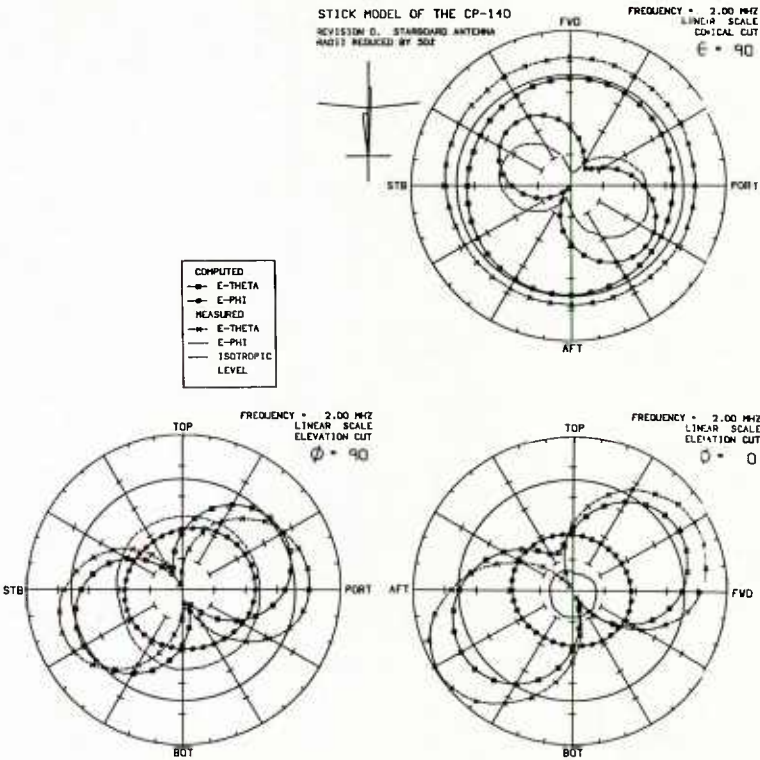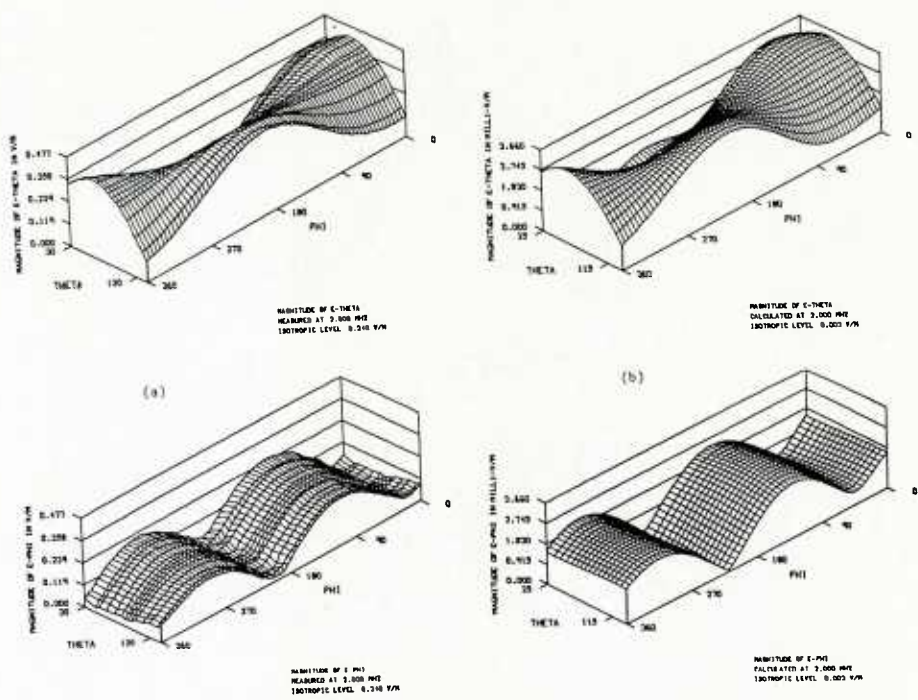
Fig. 24   Hidden-Surface Display, Conical Pattern Set,
CP-140 Simple Model, 2 MHz
(a) Measured Patterns   (b) Computed Patterns
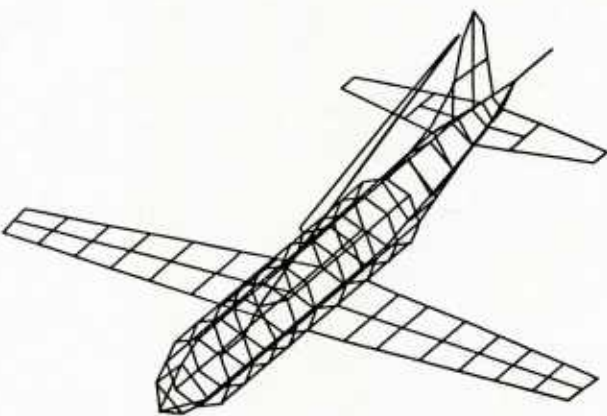
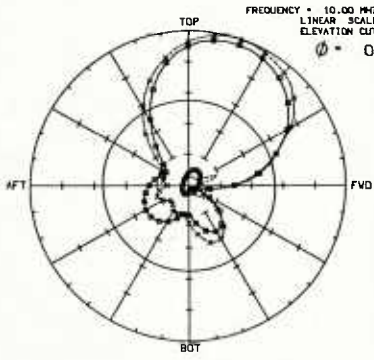
Fig. 25   3-D View of CP-140 Complex Model
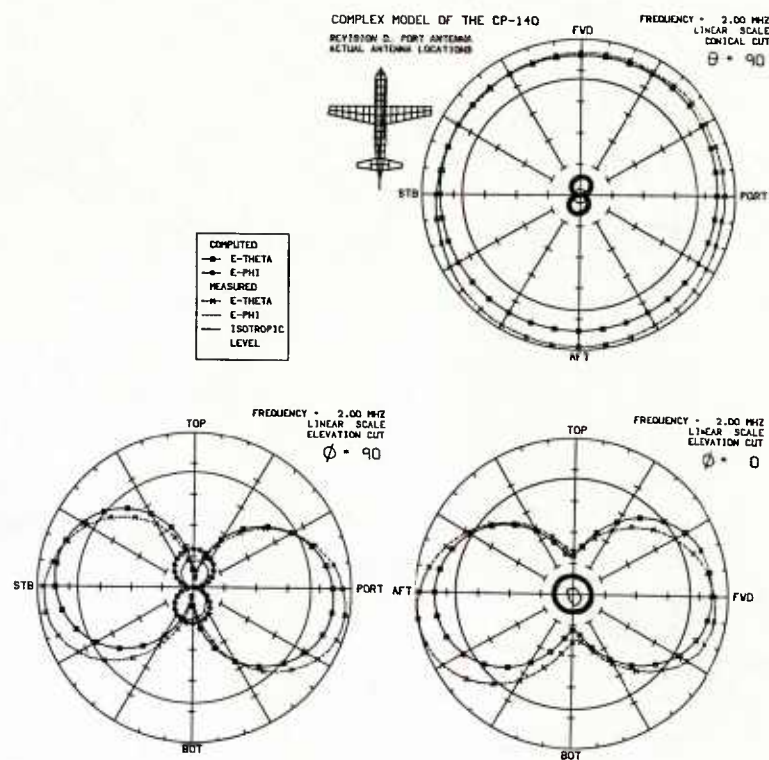
Fig. 26(a)   Principal Plane Patterns, CP-140 Complex Model
              HF1, 2 MHz
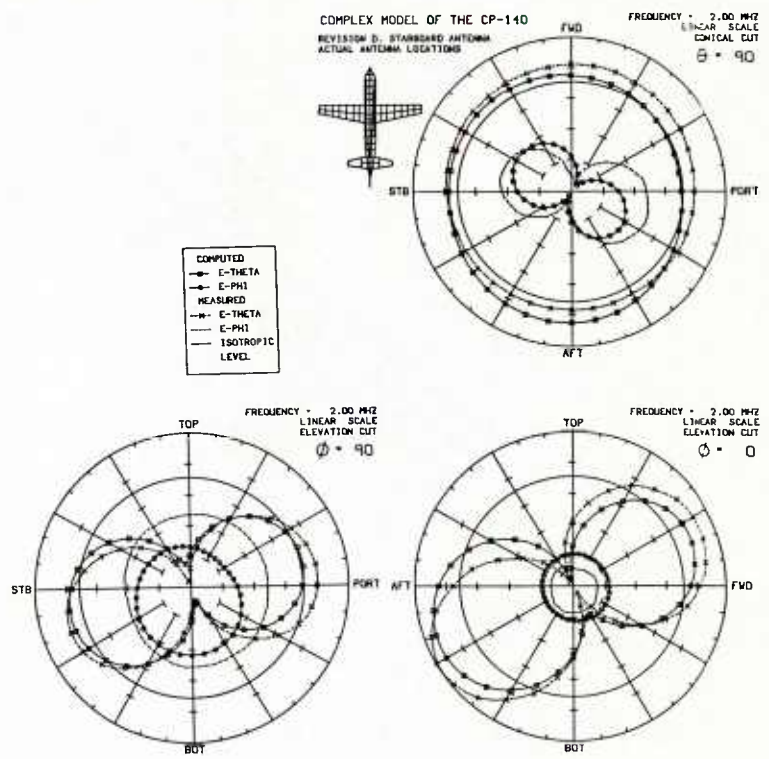
Fig. 26(b)   Principal Plane Patterns, CP-140 Complex Model
              HF2, 2 MHz
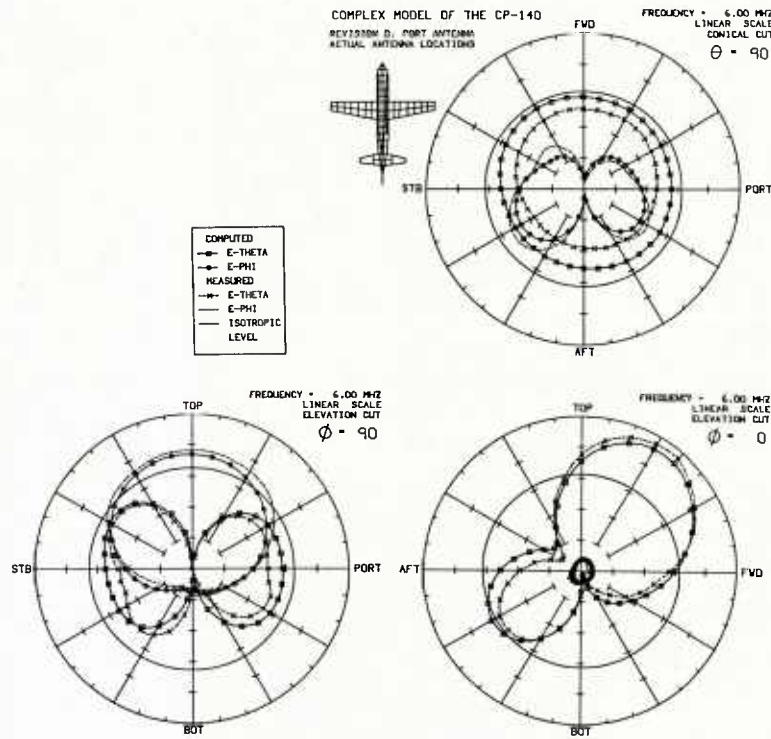
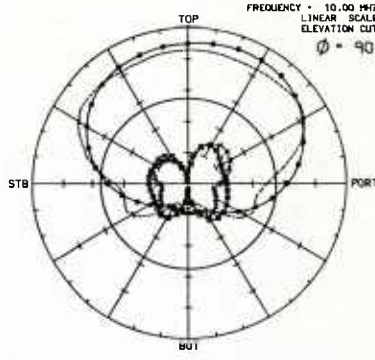Fig. 26(c)   Principal Plane Patterns, CP-140 Complex Model
HF1, 6 MHz
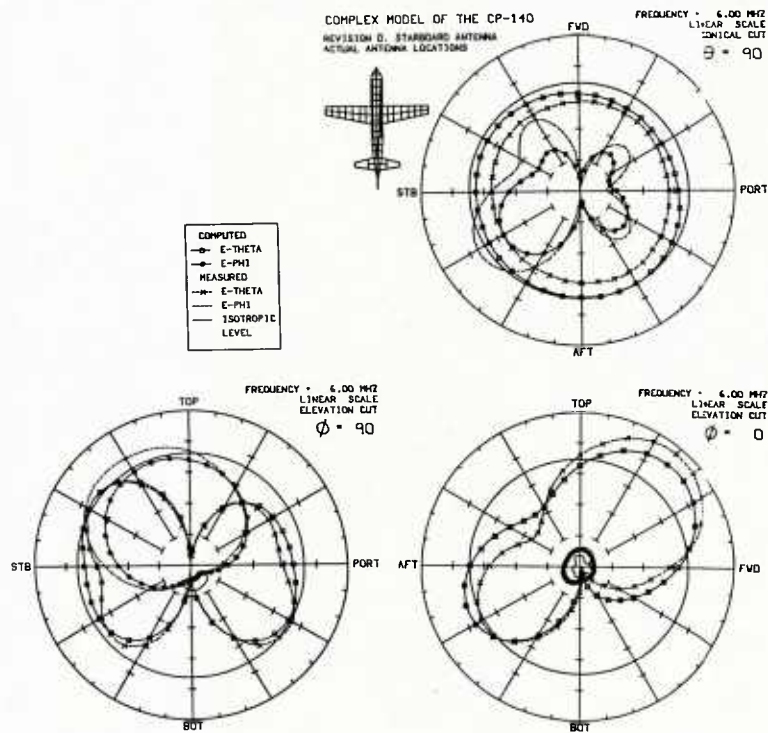
Fig. 26(d)   Principal Plane Patterns, CP-140 Complex Model
HF2, 6 MHz

Fig. 27(a)

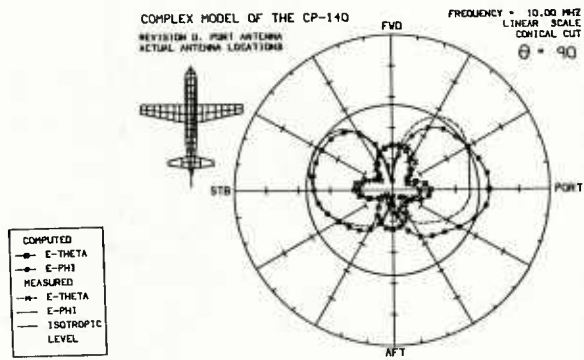Principal Plane Patterns, CP-140
Complex Model, Port Antenna,
10 MHz
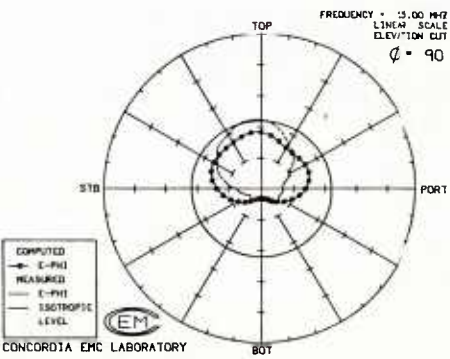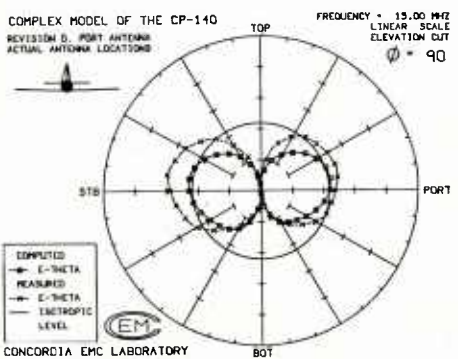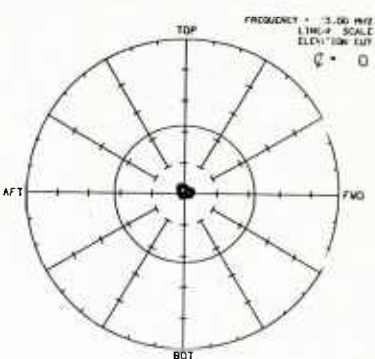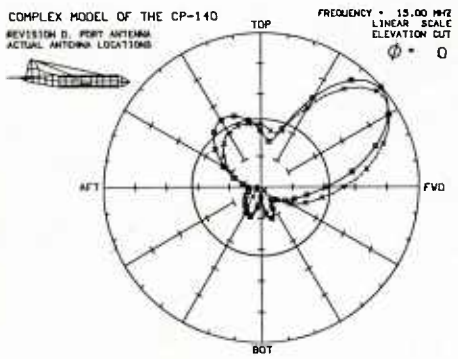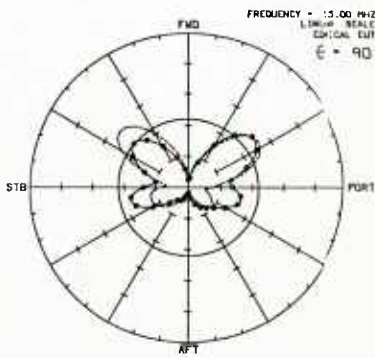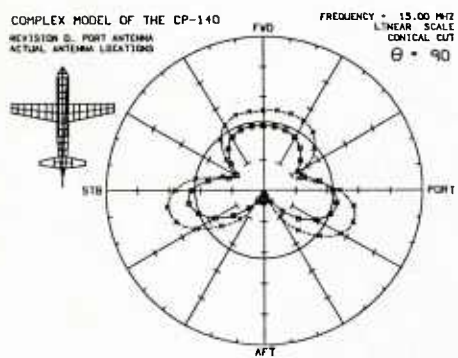
Fig. 27(b)

Principal Plane
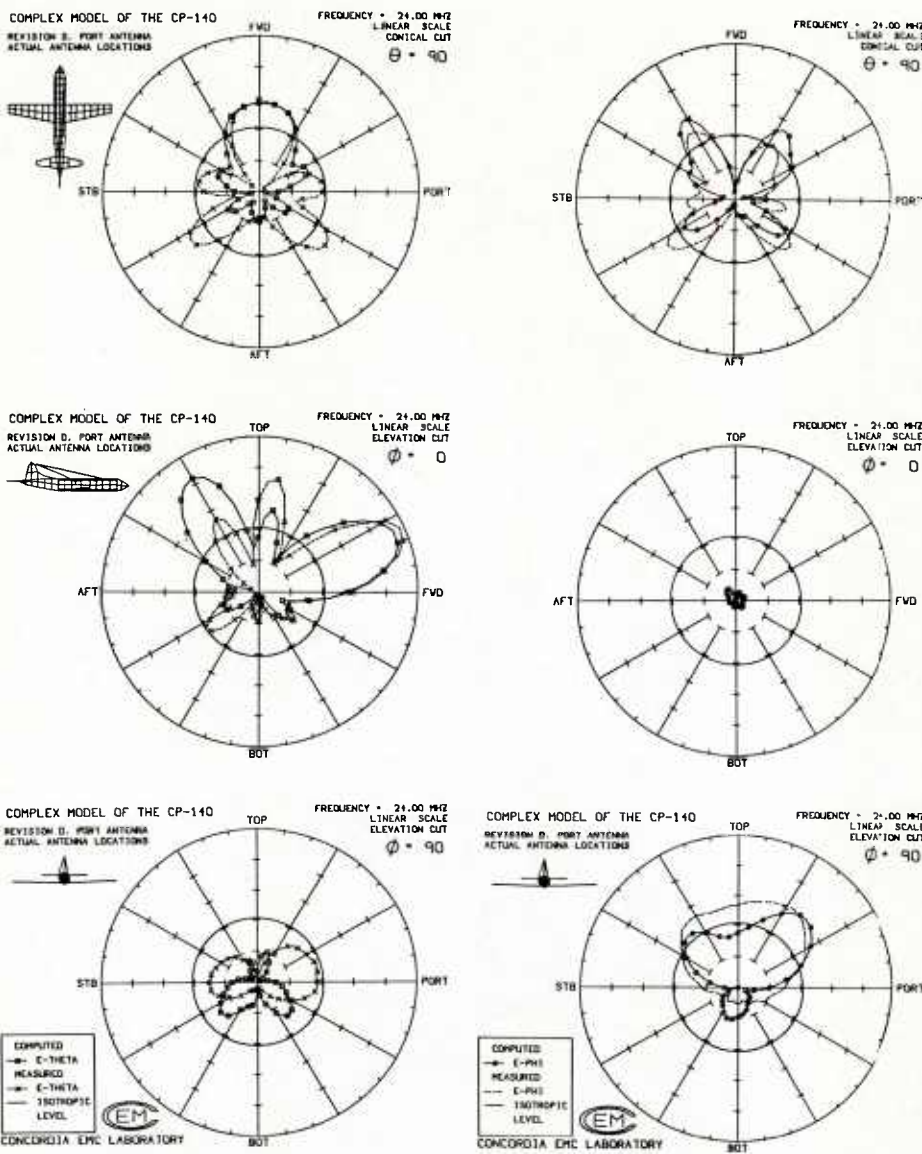Patterns, CP-140
Complex Model,
Port Antenna
15 MHz

Fig. 27(c)
Principal Plane
Patterns, CP-140
Complex Model,
Port Antenna
20 MHz

Fig. 29(b)   Hidden-Surface Plots, Radiation Pattern
Conical Set, CP-140 Complex Model HF1,
20 MHz

Fig. 28(a)

Principal Plane
Patterns, CP-140
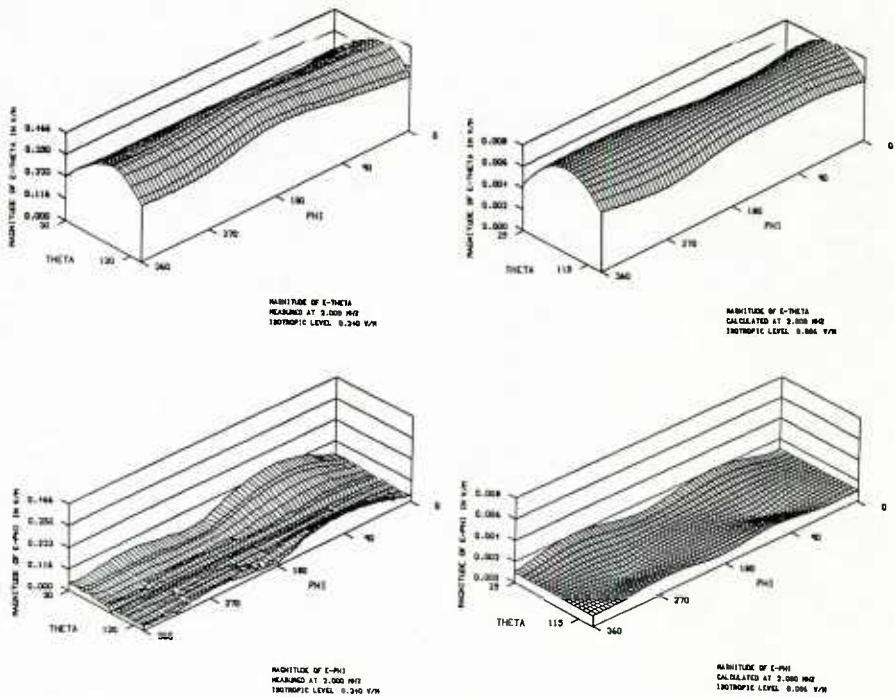Complex Model,
Port Antenna
24 MHz

Fig. 29(a)   Hidden-Surface Plots, Radiation Pattern
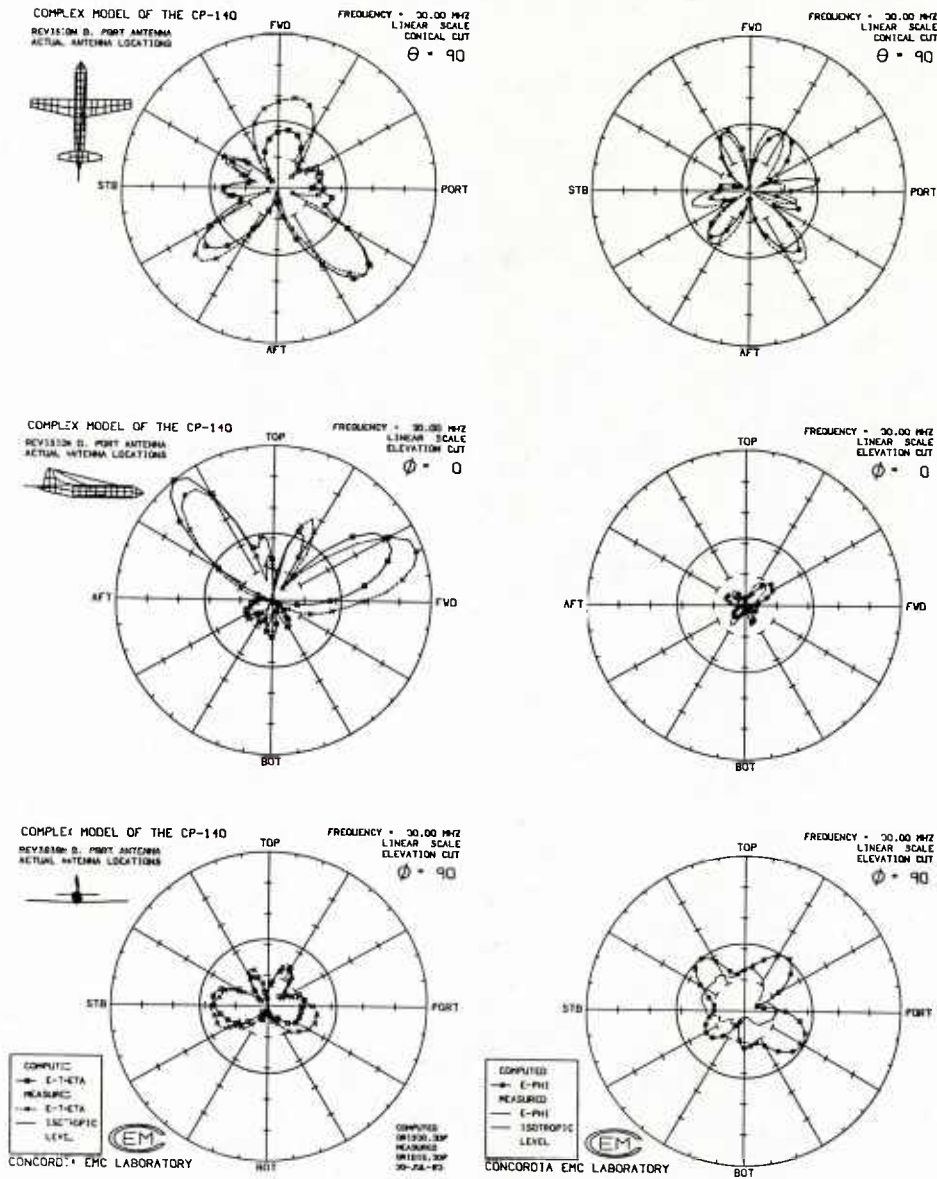Conical Set, CP-140 Complex Model HF1,
2 MHz

Fig. 28(b)

Principal Plane
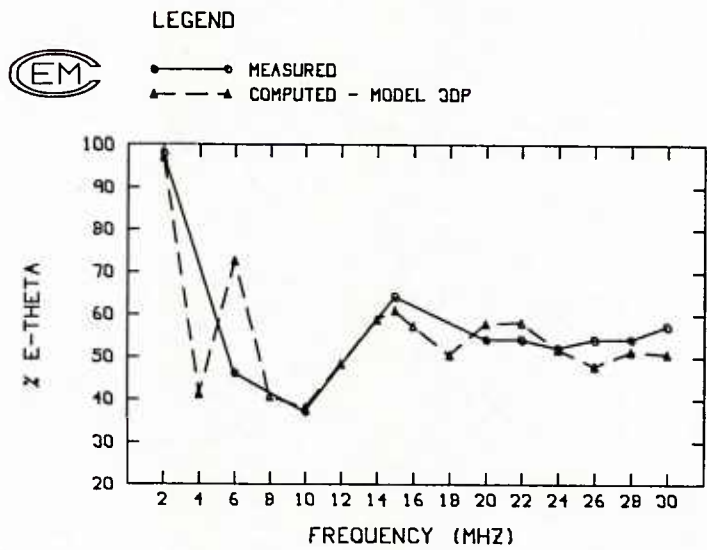Patterns, CP-140
Complex Model,
Port Antenna,
30 MHz

Fig. 30   % E_θ vs Frequency, CP-140 Complex Model, HF1
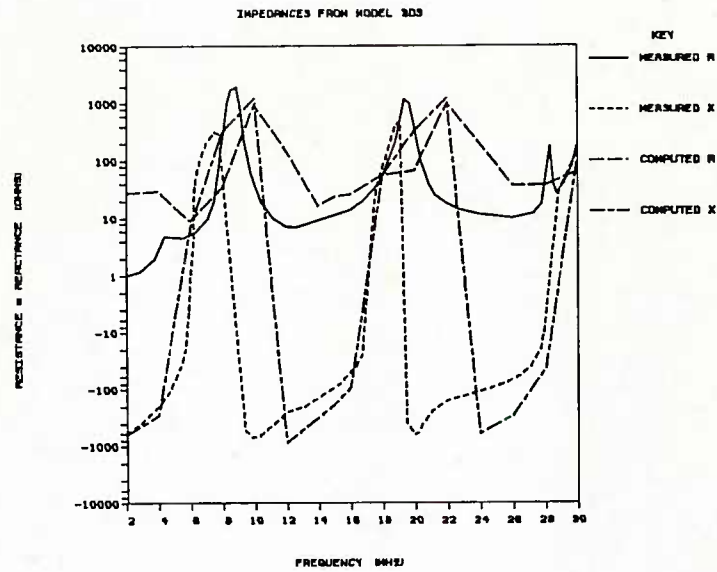
Fig. 31   Impedance vs Frequency, CP-140 Complex Model, HF2
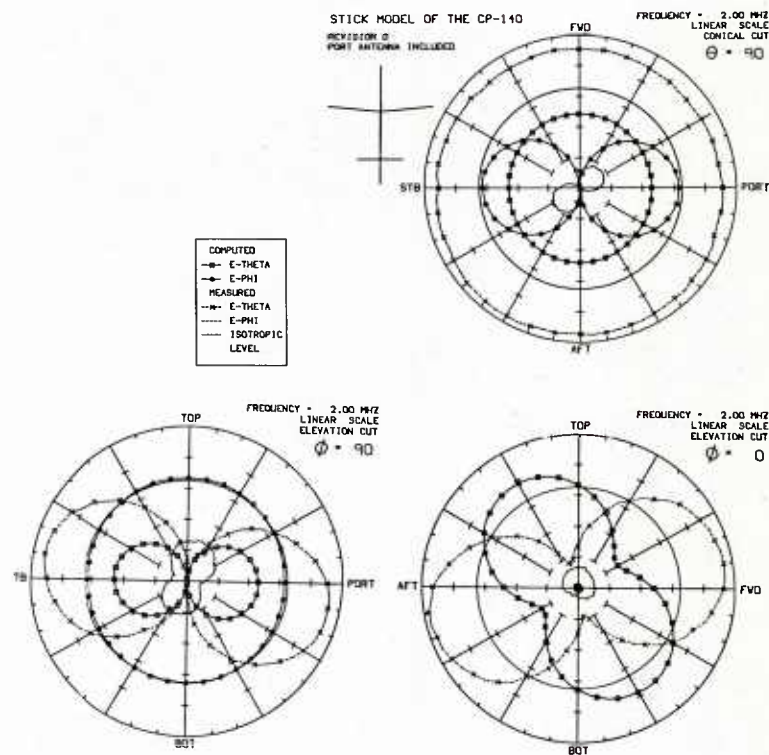
Fig. 32   Principal Plane Patterns, P-3C Configuration,
Simple Model, Port Antenna Alone, 2 MHz

Fig. 33 Current Distribution, P-3C Configuration,
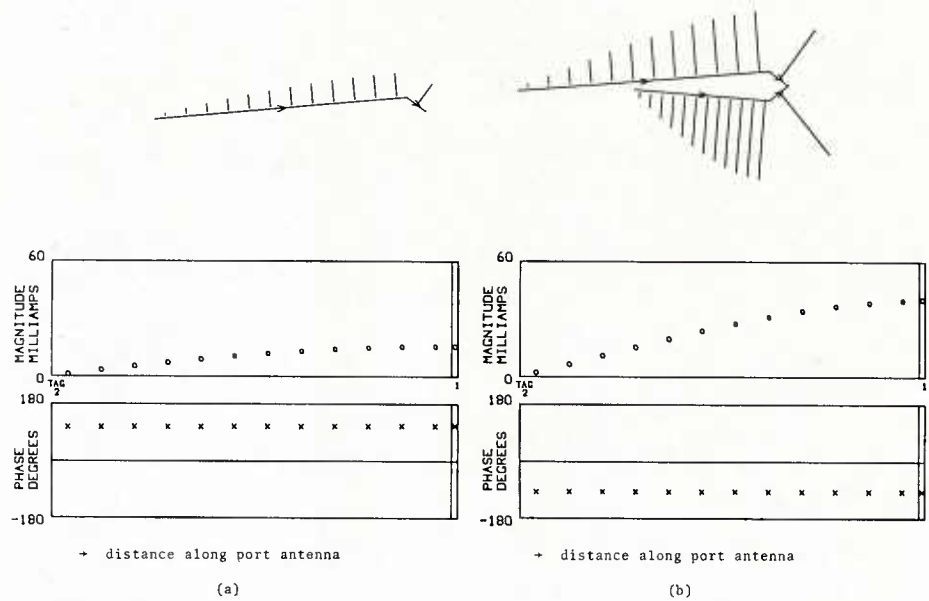Simple Model
(a) Port Antenna Alone
(b) Both Antennas in Place; Port Excited
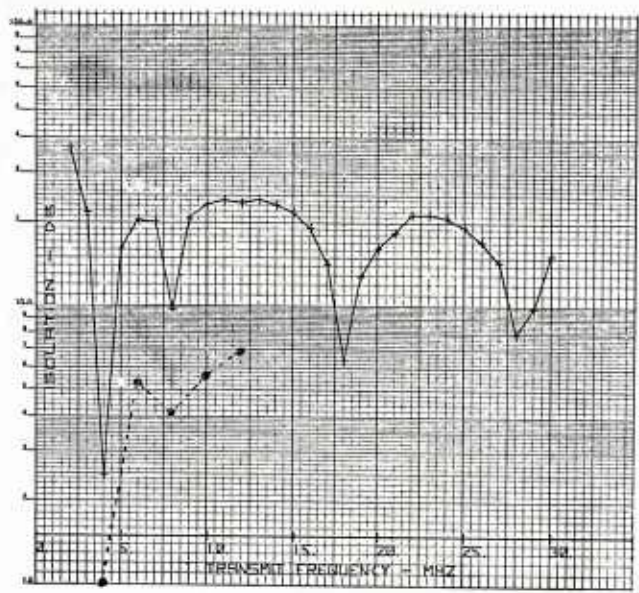
Fig. 34 Measured Isolation Values, HF Antennas, P-3C
Configuration. Lockheed Data plus NEC maximum
coupling values

HF1 excited
HF2 tuned to 4 MHz
○ NEC computed values "CP" option
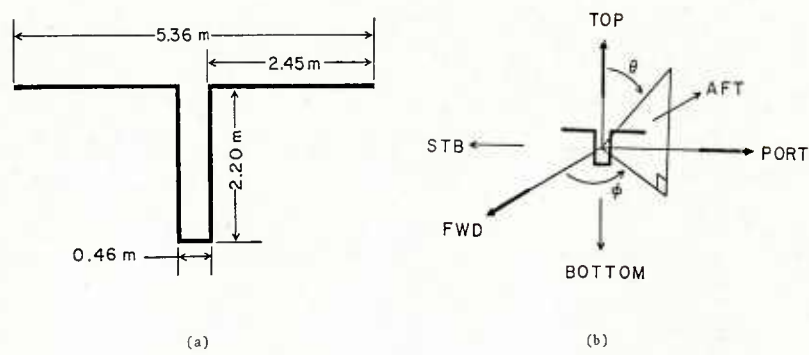
Fig. 35 (a) Dipole Dimensions and (b) Reference Coordinate System
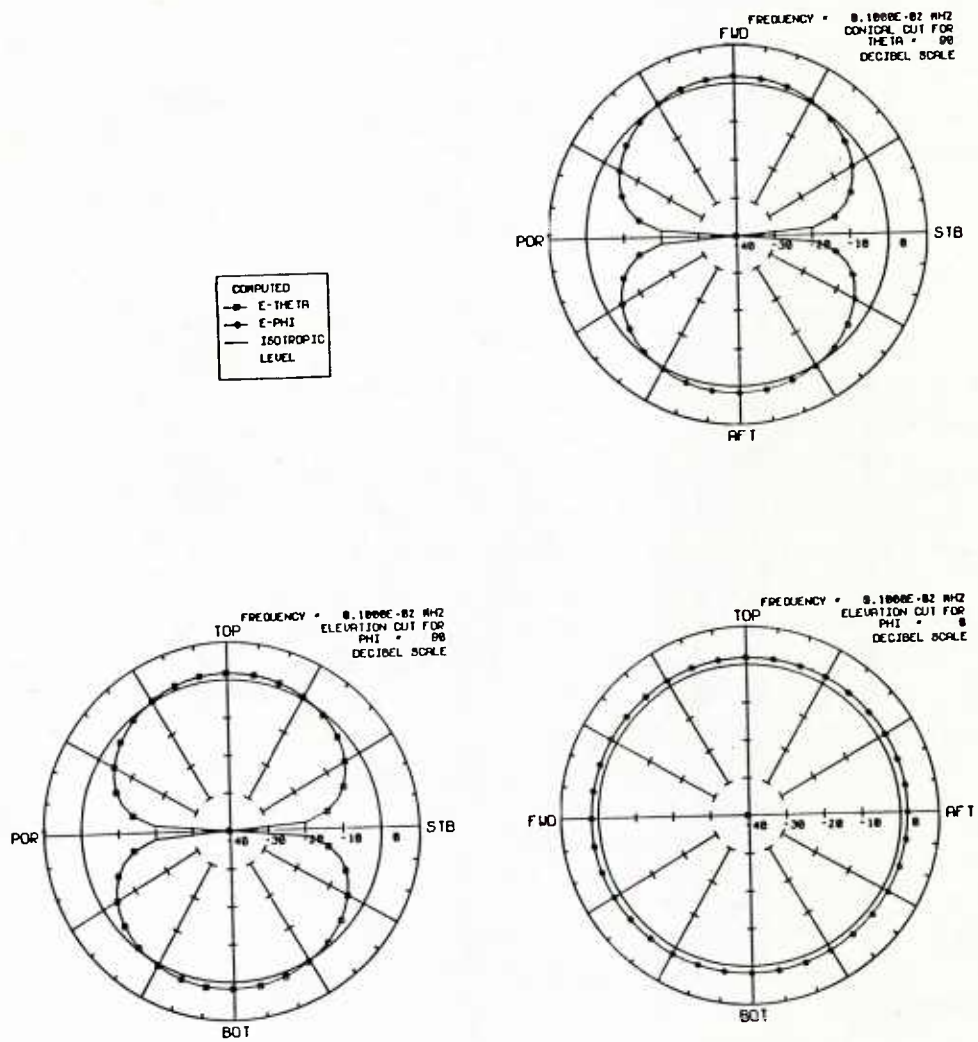
Fig. 36 Principal Plane Patterns, 10 MHz, Dipole Alone
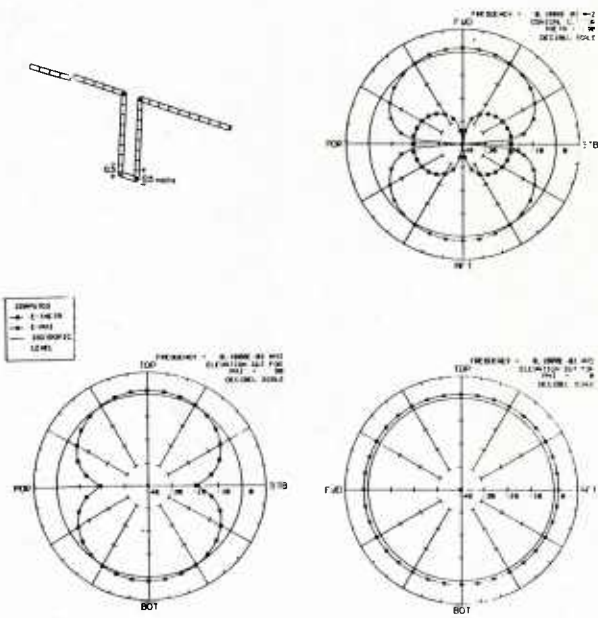
Fig. 37

Computer Model Feedline and Dipole
and Principal Plane Patterns, 10 MHz
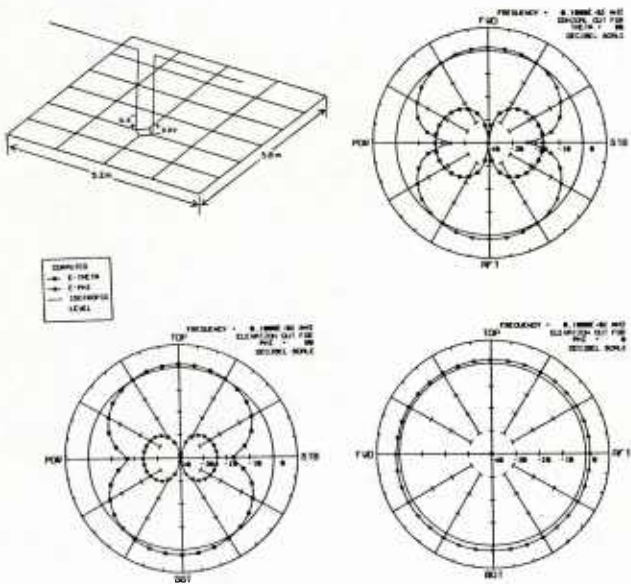
Fig. 38

Pallet, Feedline and Dipole, and
Principal Plane Patterns, 10 MHz
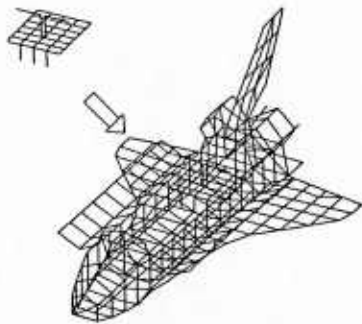
Fig. 39   Wire Grid Model of the Space Shuttle Orbiter
and Dipole
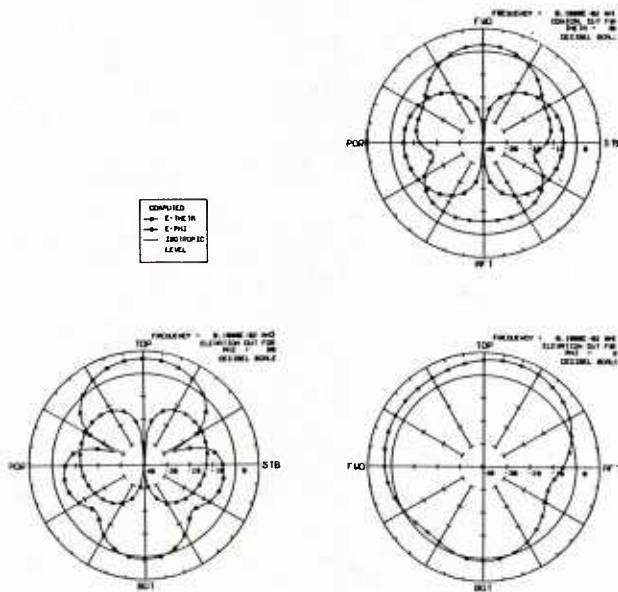
Fig. 40   Principal Plane Patterns, Complete Model, 10 MHz
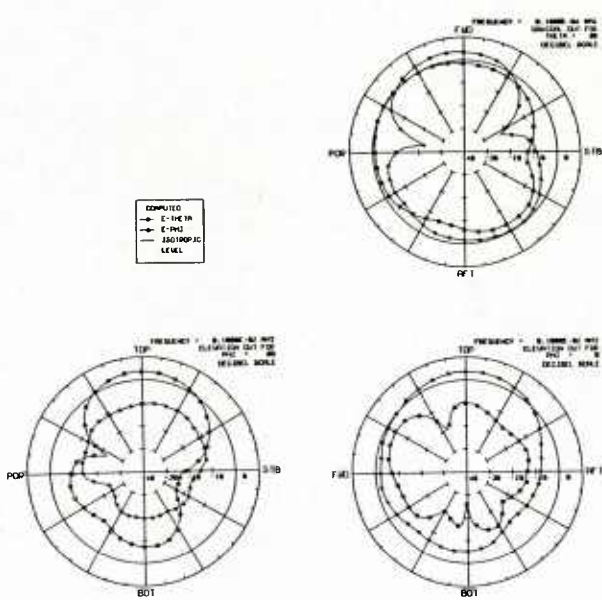
Fig. 41

Measured Principal Plane Patterns,
Complete Model, 10 MHz
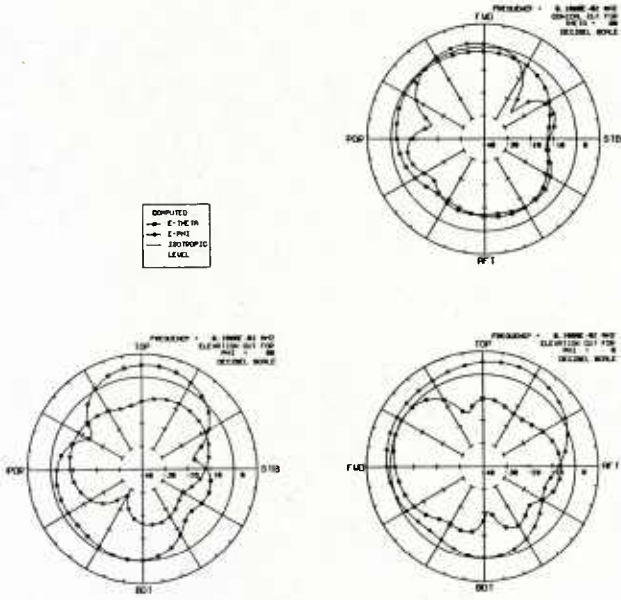
Fig. 42

Computed Principal Plane Patterns
Complete Model, 10 MHz,
20% Feedline Imbalance
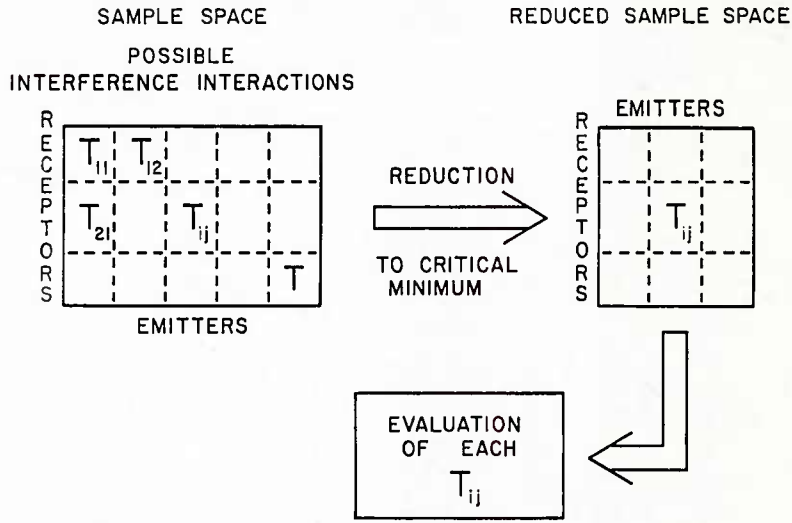
Fig. 43   EMC Analysis Process

(3.01-00)
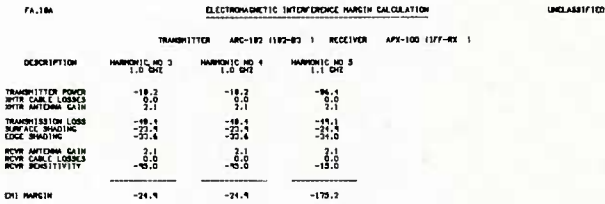
Fig. 44   Typical AAPG EMI Margin Display

ELEVATION   25., AZIMUTH   25. (DEGREES)

(1.01-01)
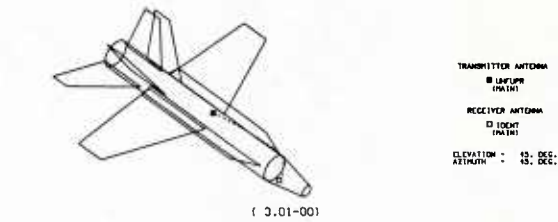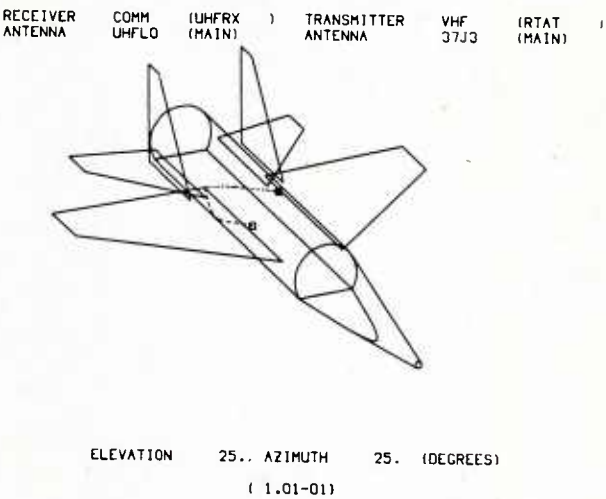
Fig. 45   Typical AAPG Close-Up Display
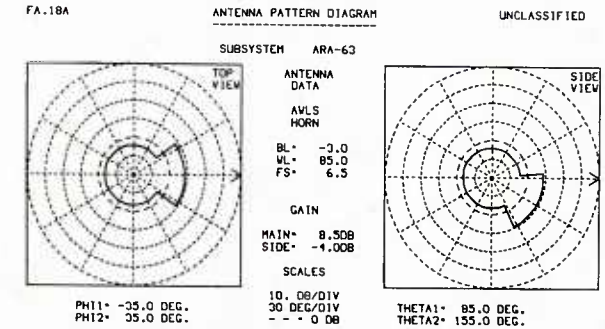
Fig. 46
Typical AAPG Antenna Pattern Display

Fig. 47

Typical AAPG Antenna Re-Location
Display
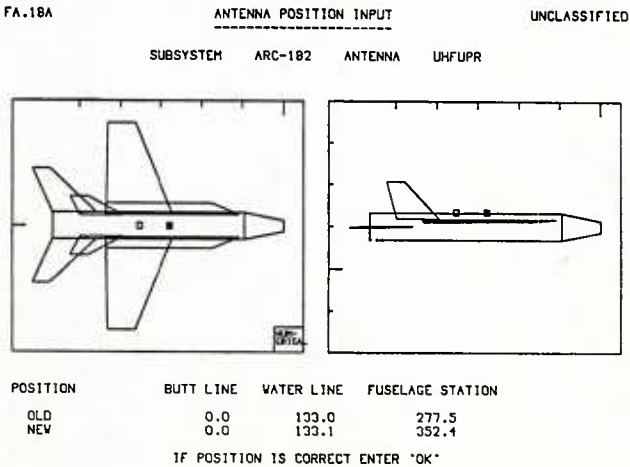
TABLE 2-1

COMPARISON OF PATH LENGTHS

PATH	FULL MODEL	SIMPLE MODEL	ERROR ON SIMPLE MODEL
1	1331 in.	1388 in.	+ 4.3%
2	472 in.	494 in.	+ 4.7%
3	1222 in.	1344 in.	+ 10%
4	1356 in.	1191 in.	- 12.2%
5	459 in.	527 in.	+ 15%
6	547 in.	525 in.	- 4.0%

Path 1. Wing tip - fuselage - top vert. stab.
2. Horizontal stab to top of vert. stab.
3. Nose along fuselage to tip of vert stab.
4. Wing tip to Wing tip.
5. Tip of Tail Boom to top of vert.
6. Stabilizer Tip to Stablizer Tip.

TABLE 2-2

PROGRAM CHECK VERSION 2 REVISION B

NECIN FILE NAME:	ORIMOD.3D
CHECK FILE NAME:	ORIC30.3D
FREQUENCY:	30.00 MHZ
WAVELENGTH:	10.00 M
EK OPTION:	USED

| WIRE TAG #	#	# SEG	ABSOLUTE SEG #S	RADIUS (M)	LENGTH OF WIRE (M)	LENGTH OF SEGS (M)	SEG/ WAVE	SEG/ RADIUS	INFO
1	1	1	1-) 1	0.0100	0.3052	0.3052	0.0305	30.52	
2	2	11	2-) 12	0.0100	19.7821	1.7984	0.1798	179.84	W
3	3	1	13-) 13	0.5030	1.9902	1.9902	0.1990	3.96	E
4	4	1	14-) 14	0.5030	2.0490	2.0490	0.2049	4.07	E
5	5	1	15-) 15	0.5030	2.0241	2.0241	0.2024	4.02	F

KEY TO THE ABOVE TABLE.

UNDER THE INFO COLUMN IS THE HIGHEST LEVEL OF ERROR DETECTED
FOR EACH INDIVIDUAL WIRE:
' ' = ACCEPTABLE
'N' = NOTE
'W' = WARNING
'E' = ERROR
* * * * *

INDIVIDUAL INCOMPATIBILITIES

TAG #	TYPE OF ERROR	ZERO LENGTH	SEG/WAV	SEG/RAD	WAV/RAD
2			W		
3			W		E
4			E		E
5			E		E

KEY TO THE ABOVE TABLE:

ZERO LENGTH	ERROR.	LENGTH OF WIRE < .01 M
SEG/WAV	NOTE:	.05 < SEG/WAVE < .1
	WARNING:	.10 < SEG/WAVE < .2
	ERROR:	SEG/WAVE > .2 OR < .001
SEG/RAD	WARNING:	2.0 < SEG/RAD < 8 WITHOUT EK OPTION
		0.5 < SEG/RAD < 2 WITH EK OPTION
	ERROR:	SEG/RAD < 2.0 WITHOUT EK OPTION
		SEG/RAD < 0.5 WITH EK OPTION
WAV/RAD	ERROR:	WAVE/RAD < 30
* * * * * *

INCOMPATIBILITIES AT JUNCTIONS

1ST TAG #	2ND TAG #	TYPE: COINCIDENCE	SEG/SEG	RAD/RAD	SEG/RAD
1	2			E	
1	212		E	E	E
1	213		E	E	E
1	295		E	E	E
1	296		E	E	E

KEY TO THE ABOVE TABLE:

COINCIDENCE	ERROR:	BOTH WIRES NEARLY OR EXACTLY COINCIDE
SEG/SEG	ERROR:	LONGER SEGMENT/SHORTER SEGMENT > 5
RAD/RAD	WARNING:	LONGER RADIUS/SHORTER RADIUS > 5
	ERROR:	LONGER RADIUS/SHORTER RADIUS > 10
SEG/RAD	ERROR:	ONE SEGMENT/OTHER RADIUS < 2

EFFECTS OF NONLINEAR LOADS ON ANTENNAS AND SCATTERERS
by
J. A. Landt
Los Alamos National Laboratory
P.O. Box 1663
Los Alamos, NM 87545

ABSTRACT

Nonlinear loads on antennas can be used to advantage or may degrade the performance of a communications system. Nonlinear elements are routinely used to protect sensitive receivers from high-power signals including high-power microwaves and EMP (electromagnetic pulse). Time-varying loading of antennas can be used to modulate the radar backscatter cross section to produce sidebands at the modulation frequency. Nonlinear elements can be used to detect the electromagnetic energy incident on an antenna, and thus be used as a measurement technique. Nonlinear loads can also be used for pulse shaping of the fields radiated by pulse-excited antennas. Active loads can be used to increase the performance of electrically small antennas and closely coupled arrays. Alternatively, undesired semiconducting junctions on structures near antennas can produce intermodulation products that can seriously degrade performance (this is often called the "rusty-bolt" effect).

This paper reviews the techniques available for analyzing these effects and gives representative examples. A time-stepping procedure is treated in detail.

I. INTRODUCTION

Essentially all radio communications and radar systems use nonlinear elements. Signals are detected, up-converted, down-converted, modulated, and processed. These operations are nonlinear, and are usually accomplished in electronics that are separate and distinct from the radiating elements of the system. If a nonlinear element is intimate with an antenna, unlike those in the conventional applications given above, the performance of the antenna can be affected. Then, a combined electromagnetic and network approach must be used to analyze the performance of the system. This paper summarizes the applications, effects, and analysis techniques for nonlinearly loaded antennas of this latter class.

Effects and applications include production of intermodulation products, radar cross section modulation, signal detection, protection, matching, and waveshape control. The literature and solution techniques are not extensive for nonlinearly loaded antennas, but several analytical, numerical, and experimental approaches have been developed and will be outlined here.

II. EFFECTS AND APPLICATIONS

A. The Rusty-Bolt Effect

Metal oxides can act like semiconductors. When two (or more) metallic structures are electrically connected by an oxide (a rusty bolt), the structure can produce undesirable nonlinear effects. Such a structure can cause mixing of signals, producing intermodulation products that can appear as interference in communication systems. This effect has been troublesome, especially on board ship (1). A method has been developed to easily identify sources of interference (2).

Production of intermodulation products can be qualitatively explained. Consider a nonlinear element placed between two metallic structures that can serve as antennas. In the present case, where interfering intermodulation products are produced, the metallic structures are unintentional antennas (such as guy wires and ladders). Fields produced by local transmitters and antennas will cause currents to flow on nearby metallic structures. These currents have the same frequency as the transmitter if no nonlinear effects are present, resulting in scattered fields at the same frequency as the transmitter. If there is a nonlinear element on the scattering structure, the nonlinear element will convert a portion of the current at the fundamental frequency into harmonics. These harmonic currents will radiate, causing signals at the harmonic frequencies to be present in the fields near by the nonlinear element. (A popular application of this harmonic production is the system used by retail stores and libraries to identify items to prevent theft.) Such harmonic generation is normally of little concern in producing interference. The signals fall off rapidly from the nonlinear element and are widely separated in frequency from the fundamental. For the production of harmonics to be efficient, the metallic structure must serve as a reasonably efficient antenna at the frequencies involved. For most inadvertent antennas, this is not likely to be the case beyond the first several harmonics.

Now consider the case when there are two local transmitters operating at different frequencies. The nonlinear element will cause mixing of these signals and produce currents and radiated fields at all combinations of multiples of the sums and differences of the two transmitted frequencies. Under this condition, one of these intermodulation products may fall in the band of a local receiver. If this happens, the sensitivity of this receiver can be severely reduced when the two interfering transmitters are active. This can happen even if the transmitters are spectrally pure and far outside the band of the receiver, because of the production of intermodulation products described here. This source of interference is one of several considered in electromagnetic compatibility studies of closely based communications systems (3),(4).

For example, if two frequencies are transmitted:

$$E_t = E_1 \cos 2\pi f_1 t + E_2 \cos 2\pi f_2 t \quad ,$$

intermodulation products can be produced of the form

$$E_i = E_Q \cos (2\pi m f_1 \pm 2\pi n f_2) \, t$$

where $n = 0, 1, 2, \cdots$
          $m = 0, 1, 2, \cdots$

and where $Q = n + m$ is defined as the order of the intermodulation product. Consider the case where $f_1 = 141.25$ MHz and $f_2 = 159.32$ MHz. The third-order intermodulation products occur at frequencies of 123.18, 177.39, 423.75, 441.82, 459.89, and 477.96 MHz. This particular example has been treated by Schuman (5), and will be covered in this lecture in more detail later.

Three conditions must be met for the production of intermodulation products that could cause interference. First, a semiconducting or nonlinear contact must be present. Second, the metallic structure which contains the nonlinear contact must be an effective antenna at the frequencies of the local transmitters. Third, the metallic structure must be an efficient antenna at the frequency of the intermodulation product or there must be a relatively low-loss path for the intermodulation signal to reach a receiver. The latter case can occur if the nonlinearity exists in the receiver coaxial cable braid, for example Ref. (6). Nonlinearities in metal contacts have also been studied by Arazm and Benson (7).

A method of locating significant sources of intermodulation interference has been developed (2). This technique will be summarized later in Section V.

Analytical and numerical techniques have been developed that can be used to study the production of intermodulation signals. These will be summarized in Sections III and IV.

B.   Transient Protectors and Limiters

Nonlinear elements are used routinely to protect sensitive receivers from static discharge, lightning, nuclear electromagnetic pulse, and high-power microwaves. Standard protection devices include spark gaps, electrical-surge arrestors, TR (transmit-receive) tubes, diodes, and other passive and active devices. The performance of these devices is affected by the antennas and circuits in which they are used.

Figure 1 shows a simple back-to-back diode limiter for a dipole antenna and 50-Ω load. The numerical procedures outlined in Sections III and IV can be used to study the performance of this arrangement. The load voltage is shown in Fig. 2 for a dipole length of 15 cm, a radius of 0.1 cm, an incident frequency of 1 GHz, an incident field of 1000 V/m, and Hewlett-Packard HP-2835 hot-carrier diodes. The circuit model of the diode includes a bulk resistance of 5.26 Ω and a constant junction capacitance of 1 pF. The computer code described in Section IV was used to calculate the performance of this antenna-limiter as a function of incident field strength.

The current through one of the diodes is shown in Fig. 3 for the same incident field strength. Figure 4 summarizes the performance of this limiter, where the load voltage is plotted as a function of incident field strength. The diodes do not conduct appreciable current for load voltages less than about 0.3 V, and below this level, the load voltage is approximately linearly related to the incident field strength. The constant of proportionality can be obtained using the well-known properties of dipole antennas (8). The equivalent circuit appropriate for voltages less than about 0.1 V is shown in Fig. 5. Here, Z_A is the antenna impedance (86.5 + j 41.7 Ω at 1 GHz), Z_D is the load impedance due to the two diodes (2.63 - j 80 Ω), and h_e is the effective height of the antenna (0.64 $\times$ 0.15 cm). This gives $V_L/E^i = 0.032 \lfloor -40.7°$. This line is labeled "no limiter action" in Fig. 4. At very high voltages, the diode characteristics will be dominated by bulk resistance and, again, the load voltage will vary approximately linearly with incident field strength. This curve is labeled "diode bulk resistance asymptote" in Fig. 4. The performance of the limiter goes smoothly between these two asymptotes. Limiting action occurs for voltages above about 0.3 V. The power rating of the diode is about 200 mW. This level is reached at an incident field strength of about 200 V/m. The reverse breakdown rating of this diode is 5 V, which is reached at an incident field strength of about 1000 V/m. At 1000 V/m incident, the antenna would deliver more than 30 V to the load without the limiter, far exceeding the rating of the diodes. This example illustrates that the interaction of the antenna with the nonlinear elements must be properly accounted for to obtain a true representation of the performance. The transient solution also shows that the load voltage builds up slowly and that initial transients will not exceed the diode voltage ratings at an incident field strength of 1000 V/m or less. It can be concluded that this simple limiter is inadequate for continuous operation for fields above 200 V/m and for pulsed fields above 1000 V/m. Low level signals will not be degraded. The limiter will produce harmonics; data on the harmonic content can be obtained by Fourier transform of Fig. 2.

Additional examples of limiters can be found in Section IV.

C.   Power Conversion

Novel applications of the conversion of radio frequency and microwave fields to direct current have been proposed. Landt (9) has developed a method of monitoring leakage from microwave ovens (at levels of 1 mW/cm^2 or less) by powering a light-emitting diode solely from the incident microwave energy. Several similar devices have been marketed that use this method. This principle has also been used to power electronic transponders (10). At higher power densities, Brown (11) powered a small, tethered helicopter solely from the energy in a microwave beam. In another application, the receiver portion of the Solar-Powered Satellite converted microwave energy to direct current for commercial power applications (12, 13).

D.   Radar Cross-Section Modulation

The radar cross section of an antenna can be modulated by a time-varying load placed at the antenna terminals. This effect has been put to practical use in a telemetry system (10). "False Doppler shifts"

can also be generated by radar cross-section modulation. Koelle and Depp (14) developed a novel radar system based on modulated backscatter. This system could accurately measure to zero Doppler shift, which is very difficult with more conventional systems.

E. Field Measurement Techniques

A variety of field measurement techniques rely on nonlinear loading of antennas and scatterers. A microwave field can be mapped by modulating the cross section of a dipole and measuring the result in a homodyne receiver (15). Microwave imagery tomographs have been produced using an array of diode-loaded dipoles (16). Methods of measuring transient fields using short dipoles that have nonlinear loads have been developed (17,18). Cases were considered where the dipole contains tapered resistive loading combined with a nonlinear load. Other techniques have also been developed to measure fields using the voltages detected by diode-loaded antennas.

F. Pulse-Shaping Radiated Fields

It is possible to use a nonlinear load to pulse-shape the field radiated by an antenna driven by an impulse generator. One may wish to reduce the late-time ringing, for example, to extend the low-frequency response of a transient electromagnetic range.

G. Active Antennas and Arrays

The performance of electrically small receiving antennas can be improved by loading the antenna with an active element (19-22). The active element serves both to transform (or match) impedance and amplify the received signals. The instabilities and resonances of actively loaded antennas have also been studied (23). In addition, active loading can be used to improve performance of arrays, both for reception (24, 25) and emission (26). Active transmitting antennas have also received attention (27). The interested reader is referred to these works and to Lecture Number 5 of this series, given by Prof. H. Lindenmeir.

III. REVIEW OF ANALYSIS TECHNIQUES

A. Use of Circuit Analysis

Nonlinear circuit-analysis techniques can be used to study the nonlinear loading of antennas. To employ this method, a circuit model of the antenna is needed. The circuit model of the antenna must adequately represent the antenna characteristics over a wide bandwidth. It is often difficult to estimate the required detail a priori and, consequently, one is left with the task of verifying the adequacy of the antenna model. Several circuit techniques may be used. Aprille and Trick (28) present a method of finding the steady-state response of nonlinear circuits for periodic inputs. The procedure involves integrating the system equations.

Nahas (13) modeled a dipole as a transmission line. The dipole was attached to filters and rectifiers, and a set of differential equations was derived from the resulting circuit. Skin-effect losses were also included using lumped circuit elements. The set of equations was solved numerically using a predictor-corrector integration method in the time domain. The analysis was extended by Gutmann and Borrego (29) to study parallel and series combinations of the dipole converter sections analyzed by Nahas. This latter work used a much simplified model for the antenna. Gutmann and Camnitz (30) have also described a method of determining the harmonic levels in nonlinear networks.

Electrically short dipoles and traveling-wave linear antennas with nonlinear loads have been studied by Kanda (17,18). The short dipole circuit model was a capacitor in series with a voltage source (for receiving). For simple nonlinear loads, an analytical solution was found in terms of the Anger function of imaginary order and imaginary argument. A numerical technique was also used to solve the circuit nodal equations using a time-stepping finite difference equation method. Kanda found that the solutions obtained by these two methods agreed closely. The traveling wave antenna was also analyzed with the time-stepping finite difference approach, but using a slightly different circuit model for the antenna.

Computer codes are available to analyze the transient response of circuits with nonlinear elements. These include NET II and SCEPTRE. Any of these codes could be used to find the response of a nonlinearly loaded antenna if a suitable circuit model for the antenna is available. Liu and Tesche (31) have devised a procedure that eliminates the need to derive a circuit model for the antenna. This procedure begins by finding the broadband antenna input impedance and short circuit current in the frequency domain. Although they obtained these quantities for a linear dipole using a frequency domain moment method technique, the procedure is not limited to this class of antennas. In addition, any procedure, including measurement, can be used to find the antenna characteristics. The next step is to formally transform the short circuit current and input admittance to the time domain. These quantities are then used in a transient analysis of the circuit containing these elements and the nonlinear loads. For a simple nonlinear voltage-current relationship for the nonlinear load, Liu and Tesche used Lalesco's nonlinear integral equation which was solved by an iterative approach. Liu (32) also compared the numerical solutions with measurements. The procedure was validated by good agreement between calculations and measurements for a resistively loaded dipole. The agreement was not as good for a diode loaded dipole, indicating that the circuit model for the diode was inadequate.

Volterra series can be used to analyze nonlinear circuits, including antennas (33,34). Sarkar and Weiner applied the technique to approximate the volt-ampere characteristic of the nonlinear load using measurements, and subsequently predicted scattered signals at different incident power levels. This technique is best when applied to weak nonlinearities, but gives good results for low levels of intermodulation without the use of an FFT.

B. Electromagnetic Solutions

Several time-domain electromagnetic computer codes have been developed that include nonlinear loading. Nonlinear elements are easily included in the time-domain techniques.

Schuman (5) adopted the thin-wire time-domain solution of Sayre and Harrington (35) to include loading by a single nonlinear load describable by a current as a polynominal function of voltage. He applied the procedure to the harmonic mixing of two incident signals of different frequencies.

Liu and Tesche (31) adopted a space-time-domain integral equation of Hallen's type for nonlinear loading. Their approach was implemented for a linear dipole with a nonlinear diode-like load described by two piecewise linear curves.

Chipman (36) modified a time-stepping finite difference solution for antennas and scatterers to include loading by a nonlinear load. In this approach, the volume surrounding the antenna is subdivided, and a time-stepping solution of Maxwell's equations in this volume is found. This approach is also suitable for analyzing antennas immersed in plasmas (37); this is the topic to be discussed by Dr. Balmain in this lecture series.

Landt (38) modified a thin-wire time-domain computer code (39) to permit loading antennas with circuits. The circuits can contain nonlinear as well as linear elements. A somewhat simpler approach was used to include loading effects of single or multiple nonlinear elements (40). These approaches permit flexibility in the antenna geometry and circuit description. These computer codes have been used to study a wide variety of nonlinear loading problems.

IV. ADAPTATION OF A THIN WIRE TIME DOMAIN (TWTD) COMPUTER CODE FOR NONLINEAR ANALYSIS

A. Introduction

TWTD is the brainchild of E. K. Miller, A. J. Poggio, and G. J. Burke (40). The original version of TWTD was developed in the early 1970s. Although the code has been extensively modified, the original mathematical basis remains unchanged to date. TWTD is still widely used which attests to the solidity of the formulation and numerical treatment. TWTD finds the transient electromagnetic response of thin wire conductive objects. The solution is formulated as an initial value problem and proceeds by time stepping. As such, TWTD can be easily modified to include nonlinear loading effects. The details of this approach are given here.

B. Mathematical Background

The treatment given here follows the original work (40). The goal is to treat nonlinear loading of antennas and scatterers. There are a variety of ways of doing this, as attested to by the other approaches summarized in this paper. In general, for transient solution, formulation in the time domain is more efficient than transform techniques; this is especially true if nonlinearities are involved. Here, we wish to develop a solution for thin wire structures. We choose the electric field integral equation formulation instead of magnetic field or vector potential formulations. This choice usually leads to better numerical stability and wider applicability than other approaches.

The derivation of the thin-wire electric field integral equation will be summarized here. A complete development can be found in the references.

The starting point is the well-known time dependent Maxwell's equations,

$$\nabla \times \vec{E} = - \frac{\partial \vec{B}}{\partial t} \tag{1a}$$

$$\nabla \times \vec{H} = \frac{\partial \vec{D}}{\partial t} + \vec{J} \tag{1b}$$

$$\nabla \cdot \vec{D} = \rho \tag{1c}$$

$$\nabla \cdot \vec{B} = 0 \tag{1d}$$

the continuity of charge,

$$\nabla \cdot \vec{J} + \frac{\partial \rho}{\partial t} = 0 \tag{2}$$

and the constituative relations,

$$\vec{D} = \varepsilon \vec{E} \tag{3a}$$

$$\vec{B} = \mu \vec{H} . \tag{3b}$$

The permittivity and permeability of the medium are ε and μ, respectively. The electric field is denoted by $\vec{E}$, the magnetic field by $\vec{H}$, the charge density by ρ, and the current density by $\vec{J}$. Rationalized MKS units are used here. $\vec{D}$ and $\vec{B}$ are the electric and magnetic flux densities, respectively.

Many methods are available for solving Maxwell's equations. For time-dependent boundary value problems, it is convenient to employ potentials. The field quantities are expressed in terms of retarded potentials:

$$\vec{B} = \nabla \times \vec{A} \tag{4a}$$

$$E = -\nabla\phi - \frac{\partial \vec{A}}{\partial t} \tag{4b}$$

where, using the Lorentz gauge, the retarded potentials are expressed in terms of integrals over current and charge:

$$\phi = \frac{1}{4\pi\varepsilon} \int_v \frac{\rho(\vec{r}', t - \frac{R}{v})}{R} dv \tag{5a}$$

$$\vec{A} = \frac{\mu}{4\pi\varepsilon} \int_v \frac{\vec{J}(\vec{r}', t - \frac{R}{v})}{R} dv \tag{5b}$$

$$v = \frac{1}{\sqrt{\mu\varepsilon}} \tag{5c}$$

$$R = |\vec{R}| = |\vec{r} - \vec{r}'| \quad . \tag{5d}$$

Here, $\vec{r}'$ is the position of the source and $\vec{r}$ is the field point (or the position of the observer).

The reader is referred to texts for development of the retarded potentials (41,42).

Since the boundary conditions will be expressed in terms of electric fields tangent to conducting surfaces and, since there are numerical reasons to use an electric field integral equation approach for thin wires, the potentials are used here to derive the electric field integral equation. In free space, $\varepsilon = \varepsilon_0$, $\mu = \mu_0$. The velocity of light, c, is:

$$c = \frac{1}{\sqrt{\mu_0\varepsilon_0}} . \tag{6}$$

Define the retarded time t':

$$t' = t - \frac{R}{c} \quad . \tag{7}$$

The desired electric field integral equation follows directly from Eqs. (2), (4), and (5). Here, the mathematical details are provided since this approach yields insight into the relationships between time, retarded time, and source distributions.

Consider the first term of Eq. (4b):

$$\nabla\phi = \frac{1}{4\pi\varepsilon} \int_v \nabla \left(\frac{\rho(\vec{r}', t')}{R}\right) dv \tag{8a}$$

$$= \frac{1}{4\pi\varepsilon} \int_v \left[\rho(\vec{r}', t') \nabla (\frac{1}{R}) + \frac{1}{R} \nabla\rho(\vec{r}', t') \right] dv \quad . \tag{8b}$$

It can be easily shown that

$$\nabla (\frac{1}{R}) = - \frac{\vec{R}}{R^3} \quad . \tag{9}$$

The divergence of the charge density requires more care. The divergence is formed using partial derivatives at constant time, t. The retarded potentials require expressing the sources in terms of retarded time, t', however. In rectangular coordinates, the gradient is defined as:

$$\nabla\rho = \frac{\partial\rho}{\partial x} \hat{a}_x + \frac{\partial\rho}{\partial y} \hat{a}_y + \frac{\partial\rho}{\partial z} \hat{a}_z \quad , \tag{10}$$

where $\hat{a}_x$, $\hat{a}_y$, and $\hat{a}_z$ are the conventional unit vectors in the x, y, and z directions, respectively. Consider the first term of Eq. (10):

$$\frac{\partial \rho}{\partial x} = \frac{\rho(\vec{r}', t')}{\partial t'} \cdot \frac{\partial t'}{\partial x} \quad . \tag{11}$$

using the formalism of partial derivatives. If the solution is limited to charges and currents bound to conducting surfaces (where the boundary conditions will be enforced), the vector $\vec{R}$ is time invarient. Then, it can be shown that

$$\frac{\partial t'}{\partial x} = -\frac{(x - x')}{cR} \tag{12}$$

It follows that

$$\nabla \rho(\vec{r}', t') = -\frac{\vec{R}}{cR} \frac{\partial \rho(\vec{r}', t')}{\partial t'} \quad . \tag{13}$$

Also

$$\frac{\partial \vec{J}}{\partial t} = \frac{\partial \vec{J}}{\partial t'} \cdot \frac{\partial t'}{\partial t} = \frac{\partial \vec{J}}{\partial t'} \quad . \tag{14}$$

Combining equations (4), (5), (6), (8), (9), (13), and (14) yield the desired equation:

$$\vec{E}(r,t) = \frac{\mu_0}{4\pi} \int_V \left[c^2 \frac{\vec{R}}{R^3} \rho(r',t') + c \frac{\vec{R}}{R^2} \frac{\partial \rho(\vec{r}',t')}{\partial t'} - \frac{1}{R} \frac{\partial \vec{J}(\vec{r}',t')}{\partial t'} \right] dv \quad . \tag{15}$$

Next, the conventional thin wire approximations are invoked. Consider Fig. 6. The total current flowing on the wire is approximated by assuming that the current is restricted to a filament described by the curve $C(\vec{r})$.

The vector $\vec{r}$ is arbitrary in general, but in Fig. 6, $\vec{r}$ is chosen at the surface of the wire, and $\hat{s}$ is tangent to the surface of the wire and parallel to the axis of the wire at position $\vec{r}$.

The integral over the cross section of the wire gives

$$\int_A \vec{J}(\vec{r}', t') \, dA = I(\vec{r}',t') \, \hat{s}' \tag{16a}$$

and

$$\int_A \rho(\vec{r}', t') \, dA = q(\vec{r}',t') \tag{16b}$$

when $\hat{s}'$ is a unit vector tangent to the curve $C(\vec{r})$ at the point $\vec{r}'$. With these approximations, Eq. (2) reduces to

$$\frac{\partial I}{\partial s'} + \frac{\partial \rho}{\partial t} = 0 \quad . \tag{17a}$$

From Eq. (7)

$$\frac{\partial \rho}{\partial t} = \frac{\partial \rho}{\partial t'} \cdot \frac{\partial t'}{\partial t} = \frac{\partial \rho}{\partial t'} \quad . \tag{17b}$$

Combining

$$\vec{E}(r,t) = \frac{\mu_0}{4\pi} \int_{C(r)} \left[\frac{c^2 \vec{R}}{R^3} q(r',t') - \frac{c\vec{R}}{R^2} \frac{\partial I(\vec{r}',t')}{\partial s'} - \frac{\hat{s}'}{R} \frac{\partial I(\vec{r}',t')}{\partial t'} \right] ds' \quad , \tag{18}$$

which is identical to Eq. (7) of Ref. (39).

Several methods of specifying the source excitation are possible. Here it is assumed that an applied electric field, $\vec{E}^I(\vec{r},t)$, is known. For example $\vec{E}^I(\vec{r},t)$ could be the field of an incident plane wave. For a second example, the wire can be driven as an antenna by specifying a nonzero E^A over a limited source region. To solve for the currents, the total electric field tangent to the wire is set equal to zero. Consider Fig. 6. The unit vector $\hat{s}$ is parallel to the wire axis and located at the surface of the wire. Then, the boundary condition yields:

$$\hat{s} \cdot (\vec{E}^I + \vec{E}) = 0 \tag{19}$$

or

$$\hat{s} \cdot \vec{E}^I(r,t) = \frac{\mu_0}{4\pi} \int_{C(r)} \left[\frac{\hat{s} \cdot \hat{s}'}{R} \frac{\partial I(\vec{r}',t')}{\partial t'} + c \frac{\hat{s} \cdot \vec{R}}{R^2} \frac{\partial I(\vec{r}',t')}{\partial s'} - c^2 \frac{\hat{s} \cdot \vec{R}}{R^3} q(\vec{r}',t') \right] ds' \quad . \tag{20}$$

This equation will be solved numerically using the method of moments. Note that the minimum value of R is a, the wire radius, and consequently, Eq. (20) contains no singularities. The charge can be related to the current through Eq. (2).

C. Numerical Solution

It will be instructive to develop the numerical solution for Eq. (20) before consideration of non-linear loading. The numerical procedure is outlined here with the aim of emphasizing the form of the solution instead of deriving the specific equations to be implemented in a computer code.

Causality is enforced in Eq. (20) through the retarded time. Fields anywhere on the structure are because of currents and charges at earlier times. Therefore, it is possible to formulate the solution as an initial value problem to be solved by a time-stepping procedure without resorting to matrix inversion. It will be found to be advantageous to use smooth basis functions, to use interpolation for the currents on the structure, and to permit distances between different portions of the structure to be very small. This in general will require matrix inversion to solve for the currents at the present time step, but the solution still proceeds in a time-stepping fashion. This will become evident as the solution is developed.

The basic steps in the solution are:

1. The structure geometry is approximated by a set of wire segments. While curved segments could be used, here the segments are restricted to be thin circular cylinders. This set of segments forms a piecewise linear approximation to the original geometry.

2. The currents at the centers of the segments are the unknowns for which a solution is desired.

3. Equation (20) will be enforced at the center of each segment, but with $\hat{s}$ residing on the surface of the cylinder and the current on the axis of the cylinder as discussed earlier.

4. A constant time step increment is used. The solution is found at a set of discrete times, starting with $t = 0$ and separated in time by a constant time step. In general, a segment length should be the same order as the time step times the velocity of light.

5. A 9-point Lagrangian interpolation function in space and time is used for the current basis function. This choice permits the integrals in Eq. (20) to be evaluated analytically.

The formal reduction of Eq. (20) to a linear system using the approach outlined above is tedious, and the interested reader is referred to Miller (39). After the notation of Eq. (22) in Ref. (39), the system equation, in matrix form, is

$$\underline{E}_v^I + \underline{E}_v^S = \underline{\underline{Z}} \, \underline{I}_v \quad , \tag{21}$$

for $v = 1, 2, \cdots, N_T$.

Here, v is the number of the time step; $\underline{E}_v^I$ is the driving (incident) electric field tangent to the wire; $\underline{\underline{Z}}$ is an impedance matrix; and $\underline{I}_v$ is the unknown current at the time step v. Underlined quantities denote a matrix quantity. $\underline{E}_v^S$ represents the "scattered" electric field tangent to the wire. This field is due to retarded currents and charges on the structure found at earlier time steps. Thus, $\underline{E}_v^S$ is known for the present time step. An element of $\underline{E}_v^S$ can be written as

$$E_{v,j}^S = \underline{S} \left[\underline{\underline{X}}_j \underline{I}_p + \underline{\underline{W}}_j \underline{C}_p \right] \underline{S}' \quad , \tag{22}$$

where, for the ith segment,

$$C_{p,i} = \int_{t=-\infty}^{t=p} I_i(\tau) d\tau \quad . \tag{23}$$

$\underline{S}$ and $\underline{S}'$ are single row (or column) matrices comprised entirely of ones. $\underline{C}_p$ and $\underline{I}_p$ are arrays constructed from currents found at past time steps. The matrices $\underline{\underline{X}}$, $\underline{\underline{W}}$, $\underline{I}_p$, and $\underline{C}_p$ include the effects of time retardation. Note that the values of $C_{p,i}$ are not charge density. If desired explicitly, the linear charge density along the wire can be obtained from

$$q_i(t) = - \frac{\partial}{\partial s} C_i(t) \quad , \tag{24}$$

where s represents distance along the wire.

The matrices $\underline{\underline{Z}}$, $\underline{\underline{W}}$, and $\underline{\underline{X}}$ depend only upon geometrical constants of the structure and upon the value of the time-step increment. Thus, these matrices are time invariant. They are calculated once and stored. The solution is obtained in a time-stepping fashion, solving for $\underline{I}_v$ at each time step. Normally, the inverse of $\underline{\underline{Z}}$ is calculated only once but is used at each time step. The wave-like nature of the propagation of the current along the wire is hidden in the matrices $\underline{\underline{Z}}$, $\underline{\underline{X}}$, and $\underline{\underline{W}}$. The matrix $\underline{\underline{Z}}$ contains off-diagonal elements due to the use of current interpolation. The final computer code is general and easily used. Geometry, segmentation, value of the time step, and incident field are input by an input deck. No code modifications are required to solve a wide variety of problems (43,44).

Implementation of loading of the wire involves modification of Eq. (21) and subsequent modifications of the $\underline{\underline{Z}}$, $\underline{\underline{X}}$, and $\underline{\underline{W}}$ matrices.

D. Loading

1. Linear Loading. Linear loading of the wire structure with resistance, inductance, and capacitance is straightforward. For any given segment, the electric field caused by loading, $E_{v,i}^{\ell}$ is approximated by

$$E_{v,i}^{\ell} = \frac{V_i^{\ell}}{\delta_i} \tag{25}$$

where δ_i is the length of the ith segment. For resistors

$$V_i^R = R_i I_i \quad , \tag{26}$$

for inductors

$$V_i^L = L_i \frac{dI_i}{dt} \quad , \tag{27}$$

for capacitors

$$V_i^C = \frac{1}{C_i} \int_{-\infty}^{t} I_i(\tau)d\tau \quad , \tag{28}$$

and where

$$V_i^{\ell} = V_i^R + V_i^L + V_i^C \quad . \tag{29}$$

Here, R_i, L_i, and C_i are respectively the resistance, inductance, and capacitance of the series loading applied to the ith segment.

Implementation of these equations proceeds using the quadratic interpolation function for the current as a function of time. Note that the field to be added is needed for Eq. (21). This field is approximated by Eq. (25). It has been found that the approximation of Eq. (25) works poorly if the loading field is confined to a region on the wire with much less extent than $c\Delta t$. Here c is the velocity of light and Δt is the time step.

2. Nonlinear Loading of Selected Segments. Several schemes can be employed to implement nonlinear loading. Two will be considered here in detail.

Method 1. The most straightforward method is simply to adjust the arrays $\underline{Z}$, $\underline{X}$, and $\underline{W}$ at each time step according to the form of nonlinear loading desired. Consider the straight-line diode-like characteristic shown in Fig. 7. If V is positive, then let

$$R = R_f \quad . \tag{30a}$$

If V is negative, then let

$$R = R_r \quad . \tag{30b}$$

Consequently, to reflect this nonlinear loading of a segment, at each time step, the $\underline{Z}$ array must be adjusted according to the sign of the sum of the fields E^I and E^S for that segment. This method requires that $\underline{Z}^{-1}$ (the inverse of $\underline{Z}$) must be found at each time step, or that two $\underline{Z}^{-1}$ matricies must be stored. This requires a substantial penalty in either computer time or storage. If more than a single segment is to be loaded, this method has an advantage, however. For example, every segment could be loaded with a diode. Each diode could be turned "on" or "off" separately, depending upon the sum of E^I and E^S for each segment individually.

Method 2. An alternate scheme can be employed, provided the time-varying loading modifies only the $\underline{Z}$ matrix (that is, time-varying resistance). Consider the loading added explicitly to Eq. (21) in terms of a time-varying impedance $\underline{Z}_L$:

$$\underline{E}_v^I + \underline{E}_v^S = \underline{Z} \, \underline{I}_v + \underline{Z}_L \, \underline{I}_v \quad . \tag{31}$$

In the previous scheme, $(\underline{Z} + \underline{Z}_L)^{-1}$ was computed at each time step. For the present case, however, partition $\underline{Z}_L$ to isolate its null components ($\underline{0}$ is the null matrix):

$$\underline{Z}_L = \begin{bmatrix} \underline{Z}_{L1} & \vdots & \underline{0} \\ - - & \vdots & - - \\ \underline{0} & \vdots & \underline{0} \end{bmatrix} \quad , \tag{32}$$

and partition $\underline{Z}$ to conform to $\underline{Z}_L$:

$$\underline{\underline{Z}} = \begin{bmatrix} \underline{\underline{Z}}_{11} & \vdots & \underline{\underline{Z}}_{12} \\ - - - & \vdots & - - \\ \underline{\underline{Z}}_{21} & \vdots & \underline{\underline{Z}}_{22} \end{bmatrix} \quad , \tag{33}$$

Then, Eq. (31) becomes (partitioning $\underline{E} = \underline{E}^I + \underline{E}^S$ and $\underline{I}$ also):

$$\begin{bmatrix} \underline{E}_{1v} \\ - - - \\ \underline{E}_{2v} \end{bmatrix} = \left\{ \begin{bmatrix} \underline{\underline{Z}}_{11} & \vdots & \underline{\underline{Z}}_{12} \\ - - - & \vdots & - - \\ \underline{\underline{Z}}_{21} & \vdots & \underline{\underline{Z}}_{22} \end{bmatrix} + \begin{bmatrix} \underline{\underline{Z}}_{L1} & \vdots & \underline{0} \\ - - - & \vdots & - - \\ \underline{0} & \vdots & \underline{0} \end{bmatrix} \right\} \begin{bmatrix} \underline{I}_{1v} \\ - - - \\ \underline{I}_{2v} \end{bmatrix} \quad . \tag{34}$$

$\underline{I}^u$ is defined as the "unloaded" current:

$$\underline{E}_v = \underline{\underline{Z}} \; \underline{I}^u_v \quad . \tag{35}$$

Multiplying Eq. (35) by $\underline{\underline{Z}}^{-1}$ yields:

$$\begin{bmatrix} \underline{I}^u_{1v} \\ - - - \\ \underline{I}^u_{2v} \end{bmatrix} = \left\{ \begin{bmatrix} \underline{U} & \vdots & \underline{0} \\ - - & \vdots & - - \\ \underline{0} & \vdots & \underline{U} \end{bmatrix} + \underline{\underline{Z}}^{-1} \begin{bmatrix} \underline{Z}_{L1} & \vdots & \underline{0} \\ - - - & \vdots & - - \\ \underline{0} & \vdots & \underline{0} \end{bmatrix} \right\} \begin{bmatrix} \underline{I}_{1v} \\ - - - \\ \underline{I}_{2v} \end{bmatrix} \quad . \tag{36}$$

$\underline{U}$ is the unity matrix. Note that $\underline{I}^u_v$ can be found at each time step from Eq. (35) and independent of loading. Partition $\underline{\underline{Z}}^{-1}$ also:

$$\underline{\underline{Z}}^{-1} = \begin{bmatrix} \underline{\underline{Z}}_{11}^{-1} & \vdots & \underline{\underline{Z}}_{12}^{-1} \\ - - - & \vdots & - - - \\ \underline{\underline{Z}}_{21}^{-1} & \vdots & \underline{\underline{Z}}_{22}^{-1} \end{bmatrix} \quad , \tag{37}$$

(Note that $\underline{\underline{Z}}_{11}^{-1}$ is not the inverse of $\underline{\underline{Z}}_{11}$ and likewise for $\underline{\underline{Z}}_{12}$, $\underline{\underline{Z}}_{21}$, and $\underline{\underline{Z}}_{22}$.)

$$\begin{bmatrix} \underline{I}^u_{1v} \\ \\ \underline{I}^u_{2v} \end{bmatrix} = \begin{bmatrix} \underline{U} + \underline{\underline{Z}}_{11}^{-1} \; \underline{\underline{Z}}_{L1} & \vdots & \underline{0} \\ - - - - - - - - - - - - & \vdots & - - - \\ \underline{\underline{Z}}_{21}^{-1} + \underline{\underline{Z}}_{L1} & \vdots & \underline{U} \end{bmatrix} \begin{bmatrix} \underline{I}_{1v} \\ - - - \\ \underline{I}_{2v} \end{bmatrix} \quad . \tag{38}$$

The currents on the loaded segments, $\underline{I}_{1v}$, are then found from

$$\underline{I}_{1v} = (\underline{U} + \underline{\underline{Z}}_{11}^{-1} \; \underline{Z}_{L1})^{-1} \; \underline{I}^u_{1v} \quad , \tag{39}$$

and subsequently the remainder of the currents, $\underline{I}_{2v}$ are found from

$$\underline{I}_{2v} = \underline{I}^u_{2v} - (\underline{\underline{Z}}_{21}^{-1} \; \underline{\underline{Z}}_{L1}) \; \underline{I}_{1v} \quad . \tag{40}$$

If all the segments are not loaded, then $\underline{\underline{Z}}_{L1}$ is less than an $n \times n$ matrix (where n is the total number of segments), and the inversion to be performed in Eq. (39) requires less time than the inversion in Eq. (31) for $(\underline{\underline{Z}} + \underline{\underline{Z}}_{L1})^{-1}$.

If a single segment is to be loaded, Eq. (39) reduces to a simple form, and very little penalty in computer time and storage is incurred. This is because Eqs. (39) and (40) can be solved explicitly for each segment individually and do not involve inversion of matrices. For a single-segment loading, the matrix equation, Eq. (39), reduces to the algebraic equation (for loading the segment labeled 1):

$$I_{1v} = \frac{I^u_{1v}}{(1 + Z_L Z_{11}^{-1})} \quad . \tag{41}$$

For the remaining segments, Eq. (40) reduces to

$$I_{jv} = I^u_{jv} - \frac{Z_{j1}^{-1} Z_L}{(1 + Z_{11}^{-1} Z_L)} \; I^u_{1v} \quad , \tag{42}$$

for $j = 2$ to N. (N is the total number of segments.) Here, the terms Z_{ij}^{-1} are the elements of the matrix $\underline{\underline{Z}}^{-1}$:

$$\underline{Z}^{-1} \doteq \begin{bmatrix} Z_{11}^{-1} & Z_{21}^{-1} & - - - - - - - - - - - - \\ Z_{21}^{-1} & Z_{22}^{-2} & \diagdown \\ \cdot & & \diagdown \\ \cdot & & \diagdown \\ \cdot & & \diagdown \\ Z_{j1}^{-1} & & Z_{jj}^{-1} \diagdown \\ \cdot & & & \diagdown \\ \cdot & & & \diagdown \\ \cdot & & & \diagdown \\ Z_{n1}^{-1} & & & \diagdown & Z_{21}^{-1} \end{bmatrix} \qquad (43)$$

Implementation of Eqs. (41) and (42) is straightforward. First, $\underline{Z}^{-1}$ is found and stored. Then, at each time step, I_v^u is calculated and subsequently modified according to Eqs. (41) and (42) and according to the desired Z_L at that time step.

3. Loading with a Circuit. The implementation of circuit analysis proceeds directly from Eqs. (41) and (42) or alternately from a modification of Eq. (21). Consider the network shown in Fig. 8. Norton's equivalent circuit of the antenna is to the left of points A-A' and stems directly from Eq. (21). The "short circuit," or "unloaded," antenna current at the terminals A-A' is I_v^u. The load current, I_v^ℓ (also the loaded antenna current) can be written as

$$I_v^\ell = \frac{I_v^u}{1 + \dfrac{Y_{11} V_v^\ell}{I_v^\ell}} \qquad . \qquad (44)$$

This expression is exactly the same as Eq. (41), if $Y_{11} = Z_{11}^{-1}$, and if Z_L is defined as V_v^ℓ / I_v^ℓ.

This observation provides a simple, yet powerful technique of loading the wire structure with a circuit. From the circuit standpoint, Norton's equivalent of the antenna is the simple circuit to the left of terminals A-A' in Fig. 8. I_v^u is the short-circuit current on the segment to be loaded, and Y_{11} is the self-admittance term of the segment to be loaded in the matrix $\underline{Z}^{-1}$ of Eq. (21).

The solution is obtained as follows. First, the matrices $\underline{Z}$, $\underline{X}$, and $\underline{W}$ are found as usual; then $\underline{Z}^{-1}$ and Z_{j1}^{-1} are calculated; the solution then proceeds by time stepping. At each time step, Eq. (21) is solved for the "unloaded" or "short circuit" current. This solution, along with $\underline{Z}^{-1}$, is used to construct Norton's equivalent circuit for the antenna as in Fig. 8 and Eq. (44). This equivalent circuit is used in a nodal analysis of the circuit using quadratic interpolation functions for the transient nodal voltages, solving for V_v^ℓ and I_v^ℓ. The unloaded currents and the solution of the circuit (with the antenna equivalent circuit attached) may be combined to yield the total solution in several different ways.

a. An "equivalent" impedance approach defines Z_L as V_v^ℓ / I_v^ℓ and inserts this value directly in Eqs. (41) and (42). However, this procedure has numerical problems, whenever I_v^u is very small and I_v^ℓ is not.

b. An alternative is to write Eq. (21) to include the field due to circuit loading as $\underline{E}_v^\ell$:

$$\underline{E}_v^I + \underline{E}_v^S = \underline{Z}\, \underline{I}_v + \underline{E}_v^\ell \qquad . \qquad (45)$$

$\underline{E}_v^\ell$ can be obtained from V_v^ℓ by using (25).

Proceeding,

$$\underline{I}_v = \underline{Z}^{-1}(\underline{E}_v^I + \underline{E}_v^S) - \underline{Z}^{-1}\underline{E}_v^\ell \qquad , \qquad (46)$$

or

$$\underline{I}_v = \underline{I}_v^u - \underline{Z}^{-1}\underline{E}_v^\ell \qquad . \qquad (47)$$

For the single-port loading of the ith segment, the current on the jth segment becomes (for $j = 1$ to N):

$$I_j = I_j^u - Y_{ji}E_v^\ell \qquad . \qquad (48)$$

The quantities E_v^ℓ and I_j^u were found above. The solution continues by then considering the next time step.

For the present applications, the capability of a large circuit code (such as SCEPTRE or NET II) was not required. Consequently, a new code was developed to solve the time-domain nodal equations. This code was tailored to the present needs and constructed making full use of the attributes of the electromagnetic portion of the solution (that is, the interpolation functions). The basis for the analysis is the normal nodal equations of conservation of current at a node:

$$\sum_{j=1}^{n} I_j = 0 \quad . \tag{49}$$

The currents are expressed in terms of the node voltages (unknown) and the values of the circuit elements.

A quadratic interpolation function is used to represent the time history of the node voltages in terms of the sampled values. Consider Fig. 9. A quadratic curve is passed through the points (t_2, V_2), (t_1, V_1), and (t_0, V_0). The values of V_2 and V_1 are known from solutions obtained at earlier time steps. The value V_0 is the unknown voltage at the present time, t_0. The solid portion of the quadratic curve is used as the interpolation function for $V(t)$ between t_1 and t_0. Using this function, it can be shown that for a constant time step of δ (that is, $\delta = t_0 - t_1 = t_1 - t_2$) and at time t_0, the current through a resistor of R Ω is

$$I_R = \frac{1}{R} V_0 \quad , \tag{50}$$

the current through an inductor of L henries is

$$I_L = \frac{1}{L} \left[\frac{5\delta}{12} V_0 + \frac{2\delta}{3} V_1 - \frac{\delta}{12} V_2 + \int_{-\infty}^{t_1} V(\tau) d\tau \right] \quad , \tag{51}$$

and the current through a capacitor of C farads is

$$I_C = C \left[\frac{3}{2\delta} V_0 - \frac{2}{\delta} V_1 + \frac{1}{2\delta} V_2 \right] \quad . \tag{52}$$

Similar expressions can be developed for circuit elements that vary with time.

Several methods can be used to treat nonlinear elements. A method that has been found to give good results is outlined here. Consider the volt-ampere (vi) characteristic shown in Fig. 10. Each nonlinear element in the circuit is assigned a value R_{eq}. This value is obtained from the R_{eq} found at the previous time step. For the first time step, R_{eq} is set equal to dV/dI at V = 0. These values of "equivalent resistance" are inserted into the nodal equations and a solution if obtained. For each nonlinear element, the solution is checked to see if it lies on the characteristic curve (to some desired accuracy). If the solution is correct for each nonlinear element, the loaded antenna currents are found using Eq. (48), and the next time step is considered. If the characteristic curves are not satisfied, an iteration process is used to obtain a correct solution. This iteration involves the circuit analysis only and does not require new electromagnetic solutions.

Iteration proceeds by determining a load line for the circuit at each nonlinear element and subsequently the intersection of this load line with the nonlinear element's vi curve. R_{eq} is defined as V_i/I_i of Fig. 10. To obtain the load line, the values of R_{eq} of the previous iteration are used for other nonlinear elements. Since the load line is influenced by these other nonlinear elements, the solution obtained using all the new values of R_{eq} may not fit the characteristic curves. Consequently, an iteration proceeds until the solution satisfies the characteristics of all the elements of the circuit. Presently, the solution is terminated with a warning if 20 iterations fail to give 0.1% agreement between the current on the vi curve and the current obtained by V/R_{eq}. Analytical solutions can be obtained for certain types of nonlinear elements (and thus avoid the iteration process), but a penalty is paid for lack of generality.

Loading the antenna at more than one location follows directly from Eq. (47). The procedure is identical to that presented here for single-port loading with the addition of voltage-controlled current sources in the nodal solution to account for the terms of $\underline{Z}^{-1} \underline{E}_v^e$ from Eq. (45).

E. Numerical Results

1. Production of Intermodulation Products. Schuman (5) calculated the current through a nonlinear load at the center of a dipole. The vi characteristic of the load is $i = -0.08 v + 3.92 v^3$ where i is in milliamperes and v is in volts. Consider the equivalent circuit shown in Fig. 8. At each time step, the proper solution is the intersection of the vi curve of the nonlinear load with the load line characterized by I^u and Y_{11}, as in Fig. 10. This, in general, would require that the roots of a polynomial be found [as in Ref. (5)]. An alternate method is to approximate the nonlinear vi curve with a series of straight line segments. Such an approximation is shown in Fig. 11. The load current was found using the present technique for the same case as in Ref. (5) and using the 11-segment straight-line approximation of Fig. 11. These results are plotted in Fig. 12. A broadside electric field was incident on a dipole of length 0.966 m. The field was $E^i = 0.25 [\cos(2\pi f_1 t) + \cos(2\pi f_2 t)]$ V/m, where $f_1 = 141.25$ MHz and $f_2 = 159.32$ MHz. The wire radius was 0.003 m, and 19 wire segments were used to represent the linear antenna. The results given in Fig. 12 agree closely with those of Ref. (5). Note that the sidebands presented in Fig. 12 are not as evident in the back-scattered field shown in Fig. 13. The load current found using the three-segment, straight-line approximation is shown in Fig. 14. Note that the same beat-frequency pattern is obtained as in Fig. 12, but the oscillations are absent when the current is near zero. These oscillations are apparently due to the negative resistance region of the nonlinear load. Computer time was 13.1 and 10.7 s on a CDC 7600 for Figs. 12 and 14, respectively, for the 760 time steps shown.

2. Loading with Diodes. Lui and Tesche (31) gave results for a dipole loaded at its center with a nonlinear resistor. The resistance was represented by 50 Ω in the "forward" direction and 5000 Ω in the "reverse" direction. For this type of load, the calculations can be "normalized" as in Ref. (31). (Note that this is not possible for arbitrary nonlinear loading.) To match the results, a dipole length of L = 1 m and a diameter of 6.739×10^{-3} m were chosen; 19 wire segments were used to model the antenna.

The broadside incident field was a 1-V/m step function with the electric field parallel to the wire and in the direction tending to cause current to flow initially in the "forward" direction. The results shown in Fig. 15 are essentially the same as found in Ref. (31). The computer time required for the solution of Fig. 15 was 1.7 s on a CDC 7600. The radiating properties of this antenna are shown in Fig. 16. Here, a voltage source was applied in series with the diode. The form of the voltage was $V = [\exp - \{a(t - t_0)\}^2]V$, where $a = 1.73 \times 10^9 \text{ s}^{-1}$ and $t_0 = 1.76 \times 10^{-9}$ s. The diode limits the flow of current at the center of the antenna to the very early portion of the response. As in the scattering case, a strong second harmonic exists in the radiated field as given in Fig. 17. Loading each of the 19 segments of the antenna with a nonlinear resistor identical to that used above gives quite different results. Late-time ringing of the far field is greatly reduced and indicates that pulse shaping of the radiated field is possible, as shown in Fig. 18.

3. Loading with Circuits. Nahas (13) and Liu (32) have noted that poor agreement between calculations and experiments is obtained for high-frequency circuits containing the simple models of diodes used here. More complete models are required. Junction capacitance as well as lead inductance and package capacitance can have strong effects on circuit performance. To illustrate this effect, along with demonstrating the capability of the present technique, consider the voltage doubler circuit shown in Fig. 19. The two diodes used for the voltage doubler are HP 5082-2835 hot-carrier diodes. Their low-frequency vi characteristics were represented by two straight-line segments. For voltages below 0.35 V, the diode is considered pure resistance of 10 MΩ. At a forward voltage of 0.35 V and greater, the slope of the vi characteristics is represented by a dynamic resistance of 0.1 Ω and a bulk resistance of 2.9 Ω. A linear dipole was chosen for the present calculations, although other antenna types could have been used. The dipole length was 5.47 cm and the radius was 0.05 cm; 19 segments were used to model the dipole. The low-frequency load is a diode, modeled with two straight-line segments similar to the high-frequency, hot-carrier diodes. The "off" resistance was chosen to be 10 MΩ, the "turn-on" voltage to be 1.55 V, and the forward dynamic resistance to be 0.7 Ω with a bulk resistance of 10 Ω. A sinusoidal field with power density of 1 mW/cm^2 at a frequency of 2450 MHz illuminated the antenna from broadside with an electric field parallel to the dipole. The resulting current through the low-frequency diode is shown in Fig. 20. Note that some time elapses before the output voltage level builds up to 1.55 V (and consequently turns the low-frequency diode "on"). The late time response contains considerable ripple due to the small value of bypass capacitors in the circuit. A slightly different and more realistic model of the actual circuit is shown in Fig. 21. Here, the junction capacitance was taken as constant at a value of 1 pF for the hot-carrier diodes and 5 pF for the low-frequency diode. The current through the junction of the low-frequency diode is shown in Fig. 22 for the same incident field that was used in Fig. 20. Note that more time is required to reach steady state and that the current has reduced by a factor of ~5. The more complete solution, as given by Fig. 22, was found to reflect the actual circuit performance, while the results shown in Fig. 20 did not. A model is shown in Fig. 23 of an antenna and circuitry of a transponder in use in an electronic identification system (10). The wire-grid model of the antenna contains 37 segments. The segment lengths are 1.2 cm parallel to the major axis of the antenna. Normal to the major axis, the segment lengths are 1.0 cm. The wire radius is 0.1 cm. The antenna is embedded in a lossless, homogeneous, isotropic medium with a dielectric constant of 9. A time-step increment of 1.2×10^{-10} s was employed. The diodes labeled D_1 and D_2 have the normal exponential voltage current relationship: $I = I_s [\exp (\theta V) - 1]$, for $\theta = 35.8 \text{ V}^{-1}$ and $I_s = 1.486 \times 10^{-8}$ A. The voltage-current relationship for the resistor R_1 consists of three straight-line segments. Below 2.50 V, $\Delta I/\Delta V = 4 \times 10^{-5}$ S; between 2.50 and 2.55 V, $\Delta I/\Delta V = 1.84 \times 10^{-2}$ S; and above 2.55 V, $\Delta I/\Delta V = 4 \times 10^{-5}$ S. The voltage across R_1 is shown in Fig. 24 when the antenna is illuminated from broadside by a sinusoidal field with a field strength of 16 V/m and a frequency of 462.662 MHz. This calculation indicates that the load resistor, R_1, switches its state at about 95 ns after the field illuminates the antenna, and that disruptive switching transients will not occur.

4. Pulse Shaping of Radiated Fields. Shaping the field radiated from a pulse-excited antenna has been studied by many workers. Resistive loading can be used to reduce late-time ringing (45), but reduced far field strengths result. A diode placed in series with the excitation voltage restricts the driving point current on dipole antennas (31,46), but causes the far field to ring at twice the fundamental frequency of the dipole. Miller and Landt (46) have shown that loading a linear dipole with a multiplicity of diodes distributed along the dipole eliminates the late-time ringing. Here, we will investigate an alternative to these loaded methods. Figure 25 shows the driving point current of a linear dipole antenna loaded with a nonlinear element of a resistance of 0 Ω in the forward direction and 700 Ω in the reverse direction. For these calculations, the dipole length, L, was 1 m and the dipole fatness parameter, Ω, was 10, where $\Omega = 2 \ln (L/r)$ and r is the wire radius. The wire was divided into 49 segments for the numerical solution. The excitation voltage was $V = \exp [-a^2(t - t_0)^2]$ for $a = 3.25 \times 10^9 \text{ s}^{-1}$ and $t_0 = 1.389 \times 10^{-9}$ s. The nonlinear element was placed in series with the excitation voltage at the center of the dipole. Note that the late-time ringing of the feedpoint current is much reduced, but the magnitude of the first pulse of current is not limited by the nonlinear element. The broadside radiated electric field strength in the far field is shown in Fig. 26. The fields have been normalized by the radial distance from the dipole to the observation point. Note that the late-time ringing is greatly reduced and that the peak field strengths of the early pulses have not been diminished by the nonlinear element. Figure 27 shows the radiated far field for the same parameters of Figs. 1 and 2, except that the reverse resistance is 400 Ω instead of 700 Ω. Only minor differences in the radiated field are noted between Figs. 26 and 27.

5. Limiting of Load Current. Devices are often employed to protect equipment from excessive voltages or currents delivered by antennas, i.e., lightning protection and EMP hardening. Here, we will examine the response of nonlinear elements that limit (or clip) the current with a series load. A dipole 10 m long and 2 mm in diameter was divided into 49 segments. A plane wave illuminated the dipole from broadside with the electric field parallel to the dipole. The time history of the electric field was a typical EMP waveform: $E(t) = 5.25 \times 10^4 [\exp(-4.00 \times 10^6 t) - \exp(-4.76 \times 10^8 t)]$ V/m. A 50-Ω load and a current-limiting nonlinear element were placed in series at the center of the dipole. Fig. 28 shows the current through the nonlinear element for clipping at a level of 25 A (or 1250 V across the 50-Ω load). (A current of ~430-A peak is delivered in the absence of the nonlinear element.) The voltage across the nonlinear element is shown in Fig. 29. In this example, the initial current charges up the dipole, and the nonlinear element becomes a high resistance when limiting the current (a maximum of ~16,000 Ω). This results in a voltage that keeps the nonlinear element in a current-limiting mode for several cycles of

the natural resonant frequency of the antenna. The power capability of the element must be at least 10 MW and will dissipate about 0.04 J. Figure 30 shows the current resulting if the limiting is raised to 50 A. The voltage across this element is shown in Fig. 31. In this case, the power capability of the element must be about 18 MW, but only about 0.03 J is dissipated in the nonlinear element. Because ~0.1 J will be delivered to the unprotected 50-Ω load, much of the energy collected by the dipole is reradiated and not dumped in the protection device.

6. Loading with Time-Dependent Elements. The use of a time-varying load has some interesting possibilities, including a shifting of the apparent frequency of the scattered field to provide a "false" Doppler shift. To study this possibility, a linear dipole 9 m long and 0.2 m in radius was divided into 9 segments and illuminated from broadside with a sinusoidal wave of 16 MHz and 1-V/m peak electric field parallel to the dipole. A time-varying resistance was placed at the center of the dipole with a value

$$R(t) = 500 \ [1 + \sin(\omega t)] \ \Omega \ ,$$

where $\omega = 2\pi f$ and f is frequency. The resulting backscattered field is greatly altered from the no-load case and is shown in Fig. 32 for a resistance modulation frequency f of 4 MHz. The spectrum of this field is shown in Fig. 33. Significant energy has been placed in sidebands with frequencies offset in multiples of 4 MHz from the 16-MHz incident wave. Miller and Landt (46) presented similar results, but for a resistance varying in a square-wave fashion between 0 and 1000 Ω. The results are similar, but slightly more energy is transferred to the higher sidebands in the square-wave case. Figure 34 shows the backscattered field strength if the resistance modulating frequency f is 5 MHz, and thus not locked to the frequency of the incident wave. In this case, the beat-frequency pattern is more complicated than that shown in Fig. 32. The spectrum of the backscattered field is shown in Fig. 35 and, again, significant amounts of energy have been placed in sidebands now offset at multiples 5 MHz from the frequency of the incident wave. It is also interesting to note that practical schemes can be used to produce time-varying resistance; several of these (including using field effect transistors) require little power and are completely quiet electromagnetically, acting only as passive (but nonlinear) reflectors.

F. Summary

The mathematical background of a time-stepping computer code has been outlined in this section, and numerical examples have been given. This computer code analyses thin-wire antennas loaded by networks containing current sources, resistors, inductors, capacitors, and elements with nonlinear vi characteristics. The solution is obtained in a single computer execution and proceeds by time stepping. The capability of the technique has been demonstrated by consideration of circuits attached to linear dipoles and wire-grid antennas. It has been demonstrated that complete models of circuit elements are required at high frequencies if reasonable agreement is to be achieved between calculations and experiments.

Numerical examples include (1) production of intermodulation products (the rusty-bolt effect); (2) effect of diode loading; (3) response of antennas loaded by circuits; (4) pulse shaping of radiated fields; (5) performance of current limiters; and (6) spectrum-spreading and modification using time-varying loads.

V. DEVICE CHARACTERISTICS AND MEASUREMENT TECHNIQUES

Satisfactory prediction of the effects of nonlinear loading depends upon the adequacy of the model of nonlinear elements. Routinely, effects of junction capacitance, bulk resistance, and package inductance and capacitance must be included in models for high-frequency diodes in addition to the low-frequency vi characteristics. Cullen and An (47) have investigated the characteristics of the Schottky diode. Other nonlinear elements, such as transient suppressors, are also of interest. Kleiner (48) considered electrical-surge arrestors.

Undesired nonlinearities can produce intermodulation products. Arazm and Benson (7) have studied the nonlinearities in metal contacts. They measured the properties of joints of similar and dissimilar metals and found that the surface properties of the metals were of prime importance. Coaxial cable braids can also cause intermodulation interference. Amin and Benson (6,49), studied this type of nonlinearity and found that oxides on copper-wire braids are important in determining the generation of intermodulation products. Nonlinear effects have also been studied by other workers (50,51).

Undesired nonlinear effects can produce significant intermodulation interference when several high-power transmitters and receivers are located closely together (ships and aircraft). Elsner (1) studied nonlinear environmental sources of interference on a decommissioned aircraft carrier. They found that major sources of interference included metallic lifelines (at turnbuckles), deck expansion joints, anchor chains, ladders, guy wires, and similar structures. Sources of interference were eliminated during the testing, providing conclusive evidence that a ship could be "cleaned up." The electromagnetic compatibility of many colocated transmitters and receivers has been studied by Lustgarten (3). Algorithms to identify frequencies likely to create intermodulation problems have been developed by Morito (4).

Chase (2) developed a simple, but effective, procedure to identify significant sources of intermodulation interference. Two operational frequencies were chosen, all other transmitters were turned off. A convenient portion of the spectrum was swept. The lowest order of the intermodulation product was calculated for several of the largest interfering signals. The strength of the signal, in relation to the lowest order of the intermodulation product, provided insight of the source(s) of intermodulation. If the signal decreases as the order increases, it is generally found that a single source is generating the interference. A suitable interference frequency was selected, and a narrow-band portable receiver and direction-finding antenna were used to survey the ship and locate the source of interference.

VI. SUMMARY

Nonlinear loads on antennas can be used to advantage or may degrade the performance of a communications system. Nonlinear elements are routinely used to protect sensitive receivers from high-power

signals including high-power microwaves and EMP. Time-varying loading of antennas can be used to modulate the radar backscatter cross section to produce sidebands at the modulation frequency. Nonlinear elements can be used to detect the electromagnetic energy incident on an antenna, and thus can be used as a measurement technique. Nonlinear loads can also be used for pulse shaping of the fields radiated by pulse-excited antennas. This has application in base-band radar and obtaining desired transient fields for laboratory purposes. Alternatively, undesired semiconducting junctions on support structures near antennas can produce intermodulation products that can seriously degrade performance (this is often called the rusty-bolt effect).

This paper reviews the techniques available for analyzing these effects and gives representative examples. A time-stepping procedure is treated in detail. Nonlinearities caused by plasma sheaths surrounding antennas are not considered.

Several techniques have been employed to analyze nonlinearly loaded antennas. Equivalent circuit models of antennas can be used to describe antenna performance. The nonlinear elements are combined with these antenna models, and the resulting system is solved by using standard computer codes that solve transient nonlinear circuits or derivation of differential equations describing system behavior followed by solution of these equations. Weak nonlinearities have been studied using a Volterra series approach, and measurements of nonlinear response at a given power level were used to predict respones at different power levels. Wide-band-frequency domain antenna response has also been used to compute the time-dependent currents and voltages across nonlinear loads. Several time-stepping procedures have been developed that combine analysis of nonlinear loads with integral equation analysis of the antenna structure. Finite-difference antenna solutions have also been modified to include nonlinear loading.

These studies have shown that care must be taken in the specification of the nonlinear load portion of the system. Stray capacitance and inductance are important at radio and microwave frequencies. Nonlinear loads can produce interfering intermodulation products. For this to occur, the structures, acting like antennas, must be effective at the frequencies of all the signals involved. These intermodulation products can degrade communications systems performance. A simple method is presented that permits identification and location of poorly grounded structures that cause the interfering signals. Performance of a system that uses modulated backscatter as part of a communication link is discussed.

REFERENCES

1. R. F. Elsner, M. J. Frazier, L. S. Smulkstys, and E. Wilson, "Environmental interference study aboard a naval vessel," IEEE Electromagn. Compat. Symp. Rec., July 1968, pp. 330-338.

2. W. M. Chase, J. W. Rockway, and G. C. Salisbury, "A method of detecting significant sources of intermodulation interference," IEEE Trans. Electromagn. Compat., Vol. EMC-17, No. 2, May 1975, pp. 47-50.

3. M. N. Lustgarten, "COSAM (co-site analysis model)," IEEE Electromagn. Compat. Symp. Rec., July 1970, pp. 394-406.

4. S. Morito, H. M. Salkin, and K. Mathur, "Computational experience with a dual backtrack algorithm for identifying frequencies likely to create intermodulation problems," IEEE Trans. Electromag. Combat., Vol. EMC-23, No. 1, February 1981, pp. 32-36.

5. H. K. Schuman, "Time-domain scattering from a nonlinearly loaded wire," IEEE Trans. Antennas Propagat., Vol. AP-22, No. 4, July 1974, pp. 611-613.

6. M. B. Amin and F. A. Benson, "Non-linear effects in coaxial cables at microwave frequencies," Electron Lett., Vol. 13, No. 25, Dec. 1977, pp. 768-770.

7. F. Arazm and F. A. Benson, "Nonlinearities in metal contacts at microwave frequencies," IEEE Trans. Electromagn. Compat., Vol. EMC-22, No. 3, Aug. 1980, pp. 142-149.

8. R. W. P. King, The Theory of Linear Antennas, first edition, Cambridge, Mass., Harvard University Press, 1956, pp. 168-182.

131-15

9. J. A. Landt, "Microwave detector for the masses," Proc. National Radio Science Meeting, Boulder, CO, 9-13 January 1978, p. 58.

10. A. R. Koelle, S. W. Depp, J. A. Landt, and R. E. Bobbett, "Short-range passive telemetry by modulated backscatter of incident CW RF carrier beam." in Biotelemetry III, edited by T. B. Fryer, H. A. Miller, and H. Sandler, Academic, New York, 1976, pp. 337-340.

11. W. C. Brown, J. R. Mims, and N. I. Heenan, "An experimental microwave-powered helicopter," IEEE Int. Conv. Rec., Vol. 13, part 5, 1965, pp. 225-235.

12. P. E. Glaser, "Power without pollution," J. Microwave Power, Vol. 4, 1970, pp. 211-222.

13. J. J. Nahas, "Modeling and computer simulation of a microwave-to-dc energy conversion element," IEEE Trans. Microwave Theory Tech., Vol. MTT-23, Dec. 1975, pp. 1030-1035.

14. A. R. Koelle and S. W. Depp, "Doppler radar with cooperative target measures to zero velocity and senses the direction of motion," IEEE Proc., Vol. 65, No. 3, March 1977, pp. 492-493.

15. R. J. King, Microwave homodyne systems, London, C. F. Hodgson & Son Ltd., 1978, p. 128.

16. G. Collignon, Y. Michel, F. Robin, J. Saint, and J. C. Bolomey, "Fast near field antenna probing by means of the modulated scattering technique," 1982 APS Symposium Digest, IEEE Antenn. and Propagat. Society meeting, 24-28 May 1982, Albuquerque, NM, pp. 214-217.

17. M. Kanda, "Analytical and numerical techniques for analyzing an electrically short dipole with a non-linear load," IEEE Trans. Angennas Propagat., Vol. AP-28, No. 1, Jan. 1980, p. 71.

18. M. Kanda, "The time-domain characteristics of a traveling-wave linear antenna with linear and non-linear parallel loads," IEEE Trans. Antenna Propagat., Vol. AP-28, No. 2, Mar. 1980, p. 267.

19. H. Lindenmeier and G. Flachenecker, "Breitbandige transistorierte Empfangsantennen im Frequenzbereich zwischen 10 kHz und 10 MHz," Nachrichtentech. F., Vol. 45, 1972, pp. 140-145.

20. J. F. Hopf and H. K. Lindenmeier, "Fast tunable active receiving antennas," Radio Science, Vol. 16, No. 6, 1981, pp. 1143-1147.

21. E. H. Nordholt and D. Van Willigen, "A new approach to active antenna design," IEEE Trans. Antennas Propagat., Vol. AP-28, No. 6, November 1980, pp. 904-910.

22. A. J. Bahr, "On the use of active coupling networks with electrically small receiving antennas," IEEE Trans. Antennas Propagat., Vol. AP-25, No. 6, November 1977, pp. 842-845.

23. P. L. Fanson and Ku-Mu Chen, "Instabilities and resonances of actively and passively loaded antennas," IEEE Trans. Antennas Propagat., Vol AP-22, No. 2, March 1974, pp. 344-347.

24. M. M. Dawoud and A. P. Anderson, "Experimental verification of the reduced frequency dependence of active receiving arrray," IEEE Trans. Antennas Propagat., Vol. AP-22, No. 2, March 1974, pp. 342-344.

25. J. P. Daniel, "Reduction of mutual coupling between active monopoles: application to superdirective receiving arrays," IEEE Trans. Antennas Propagat., Vol AP-25, No. 6, Nov. 1977, pp. 737-741.

26. J. P. Daniel, "Mutual coupling between antennas for emission or reception-application to passive and active dipoles," IEEE Trans. Antennas Propagat., Vol. AP-22, No. 2, Mar. 1974, pp. 347-349.

27. T. S. M. Maclean and G. Morris, "Short range active transmitting antenna with very large height reduction," IEEE Trans. Antennas Propagat., Vol. AP-23, No. 2, Mar. 1975, pp. 286-287.

28. T. J. Aprille, Jr., and T. N. Trick, "Steady-state analysis of nonlinear circuits with periodic inputs," Proc. IEEE, Vol. 60, Jan. 1972, pp. 108-114.

29. R. J. Gutmann and J. M. Borrego, "Power combining in an array of microwave power rectifiers," IEEE Trans. Microwave Theory Tech., Vol. MTT-27, Dec. 1979, pp. 958-968.

30. R. J. Gutmann and L. H. Camnitz, "Determination of harmonic levels in nonlinear networks by computer simulation," IEEE Trans. Electromag. Compat., Vol. EMC-24, No. 1, Feb. 1982, p. 50.

31. T. K. Liu and F. M. Tesche, "Analysis of antennas and scatterers with nonlinear loads," IEEE Trans. Antennas Propagat., Vol. AP-24, No. 2, Mar. 1976, pp. 131-139.

32. T. K. Liu, F. M. Tesche, and F. J. Deadrick, "Transient excitation of an antenna with a nonlinear load: Numerical and experimental results," IEEE Trans. Antennas Propagat., Vol. AP-25, No. 4, July 1977, pp. 539-541.

33. T. K. Sarkar, and D. D. Weiner, "Scattering analysis of nonlinearly loaded antennas," IEEE Trans. Antennas Propagat., Vol. AP-24, No. 2, Mar. 1976, pp. 125-131.

34. B. J. Leon and D. J. Schaeffer, "Volterna series and Picard iteration for nonlinear circuits and systems," IEEE Trans. Circuits Syst., Vol. CAS-25, Sept. 1978, pp. 789-793.

35. E. P. Sayre and R. F. Harrington, "Time domain radiation and scattering by thin wires," Appl. Sci. Res., Vol. 20, Sept. 1972, pp. 413-444.

36. M. A. Chipman, "Finite difference solutions for antennas with nonlinear loads," Proc. URSI Sympos. Electromag. Wave Theory, Stanford University, June 20-24, 1977, pp. 185-187.

37. D. E. Merewether and T. F. Ezell, "The interaction of cylindrical posts and radiation-induced electric field pulses in ionized media," IEEE Trans. Nuclear Science, Vol. NS-21, No. 5, Oct. 1974, pp. 4-13.

38. J. A. Landt, "Network loading of thin-wire antennas and scatters in the time domain," Radio Sci., Vol. 16, No. 6, Nov.-Dec. 1981, pp. 1241-1247.

39. E. K. Miller, A. J. Poggio, and G. J. Burke, "An integro-differential equation technique for the time-domain analysis of thin wire structures: I. The numerical method," J. Comput. Phys., Vol. 12, May 1973, pp. 24-48.

40. J. A. Landt, E. K. Miller, and F. J. Deadrick, "Time domain modeling of nonlinear loads, " IEEE Trans. Antennas Propagat., Vol. AP-31, No. 1, Jan. 1983, pp. 121-126.

41. S. Ramo, J. R. Whinnery, and T. VanDuzer, Fields and Waves in Communication Electronics, New York, John Wiley & Sons, 1967, p. 263.

42. E. C. Jordan and K. G. Balmain, Electromagnetic Waver and Radiating Systems, second edition, Englewood Cliffs, New Jersey, Prentice-Hall, 1968, p. 311.

43. M. Van Blaricum and E. K. Miller, Lawrence Livermore National Laboratory, "TWTD: A computer program for the time-domain analysis of thin-wire structures," October 1972, report number UCRL-51277.

44. J. A. Landt, E. K. Miller, and M. Van Blaricum, Lawrence Livermore National Laboratory," WT-MBA/LLLIB: A computer program for the time-domain electromagnetic response of thin-wire structures," May 1974, report number UCRL-51585.

45. E. K. Miller and J. A. Landt, "Short-pulse characteristics of the conical spiral antenna," IEEE Trans. Antennas Propagat., Vol. AP-25, Sept. 1977, pp. 621-626.

46. E. K. Miller and J. A. Landt, "Direct time-domain techniques for transient radiation and scattering from wires," Proc. IEEE, Vol. 68, No. 11, Nov. 1980, pp. 1396-1423.

47. A. L. Cullen and T. Y. An, "Microwave characteristics of the Schottky-barrier diode power sensor," IEE Proc., Vol. 129, No. 4, Aug. 1982, pp. 191-198.

48. C. T. Kleiner, E. D. Johnson, L. R. McMurray, and F. T. Suzuki, "An electrical surge arrestor (ESA) model for electromagnetic pulse analysis," IEEE Trans. Nuclear Science, Vol. NS-24, No. 6, Dec. 1977, p. 2352-2356.

49. M. B. Amin and F. A. Benson, "Coaxial cables as sources of intermodulation interference at microwave frequencies," IEEE Trans. Electromagn. Compat., Vol. EMC-20, Aug. 1978, pp. 376-384.

50. M. Bayrak and F. A. Benson, "Intermodulation products from nonlinearities in transmission lines and connectors at microwave frequencies," Proc. Inst. Elect. Eng., Vol. 122, No. 4, Apr. 1975, pp. 361-367.

51. J. A. Betts and D. R. Ebenezer, "Intermodulation interference in mobile multiple-transmission communication systems operating at high frequencies (3~30 MHz)," Proc. Inst. Elect. Eng., Vol. 120, No. 11, Nov. 1973, p. 1337.
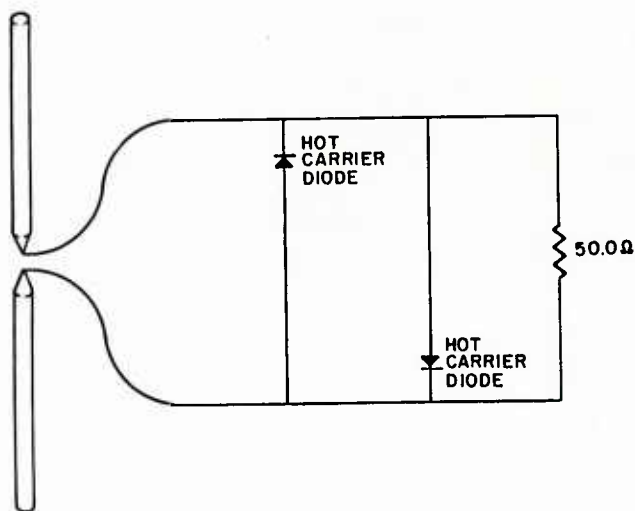
Fig. 1. Dipole with 50-Ω load and shunt diode limiters.
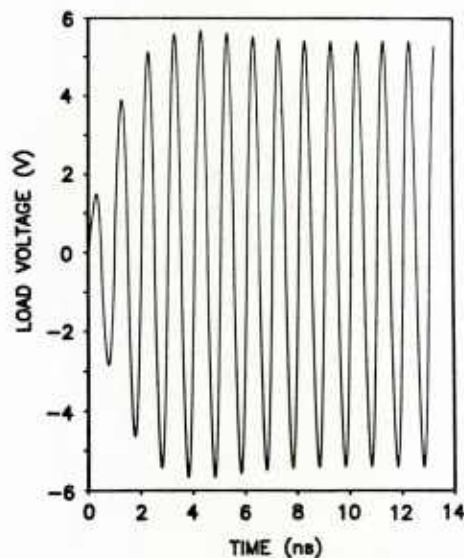
Fig. 2. The voltage across the 50 Ω load of Fig. 1.
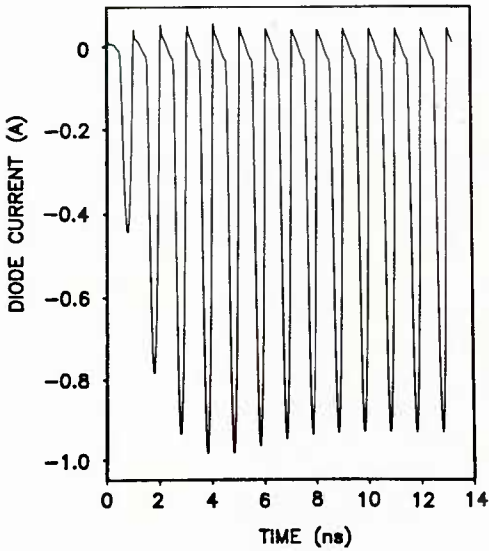
Fig. 3. The current through a diode of Fig. 1.
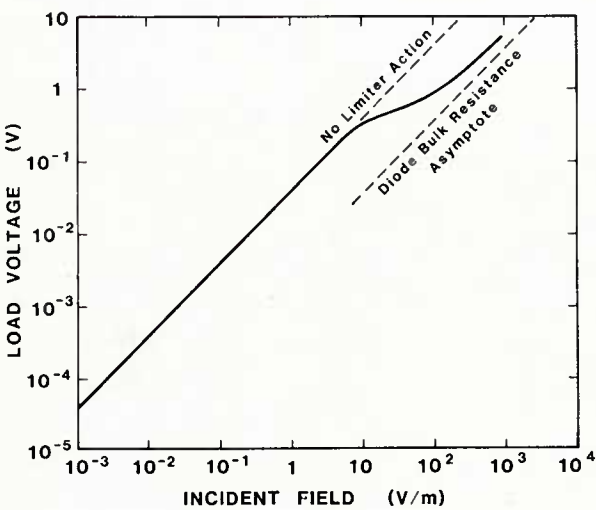
Fig. 4. Performance of the limiter circuit in Fig. 1.
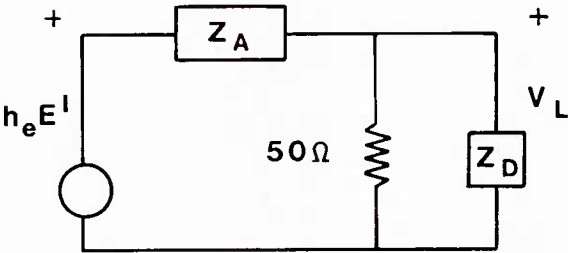
Fig. 5. Equivalent circuit used for the asymptotic response of the circuit of Fig. 1.
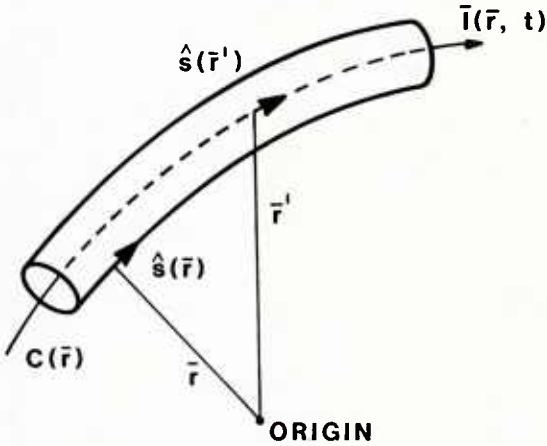
Fig. 6. Geometry for thin-wire electric-field integral equation.
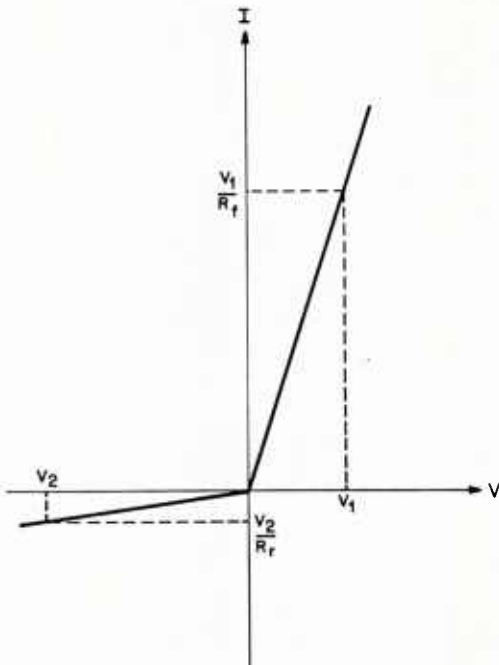
Fig. 7. The volt-ampere characteristics of an idealized diode-like nonlinear element.
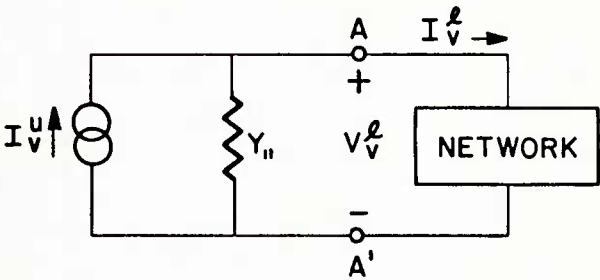
Fig. 8. A network connected to the Norton's equivalent of the antenna.
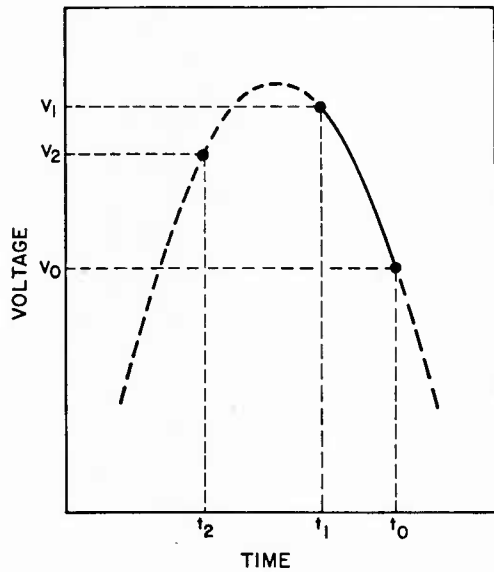
Fig. 9. Illustration of the portion of a quad-
ratic function used as an interpola-
tion function.
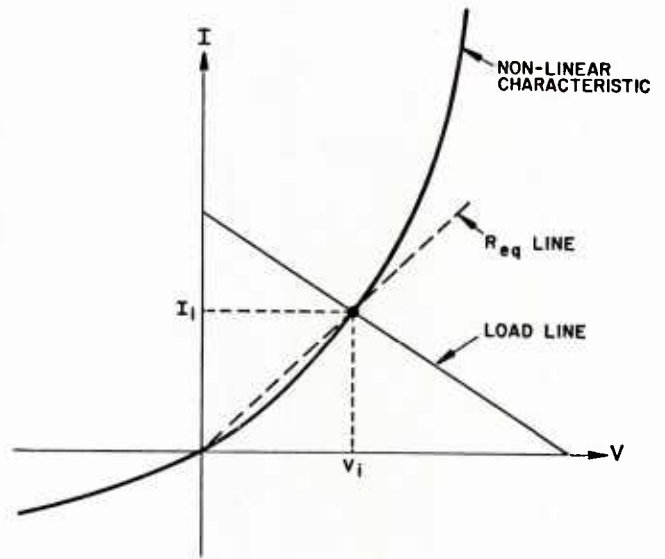
Fig. 10. The volt-ampere characteristics of a
nonlinear element and the circuit load
line.
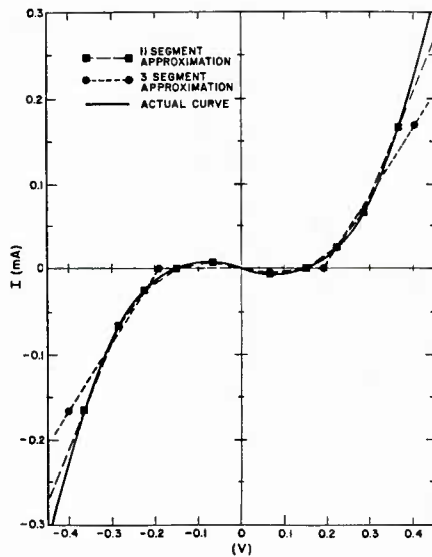
Fig. 11. Straight-line approximations of the
volt-ampere characteristics of a non-
linear load.
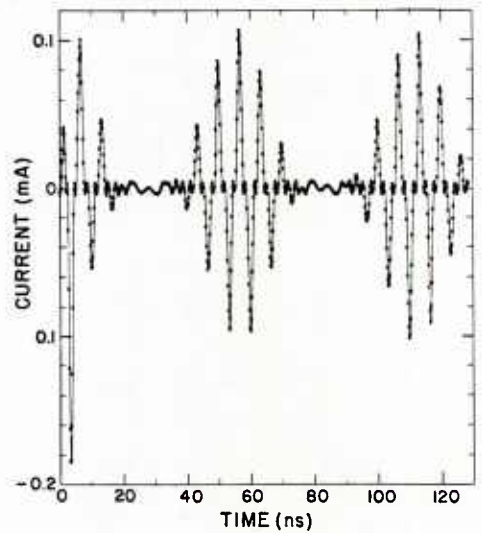
Fig. 12. The load current resulting when a two-
frequency wave illuminates a dipole
loaded at its center with the 11-
segment approximation of Fig. 11.
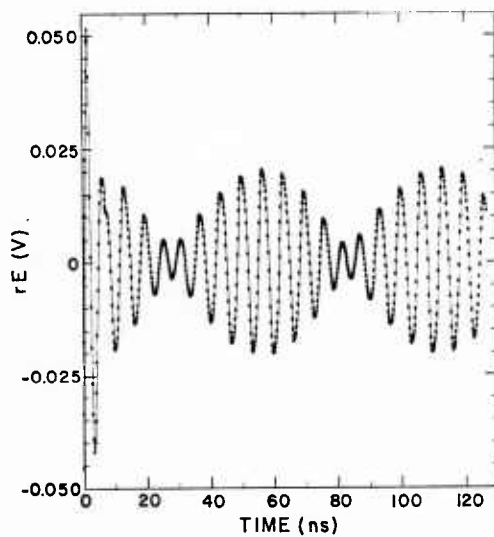
Fig. 13. The backscattered field corresponding
to the current of Fig. 12.
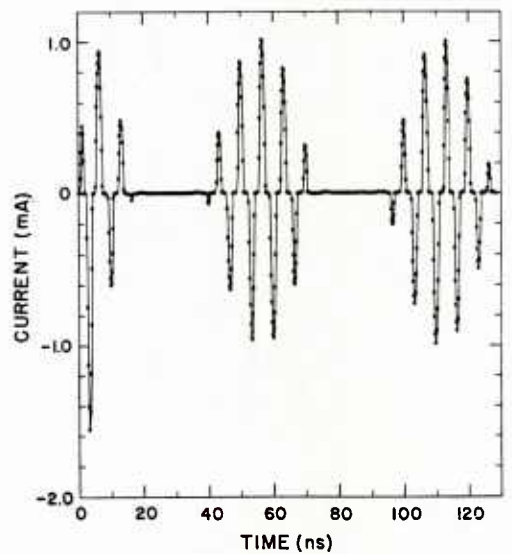
Fig. 14. The load current resulting from the
three-segment approximation of Fig. 11.
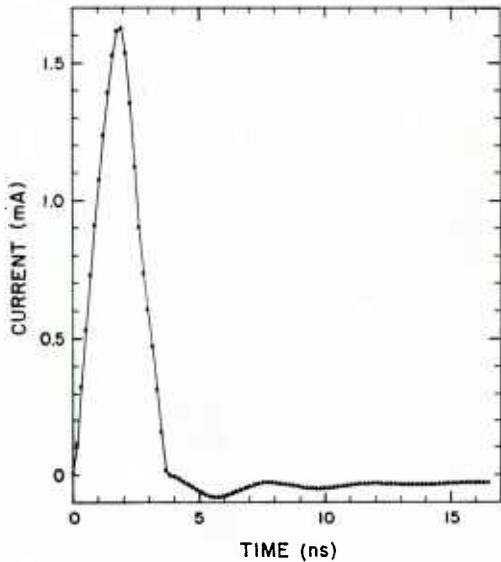
Fig. 15. The current at the center of a dipole loaded with a diode and illuminated by a step function electromagnetic field.
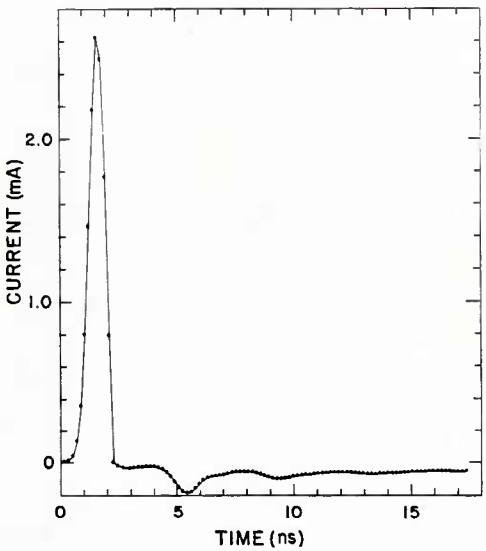
Fig. 16. The current at the center of a dipole loaded with a diode and excited as an antenna with a Gaussian pulse of voltage.
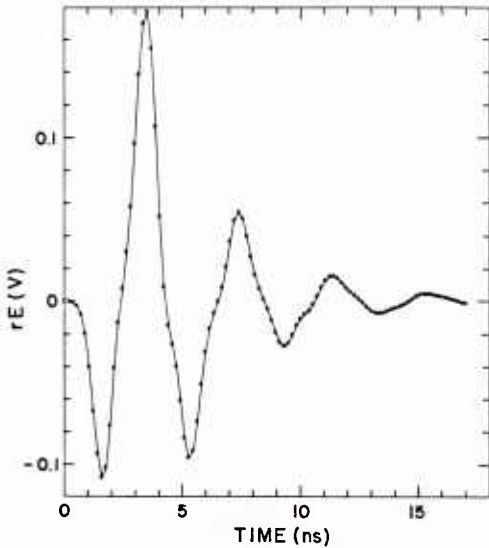
Fig. 17. The broadside radiated fields corresponding to Fig. 16.
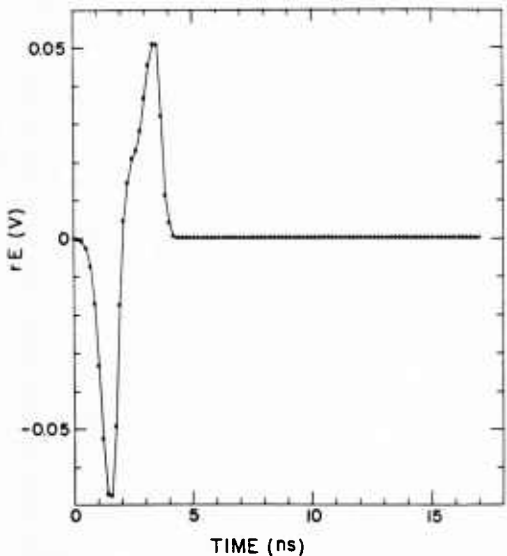
Fig. 18. The broadside radiated fields of a dipole loaded with 19 diodes distributed along the length of the dipole and excited as an antenna by a Gaussian pulse of voltage.
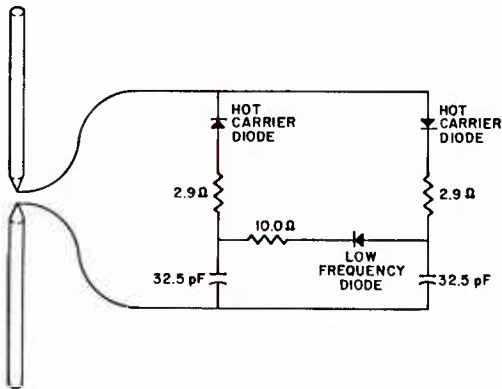
Fig. 19. A dipole loaded with a circuit.
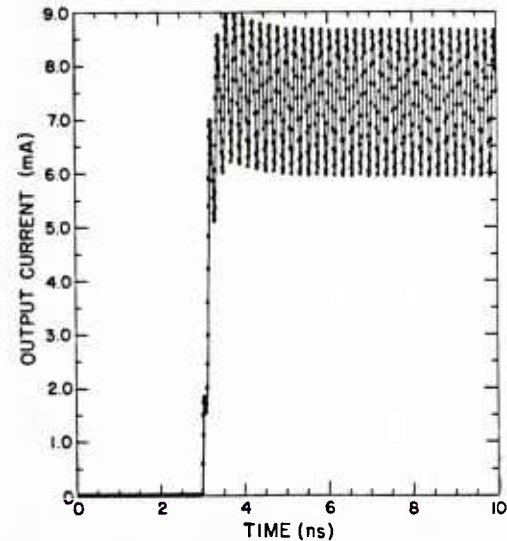
Fig. 20. The current flowing through the low-frequency diode of Fig. 19 when illuminated by a 2450-MHz electromagnetic field.
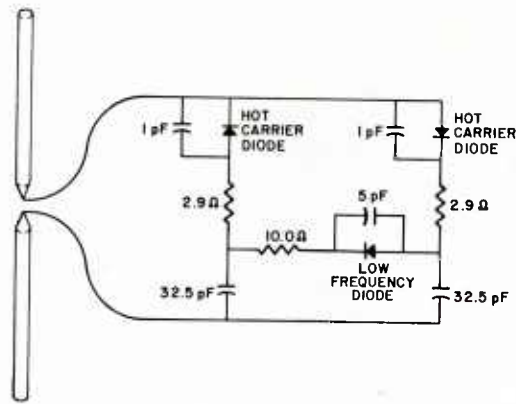
Fig. 21.   A more complete model of the circuit.
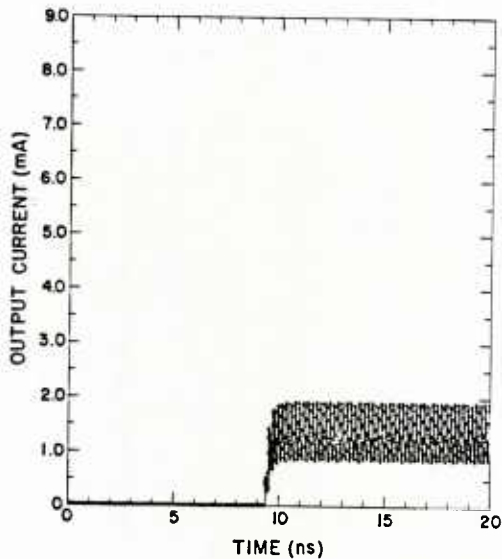
Fig. 22.   The current flowing through the low-frequency diode of Fig. 21.
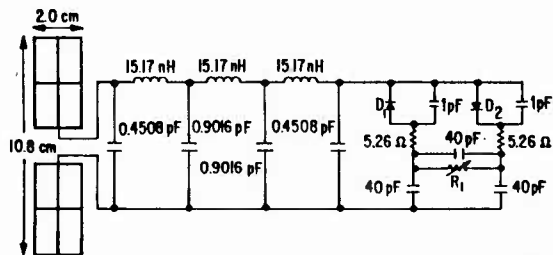
Fig. 23.   Diagram of a circuit attached to a wire-grid paddle antenna.
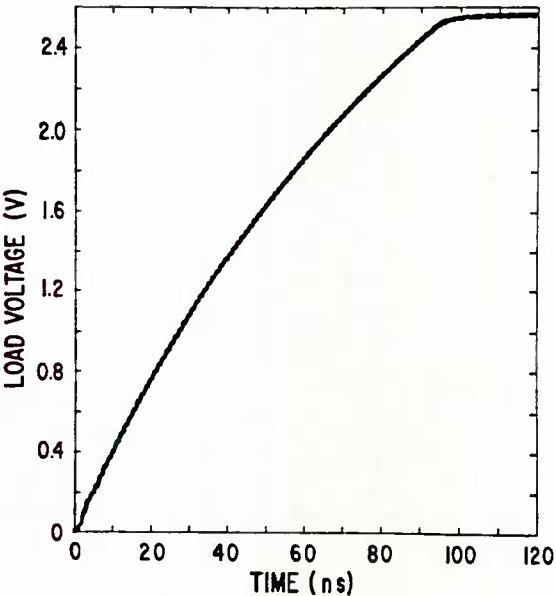
Fig. 24.   The voltage across R_1 of Fig. 23.
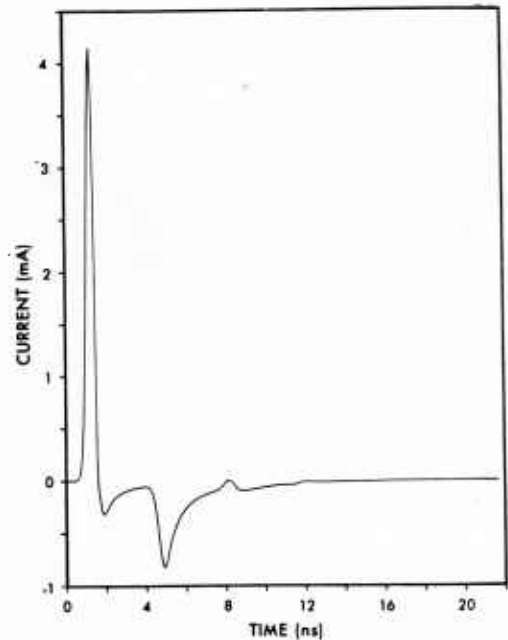
Fig. 25.   Driving point current of a pulse-excited dipole antenna loaded by a nonlinear resistance with a value of $0 \ \Omega$ in one direction and $700 \ \Omega$ in the reverse direction.
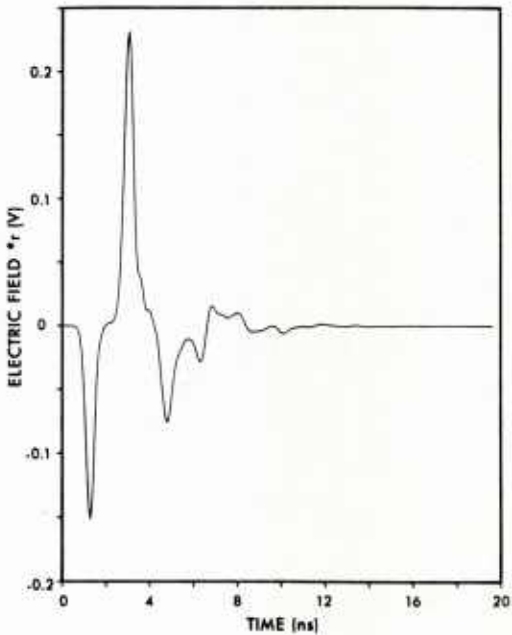
Fig. 26.   Electric field radiated broadside from the antenna of Fig. 25.
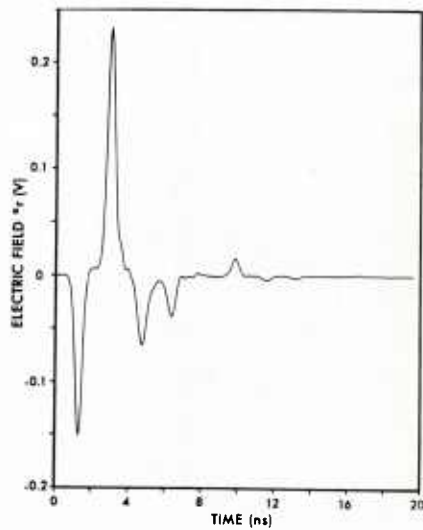
Fig. 27. Electric field radiated by the example of Fig. 25 but with a reverse resistance of 400 Ω.
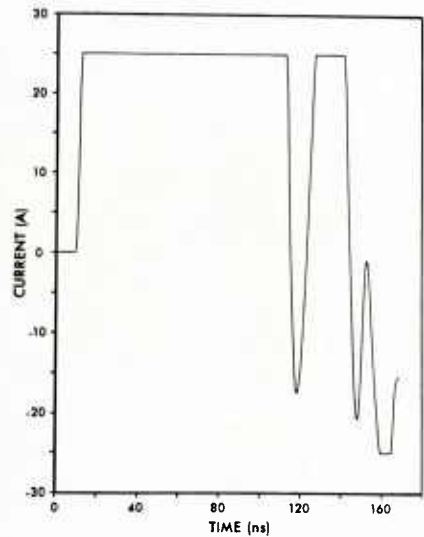
Fig. 28. EMP response of a dipole antenna loaded by a nonlinear element that limits the current at the center of the antenna to 25 A.
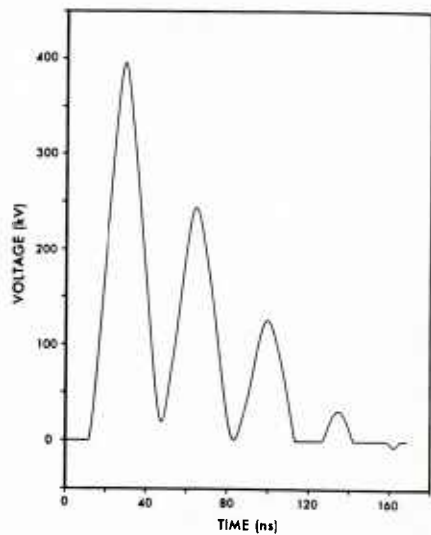
Fig. 29. Voltage across the nonlinear element of Fig. 28.
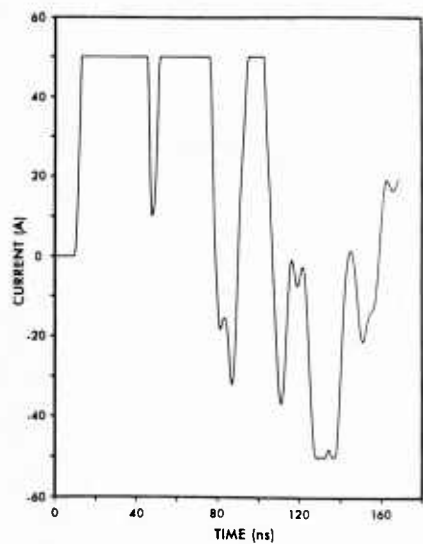
Fig. 30. EMP response of the antenna of Fig. 28 with a current limit of 50 A.
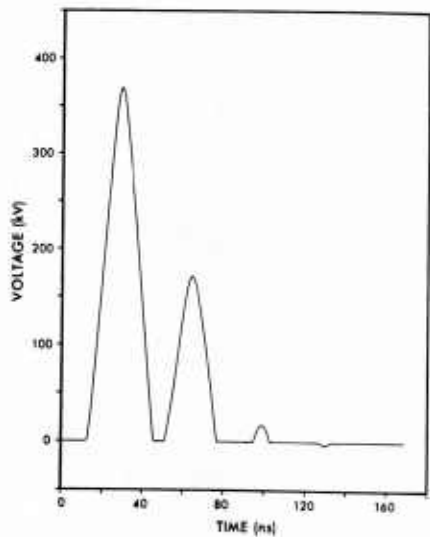
Fig. 31. Voltage across the nonlinear element of Fig. 30.
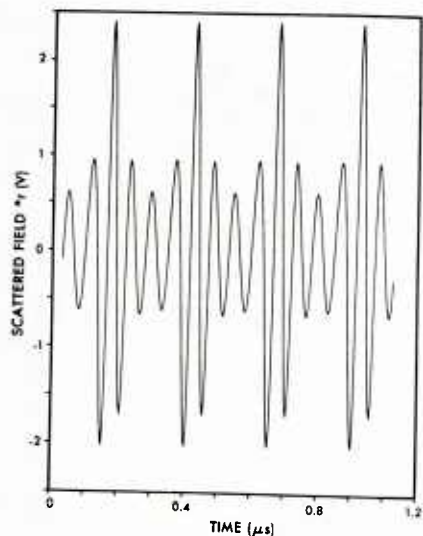
Fig. 32. Electric far field scattered from a dipole antenna illuminated by a 16-MHz sinusoidal wave and loaded by a resistance varying in a sinusoidal fashion at 4 MHz.
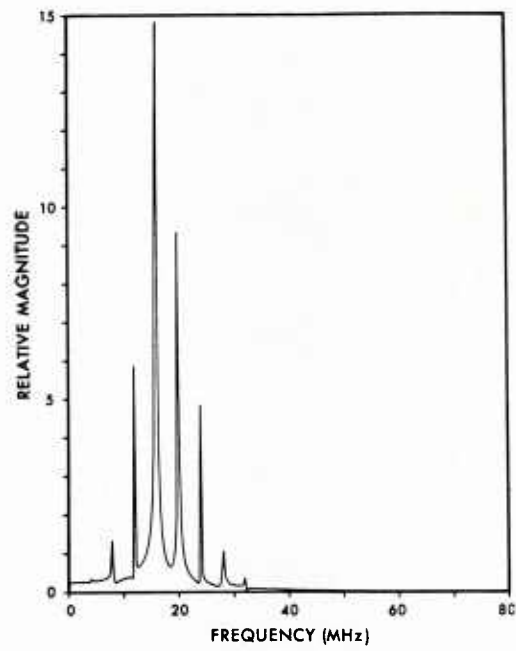
Fig. 33.   Spectrum of the waveform of Fig. 32.
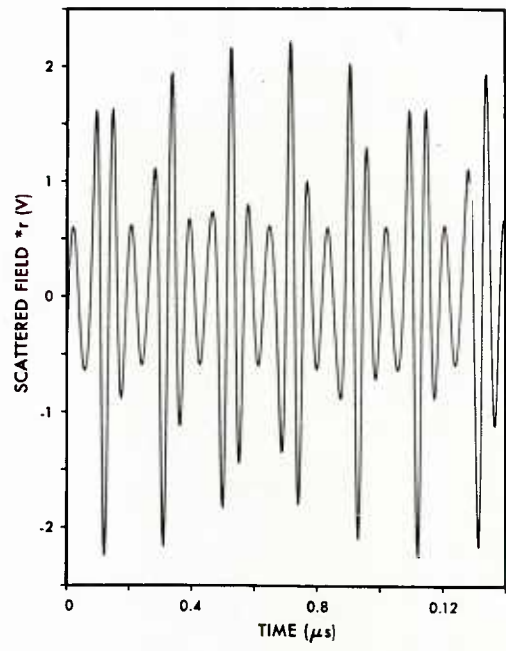
Fig. 34.   Electric far field of the example of Fig. 32 for a resistance varying at 5 MHz.
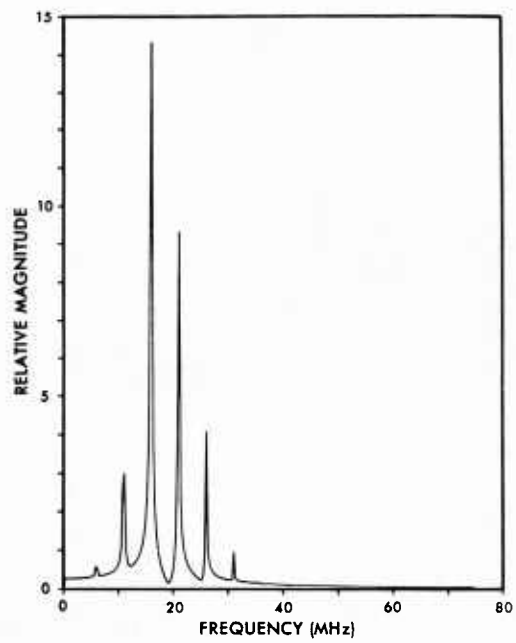
Fig. 35.   Spectrum of the waveform of Fig. 34.

PERFORMANCE OF ANTENNAS IN PLASMAS

by
K.G. Balmain
Professor
Department of Electrical Engineering
University of Toronto
Toronto, Ontario
Canada M5S 1A4

SUMMARY

The Waves in Space Plasmas (WISP) facility is expected to be flown on the Space Shuttle in 1987. The payload will include Spacelab, a 300 m tip-to-tip dipole antenna for wave launching and reception, and a small subsatellite for remote signal reception and plasma diagnostics. The objectives are to study wave injection and propagation in the ionospheric plasma, and to use these phenomena to probe the structure and morphology of the ionosphere. To achieve these objectives, it is essential to understand how much the properties of a long dipole antenna are affected by the surrounding anisotropic plasma medium. This paper summarizes the WISP project with emphasis on antenna-related aspects, and reviews the state of the art on the subject of antennas in plasmas.

INTRODUCTION

In 1987 the Space Shuttle will carry Spacelab 6 into near-circular orbit in the ionosphere, spanning a range of altitudes not far above the F-region maximum in electron density. A 300 m tip-to-tip dipole antenna will be extended outward from the Shuttle's cargo bay, and a small subsatellite will be picked out of the cargo bay by the Remote Manipulator System and then spun up and released into its own orbit close to that of the Shuttle Orbiter. At this time there will commence a week-long sequence of experiments mainly involving VLF to HF transmissions from the Orbiter to the subsatellite, comprising the operational part of a project known as Waves in Space Plasmas, or WISP. This is a joint cooperative project involving the United States and Canada, with the VLF experiments funded by NASA and the HF experiments funded by the National Research Council of Canada.

The experiments to be carried out are numerous. Large-scale ionospheric structures will be studied, with special attention to gravity waves, travelling ionospheric distur- bances and equatorial bubbles. Plasma irregularities and ducts will be probed both directly and also remotely in a "radar" configuration. Measurements will be made on wave modes launched by the antenna, as well as wave-wave coupling, parametric coupling, and scatter from electrostatic waves. Naturally occurring instabilities will be observed, and at high transmitter power levels, instabilities and growing waves will be induced artificially.

The properties of the antenna operating in its anisotropic, inhomogeneous and non- linear environment must be studied in depth as part of the project, not only to permit interpretation of the experiments already mentioned, but also as scientific objectives in their own right. The Orbiter-to-subsatellite transmissions over moderate distances can be viewed as the operation of an "antenna range in space", permitting measurement of the dipole's radiation pattern under the strong influence of the anisotropy of its surroundings. At short distances, near-field phenomena such as resonance cones should be measurable. At the antenna terminals, measurements of input impedance and nonlinear effects will be particularly important. The high signal levels close to the antenna may cause increased ionization in the surrounding gas and may induce electrostatic charge accumulation on the Orbiter's nearby insulating surfaces.

The following will be an overview of the entire WISP project, emphasizing those aspects pertaining to antenna performance and including recent experimental and theoreti- cal results on the input impedance and radiation patterns of antennas in plasmas.

THE WISP SPACE SHUTTLE PROGRAM

The essential elements of the WISP instrument payload are shown in Fig.1 in their positions on the Space Shuttle Orbiter. The forward part of the cargo bay is occupied by Spacelab with its complement of scientific instruments and experiment control apparatus. The aft part of the cargo bay is occupied by a pallet containing the dipole antenna and the VLF and HF subsystems of WISP, as well as a low light level TV camera which is pri- marily intended to monitor atmospheric emissions as part of another scientific program. Also shown on the pallet is the subsatellite or Recoverable Plasma Diagnostics Package (RPDP) which will be picked up by the Remote Manipulator System (RMS) and held for local signal measurements and plasma diagnostics, or released into a nearby orbit for distant measurements. The most recent plans call for the RPDP to be stowed elsewhere and require more insulation around the antenna terminals, resulting in a WISP pallet configured as shown in Fig.2. One version of the RPDP under consideration is shown in Fig.3, with an array of dipole and loop antennas able to respond to any component of electric or magnetic

fields. As part of another program, a particle beam injector will also be available. Although not yet given final NASA approval, the first flight is tentatively planned for a late 1987 launch into a 57° inclination orbit in an altitude range of 325-500 km. The entire mission will take approximately seven days and will include several experiments in addition to WISP.

The VLF subsystem will operate in the frequency range 1 - 100 kHz at power levels up to 3kW and antenna dc bias up to ± 2 kV. The HF subsystem will operate in the frequency range 100 kHz - 30 MHz at power levels up to 500 W and antenna dc bias up to ± 300 V. At all frequencies, antenna voltage, current and impedance will be measured, and signal reception will be possible both at the Orbiter and at the RPDP. The receiving systems will have phase measurement capability and at HF will be able to measure Doppler shifts to ± 1.6 kHz. Under stepwise control will be all significant parameters such as frequency, pulse length, pulse rate, power level and antenna length. The orbiter orientation and position relative to the RPDP can be controlled. As an antenna-in-plasma laboratory, the system will have most of the advantages of an earthbound laboratory without the major disadvantage of finite dimensions and nearby walls.

Some aspects of the WISP scientific program are depicted in Fig.4. A review of the entire WISP program which emphasizes the VLF experiments has been presented by Fredricks and Taylor [1], the VLF antenna and transmitter have been discussed by Inan et al. [2], and the HF experiments have been described by James [3].

At VLF, the study of wave-particle interactions is crucial. It is expected that the interaction between waves and the naturally occurring high-energy radiation belt particles will produce nonlinear wave growth which can be measured by the RPDP. It is also expected that VLF emissions will trigger instabilities that result in augmented particle precipitation into the ionosphere producing increases in ionization, X-rays and light emissions or, in other words, an artificial aurora. In addition to the wave-particle interactions, it will also be important to study whistler-mode propagation, especially the degree to which whistler waves are ducted by magnetic-field-aligned enhancements or depletions in electron density.

It is known that auroral precipitation is an important source of a long-wavelength phenomenon known as the Travelling Ionospheric Disturbance (TID) which is the ionospheric manifestation of the atmospheric gravity wave phenomenon. The TIDs will be studied using transmissions from the WISP/HF subsystem to the RPDP. It is expected that range and Doppler measurements will permit the wave vectors of TIDs to be deduced.

Another ionospheric phenomenon accessible to WISP/HF will be the large-scale plasma-density-depleted regions which occur near the magnetic equator and slowly rise from the bottomside into the topside of the ionosphere. These "equatorial bubbles" cause unexpectedly severe scintillations on communications links with synchronous-orbit spacecraft. The combined functions of "in situ" plasma measurements and remote sounding available on WISP/HF should permit detailed mapping not only of bubble structures but also of field-aligned HF ducts. Near the upper end of the HF frequency range the antenna will be shortened and the system used in a radar mode to study the size and distribution of E-region and F-region electron density irregularities.

As in the VLF case, at HF the interaction of waves and particle beams can be studied, using both naturally occurring particle beams and artificial ones emitted by instruments on the Shuttle Orbiter. With the WISP transmitter off but the beam on, the inherent instabilities can be studied by measuring their emissions. With the transmitter on, convective growth or damping of the waves transmitted to the RPDP can be identified.

For moderate separations between the Orbiter and the RPDP the surrounding plasma will be generally uniform, making possible tests on fundamental properties of wave propagation in anisotropic media, including phase and group delay, polarization, power flux, mode coupling, and collisionless damping. In other words it should be possible to measure directly the dispersion relations for characteristic waves, by measuring the signals received with the appropriate characteristic polarizations.

At close range, with the RPDP held in a sequence of programmed positions on the end of the RMS arm, the antenna near field can be measured as well as the properties of the nearby plasma, in search of plasma heating and particle acceleration effects. The RPDP should also permit study of both the sheath and the wake regions around the Orbiter and the dipole antenna. With the RPDP released but still at close range, it will be able to search for the high-field regions known as "resonance cones". These high-field regions originate at the ends and centre of a dipole and have axes parallel to the magnetic field as depicted in Fig.5. At greater distances from the Orbiter, the resonance cones become weaker and less well defined, merging into the radiation pattern of the antenna which will be measured directly for the first time in the ionosphere.

The antenna impedance will be important for reasons of both local plasma diagnostics and effects on system performance due to mismatch losses. The measurements of antenna impedance will permit tests of various theories, tests which are difficult at best in confined laboratory plasmas and impossible in the laboratory for antennas which are relatively long.

WISP ANTENNA IMPEDANCE ESTIMATION

The VLF input impedance at low signal level has been discussed by Inan et al [2] who conclude that the best theoretical model presently available is the ion sheath impedance of Mlodnosky and Garriott [4] in series with the cold-plasma impedance which is predominantly real (radiation resistance) in this frequency range. The Mlodnosky and Garriott model for the ion sheath impedance comprises a vacuum-gap capacitance in parallel with a resistance which is the slope of the nonlinear DC voltage-current curve at floating potential, this potential being established by setting to zero the sum of the random electron and ion currents to the antenna plus the "ram" ion current due to the antenna velocity (7 km/sec for WISP).

At MF and HF, the antenna can be long in terms of free-space wavelengths, a situation for which there exists no comprehensive theory. Nevertheless some estimate of antenna impedance is required for purposes of instrument design.

Existing theories of long antennas in plasma do not include collisionless damping effects. For impedance estimation, one is therefore obliged to use an artificially high coefficient of collisional damping, fixing its value by comparison with experiment. Rocket experiments in the F region on a dipole 4 m long (tip-to-tip) indicate an input resistance at the plasma frequency of the order of 100,000 ohms but corresponding cold plasma calculations predict about 30 megohms which means that the actual F-region electron-molecule collision frequency would have to be artificially inflated by a factor of about 500 to bring the cold-plasma calculations into agreement with experiments at the plasma frequency.

Recent theoretical work on an isotropic-plasma, kinetic-theory approach to calculating sheath losses and finite input resistance below the plasma frequency [7,8,9] is for short dipoles only and appears to be extendable to long antennas only with difficulty. Therefore the approach to be used here will be to go back to the results of Mlodnosky and Garriott [4] to derive a sheath-region conductivity which can be added to any cold-plasma, vacuum-gap representation of the antenna-plasma interface. For a parallel-plate geometry and zero antenna velocity, this procedure gives the conductivity

$$\sigma = \sqrt{2\pi} \sqrt{\frac{m_e \, T_i}{m_i \, T_e}} \; \varepsilon_o \; f_N \frac{d}{\lambda_D} \tag{1}$$

where m_e = electron mass

m_i = ion mass

T_e = electron temperature

T_i = ion temperature

ε_o = permittivity of a vacuum

f_N = plasma frequency (Hz)

d = sheath thickness

λ_D = Debye length = $\sqrt{\varepsilon_o \, k \, T_e / N e^2}$

k = Boltzmann's constant

e = electron charge magnitude.

Substitution of values appropriate to the F region together with a sheath thickness of 5 λ_D yields conductivities in the range 10^{-6} to 10^{-5} S/m.

The simplest available theory which takes into account both plasma anisotropy and wave propagation along a dipole antenna is that of Adachi, Ishizone and Mushiake [10]. It employs the cold-plasma permittivity matrix in the derivation of the capacitance per unit length of an isolated wire, followed by the substitution of this capacitance into the expression for the input impedance of an open-ended transmission line. Examples of impedance calculations are shown in Figs.6 through 8, using the Adachi formulation together with an augmented collision frequency and a sheath-region conductivity.

When such a slightly-conductive, vacuum gap ion sheath region is surrounded by a dense plasma, it is clear that the configuration is much like that of a coaxial cable and should support waves which are attenuated and which propagate at a velocity below that of light in a vacuum (because the high-density plasma in effect reduces the capacitance per unit length of the sheath region). That these sheath waves on an antenna should produce a family of sheath-wave resonances was first recognized by Marec and Mourier [11].

For a very short dipole, the first sheath-wave resonance may be interpreted as the series-resonance between an inductive plasma and a capacitive sheath. This can be seen in Fig.6 as a reactance zero-crossing accompanied by a small "bump" in resistance just below 4 MHz. For a long dipole there are multiple sheath-wave resonances which are visible in Fig.7 at frequencies below 2 MHz. These waves experience an attenuation which increases with increasing frequency, and above 2 MHz it is clear that such a wave is negligible in magnitude by the time it has arrived back at the terminals after being reflected at the end of the antenna. In Fig.8, what appears to be a small sheath-wave effect is visible just above 1.0 MHz.

In general, the anisotropic-medium theory of Adachi does not predict radiation, so the resonances above the upper hybrid frequency do not exhibit the radiation damping that would exist in reality. However, for isotropic media, the numerical method developed by Richmond [12] can be used. It includes a dielectric sheath which can be. specified as a vacuum region with the conductivity already derived, plus a surrounding medium which can be specified to have the complex permittivity of isotropic, cold plasma. This program was the one used to determine the augmented collision frequency by matching calculated with experimental resistances at the plasma frequency for a short dipole.

The numerical method described above was applied to the case of a 200 m tip-to-tip dipole antenna. The effect of radiation damping above the plasma frequency is clearly in evidence in Fig.9. Sheath-wave resonances at frequencies below the plasma frequency are very much in evidence in Fig.10 which closely resembles (as it should) the low-frequency half of Fig.7. Corresponding to Fig.10, a resonant and an antiresonant sheath-wave current distribution are shown in Fig.11.

The foregoing impedance estimates for long antennas are the best readily available at the present time. In spite of their obvious inadequacies they do suggest that the WISP antenna impedance will be controlled by the medium and will undergo large gyrations as the frequency changes. Other calculations (not shown) indicate that there will be significant dependence of impedance on both antenna orientation and antenna length.

PROGRESS ON ANTENNAS IN PLASMA, DATING FROM 1978

The subject of antennas in plasmas has been reviewed sporadically over the last sixteen years or so, covering progress up to 1978. Some of the principal review papers and books are those by Bachynski [13], Kaiser and Tunaley [14], Wait [15], Thomas and Landmark [16], Andronov and Chugunov [17], Ohnuma [18], and Balmain [19,20]. This indicates a high level of research activity, due to the fact that a plasma medium can very greatly affect the properties of an antenna immersed in it. For example, when an antenna in the ionosphere is given a high-power RF pulse, there follows a great variety of linear and nonlinear phenomena in the forms of echoes or resonances. The richness of these phenomena is demonstrated in the recent work by Benson [21]. As another example, in his studies of HF wave propagation between two satellites, James [22,23,24] found that the dependence of the antenna input impedance on the plasma properties had a significant effect. In a further satellite study, James [25] found that it was necessary to assume a 1 m radius sheath around the antenna in order to make the impedance theory of Adachi et al [10] predict (approximately) the measured voltage magnitude at the output of the 0.1-20 MHz sounder transmitter; this constitutes evidence that the sounder transmissions were severely perturbing the plasma around the antenna.

In a continuation of earlier work on the impedance of a short rocket-mounted dipole [5,6], Meyer-Vernet [26] achieved fairly good agreement between ionospheric impedance measurements and a hydrodynamic tensor-pressure theory with a vacuum gap representation of the ion sheath (Fig.12). The only discrepancy was in the frequency range just below the plasma frequency, where the measured resistance was much higher than the calculated value. It was argued [7] that an accurate resistance prediction could be achieved using kinetic theory with an accurate representation of the inhomogeneous sheath region, or possibly even without such a representation [8].

Laboratory measurements have been important aids in the development of impedance theories. Sawaya et al [27] measured monopole impedance in a large chamber (Fig.13) and were able to observe the oblique resonance (at 130 MHz in Fig.14) which occurs when the antenna wire is parallel to the resonance cone. Taking ion motion into account, Hoyano et al[28] were able to identify the lower-hybrid resonance (LHR) in impedance measurements on a wire monopole antenna. There are clearly advantages to making laboratory impedance measurements on monopole antennas over a ground plane, but it has been shown by Matin et al [29] that the familiar image principle is inapplicable in a magnetized plasma with the magnetic field oblique (neither parallel nor perpendicular to the monopole); fortunately the differences in calculated impedance are not great and so, for many purposes, dipole theory is adequate to predict the impedance of a monopole antenna.

A spherical RF probe is potentially useful for magnetoplasma diagnostics if its impedance is known: Fujita and Adachi [30] used fluid theory to analyse this case, thus unifying previous theories and also showing that the charge density is uniform over the surface of the sphere in spite of the anisotropy of the medium. For isotropic plasmas, Ohnuki and Adachi [31] measured the impedance of disc shaped antennas used to radiate electron plasma waves; they achieved fairly good agreement with theory [32] above plasma frequency but carried out no comparison below plasma frequency. Elgin [33] derived a kinetic theory formulation of the impedance of a parallel-plate isotropic plasma "capacitor" but presented no numerical results. Hsieh [34] calculated the current distribution and radiation resistance of a cylindrical dipole in a warm, isotropic plasma, finding significant end-cap effects. Ancona [35] showed how small antenna impedance in weakly dissipative media could be extrapolated from knowledge of impedance in vacuum at a complex frequency. Nakagawa [36] studied an oscillating dipole in a moving, compressible plasma and noted a tendency toward negative resistance for velocities greater than the electron thermal velocity.

The full electromagnetic radiation fields of a current element have been computed by Giles [37] for a warm, magnetized plasma. His calculations are based on the properties of the refractive index surfaces and they demonstrate clearly how contributions from two different parts of the same refractive index surface can produce interference undulations in radiation patterns. Such undulations are clearly shown in Fig.15 which is a graph of the wave field strength as a function of polar angle θ at a radius of approximately a free-space wavelength, near a resonance cone at $\theta = 74°$. This graph is for an electric current element perpendicular to the magnetic field. For a magnetic current element (small loop) parallel to the magnetic field, the radiation pattern is as shown in Fig.16, with the resonance cone still visible but with the undulations raised considerably in magnitude. In general it is clear that the radiation pattern has some features characteristic of the anisotropic medium, and other features associated with the type and orientation of the source. This and other similar data indicate that one cannot measure the radiation pattern of an antenna simply by rotating it.

Laboratory measurements of antenna radiation patterns are usually impossible for long-wavelength modes of propagation because plasma vacuum chambers are necessarily small and have walls which reflect all types of radiated waves. Of course this provides one of the main reasons for the existence of the WISP program, that of being able to perform radiation experiments in a plasma of (relatively) limitless extent. In the laboratory, where initial measurements must still be made, one might choose to perform antenna radiation experiments over a ground plane. Matin et al [38] have shown that, in general for an inclined monopole over a ground plane, image theory in its familiar form no longer is valid and the phenomena of lateral waves and wave shedding from the ground plane may exist. This means that the radiation pattern of a monopole antenna over a ground plane can be quite different from that of the corresponding dipole antenna.

Resonance cones emanating from point sources have been studied extensively under linear (low signal level) conditions, usually theoretically under the quasi-static assumption, and experimentally at close range. Storey et al [39] showed that the interference undulations may lie either inside or outside the resonance cone, depending on the distance from the source. At very short distance the interference structure and even the cone itself may disappear, according to Thiel and Décréau [40]. The inclusion of electromagnetic effects was found by Kuehl [41] to produce some reduction in cone amplitude and a small angular shift. Exactly at the plasma and upper hybrid frequencies the quasi-static radiation patterns calculated by Thiel and Debrie [42] showed dependence on both the anisotropic medium and the orientation of the current-element sources (Fig.17).

The presence of a drifting plasma causes the resonance cone angle to shift relative to its stationary-plasma value. Storey and Thiel [43] found the correction factors necessary to permit deduction of the electron density, temperature and drift velocity from cone field measurements. Lucks and Krämer [44] included ion motion as well as electron drift and studied the shift of the cone angle in the vicinity of the lower-hybrid resonance. Mourgues et al [45] found Cerenkov cone effects in the case of a drifting isotropic plasma when the drift velocity was of the same order of magnitude as the thermal velocity. Singh [46] found both a Cerenkov cone and a split resonance cone in a streaming anisotropic plasma.

Because of the relatively high signal levels in resonance cones, their nonlinear behaviour is important. Under dipole excitation and assuming only ponderomotive-force nonlinearities, Kuehl [47] has identified some cone distortion, especially near the plasma and upper-hybrid frequencies. For the case of converging resonance cones from a wire-ring exciter (Fig.18), Wang and Kuehl [48] predicted a nonlinear shift of the focal point toward the exciter, and Wilson and Wang [49] confirmed this effect experimentally. Kuehl [50] then deduced that the nonlinear focal shift could be either toward or away from the exciter, depending on the frequency and the plasma parameters, and the shift effect would be strongest near the lower-hybrid, upper-hybrid and plasma frequencies.

Nonlinear effects have also been studied by Lavergnat et al [51] in the context of the mixing of two signals at slightly different frequencies, with the two signals being applied either to the same RF probe or to adjacent probes; the measurements and some calculations suggested that the nonlinear effects occur in the near field but nevertheless outside the sheath, and that these effects could be used to deduce sheath thickness.

The radiation patterns of quasi-static electron cyclotron waves radiated from a point source have been studied by Ohmori et al [52], with fairly good agreement between theory and experiment. In somewhat similar experiments, Lembège observed high-field cones related to the inflection points in refractive index surfaces [53], and also noted interference between the cold plasma field and the cyclotron harmonic wave field [54].

Ion acoustic waves have short enough wavelengths to be useful in laboratory studies. Nakamura and Nomura [55] achieved good agreement between theoretical and experimental radiation patterns for monopole antennas. Khazei et al [56] constructed and tested a quadrupole ion acoustic wave array consisting of four gridded hemispheres. Khazei et al [57] used a square plate as an antenna to launch short-pulse, nonlinear ion-acoustic solitons, noting a distinction between near and far fields similar to that for aperture antennas in free space.

Electron plasma waves in isotropic plasma are also convenient for laboratory studies. Ohnuki and Adachi [58] predicted the radiation patterns of oblate spheroidal antennas, and Ohnuki et al [59] measured similar patterns in the laboratory, using both solid and mesh disc antennas.

Plasmas in cylindrical discharge tubes are inhomogeneous, with the electron density dropping off rapidly near the walls. With an axial magnetic field applied, a localized

source in the centre of the tube can generate a resonance cone which is reflected from the density gradient near the walls, and even multiple reflections are possible. This phenomenon has been studied both theoretically and experimentally by Ohnuma [60] and by Ohnuma and Gonfalone [61]. Ohnuma [62] showed that such resonance cone phenomena allowed field penetration through a plasma layer, and that the layer density profile could be deduced from the cone trajectory. Ohnuma and Lembège [63] deduced the magnitude and direction of a diverging magnetic field by measuring cone trajectories. Sanuki et al [64] made a warm-plasma theoretical study of resonance cones in an inhomogeneous plasma column due to a point source, and Ohnuma et al [65] carried out comparisons between theory and experiment for frequencies below the plasma frequency. A kinetic-theory extension of this work was done by Ohnuma et al [66]. We are reminded that the use of the cold-plasma representation for an inhomogeneous plasma predicts high power absorption in the region of plasma resonance, in the analysis by Weenink [67] of an ion-sheathed slot antenna. For similar reasons, Adachi and Ohnuki [68] find in their analysis of a plasma-filled waveguide that homogeneous cold-plasma multilayers cannot properly represent a smoothly-varying density gradient.

Cyclotron harmonic waves (Bernstein modes) had been thought to propagate essentially unattenuated only in the direction perpendicular to the magnetic field. Lembège and Gonfalone [69] carefully mapped the field of a point source in a large laboratory magneto-plasma and used the results to measure the plasma density and thermal velocity. They found that the cyclotron harmonic waves did not propagate in a direction strictly transverse to the magnetic field but rather were concentrated on surfaces of revolution around the magnetic field direction. Thiel and Lembège [70] found that cyclotron harmonic waves could be detected in any direction and their field distributions showed good agreement between theory and experiment.

There is renewed interest in the performance of helical or loop antennas in plasma. Hwang and Gould [71] used two-turn loop impedance measurements near the ion cyclotron frequency to demonstrate 80% efficiency in power delivery to a Tokamak plasma. Balmashov et al [72] used a helix to launch whistler waves in a laboratory magnetoplasma; they varied the helix length to optimize wave launching, and found they could selectively launch waves in different radial regions of their cyclindrically inhomogeneous plasma. Blackwell and Cross [73], used a helical RF coil to launch magneto-acoustic (Alfvén) waves in a cylindrical plasma column.

It must not be forgotten that a passive antenna in a plasma picks up noise from its surroundings. Couturier et al [74] have compared their theoretical noise calculations with observations from the satellite ISEE 3. Sentman [75] has calculated the cyclotron harmonic wave noise spectra to be expected at the terminals of 50 m and 100 m dipoles in synchronous orbit.

CONCLUSIONS

In spite of an intensive research effort spanning three decades, there exists no generally applicable theory of long dipole antennas in plasma, at least none adequate to predict the current distribution, input impedance and radiation fields of the WISP 300 m antenna. This is certainly true for low-level fields (linear case) although now there is a large scientific literature on the response of a plasma to current elements and point charges. As for high-level fields (nonlinear case), there are now some promising analyses available for the resonance-cone fields of point charges and charge rings. Thus the foundations are firmly in place for future advances in the study of antennas in plasma.

ACKNOWLEDGMENTS

REFERENCES

1. Fredricks, R.W., and W.W.L. Taylor. Waves in space plasmas program. Proceedings of the 1981 NRL/ONR Symposium on the Effect of the Ionosphere on Radio Wave Systems.

2. Inan, U.S., T.F. Bell, R.A. Helliwell, and K.P. Katsufrakis. A VLF transmitter on the Space Shuttle. Adv. Space Res., Vol.1, COSPAR, 1981, pp.235-239.

3. James, H.G. High frequency radio experiments with the WISP system on Spacelab. Adv. Space Res., Vol.1, COSPAR, 1981, pp.241-244.

4. Mlodnosky, R.F., and O.K. Garriott. The VLF admittance of a dipole in the lower ionosphere. Proc. International Conf. on the Ionosphere, Institute of Physics and Physical Society, London, 1963, pp.484-491.

5. Vernet, N., R. Manning, and J.L. Steinberg. The impedance of a dipole antenna in the ionosphere, 1, Experimental study. Radio Sci., Vol.10, No.5, 1975, pp.517-527.

6. Meyer, P., and N. Vernet. The impedance of a dipole antenna in the ionosphere, 2, Comparison with theory. Radio Sci., Vol.10, No.5, 1975, pp.529-536.

7. Meyer-Vernet, N., P. Meyer, and C. Perche. Losses due to the inhomogeneous sheath surrounding an antenna in a plasma. Radio Sci., Vol.13, No.1, 1978, pp.69-73.

8. Singh, N. A boundary-value problem treatment of an electric dipole in a warm isotropic plasma using the multiple water bag model. Radio Sci., Vol.13, No.4, 1978, pp.625-637.

9. Singh, N. Low-frequency radiation from an electric dipole in an isotropic plasma. Radio Sci., Vol.14, No.1, 1979, pp.43-47.

10. Adachi, S., T. Ishizone, and Y. Mushiake. Transmission line theory of antenna impedance in a magnetoplasma. Radio Sci., Vol.12, No.1, 1977, pp.23-31.

11. Marec, J., and G. Mourier. Sur la propagation des ondes de surface et la nature des résonances électrostatiques de gaine. C.R. Acad. Sci. Paris, Vol.271, 1970, pp.367-370.

12. Richmond, J.H. Computer program for thin-wire structures in a homogenous conducting medium. NASA Contractor Report CR-2399, 1974.

13. Bachynski, M.P. Sources in plasmas. RCA Rev., Vol.28, No.1, 1967, pp.111-152.

14. Kaiser, T.R., and J.K.E. Tunaley. Radio-frequency impedance probes. Space Sci. Rev., Vol.8, 1968, pp.32-73.

15. Wait, J.R. Electromagnetics and Plasmas. Holt, Rinehart and Winston, Inc., New York, 1968, 144 pp.

16. Thomas, J.O., and B.J. Landmark (eds.). Plasma Waves in Space and Laboratory, Vols.1 and 2, Edinburgh Univ. Press, 1969.

17. Andronov, A.A., and Yu. V. Chugunov. Quasisteady-state electric fields of sources in dilute plasma. Sov. Phys., Uspekhi, Vol.18, No.5, 1975, pp.343-360.

18. Ohnuma, T. Radiation phenomena of plasma waves, Parts 1-3. IEEE Trans. Plasma Sci., Vol. PS-6, No.4, 1978, pp.464-523.

19. Balmain, K.G. Antennas in plasma: characteristics as functions of frequency. Radio Sci., Vol.7, No.8-9, 1972, pp.771-775.

20. Balmain, K.G. The properties of antennas in plasmas. Annales des Télécommunications, Vol.35, Nos.3-4, 1979, pp.273-283.

21. Benson, R.F. Stimulated plasma instability and nonlinear phenomena in the ionosphere. Radio Sci., Vol.17, No.6, 1982, pp.1637-1659.

22. James, H.G. Wave propagation at medium frequencies between two ionospheric satellites, 1, General results. Radio Sci., Vol.13, No.3, 1978, pp.531-542.

23. James, H.G. Wave propagation at medium frequencies between two satellites, 2, Whistler-mode pulses. Radio Sci., Vol.13, No.3, 1978, pp.543-558.

24. James, H.G. Wave propagation experiments at medium frequencies between two ionospheric satellites, 3, Z mode pulses. J.Geophys. Res., Vol.84, No.A2, 1979, pp.499-506.

25. James, H.G. Tests of impedance theories for a transmitting dipole in an ionospheric plasma. IEEE Trans. Antennas Propagat., Vol.AP-28, No.5, 1980, pp.623-630.

26. Meyer-Vernet, N. Impedance of a short antenna in a warm magnetoplasma: Experiment and comparison with theory. Radio Sci., Vol.13, No.6, 1978, pp.1059-1068.

27. Sawaya, K., T. Ishizone, and Y. Mushiake. Measurement of the impedance of a linear antenna in a magnetoplasma. Radio Sci., Vol.13, No.1, 1978, pp.21-29.

28. Hoyano, A., S. Ohnuki, S. Adachi, and T. Ohnuma. Resonance of a wire antenna near the lower hybrid frequency in an RF-generated magnetoplasma. Proc. IEEE, Vol.67, No.1, 1979, pp.170-171.

29. Matin, M.A., K. Sawaya, T. Ishizone, and Y. Mushiake. Impedance of a monopole antenna over a ground plane and immersed in a magnetoplasma. IEEE Trans. Antennas Propagat., Vol.AP-28, No.3, 1980, pp.332-341.

30. Fujita, T., and S. Adachi. Impedance of a spherical probe immersed in a warm magnetized plasma. Radio Sci., Vol.16, No.3, 1981, pp.399-408.

31. Ohnuki, S., and S. Adachi. Radiation impedances of disc-shaped antennas for an electron plasma wave. IEEE Trans. Plasma Sci., Vol.PS-9, No.1, 1981, pp.16-18.

32. Ohnuki, S., S. Adachi, and T. Ohnuma. Theoretical analysis on radiation and reception characteristics of an oblate spheroidal antenna for electron plasma waves. J. Appl. Phys., Vol. 49, No.1, 1978, pp.138-145.

33. Elgin, J.N. The plasma capacitor problem. J. Plasma Phys., Vol.25, Part 1, 1981, pp.175-192.

34. Hsieh, H.C. Current distribution of a cylindrical antenna in a warm plasma. IEEE Trans. Plasma Sci., Vol. PS-9, No.2, 1981, pp.52-57.

35. Ancona, C. On small antenna impedance in weakly dissipative media. IEEE Trans. Antennas Propagat., Vol.AP-26, No.2, 1978, pp.341-343.

36. Nakagawa, K. Radiation resistance of an oscillating dipole in a moving compressible plasma. IEEE Trans. Antennas Propagat., Vol.AP-28, No.1, 1980, pp.65-70.

37. Giles, M.J. On the emission of radiation from a localized current source in a magnetoplasma. J. Plasma Phys., Vol.19, Part 2, 1978, pp.201-225.

38. Matin, M.A., Y. Mushiake, T. Ishizone, and K. Sawaya. Radiation from a small monopole in a uniaxially anisotropic plasma. IEEE Trans. Antennas Propagat., Vol.AP-30, No.2, 1982, pp.235-240.

39. Storey, L.R.O., J. Thiel, and R.W. Boswell. Location of the interference structure near the lower oblique (whistler) resonance cone. Phys. Fluids, Vol.23, No.3, 1980, pp.654-655.

40. Thiel, J., and P.M.E. Décréau. Excitation of the plasma and lower oblique resonances in a Maxwellian magnetoplasma of weak density. Phys. Fluids, Vol.23, No.11, 1980, pp.2334-2335.

41. Kuehl, H.H. Electromagnetic effects on plasma resonance cones. IEEE Trans. Plasma Sci., Vol.PS-9, No.3, 1981, pp.104-108.

42. Thiel, J., and R. Debrie. Electrostatic waves potential at the plasma and upper-hybrid resonances. J. Plasma Phys., Vol.25, Part 2, 1981, pp.239-254.

43. Storey, L.R.O., and J. Thiel. Thermal and field-aligned-drift effects near the lower oblique resonance. Phys. Fluids, Vol.21, No.12, 1978, pp.2325-2335.

44. Lucks, K., and M. Krämer. Measurements of resonance cones influenced by ion dynamics and electron drift motion. Plasma Physics, Vol.22, 1980, pp.879-892.

45. Mourgues, G., E. Fijalkow, and M.R. Feix. Forced oscillations generated by a point antenna in a drifting plasma. Plasma physics, Vol.22, 1980, pp.367-399.

46. Singh, N. Resonance cones in non-Maxwellian plasmas. Radio Sci., Vol.15, No.4, 1980, pp.881-889.

47. Kuehl, H.H. Nonlinear resonance cone surfaces. IEEE Trans. Plasma Sci., Vol.PS-7, No.4, 1979, pp.201-204.

48. Wang, W.S., and H.H. Kuehl. Converging nonlinear resonance cones. Phys. Fluids, Vol.22, No.9, 1979, pp.1707-1715.

49. Wilson, J.R., and K.L. Wong. Nonlinear converging resonance cones. Phys. Fluids, Vol.23, No.3, 1980, pp.566-572.

50. Kuehl, H.H. Converging nonlinear resonance cone trajectories. Phys. Fluids, Vol.23, No.7, 1980, pp.1355-1358.

51. Lavergnat, J., J.M. Illiano, J.Y. Delahaye, and R. Ney. Nonlinear effects in the vicinity of a radio frequency probe. Plasma Physics, Vol.22, 1980, pp.57-67.

52. Ohmori, S., T. Ohnuma, and S. Adachi. Angular potential patterns of electrostatic electron cyclotron waves radiated from a point source. Radio Sci., Vol.13, No.6, 1978, pp.1053-1057.

53. Lembège, B. Antenna radiation pattern of cyclotron harmonic waves in a hot magnetoplasma. Radio Sci., Vol.14, No.3, 1979, pp.487-502.

54. Lembège, B. Cyclotron harmonic waves detected in the direction parallel to the magnetostatic field. Phys. Fluids, Vol.23, No.10, 1980, pp.2128-2133.

55. Nakamura, Y., and Y. Nomura. Near field and damping effects on the radiation of ion acoustic waves from antennas. Radio Sci., Vol.14, No.6, 1979, pp.1175-1181.

56. Khazei, M., J.M. Bulson, and K.E. Lonngren. Quadrupole radiation of ion-acoustic waves. IEEE Trans. Plasma Sci., Vol.PS-10, No.3, 1982, pp.195-198.

57. Khazei, M., B. Nelson, C. Chan, and K. Lonngren. Radiation characteristics of ion acoustic solitons launched from an antenna. IEEE Trans. Plasma Sci., Vol.PS-9, No.3, 1981, pp.101-103.

58. Ohnuki, S., and Adachi, S. Radiation and reception characteristics of an oblate spheroidal antenna for electron plasma waves: 1. Theory. Radio Sci., Vol.16, No. 4, 1981, pp.569-578.

59. Ohnuki, S., S. Adachi, and T. Ohnuma. Radiation and reception characteristics of an oblate spheroidal antenna for electron plasma waves: 2. Experiment. Radio Sci., Vol.16, No.4, 1981, pp.579-585.

60. Ohnuma, T. Trapped high-frequency field in an inhomogeneous plasma. IEEE Trans. Plasma Sci., Vol.PS-6, No.4, 1978, pp.524-526.

61. Ohnuma, T., and A. Gonfalone. Duct propagation of localized radio-frequency fields along an inhomogeneous magnetoplasma column. Radio Sci., Vol.14, No.1, 1979, pp. 141-145.

62. Ohnuma, T. Penetration of localized radio frequency fields through an inhomogeneous magnetoplasma. IEEE Trans. Plasma Sci., Vol.PS-7, No.3, 1979, pp.164-166.

63. Ohnuma, T., and B. Lembège. Determination of magnetic field lines by measuring trajectories of lower hybrid cones. IEEE Trans. Plasma Sci., Vol.PS-7, No.4, 1979, pp.234-235.

64. Sanuki, H., T. Watanabe, and T. Ohnuma. Theoretical analysis of the resonance cone in an inhomogeneous plasma column. IEEE Trans. Plasma Sci., Vol.PS-8, No.2, 1980, pp.60-63.

65. Ohnuma, T., T. Watanabe, and H. Sanuki. Reflection of oblique electron thermal modes in an inhomogeneous magnetized plasma. Radio Sci., Vol.16, No.2, 1981, pp.257-259.

66. Ohnuma, T., T. Watanabe, and H. Sanuki. Oblique electron thermal waves in a magnetized plasma. IEEE Trans. Plasma Sci., Vol.PS-10, No.1, 1982, pp.27-32.

67. Weenink, M.P.H. Resonant energy absorption in the ion sheath of a plate antenna. Radio Sci., Vol.17, No.2, 1982, pp.411-419.

68. Adachi, S., and S. Ohnuki. Failure of homogeneous multilayer approximation for transversely nonuniform plasma waveguides. Radio Sci., Vol.17, No.3, 1982, pp. 539-544.

69. Lembège, B., and A. Gonfolane. Cyclotron harmonic wave propagation in a large magnetoplasma. Plasma Phys., Vol.20, No.9, 1978, pp.879-889.

70. Thiel, J., and B. Lembège. Electrostatic electron cyclotron radiation from a point source. Phys. Fluids, Vol.25, No.3, 1982, pp.551-565.

71. Hwang, D.Q., and R.W. Gould. Measurements of the complex loading impedance of the magnetosonic cavity modes. Phys. Fluids, Vol.23, No.3, 1980, pp.614-623.

72. Balmashov, A.A., J.P. Lynov, P. Michelsen, and J. Juul Rasmussen. Excitation of whistler waves by a helical wave structure. J. Phys. D: Appl. Phys., Vol.14, No. 10, 1981, pp.1803-1809.

73. Blackwell, B.D., and R.C. Cross. Measurements of the impedance of a magneto-acoustic wave-launching antenna. J. Plasma Phys., Vol.22, Part 3, 1979, pp.499-514.

74. Couturier, P., S. Hoang, N. Meyer-Vernet, and J.L. Steinberg. Quasi-thermal noise in a stable plasma at rest: Theory and observations from ISEE 3. J. Geophys. Res., Vol.86, No.A3, 1981, pp.11,127-11,138.

75. Sentman, D.D. Thermal fluctuations and the diffuse electrostatic emissions. J. Geophys. Res., Vol.87, No.A3, 1982, pp.1455-1472.
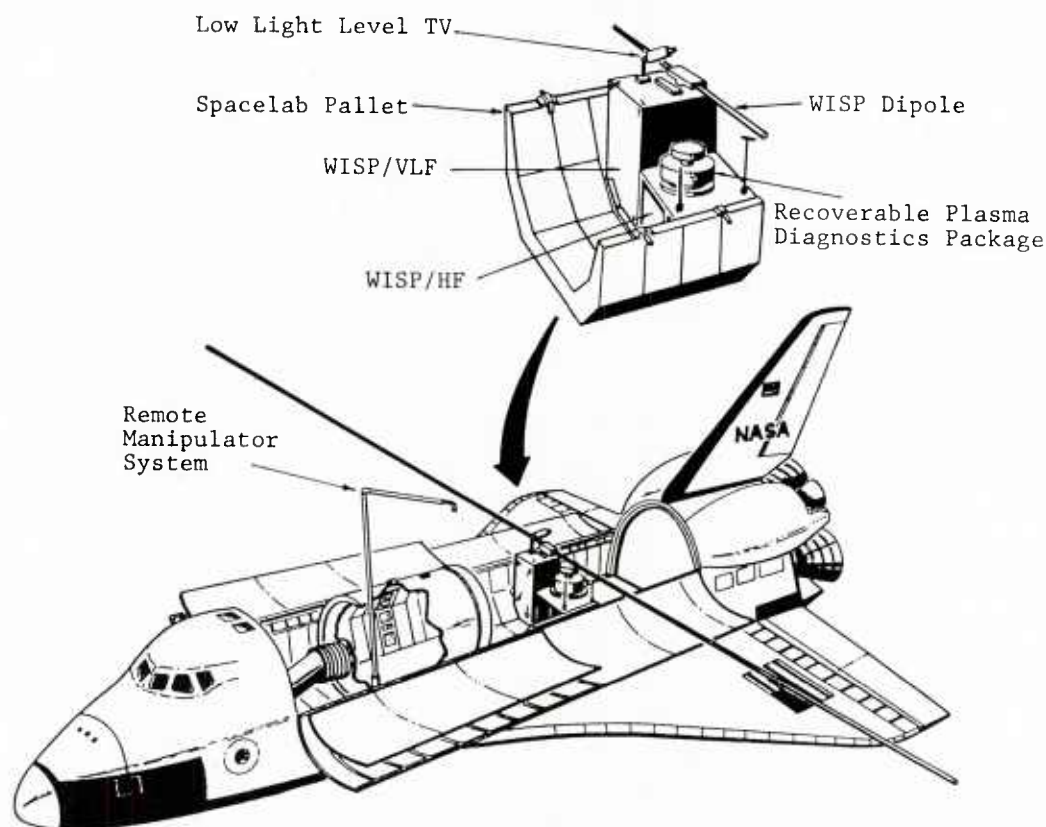
Fig.1 WISP Instrumentation (original version)
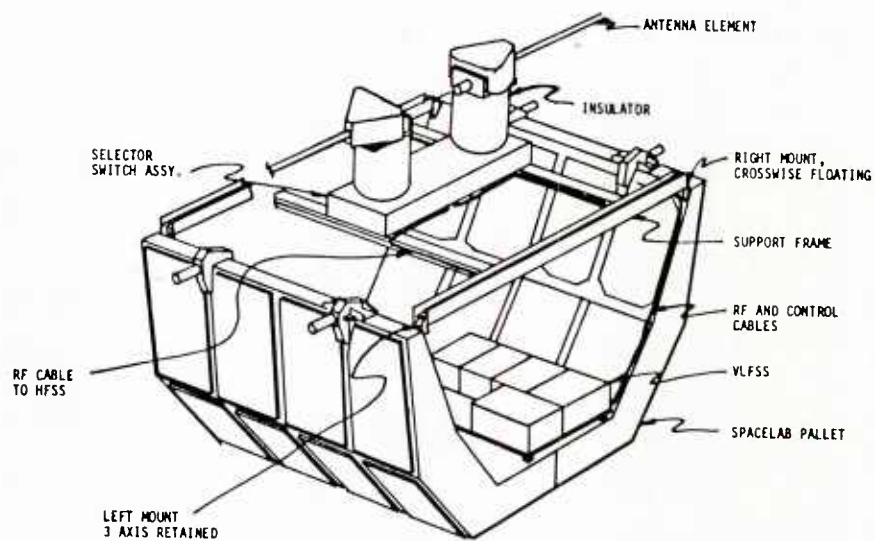
Fig.2   WISP Dipole Antenna Sub-System (recent version)
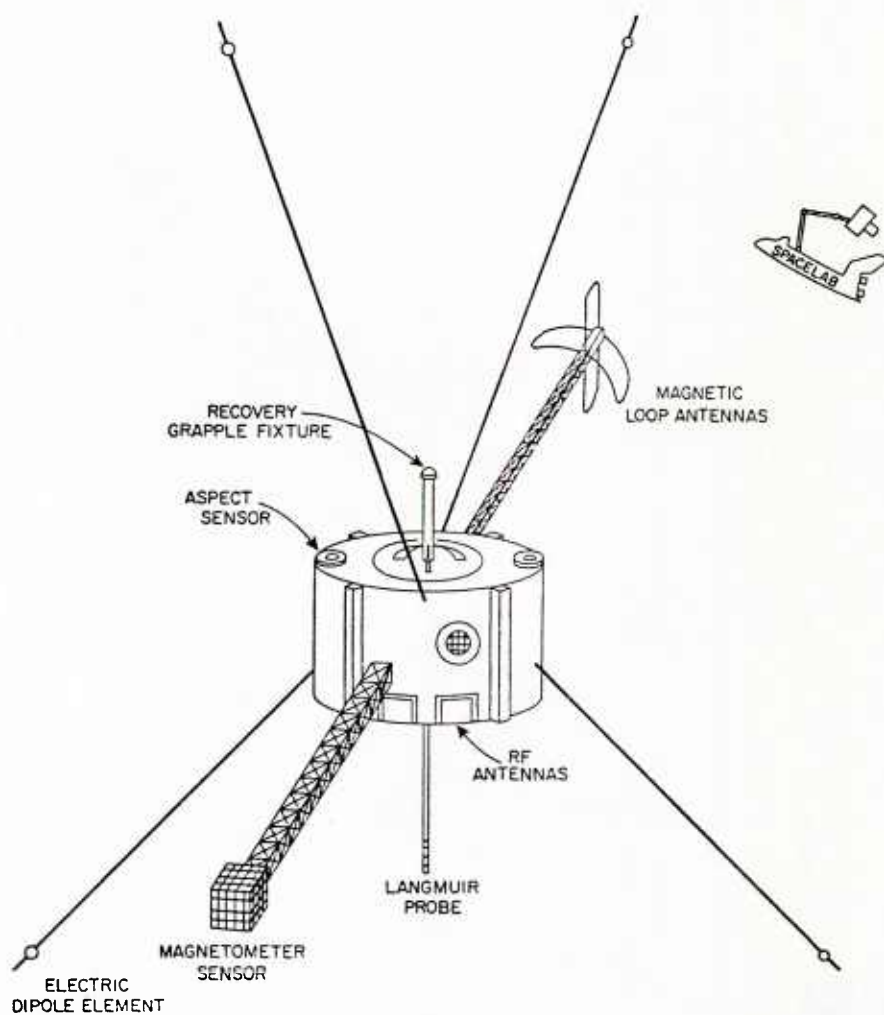
Fig.3   Recoverable Plasma Diagnostics Package (RPDP)
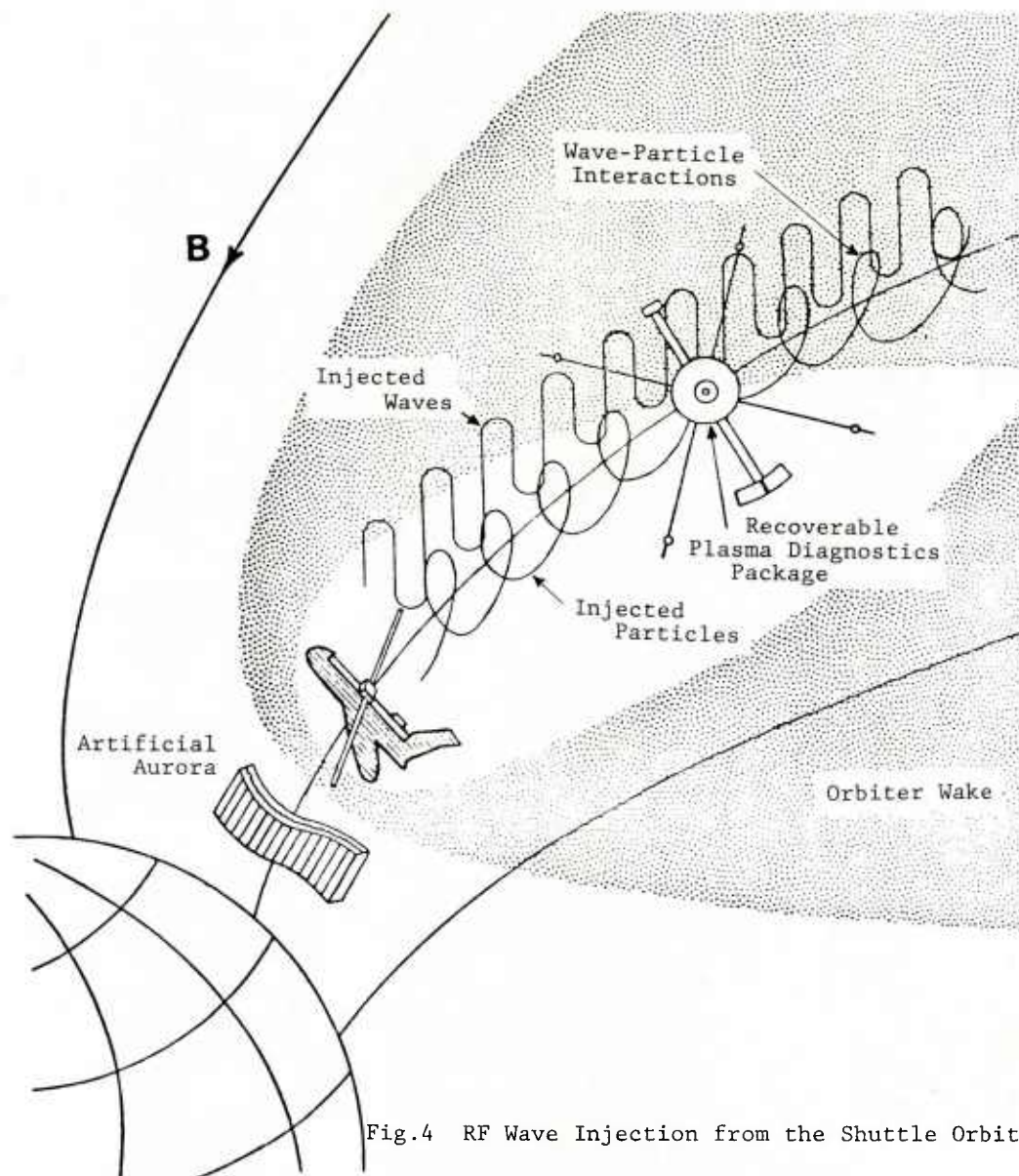
Fig.4 RF Wave Injection from the Shuttle Orbiter

$$\epsilon_r = \begin{bmatrix} K' & jK'' & 0 \\ -jK'' & K' & 0 \\ 0 & 0 & K_o \end{bmatrix}$$

$$\tan \theta = \sqrt{\frac{-K'}{K_o}}$$
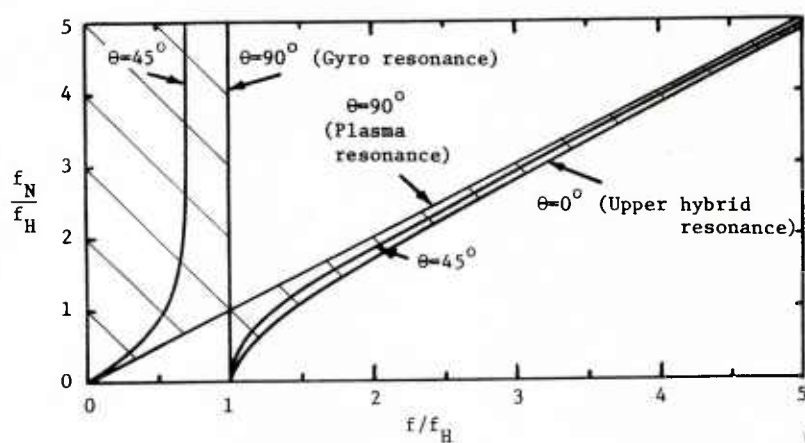
Magnetoplasma resonant frequencies.
The angle θ is the angle of the
high-field resonance-cone
direction with respect to the
magnetic field.
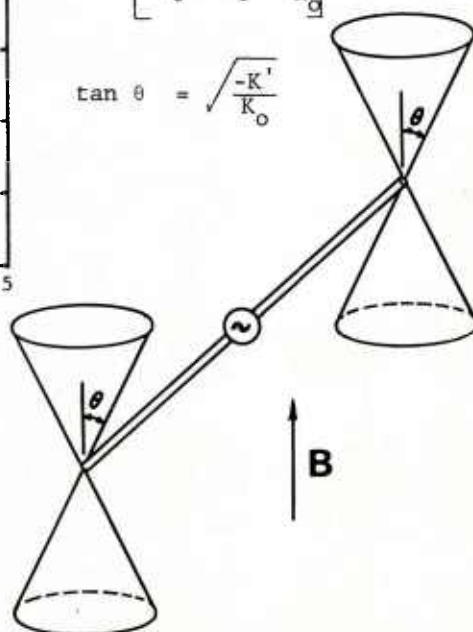
Fig.5 The resonant frequencies for an electron-
only magnetoplasma. The resonance cones
(depicted at right) occur in the parameter
regions shown shaded (above).

DIPØLE IN MAGNETØPLASMA

MODIFIED ADACHI'S FORMULA

PLASMA FREQUENCY   = 1.000×10^7 HERTZ

CYCLOTRON FREQUENCY= 1.000×10^6 HERTZ

COLLISION FREQUENCY= 6.300×10^5 1/SEC

DEBYE LENGTH   = 5.000×10^{-3} METERS

ORIENTATION ANGLE = 0.000×10^0 DEGREES

ANTENNA HALF-LENGTH= 3.000×10^0 METERS

ANTENNA RADIUS   = 3.000×10^{-2} METERS

SHEATH CONDUCTIVITY= 1.000×10^{-5} MHOS/M
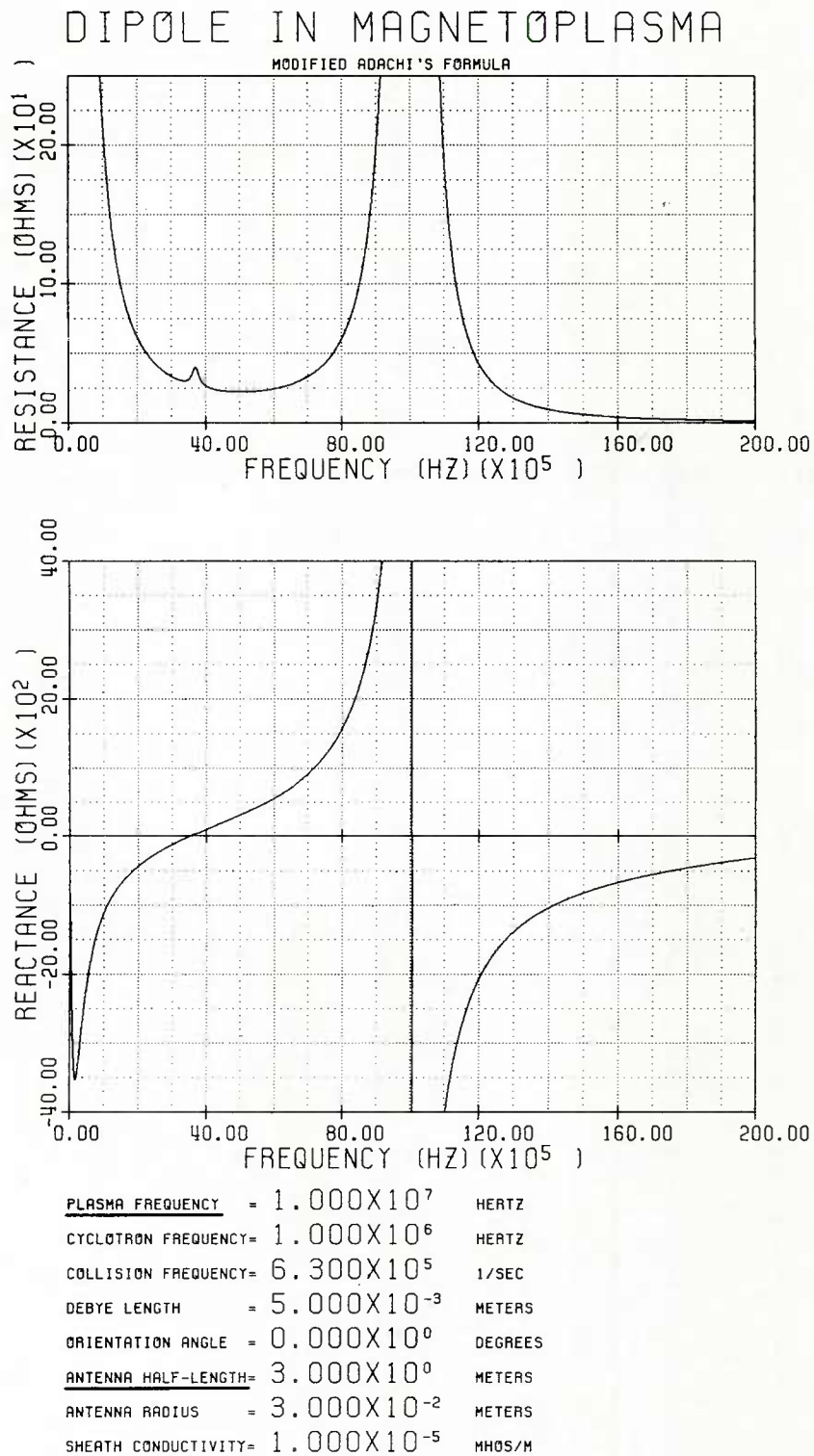
Fig.6   Short dipole input impedance as calculated using the
theory of Adachi et al [10], modified by the inclusion
of sheath-region conductivity. Dipole tip-to-tip
length = 6 m; f_N = 10 MHz; f_H = 1.0 MHz.

DIPOLE IN MAGNETOPLASMA

Fig.7 Long dipole input impedance as calculated using the
theory of Adachi et al [10],modified by the inclusion
of sheath-region conductivity. Dipole tip-to-tip
length = 200 m; f_N = 10 MHz; f_H = 1.0 MHz.

DIPOLE IN MAGNETOPLASMA

MODIFIED ADACHI'S FORMULA

PLASMA FREQUENCY = 2.000×10^6 HERTZ
CYCLOTRON FREQUENCY= 1.000×10^6 HERTZ
COLLISION FREQUENCY= 1.300×10^5 1/SEC
DEBYE LENGTH = 5.000×10^{-3} METERS
ORIENTATION ANGLE = 0.000×10^0 DEGREES
ANTENNA HALF-LENGTH= 1.000×10^2 METERS
ANTENNA RADIUS = 3.000×10^{-2} METERS
SHEATH CONDUCTIVITY= 2.000×10^{-6} MHOS/M
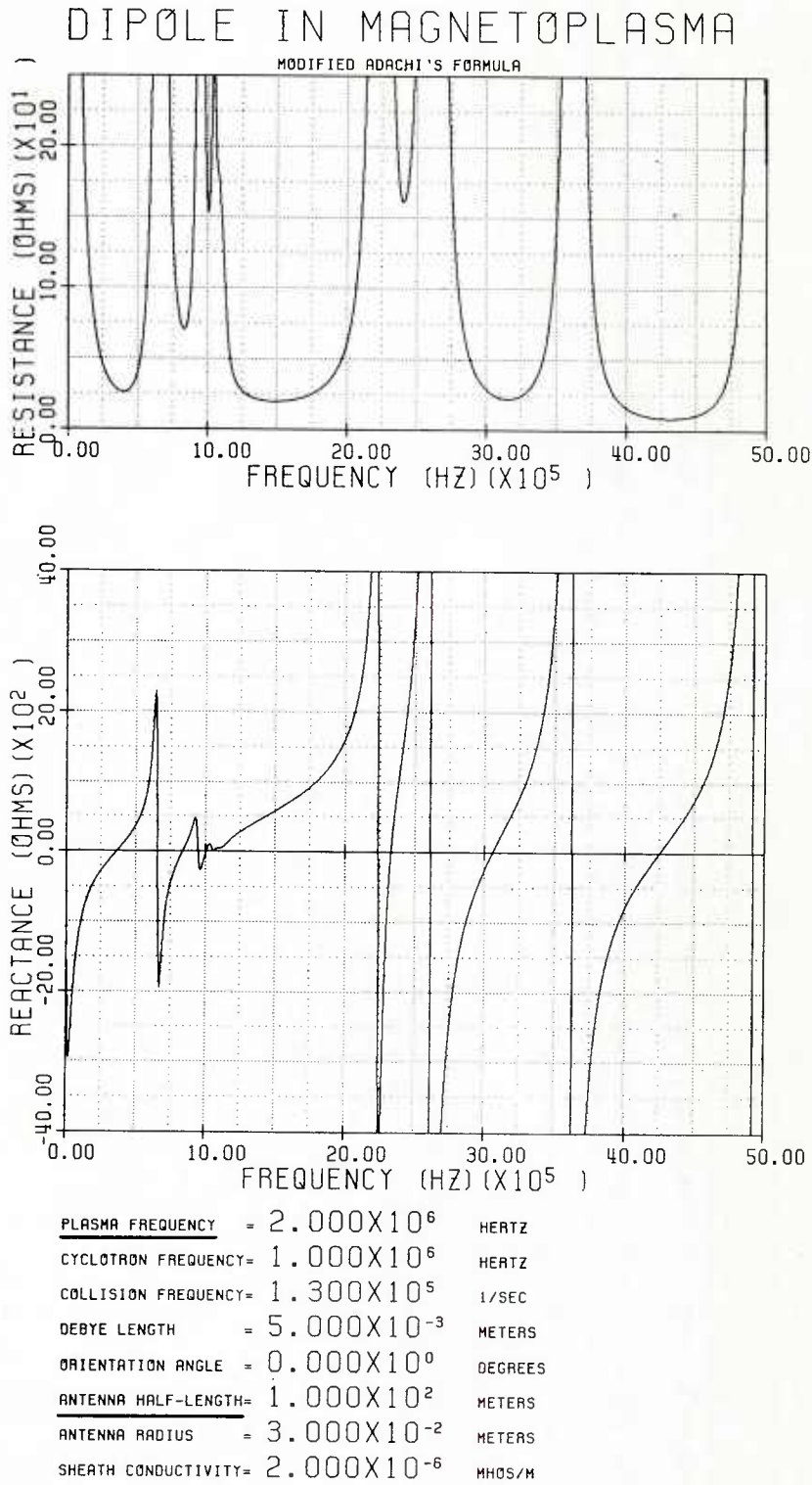
Fig.8 Long dipole input impedance as calculated using the
theory of Adachi et al [10],modified by the inclusion
of sheath-region conductivity. Dipole tip-to-tip
length = 200 m; f_N = 2.0 MHz; f_H = 1.0 MHz.
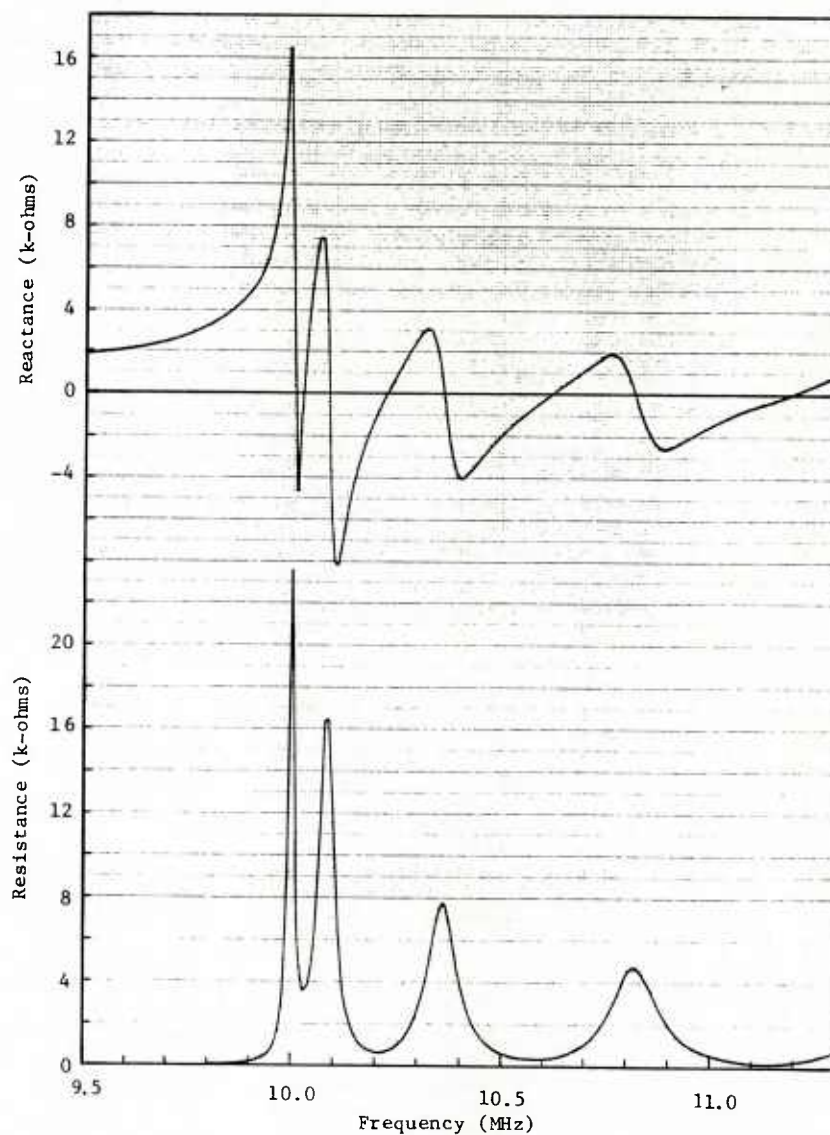
Impedance of long dipole near the
plasma frequency, from moment-
method computation. Parameters:
f_N = 10 MHz, ν = 0.1 MHz, λ_D = 5 mm
(sheath thickness = 5 λ_D), half
length H = 100 m, radius ρ = 3 cm,
sheath conductivity σ = 10^{-5}S,
number of segments = 80.

Fig.9 Long dipole input impedance as calculated using the
numerical method of Richmond [12], modified by the
inclusion of sheath-region conductivity. This cal-
culation includes radiation at frequencies above 10
MHz.
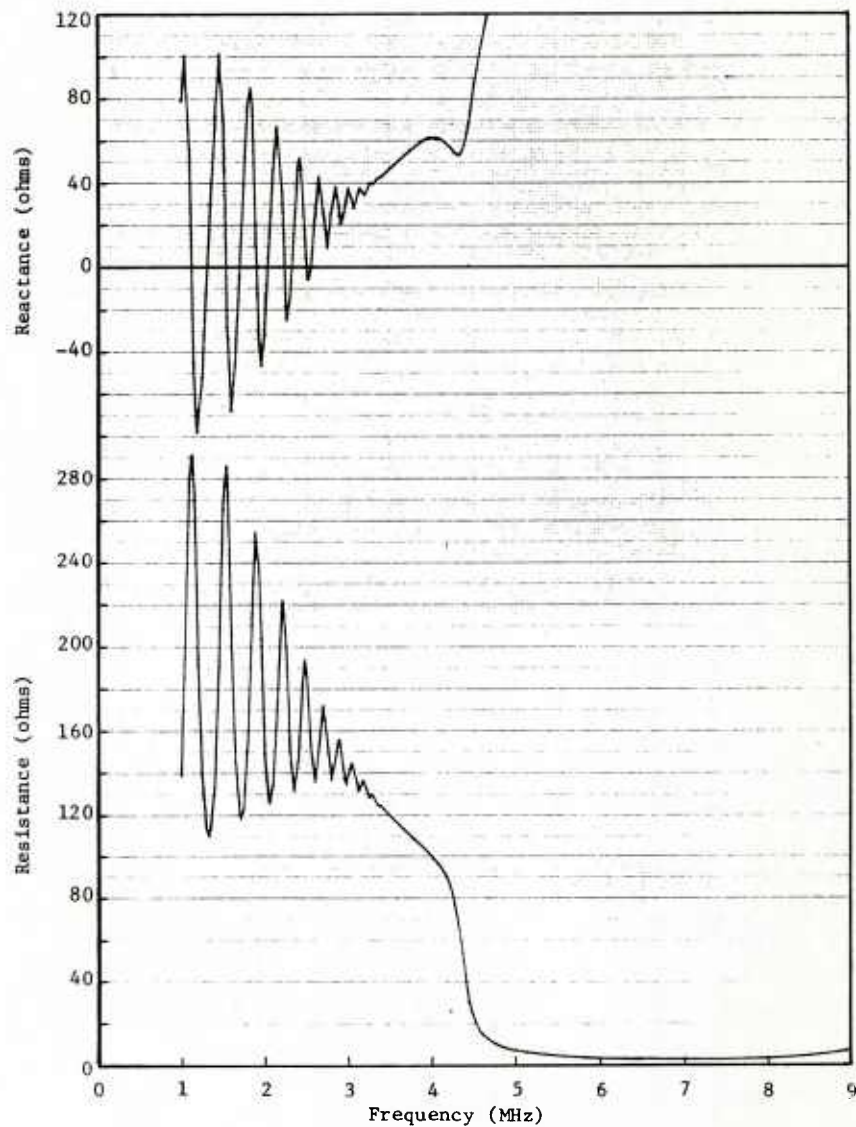
Impedance of long dipole below the
plasma frequency, from moment-
method computation. Note especially
the sheath-wave resonances.
Parameters: f_N = 10 MHz, ν = 0.1 MHz,
λ_D = 5 mm (sheath thickness = 5 λ_D),
half length H = 100 m, radius
ρ = 3 cm, sheath conductivity
$\sigma = 10^{-5}$S, number of segments = 80.

Fig.10   Long dipole input impedance as calculated using the
numerical method of Richmond [12], modified by the
inclusion of sheath-region conductivity. This cal-
culation predicts sheath-wave resonances at fre-
quencies below 5 MHz. No radiation can occur at any
frequency on the above graph because the frequency
is lower than the plasma frequency.
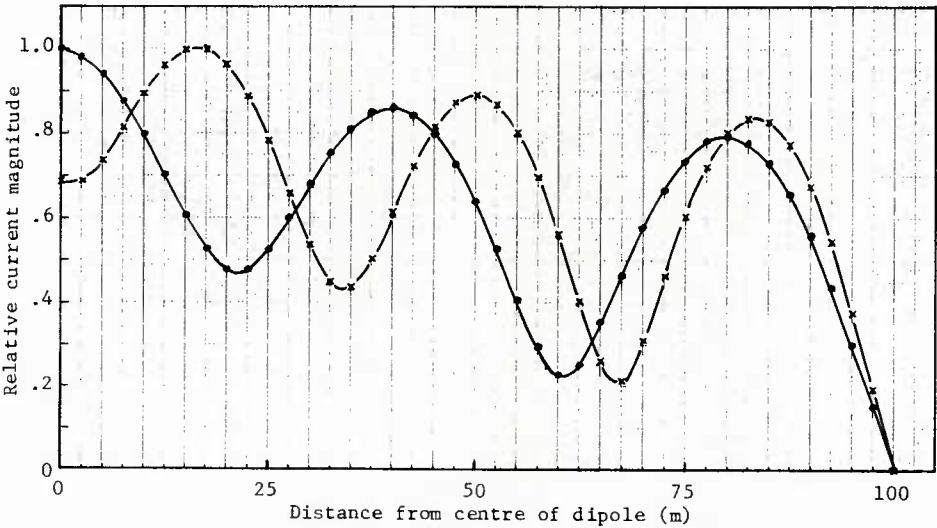
Fig.11 Current-magnitude distribution for a long dipole in
region of sheath-wave propagation. Dots: 1.330 MHz.
Crosses: 1.530 MHz. Parameters: F_N = 10 MHz,
ν = 0.1 MHz, λ_D = 5 mm (sheath thickness = 5 λ_D),
half length H = 100 m, radius ρ = 3 cm, sheath con-
ductivity σ = 10^{-5}S/m, number of segments = 80.
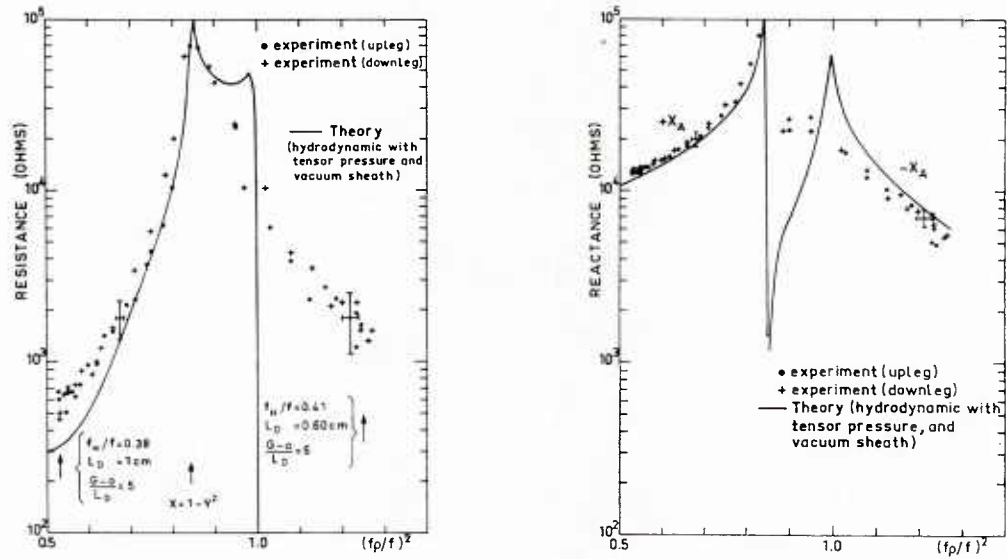
Fig.12 Dipole impedance: Comparison between tensor pressure theory
and an ionospheric experiment with a dipole of tip-to-tip
length 4 m, f = 2.7 MHz, -2 V bias, perpendicular to magnetic
field. Reference: Meyer-Vernet [26].
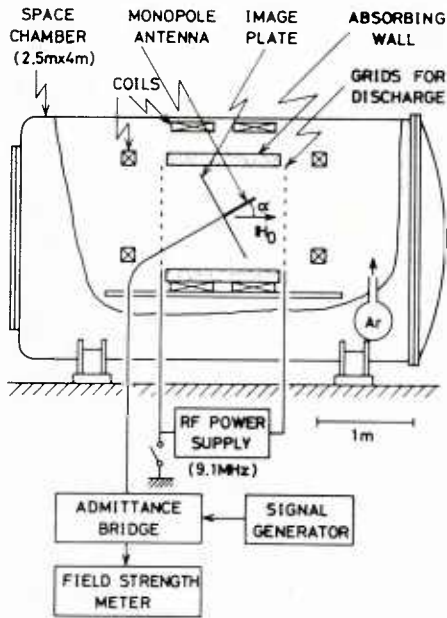
Fig.13 Plasma chamber for measurements on monopole antenna in plasma. Reference: Sawaya et al [27].
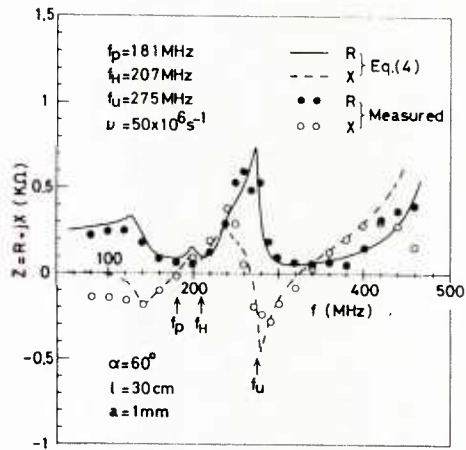
Fig.14 Laboratory impedance measurements and theory for monopole inclined with respect to magnetic field. Reference: Sawaya et al [27].
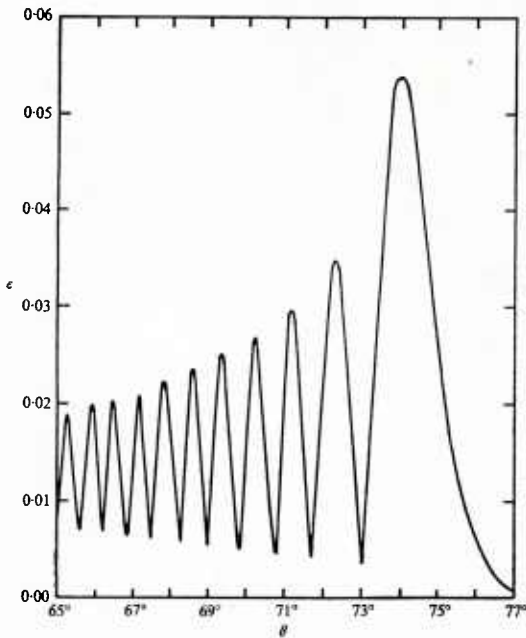
Fig.15 Radiated field magnitude as a function of polar angle near the resonance cone for an electric current element perpendicular to the magnetic field. $X = 1.1$, $Y = 1.7$. Reference: Giles [37].
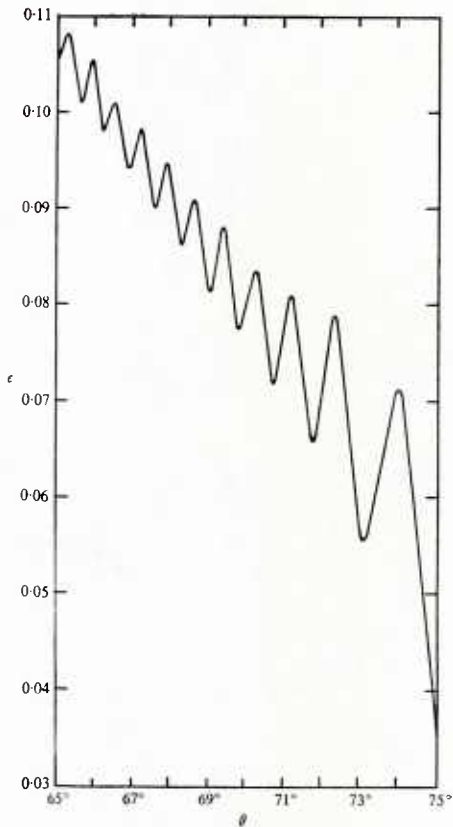
Fig.16 Radiated field magnitude as a function of polar angle near the resonance cone for a magnetic current element parallel to the magnetic field. $X = 1.1$, $Y = 1.7$. Reference: Giles [37].
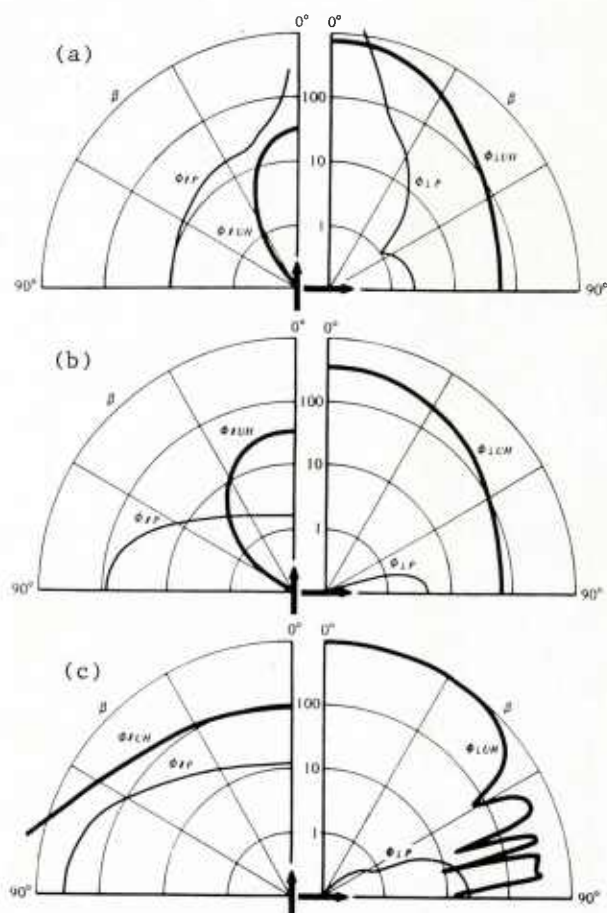
Fig.17 Magnitude of the quasi-static potential as a function of angle at the plasma and upper-hybrid frequencies. Parallel and perpendicular orientations of current element with respect to magnetic field are shown. Reference: Thiel and Debrie [42]. (a) $f_N/f_H = 0.3$, (b) $f_N/f_H = 1.3$, (c) $f_N/f_H = 2.5$.

Fig.18 Converging resonance cone due to ring-shaped wire exciter. Reference: Wang and Kuehl [48].

AGARD Lecture Series No.131 Advisory Group for Aerospace Research and Development, NATO THE PERFORMANCE OF ANTENNAS IN THEIR OPERATIONAL ENVIRONMENT Published September 1983 250 pages Lecture Series No.131, concerned with the performance of antennas in their operational environment, is sponsored by the Electromagnetic Wave Propagation Panel of AGARD and implemented by the Consultant and Exchange Programme. Antennas can provide gain in any direction, and the effect of the operating environment on this parameter is P.T.O	AGARD-LS-131 Antennas Performance	AGARD Lecture Series No.131 Advisory Group for Aerospace Research and Development, NATO THE PERFORMANCE OF ANTENNAS IN THEIR OPERATIONAL ENVIRONMENT Published September 1983 250 pages Lecture Series No.131, concerned with the performance of antennas in their operational environment, is sponsored by the Electromagnetic Wave Propagation Panel of AGARD and implemented by the Consultant and Exchange Programme. Antennas can provide gain in any direction, and the effect of the operating environment on this parameter is P.T.O	AGARD-LS-131 Antennas Performance
AGARD Lecture Series No.131 Advisory Group for Aerospace Research and Development, NATO THE PERFORMANCE OF ANTENNAS IN THEIR OPERATIONAL ENVIRONMENT Published September 1983 250 pages Lecture Series No.131, concerned with the performance of antennas in their operational environment, is sponsored by the Electromagnetic Wave Propagation Panel of AGARD and implemented by the Consultant and Exchange Programme. Antennas can provide gain in any direction, and the effect of the operating environment on this parameter is P.T.O	AGARD-LS-131 Antennas Performance	AGARD Lecture Series No.131 Advisory Group for Aerospace Research and Development, NATO THE PERFORMANCE OF ANTENNAS IN THEIR OPERATIONAL ENVIRONMENT Published September 1983 250 pages Lecture Series No.131, concerned with the performance of antennas in their operational environment, is sponsored by the Electromagnetic Wave Propagation Panel of AGARD and implemented by the Consultant and Exchange Programme. Antennas can provide gain in any direction, and the effect of the operating environment on this parameter is P.T.O	AGARD-LS-131 Antennas Performance

fundamentally important for the performance of radio systems. Yet the effect of the environment on antennas is often overlooked. The performance of the antenna is more usually specified in terms of its operation over a perfectly conducting flat ground plane.

This Lecture Series covers: techniques for measurement/prediction (numerical and experimental modelling); performance of fixed and transportable antennas (terrain effects, masts and building effects, re-radiation by supporting towers); performance of mobile antennas (effects of supporting platforms such as aircraft, ships and automobiles); performance of antennas in plasmas.

PAL   31 JAN   ≠915/5000   15.380

U209784

AGARD

NATO ⊕ OTAN

7 RUE ANCELLE · 92200 NEUILLY-SUR-SEINE

FRANCE

Telephone 745.08.10 · Telex 610176

DISTRIBUTION OF UNCLASSIFIED AGARD PUBLICATIONS

AGARD does NOT hold stocks of AGARD publications at the above address for general distribution. Initial distribution of AGARD publications is made to AGARD Member Nations through the following National Distribution Centres. Further copies are sometimes available from these Centres, but if not may be purchased in Microfiche or Photocopy form from the Purchase Agencies listed below.

NATIONAL DISTRIBUTION CENTRES

BELGIUM
Coordonnateur AGARD — VSL
Etat-Major de la Force Aérienne
Quartier Reine Elisabeth
Rue d'Evere, 1140 Bruxelles

CANADA
Defence Science
Department of [
Ottawa, Ontario

DENMARK
Danish Defence
Østerbrogades K
Copenhagen Ø

FRANCE
O.N.E.R.A. (Dir
29 Avenue de la
92320 Châtillon

GERMANY
Fachinformation
Physik, Mathema
Kernforschungsz
D-7514 Eggenste

GREECE
Hellenic Air For
Research and De
Holargos, Athens

ICELAND
Director of Aviation
c/o Flugrad
Reykjavik

ITALY
Aeronautica Militare
Ufficio del Delegato Nazionale all'AGARD
3, Piazzale Adenauer
Roma/EUR

GE)

UNITED KINGDOM
Defence Research Information Centre
Station Square House
St. Mary Cray
Orpington, Kent BR5 3RE

UNITED STATES
National Aeronautics and Space Administration (NASA)
Langley Field, Virginia 23365
Attn: Report Distribution and Storage Unit

THE UNITED STATES NATIONAL DISTRIBUTION CENTRE (NASA) DOES NOT HOLD
STOCKS OF AGARD PUBLICATIONS, AND APPLICATIONS FOR COPIES SHOULD BE MADE
DIRECT TO THE NATIONAL TECHNICAL INFORMATION SERVICE (NTIS) AT THE ADDRESS BELOW.

PURCHASE AGENCIES

Microfiche or Photocopy
National Technical
Information Service (NTIS)
5285 Port Royal Road
Springfield
Virginia 22161, USA

Microfiche
Space Documentation Service
European Space Agency
10, rue Mario Nikis
75015 Paris, France

Microfiche or Photocopy
British Library Lending
Division
Boston Spa, Wetherby
West Yorkshire LS23 7BQ
England

Requests for microfiche or photocopies of AGARD documents should include the AGARD serial number, title, author or editor, and publication date. Requests to NTIS should include the NASA accession report number. Full bibliographical references and abstracts of AGARD publications are given in the following journals:

Scientific and Technical Aerospace Reports (STAR)
published by NASA Scientific and Technical
Information Facility
Post Office Box 8757
Baltimore/Washington International Airport
Maryland 21240, USA

Government Reports Announcements (GRA)
published by the National Technical
Information Services, Springfield
Virginia 22161, USA